

UNCLASSIFIED

AD NUMBER	
AD373861	
CLASSIFICATION CHANGES	
TO:	unclassified
FROM:	confidential
LIMITATION CHANGES	
TO:	Approved for public release, distribution unlimited
FROM:	Distribution authorized to U.S. Gov't. agencies and their contractors; Administrative/Operational Use; 31 MAR 1966. Other requests shall be referred to Air Force Rocket Propulsion Lab., AFSC, Edwards AFB, CA.
AUTHORITY	
DoD 5200.1-r, 31 Dec 1972; AFRPL ltr, 7 May 1973	

THIS PAGE IS UNCLASSIFIED

GENERAL DECLASSIFICATION SCHEDULE

**IN ACCORDANCE WITH
DOD 5200.1-R & EXECUTIVE ORDER 11852**

THIS DOCUMENT IS:

**Subject to General Declassification Schedule of
Executive Order 11852-Automatically Downgraded at
2 Years Intervals- DECLASSIFIED ON DECEMBER 31, 1972**

BY

**Defense Documentation Center
Defense Supply Agency
Cameron Station
Alexandria, Virginia 22314**

SECURITY

MARKING

The classified or limited status of this report applies to each page, unless otherwise marked.

Separate page printouts MUST be marked accordingly.

THIS DOCUMENT CONTAINS INFORMATION AFFECTING THE NATIONAL DEFENSE OF THE UNITED STATES WITHIN THE MEANING OF THE ESPIONAGE LAWS, TITLE 18, U.S.C., SECTIONS 793 AND 794. THE TRANSMISSION OR THE REVELATION OF ITS CONTENTS IN ANY MANNER TO AN UNAUTHORIZED PERSON IS PROHIBITED BY LAW.

NOTICE: When government or other drawings, specifications or other data are used for any purpose other than in connection with a definitely related government procurement operation, the U.S. Government thereby incurs no responsibility, nor any obligation whatsoever; and the fact that the Government may have formulated, furnished, or in any way supplied the said drawings, specifications, or other data is not to be regarded by implication or otherwise as in any manner licensing the holder or any other person or corporation, or conveying any rights or permission to manufacture, use or sell any patented invention that may in any way be related thereto.

CONFIDENTIAL

AERONUTRONIC LOG NO 5789-66

373861

AFRPL-TR-66-63

(UNCLASSIFIED TITLE)

AN INVESTIGATION AND FEASIBILITY DEMONSTRATION
OF
NOZZLES FOR RESTARTABLE SOLID ROCKET MOTORS

Final Technical Report

W. H. Armour, et al.
Aeronutronic Division of Philco Corporation

TECHNICAL REPORT AFRPL-TR-66-53

April 1966

In addition to security requirements which must be met, this document is subject to special export controls and each transmittal to foreign governments or foreign nationals may be made only with prior approval of AFRPL (RPPR-STINFO), Edwards, California 93523.

Air Force Rocket Propulsion Laboratory
Research and Technology Division
Air Force Systems Command
Edwards Air Force Base, California

AERONUTRONIC
DIVISION OF PHILCO CORPORATION
A SUBSIDIARY OF *Ford Motor Company*,
FORD ROAD/NEWPORT BEACH, CALIFORNIA

CONFIDENTIAL

**Best
Available
Copy**

"When U. S. Government drawings, specifications, or other data are used for any purpose other than a definitely related Government procurement operation, the Government thereby incurs no responsibility nor any obligation whatsoever, and the fact that the Government may have formulated, furnished, or in any way supplied the said drawings, specifications, or other data, is not to be regarded by implication or otherwise, or in any manner licensing the holder or any other person or corporation, or conveying any rights or permission to manufacture, use, or sell any patented invention that may in any way be related thereto."

CONFIDENTIAL

AFRPL-TR-65-53

Secondary Publication No. C-3617

In addition to security requirements which must be met, this document is subject to special export controls and each transmittal to foreign governments or foreign nationals may be made only with prior approval of AFRPL (RPPR-STINFO), Edwards, California 93523.

FINAL REPORT

**AN INVESTIGATION AND FEASIBILITY DEMONSTRATION
OF NOZZLES FOR RESTARTABLE SOLID ROCKET MOTORS (U)**

Prepared for: Rocket Propulsion Laboratory
Research and Technology Division
Air Force Systems Command
Edwards, California

Under Contract: AF 04(611)-9904

Prepared by: W. H. Armour, R. M. Edmiston, H. L. Moody,
J. G. Baetz, E. L. Kane

Approved by: *D. A. Carrison*
D. A. Carrison, Manager
Propulsion Engineering Department

31 March 1966

AERONUTRONIC
DIVISION OF PHILCO CORPORATION
A SUBSIDIARY OF *Ford Motor Company*,
FORD ROAD NEWPORT BEACH CALIFORNIA

NOTICE: This material contains information affecting the National Defense of the United States within the meaning of the Espionage Laws, Title 18 U.S.C., Sections 793 and 794, the transmission or revelation of which in any manner to an unauthorized person is prohibited by law.

DOWNGRADED AT 3 YEAR INTERVALS; DECLASSIFIED AFTER 12 YEARS

CONFIDENTIAL

ABSTRACT

Analytical and empirical studies were conducted to define and investigate problems associated with restartable solid propellant rocket nozzles. Thermal analysis covered the complete temperature history from startup through cooldown of the duty cycle. In addition to conventional convection, conduction, and radiation, the effects of the pyrolysis gases of charring ablators were included. The structural analysis included the investigation of the thermo-elastic behavior of cylindrical and washer inserts, the existence of plastic zones, the effects of contact pressures in stacked washer inserts, and the effects of property degradation of tungsten due to grain growth. The materials investigation included tungsten-carbon reactions, tungsten grain growth and the resulting effects on properties, and the high temperature c-direction compressive deformation of pyrolytic graphite. Rocket nozzle firings were used for verification of analyses and further problem definition. It was found that the strength of tungsten is degraded by 50 percent or more with very slight grain growth. Large permanent c-direction compressive deformations are attainable in pyrolytic graphite above 2600°C with stresses of 7000 psi in 30 seconds. Ablation of char-forming insulators provides the principal mode of cooldown by the pyrolysis process and by heat transfer to the resulting gases as they leave the nozzle. Radiation was found to be an order of magnitude lower in significance. Higher thermal loads result from initial uniform ambient temperature conditions than from restarting from any point during cooldown. Thermal stress design charts have been constructed for the candidate throat materials. A very simple design chart based on brittle fracture and yielding which requires knowledge of only the chamber pressure and throat diameter has been devised. Tests showed the analysis techniques developed to be satisfactory. With these analytical techniques, limitations on duty cycles can be determined. These limitations are couplings of firing times and cooldown times. The results of rocket firing tests are presented. The current capability of analyzing restartable nozzles is assessed and major problems which require further investigation are defined.

CONTENTS

SECTION	PAGE
1 INTRODUCTION.	1-1
2 THERMAL AND CORROSION ANALYSIS	
2.1 Convection Heat Transfer	2-1
2.2 Conduction-Ablation.	2-7
2.3 Radiation.	2-9
2.4 Application of Thermal Analysis.	2-10
3 STRUCTURAL ANALYSIS	3-1
3.1 Problem Definition	3-2
3.2 Elastic Analysis	3-10
3.3 Anelastic Behavior	3-47
3.4 Development of Theory for Stacked Pyrolytic Graphite Washer Inserts.	3-58
3.5 Thermal Fatigue.	3-65
3.6 Changes in Material Characteristics.	3-83
3.7 Unique Loading Effects	3-88
4 MATERIALS STUDIES .	
4.1 Literature Survey.	4-1
4.2 Tungsten Grain Growth.	4-3
4.3 Tungsten-Carbon Reaction Studies	4-15
4.4 Alumina Studies.	4-25
4.5 High Temperature c-Direction Compressive Deformation of Pyrolytic Graphite.	4-27
4.6 Thermal Fatigue Tests.	4-40

CONTENTS (Continued)

SECTION		PAGE
5	ROCKET MOTOR TESTS.	5-1
	5.1 Nozzle Throat Sections	5-5
	5.2 Nozzle Entrance Sections	5-8
	5.3 Nozzle Exit Sections	5-11
	5.4 Nozzle Insulation.	5-11
6	DEVELOPMENT MOTOR TESTS	
	6.1 Development Nozzle Throat Sections	6-1
	6.2 Development Nozzle Entrance Sections	6-8
	6.3 Development Nozzle Exit.	6-10
	6.4 Development Nozzle Insulation.	6-10
7	DEMONSTRATION TESTS	
	7.1 Test Conditions.	7-1
	7.2 Duty Cycle	7-1
	7.3 Nozzle Design.	7-3
	7.4 Test Results	7-5
8	COMPARISON OF ANALYTICAL AND EXPERIMENTAL DATA.	8-1
	8.1 Entrance Sections.	8-2
	8.2 Throat Sections.	8-6
	8.3 Exit Sections.	8-61
	8.4 Insulation	8-62
	8.5 Alumina Deposition	8-72
9	CONCLUSIONS	
	9.1 Summary of Results.	9-1
	9.2 Residual Problem Areas.	9-5
APPENDICES		
A	CONVECTION HEAT TRANSFER	
	A.1 Boundary Layer Solution.	A-1
	A.2 Free-Stream Nozzle flow.	A-7

CONTENTS (Continued)

APPENDICES	PAGE
B-- RADIATIVE HEAT TRANSFER	
B.1 Cooldown Period.	B-1
B.2 Application of Cooldown Radiative Analyses	B-10
B.3 Firing Period.	B-10
B.4 Surface Emissivity	B-14
C CONDUCTION-ABLATION HEAT TRANSFER	
C.1 Internal Energy Balance.	C-1
C.2 Pyrolysis.	C-2
C.3 Gas-Char Reactions	C-5
C.4 Thermophysical Properties.	C-7
C.5 Gas Momentum and Mass Balance.	C-9
C.6 Flame Front Boundary Conditions.	C-11

ILLUSTRATIONS

FIGURE		PAGE
2-1	Propellant Enthalpy as a Function of Temperature. . . .	2-3
2-2	Propellant Gas Constant as a Function of Temperature. .	2-4
2-3	Density-Enthalpy Correlation.	2-6
2-4	Gas Side Heat Transfer Coefficient; Wall Temperature, and Wall Contour, Real Gas Analysis	2-8
2-5	Schematic of Deposition Phenomenon.	2-18
2-6	Temperature Versus Time with and without Al_2O_3 Deposition for Rocket Motor Test 10	2-21
2-7	Materials Comparison Plot of Surface Temperature-Time Profile at Throat	2-24
2-8	Temperature-Time Profile at Throat Section for Tungsten Shell Backed with ATJ Graphite.	2-25
	Free Stream Stagnation Temperature During Soak Period after 20 Sec Firing	2-28
2-9	Nozzle Surface Temperature Distribution after Shutdown.	2-30
2-11	Nozzle Surface Temperature Distribution with Radiation and Conduction Cool Down at 396 Seconds after Shutdown.	2-31

ILLUSTRATIONS (Continued)

FIGURE		PAGE
2-12	Change in Heat Content for Throat Insert due to Ablation and Radiation.	2-33
2-13	Comparison of Wedge and Washer Pyrolytic Graphite Throat Insert.	2-34
2-14	Temperature Profile for Pyrolytic Graphite Throat Washer with Asbestos Phenolic Insulator.	2-37
2-15	Temperature Profile for Pyrolytic Graphite Throat Washer Insulated with Pyrolytic Graphite and Asbestos Phenolic	2-38
2-16	Pyrolytic Graphite Throat Insert Thermal History with Various Backup Insulators	2-39
2-17	Decomposition of Ablating Nodes	2-40
2-18	Axial Gas Side Surface Temperature Profile for 1-1/4 In. As-Deposited P.G. Nozzle.	2-41
2-19	Radial Temperature Distribution in Ablator at Throat Location (for Nozzle of Figure 2-18).	2-43
2-20	Total Change in Throat Insert Heat Content During Soak.	2-44
2-21	Effect of Initial Char Thickness and Throat Insert Heat Content on Heat Dissipated During Soak	2-45
2-22	Influence of Total Heat Content for Tungsten Shell (0.15 In.) and ATJ Graphite Throat Insert on Firing Time.	2-48
2-23	Influence of Heat Content for Pyrolytic Graphite Throat Insert on Firing Time.	2-49
2-24	Total Heat Content for As-Deposited Pyrolytic Graphite Throat Insert Versus Firing Time.	2-50

ILLUSTRATIONS (Continued)

FIGURE		PAGE
2-25	Total Heat of Pyrolytic Graphite Versus Temperature . .	2-52
2-26	Heat Content of Edge Grain As-Deposited P.G. Throat Insert Versus Firing Time	2-55
2-27	Heat Content of Annealed P.G. Throat Insert Versus Firing Time	2-56
2-28	Heat Content for Tungsten Shell and ATJ Graphite Throat Insert Versus Firing Time	2-57
2-29	Thermal History of Pyrolytic Graphite Throat Insert . .	2-58
2-30	Influence of Alumina Deposition on Heat Content of P.G. Throat Insert	2-59
2-31	Backup Material Effect on Firing Time	2-62
2-32	Firing Time for Surface Temperature to Reach 5500°F for Tungsten Backed with ATJ Throat Inserts	2-63
3-1	Pyrolytic Graphite Plates Shown in Section.	3-6
3-2	Elephant's Footing in Nozzle Fired under Contract No. AF 04(611)-8387	3-7
3-3	Coupling of Temperature Shape and Geometry in the Stress Response of a Hollow Cylinder.	3-14
3-4	Flame Side Temperature of Insert up to Maximum Temperature Difference Across Insert.	3-17
3-5	Temperature Difference Across Insert Wall	3-18
3-6	Nozzle Throat Heat Transfer Parameter	3-19
3-7	Thermal Conductivity of Tungsten and ATJ Graphite . . .	3-20
3-8	Temperature Distribution Exponent	3-21

ILLUSTRATIONS (Continued)

FIGURE		PAGE
3-9	The Thermal Loading Parameter f_n	3-22
3-10	Thermal Stress Design Chart for ATJ Graphite Long Cylinder Backside Tensile Failure	3-34
3-11	Thermal Stress Design Chart for Tungsten Long Cylinder Backside Tensile Failure	3-35
3-12	Design Chart for Pyrolytic Graphite Inner Surface Compression	3-38
3-13	Pyrolytic Graphite Inner Surface Compressive Response Structural Chart.	3-39
3-14	Tungsten Long Cylinder Outer Surface Tensile Response Structural Chart.	3-40
3-15	Tungsten Short Cylinder Outer Surface Tensile Response Structural Chart.	3-41
3-16	Coordinate System Used for Conical Sections	3-44
3-17	Tungsten Long Cylinder Inner Surface Compressive Yield Chart	3-55
3-18	Effect of the Maximum Temperature in the Cycle on the Fatigue Life (Minimum Temperature 40°C) (From Reference 3-30)	3-68
3-19	Intergranular Cracks at Inner Surface of Tungsten Washer Fired Once (14X)	3-75
3-20	Intergranular Cracks at Inner Surface of Tungsten Washer Fired Once (100X).	3-76
3-21	Tungsten Outer Surface Tensile Response Chart for Degraded Strength	3-85
3-22	The Effect of Grain Growth on Throat Insert Design. . .	3-86

ILLUSTRATION (Continued)

FIGURE		PAGE
4-1	Tensile Specimen Used for Tungsten Grain Growth Evaluation.	4-4
4-2	Arc Cast Tungsten Sample 2, 2 Cycles to 2400°C, Largest Grain (100X).	4-6
4-3	Arc Cast Tungsten Sample 3, 5 Cycles to 2400°C, Largest Grain (100X).	4-6
4-4	Arc Cast Tungsten Sample 5, 10 Cycles to 2400°C, Largest Grain (100X).	4-7
4-5	Arc Cast Tungsten Sample 6, 10 Minutes at 2400°C, Largest Grain (100X).	4-7
4-6	Arc Cast Tungsten As-Received (200X).	4-8
4-7	Arc Cast Tungsten Sample 1, 1 Cycle to 1850°C, Largest Grain and Grain at Fracture (200X).	4-8
4-8	Arc Cast Tungsten Sample 2, 2 Cycles to 2400°C, Grain at Fracture (200X).	4-9
4-9	Arc Cast Tungsten Sample 3, 5 Cycles to 2400°C, Grain at Fracture (200X).	4-9
4-10	Arc Cast Tungsten Sample 5, 10 Cycles to 2400°C, Grain at Fracture (200X).	4-10
4-11	Arc Cast Tungsten Sample 6, 10 Minutes at 2400°C, Grain at Fracture (200X).	4-10
4-12	As-Received Arc Cast Tungsten, Sample 7, at Fracture (400X).	4-11
4-13	Arc Cast Tungsten, 10 Cycles to 2400°C, Crack Developed During Heating Cycle (100X)	4-11

ILLUSTRATIONS (Continued)

FIGURE		PAGE
4-14	Arc Cast Tungsten, 10 Cycles to 2400°C, Crack Developed During Heating Cycle (200X).	4-12
4-15	Variation of Young's Modulus and Tensile Strength of Arc Cast Tungsten with Grain Size.	4-14
4-16	Grain Growth in Gas Pressure Bonded Tungsten. Above: As-Received. Below: After 5 Minutes at 2500°C.	4-16
4-17	Typical Time-Temperature Curve for Tungsten-Carbon Experiments.	4-18
4-18	Tungsten-Carbon Experiment No. 4 Showing Melting at the Interface.	4-21
4-19	Tungsten-Carbon Experiment No. 6 Showing Slight Surface Changes.	4-22
4-20	Tungsten-Carbon Experiment No. 16 Showing Liquid Phase Formed and Deformation of Tungsten	4-23
4-21	Tungsten-Carbon Experiment No. 25 Showing Liquid Phase Which Occurred When Using ThO ₂ as a Diffusion Barrier.	4-24
4-22	Pyrolytic Graphite Compressive Deformation Apparatus	4-28
4-23	Typical Temperature Response of Specimens.	4-30
4-24	Time Dependence of Deformation - Phase 1 HTM Material.	4-33
4-25	Temperature Dependence of Deformation - Phase 1 HTM Material	4-33
4-26	Time Dependence of Deformation - Phase 2 STC Material.	4-35
4-27	Temperature Dependence of Deformation - Phase 2 STC Material	4-35
4-28	Deformation Surface for Constant Temperature	4-37

ILLUSTRATIONS (Continued)

FIGURE		PAGE
4-29	Deformation Surface for Constant Time of 30 Seconds. . .	4-37
4-30	Constant Stress Surface.	4-37
4-31	Deformation Versus Time for Repeated Loading	4-38
4-32	Accumulative Deformation Versus Time for Repeated Loading	4-38
4-33	Thermal Fatigue Samples after Test	4-41
5-1	Nozzle Throat Material Candidates for Restartable Solid Propellant Rocket Motors	5-6
5-2	Duty Cycle Limits Pyrolytic Graphite Throats	5-7
5-3	Nozzle Entrance Material Candidates for Restartable Solid Propellant Rocket Motors	5-9
5-4	Duty Cycle Limits - ATJ Graphite Entrances	5-10
5-5	Maximum Allowable Firing Time Versus Thickness for Entrance Sections.	5-12
5-6	Duty Cycle Limits - Carbon Cloth Phenolic Entrances. . .	5-13
5-7	Nozzle Insulation Material Candidates for Restartable Solid Propellant Rocket Motors	5-14
5-8	Duty Cycle Limits Asbestos Phenolic Insulation Behind Entrance Section	5-19
5-9	Duty Cycle Limits - Asbestos Phenolic Insulation Behind Throat Section	5-20
5-10	Maximum Allowable Firing Time Versus Thickness for Entrance Insulation.	5-21
5-11	Maximum Allowable Firing Time Versus Thickness for Throat Insulation.	5-22

ILLUSTRATIONS (Continued)

FIGURE		PAGE
6-1	Restart Development Test No. 1 Materials Performance. .	6-3
6-2	Restart Development Test No. 2 Materials Performance. .	6-4
6-3	Restart Development Test No. 3 Materials Performance. .	6-5
6-4	Restart Development Test No. 4 Materials Performance. .	6-6
6-5	Restart Development Test No. 5 Materials Performance. .	6-7
7-1	Proposed Demonstration Nozzle Duty Cycle.	7-2
7-2	Nozzle Design for Demonstration Test.	7-4
7-3	Restart Demonstration Test No. 1 Nozzle Performance . .	7-6
7-4	Demonstration Duty Cycle as Actually Fired.	7-8
7-5	Demonstration Nozzle Chamber Pressure Versus Cumulative Firing Time	7-10
7-6	Demonstration Nozzle Cumulative Throat Erosion Rate Versus Cumulative Firing Time	7-11
7-7	Erosion Rates of Exit Cone Segments Versus Expansion Ratio for Demonstration Nozzle.	7-13
7-8	Demonstration Nozzle Throat After 75 Seconds Firing Time.	7-14
7-9	Demonstration Nozzle Throat and Exit Cone After 75 Seconds Firing Time.	7-15
7-10	Demonstration Nozzle Throat Cross Section After Test (200 Seconds)	7-16
7-11	Demonstration Nozzle Contour After Test (200 Seconds) .	7-17

ILLUSTRATIONS (Continued)

FIGURE		PAGE
8-1	Surface Temperature Versus Firing Time for 1.25 inch As-Deposited P.G. Development Nozzle (Test No. 3) . . .	8-3
8-2	Development Nozzle ATJ Entrance Sections.	8-5
8-3	Al ₂ O ₃ Deposition on Nozzle Throat Versus Time	8-8
8-4	Conduction - Ablation Program Calculations of Total Heat Flux Over a Range of Assumed h_{eff} Values.	8-10
8-5	Comparison of the Heat Transfer Coefficients Obtained from the Real Gas Boundary Layer Analysis and the Bartz Correlation	8-13
8-6	Comparison of the Heat Transfer Coefficients Obtained from the Real Gas Boundary Layer Analysis and the Perfect Gas Analysis of Reference K1.	8-14
8-7	Analytical and Experimental Comparisons of Duty Cycle Limitations on Rocket Motor Tests	8-15
8-8	Predicted Pyrolytic Graphite Inner Surface Temperature and Axial Stress - Rocket Motor Test Nozzles.	8-19
8-9	Predicted Axial Stress Distribution of Pyrolytic Graphite Rocket Motor Test Nozzles.	8-21
8-10	Predicted Axial Stress Distribution in Pyrolytic Graphite - Demonstration Test Nozzles	8-22
8-11	Wrinkles and Erosion Groove in Annealed Pyrolytic Graphite Rocket Motor Test 6.	8-24
8-12	Edge View of Kinks in Annealed Pyrolytic Graphite Rocket Motor Test 6	8-25
8-13	Short Cylinder Length Limits (Tungsten)	8-27
8-14	Sectioned Insert of Rocket Motor Test No. 7	8-34

ILLUSTRATIONS (Continued)

FIGURE		PAGE
8-15	Backside View of Insert of Rocket Motor Test No. 8. . .	8-37
8-16	View from Upstream of Insert of Rocket Motor Test No. 8	8-38
8-17	Fracture Surface of Insert of Rocket Motor Test No. 8 .	8-39
8-18	Sectioned Insert of Rocket Motor Test No. 8	8-40
8-19	Sectioned Insert of Rocket Motor Test No. 8	8-41
8-20	Insert of Rocket Motor Test No. 12.	8-44
8-21	Sectioned Insert of Rocket Motor Test No. 12.	8-45
8-22	View from Upstream of Insert of Rocket Motor Test No. 13.	8-47
8-23	Fracture Surface of Insert of Rocket Motor Test No 13.	8-48
8-24	Sectioned Insert of Rocket Motor Test No. 13	8-49
8-25	Upstream View of Insert of Development Test No. 2. . .	8-50
8-26	Sectioned Insert of Development Test No. 2	8-51
8-27	Sectioned Insert of Development Test No. 2	8-52
8-28	Sectioned Insert of Development Test No. 4	8-55
8-29	Sectioned Insert of Development Test No. 4	8-56
8-30	Sectioned Insert of Development Test No. 4	8-57
8-31	Predicted and Measured Thermal Response of Throat Insert for Development Test D-3.	8-63
8-32	Predicted and Measured Thermal Response of Throat Insert for Demonstration Test.	8-64

ILLUSTRATIONS (Continued)

FIGURE		PAGE
8-33	Initial Chamber Pressure Versus Time Comparison.	8-66
8-34	Rate of Enthalpy Change of Throat Washer Versus Soak Time for As-Deposited P.G. Development Motor Firing	8-67
8-35	Rate of Enthalpy Change of Throat Washer Versus Soak Time for Demonstration Motor Firing	8-68
8-36	Char Growth Versus Cumulative Firing Time Restart Development Nozzle	8-70
8-37	Char Growth Versus Cumulative Firing Time Restart Demonstration Nozzle	8-71
8-38	Nozzle Throat Radius Change Versus Firing Time Restart Rocket Motor Test No. 3 (As-Deposited Pyrolytic Graphite)	8-73
8-39	Nozzle Throat Radius Change Versus Firing Time Restart Rocket Motor Test No. 4 (Heat Treated Pyrolytic Graphite)	8-74
8-40	Nozzle Throat Radius Change Versus Firing Time Restart Rocket Motor Test No. 6 (Annealed Pyrolytic Graphite).	8-75
8-41	Nozzle Throat Radius Change Versus Firing Time Restart Rocket Motor Tests 9, 10 and 11.	8-76
8-42	$\int_0^t \delta dt$ Versus Cycle Number.	8-78
A-1	Incompressible Skin Friction Coefficient as a Function of the Momentum Thickness Reynolds' Number	A-5
B-1	Coordinate System for the Shape Factor Analysis of a Rocket Nozzle.	B-4
B-2	Absorption Coefficient of a Carbon Particle Cloud Versus Area Ratio for Optical Thin Condition	B-11
B-3	Absorption Coefficient of a Carbon Particle Cloud Versus Area Ratio for Optical Thin Condition	B-12
C-1	Pyrolysis of Phenolic Resin on Reinforcement Free Basis.	C-4
C-2	Average Specific Heat at Constant Pressure of Pyrolysis Products of Phenolic Resin	C-6

TABLES

TABLE		PAGE
2.1	Heat Transfer Mechanisms Included in the Thermal Analysis.	2-12
2.2	Materials and Nozzle Configuration Studied in Thermal Analysis.	2-13
2.3	Empirical Equations of Throat Thermal Response During Firing and Equilibration Periods (Nozzle Configurations of Figures 2-7 and 2-8)	2-26
2.4	Energy Dissipated by Heat Transfer Mechanisms During Soakback at Throat Location for 1.25-Inch Nozzle (Predicted)	2-42
3.1	Application of Limiting Equations to Nozzle Insert Materials	3-32
3.2	Material Properties	3-32
3.3	Values of Surface Tension	3-77
4.1	Tungsten Grain Growth Heating Conditions.	4-5
4.2	Summary of Tungsten Carbon Experiments.	4-20
4.3	Pyrolytic Graphite Compressive Deformation Data Phase I - HTM Material	4-32

TABLES (Continued)

TABLE		PAGE
4.4	Pyrolytic Graphite Compressive Deformation Data Phase 2 - STC Material	4-34
4.5	Preliminary Thermal Fatigue Test Data	4-42
5.1	Restart Rocket Motor Tests - Summary.	5-2
5.2	Nozzle Materials and Fabrication Procedures	5-15
5.3	Entrance Insulator Evaluation - Rocket Motor Tests. . .	5-17
5.4	Throat Insulator Evaluation - Rocket Motor Tests. . . .	5-18
6.1	Restart Development Tests - Summary	6-2
6.2	Entrance Insulator Evaluation - Development Motor Tests	6-11
6.3	Throat Insulator Evaluation - Development Motor Tests .	6-11
7.1	Restart Demonstration Nozzle Throat Performance	7-9
7.2	Insulator Evaluation - Demonstration Motor Test	7-12
8.1	Pyrolytic Graphite Test Utilization	8-17
8.2	Tungsten Test Insert Data	8-28
8.3	Tungsten Insert Data.	8-30
8.4	Tungsten Insert Summary	8-33
8.5	X-Ray Diffraction Data of Rocket Motor Test No. 7 Samples	8-35
8.6	X-Ray Diffraction Analysis of Rocket Motor Test No. 8 Samples	8-43
8.7	X-Ray Diffraction Analysis Data Development Test No. 2 Samples	8-53

TABLES (Continued)

TABLE		PAGE
8.8	X-Ray Diffraction Analysis Data Development Test No. 4 Samples.	8-58
8.9	Tungsten Grain Size and Temperature History Summary. . .	8-60
C.1	Arrhenius Pyrolysis Rate Laws for Phenolic Resins. . . .	C-3
C.2	Virgin and Char Thermal Conductivities of Asbestos and Silica Phenolic.	C-8
C.3	Virgin and Char Densities and Specific Heats for Various Ablating Materials	C-10

SECTION 1

INTRODUCTION

This Air Force program was initiated to define the problems associated with nozzles undergoing restart and cyclical operations, to investigate these problems, and to demonstrate with actual firings that such nozzles can be successfully designed and tested. An approach which emphasized analytical studies was undertaken combining thermal, structural, and corrosion analyses supported by laboratory studies of materials and by rocket motor tests. The scope of the program was limited to an initial effort; it was realized that all problems could not be investigated in a single 12-month effort. Definition of problems which require further investigation was also included within the scope.

The underlying philosophy to the analytical approach taken was that a better understanding of the behavior of the nozzle could be achieved. The influences of the many parameters involved could be assessed, and judicious variations in these quantities could be made in order to design nozzles with a higher probability of survival. This is contrasted with the build-and-test approach from which a success or failure data point is obtained. If the point comes up failure, some basis for making design changes is necessary. It was the philosophy of this program that analysis formed the proper basis.

The program emphasis was placed on the restartable aspects of the subject. This naturally points to the cyclical nature of the nozzle operation. Some problems are common to both single firing and restartable nozzles; for instance a restartable nozzle will respond exactly the same as a single firing nozzle, the only difference being in the number of times the same events occur. Thus, it immediately appears that there may be some problems which can be attacked independently of the cyclic phenomenon. On the other

hand, if some residual effects remain after a firing or a series of firings, the prior history becomes important to the investigation. In this case, some problems unique to restartable nozzles may be defined. Such unique problems may arise from changed initial conditions. As a result of previous firings, some preload may exist on the nozzle components, or the temperature distribution may be different from a uniform ambient temperature. Alteration of material properties as a result of prior firings presents a material which will respond differently in subsequent firings.

It can be appreciated that, although the investigations were conducted in several disciplines, a great deal of interplay was necessary between these in order to bring the program into a coherent and unified effort. The operating conditions and nozzle contour dictate the input conditions to the thermal investigation. The thermal output becomes the input to the structural analysis. Material properties both influence and limit the responses obtained from both the thermal and structural disciplines. Temperature limits established from corrosion considerations limit the firing time. The cooldown history influences the loadings and the allowable firing times for subsequent operation. Thus, a great many interdisciplinary influences exist.

For purposes of the analytical investigations, the entrance and exit sections were considered to be cone frustums. Moreover, for the structural analyses, the throat was considered to be a cylindrical section. Additional limitations placed on the scope of this study included the operating conditions which were: 700 psia chamber pressure, 6200°F stagnation temperature, and a total firing time of 200 seconds with up to 40 restarts. Later in the program, the 40 restart requirement was reduced by the Air Force to approximately 20 since this reflected a more realistic requirement. The final demonstration test consisted of 18 restarts. CYI-75, an aluminumized propellant, was chosen for simulation in the nozzle firing tests.

A limited number of materials was selected for investigation within this program. Since many of the problems in a nozzle are associated with particular materials and since different materials require different analytical considerations, it was necessary to couple the materials with the analyses in order to maintain the program perspective. The materials investigated were reinforced plastics, tungsten, pyrolytic graphite, and polycrystalline graphite. These materials have been the most widely used in nozzles and are deemed at present to be the most important for this application. The reinforced plastics were limited to use as backup insulators and as flame surface material in the conical portions of the nozzle. Tungsten was limited to use as a throat insert material.

ATJ graphite was chosen as a representative polycrystalline graphite even though there are more erosion resistant grades available. ATJ lends itself nicely to analysis since, relatively speaking, most of its properties are known. Thus, it is used to represent a class of materials. For tungsten, two types were studied: arc cast and Allied Chemical Corporation's gas pressure bonded microspheres. These are considered to be representative grades of this material. Pyrolytic graphite in several forms was investigated: the shell of revolution (c-direction normal to the surface) and the edge grain washer configuration utilizing as-deposited, annealed, and heat treated material. The scope of the study was thus limited to those problems which may be encountered in using these classes of materials.

Some of the problems investigated in this program were: tungsten grain growth and the effects on nozzle performance; alumina deposition and its influence on thermal behavior; plastic deformation of pyrolytic graphite and the effects of nozzle shape and performance; char layer growth of ablating plastics and the effects of pyrolysis and convection of the pyrolysis gases on the heat transfer analysis; the relative effects of radiation, conduction, and pyrolysis on nozzle cooling; the effect of long heat soak times on nozzle materials; the thermoelastic response of nozzle components; the plastic behavior of throat inserts; and the relative performances of nozzle materials when fired under identical conditions. The end product of these investigations will be a compilation of analytical techniques from which operational duty cycles can be defined. Combinations of firing times and cooldown times for other given operating conditions define a duty cycle.

This report summarizes the work accomplished during the program. Reference is made to much of the effort contained in the Quarterly Technical Reports^{1.1,1.2,1.3}. A complete description of the three rocket test series and a comparison of the analytical and experimental results are given. Problem areas which were felt to be important initially in the program were investigated. Some of these were not as serious as originally contemplated. Also, new problems were uncovered. These are discussed in the summary and conclusion sections of this report.

REFERENCES

- 1.1 Armour, W. H., et al., "An Investigation and Feasibility Demonstration of Nozzles for Restartable Solid Rocket Motors," Contract AF 04(611)-9904, First Quarterly Report RPL TDR-64-112, Aeronutronic Publication No. U-2794, 21 September 1964.
- 1.2 Armour, W. H., et al., "An Investigation and Feasibility Demonstration of Nozzles for Restartable Solid Rocket Motors," Contract AF 04(611)-9904, Second Quarterly Report RPL TDR-64-168, Aeronutronic Publication No. C-2952, 20 December 1964.
- 1.3 Armour, W. H., et al., "An Investigation and Feasibility Demonstration of Nozzles for Restartable Solid Rocket Motors," Contract AF 04(611)-9904, Third Quarterly Report RPL TDR-65-53, Aeronutronic Publication No. C-3023, 22 March 1965.

SECTION 2

THERMAL AND CORROSION ANALYSIS

This section describes the analytical treatment of the thermal problem encountered in nozzles for restartable solid rocket motors. A description of the analytical techniques used is given, with some of the details contained in appendices. A comparison of the results of these analyses or predicted performance with those results obtained during the test phases of this program are given in a separated section (Section 8) for continuity.

2.1 CONVECTION HEAT TRANSFER

2.1.1 INTRODUCTION

Although the large number of turbulent boundary layer heat transfer theories employed in the past have indicated a high level of interest among researchers, no particular theory has given a suitable correlation to high temperature ($T_e > 3000^\circ\text{F}$) rocket nozzle heat transfer data. In the development of nozzle systems for use with advanced solid propellants, failure is often traced to inadequate thermal design, especially in the inlet section just upstream of the throat. Although such failures are structural, it can be inferred that an accurate knowledge of the thermal loading in the region of failure is a prerequisite to the performance of structural analysis or redesign. Clearly, cyclic operation of the nozzle will have a tendency to magnify any inaccuracies which are introduced by the thermal analysis. It is currently believed that convective heat transfer theory may be deficient in its treatment of (1) pressure gradient influence, (2) thermochemistry effects, (3) inviscid flow field characterization, (4) skin friction, (5) the local similarity assumption, (6) Reynolds' heat transfer analogy, and (7) surface roughness effects. It is also recognized that the adequacy of existing theory is limited by the incomplete understanding of turbulence, combustion, and two phase flow phenomena in rockets.

Early in this program it was concluded that the boundary layer theory of Elliott, Bartz, and Silver^{2.1} could be extended to improve the treatment of effects (1) through (4). Effects (5), (6), and (7) are of such a nature that an entire reprogramming of the analysis would be necessary; such an expenditure of time and effort was not considered warranted at the time. It should be noted that in-house analytical work has been undertaken in recent months to investigate these topics, and in addition, the effects of injectant gas mass transport is also under some scrutiny. The primary objective of implementing effects (1) through (4) is to improve the agreement of theory with available experimental data. When necessary, the calculation technique of Reference 2.1 was used in its unrevised form.

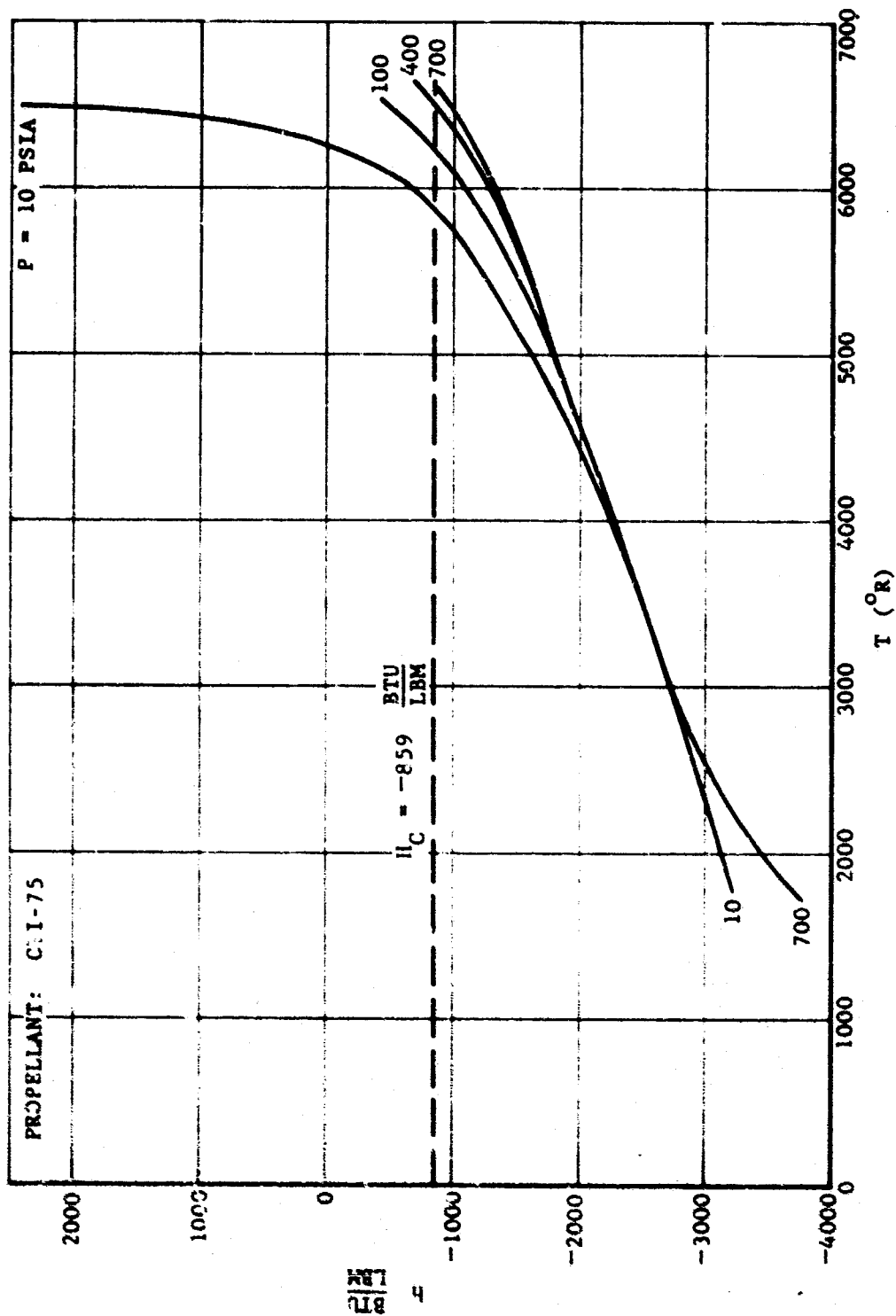
2.1.2 THERMOCHEMICAL EQUILIBRIUM PROGRAM

Because of the very high flow temperatures it was deemed that inclusion of effect (2) would be the most important; consequently, much of the effort was directed towards the combination of a suitable equilibrium thermochemistry program with a properly modified adaptation of the Reference 2.1 analysis. In order to discuss this combination it is necessary to discuss the Aeronutronic equilibrium program.

Determination of the various equilibrium propellant state properties as a function of two assigned conditions is accomplished by application of the minimum free energy ($F = h - p/p_0 - TS$) technique originally derived by White, et al. (Reference 2.2), and extended to multiphase flow by Oliver, et al. (Reference 2.3). Calculation of the equilibrium composition requires the finding of a non-negative set of mole fractions which will minimize the total free energy of the system while satisfying the mass balance requirement.

There are two ways of applying this program in the calculation of thermodynamic properties for use in the heat transfer analysis. First, an unburned propellant composition is assigned, and the resulting state properties, mole fractions, mixture molecular weight, etc., are computed at a number of selected temperatures and pressures. Figures 2-1 and 2-2 illustrate the static enthalpy and gas constant, respectively, as a function of temperature and pressure for the CYI-75 propellant. The boundary layer theory, described in Paragraph 2.1.3 and in Appendix A, requires as input data, the specification of wall temperature, enthalpy (h), and gas constant (R/W_m). It is assumed that chemical equilibrium is maintained at the wall surface, and in the definition of a suitable density versus enthalpy expression, throughout the entire boundary layer thickness. With the arbitrary selection of the wall temperature, the local wall pressure (and thus H_w and $R/W_{m,w}$), may be hand calculated by a simple one-dimensional perfect gas analysis based on the chamber specific heat ratio (as calculated by the equilibrium program at the chamber state point). This method of calculating the pressure dependence on the nozzle contour is accurate enough because enthalpy and gas constant are nearly insensitive to changes in pressure over a wide range of temperatures (Figures 2-1 and 2-2). The accuracy of this method in determining the

CONFIDENTIAL



FO2968 C

FIGURE 2-1. PROPELLANT ENTHALPY AS A FUNCTION OF TEMPERATURE

CONFIDENTIAL

CONFIDENTIAL

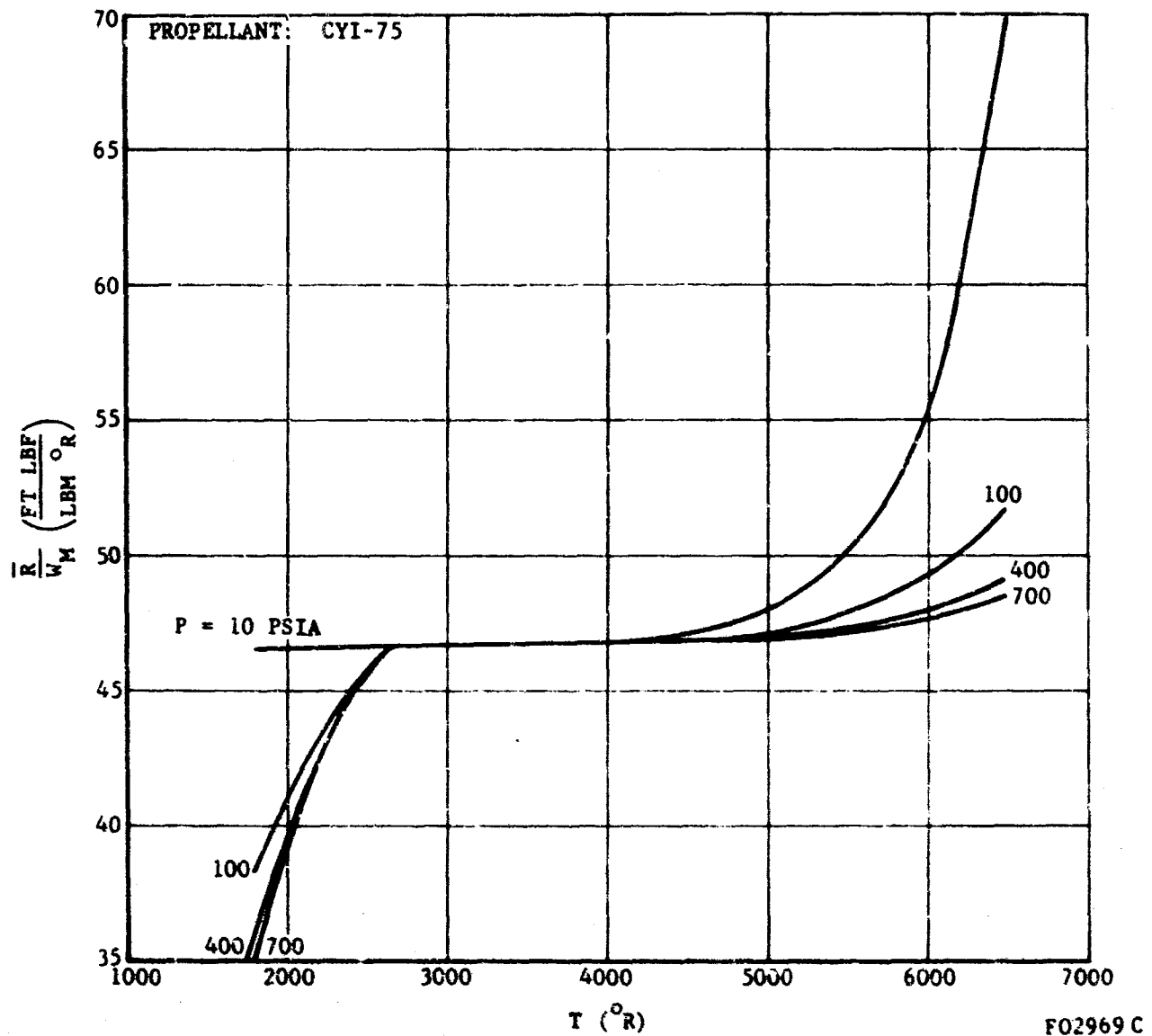


FIGURE 2-2. PROPELLANT GAS CONSTANT AS A FUNCTION OF TEMPERATURE

CONFIDENTIAL

CONFIDENTIAL

local wall values of h and \bar{R}/Wm is somewhat reduced in the low and high temperature ranges; however, it is still assumed to be suitable over these ranges.

Figure 2-3 illustrates a plotting of equilibrium density versus enthalpy over a range of conditions between the wall values ($T_w = 2000^\circ R$) and the inviscid stream. Various authors, in particular Fay and Riddell,^{2,4} have assumed analytic density - enthalpy fits; it is assumed in these calculations that a linear correlation between the wall and inviscid stream is suitable, so that

$$\frac{\rho_e}{\rho} = \frac{\rho_e}{\rho_w} + \left(1 - \frac{\rho_e}{\rho_w}\right) \left(\frac{h - h_w}{h_e - h_w}\right) \quad (2.1)$$

the linear correlations are also shown in Figure 2-3. It is seen that the linear approximation is quite accurate, at least for the propellant in question. The ρ_e/ρ and $(h-h_w)/(h_e-h_w)$ values were computed at five different temperatures for a single pressure, the boundary layer edge temperature (subscript e) having been determined by travelling along an isentrope from the assumed chamber condition. It should be mentioned that recent correlations have been performed with Be propellant formulations, with these equilibrium compositions also exhibiting a near-linear density-enthalpy dependence. This method thus shows some generality.

The second application of the equilibrium program involves the evaluation of the inviscid stream state properties along an isentrope starting at the assumed chamber conditions. This procedure solves for the local flow conditions along an individual streamline; the relating of this streamline to the actual flow geometry in the nozzle is achieved by specifying additional fluid dynamic conservation relations (Appendix A). A series of pressures are chosen at which the state properties are evaluated; use of these properties in the conservation relations is made by linear interpolation between the adjacent state points.

2.1.3 DETERMINATION OF THE HEAT TRANSFER COEFFICIENT

Discussed in Appendix A are the features of the gasdynamic boundary layer analysis developed during this contract. In this paragraph is presented a calculated gas side heat transfer coefficient distribution along the surface of the 1.25-inch throat diameter nozzle. The input conditions are the wall temperature, enthalpy, and gas constant distributions, the chamber conditions with the resulting equilibrium table evaluated over a range of pressures down to the exit condition, an assumed initial momentum thickness at the start of boundary layer growth (a small but non-zero factor), and various constant parameters, such as the Prandtl number, viscosity power, etc. Except for the addition of enthalpy and gas constant versus axial length distributions, and choice of one- or two-dimensional free stream

CONFIDENTIAL

PLOTTED CONDITIONS			A			O		
X	P (PSIA)	T (°R)	P	T		P	T	
e-700	700	6630	400	6250		100	5350	
	700	5000	400	5000		100	5000	
	700	4000	400	4000		100	4000	
	700	3000	400	3000		100	3000	
w-700	700	2000	400	2000		100	2000	

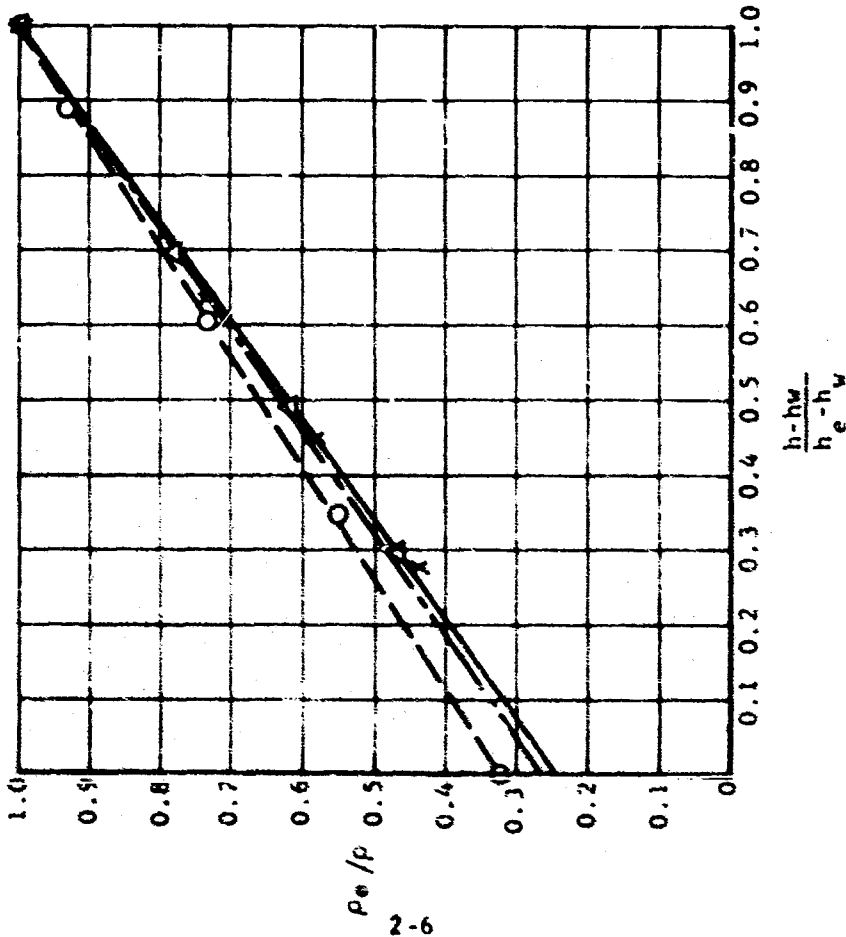
PROPELLANT COMBINATION: CYI-75

$P_c = 700 \text{ PSIA}$
 $T_c = 6630 \text{ }^\circ\text{R}$
 $T_w = 2000 \text{ }^\circ\text{R}$

$\frac{\rho_e}{\rho} = \frac{\rho_e}{\rho_w} + \left(1 - \frac{\rho_e}{\rho_w}\right) \left(\frac{h - h_w}{h_e - h_w}\right)$

$P = 700 \text{ PSIA}$
 $P = 400 \text{ PSIA}$
 $P = 100 \text{ PSIA}$

F02970 C



CONFIDENTIAL

FIGURE 2-3. DENSITY-ENTHALPY CORRELATION

CONFIDENTIAL

solutions, the input format is virtually identical to the one given in Reference 2.1. Figure 2-4 shows the calculated gas side heat transfer coefficient along with the original nozzle contour (before erosion and/or deposition had occurred), and the assumed wall temperature, which is approximately the high steady-state value. The one-dimensional inviscid stream choice $PAU = \dot{m}$ was made for the solution illustrated here. The maximum heat transfer coefficient is calculated to be at the throat because of the one-dimensional inviscid stream assumption; in actuality, the maximum point is at the intersection of the sonic line with the wall boundary layer, slightly upstream of the throat. Because of budget limitations the two-dimensional inviscid stream solution was not employed in any calculations, although it was programmed and is available for use. Details are given in Part 2 of Appendix A.

The calculated gas side heat transfer coefficients (with a maximum value of $0.00818 \text{ Btu/in.}^2\text{sec}^{\circ}\text{R}$), is generally not the value experimentally measured by nozzle wall thermocouples; the presence of ablation and/or deposition gives a measured value that is significantly lower than that predicted by the boundary layer analysis. The effects of deposition and comparison of the analytically predicted heat transfer coefficient, both as calculated and as modified by the influence of deposition, are given in Section 8 of this report. As can be seen, the comparison of this theory and actual results obtained during test are remarkably good. Also shown are comparisons with previously used techniques for predicting rocket nozzle heat transfer.

2.2 CONDUCTION-ABLATION

The determination of the thermal response of the structural and insulation components of a rocket motor subjected to any stop-start duty cycle, requires the use of a conduction analysis which is capable of handling time dependent convective and radiative boundary conditions and thermal and chemical degradation of materials. The time dependent convective and radiative boundary conditions must also be incorporated in the conduction analysis in such a manner that boundary layer mass injection and deposition can be included in the thermal analysis. The influence of ablation in an un-cooled nozzle thermal response during soak or cooldown periods requires coupling of the conduction and ablation modes of heat transfer. The ablation analysis must be applied to the conduction analysis in such a manner that ablation of the surface material as well as the heat sink backup insulation material can be predicted.

The conduction analysis employed in this program was a modified version of an existing transient, three-dimensional conduction program. The program was modified to handle the thermal and chemical degradation of materials at any location in a rocket motor. This program is able to handle time, temperature or position dependent thermophysical material properties, and boundary conditions. A detailed description of this program is given in Appendix C.

CONFIDENTIAL

THIS PAGE IS UNCLASSIFIED

CONFIDENTIAL

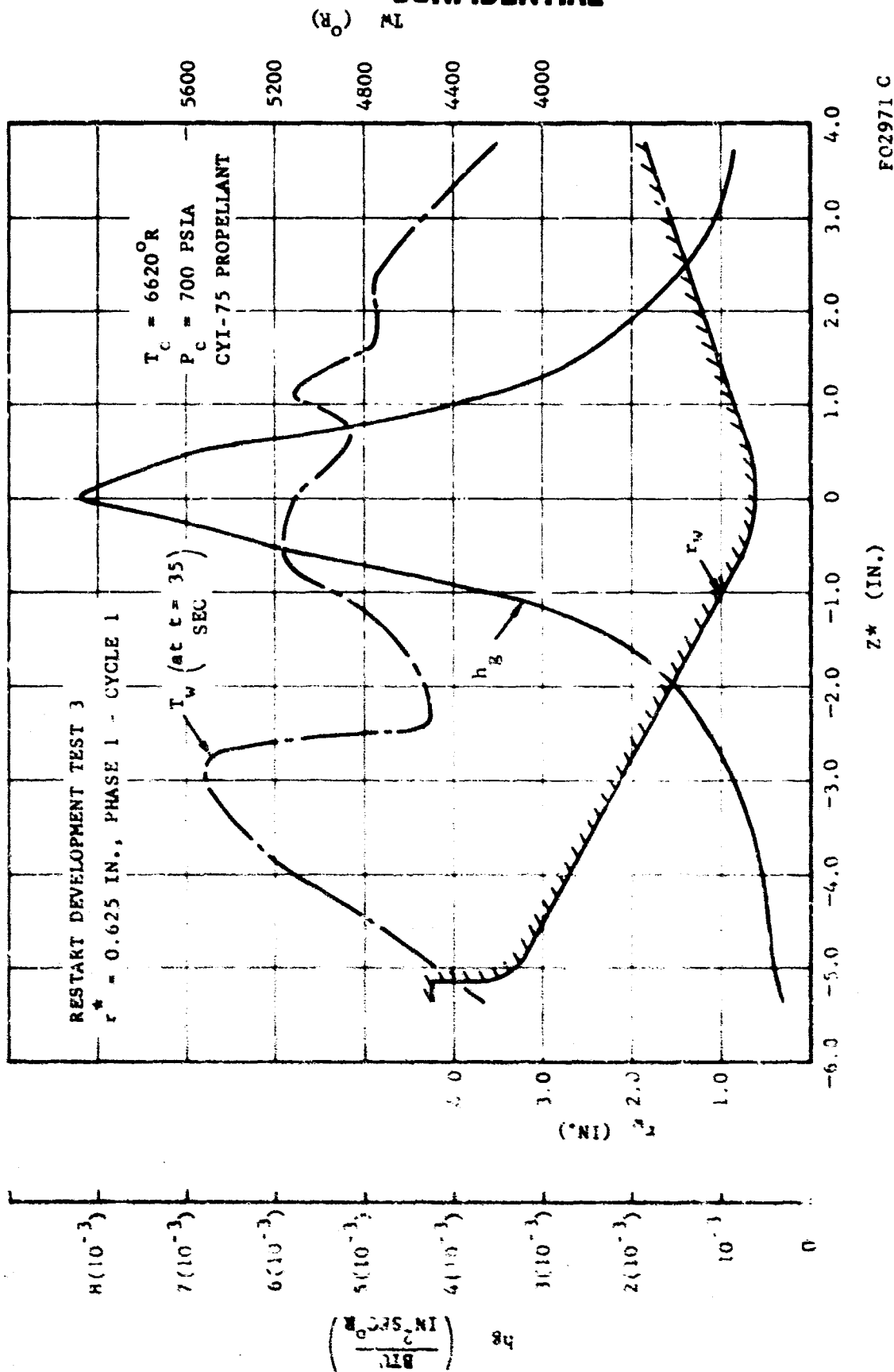


FIGURE 2-4. GAS SIDE HEAT TRANSFER COEFFICIENT, WALL TEMPERATURE, AND WALL CONTOUR, REAL GAS ANALYSIS

CONFIDENTIAL

Since the basic program requirements of the thermal analysis were to (1) generate data that will enable intelligent selections of guidelines for restart duty cycles, (2) define thermal and structural response capabilities of nozzle configurations, and (3) determine limitations upon restart; the conduction-ablation program was employed in this program using two different techniques. The first technique consisted of dividing the nozzle into three sections (i.e., entrance, throat insert, and exit cone). The conduction-ablation program was applied to each section of the rocket motor during the firing and equilibration periods (equilibration period is defined as that time between nozzle shut down and the time to reach 90 percent of a radial isothermal condition in the heat sink materials). This technique resulted in the determination of the amount of heat absorbed by the nozzle materials during firing and the time to reach radial isothermal conditions in the heat sink materials. To apply the results of this technique to restartable motors requires the assumption that these motor sections are thermally independent of one another during firing and equilibration periods. Use of this assumption during the soak back period is, however, invalid, as axial conduction and radiation interchange between these sections becomes significant. Therefore, in determining the thermal response of the rocket motor during soak period, a second technique was used in applying the conduction-ablation program. This technique consisted of analyzing the three nozzle sections to determine the change in heat content of the heat sink and the thermal response characteristics of the insulators during soak back.

The application of the conduction-ablation program, with the various inputs from the convection and radiation analysis, to selected stop-start nozzle configurations is presented in Paragraph 2.4.

2.3 RADIATION

A portion of the effort expended in this program has been devoted to the development of practical analytical tools which can be used to evaluate the radiant energy exchange mechanisms in restartable solid motors. It is apparent that (1) surface to surface, (2) surface to fluid phases, and (3) surface to ambient environment radiation exchanges can occur. The determination of the importance of these types of radiative transfer to the thermal behavior of the structural and insulation components of a restartable nozzle requires dividing the analytical radiation model into two parts. Each part is applied to the rocket motor at the appropriate period of motor operation; that is, during firing and soak periods.

During firing the chamber and nozzle surfaces exchange radiative energy with the combustion products. For combustion products that are characteristic of aluminized propellants, the cloud transmissivities in the chamber and nozzle regions are such that the radiative energy transferred from surface to surface is unimportant. During firing, radiative transport is then dependent on the emission characteristics of the combustion products and,

of course, chamber and nozzle surface emissivities. However, the analytical determination of the emissive characteristics of the aluminized cloud is complicated by the scattering experienced by dispersed alumina particles. In addition, the effect of alumina deposition and chemical reactions at the chamber and nozzle surfaces complicate the specification of surface emissivity.

For this program, the emissivity of the surface of exposed materials were regarded as a function of the material only. The effects of deposition, chemical reactions, and surface temperature were omitted because of the inaccuracies in predicting alumina cloud emission and the complications in analyzing the mechanisms of deposition (surface coverage by alumina must be defined as a function of position and time). The emissive properties of the combustion products were obtained from experimental data acquired from aluminized solid propellant motor firings. These data were obtained from Reference B.5. The data of Reference B.5 were extrapolated to the rocket motors of this program using a modification of the technique developed in Reference B.6. A detailed technical discussion of the technique used in this program is presented in Appendix B.

During soak periods, radiative transfer will exist between the various rocket motor inner surfaces, the inner surfaces and the ambient environment (via the exit cone), and the inner surfaces and the free stream. To determine the importance of inner surface-free stream radiative transfer, the quantities of absorbing species in the free stream were calculated using (1) experimentally obtained cool down chamber pressures and free stream stagnation temperatures, and (2) thermochemical calculations performed on the insulating materials pyrolysis products. A simplified optically thin radiation analysis was then applied to various rocket motor contours using the calculated quantities of absorbing species. The resulting surface-free stream radiative transfer was compared to surface-surface and surface-ambient environment radiative transport and the energy dissipated by ablation. The former was found to be insignificant compared to these other modes.

The radiative transport between surface-surface and surface-ambient environment was determined using a modified form of the analysis presented in Reference B.2. This modified analysis predicts the effective view factors (gray wall view factors) from (1) one motor surface element to another and (2) the surface elements to the ambient environment. A detailed discussion of the soak back analyses is presented in Appendix B.

2.4 APPLICATION OF THERMAL ANALYSIS

2.4.1 INTRODUCTION

During this program, the heat transfer analyses described in Paragraphs 2.1, 2.2, and 2.3 were applied to a number of different nozzle designs in an effort to (1) define problem areas and/or limitations of the heat transfer analysis, (2) generate data that enables intelligent selection of restart duty cycles

for specific designs, (3) generate data that enables intelligent selection of nozzle designs for a given duty cycle, and (4) integrate the thermal effort with the test effort. The results obtained in these areas are presented and discussed in this paragraph by dividing the thermal history of a restartable rocket motor nozzle into two periods: firing and soak. The heat transfer mechanisms considered in the thermal analysis for these periods are summarized in Table 2.1. The effect and importance of each heat transfer mechanism in the thermal response was determined by comparing the analytical predictions with the results acquired in the test effort. Also, by comparing the analytical results with the test results, the limitations of the heat transfer analysis were determined.

From a thermal standpoint there are two criteria with which to design an uncooled restartable rocket motor nozzle. The first requires that neither the entrance section nor throat insert surface temperature reach a level at which excessive surface regression will be experienced. Therefore, it is required that the nozzle entrance and throat exhibit good heat sink properties. By fulfilling this criterion, undue loss in motor performance from thermal response constraints is eliminated. The second criterion for restart purposes requires that a minimum amount of energy be absorbed by the heat sink materials. Minimizing the energy absorbed by the heat sink implies that the amount of ablative material consumed in dissipating this energy is also minimized. (This criterion is based on the fact that for the configurations studied in this program, heat dissipated by ablation is far greater than by radiation). These design criteria imply opposing constraints on the thermal limitations, thus resulting in an optimization of the heat sink material and thickness. However, in this program the limitation on surface regression imposed by the first criterion was considered of primary importance and used as the only constraint in the thermal design.

Since there are a large number of contours and material combinations that are feasible for uncooled nozzle designs, the thermal effort considered only those combinations that exhibited desirable traits in the motor firings of this program. The materials and nozzle configurations used in the thermal analysis are listed in Table 2.2. As Table 2.2 indicates, the major effort of the thermal analysis was focused on the throat insert section of the nozzle. This was attributed to the imposed limitations of throat regression and the fact that the net wall heat flux is substantially larger in this area than in the entrance and exit sections. The thermal analysis divided the rocket motor into three sections (entrance, throat, and exit) for determining the thermal limitations during firing and equilibration periods. This technique is valid only if these sections are thermally independent. During firing, axial conduction and film cooling will make these sections thermally dependent. However, the radial conduction is considerably greater than axial conduction and the effect of film cooling is negligible when compared to deposition, thereby verifying this approach during firing.

TABLE 2.1

HEAT TRANSFER MECHANISMS
INCLUDED IN THE THERMAL ANALYSIS

<u>Rocket Motor Period</u>	<u>Heat Transfer Mechanism</u>	<u>Rocket Motor Location Where Applied</u>
Firing	Convection	Combustion products and gas side surfaces
	Radiation	Combustion products and gas side surface
	Internal ablation	Reinforced plastics
	Surface regression due to chemical attack	Assumed maximum design surface temperature
	Two-dimensional conduction	Entrance, throat insert, and exit
Soak (cool down)	Convection	Pyrolysis products in motor free stream and gas side surfaces
	Radiation	Pyrolysis products in rocket motor free stream and gas side surface, interchange between gas side surfaces, gas side surfaces and ambient environment
	Internal ablation	Reinforced plastics
	Two-dimensional conduction	Entrance, throat insert, and exit

TABLE 2.2
MATERIALS AND NOZZLE CONFIGURATIONS
STUDIED IN THERMAL ANALYSIS

Throat Diameter	Entrance		Throat Inset		Exit Cone	
	Flange Front	Backup Insulator	Heat Sink	Backup Insulator	Flange Front	Backup Insulator
5/8 in.			PG - 3.0 in. OD ATJ Backup - 3.72 in. OD	ATJ Perfectly Insulated		
			PG - 2.21 in. OD ATJ Backup - 2.93 in. OD	ATJ Perfectly Insulated		
			PG - 1.40 in. OD ATJ Backup - 2.12 in. OD	ATJ Perfectly Insulated		
			PG - 3.0 in. OD	PG Perfectly Insulated		
			Annealed PG - 1.0 in. OD ATJ Backup - 3.72 in. OD	ATJ Perfectly Insulated		
			Tungsten - 0.800 in. thick ATJ Backup - 3.00 in. OD	ATJ Perfectly Insulated		
			Tungsten - 0.180 in. thick ATJ Backup - 3.00 in. OD	ATJ Perfectly Insulated		
			PG - 4.00 in. OD ATJ Backup - 4.50 in. OD	ATJ Perfectly Insulated		
			PG - 3.25 in. OD ATJ Backup - 3.75 in. OD	ATJ Perfectly Insulated		
	ATJ Graphite Washers to 4 of 9.5 30° Entrance	ATJ Perfectly Insulated	PG - 5.00 in. OD ATJ Backup - 5.50 in. OD	ATJ Perfectly Insulated	ATJ and CX Graphite 20° Exit Cone	ATJ and CX Perfectly Insulated
1-1/4 in.	ATJ Graphite Washers to 4 of 9.5 30° Entrance	Asbestos Phenolic	PG - 5.00 in. OD ATJ Backup - 5.50 in. OD	Asbestos Phenolic 6.50 in. OD	ATJ and CX Graphite 20° Exit Cone	ATJ and CX Perfectly Insulated
	ATJ Graphite Washers to 4 of 9.5 30° Entrance	ATJ Perfectly Insulated	PG Wedge - 4.00 in. OD ATJ Backup - 5.50 in. OD	ATJ Perfectly Insulated	ATJ and CX Graphite 20° Exit Cone	ATJ and CX Perfectly Insulated
			Tungsten - 0.180 in. thick ATJ Backup - 7.70 in. OD	ATJ Perfectly Insulated		
			Tungsten - 0.150 in. thick ATJ Backup - 7.50 in. OD	ATJ Perfectly Insulated		
			Tungsten - 0.150 in. thick ATJ Backup - 7.50 in. OD	Asbestos Phenolic 10.0 in. OD		
			Annealed PG - 7.50 in. OD	Annealed PG Perfectly Insulated		
			PG - 8.50 in. OD	PG Perfectly Insulated		
			PG - 7.50 in. OD	PG Perfectly Insulated		
			PG - 7.50 in. OD	Asbestos Phenolic		
			PG - 7.50 in. OD	Silica Phenolic		
2-1/2 in.			PG - 7.50 in. OD	PG Shell and Asbestos Phenolic		
			PG - 7.50 in. OD	Cast Carbon		
			PG - 7.50 in. OD	PG Perfectly Insulated	ATJ Graphite 3/8 in. thick 4 from 4 to 4 20° Exit	ATJ and Carbon Cloth Phenolic Perfectly Insulated
			PG - 7.50 in. OD	PG Perfectly Insulated	ATJ Graphite 3/8 in. thick 4 from 4 to 4 20° Exit Carbon Cloth Phenolic 5/8 in. thick 4 from 4 to 4	ATJ and Carbon Cloth Phenolic Perfectly Insulated
	ATJ Graphite Cone - 1.650 in. thick 15° Entrance	Asbestos Phenolic	PG - 7.50 in. OD	PG Perfectly Insulated		
	Graphite Cloth Phenolic Cone - 1.650 in. thick	Graphite Cloth Phenolic Perfectly Insulated	PG - 7.50 in. OD	PG Perfectly Insulated		

During the equilibration period (period during soak that the radial isothermal condition is approached), radiative and axial conductive energy transport between these sections will exist. However, for the nozzles studied, it has been found that the magnitude of radiative and conductive interchange during this period is considerably less than the cool-down component of ablation.

2.4.2 FIRING PERIOD

To determine the thermal and structural limitations of restartable nozzles, it is required that the thermal analysis predicts (1) the radial and axial temperature distributions in the heat sink material during firing, (2) the internal ablation rates of the reinforced plastic materials, and (3) the surface regression rates of the gas side surface materials. To eliminate the analytical complications and questionable assumptions involved in predicting surface regression (see Paragraph 2.5 and Appendix C), the determination of surface regression was relaxed by imposing a maximum material design temperature. This temperature represents the thermal level above which excessive surface regression may be expected to occur. This temperature restriction was applied as a thermal limitation to the throat region. The no surface regression boundary condition was applied to the entrance section of the nozzle; however, the maximum design temperature was not considered as a thermal limitation. This approach in applying the thermal analysis to the entrance section is reasonable since this section may experience a certain amount of surface regression and not result in a significant change in motor performance. The temperature distribution and heat absorbed by the heat sink materials of Table 2.2 were determined for the firing period using the convection, radiation, and conduction-ablation analyses developed in this program. Early in the program the convective boundary conditions were calculated from the Bartz heat transfer correlations mentioned in Paragraph 2.1.3. This boundary condition was applied to the conduction-ablation analysis assuming no alumina deposition. The effect of alumina deposition on heat transfer is discussed in Paragraph 2.4.3 and Section 8.

The following paragraphs present phenomena, problem areas and results that were analytically investigated or obtained for the firing period.

a. Alumina Deposition. From the test results of this program a primarily physical model of the alumina deposition phenomena has been formulated. This model considers that initially, deposition occurs at specific locations on the nozzle gas side surface as a direct result of particle impingement. The initial location and rate of particle impingement has been found to depend on the motor contour, propellant geometry, particle size, and chamber conditions. Of the total particles that impinge on the surface, part will re-enter the gas stream and part will remain on the surface. The quantity that remains on the surface is thought to depend on the porosity, surface roughness and temperature of the surface material

(mechanical attachment); the particle velocity, size and angle with respect to surface (momentum effects); and the type of chemical reactions occurring between alumina and the surface material (chemical attachment, see Section 4). Mechanical attachment is formed by the solidification of the liquid alumina on cold graphite. This type of bond is weak and might be easily released by thermal stresses and gas shear loading. Chemical attachment on carbon is formed by the following reaction:



The Al_4C_3 layer is stable with respect to both carbon and Al_2O_3 , forming a strong chemical bond. (This reaction is highly dependent on pressure and temperature.) Further results of alumina layers on graphite were obtained during the laboratory studies and are reported in Section 4 of this report. The formation of a deposit at specific locations on the surface will cause an irregularity in the motor contour; thereby causing the particle impingement rate to possibly increase. The deposit will be heated by the free stream (via convection and radiation) and cooled by the motor surface material (via conduction). As the deposit thickness increases, the deposit's gas surface will approach the melting point. The time the deposit surface reaches the melting point depends upon the deposit thickness, heating rate, and thermal conductivity of the motor surface material. Once this occurs, the free stream wall shear will cause the liquid portion of the deposit to flow downstream. (Also, the free stream particles impinging on the liquid deposit will not be able to re-enter the free stream as readily as when impingement occurs on a solid surface, thus increasing the deposition rate.) The manner in which the deposit flows downstream will depend on the chemical reactions and wetting that occurs between alumina and the surface material. If the deposit wets the wall, which occurs when Al_4C_3 is present, the radial velocity profile in the liquid will be nearly linear and the liquid flow will resemble Couette flow. As the alumina flows downstream, the portion of the deposit coming in contact with an exposed portion of the surface material will generally solidify (depending upon the surface temperature before deposition and the thermal conductivity of the material). As the layer builds up, the gas side surface of the deposit will re-melt and proceed to flow downstream. Therefore, when the local surface material's temperature is above the melting point of alumina and particle impingement is not present, the alumina mass entering and leaving a location are equal. As the firing proceeds, the locations that initially caused the occurrence of deposition will increase in temperature (locations of particle impingement) therefore causing the deposition thickness at this location to decrease. The decrease in alumina thickness will, in turn, cause the deposition or particle impingement rate to decrease (reduction in discontinuity of contour). Therefore, the alumina mass flow may be expected to logarithmically approach a constant value. Also, at the time when the aft closure, entrance, and throat surface temperature are above the melting point of alumina, the variation of the deposit thickness in these sections will depend on the area ratio change (thickness change due to circumferential change in contour), free stream velocity, wall shear, and local impingement.

When the deposition mass flow is approaching a constant value in the aft closure, entrance, and throat sections, the behavior of the deposit in the exit cone will not necessarily be similar. The wall heat flux in the exit cone is considerably less than in the other sections, thereby requiring a longer time to reach the Al_2O_3 melting point. With a deposit in the exit cone flow separation and shock waves are likely to be experienced. Also, due to low pressures, the formation of Al_4C_3 may not occur. Therefore, due to the complicated flow field alteration and pressure-temperature dependence of Al_4C_3 formation in the exit cone, the deposit behavior in this section may be expected to be very complicated. The transient behavior of the plume observed in aluminized propellant firings is indicative of the complicated deposition behavior experienced in the exit cone; i.e., plume separation and the transient behavior of sparks in the periphery of the plume.

As the gas side surface in the entrance rises above the melting point of Al_2O_3 , the mechanisms causing the attachment of impinging particles will change. The mechanical attachment mechanism undergoes a severe change since Al_2O_3 will no longer solidify at the wall. Also, the importance of the chemical attachment, via the formation of $\text{Al}_4\text{C}_3(\text{s})$, is decreased since $\text{Al}_4\text{C}_3(\text{s})$ becomes unstable with respect to $\text{Al}(\text{g})$ and $\text{CO}(\text{g})$. For a total pressure of 1000 psia, the formation of Al_4C_3 will occur below approximately 5500°F; above this temperature the Al_4C_3 is unstable. This temperature is strongly dependent on pressure (lower pressure corresponds with lower temperature). Therefore, if the surface temperature exceeds the pressure dependent critical temperature, the importance of the chemical attachment mechanism decreases. With this, the wettability of Al_2O_3 on the surface is decreased and the Al_2O_3 that does deposit on the surface (amount significantly decreased) will not wet the surface. The alumina deposit at this temperature level may be expected to be of the bead or droplet type.

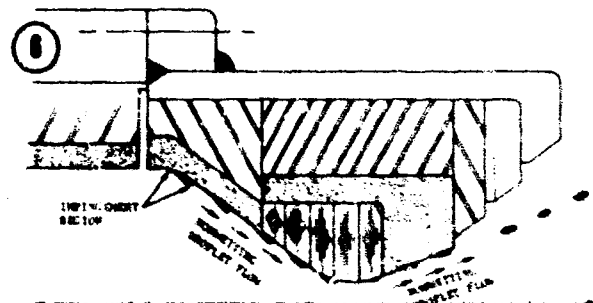
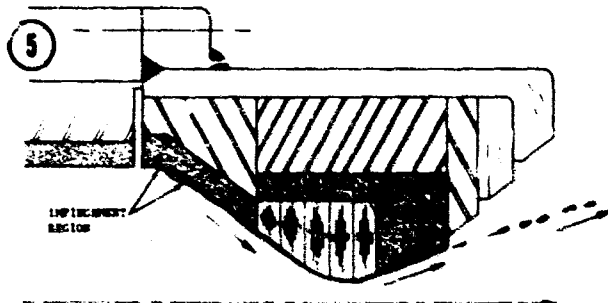
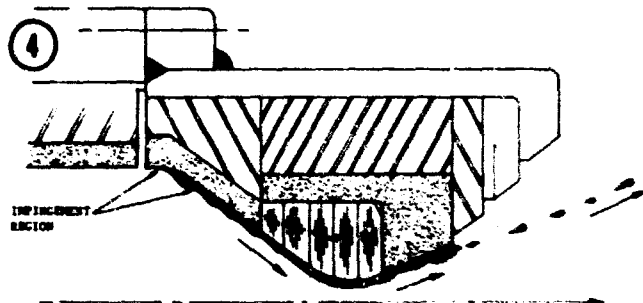
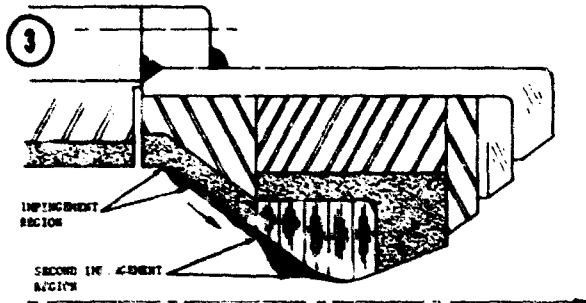
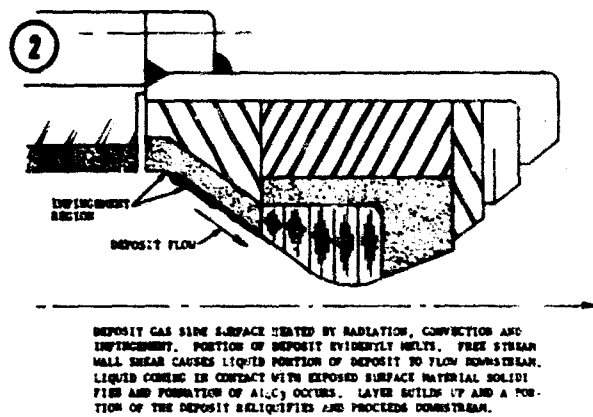
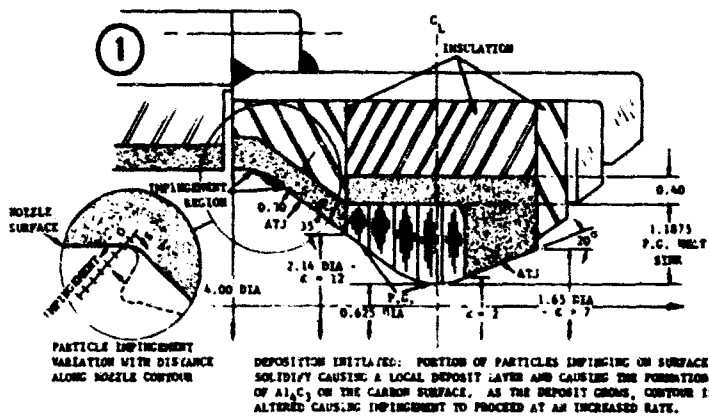
The above discussion was applicable to polycrystalline graphite entrance and aft closure section. When a gas side surface ablator is employed in these sections, the deposition will be altered by surface chemical reactions, pyrolysis gas mass flow, and surface regression. There are three basic types of ablators that are usually employed; high temperature-hard char (carbon or graphite cloth phenolics), low temperature-hard char (asbestos or silica phenolics) and low temperature-soft char (elastomeric materials). When the high or low temperature-hard char are employed, the large pyrolysis mass flow experienced early in the firing will delay the formation of a deposit on the ablator surface. As the pyrolysis mass flow decreases, the deposition rate will increase causing a buildup of alumina. The deposition rate will depend on the pyrolysis mass flow, surface chemical reactions, and mechanical attachment mechanisms. For carbon or graphite phenolics, the formation of Al_4C_3 will be the primary surface chemical reaction and provide means by which alumina will wet the surface. For the asbestos or silica phenolics, a phase change and/or chemical reaction will occur in the reinforcement material causing a viscous liquid to be formed.

This viscous liquid will promote deposition. After deposition is initiated the pyrolysis mass flow will cause the deposit to build up in beads and flow along the surface in droplet type flow. Due to the low thermal conductivities of ablators, the surface temperature will increase at a high rate as compared to the polycrystalline graphites. This will cause Al_4C_3 to become unstable in a relatively short time, thereby causing a decrease in the deposition rate. From this it can be deduced that when carbon or graphite cloth phenolics are employed in regions of the nozzle experiencing impingement, the deposition rate at these locations will be very low. However, for asbestos or silica phenolics, an increase in surface temperature will cause an increase in the amount of viscous liquid formed (produced by phase changes and/or chemical reactions involving reinforcement) thereby causing an increase in deposition. As noted above the alumina will flow downstream on the ablator in a bead or droplet type flow.

When tungsten is used as the gas side surface material, the alumina behavior will depend primarily on the tungsten heat sink thickness, tungsten backup material, and upstream deposition phenomena. It has been found from laboratory investigations (Section 4) that alumina will wet tungsten, therefore, the deposition behavior on tungsten will depend on the transient tungsten surface temperature and upstream deposit behavior.

A schematic of the above physical model is presented in Figure 2-5 for a typical rocket motor configuration. Important alterations that may occur in the deposition behavior of Figure 2-5 are listed below:

- (1) In step (3) the buildup of a deposit on the upstream P.G. surface will cause a severe decrease in local area ratio causing the local wall shear to increase. A level of wall shear may be reached that exceeds the shear force of the deposit-wall attraction. If this occurs, the deposit will be extruded through the exit cone causing a considerable amount of large alumina particles in the periphery of the plume. After the deposit is removed from the P.G., step (2) will follow; however, the P.G. surface temperature will be at a higher level than experienced when step (2) was encountered the first time. The above phenomena may also be expected to occur in step (4).
- (2) In step (3) the alumina deposited on the P.G. washers will cause the local heat flux and wall gas shear to increase. Depending upon the upstream mass flow to this section, a level of heat flux and wall shear may be reached that will cause a large increase in the liquification rate



F02982U

FIGURE 2-5. SCHEMATIC OF DEPOSITION PHENOMENON

of solid alumina. If the amount of liquid formed at this time exceeds the amount supplied via upstream impingement, a large increase in liquid mass flow will be experienced. When this large mass flow comes in contact with the exit cone surface, where the formation of Al_4C_3 has not occurred to any great extent, the deposit will not significantly wet the surface. Since the momentum of the liquid is fairly high and the deposit is in the form of droplets (nonwetting) the deposit will be forced out through the exit cone. This is shown in step (4).

- (3) During any of the five steps in Figure 2-5 chemical and/or mechanical surface regression may be experienced. That is, particle impingement, spallation, cracking, erosion or chemical attack that results from high heating rates, surface shear, and non-uniform coverage of the wall with deposit may cause surface regression. Since the surface regression rate is not necessarily uniform in the axial or circumferential direction, the contour may be expected to become irregular. Irregularity in contour may promote more sites for impingement, causing the deposition rate to increase.
- (4) In restartable nozzles, the firing time may be such that at shutdown, either steps (2), (3), (4), or (5) are applicable. As the nozzle cools thermal stresses will be encountered in the solid deposits causing possible cracking of the attached alumina. Also, Al_4C_3 hydrolyzes at low temperatures thereby reducing the chemical bond between alumina and the carbon wall. The presence of pyrolysis gas in the free stream during soak will induce a gas shear on the deposit in the entrance and throat region. From these phenomena a portion of the deposit present at shutdown may be removed from the nozzle; the location and amount of deposition remaining depending on (1) the thickness of deposit at shutdown, (2) the physical state of the deposit at shutdown, (3) the gas shear

during soak, and (4) temperature history during soak. If a deposit is present on the subsequent startup, step (1) will be altered. The initial deposit should cause deposition to proceed at a rate greater than the first firing. The initial deposit is heated and continues to flow downstream, step (2).

Comparisons of the above physical model with the motor tests of this contract are presented in Section 8.

As can be seen from the above, to develop an analytical model for the deposition phenomena will require (1) the prediction of the transient deposition or impingement rates experienced in the motor; (2) the specification of such property data as liquid alumina thermal conductivity, density, specific heat and viscosity; and (3) investigation of the mechanisms affecting alumina wetting and attachment of the gas side surface materials. At the present time the above parameters have not been determined. Therefore, to determine the effect of alumina deposition on the rocket motor's behavior, a semiempirical technique was employed in this program. From the test effort of this contract the transient deposit thickness at the nozzle throat was determined using the analysis presented in Paragraph 8.7. The alumina deposition thickness specified by the test data was applied to the conduction program using a moving wall boundary. The variable alumina thickness was divided into incremental volumes so that the liquid and solid layers were separated and the free stream convective and radiative boundary conditions applied to the alumina surface. The convective heat transfer coefficients were made a function of wall temperature and throat diameter and the radiation boundary condition was eliminated due to the low alumina surface emissivity. The results of this analysis are presented in Figure 2-6 with experimentally obtained backwall temperature used as a comparison. The time at which the amount of alumina entering and removed from throat location are equal is 19 seconds as predicted by the thermal analysis (alumina layer totally liquified). Referring to Figure 8-41, Test No. 10, this condition was reached at 20 seconds. This correlation is sufficient to verify the method used in the thermal analysis. However, the predicted ATJ-PG interface temperature does not compare with the test data. The deviation in the latter portion of the firing may be attributed to the convective heat transfer coefficient used in the analysis. As discussed in Section 8 the actual gas side heat transfer coefficient is expected to be greater than the value predicted by the modified Bartz correlations. Therefore, use of the Bartz heat transfer coefficient as the gas side heat transfer coefficient, when the alumina deposit is considered, will cause the amount of heat absorbed during firing to be less than the actual amount. The difference in the ATJ-PG interface temperature (predicted and measured) in the first five seconds is caused by the start transient that was experienced during firing. That is, the thermal analysis assumed a step change in chamber pressure at startup; whereas, the actual pressure was transient and required approximately 3.5 seconds to reach a steady value.

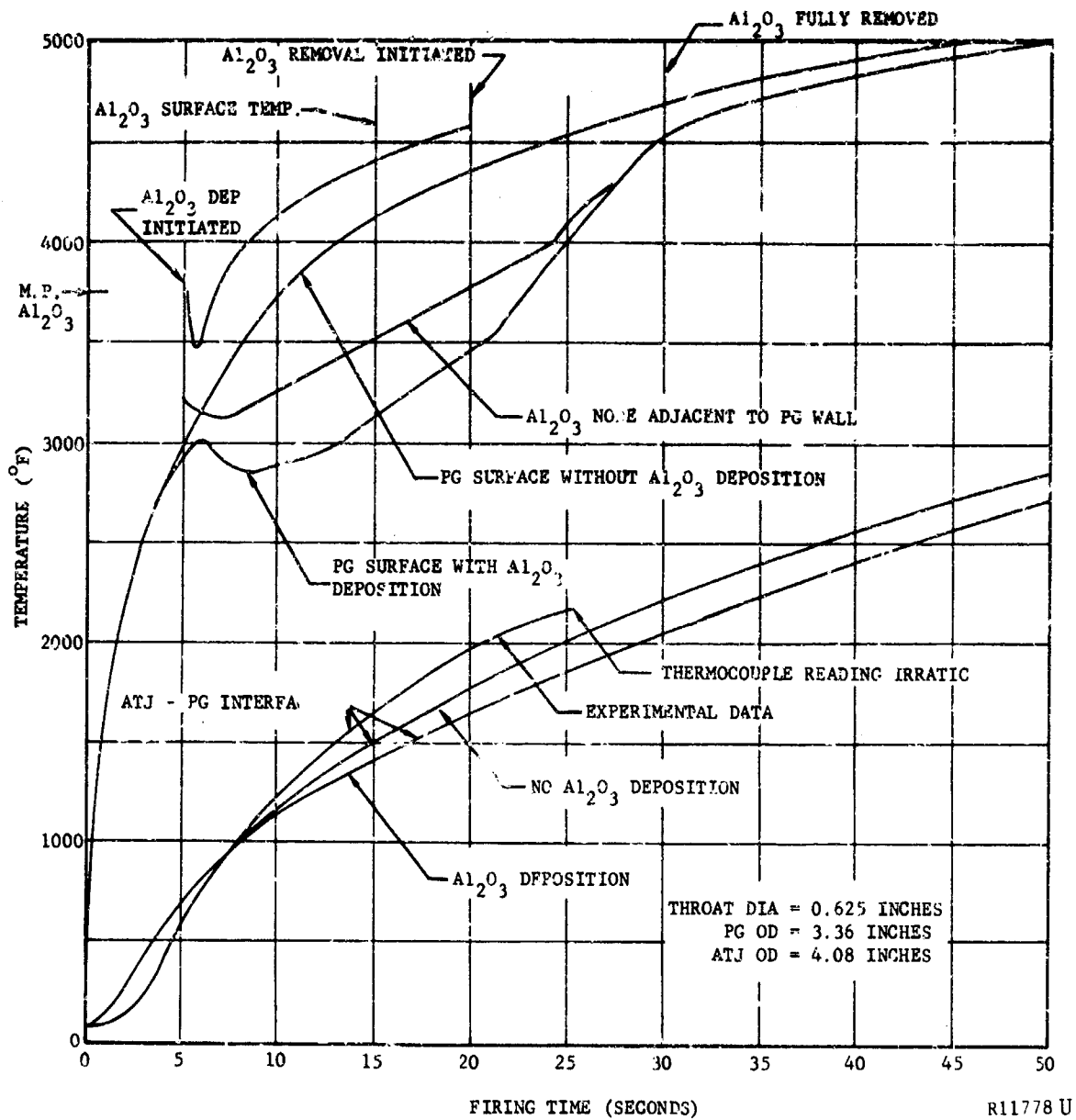


FIGURE 2-6. TEMPERATURE VERSUS TIME WITH AND WITHOUT Al₂O₃ DEPOSITION FOR ROCKET MOTOR TEST 10.

Also shown in Figure 2-6 are the analytical results for the case with no alumina deposition. The difference in surface temperature with and without alumina deposition is pronounced during the times at which alumina is on the wall. With the removal of alumina the surface temperature then approaches the no alumina case. The reason for the decrease in surface temperature after alumina deposition is initiated is due to the reduction in heat input to the wall by the alumina. That is, the heat conducted away from the surface to the internal material is greater than the heat input from the alumina layer and will result in a lowering of the surface temperature.

The effect of alumina deposition on the transient temperature response of rocket motor heat sink material is significant as shown in Figure 2-6. Therefore, in performing thermal calculations without including the effect of deposition, the predicted heat sink temperature levels will be conservative during the time the deposit is present (the conservatism will of course depend on the deposit thickness). Since an analytical solution of the deposition phenomena does not exist an alternate approach was undertaken in this program. It was found, for all practical purposes, that the heat absorbed in the motor firings of this program (in which deposition did occur) compared reasonably well to the analytical prediction (the analysis of which did not include deposition) if the modified Bartz correlation was employed in predicting the convective boundary condition. This conclusion is evident in Figure 8-31 of Section 8.

b. Internal Ablation. The ablation experienced in the heat sink backup materials (reinforced plastics) during the firing period has been analyzed and found to be unimportant during this period. Figure 8-31 presents a correlation between experimentally obtained temperatures and two analytical predictions, one considering backup material ablation and the other considering only heat conduction to the backup material (no ablation). Although this type of correlation is approximate, i.e., dependent on the deposition phenomena, it does indicate the relative importance of ablation. The predicted backwall temperature (considering ablation) is approximately 100°F less than the measured value at the time of shutdown as Figure 8-31 indicates. After shutdown, the measured backwall temperature undergoes a large decrease in temperature instead of a rise as predicted in both analytical predictions. This indicates that during firing, the heat absorbed by ablation was negligible in the backup material. Due to the high chamber pressure and slope of the pressure curve (increasing with time) the pyrolysis gas leaving the char layer was very small (gas stored in char). At shutdown, the large decrease in chamber pressure caused the pyrolysis gas flow to increase, thereby cooling the ablator char and the heat sink backwall. After the pyrolysis gas stored in the char during firing was depleted, the backwall temperature rises due to heat sink equilibration. This backwall temperature behavior was evident on all pyrolytic graphite inserts that underwent a long continuous firing (backwall temperature reaching a level at which ablation is initiated).

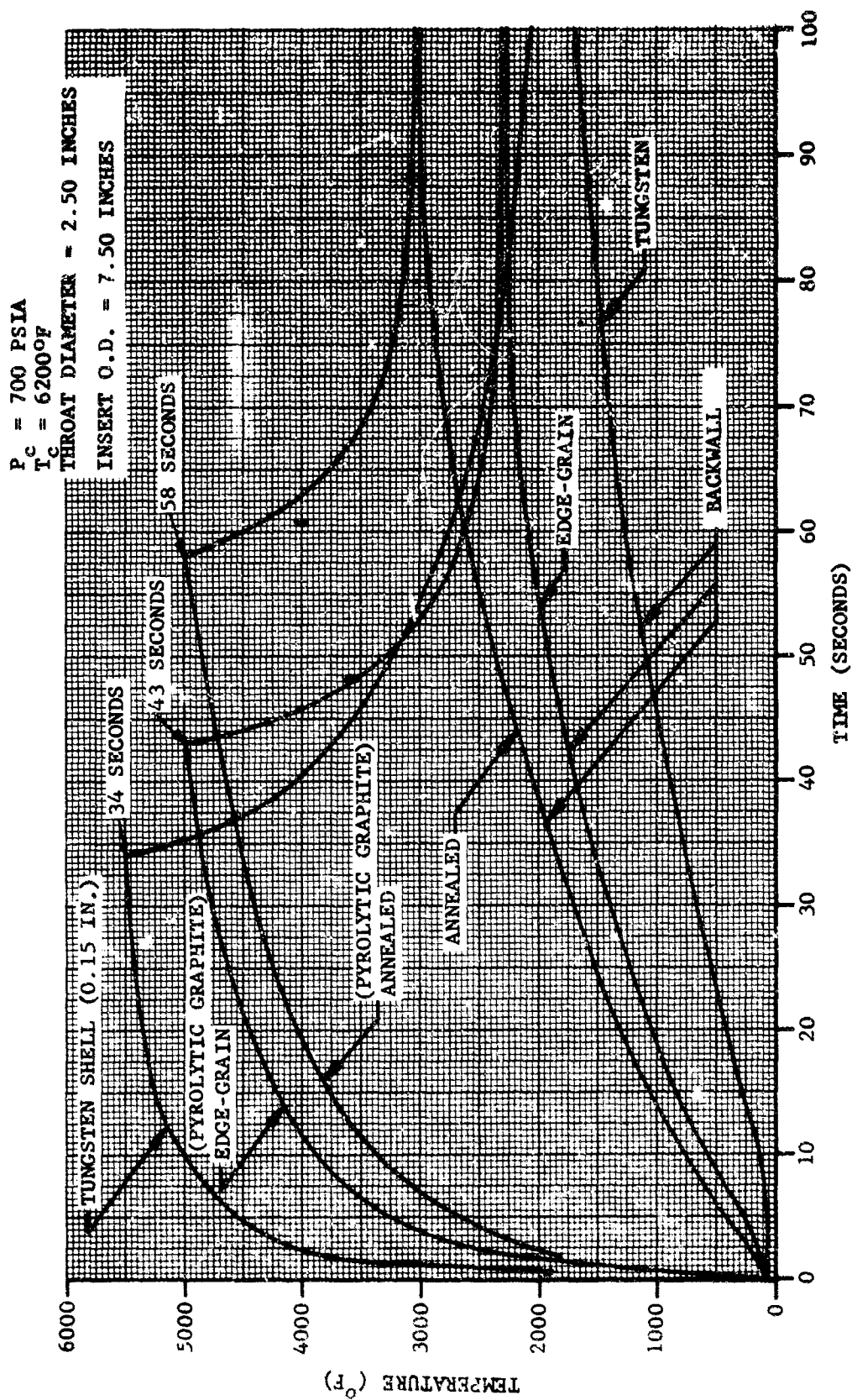
c. Temperature Profiles. As was mentioned in Paragraph 2.4.2a, the presence of alumina deposition will strongly affect the temperature profiles of a rocket nozzle during firing. Therefore, to fulfill the objectives of this contract, the thermal analysis which does not consider deposition, was applied to the nozzle configurations of Table 2.2 to predict such thermal characteristics as the heat absorbed during firing and the firing time required to reach the maximum design temperature (these characteristics are presented in Paragraph 2.4.4). The heat sink temperature distributions obtained from these calculations are conservative regarding temperature level and radial temperature gradient during the time an appreciable amount of deposit exists. During the time before deposition is initiated and the time after the deposit is removed, the surface temperature level may be considered accurate as is evident in Figure 2-6.

Figures 2-7 and 2-8 are examples of the throat surface temperature histories that were determined in this program. Empirical equations of the temperature response during the firing and equilibration periods were determined for the inserts of Figures 2-7 and 2-8 and are presented in Table 2.3. In comparing the various insert materials of Figures 2-7 and 2-8, the effect of insert thermal conductivity on the time required to reach the maximum design temperature (5000°F for P.G. and 5500°F for tungsten) is evident. The tungsten shell-ATJ graphite insert is inhibited by the low thermal conductivity of ATJ; whereas annealing pyrolytic graphite is shown to be beneficial. Also, the equilibration time is shorter for the annealed P.G. insert than the as-deposited P.G. or tungsten inserts.

2.4.3 SOAK PERIOD

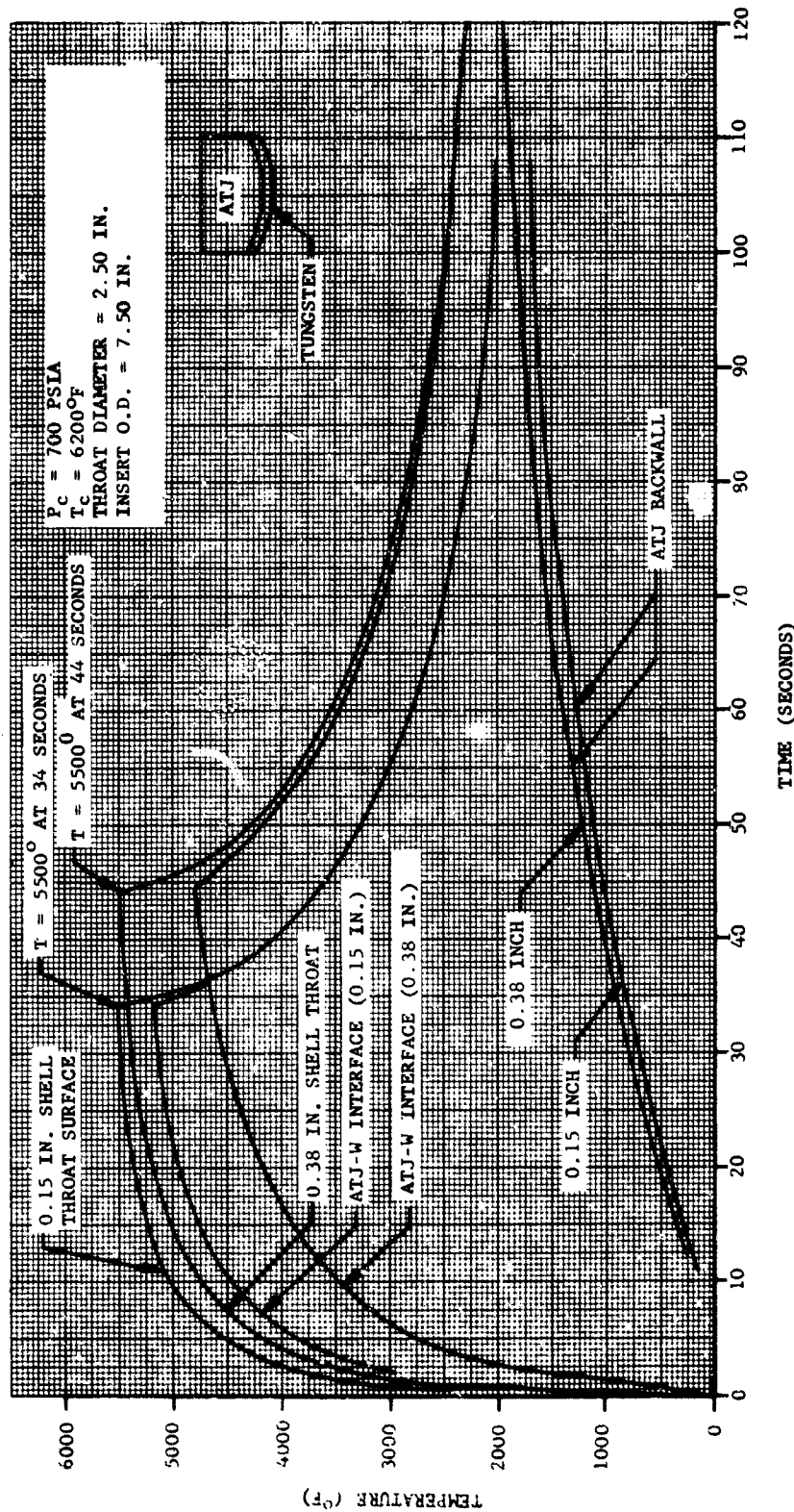
One of the parameters that determine the ability or capability of a rocket motor to refire is amount of heat that has been dissipated during the cool-down period. To determine the heat dissipated in the critical regions of a nozzle; i.e., entrance, throat, and exit; requires definition of the important modes of heat transfer that prevail during this period. The heat transfer modes studied and defined in this contract have been presented in Table 2.1 and are discussed below.

a. Convective Heat Transfer. During soak back, the rocket motor's free stream is composed primarily of the pyrolysis products that result from material thermal and chemical degradation. The heat exchanged between the free stream pyrolysis products and the motor flamefront surfaces will depend on the pyrolysis mass flow, free stream temperature, and motor surface temperature. However, since the pyrolysis gas is being injected along the total axial distance of the motor (for the motors studied in this program the heat sink materials employed in the entrance, throat, and exit sections were insulated with asbestos phenolic) the pyrolysis mass flow and free stream temperature will vary with axial position. Therefore, depending on (1) the axial temperature gradient of the flamefront surface,



RO9623 U

FIGURE 2-7. MATERIALS COMPARISON PLOT OF SURFACE TEMPERATURE -
TIME PROFILE AT THROAT



RO9609 U

FIGURE 2-8. TEMPERATURE - TIME PROFILE AT THROAT SECTION FOR TUNGSTEN SHELL BACKED WITH ATJ GRAPHITE

TABLE 2.3

EMPIRICAL EQUATIONS OF THROAT
THERMAL RESPONSE DURING FIRING AND EQUILIBRATION
PERIODS (NOZZLE CONFIGURATIONS OF FIGURES
2-7 AND 2-8)

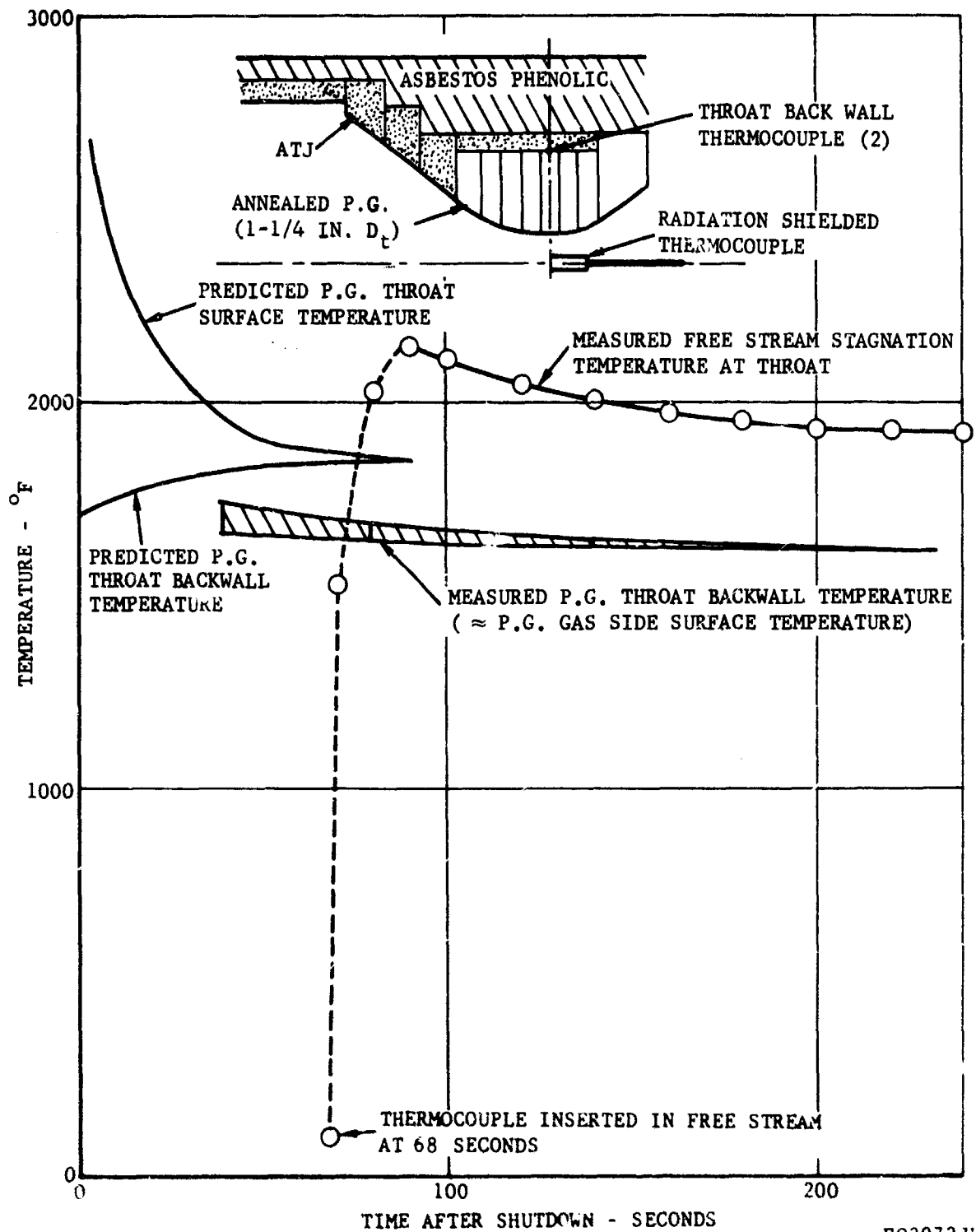
<u>Nozzle</u>	<u>Period</u>	<u>Empirical Equation</u>
As-Deposited Pyrolytic Graphite	Firing	$T = \frac{(6.54t^{1/3} - 1.368t^{1/2} - 3.43t^{1/2})10^3 + 70}{(r/r_o)^{6.8t - 0.505}}$
	Equilibration ($r=r_o$ only)	$T = (5.0 + 2.52t^{1/2} - 12.2t^{1/3} + 9.22t^{1/4})10^3$
Annealed Pyrolytic Graphite	Firing	$T = \frac{(-1.77t^{1/2} + 8.76t^{1/3} - 5.6t^{1/4})10^3 + 70}{(r/r_o)^{6.8t - 0.505}}$
	Equilibration ($r=r_o$ only)	$T = (5.0 + 2.58t^{1/2} - 12.6t^{1/3} + 9.34t^{1/4})10^3$
Tungsten Shell Backed with ATJ Graphite	Firing ($r=r_o$ only)	
	0.15 inch shell	$T = (-1.75t^{1/2} + 4.38t^{1/3} + 0.566t^{1/4})10^3 + 70$
	0.38 inch shell	$T = (-1.87t^{1/2} + 6.36t^{1/3} - 1.758t^{1/4})10^3 + 70$
	Equilibration ($r=r_o$ only)	
	0.15 inch shell	$T = (5.5 + 1.20t^{1/2} - 7.12t^{1/3} + 5.44t^{1/4})10^3$
	0.38 inch shell	$T = (5.5 + 0.747t^{1/2} - 5.08t^{1/3} + 5.71t^{1/4})10^3$

(2) the local pyrolysis gas injection rate, and (3) the degree of thermal equilibrium between the local pyrolysis gas and corresponding surface; a flamefront surface may be heated or cooled by the pyrolysis gas free stream.

In this program the amount of heat transferred between the pyrolysis gas and a nozzle throat was determined in development nozzle firing number D-1. The throat insert employed in this firing consisted of annealed P.G. washers backed with ATJ. Two thermocouples were placed on the backside of the throat washer and a radiation shielded thermocouple was inserted in the free stream at the throat axial position 68 seconds after shutdown. The resulting gas stagnation temperature and P.G. backwall temperature are shown in Figure 2-9. By comparing the two temperatures at times greater than the equilibration time the temperature difference between the P.G. surface and pyrolysis gas can be determined (i.e., backwall P.G. temperature - P.G. surface temperature at soakback times greater than the time to reach washer equilibration). From Figure 2-9 it can be seen that the P.G. insert will be heated by the pyrolysis free stream. At 160 seconds after shutdown, the convective heat flux incident on the throat washer (0.5 inch wide) was calculated using the measured temperature difference (340°F), the chamber pressure at 150 seconds (20 psia), and a convective pipe flow analysis (see Reference B.3) to be 0.03 Btu/second. Using the P.G. backwall thermocouple response at 160 seconds, the net heat dissipated from the throat washer is calculated to be 0.24 Btu/second ($q = \rho c v dT/dt$; where ρv is mass of throat washer, c is P.G. specific heat, and dT/dt is temperature slope). The heat added by pyrolysis gas convection is therefore an order of magnitude less than the net heat dissipated by the other heat transfer mechanisms present during soakback. For comparison, the predicted surface and backwall temperature of the throat washer is shown in Figure 2-9. The difference in the predicted and the measured temperature may be attributed to the conservative convective heat transfer coefficient used in the thermal analysis.

Since the pyrolysis gas in the free stream at the throat location is produced by ablation in the chamber liner, aft closure, and nozzle entrance, the soakback convective heat flux to or from the surfaces at these locations will be considerably less than at the throat. That is, as the pyrolysis gas leaves the gas side surface and enters the free stream after a high degree of thermal equilibrium has been obtained between the gas and surface, the temperature difference between the pyrolysis gas free stream and gas side surface at a specific location will depend largely on the upstream surface temperatures.

As is evident from the above discussion, the magnitude of soakback convective heat flux will depend largely on the materials employed in the rocket motor as gas side surfaces and backup insulators and their respective thickness. For the rocket motor described above (annealed P.G. throat), the chamber liner and entrance section consisted of ATJ graphite backed with asbestos phenolic. During the equilibration period, the P.G. washer



FO2972 U

FIGURE 2-9. FREE STREAM STAGNATION TEMPERATURE DURING SOAK PERIOD AFTER 20 SEC FIRING

throat insert equilibrates to a lower temperature than will the ATJ entrance and chamber heat sink. Therefore, the greatest temperature difference between the pyrolysis gas free stream and the gas side surface will occur at the throat insert. However, if a thin tungsten shell backed with ATJ graphite is employed for the insert in the above motor, the equilibration temperature response of the insert (Figure 2-7) will cause a significant decrease in soakback convection. Employing a gas side ablator in the chamber and entrance section would reduce both the pyrolysis gas temperature and mass flow during the equilibration period (i.e., heat dissipated by ablation during equilibration would consist primarily of heat stored in char rather than the heat stored in the graphite heat sink material).

b. Radiative Heat Transfer. During soakback, radiative energy exchange will occur between the surfaces of the rocket components (inside surface radiation), between these surfaces and the ambient environment, and between these surfaces and the pyrolysis products. The amount of heat exchange between the rocket motor inside surfaces and the pyrolysis products will depend on the amount of carbon precipitation experienced as the gases flow along the nozzle contour. The mechanism and parameters involved in this mode of radiative heat transfer is discussed in Appendix B. In Appendix B it is found that the amount of heat involved in this mode of radiation is negligible compared with the other heat transfer mechanisms.

The radiative exchanges between the inner surfaces of the rocket motors and between these surfaces and the ambient were found to depend on the gas side material and the exit area ratio. The importance of these modes of radiative heat transfer were determined by applying the radiation analyses of Appendix B to the 2.5-inch and 1.25-inch throat diameter - P.G. insert nozzles of Table 2.2. Figures 2-10 and 2-11 are comparison plots of the thermal response for the 2.5-inch diameter motor geometries considered. The effect of radiation on exit cone cooling can be seen by comparing the conduction only and radiation plus conduction curves (Figure 2-10). Conduction will radially equilibrate the exit cone heat sink to an isothermal condition and permit some axial energy interchange. Radiation interchange will increase the axial energy transfer and permit axial thermal equilibration at an increased rate. Utilizing carbon cloth phenolic instead of ATJ at $\epsilon > 9$ will result in a decrease in surface temperature during cooling. This decrease is attributed to the fact that only a small amount of energy is absorbed by carbon cloth phenolic during firing (i.e., carbon cloth phenolic will have a high surface temperature due to its low thermal conductivity, causing less input energy). The effect of exit area ratio on radiation cooling is shown in Figure 2-11. The effective shape factor between surface and space is increased with small exit area ratios thus increasing radiative cooling. This figure also gives an indication of the difference in radiation cooling at sea level ($\epsilon_{\text{exit}} < 9$) and space conditions ($\epsilon_{\text{exit}} \geq 40$).

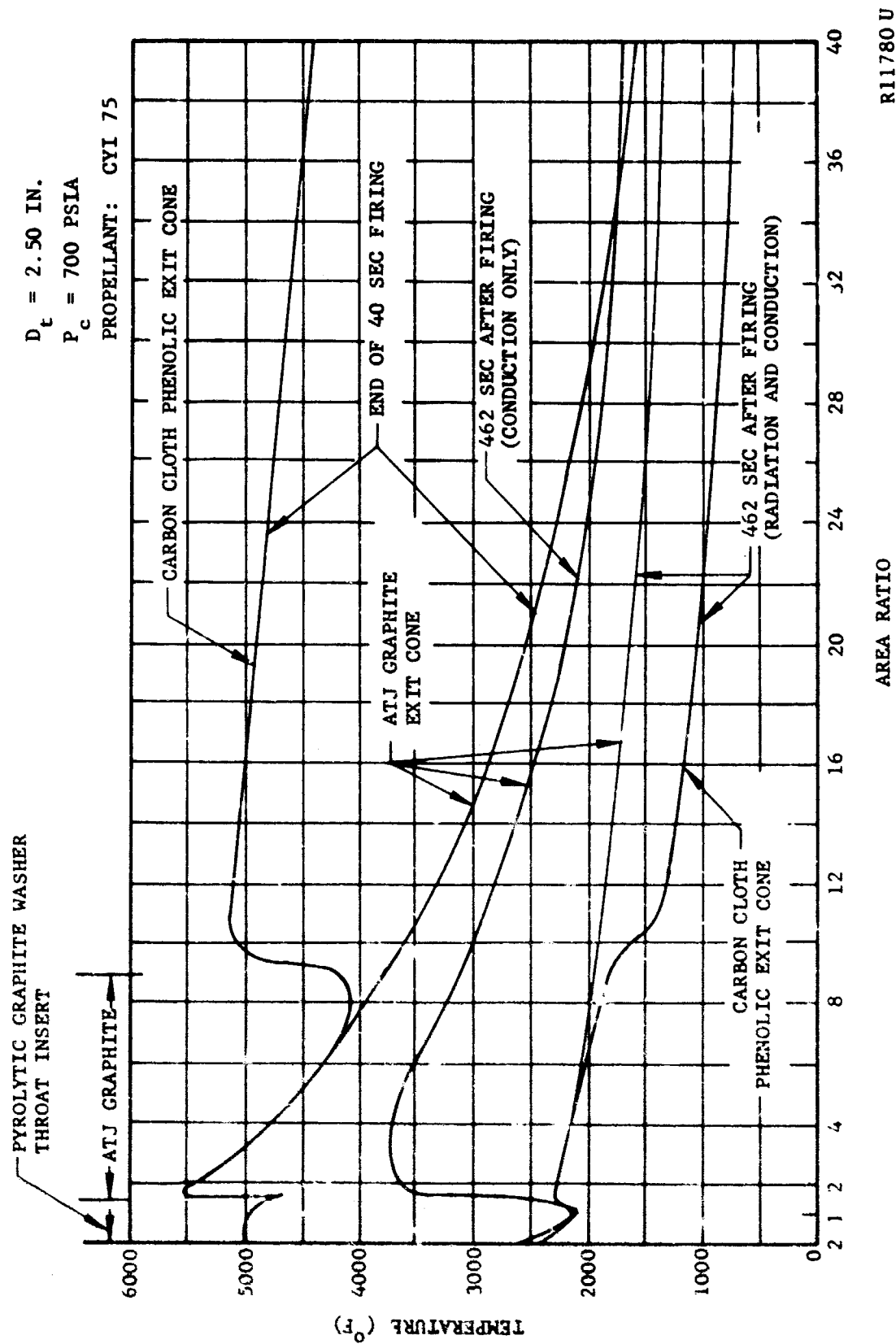


FIGURE 2-10. NOZZLE SURFACE TEMPERATURE DISTRIBUTION AFTER SHUTDOWN

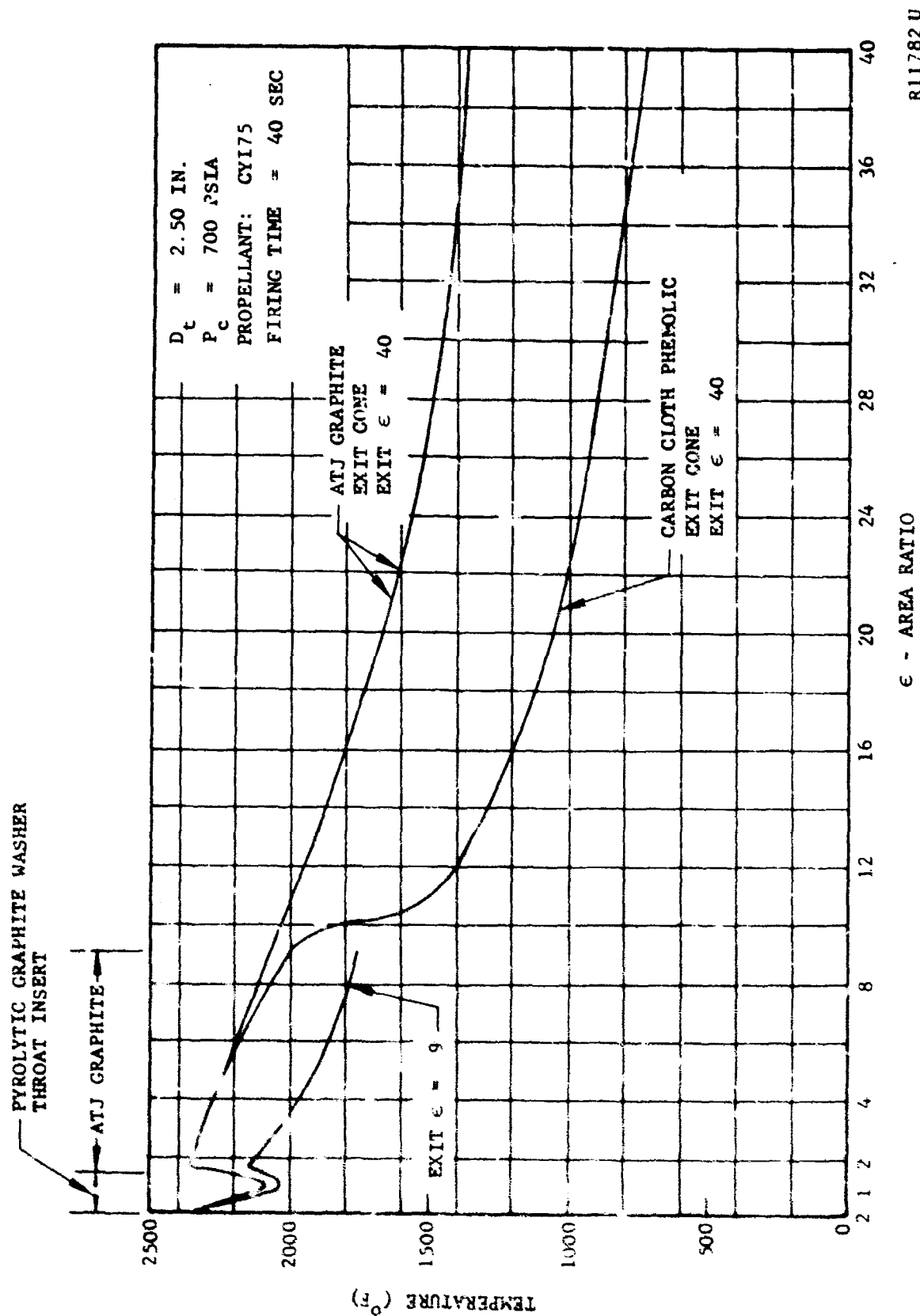


FIGURE 2-11. NOZZLE SURFACE TEMPERATURE DISTRIBUTION WITH RADIATION AND CONDUCTION COOL DOWN AT 396 SECONDS AFTER SHUTDOWN

The heat dissipated or added by radiation to the throat insert for the nozzles of Figures 2-10 and 2-11 are shown in Figure 2-12. For an exit area ratio of 9, the radiation interchange between the throat and adjacent exit and entrance section surfaces and the energy lost from the throat insert to space via the exit cone cancel at early times after firing to produce no change in insert heat content. As the exit and entrance section cool, the throat insert will experience some radiation cooling. As the time after firing increases, the temperature level of the insert will decrease, thereby decreasing radiation cooldown. An exit area ratio of 40 will substantially alter throat insert radiation cooling, as indicated in Figure 2-12. This is attributed to the decrease in effective shape factor between the insert surface and space. After firing, the pyrolytic graphite insert will equilibrate to a lower temperature level than the adjacent exit and entrance section surfaces due to the large difference in material thermal conductivity. This temperature difference will then induce radiation heating of the pyrolytic graphite throat; the amount of which will decrease with time.

The results obtained from the 1.25-inch nozzle calculations are shown in Figure 2-13. In applying the thermal analysis to this nozzle it was desired to determine the effect of P.G. a-b direction orientation on nozzle heating and cooling. The a-b plane of pyrolytic graphite was aligned parallel (wedge) and perpendicular (washer) to the nozzle axis. Both insert designs occupied the same volume. The thermal difference which may exist with the wedge design in conducting energy out of the entrance and throat regions to the exit cone (where it is lost by radiation to space) can then be determined. By increasing the energy dissipation by radiation, the insulation thicknesses required by the ablative backups are decreased. Figure 2-13 presents the results of the thermal analysis as a comparison in surface temperature for the two throat insert designs. From Figure 2-13 the washer design will reach a temperature 200°F below that of the wedge in the throat region after firing. This is attributed to heat sink usage. Due to the low thermal conductivity of pyrolytic graphite in the c-direction, heat will primarily be conducted radially in the washer design, whereas in the wedge design, heat conduction will be in both the radial and axial directions. Since the heat incident at a particular axial location may be conducted both axially and radially in the wedge design, the heat sink at this location may be at a higher energy level than that obtained in a washer design. For the type of heat fluxes resulting from an aluminized cloud, the point of maximum heat flux is significantly upstream of the throat. Therefore, the wedge design at locations downstream of the throat will obtain higher surface and backwall temperatures than that of a washer design. The decrease in surface temperature at the axial location of 3 inches is caused by the presence of pyrolytic graphite in a region of low heat flux. Radiation heating increases in the upstream direction from the throat and convection decreases; the net effect is a reduction in total energy incident at the surface. The presence of a low thermal conductivity material such as ATJ in the entrance section will result in sufficiently high surface temperatures, thus accounting for the thermal discontinuity at the ATJ-PG

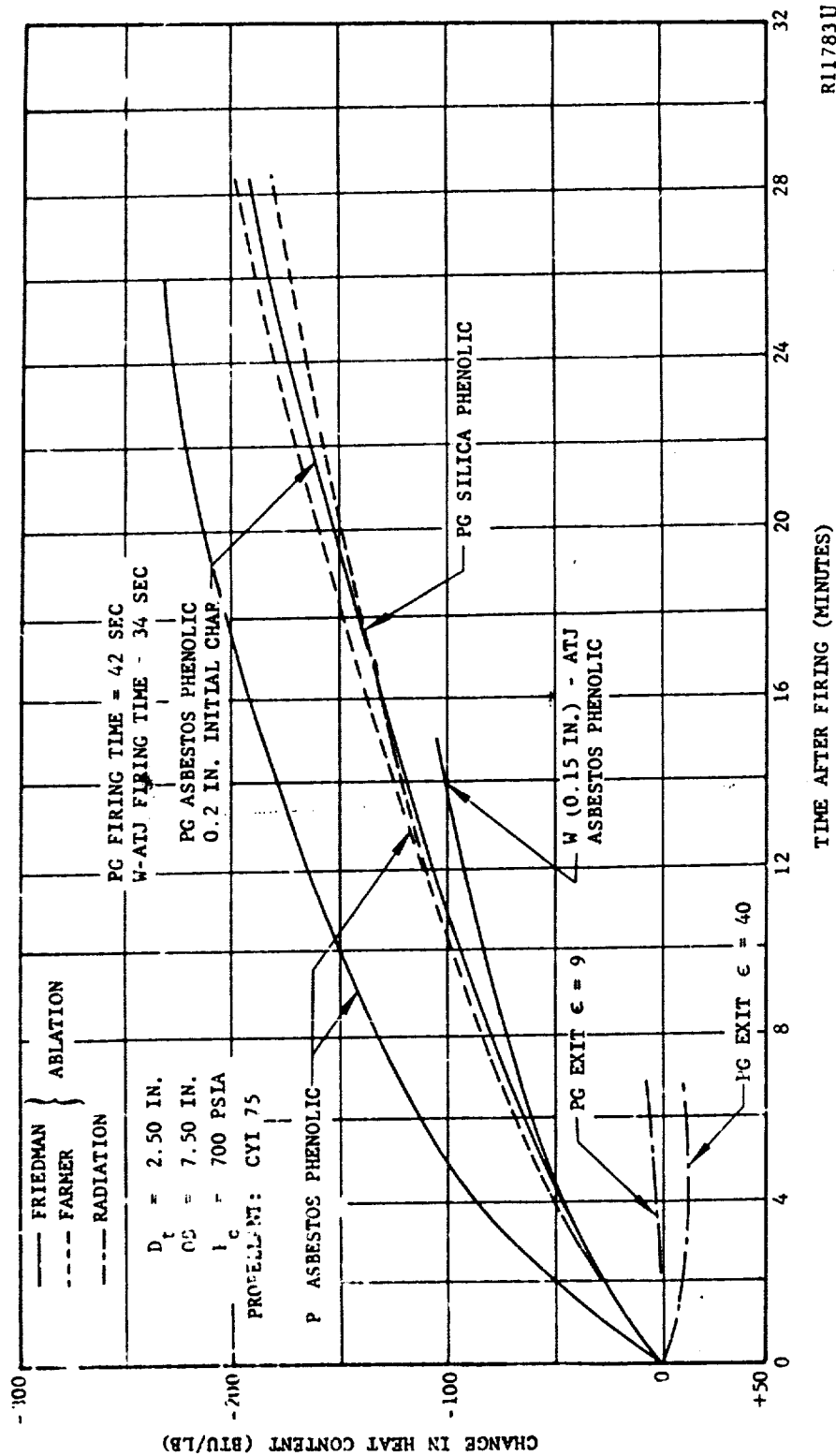


FIGURE 2-12. CHANGE IN HEAT CONTENT FOR THROAT INSERT DUE TO ABLATION AND RADIATION

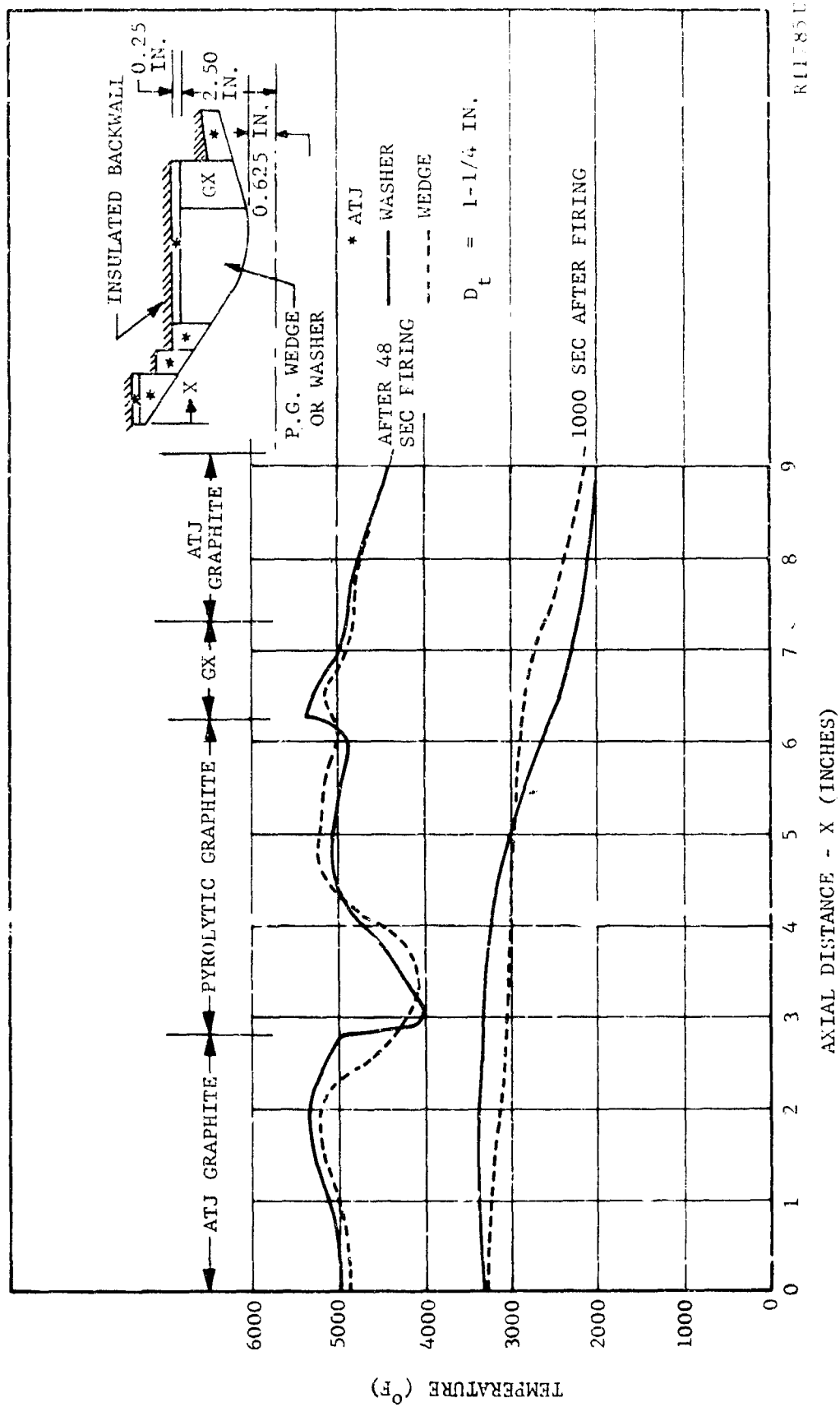


FIGURE 2-13. COMPARISON OF WEDGE AND WASHER PYROLYTIC GRAPHITE THROAT INSERT

interface ($x = 2.8$ inches). The advantage of the wedge design in radiation cooling is not significant in the throat region. The energy conducted from the entrance section to the exit cone via the wedge insert will produce (approximately) a 260°F cooler entrance than the washer. However, if a carbon or graphite cloth phenolic entrance section is employed, the axial conduction will be eliminated and the advantage of the wedge in the entrance section will be lost.

c. Ablation. The heat absorbed during firing has been found to be dissipated almost entirely by ablation for the rocket motor configurations studied in this program. Because of this observation, a significant portion of the thermal effort has been devoted to the ablation phenomena. The behavior of the ablation phenomena during firing and soak has been analytically investigated using the conduction-ablation program presented in Appendix C. This program will predict the ablation characteristics of reinforced plastics that are employed as heat sink backup insulators and gas side materials. However, in this contract, the conduction-ablation program was limited in its ability to accurately predict the ablation characteristics experienced in stop-start nozzles. This limitation was imposed by a lack of ablation property data for the reinforced plastics studied in this contract. The property data that were found to be very important in the ablation phenomena and also require further laboratory investigation consist of:

- (1) Char thermal conductivity (variation with density and temperature).
- (2) Char density as encountered in rocket motor (variable during ablation process due to coking experienced between the carbon saturated pyrolysis gas and char).
- (3) Pyrolysis gas enthalpy above 2000°F.
- (4) Reaction rates and energies involved in chemical reactions that occur between carbonaceous char and reinforcement material (silica-carbon reaction).
- (5) Pyrolysis rate law (decomposition rate) of plastic under variable heating conditions.

The application of the ablation analysis has been twofold: (1) a study of the importance of ablation in throat insert cooldown, and (2) the application of various backup materials for a throat insert insulation investigation. In the material investigation, the throat insert material was pyrolytic graphite backed with (1) asbestos phenolic, (2) silica phenolic, (3) castable carbon (a product of Atlantic Research Corporation), and (4) pyrolytic graphite insulator backed with asbestos phenolic. The Friedman pyrolysis rate law ($n = 5$) was selected for all materials (see Appendix C).

The radial temperature profiles for asbestos phenolic and pyrolytic graphite-asbestos phenolic backup are shown in Figures 2-14 and 2-15, respectively. The nozzle was fired for 43 seconds and then the insert was allowed to equilibrate, at which time the free stream surface is assumed insulated (no radiation cooldown). In Figure 2-16 the thermal history of the pyrolytic graphite insert-backup material interface is shown for various backup materials. Figure 2-16 may also be said to represent the thermal history for the total throat washer because, as Figures 2-7 and 2-8 indicate, the throat washer is isothermal after 100 seconds from firing. The decomposition of the ablating nodes is shown in Figure 2-17 for the ablative materials of Figure 2-16.

The insulating and ablative cooling properties of pyrolytic graphite shell and asbestos phenolic are found to exceed all other material configurations studied (Figure 2-16). This is attributed to the fact that the pyrolytic graphite backup (1) provides additional heat capacity to the throat insert and (2) when compared to asbestos phenolic without pyrolytic graphite, insulates the throat insert from the ablator, thus causing ablation to be delayed (approximately 35 seconds) and to proceed at a slower rate. Asbestos phenolic is found to be superior to silica from a thermal standpoint as indicated by (1) the slower pyrolysis rate (Figure 2-17) and (2) the greater cooling properties (Figure 2-16). The cooling properties of asbestos exceed silica due to (1) lower thermal conductivity of char and virgin material and (2) lower char density (i.e., greater heat capacity per pound of resin due to the greater percentage of pyrolysis products formed). The moldable carbon insulator, which behaves as a heat sink, is not too much different than the ablators in affecting the thermal history of the throat insert.

In studying the effect of initial char thickness on ablation rate, the 2.5-inch nozzle was fired from ambient with an initial asbestos phenolic char thickness of 0.20 inch, the influence of which is shown in Figure 2-16. The char is found to act similar to that of the cast carbon backup insulator except at times approaching 700 seconds. At this time, Figure 2-17 indicates ablation is initiated with the cooling mechanism of ablation influencing the thermal history of the throat insert. Therefore, when a motor is started from ambient with an initial char, the char will act as an additional heat sink and delay the initiation of virgin plastic degradation. This degradation rate will proceed at a much slower rate than the zero initial char case. The initial char thickness will also result in a more efficient usage of the degradation material than the zero char case in dissipating heat since the pyrolysis products transpire through a larger char thickness thus absorbing more heat. The effect of initial temperature level on the ablation phenomena (Figure 2-18) was obtained by refiring the 1.25-inch nozzle after a 100 second soak. The increase in heat sink energy after the second firing will cause only a slight change in ablation rate. This is due to the initial char thickness prior to the second firing.

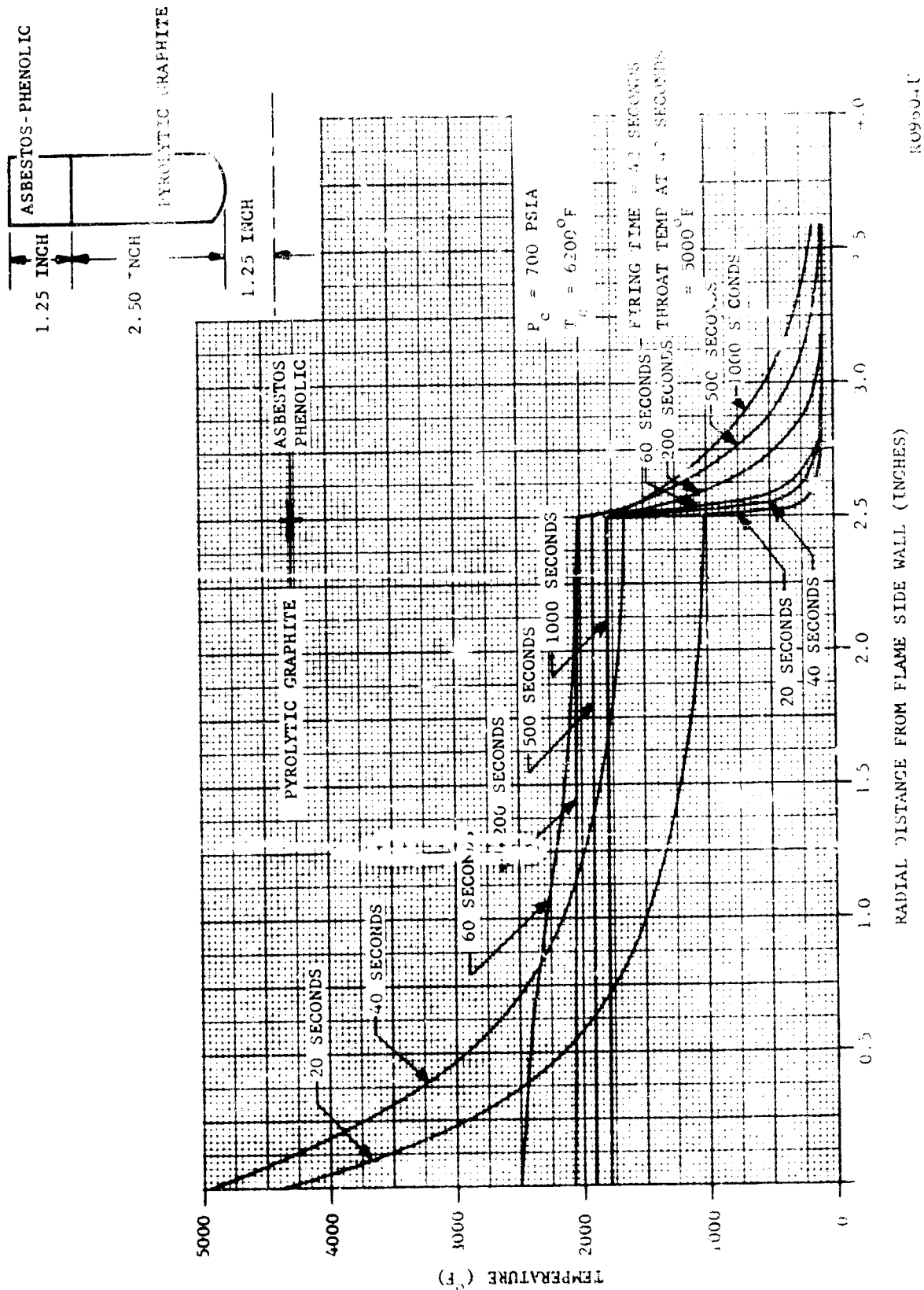


FIGURE 2-14. TEMPERATURE PROFILE FOR PYROLYTIC GRAPHITE THROAT WASHER WITH ASBESTOS PHENOLIC INSULATOR

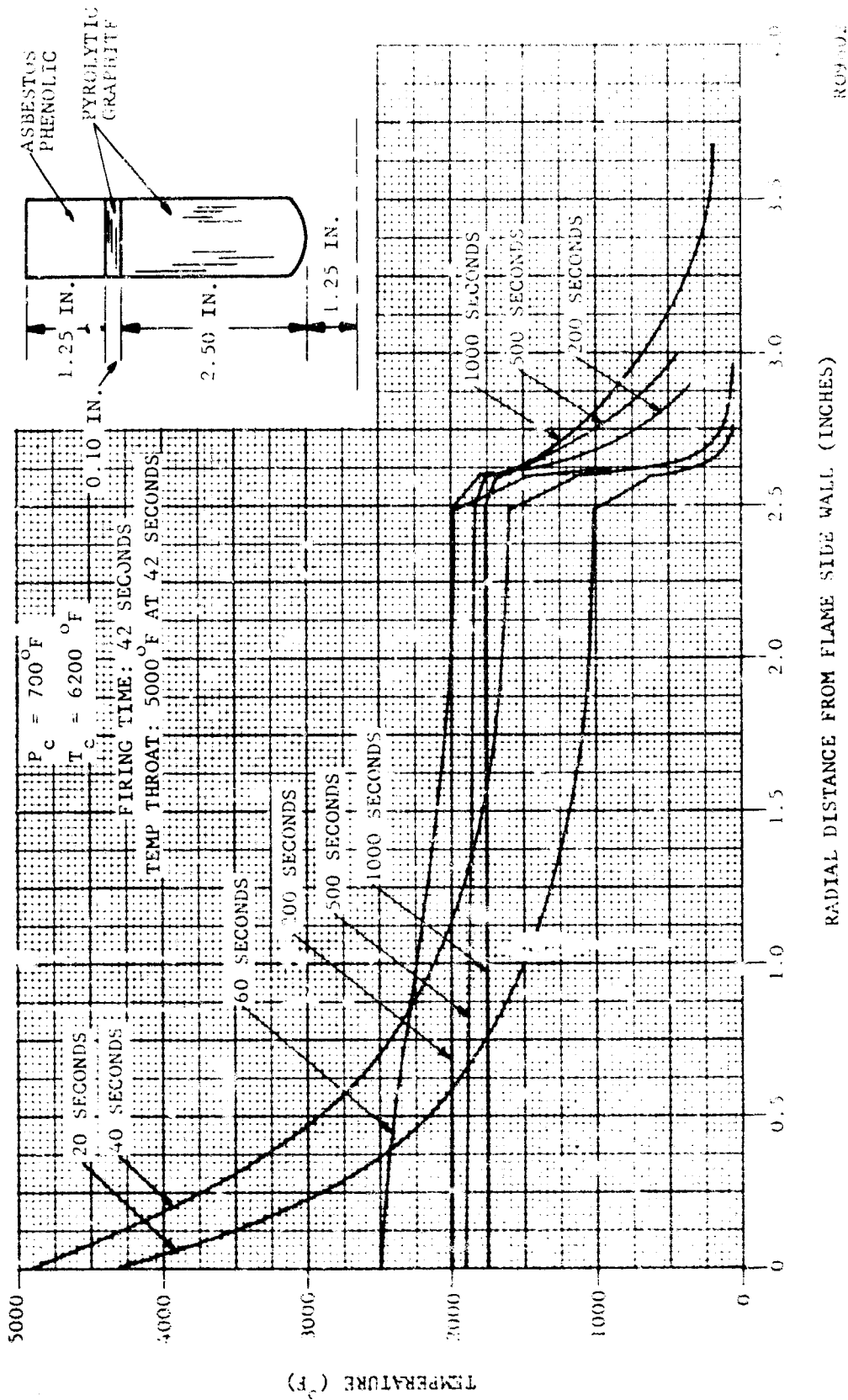
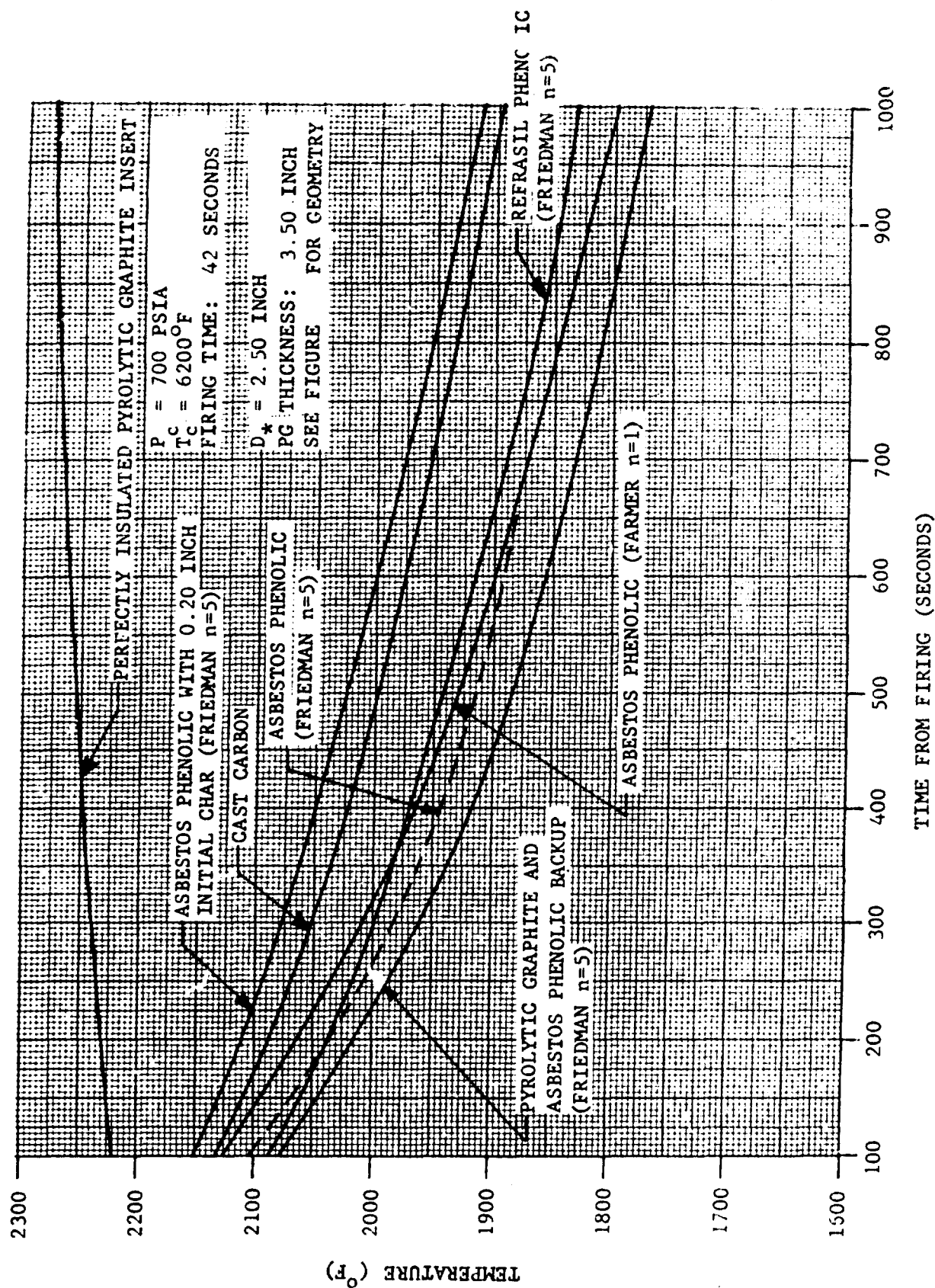


FIGURE 2-13. TEMPERATURE PROFILE FOR PYROLYTIC GRAPHITE THROAT WASHER INSULATED WITH PYROLYTIC GRAPHITE AND ASBESTOS PHENOLIC



RO9605U

FIGURE 2-16. PYROLYTIC GRAPHITE THROAT INSERT THERMAL HISTORY WITH VARIOUS BACKUP INSULATORS

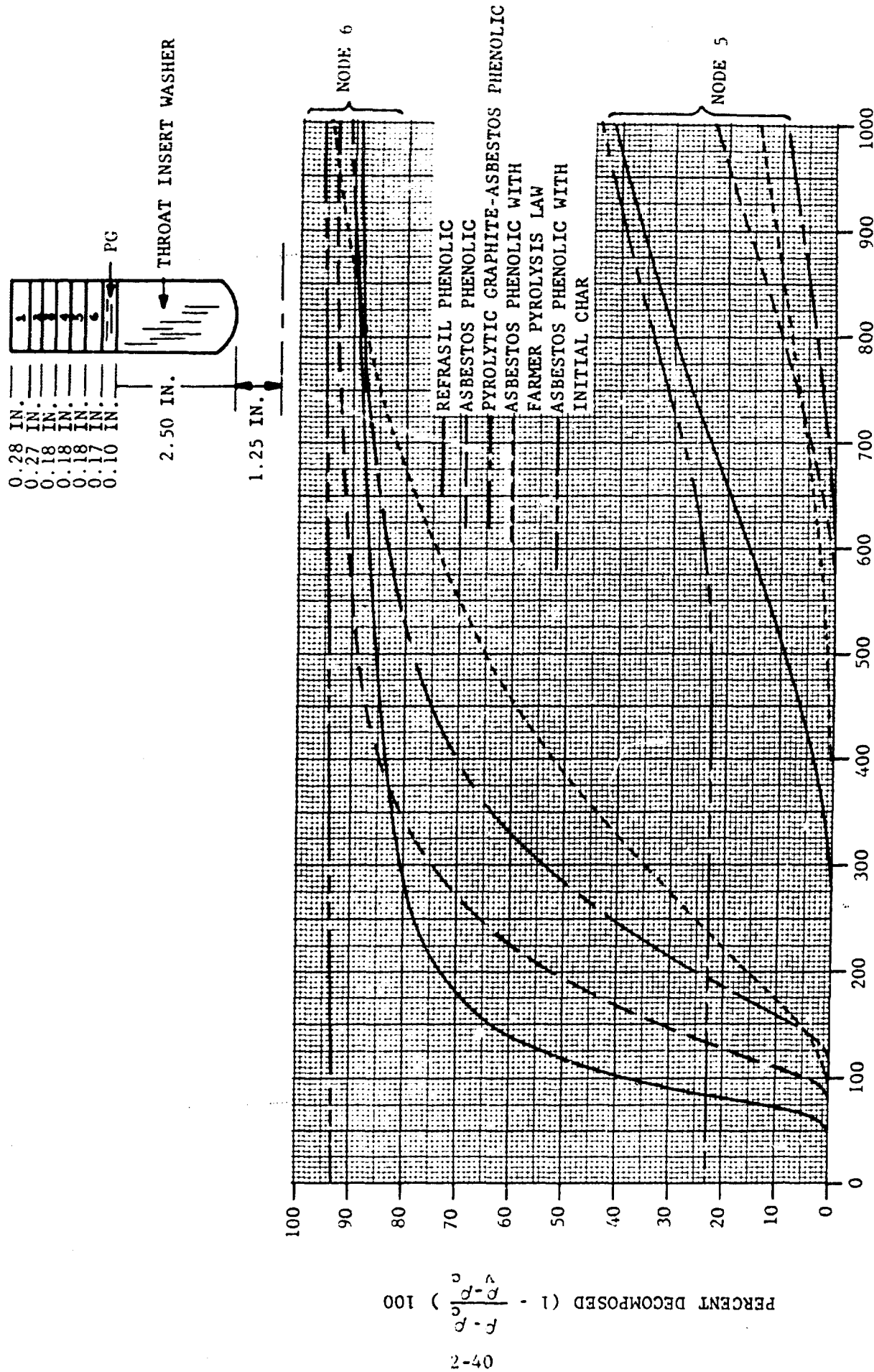


FIGURE 2-17. DECOMPOSITION OF ABLATING NODES

R09603 U

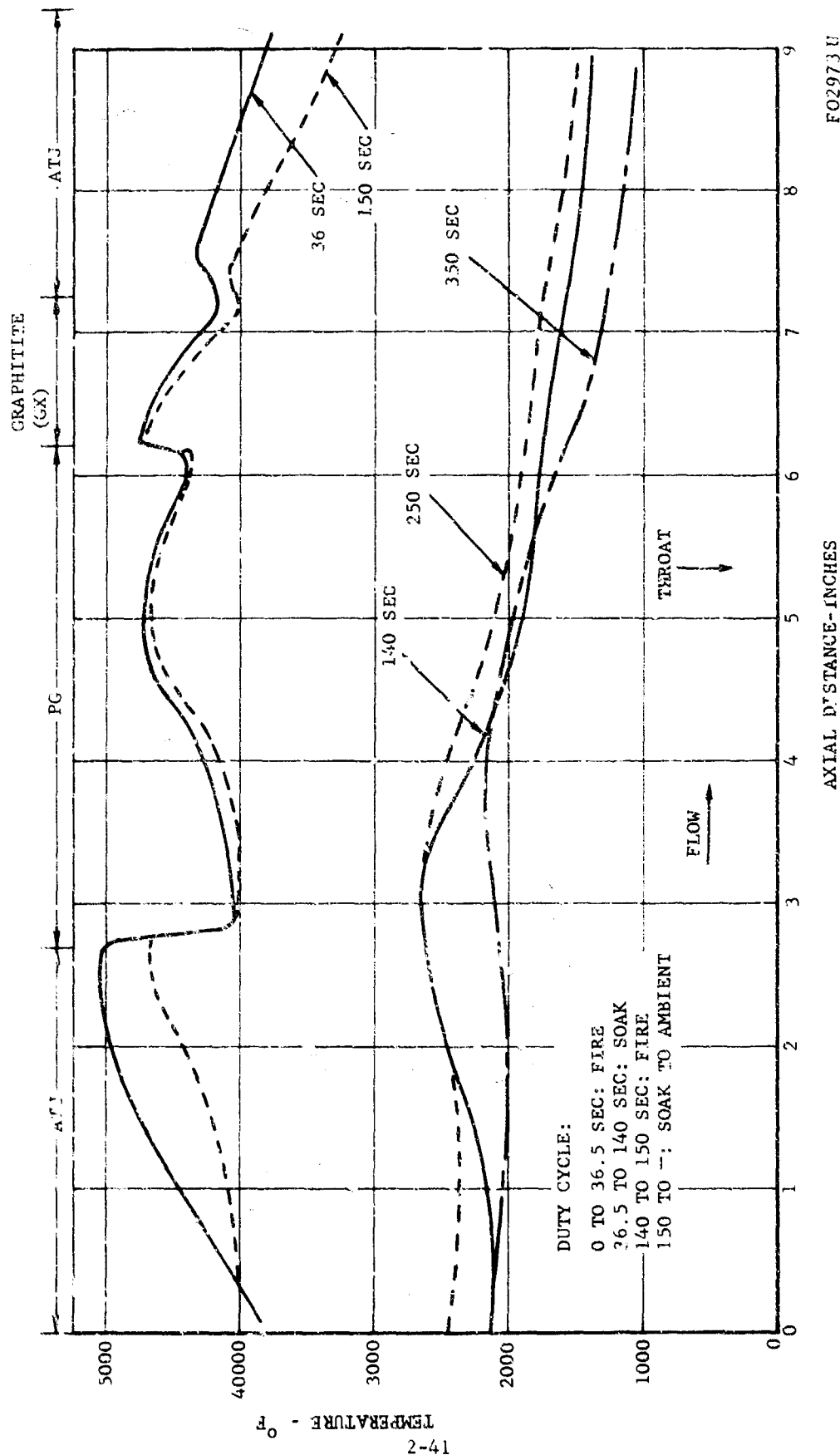
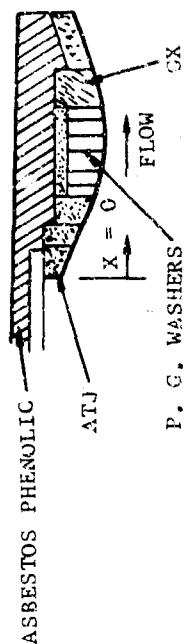


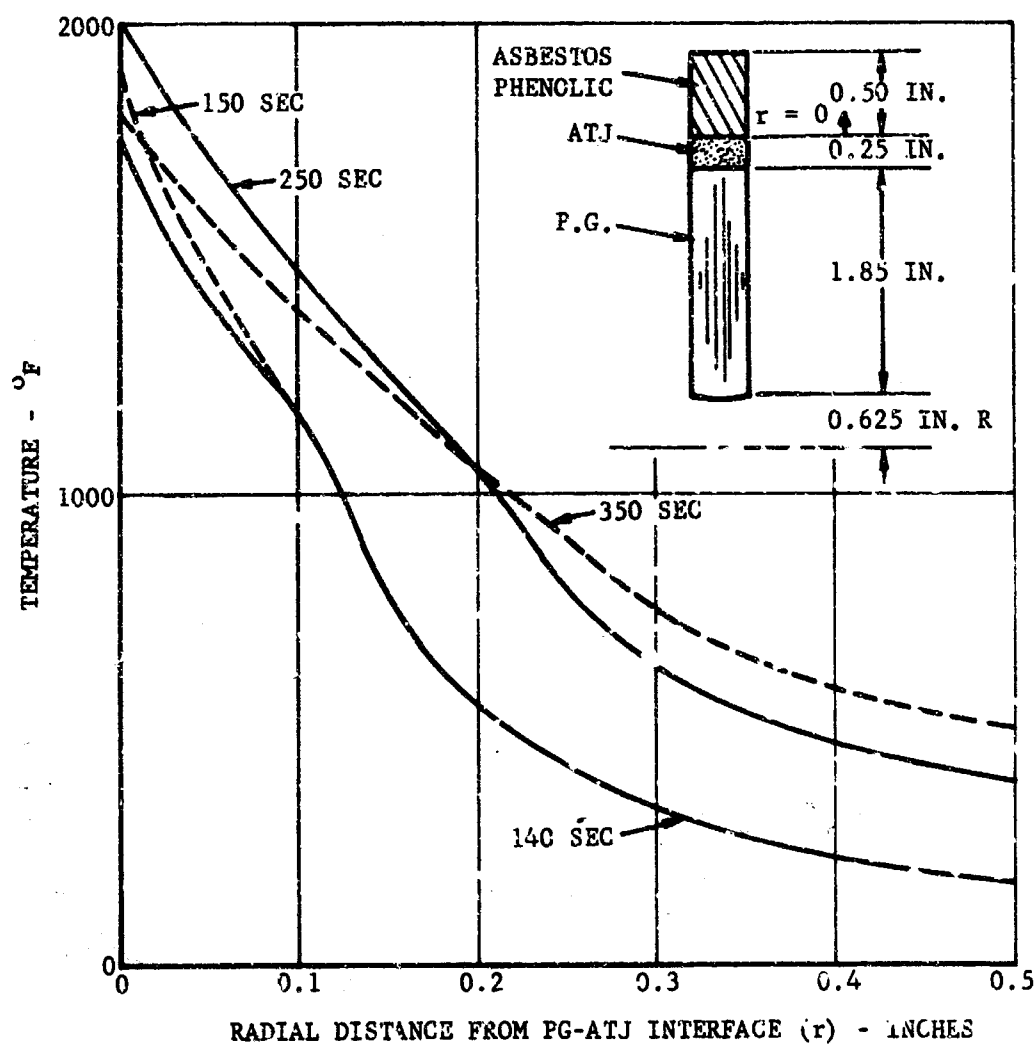
FIGURE 2-18. AXIAL GAS SIDE SURFACE TEMPERATURE PROFILE FOR 1-1/4 IN. AS-DEPOSITED P.G. NOZZLE

The predicted cooldown rates and temperature distributions of the 1.25-inch throat diameter P.G. motor (test D-2) (see Table 2.2) are shown in Figures 2-18, 2-19 and 2-20, respectively. The effect of restart on these ablation characteristics is clearly evident in Figure 2-19, i.e., increase in char temperature level and therefore ablation rate. In Figure 2-19, virgin degradation can be seen to proceed at a high rate in the 900 to 1100°F temperature range (as noted by the change in temperature gradient in this temperature range).

The enthalpy change of the throat washer during the soak period is shown in Figure 2-20 for the 2.5- and 1.25-inch P.G. inserts, respectively. (The ablation characteristics during firing have been discussed in Paragraph 2.4.2.) The effect of initial char thickness and heat sink temperature on the heat dissipated by ablation is shown in Figure 2-21. By comparing the heat dissipated from the throat washer during soakback by (1) radiation (Paragraph 2.4.3b), (2) convection (Paragraph 2.4.3a), and (3) ablation (Figure 2-12), it is concluded that for the nozzles studied in this contract, the heat absorbed by the heat sink materials in the entrance and throat regions during firing is almost solely dissipated by ablation. The radiation and conduction heat transfer mechanisms transport energy to cooler sections of the motor, where the major portion is dissipated by ablation. Table 2.4 and Figure 2-12 are a comparison of the energies dissipated by the various soakback heat transfer mechanisms for the nozzle of Figure 2-19 and Figure 2-10, respectively.

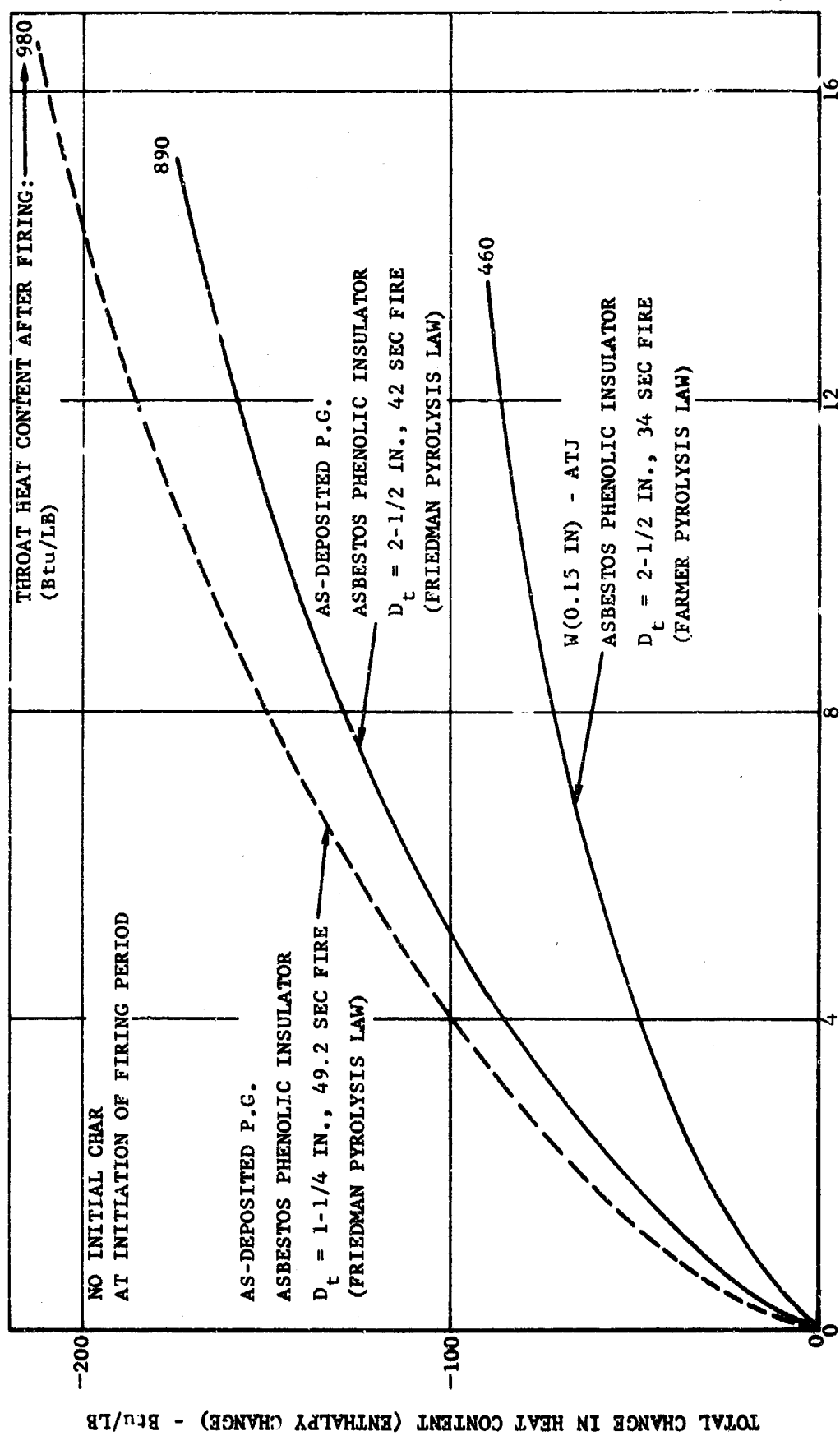
TABLE 2.4
ENERGY DISSIPATED BY HEAT TRANSFER
MECHANISMS DURING SOAKBACK AT
THROAT LOCATION FOR 1.25-INCH NOZZLE (PREDICTED)

<u>Heat Transfer Mechanism</u>	<u>Time During Soak Period</u>	<u>Throat Washer Enthalpy Change (Btu/lb-sec)</u>
Radiation - intersurface and surface to ambient environment	140 sec after shutdown	-0.04
Convection (from pyrolysis gas free stream)	140 sec after shutdown	+0.02
Ablation	140 sec after shutdown	-0.27
Total		-0.29



FJ2974 U

FIGURE 2-19. RADIAL TEMPERATURE DISTRIBUTION IN ABLATOR AT THROAT LOCATION (FOR NOZZLE OF FIGURE 2-18)



FO2975 U

FIGURE 2-20. TOTAL CHANGE IN THROAT INSERT HEAT CONTENT DURING SOAK

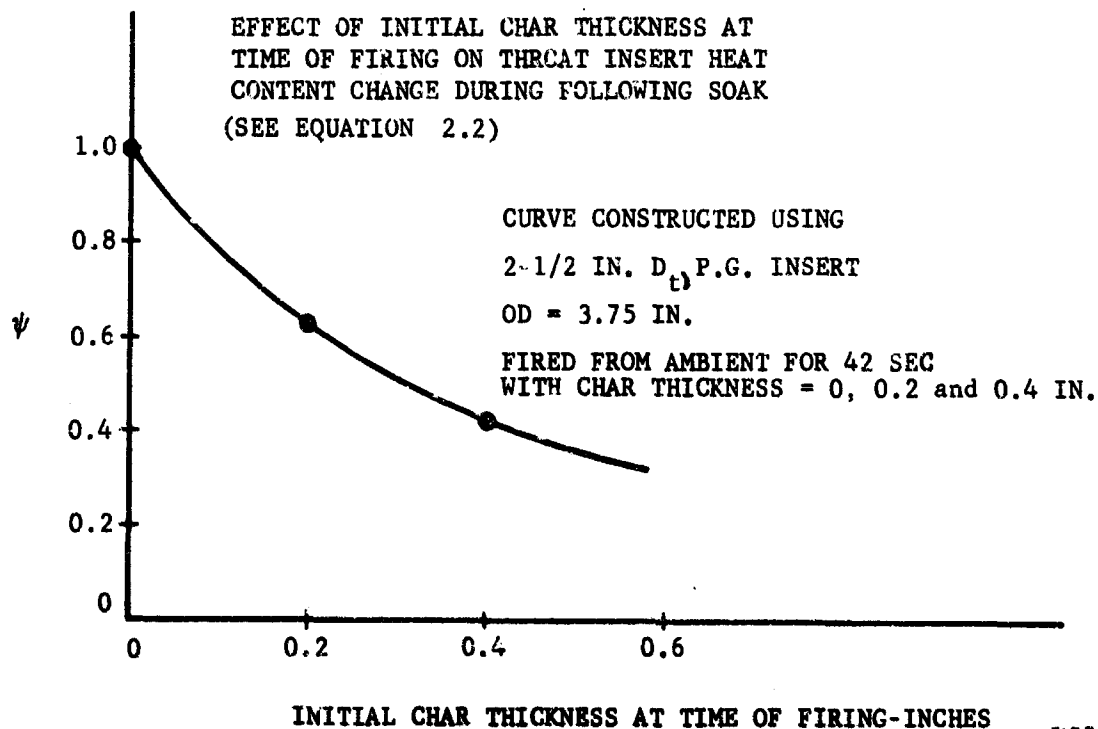
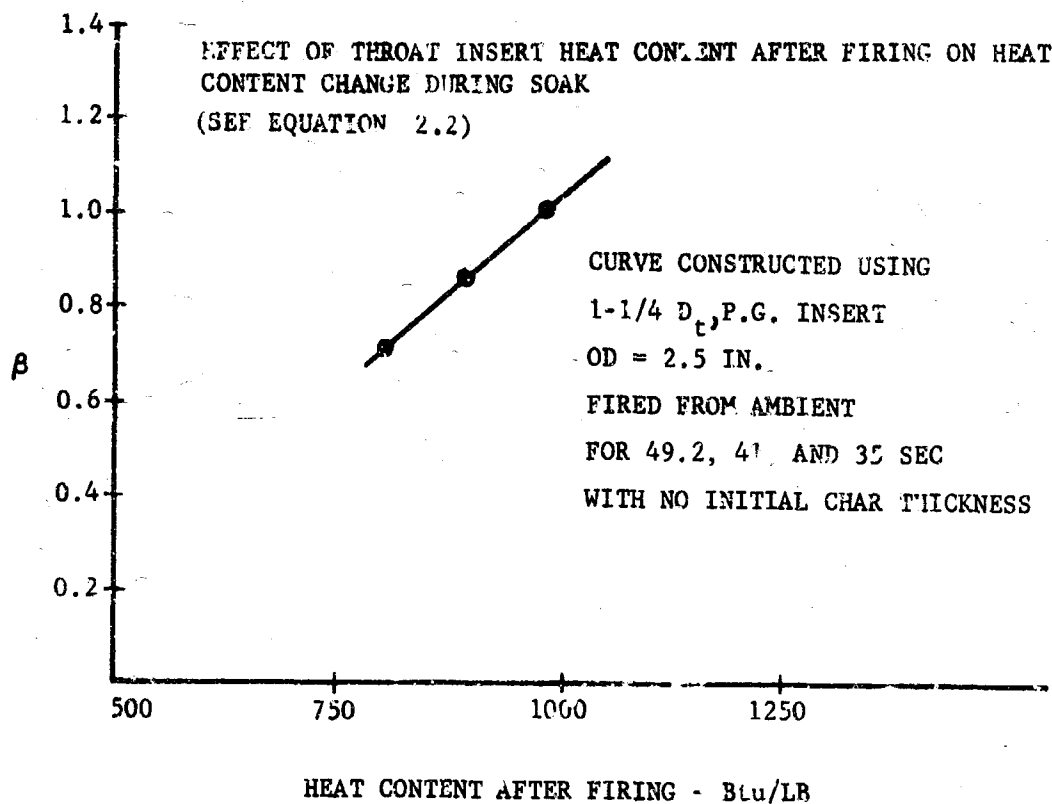


FIGURE 2-21. EFFECT OF INITIAL CHAR THICKNESS AND THROAT INSERT HEAT CONTENT ON HEAT DISSIPATED DURING SOAK

The accuracy of the above results and observations are limited by the ablation property values used in the ablation analysis. To determine the accuracy and limitations of both the results and ablation model, the ablation property data and phenomena that are considered important were investigated.

The effect of the Arrhenius pyrolysis rate law constants were studied with asbestos phenolic as the ablator. The Arrhenius constants of Friedman ($n = 5$) and Farmer ($n = 1$) were employed and the results shown in Figures 2-12, 2-16 and 2-17. The large discrepancy in ablation rate (Figure 2-17) indicates the importance of the Arrhenius constants on the ablation rate.

At the time the material investigations were performed, the char thermal conductivity of asbestos phenolic was not available. The value used in the ablation program was obtained from the weight ratio of the individual conductivities of asbestos and porous carbon. The resulting value was 3×10^{-6} Btu/in. sec^{°F}. Later in the contract, the char thermal conductivity was found to possibly be in the 10 to 20×10^{-6} Btu/in. sec^{°F} range (see Appendix C). Since the material investigation employed the 3×10^{-6} char thermal conductivity, the results of the above material investigation must be considered only from a qualitative approach. Another important phenomena that was found to occur in the ablation of the backup heat sink insulators and not considered in the analytical model was that of carbon-acecus char-reinforcement chemical reactions. In the insulators obtained from the motor firings under this contract a significant amount of SiC was found. The reaction between Si and C involves a highly endothermic chemical reaction and therefore should be considered in the ablation analysis of refrasil (silica) and asbestos phenolic (see Appendix C). Not including this reaction in the analysis then requires that the heat absorbed by this reaction must be dissipated by degradation of the virgin plastic, causing the predicted ablation rate to be greater than actually exists (see Section 8).

CONFIDENTIAL

2.4.4 DUTY CYCLE LIMITATIONS AND THROAT INSERT DESIGN

The thermal analyses of Paragraphs 2.1, 2.2 and 2.3 together with the results of Paragraphs 2.4.3 and 2.4.4 were applied to the throat insert configurations listed in Table 2.2 to establish (1) the amount of energy absorbed by the insert at various times during firing and (2) the time to reach the maximum design temperature (5000°F for PG and 5500°F for tungsten). By performing the thermal analysis on throat inserts at different temperature levels, the determination of energy input versus temperature permits the construction of a family of curves relating heat input to firing time.

The firing time at which the throat surface reaches the maximum design temperature will then restrict the maximum energy that the throat insert can absorb at the corresponding initial temperature level (initial heat content). Combining the heat content dependency on firing time with the maximum surface temperature restriction enables the construction of duty cycle curves similar to Figures 2-22, 2-23 and 2-24. Curves of this type are very versatile in selecting possible duty cycles for a given throat insert. However, curves of this nature are restricted in the following ways: (1) at the end of firing the throat insert must be nearly equilibrated (that is, approximately isothermal) before a restart is initiated, (2) alumina deposition is not considered, and (3) the start transient is assumed as a step-change in chamber pressure. Paragraph 2.4.2c shows that insert equilibration is obtained at approximately 30 seconds for pyrolytic graphite, 25 seconds for annealed pyrolytic graphite, and 80 seconds for tungsten. The effect of alumina deposition and start transients on the heat content curves is discussed elsewhere in this paragraph.

To specify the amount of energy dissipated by ablation, conduction and radiation during the soak period (and thus the energy level at which the throat insert is restarted on subsequent firings) required applying the ablation-conduction and radiation programs to the entrance, throat, and exit sections (discussed in Paragraph 2.4.3). Since the magnitude of energy absorbed by ablation is dependent upon the temperature level of the throat insert and initial char thickness (i.e., ablation rate is a function of heat input), and the energy lost by radiation from the throat insert is a function of nozzle surface temperatures, the change in insert heat content during cool-down may be expected to be dependent on the insert energy level at the time of shutdown. To analyze the ablation and radiation temperature dependence of the various throat insert configurations with the infinite number of possible duty cycles would require an expensive and lengthy thermal analysis. Therefore, as a simplification the ablation-conduction and radiation programs were applied to the energy level obtained at the end of the initial pulse for a firing time sufficient to reach the maximum surface temperature using three initial char thicknesses. From this type of analysis the effect of initial char thickness on the change in heat content during soak back can be determined (Figure 2-21). To determine the effect of insert heat

CONFIDENTIAL

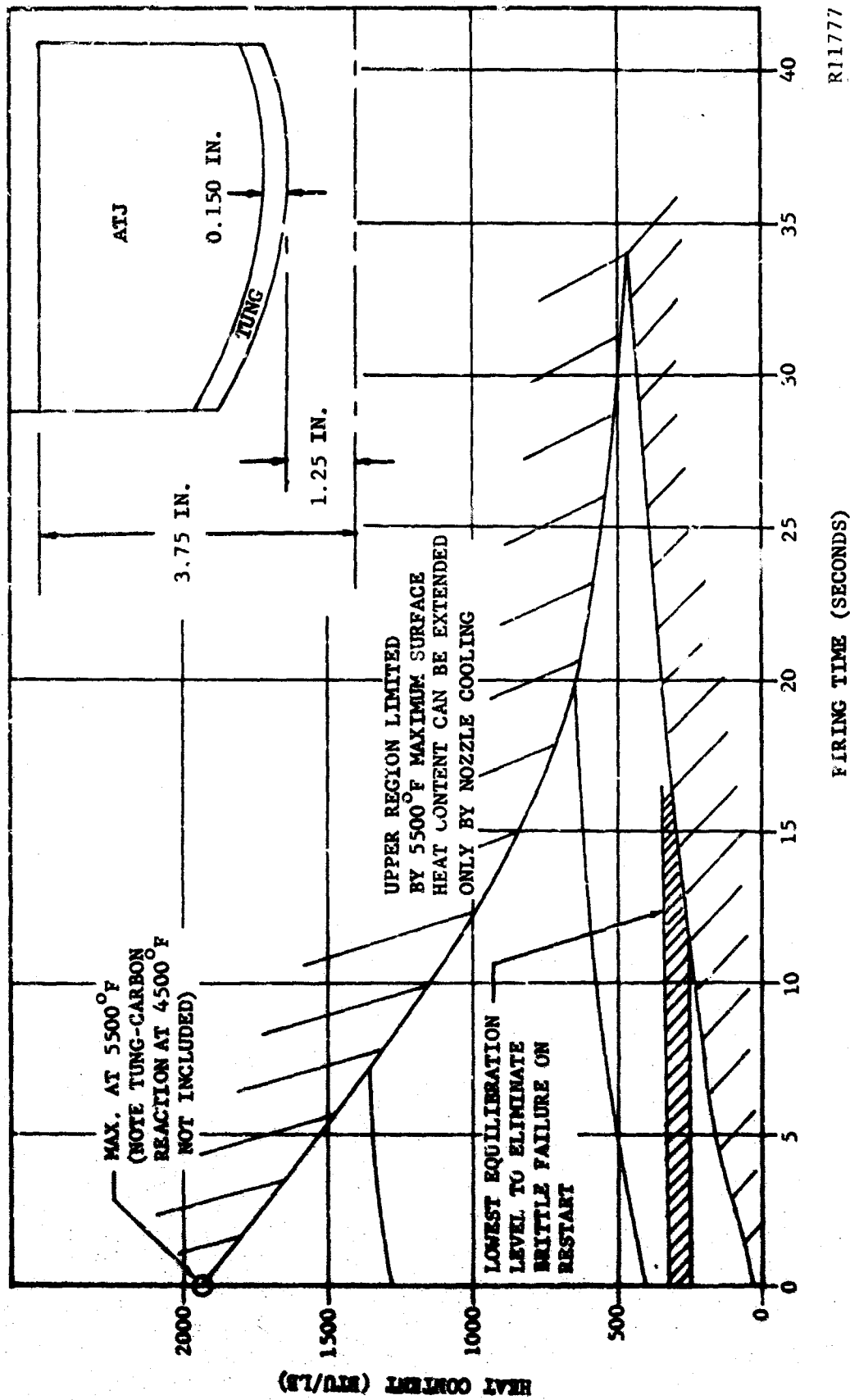
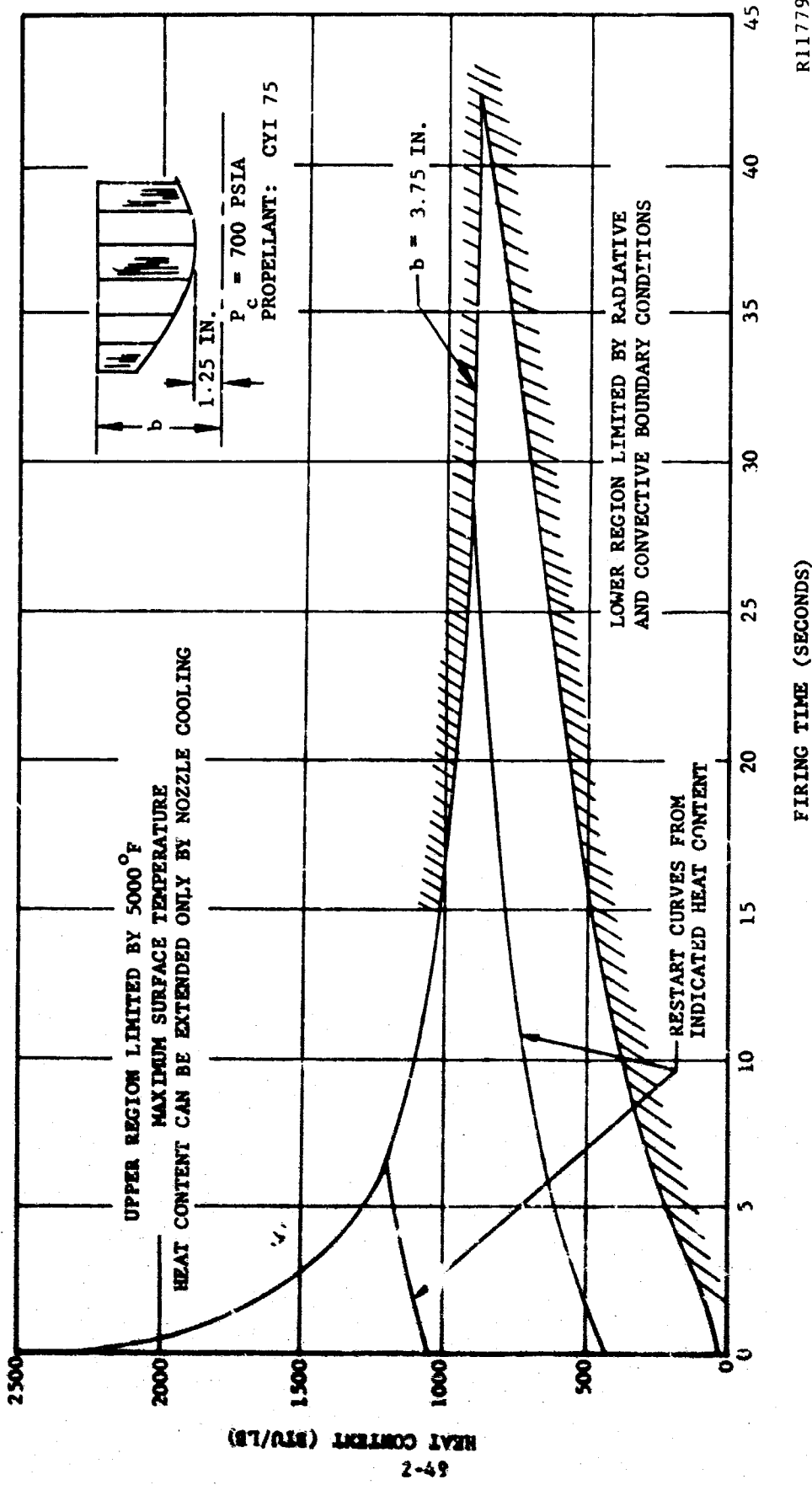


FIGURE 2-22. INFLUENCE OF TOTAL HEAT CONTENT FOR TUNGSTEN SHELL (0.15 IN.) AND ATJ GRAPHITE THROAT INSERT ON FIRING TIME

CONFIDENTIAL

CONFIDENTIAL

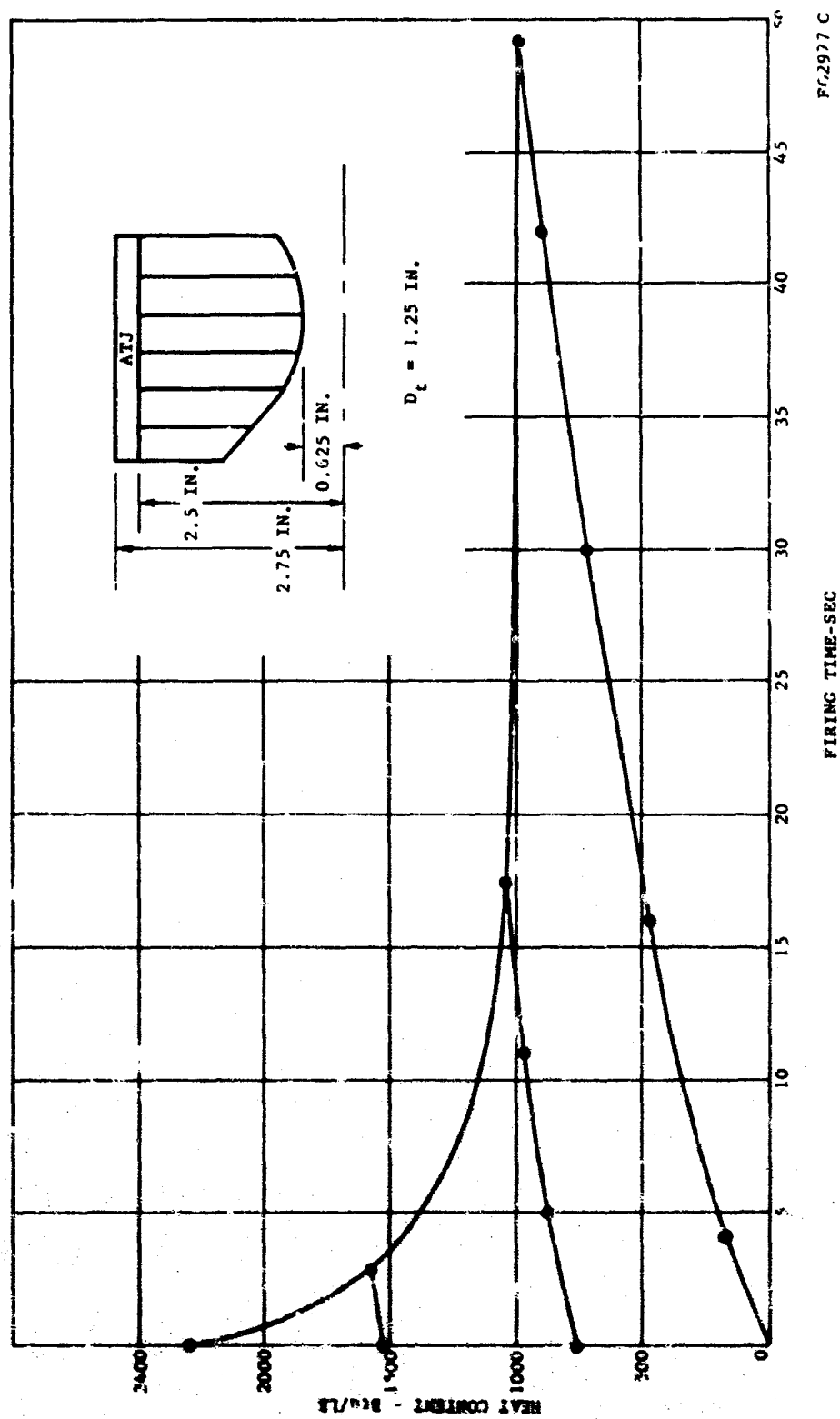


R11779 C

FIGURE 2-23. INFLUENCE OF HEAT CONTENT FOR PYROLYTIC GRAPHITE
THROAT INSERT ON FIRING TIME

CONFIDENTIAL

CONFIDENTIAL



FG2977 C

FIRING TIME-SEC

FIGURE 2-24. TOTAL HEAT CONTENT FOR AS DEP. PYROLYTIC GRAPHITE HROAT INSERT VERSUS FIRING TIME

2-50

CONFIDENTIAL

CONFIDENTIAL

content on the change in heat content during soak back, the conduction-ablation analysis was applied to a P.G. insert at various initial heat content levels with no initial char thickness (Figure 2-21). To determine the char thickness at a specific time in the duty cycle it is suggested that the empirical expression, $\Delta = Kt^{1/2}$, be employed (where Δ is the char thickness after soak to ambient and t is the cumulative firing time). The constant K is presented and discussed in Section 6 for the above nozzle configurations. Figure 2-21 was constructed using the heat content change at 10 minutes in the soak period. The ratios ϕ and β of Figure 2-21 were found to be, for all practical purposes, constant in the 0 to 18 minute soak period; however, after this time the deviation in ϕ and β is significant. From Figure 2-12, the radiation mode of insert cooldown can be seen to be considerably less than that resulting from ablation and is extremely dependent on exit area ratio. Thus, in considering throat insert cooldown for the configuration studied; the effect of radiation can be neglected.

It has been semi-empirically shown in this program that if, during the soak period, the temperature level of the insert does not reach below approximately 1500°F or 500 Btu/lb the heat dissipated by ablation, for all practical purposes, is independent of char thickness for the following soak period. This observation may be attributed to the fact that (1) the temperature level in the char and pyrolysis zone is at a sufficient level and (2) the char layer is thick enough such that the pyrolysis rate is nearly independent of char thickness.

The change in throat insert heat content during soak back is shown in Figure 2-20 for the insert configurations of Figures 2-22, 2-23, and 2-24. These heat content curves apply to Figures 2-22, 2-23, and 2-24 for no initial char thickness and a heat content level at the time of shutdown of 460, 890, and 980 Btu/lb, respectively. The effect of throat insert heat content at shutdown on the change in heat content during soak back is shown in Figure 2-21. Also, the effect of initial char thickness on the change in heat content is shown in Figure 2-21. By applying Figure 2-21 to Figure 2-20, the duty cycle limitation of the throat insert of Figures 2-23 and 2-24 can be determined using the following expression:

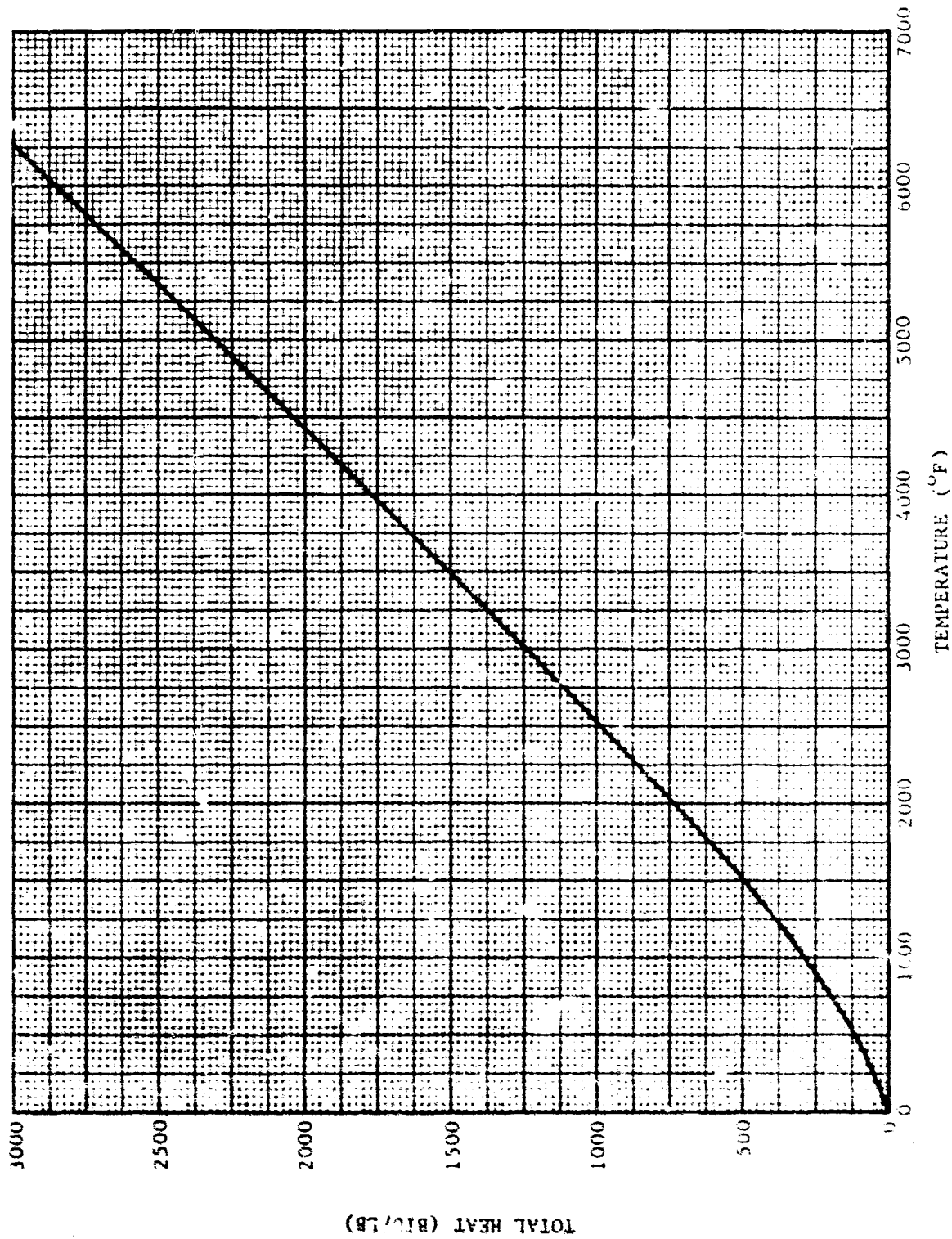
$$\Delta H = \phi \beta \Delta H_0 \quad (2.2)$$

where ΔH_0 is the change in heat content of Figure 2-20.

The pyrolytic graphite heat content versus temperature is presented in Figure 2-25 to aid in the determination of the insert temperature levels of Figures

An example of the above technique in determining duty cycle limitations is presented in the following paragraphs.

CONFIDENTIAL



RO0621 U

FIGURE 4-25. TOTAL HEAT OF PYROLYTIC GRAPHITE VERSUS TEMPERATURE

2-52

CONFIDENTIAL

THIS PAGE IS UNCLASSIFIED

CONFIDENTIAL

The initial pulse length, Figure 2-24, is chosen such that the surface temperature at the end of firing corresponds to that at which initiation of throat regression is expected. From Figure 2-24, the maximum firing time is found to be 49.2 seconds with the heat content of the insert at 980 Btu/lb. The heat content is 980 Btu/lb and the char thickness at the time of firing is zero, therefore $\phi = 1$ and $\beta = 1$ (See Figure 2-21). Then, if the soak back period is 14 minutes the change in heat content of the insert is -204 Btu/lb (Figure 2-20). Therefore, the heat content level of the insert at the initiation of the second pulse is 776 Btu/lb. If the second pulse length is chosen such that the surface temperature reaches the level at which throat regression is initiated, then, from Figure 2-24, the second pulse length is 17.4 seconds and the insert heat content is 1040 Btu/lb. Since the heat content at the end of the first soak period is above 500 Btu/lb, the heat dissipated during the second soak can be estimated from Figures 2-21 and 2-20. If the second soak period is 5 minutes, the change in heat content is $(-220+204)(1.1) = -17.6$ Btu/lb. (The change in heat content at 14 + 5 minutes minus the change in heat content at 14 minutes, and this difference multiplied by the constant found in Figure 2-21 using a heat content of 1040 Btu/lb.) The heat content at the initiation of the third pulse is then 1022 Btu/lb. If the heat content for the remaining soak periods is not below 500 Btu/lb the above procedure is followed for the remaining firings. If, however, a soak to ambient is desired after the second pulse then the final char thickness is obtained using the total firing time that the insert experienced and the correlations presented in Section 8, Figure 8-36; i.e., $\Delta = Kt^{1/2} = 0.043$ $(49.2 + 17.4)^{1/2} = 0.35$ inch. If the first pulse length after the soak to ambient is 20 seconds, the change of heat content experienced during the first soak period is found as follows: (1) from Figure 2-24 the heat content of the insert after 20 seconds is 550 Btu/lb; (2) the char thickness at the initiation of the first pulse is found from Section 8 using the total firing time prior to the soak to ambient, char thickness = 0.35 inch; (3) the parameter β is found from Figure 2-21 using the 550 Btu/lb insert heat content; (4) the parameter ϕ is found from Figure 2-21 using 0.35 inch, the initial char thickness; (5) the quantity ΔH_0 is found from Figure 2-20 using the time of this first soak period; and (6) using Equation (2.2), the change in heat content is determined. This procedure is applied to the remaining fire and soak periods.

The duty cycle curve for tungsten (Figure 2-22) has a structural restriction on the amount of cooling that can be experienced between firings. If the first or any subsequent pulse allows the insert heat content to exceed 300 Btu/lb, the heat content cannot fall below the band of Figure 2-22 in the cooling period or a structural failure of the tungsten will be experienced on subsequent startup. This band represents the transition between a ductile and brittle state for tungsten since the heat content is proportional to temperature, i.e., $H = C_p T$. For example, when the heat content of the insert of Figure 2-22 exceeds 300 Btu/lb, grain growth in the tungsten is experienced. This grain growth in turn reduces the structural strength of the tungsten. If the heat content should fall below 240 Btu/lb, the tungsten is in a brittle state and subsequent firings could result in a thermal shock failure.

CONFIDENTIAL

Structural limitations are placed on pyrolytic graphite but failure is of a different form than tungsten. Pyrolytic graphite structural failure is in the form of spalling and is discussed in another section.

Duty cycle curves similar to Figures 2-22, 2-23 and 2-24 for the throat inserts listed in Table 2.2 are presented in Figures 2-26, 2-27, and 2-28. In review, the above duty cycle curves are restricted by:

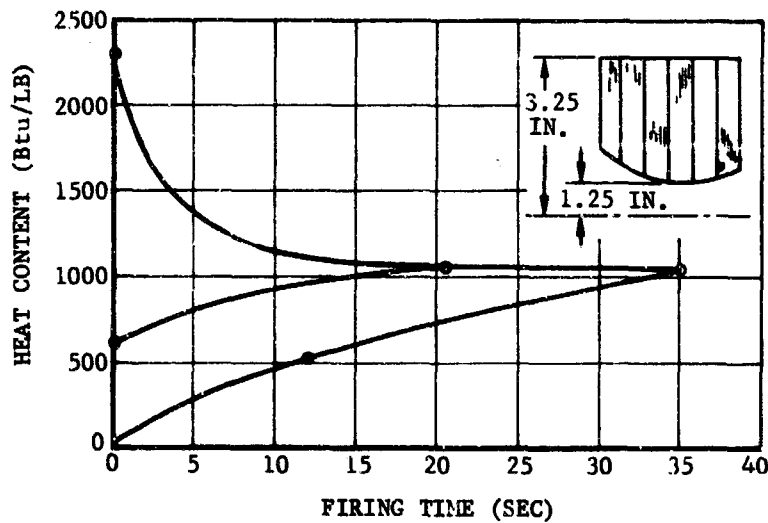
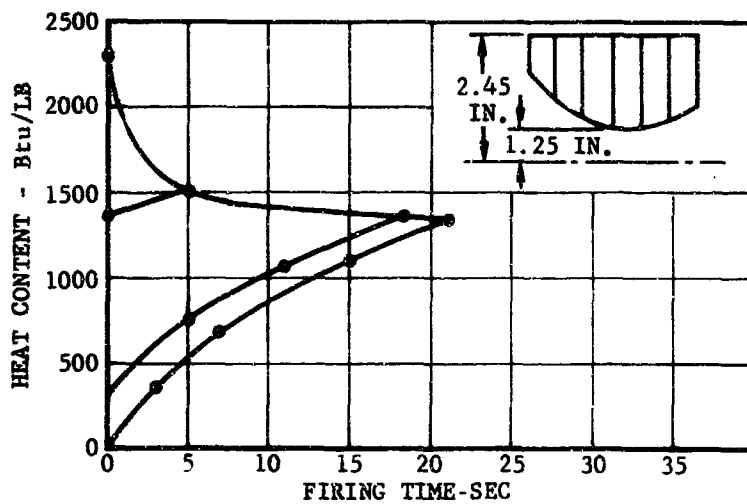
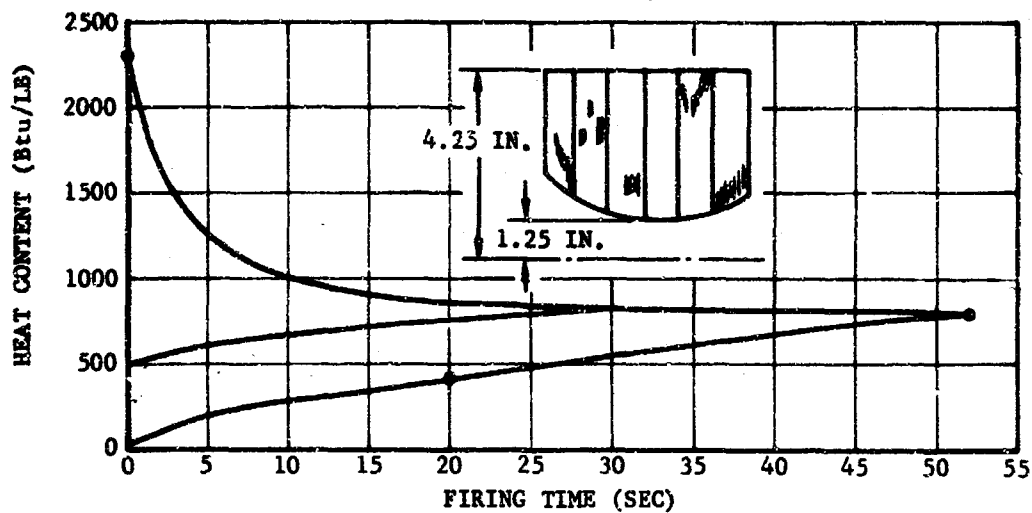
- (1) The assumption of insert equilibration to an isothermal state between firings,
- (2) the omission of alumina deposition,
- (3) the omission of startup transients,
- (4) the effect of backup material other than insulator, i.e., ATJ graphite, and
- (5) extrapolation to throat inserts not studied in this program.

The effects of these restrictions on the duty cycle curves are described below.

a. Insert Equilibration to Isothermal State. The restriction that the cooldown time be sufficient for insert equilibration to approximately reach an isothermal state (roughly 30 seconds for pyrolytic graphite, 25 seconds for annealed pyrolytic graphite, and 80 seconds for 0.150-inch tungsten) limits the duty cycle curves to cooldown periods greater than the time to reach nearly isothermal conditions. However, this restriction can be broadened from considering the fact that a pulse firing will, in the limit (cooldown time approaches zero), approach a continuous firing. For cooldown times less than 5 seconds the pulse firing may be considered continuous. This is shown very effectively in Figure 2-29. Figure 2-29 is a comparison between a continuous firing and 5 second firings with 3-second off times for a 5/8-inch diameter pyrolytic graphite throat insert. For cooldown periods greater than 5 seconds and less than the equilibration time, a significant error may result in using these duty cycle curves.

b. Alumina Deposition. The boundary conditions applied to the thermal analysis were altered so as to predict the effect of alumina deposition on the thermal behavior of the throat insert. The analysis of deposition is limited in that the deposition rate must be specified from experimental data (See Section 8). The effect of alumina deposition on the duty cycle curves shown in the previous paragraph is illustrated in Figure 2-30.

CONFIDENTIAL



FO2978 C

FIGURE 2-26. HEAT CONTENT OF EDGE GRAIN AS DEPOSITED P.G. THROAT INSERT VERSUS FIRING TIME

CONFIDENTIAL

CONFIDENTIAL

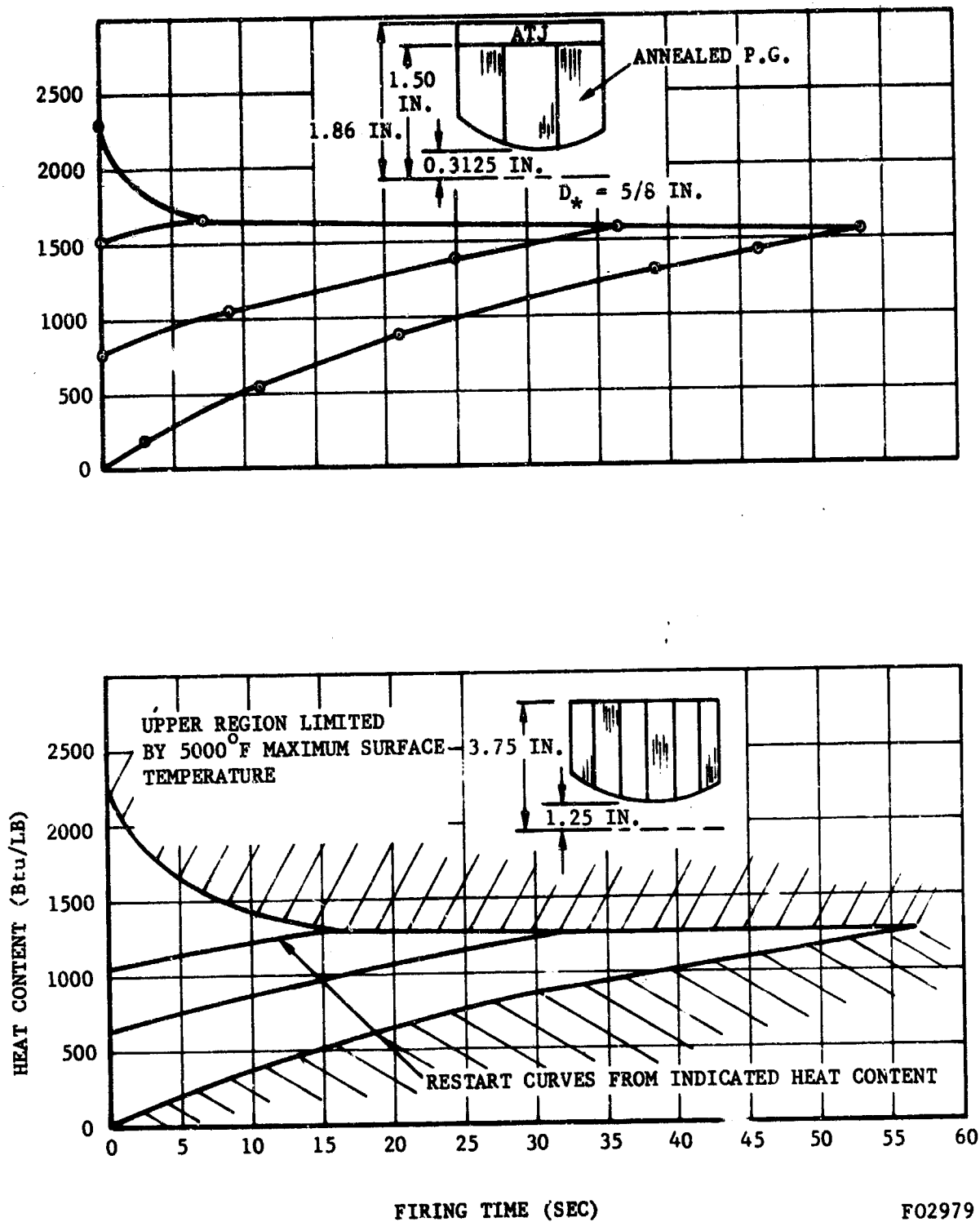
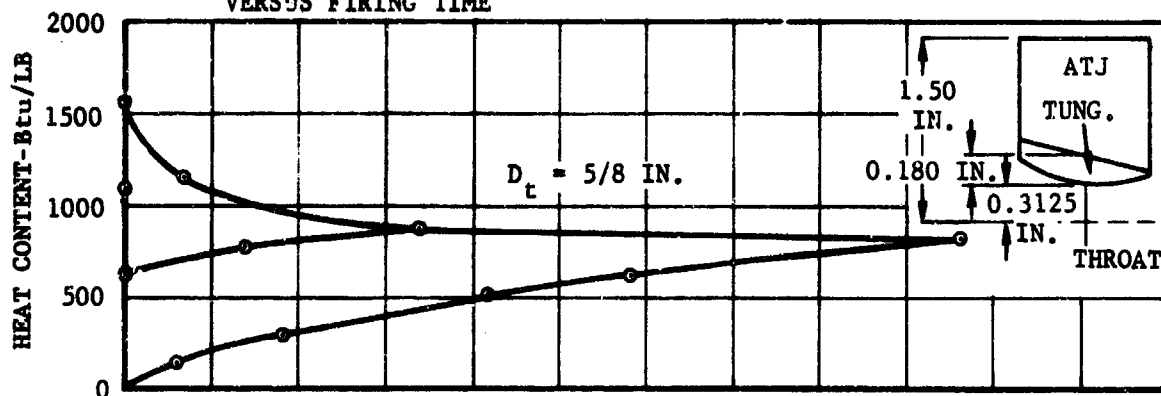


FIGURE 2-27. HEAT CONTENT OF ANNEALED P.G. THROAT INSERT VERSUS FIRING TIME

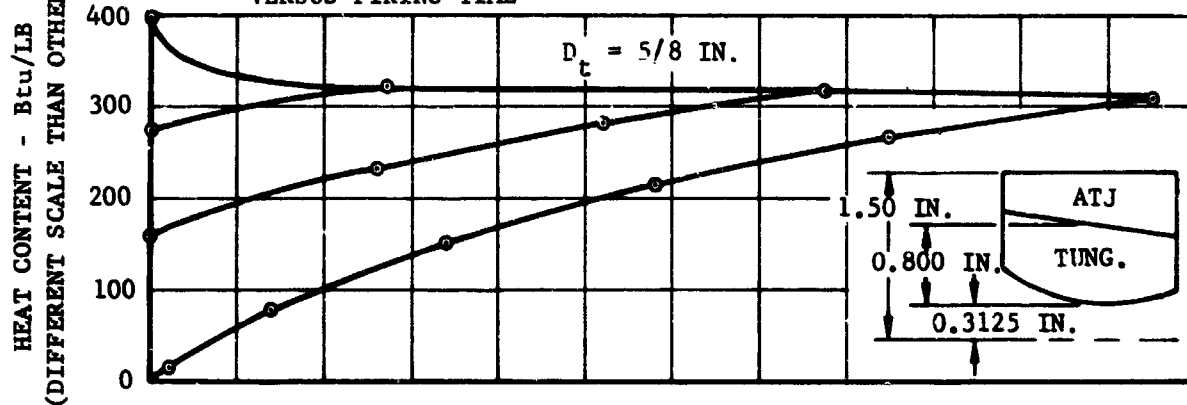
CONFIDENTIAL

CONFIDENTIAL

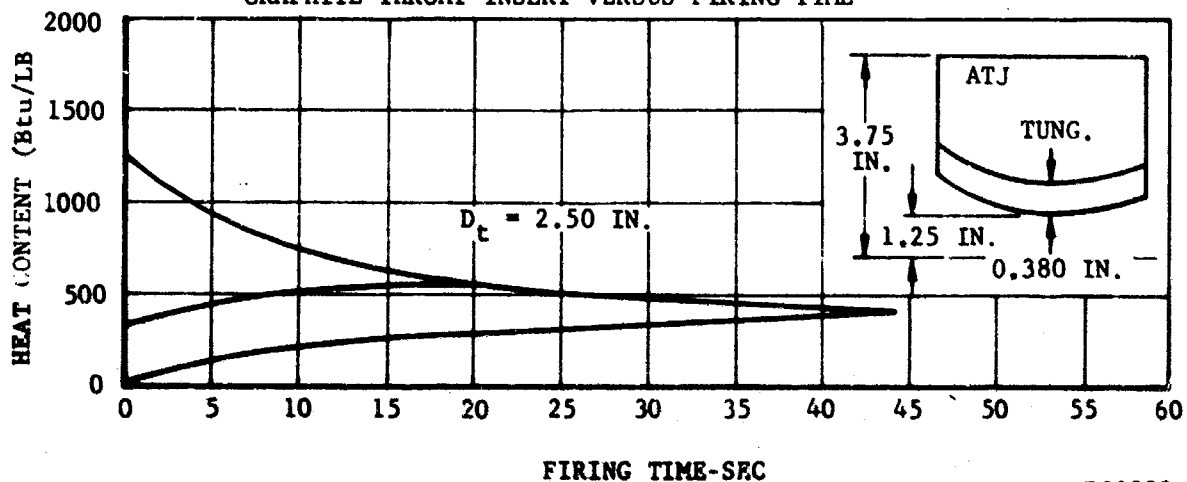
HEAT CONTENT OF TUNG. - ATJ THROAT INSERT (0.180 IN.)
VERSUS FIRING TIME



HEAT CONTENT OF TUNG. - ATJ THROAT INSERT (0.800 IN.)
VERSUS FIRING TIME



HEAT CONTENT OF TUNGSTEN - ATJ THROAT INSERT VERSUS FIRING TIME
GRAPHITE THROAT INSERT VERSUS FIRING TIME



F02980 C

FIGURE 2-28. HEAT CONTENT FOR TUNG. SHELL AND ATJ GRAPHITE
THROAT INSERT VERSUS FIRING TIME

CONFIDENTIAL

CONFIDENTIAL

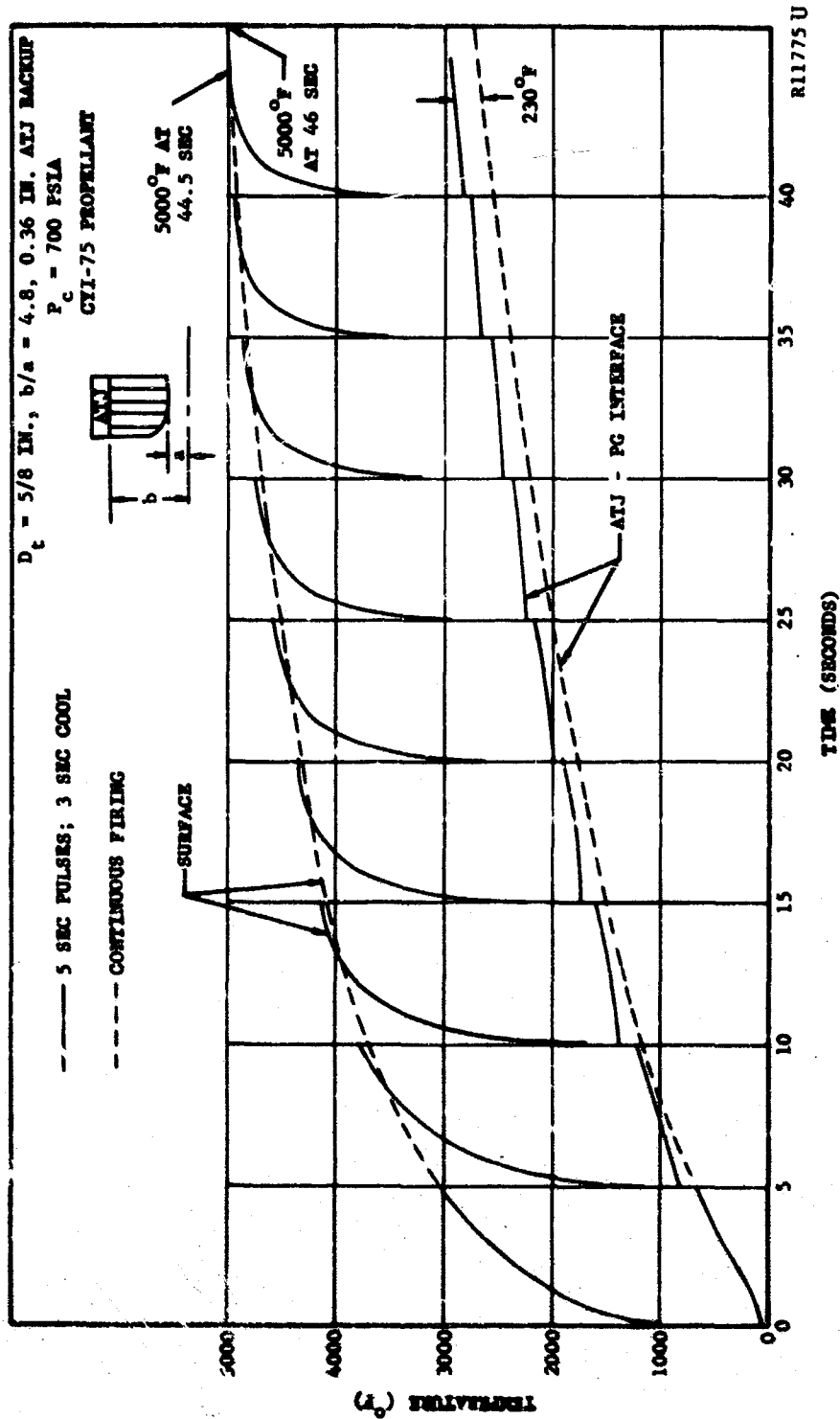


FIGURE 2-29. THERMAL HISTORY OF PYROLYTIC GRAPHITE THROAT INSERT

CONFIDENTIAL

THIS PAGE IS UNCLASSIFIED

CONFIDENTIAL

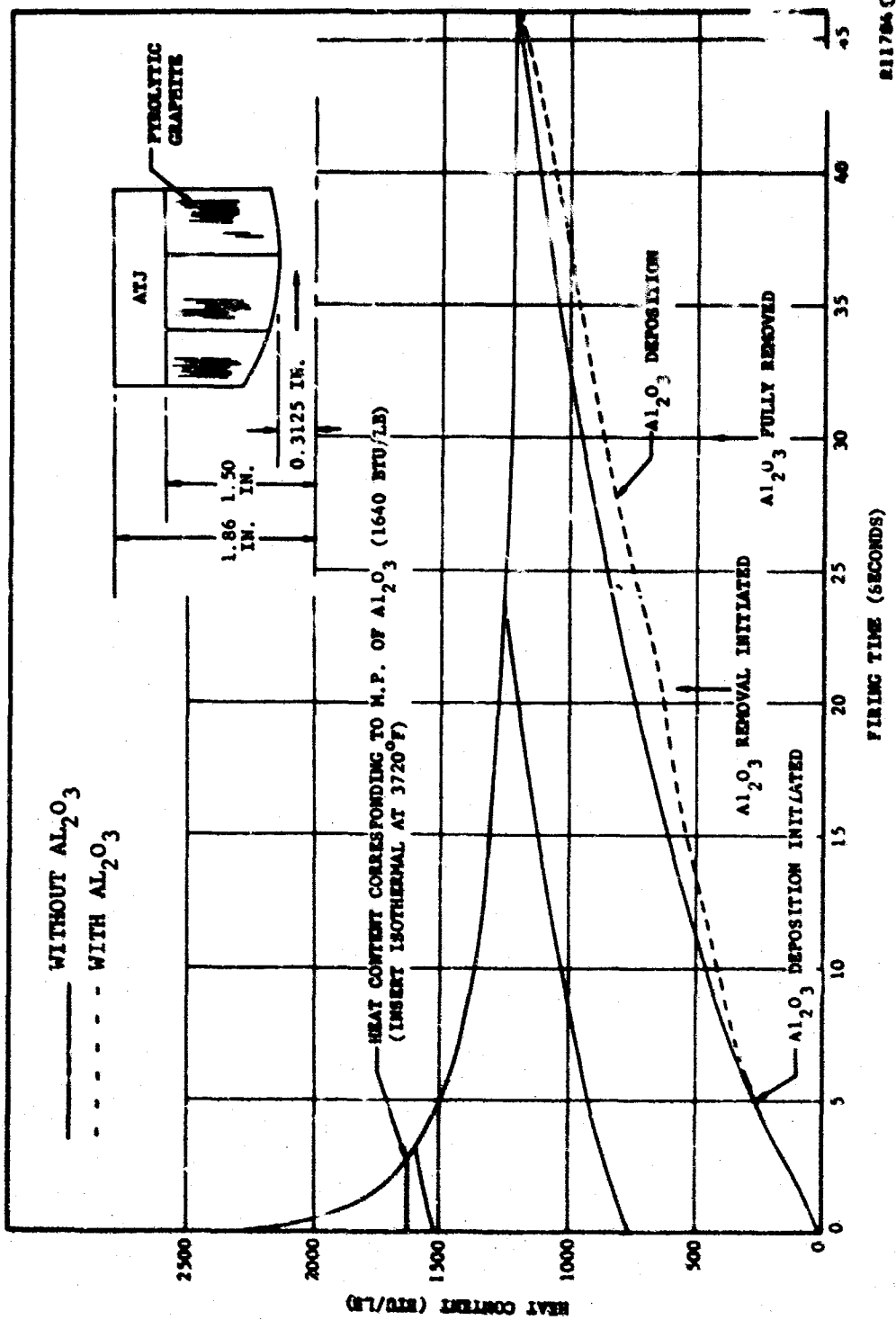


FIGURE 2-30. INFLUENCE OF ALUMINA DEPOSITION ON HEAT CONTENT OF P.G. THROAT INSET

CONFIDENTIAL

CONFIDENTIAL

Alumina reduces the heat input to the throat insert and thus increases the window of the duty cycle curves. For long firing times, the effect of alumina deposition can be neglected from a thermal standpoint; however, from structural considerations the initiation of spalling will be delayed and alumina deposition must be included.

It should be noted that the alumina deposition experienced in the solid propellant simulator at Aeromutronic may not be representative of solid propellant motors, the difference being in chamber geometry and propellant combustion (i.e. particle size and flow pattern). Consideration of alumina deposition in determining duty cycle limitations requires additional work in predicting the deposition mechanisms. Omission of alumina deposition phenomena in the thermal analysis will result in conservative thermal and structure predictions.

c. Start Transients. The thermal analyses performed in this program assume a step change in chamber pressure at startup. i.e., at $t < 0$, $P_c = 14.7$ psia and at $t \geq 0$, $P_c = 700$ psia. A step change in chamber pressure is a relatively conservative assumption for all motors. The chamber pressure trace during startup in the simulator and in solid propellant motors is not a step change, but a logarithmic function depending, of course, on igniter characteristics. The reduction in heating that is experienced with a logarithmic chamber pressure rise is sufficient to produce a 1 to 2 second temperature delay in the backwall temperature. The surface temperature will be sufficiently lower with the logarithmic pressure trace, producing a delay in thermal structural failure; as the effect of the pressure start transient on structural failure will effect tungsten to a larger extent than pyrolytic graphite. Tungsten failure is in the form of cracking and occurs at very short times from startup; whereas that of pyrolytic graphite is in the form of spallation and is found to occur at times greater than 10 seconds. The effect of pressure transient on tungsten failure is discussed in Section 3.

d. Extrapolation Technique for Throat Insert Configurations Not Studied in this Program. A throat insert has three primary parameters which determine its thermal duty cycle limitations (constant chamber conditions). These are:

- (1) Type of heat sink material or materials.
- (2) Throat diameter.
- (3) Heat sink thickness.

The heat content curves presented in this paragraph are restricted to only edge grain as deposited P.G. backed with ATJ, edge grain annealed P.G. backed with ATJ, and tungsten laced with ATJ. If a particular nozzle employs a backup material other than ATJ, the heat content curves developed

CONFIDENTIAL

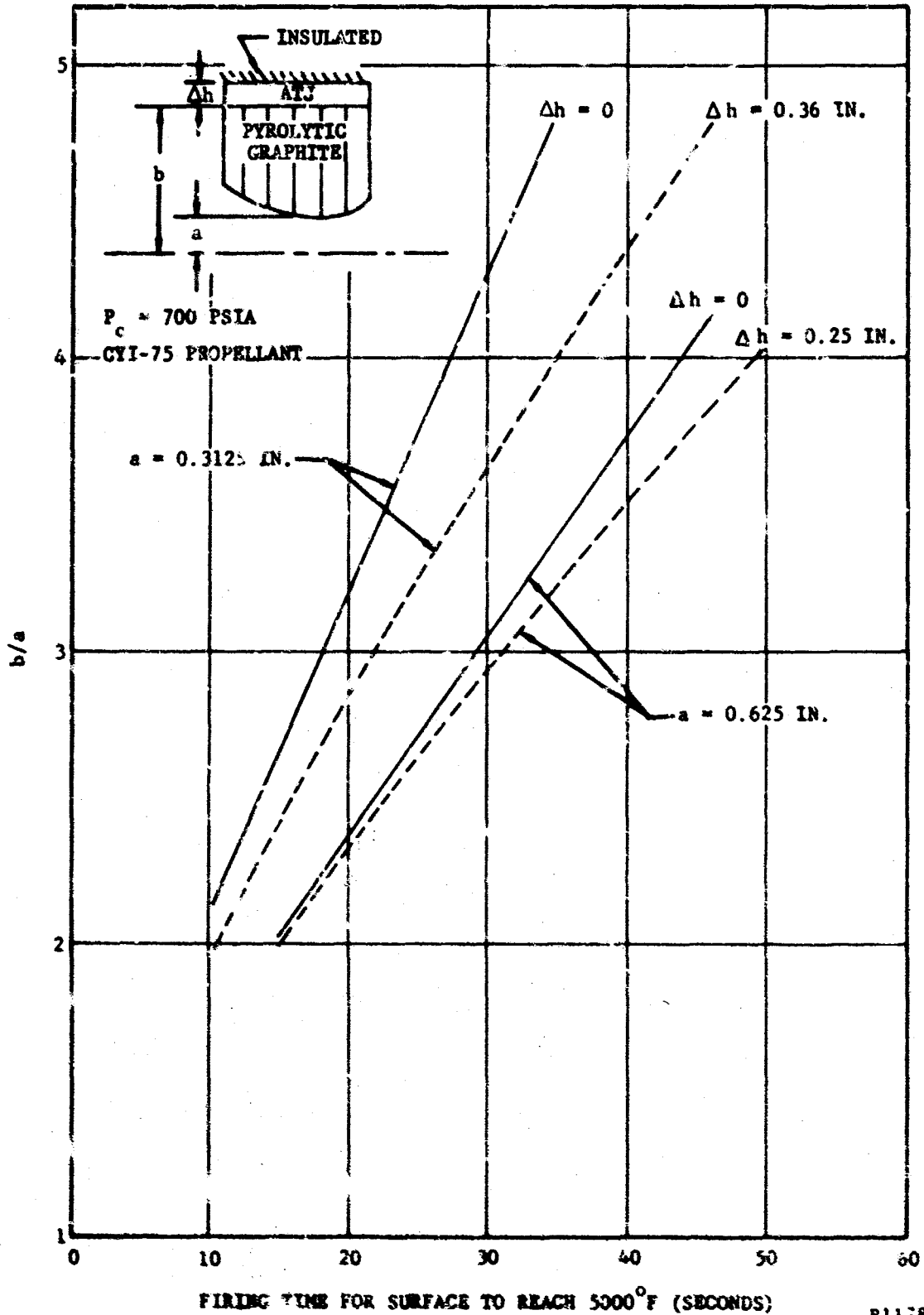
for as deposited P. G. and annealed P. G. can be applied for design purposes. That is, the effect of the backup material on thermal response is minor as shown in Figure 2-31. If, however, the backup material for the tungsten insert has a thermal conductivity much different from ATJ, then it is not permissible to use the tungsten heat content curves.

The effect of throat diameter on heat content is reflected primarily in the dependency of the heat transfer coefficient and radial heat sink change on throat diameter. The heat content curves presented in this paragraph are applicable for throat diameters of 1.25, and 2.50 inches. For design purposes other than the above, and the 1.25 to 5 inches in range, linear interpolation is permissible at constant heat sink thickness (b/a). For diameters greater than 5 inches, the heat content curves should be determined analytically.

The effect of heat sink thickness (b/a) on the time for the surface temperature to reach the maximum design temperature (5000°F for P. G. and 5500°F for tungsten) is shown in Figures 2-31 and 2-32 for P. G. and tungsten, respectively. The effectiveness of the heat sink thickness in increasing the time to reach the design surface temperature is nearly linear for all b/a values studied for P. G. For tungsten inserts, a point of diminishing returns is reached at a $b/a = 1.2$. For inserts with b/a values greatly different from those studied in this program, the heat content curves should be determined analytically.

CONFIDENTIAL

CONFIDENTIAL



R11781U

FIGURE 2-31. BACKUP MATERIAL EFFECT ON FIRING TIME

2-62

CONFIDENTIAL

THIS PAGE IS UNCLASSIFIED

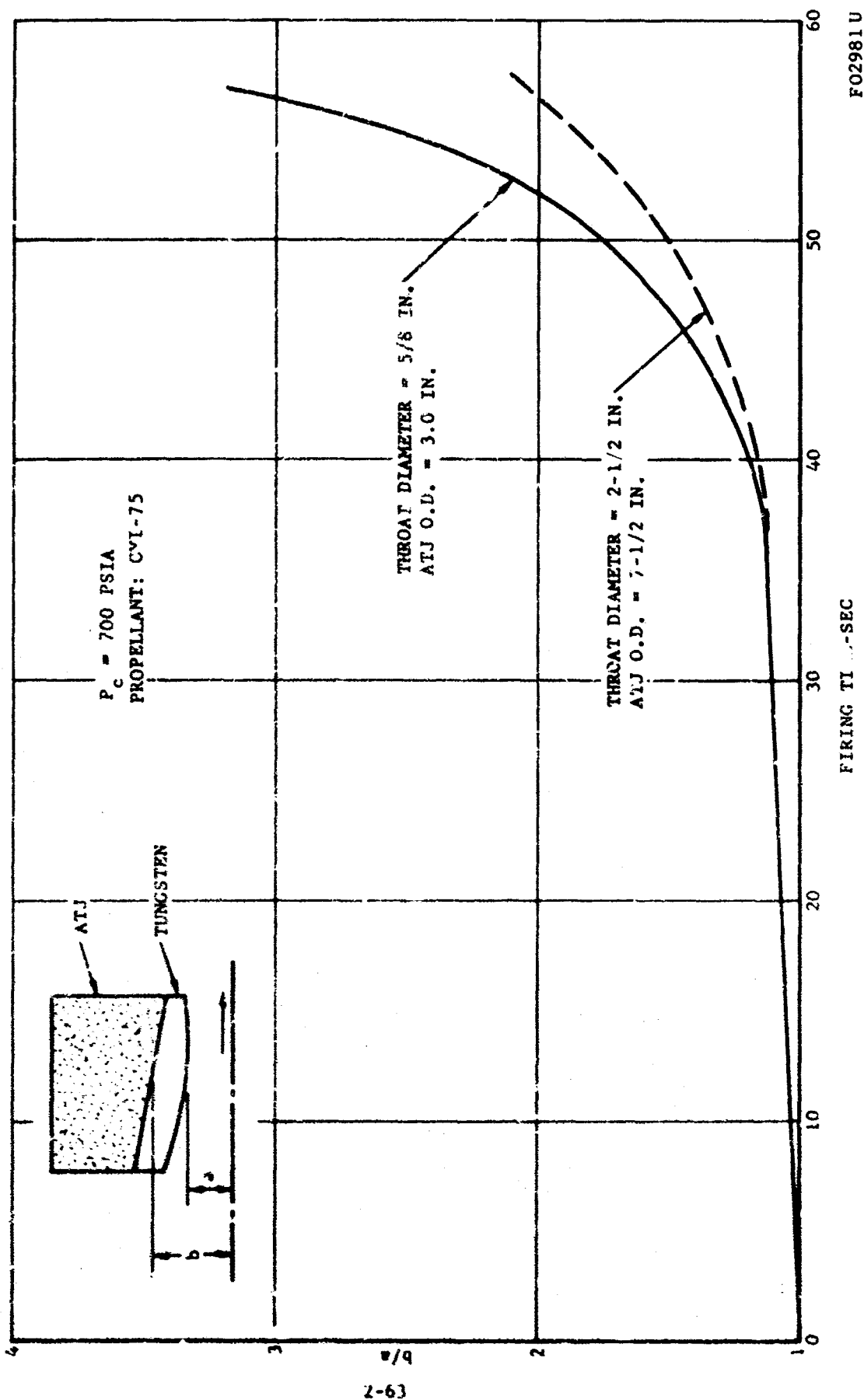


FIGURE 2-32. FIRING TIME FOR SURFACE TEMPERATURE TO REACH 5500° F FOR TUNGSTEN BACKED WITH ATJ THROAT INSERTS

REFERENCES

- 2.1 Elliot, D. G., Bartz, D. R., and Silver, S., Calculation of Turbulent Boundary-Layer Growth and Heat Transfer in Axisymmetric Nozzles, Jet Propulsion Laboratory Technical Report No. 32-387, California Institute of Technology, Pasadena, California, 15 February 1963.
- 2.2 White, W. B., Johnson, S. M., and Dantzig, G. B., "Chemical Equilibrium in Complex Mixtures," Journal of Chemical Physics, 28, pp 751-755, May 1958.
- 2.3 Oliver, R. C., Stephanou, S. E., and Baier, R. W., "Calculating Free-Energy Minimization," Chemical Engineering, pp 121-128, 19 February 1962.
- 2.4 Fay, J. A., and Riddell, F. R., "Theory of Stagnation Point Heat Transfer in Dissociated Air," Journal of the Aeronautical Sciences, 25, pp 73-85, 121, February 1958.

SECTION 3

STRUCTURAL ANALYSIS

The objective of the structural analysis was to develop sufficient analytical foundation for the determination of the structural response of the nozzle components so that ranges of allowable operation might be established. Two simple definitions were formulated to serve as guidelines in the structural area:

Failure: Any occurrence which prevents an item from functioning as desired.

Structural failure of a solid propellant nozzle: Any structural phenomenon which prevents the nozzle from meeting operational requirements.

Structural phenomena leading to failure formed the basis for the definition of problems to be considered within this area of analysis. In general, the structural phenomena which were investigated were the development of fracture surfaces, permanent deformations, and the loss of surface material as a result of structural responses. Even with the broad definitions given above, it is difficult to pinpoint an occurrence which could actually be termed a failure. For example, not every case of fracture surface development can be called a failure. In this program similar one-piece and two-piece tungsten inserts were designed and tested; structurally, they performed equally well. Had the interface of the two-piece insert been the result of a fracture, it would be difficult to call this fracture a failure.

The problems discussed in the succeeding paragraphs were defined early in the program in order to form a basis for the structural analytical efforts. As the program progressed, problem emphasis was shifted as results from tests, analysis, and outside sources became available. As a consequence, a reassessment of problems is made as the last portion of Paragraph 3.1.

A comparison of analytical predictions with test results is made in Section 6.

3.1 PROBLEM DEFINITION

In order to simplify the structural analysis, the problems are divided into two categories. One category includes problems which are common to both single-firing and to restartable nozzles. Thus, these problems for the restartable nozzle are the same as for the single-firing nozzle except that they are of a repetitive nature. The fact that they are repetitive is not considered in this category. Any effects due to repetition are considered in the second category. This second category includes problems unique to restartable nozzles. These cover the cyclic effects, cumulative effects, and unique loading effects.

A strong coupling exists between materials and structural problems. For a given material, certain phenomena occur which are not displayed by other materials. For example, the structural transformation which pyrolytic graphite undergoes at high temperature is not evident in tungsten. Likewise, tungsten's high modulus of elasticity, which is largely responsible for high tensile thermal stresses, makes the brittle-ductile transition temperature an important characteristic for this material. It is not possible, therefore, to say that certain general problems, such as thermal stress and pressure stress problems, exist, but it is necessary to consider the types of loading and the particular responses which are possible with the materials included in the study.

3.1.1 PROBLEMS COMMON TO SINGLE-FIRING AND RESTARTABLE NOZZLES

a. Elastic Behavior. Certainly one of the most important problems to be considered in restartable nozzles is the elastic response of the structure to the imposed loading. Response in the elastic range will certainly exist for the first firing, and, depending on the initial conditions, may exist for all subsequent firings. All materials considered within this program have a temperature range over which they display linear elastic behavior. Calculation of linear elastic response is not difficult if certain simplifying geometrical assumptions are considered valid. These include the absence of end-effects and axial variations in geometry. Any initial or residual stresses are merely superimposed.

(1) Development of Fracture Surfaces. Considering the thermal stresses in a nozzle which was initially at the temperature of its ambient environment, it is found that the maximum compressive stresses occur on the inner wall. But the compressive stresses in the materials under consideration do not produce fracture surfaces. The maximum tensile stresses occur at the back wall, which is still cool enough when the peak tensile stresses are attained that the wall material is brittle. This tensile response is thus in the elastic regime and is the critical stress for the development of fracture surfaces.

(2) Spallation. Spallation may be defined as the ejection of chunks of surface material. This phenomenon may occur from several causes:

- (a) The development of high stresses near the material surface caused by the reflection of an elastic wave from that surface. This is noted in hypervelocity impact where material spalls from the backside of the impacted body.
- (b) The development of large principal stresses parallel to the surface. These stresses give rise to maximum shear stresses at some angle to the surface. Considering, for example, a strength criterion, when these shear stresses (rather than the principal stress) become critical, they will cause fracture on planes oblique to the surface and allow spallation to occur.
- (c) The development of stresses from the generation of high pressure gases in porous material. This occurs in char-forming ablators where the pyrolysis gases are being generated at a fast enough rate so that the porosity of the char is not sufficient to allow their immediate escape.

Spallation from the first cause was not considered, since it was not expected that a dynamic elastic wave of sufficient severity would be generated with the loadings encountered in restartable nozzles.

Large principal stresses are, of course, created which give rise to the oblique shearing stresses. This was considered since many of the nozzle materials exhibit shear strengths of about half the tensile or compressive strengths. It is also of concern for materials which have large grain sizes and weak grain boundaries.

Spallation resulting from high internal gas pressure could be important only in the char-forming ablators.

D. Anelastic Behavior. Included in this general grouping are viscoelastic and plastic responses. Essentially, elastic behavior implies complete recovery of energy of deformation. When energy is dissipated, the behavior is anelastic.

Relatively instantaneous response on loading and subsequent unloading, accompanied by energy dissipation (and thus permanent deformation), without significant additional deformation (and energy dissipation) between the end of the loading period and beginning of unloading, is characteristic of elastic-plastic behavior. The permanent deformation and accompanying energy dissipation is considered the result of plastic straining. Thus, this ideal elastic-plastic response is a rate-insensitive energy dissipation phenomenon which leads to permanent deformation and/or residual internal stresses. It is convenient and mostly correct to think of plasticity as dissipation of mechanical energy through solid friction. Idealized linearly elastic-plastic behavior often is characterized in one dimension by a friction block in combination with a set of springs. At loads below some limit, load strain response is in accord with all elastic springs. After the frictional resistance is overcome, strain is not retarded by all the springs unless the load again drops below the friction force. This represents work hardening. Perfectly plastic behavior is represented by one spring and block in series.

Rate-dependent dissipation of mechanical energy, usually characterized as viscous or quasi-viscous flow of material, is considered to define viscoelastic effects. Continued deformation of a material after a loading period is completed and constant stress is sustained, particularly in evidence in materials operating at comparatively high temperatures, is known as creep. Reduction of stress with time from an initial stress level while maintaining a constant deformation is known as relaxation. Removal of a load from a material to which it has been applied for a period of time is often followed by a time-dependent reversal of strain, known as recovery. These are all visco-elastic phenomena. Idealized linearly, visco-elastic behavior is usually pictured as a set of elastic springs and viscous dashpots in series or parallel, characteristic of energy dissipation through flow. Like plastic behavior, visco-elastic behavior can lead to residual stresses or deformations in a material at some time after completion of its external loading history.

Although these anelastic phenomena occur in single firing nozzles, their treatment is usually not undertaken in depth. The most common treatment is to incorporate modified moduli into the elastic analysis and iterate the resulting inhomogeneous problem until a compatible solution is obtained. Only the loading phase is important in this case. However, for a restart nozzle the problem takes on added importance, since, as pointed out above, the permanent deformations which occur result in residual stresses and strains which have significance in both the subsequent unloading and loading portions of the duty cycle.

c. c-Direction Permanent Deformation in Pyrolytic Graphite (Elephant's Footing). It is known that pyrolytic graphite, when heated to high temperature, undergoes a permanent contraction in the c-direction accompanied by a permanent extension in the a-b plane. This is a time-temperature dependent phenomenon, and the degree is influenced by the characteristics of the material. Contractions up to approximately 14 percent and extensions of about 5 percent are possible. The acceleration of this phenomenon with load has been investigated in this program in the material studies, Section 4.

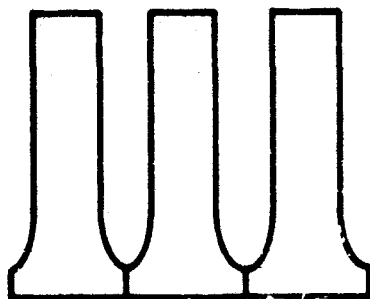
In an edge-grain or washer configuration, the hotter inner regions of the pyrolytic graphite plates will thermally expand in the c-direction to a greater degree than the cooler outer material. In section, these plates take on the appearance of an elephant's foot, as shown in Figure 3-1a. These hotter inner regions will thus be in contact and carry the axial pressure loads over a relatively narrow annulus with the result that locally high contact stresses are produced. These high-contact stresses acting in the hot material can cause c-direction permanent deformation. When the material cools, gapping between the washers results, as shown in Figure 3-1b. This raises the question of whether geometric integrity has been lost.

This phenomenon had been observed on a previous program, Contract AF 04(611)-8387. Figure 3-2 is a photograph of a sectioned nozzle where this had occurred.

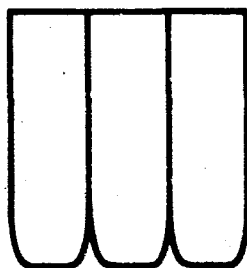
3.1.2 PROBLEMS UNIQUE TO RESTARTABLE NOZZLES

This category can be further subdivided into two broad areas. One area is concerned with the effects of changed initial conditions and the other includes cyclic and cumulative effects. Both require some or all of the prior history to be known. Some of the problems can be attacked by the correct application of analyses developed for the common problems discussed above, while others require entirely different analyses.

a. Thermal Fatigue. This was defined as a potential problem at the outset. Its treatment requires that the entire previous history of the nozzle be known. Thermal fatigue is the development of fatigue fracture surfaces resulting from repeated thermal straining into the anelastic range. It is known that nozzle materials become hot enough (assuming firing times of several seconds or greater) and stresses become great enough that anelastic deformations occur. Repeated application could lead to fracture of the nozzle material. The dearth of corroborated theory and the paucity of data on the materials under consideration made this one of the more difficult problems to assess.



(a) PG WASHER CONFIGURATION CARRYING AXIAL LEADS DURING INTERNAL HEATING



(b) C-DIRECTION PERMANENT DEFORMATION RESULTING IN GAPPING BETWEEN COOLED WASHERS.

FO4458 U

FIGURE 3-1. PYROLYTIC GRAPHITE PLATES SHOWN IN SECTION

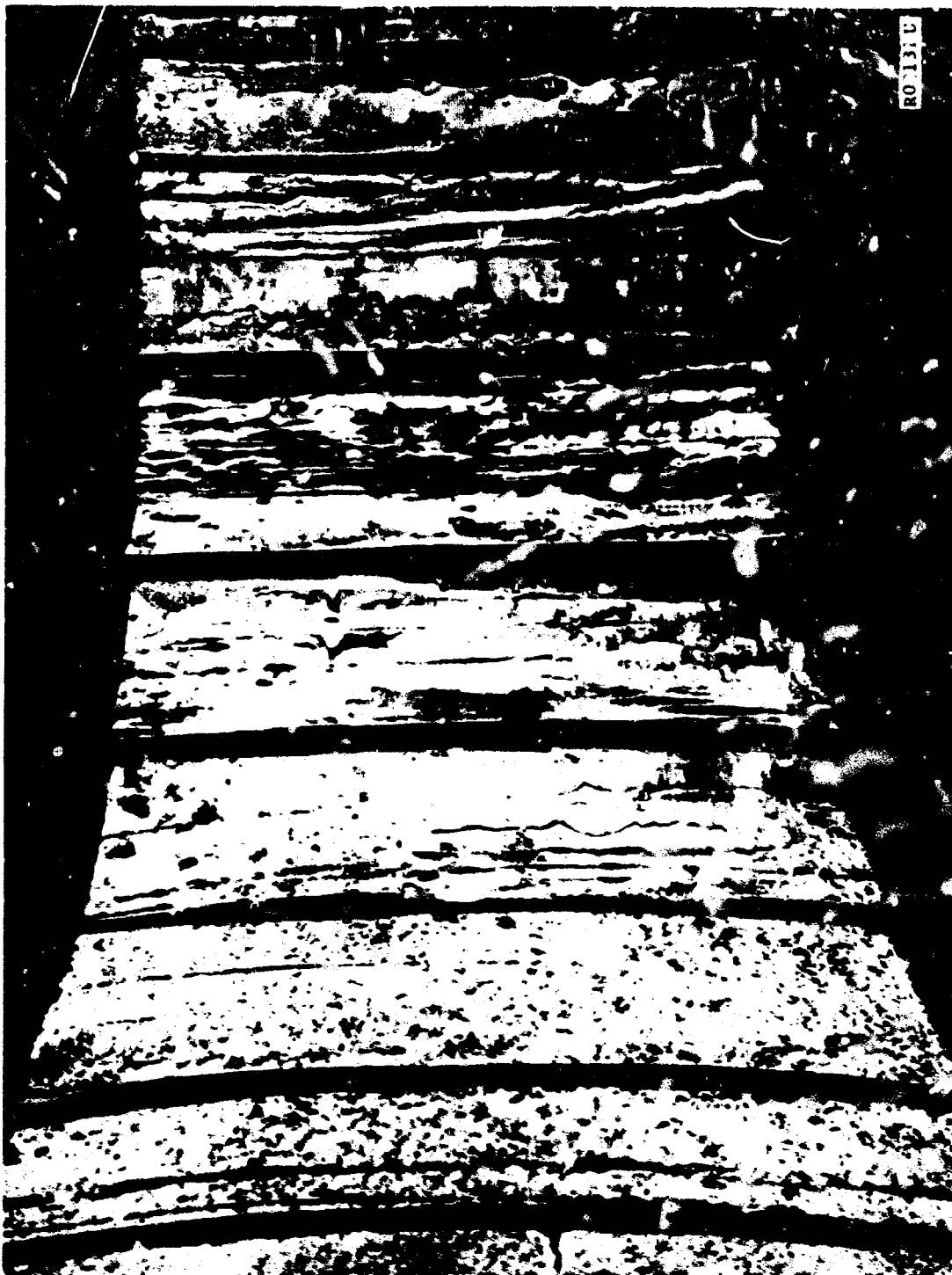


FIGURE 3-2. ELEPHANT'S FOOTING IN ROZZLE FIRED UNDER
CONTRACT NO. AF 04(611) 8387

b. Change of Material Characteristics. Examples of material characteristics changes are, according to material:

Tungsten

- Recrystallization
- Grain growth
- Carbon diffusion

Pyrolytic Graphite

- Structural transformation

Reinforced Plastics

- Char layer formation

The net implication from the structural viewpoint is that, in effect, a new material exists. Elastic constants and other quantities may be altered. Recrystallized tungsten displays a change in strength and a change in brittle-ductile transition temperature. Annealed pyrolytic graphite has different moduli, thermal expansion coefficients, and strengths than the virgin material.

Analyses which apply to the problems common to single-firing and restartable nozzles can be applied to nozzles which have undergone these changes of material characteristics provided that the resulting material properties are known and that deformations accompanying the changes are known.

The effects on the structure of partial changes or of changes which have occurred only in a portion of the nozzle material present problems of a more complex nature. It is necessary not only to be able to estimate these partial changes, but also to know the degree of property change which accompanies them.

c. Problems Caused by Unique Loading Effects. In a single-firing nozzle, the initial conditions are usually taken to be a uniform ambient temperature (and therefore no thermal stresses) and no other initial stresses. However, in a restartable nozzle, a restart can presumably occur at various stages of cool-down with attendant nonzero structural responses. Thus, the structure is not initially in a stress-free or strain-free state.

If structural components undergo permanent deformation or other changes in geometry, they may shrink away from adjacent components. This loss of contact will alter the restraint provided by the constraining structure, and this structure will not provide a load until sufficient radial deformation has occurred to bring the components into contact again.

3.1.3 PROBLEM REASSESSMENT AND ANALYTICAL SUMMARY

The results of the test phases of the program required a critical reassessment of the problems defined in the preceding paragraph. Some problems which had been defined were not observed in the firings. Others which had not been defined were observed.

The following phenomena were not observed in the test program:

- Tensile fractures in pyrolytic graphite. This problem had been analyzed, and the results indicated that it would be virtually impossible to produce such fractures. It is thus felt that no major problem could exist.
- Elephant's footing in pyrolytic graphite. As discussed in Paragraph 3.1.1c, this phenomenon had been observed in a previous program. However, it was not observed in any of the test nozzles of this program. Laboratory studies (Section 4) were conducted to define the time-temperature-load dependence of this effect. Structural analyses were developed to predict the phenomenon. Its occurrence in the Demonstrative Test nozzle was predicted, but the phenomenon failed to materialize. As a consequence, its importance as a problem is not completely well defined.
- Thermal fatigue. The experimental data which are available for the materials of interest indicate that thermal fatigue should not be a problem in restartable nozzles. No thermal fatigue was observed in any of the nozzle tests. Even though these indications are quite favorable, there is still lacking that degree of precision necessary to dismiss this problem entirely.
- Spallation in tungsten. That spallation can occur in tungsten inserts is not certain. The compressive behavior of tungsten is not well defined. In tungsten inserts, the compressive stress on the inner surface builds up rapidly, but so does the temperature. By the time the stresses have reached a magnitude equivalent to the brittle tensile strength, the temperature may have exceeded the ductile brittle transition temperature. So the question of spallation may be of only academic interest for tungsten inserts.

- Spallation in reinforced plastics. This is more commonly termed "chunking." No analysis was performed in this area. Although it was not observed in any of the tests, it is still felt to be an important problem until sufficient data are generated to the contrary.

The following phenomena were observed in the test program:

- Tensile fractures in tungsten. This problem was analyzed, and good correlation was obtained with analytical predictions.
- Anelastic deformation of tungsten. Analysis was developed for predicting this phenomenon. However, it appears that factors other than purely plastic deformation are involved and tungsten shrinkage is not fully understood.
- Spallation in pyrolytic graphite. Surface chunking was observed in some of the tests. Although there is some correlation with analytical results, the definition of spallation in pyrolytic graphite needs to be established in the materials laboratory.
- Buckling of annealed pyrolytic graphite. No instability analyses were performed for any of the materials used in the program. The buckling of annealed pyrolytic graphite was observed in the tests and was defined as a problem as a result of these observations.

Although polycrystalline graphite was initially a primary material to be investigated, it was eliminated from further consideration after the first two rocket motor tests. Since analytical work had been performed on this material prior to this elimination, the analytical work is included even though no emphasis is placed on it later in this report.

3.2 ELASTIC ANALYSIS

The development of fracture surfaces from the back wall tensile response and spallation resulting from inner surface compressive stresses were investigated in this analysis. A simplified analytical method was developed for throat inserts, treating them as hollow cylinders. A computer program was developed for the analysis of conical sections; however, convergence of the program to a solution was not obtained; as a result, no analysis was performed for these sections.

3.2.1 THERMOELASTIC RESPONSE OF THICK-WALLED CYLINDERS

The analysis of the thermoelastic response of thick-walled cylinders was attacked in a reverse manner. Instead of obtaining the structural response from a given loading and comparing this response to some allowable, the allowable responses are used to specify the loadings which can be tolerated. These loadings are then used to specify limits on the geometry of the insert or the firing duration.

A simple analytical technique was desired. This approach was limited to the throat region, which is considered to be a hollow cylinder for purposes of this study, and was applied only to the elastic response.

Since the real problem involves a temperature range in which material properties vary, this variation should be considered in order to make the analysis most meaningful. However, in order not to complicate matters, the analysis was simplified by considering constant properties. These constant properties were chosen as the most useful and meaningful values corresponding to nominal responses of the materials considered. To further simplify, temperature and space were normalized so that the shape of the loading (temperature) distribution would become apparent.

The materials which are candidates for the throat region are brittle over some portion of their operating temperature range. Those that are brittle when the limiting stress is reached can fail purely because of the elastic response. For a cylinder heated at the inner surface, the critical responses will be tension on the outer surface and compression on the inner surface. The tensile stresses can result in the development of fracture surfaces, while the compressive stresses can cause spallation. Spallation has been defined as resulting from shear stresses acting obliquely to the normal compression stress. For maximum shear stresses acting at 45 degrees to the compressive stress, the shear stresses will be half the magnitude of the compressive stress. Since for brittle materials the shear strength can be taken as half the compressive strength, the compressive stress may be taken as the critical stress.

a. Initial structural development. The approach is applied to an isotropic, homogeneous, constant-property material in the shape of a hollow cylinder which is considered to be initially stress free. Temperature, pressure, and restraint provide the loading mechanisms.

The back side (tensile) axial and circumferential thermal stresses of a long hollow cylinder are equal and are given by the expression

$$\sigma = \frac{E\alpha}{1-\nu} \left[\frac{2}{b^2 - a^2} \int_a^b T r dr - T_b \right] \quad (3.1)$$

where

σ = stress

E = modulus of elasticity

α = coefficient of thermal expansion

ν = Poisson's ratio

r = radial coordinate

a = inner radius

b = outer radius

T = temperature

T_b = back wall temperature

And the flame front side compressive axial and circumferential stress are equal and are given by the expression

$$\sigma = \frac{E\alpha}{1-\nu} \left[\frac{2}{b^2 - a^2} \int_a^b T r dr - T_a \right] \quad (3.2)$$

where

T_a = flame front wall temperature

Normalizing the radial coordinate, define

$$\xi = \frac{r - a}{b - a} \quad ; \quad 0 \leq \xi \leq 1$$

and

$$\gamma = \xi - 1/2 \quad ; \quad -1/2 \leq \gamma \leq 1/2$$

Referring the temperature to the datum of the back wall temperature, define

$$\theta = \frac{T - T_b}{T_a - T_b} \quad ; \quad 0 \leq \theta \leq 1$$

For convenience, define

$$\beta = b/a$$

In addition, define

$$f_n(\theta) = \int_0^1 \theta d\xi + 2 \frac{\beta - 1}{\beta + 1} \int_{-1/2}^{1/2} \theta \gamma d\gamma$$

Equations (3.1) and (3.2) may be rewritten

$$\sigma = \frac{E \alpha}{1 - \nu} (T_a - T_b) f_n \quad (3.3)$$

$$\sigma = \frac{E \alpha}{1 - \nu} (T_a - T_b) (f_n - 1) \quad (3.4)$$

for the back side and front side stresses, respectively. These stresses are for long hollow cylinders.

The temperature distribution can be completely described by the temperature difference $T_a - T_b$ and the shape of the distribution. Since the cylinder is being heated internally, the temperature must be a monotonically decreasing function and everywhere have a non-negative curvature. It is simple to specify polynomial distributions which satisfy these requirements. Further, it can be shown that the stress response to a given temperature distribution is bounded by the stress responses of the bounding temperatures. Thus stress responses to temperatures of the form

$$\theta = (1 - \xi)^n \quad ; \quad n \geq 1$$

can be used to bound the responses of intermediate distributions. It is found that actual temperature distributions in nozzle inserts approximate these distributions quite well. The main discrepancy occurs near the outer radius, where the area under the curve is quite small. The error in the thermal stresses which results is also quite small. The functions $f_n(\xi)$ for temperatures of this form may be easily evaluated:

$$f_n = \frac{2}{n^2 + 3n + 2} \left(1 + \frac{n}{\beta + 1} \right) \quad (3.5)$$

These functions are plotted in Figure 3-3.

In real cases, it is found that the maximum thermal stresses occur very near the time when the temperature difference $T_a - T_b$ is at a maximum. For this simplified analysis, it was assumed that the two occur simultaneously. At this point in the analysis, the dimensionless temperature θ is essentially abandoned and another normalized temperature is defined:

$$\phi = \frac{T - T_0}{T_g - T_0}$$

where

T_g = gas stream recovery temperature

T_0 = uniform initial temperature

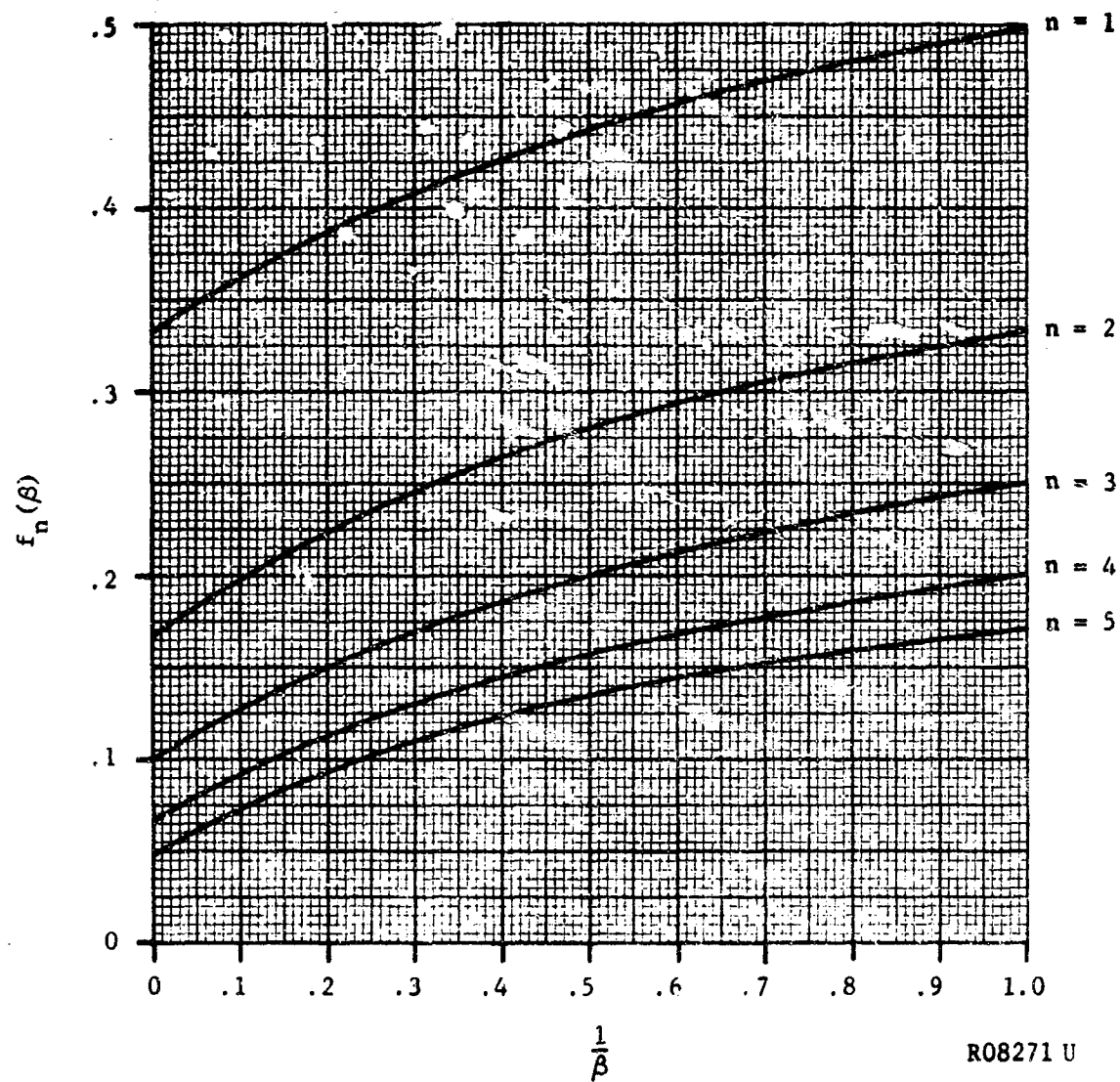


FIGURE 3-3. COUPLING OF TEMPERATURE SHAPE AND GEOMETRY IN THE STRESS RESPONSE OF A HOLLOW CYLINDER

The temperature difference between faces of the cylinder is then

$$\Delta\phi = \frac{T_g - T_b}{T_g - T_o}$$

If an allowable stress is determined, then an allowable temperature difference can be defined as the limiting loading function. Thus

$$\Delta\phi_{all} = \frac{\sigma_{all} (1 - \nu)}{E\alpha(T_g - T_o)f_n} \quad (3.6)$$

or

$$\Delta\phi_{all} = \frac{\sigma_{all} (1 - \nu)}{E\alpha(T_g - T_o)(f_n - 1)} \quad (3.7)$$

for back side and front side responses, respectively.

The thermal development was involved in determining the $\Delta\phi$ which could be attained, thus giving a quantity for comparison with the $\Delta\phi_{all}$ defined above. The thermal development, as well as the combination of the thermal and structural analyses, involved quite a bit of graphical work. These procedures are discussed in the paragraphs following.

b. Simplified Thermal Development. The thermal portion of this analysis was conducted using the published results of Hatch, et al.³⁻¹ and of Desmon and Avis.³⁻² These authors presented data showing the results of thermal response of a thick-walled cylinder to inside heating with the exterior surface of the cylinder insulated. These results are presented in nondimensional form incorporating parameters of nondimensional time, which is the Fourier Modulus, and nondimensional heat transfer parameter, which is the Biot Modulus. These data were plotted and cross-plotted for application to the present analysis. Results are predicated on obtaining a maximum attainable temperature differential and comparing this temperature differential with the maximum allowable temperature differential.

The assumption of the insulated back wall is valid if the back wall thermal gradient is quite small when the maximum temperature difference occurs. This will, of course, be satisfied if the thermal response of the back wall is small at this time.

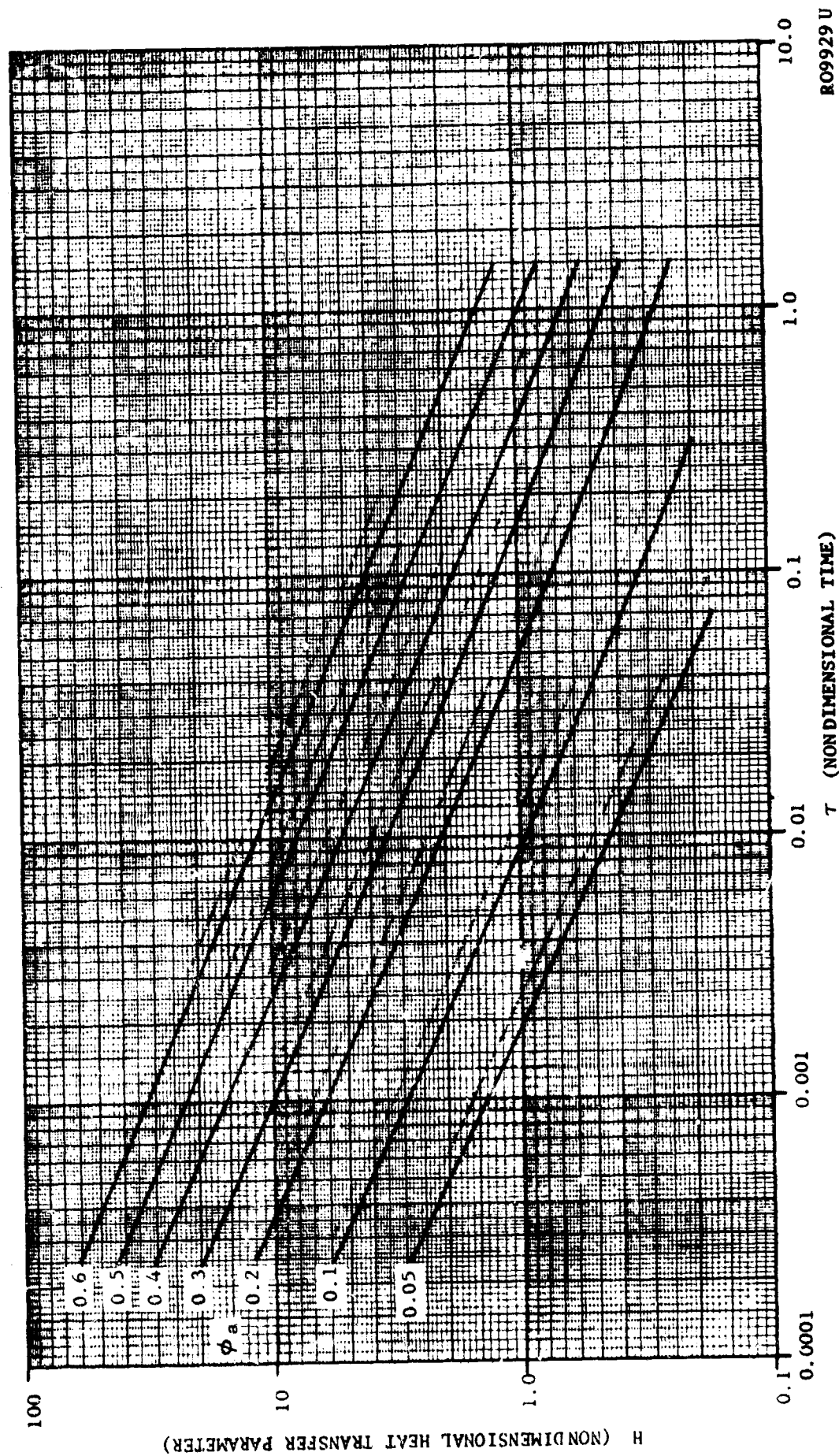
In generating parameters for use in the application of the published thermal data to the current analysis, the dimensional heat transfer coefficient was evaluated by the simplified Bartz equation which is presented as Equation (7) in Paragraph 8.2.1. The dimensionless heat transfer parameter, H , and the dimensionless time, τ , are defined with respect to the cylinder inner radius.

A plot compiled from the Hatch data showing the flame side surface temperature rise as a function of H and T is shown in Figure 3-4. This figure is used in the analysis to plot the heat transfer parameter H as a function of the surface temperature, independent of β , in order that H can be found as a function of nondimensional time.

The nondimensional temperature differential $\Delta\phi$ and the corresponding nondimensional time were taken from the Hatch data for various values of H and β . The maximum value of $\Delta\phi$ at the corresponding T and H were recorded for the various β ratios. Figure 3-5 is the resulting nondimensional cross plot. This figure illustrates the change in the temperature differential across the wall of hollow cylinders of various thickness ratios up to the time when the maximum temperature differential occurs. Note that for times up to just prior to the attainment of the maximum temperature difference through the wall, these curves are independent of the thickness ratio. The straight portion of the curve indicates that the outside surface temperature has not yet responded to the heating and that the inside surface temperature is, during this period, independent of the wall thickness. Thermally, during this time the body behaves as though it were an infinitely thick hollow cylinder.

A certain relaxation of the assumption of constant properties was made in this thermal analysis. The mean specific heat, \bar{c} , the mean conductivity, \bar{k} , and the mean heat transfer coefficient, \bar{h} , were used. These quantities were obtained by integrating between temperature limits and averaging with respect to the temperature range. The mean heat transfer coefficient is shown in Figure 3-6 as a function of wall temperature and the product $P_c D^*$. This graph was generated using the simplified Bartz equation. It applies to the propellant under consideration within this study, CYI-75. The thermal conductivity, k , and mean thermal conductivity, \bar{K} , of tungsten and ATJ graphite are shown in Figure 3-7 as a function of temperature. The value of \bar{k} corresponding to the flame side surface temperature was used for subsequent calculations.

The term f_n is a component of the thermal loading and is expressible in terms of β and the temperature distribution parameter n . Recall that the temperature distribution parameter, n , reflects the shape of the temperature distribution. The parameter n , for a given β ratio, is dependent only on the nondimensional time. The quantity n is shown in Figure 3-8 as a function of nondimensional time for given ratios of β . This figure was generated by using a best fit polynomial to express the shape of the temperature distribution. Combining Figures 3-3 and 3-8 results in Figure 3-9. This figure depicts the loading parameter f_n as a function of nondimensional time for various ratios of β .



RO9929 U

FIGURE 3-4. FLAME SIDE TEMPERATURE OF INSERT UP TO MAXIMUM TEMPERATURE DIFFERENCE ACROSS INSERT

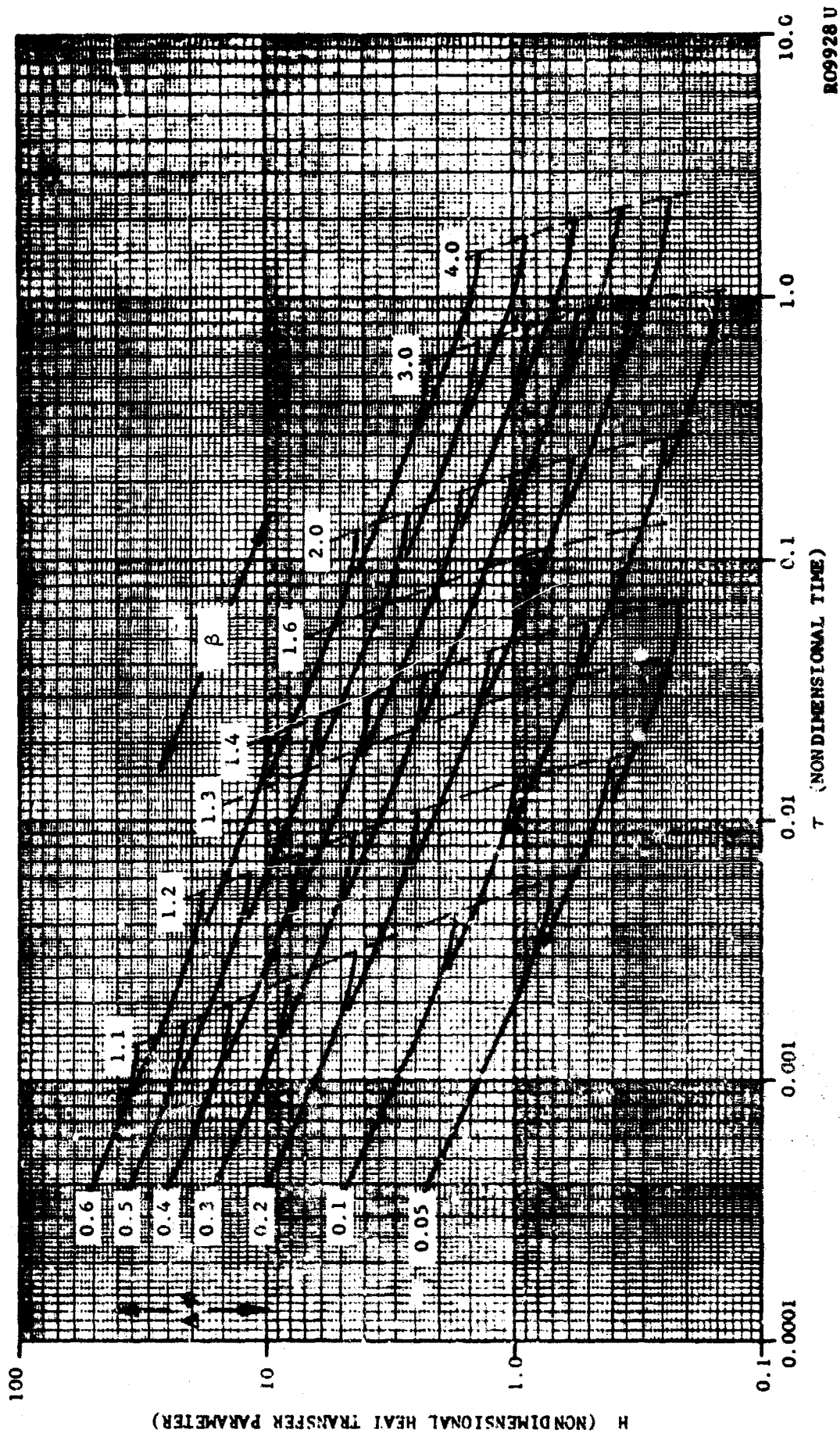
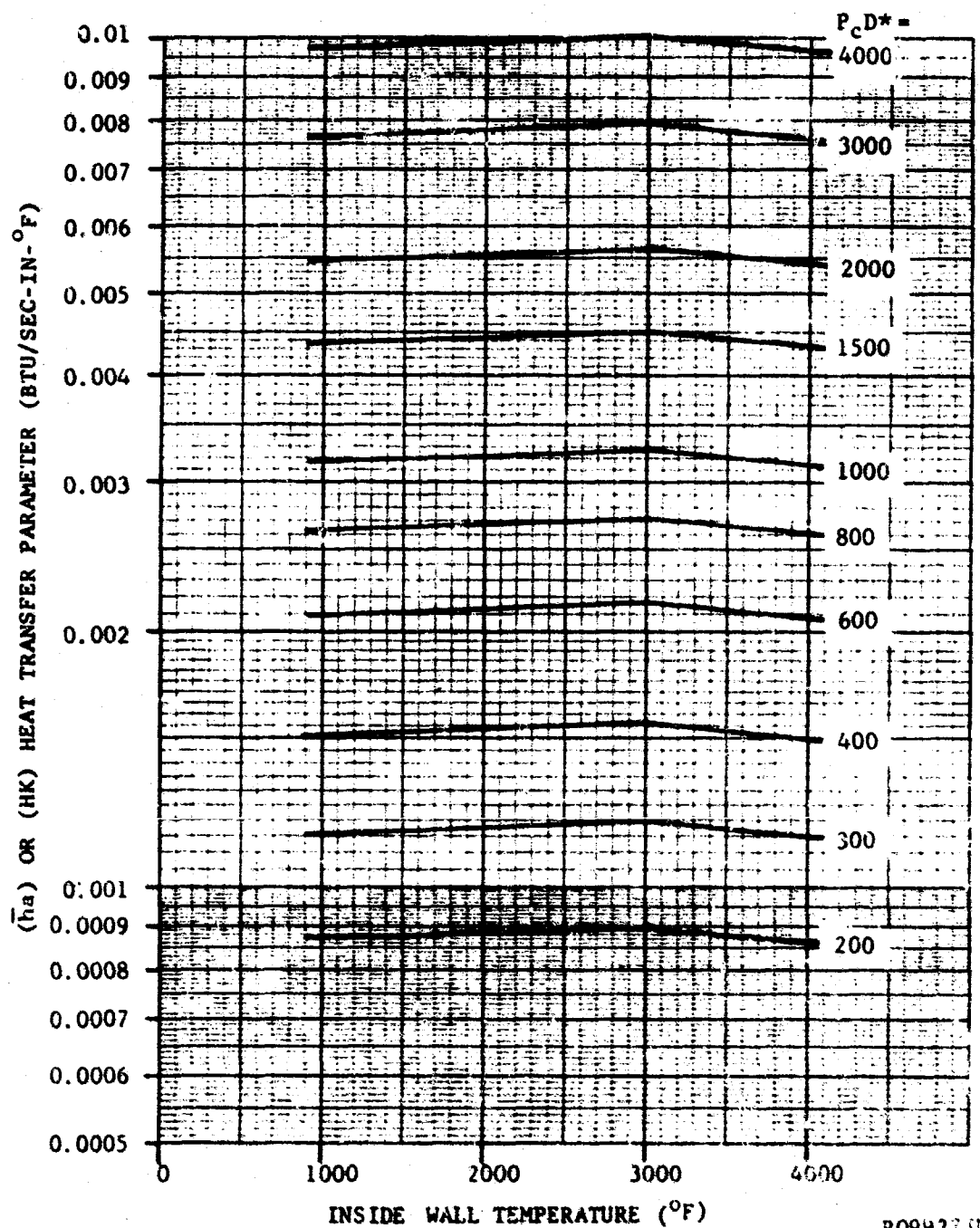


FIGURE 3-5. TEMPERATURE DIFFERENCE ACROSS INSERT WALL

RC9928 U



R09927 U

FIGURE 3-6. NOZZLE THROAT HEAT TRANSFER PARAMETER

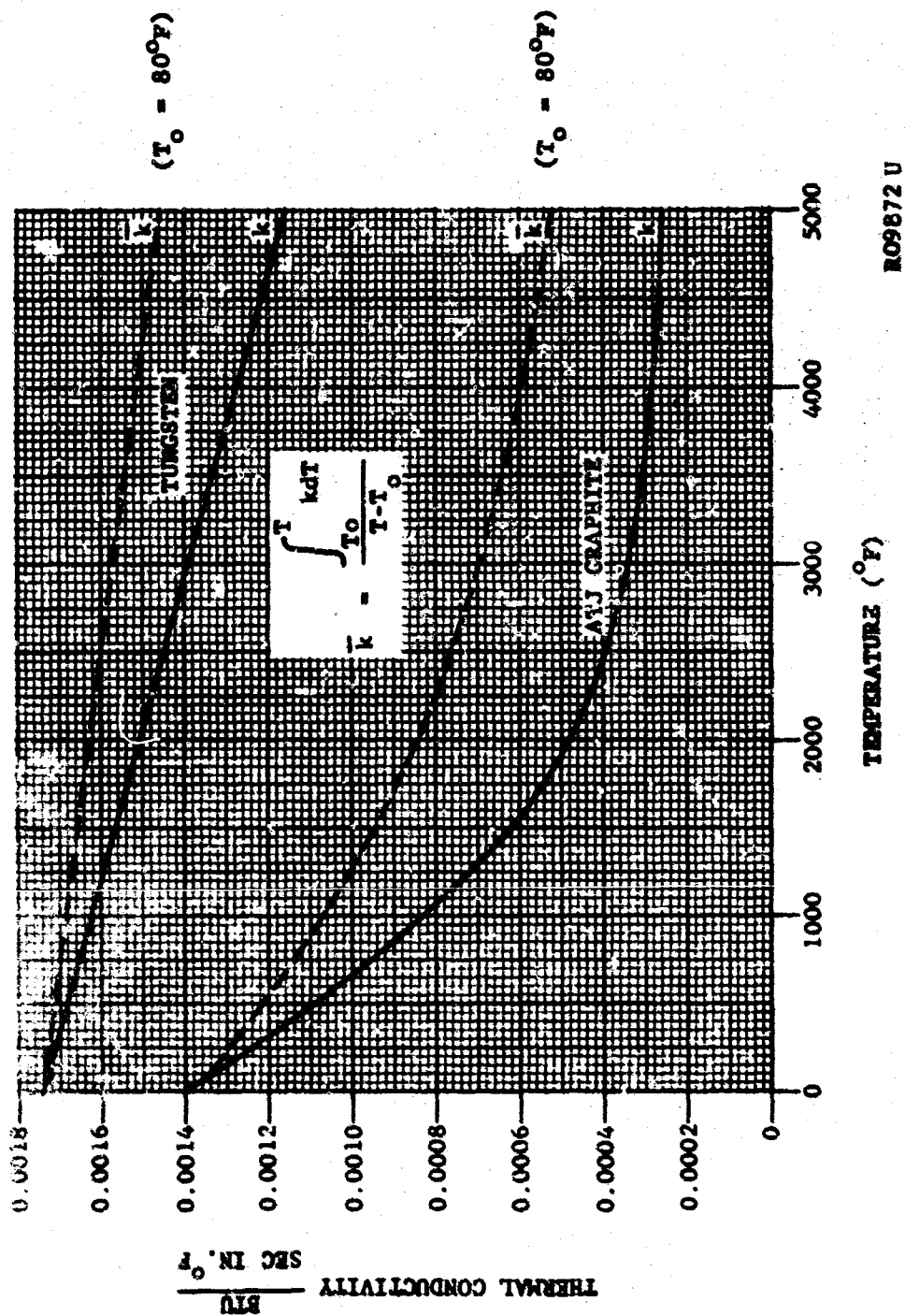
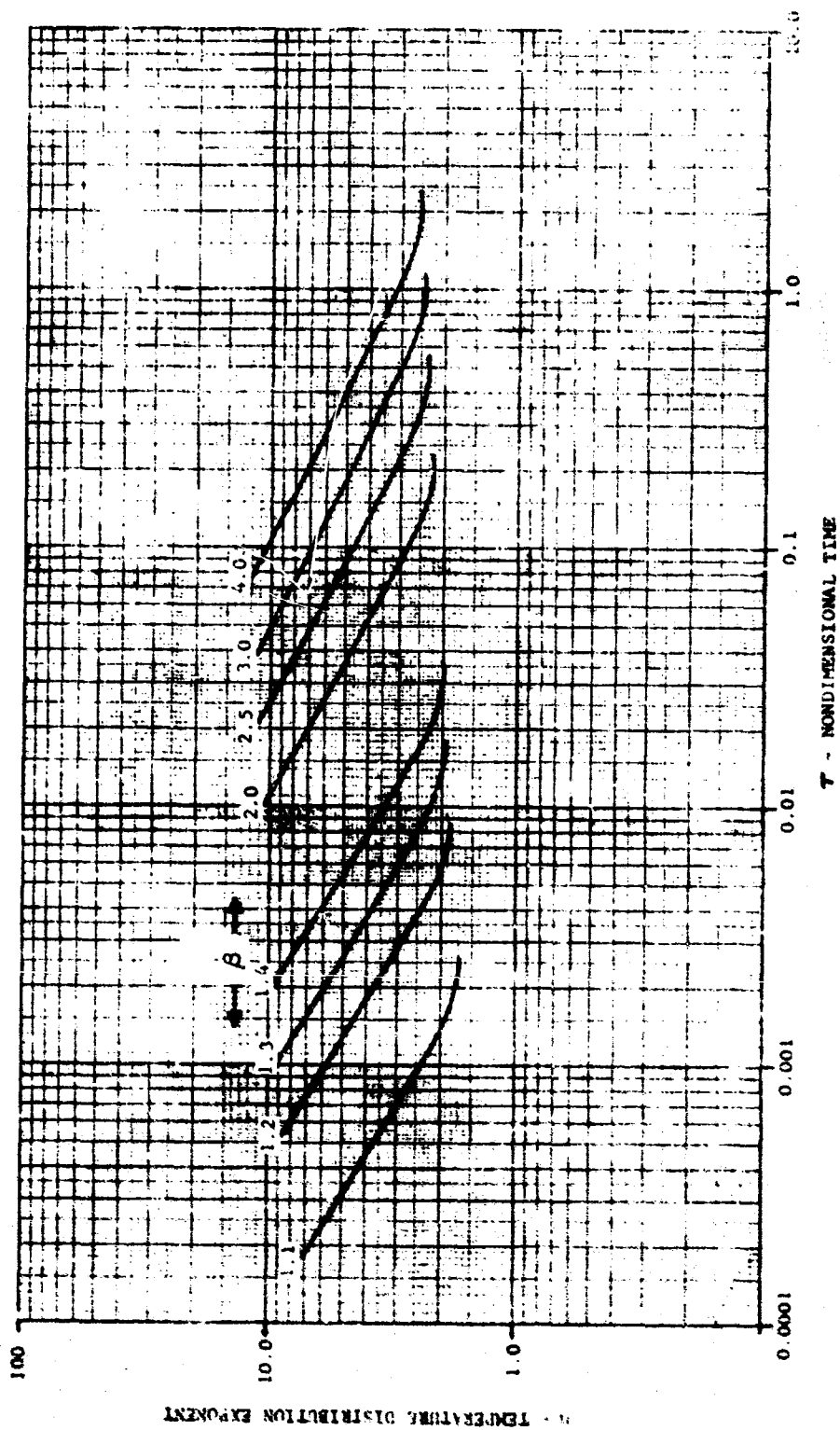


FIGURE 3-7. THERMAL CONDUCTIVITY OF TUNGSTEN AND ATJ GRAPHITE



R09869U

FIGURE 3-8. TEMPERATURE DISTRIBUTION EXPONENT

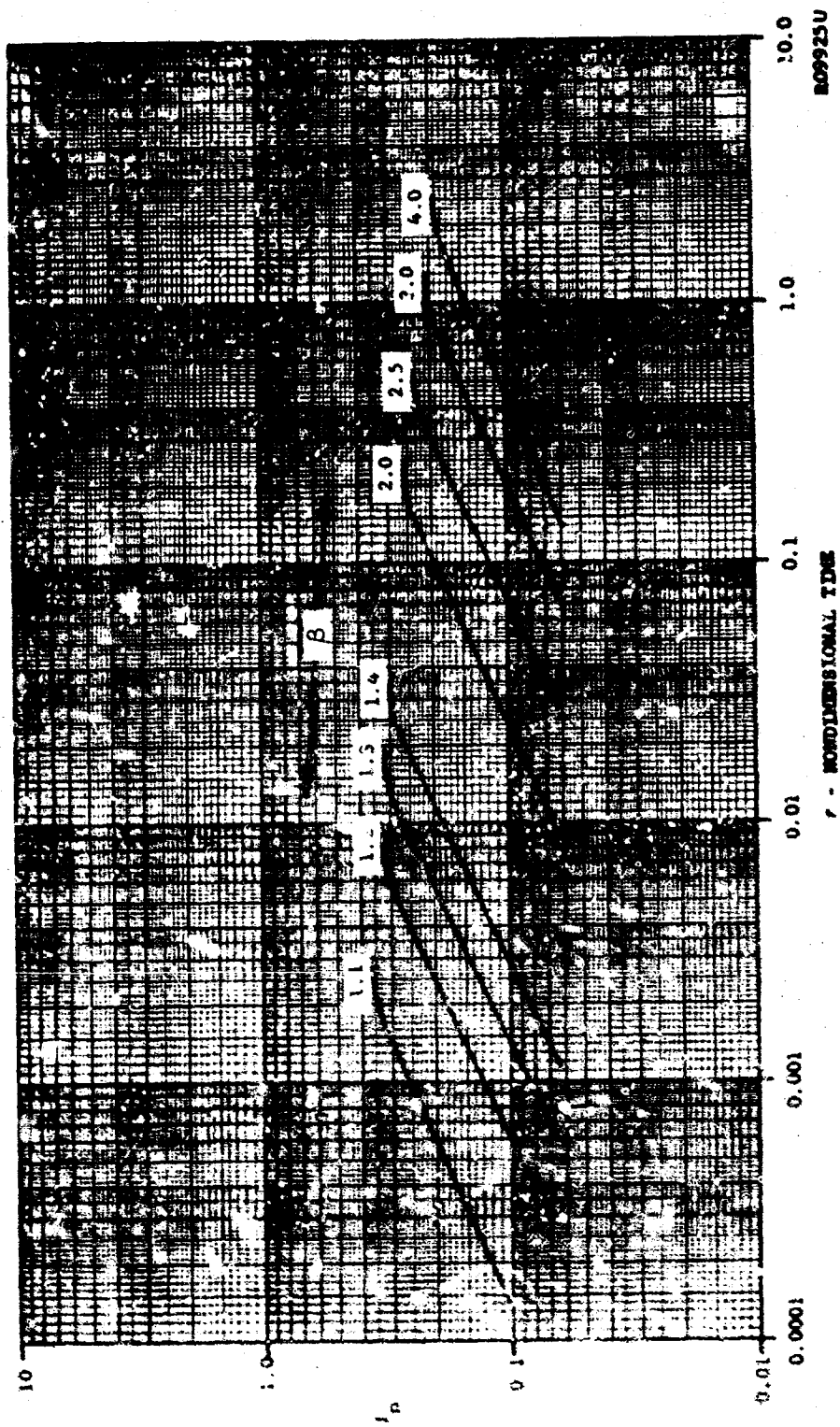


FIGURE 3-9. THE THERMAL LOADING PARAMETER I_n

At this point, the thermal development is essentially complete. All that remains is to establish the attainable $\Delta\phi$. In order to accomplish this, the data of Figure 3-5 are combined with the heat transfer parameter (as reflected by P_{CD}^*) of Figure 3-6 and conductivity data of Figure 3-7. The resulting graphs show the attainable nondimensional temperature difference as a function of nondimensional time. Graphs of the attainable $\Delta\phi$ are not shown at this point but will be presented later with the allowable temperature difference superimposed.

With the function f_n determined, as shown in Figure 3-9, an allowable may be established from Equations (3.6) and (3.7) for the simplest cases of thermal loading. Other important considerations not reflected in these equations are those of pressure, restraint, and clearance, and whether the cylinder is short or long. These factors will be discussed prior to the completion of the structural development.

c. Short Cylinders and Long Cylinders. For long cylinders, the usual assumption is that plane strain prevails. In this case, for isotropic materials with constant properties, the hoop and axial thermal stresses are equal on both radial boundaries. On the inner surface these stresses are both compressive for internal heating. And on the outer surface they are both tensile. Providing restraint to radial thermal expansion effectively superimposes a compressive stress upon the hoop thermal stresses while, to a first-order approximation, it does not affect the axial stresses. Thus, for the long cylinder, the axial stress will always represent the maximum back side stress while at the inner surface the hoop stress will almost always have the greater magnitude. (Whether the hoop or axial stress has the greater magnitude at the inner surface depends on the relative influences of the internal pressure and the back side restraint.)

For short cylinders, the condition of plane stress is usually assumed. Axial effects are neglected and the axial stress is assumed to vanish. Equations (3.3) and (3.4) give the inner and outer hoop thermal stresses for short cylinders if ν is set equal to zero. In the case of short cylinders, the hoop stress is always critical at both the inner and outer surfaces whether back side restraint exists or not.

How short is short? Cylinders which may be properly identified as washers or disks are certainly short, and for all practical purposes the axial stresses do vanish. But as disks are allowed to lengthen there is no critical length at which the axial stresses suddenly jump from zero to their long cylinder values. No, as length increases so the axial stresses build up. Below a certain length, these axial stresses can usually be safely neglected in relation to the hoop stresses, and the axial effects

which account for an increase in the hoop stresses (through the factor $1/(1-\nu)$) can also be neglected. Although this length is not precisely defined, it has been found that a cylinder can usually be considered short if

$$\lambda L \leq \frac{\pi}{4} \quad (3.8)$$

where L is the length and λ is the familiar quantity defined by

$$\lambda^4 = \frac{3(1-\nu^2)}{R^2 h^2}$$

where R is the mean radius and h is the wall thickness.

d. Influences of Pressure, Restraint, and Clearance. Still assuming a hollow cylinder, whether short or long, if an internal pressure p_a and an external pressure p_b are acting, the hoop stresses which result on the boundaries are given below.

At the inner boundary

$$\sigma_{p_a} = \frac{\beta^2 + 1}{\beta^2 - 1} p_a \quad (3.9)$$

$$\sigma_{p_b} = -\frac{2\beta^2}{\beta^2 - 1} p_b \quad (3.10)$$

At the outer boundary

$$\sigma_{p_a} = \frac{2p_a}{\beta^2 - 1} \quad (3.11)$$

$$\sigma_{p_b} = -\frac{\beta^2 + 1}{\beta^2 - 1} p_b \quad (3.12)$$

To a first-order approximation, these pressures do not influence the axial stresses. For purposes of this analysis, the radial stresses are of themselves relatively unimportant, but their influence on the radial displacement is important; both will be included in the analysis.

The internal pressure acting is, for a throat insert, due to the exhaust gases. For simplicity, this pressure may be taken as approximately 60 percent of the chamber pressure and may be considered to be uniform over the length of the insert.

The external pressure acting is not so easy to determine. It is usually not a gas pressure. (If it were, it would be close to the internal pressure, and the pressure effects would become insignificant.) Rather, it is caused by restraint to radial expansion of the insert. The magnitude of the external pressure, p_b , is difficult to estimate. It is influenced by three factors:

- (1) Initial back side clearance (between insert and backup material). A small gap can have a tremendous influence not only on the magnitude of p_b but also on the time when p_b occurs.
- (2) Relative rigidities of the insert and backup structure. These rigidities include both the thicknesses and the moduli of the two structures
- (3) The bearing strength or crushing characteristics of the insert or the backup structure (whichever is more likely to crush).

It is evident that total restraint to radial expansion cannot be provided by the backup structure - a tremendous pressure (in some cases of the order of several tens of thousands of pounds per square inch) is required for most inserts.

The radial displacements at the outer surface of the insert due to thermal effects, internal pressure, and external pressure are, respectively,

$$u_{th} = \alpha b \left[(T_a - T_b) (f_n - 1) + T_a - T_o \right] \quad (3.13)$$

$$u_{p_a} = \frac{2b}{E(\beta^2 - 1)} p_a \quad (3.14)$$

$$u_{p_b} = - \frac{b}{E} \left[\frac{\beta^2 + 1}{\beta^2 - 1} - \nu \right] p_b \quad (3.15)$$

These displacements apply to both long and short cylinders. If there should be an initial gap, u_g , between the insert and backup structure, this gap can, for purposes of analysis, be subtracted from the thermal displacement.

Good design practices usually provide a gap between pyrolytic graphite washers and the backup structure, while they provide a tight back side fit for tungsten and polycrystalline graphite inserts. These fits, as well as the backup material, influence not only the magnitude of the back side pressure developed but also the time at which this pressure is developed.

Polycrystalline graphite inserts are fitted into material which has nearly the same modulus of elasticity as the insert itself. Thus, before the backup material has heated appreciably (or a char has formed), the insert and backup material act almost as a continuous elastic body. The pressure, p_b , developed is of the order of an internal radial stress for an equivalent single elastic body. These stresses would be of the order of 1000 to 2000 pounds per square inch.

Tungsten inserts, on the other hand, are fitted into material which has less than 5 percent of the tungsten modulus. Thus, tungsten is more capable of forcing its radial displacement upon the backup material, and back side pressures in the range of 5,000 to 10,000 psi can be developed.

These back side pressures are only a fraction of those required for total restraint to expansion. The geometries of the insert and the complete backup structure influence the magnitude of the pressures developed.

The magnitude of the restraint pressure, p_b , may be estimated by considering the insert and the backup structure to be concentric cylinders with interface pressures and displacements matched. Then

$$p_b = \frac{E_1 E_2}{E_2 K_1 + E_1 K_2} \left\{ \frac{2 p_a}{E_1 (\beta^2 - 1)} + \alpha_1 \left[(T_a - T_b) (f_n - 1) + (T_a - T_o) \right] - \frac{u_g}{b} \right\} \quad (3.16)$$

where the subscripts 1 and 2 refer to the insert and backup, respectively.

$$K_1 = \frac{\beta^2 + 1}{\beta^2 - 1} - \nu_1$$

$$K_2 = \frac{c^2 + b^2}{c^2 - b^2} + \nu_2$$

c = outer radius of the backup cylinder.

In order for p_b to exist, it must be positive, which means that the quantity in the braces must be positive. For total restraint, the factor outside the braces becomes E_1/K_1 (E_2 becomes infinitely large). For no restraint, this factor vanishes.

The Poisson's ratios appearing in the definitions of the K 's represent the influence of the radial stress on the radial displacement. K_2 will, in general, be greater than K_1 , and in the range of about twice K_1 . If E_1 and E_2 are approximately equal (which is true for polycrystalline inserts), then

$$\frac{E_1 E_2}{E_2 K_1 + E_1 K_2} < \frac{1}{2} \frac{E_1}{K_1}$$

or less than 50 percent restraint is supplied. But if $E_1 \gg E_2$, which is true for tungsten inserts,

$$\frac{E_1 E_2}{E_2 K_1 + E_1 K_2} < \frac{E_2}{K_2}$$

and since

$$\frac{E_2}{K_2} \ll \frac{E_1}{K_1}$$

the restraint is very slight.

If $E_1 = 2 E_2$, which is approximately true for pyrolytic graphite inserts, then

$$\frac{E_1 E_2}{E_2 K_1 + E_1 K_2} < \frac{1}{3} \frac{E_1}{K_1}$$

For convenience let

$$\frac{E_1 E_2}{E_2 K_1 + E_1 K_2} = J \frac{E_1}{K_1}$$

It is recommended that, for simplified and approximate analyses, the factor J be taken as approximately

1/3 for polycrystalline graphite inserts

1/5 for pyrolytic graphite washer inserts

1/50 for tungsten inserts

It is further recommended that polycrystalline graphite and tungsten inserts be designed with an intimate fit between the insert and the backup structure so that u_g vanishes, and that pyrolytic graphite washer inserts be designed with a radial gap behind the insert u_g/b of about 0.002.

The back side restraint is important in long cylinders only for the front side compressive hoop stress. The magnitude of this hoop stress is increased by p_b while the axial stress is not influenced. The axial back side tensile stress is not affected by the external pressure, while the back side hoop stress is decreased by it.

For short cylinders, the back side restraint is important for both the back side and front side hoop stresses. These hoop stresses are the critical stresses since the axial stresses are assumed to vanish. The back side hoop stress is decreased by the presence of p_b while the magnitude of the front side hoop stress is increased.

The critical stresses may now be defined. For short cylinders, the hoop stress is critical on both the inner surface and the outer surface. At the outer surface

$$\sigma_{\theta} = E\alpha(T_a - T_b)f_n + \frac{2p_a}{\beta^2 - 1} - \frac{\beta^2 + 1}{\beta^2 - 1} \frac{EJ}{K} \left\{ \frac{2p_a}{\beta^2 - 1} + \alpha[(T_a - T_b)(f_n - 1) + (T_a - T_o)] - \frac{u_g}{b} \right\} \quad (3.17)$$

and at the inner surface

$$\sigma_{\theta} = E\alpha(T_a - T_b)(f_n - 1) + \frac{\beta^2 + 1}{\beta^2 - 1} p_a - \frac{2\beta^2}{\beta^2 - 1} \frac{EJ}{K} \left\{ \frac{2p_a}{\beta^2 - 1} + \alpha[(T_a - T_b)(f_n - 1) + (T_a - T_o)] - \frac{u_g}{b} \right\} \quad (3.18)$$

Subscripts have been dropped on E , K , and α and the quantities are those of the insert. The restraint stress is active if the quantity in the braces is positive. In each of these equations, the first term on the right is the direct thermal stress; the second term is the direct internal pressure stress; and the third term is the restraint stress.

For long cylinders, the value of the maximum stress on the outer boundary is always given by the axial stress. For no pressure effects, the axial and hoop stresses are equal and, theoretically, the insert could fail from either stress. With restraint stresses acting, the hoop stress is reduced while the axial stress is unaffected. Thus, the magnitude of the maximum stress is given by

$$\sigma_z = \frac{E\alpha}{1-\nu} (T_a - T_b) (f_n - 1) \quad (3.19)$$

On the inner surface, if there are no pressure effects, the hoop and axial stresses are again equal. If restraint stresses are acting, the magnitude of the hoop stress is increased, while the axial stress is not affected. The hoop stress at the inner boundary is

$$\sigma_\theta = \frac{E\alpha}{1-\nu} (T_a - T_b) (f_n - 1) + \frac{\beta^2 + 1}{\beta^2 - 1} p_a \quad (3.20)$$

$$- \frac{2\beta^2}{\beta^2 - 1} \frac{EJ}{K} \left\{ \frac{2p_a}{(\beta^2 - 1)} + \alpha \left[(T_a - T_b) (f_n - 1) + (T_a - T_o) \right] - \frac{u_E}{b} \right\}$$

where, again, the quantity in the braces must be positive in order for the restraint stress to be active. Both of these equations for the long cylinder tacitly assume that the compressive restraint hoop stress is great enough to overpower the tensile stress caused by the internal pressure. In actual cases involving practical nozzle designs, this is a valid assumption. By the time the stresses have grown to the point where they are approaching their maximum values, the restraint stresses have become active and do, in fact, more than overcome the internal pressure stresses.

c. Completed Structural Development. It now remains to establish an allowable temperature difference with considerations from the structural portion of the analysis to compare to the attainable temperature difference developed in the thermal portion of the analysis. This must be done in order to develop limits on the insert design or the nozzle operation.

If the stresses defined by Equations (3.17) through (3.20) are at their allowable values, then the temperature differences, $T_g - T_p$, are at their allowable values. Allowable temperature differences may then be defined in terms of the allowable stresses.

For the short cylinder, at the outer boundary

$$\Delta\phi_{all} = \frac{\sigma_{all} (\beta^2 - 1) - 2p_a + \frac{EJ}{K} [\beta^2 + 1] \left[\frac{2p_a}{(\beta^2 - 1)E} - \frac{u_g}{b} + \alpha(T_g - T_o) \phi_a \right]}{E\alpha (T_g - T_o) \left[f_n (\beta^2 - 1) - \frac{J}{K} (\beta^2 + 1) (f_n - 1) \right]} \quad (3.21)$$

And at the inner boundary

$$\Delta\phi_{all} = \frac{\sigma_{all} (\beta^2 - 1) - (\beta^2 + 1) p_a + 2\beta^2 \frac{EJ}{K} \left[\frac{2p_a}{(\beta^2 - 1)E} - \frac{u_g}{b} + \alpha(T_g - T_o) \phi_a \right]}{E\alpha (T_g - T_o) (f_n - 1) \left[\beta^2 - 1 - 2\frac{J}{K} \right]} \quad (3.22)$$

For the long cylinder, at the outer boundary

$$\Delta\phi_{all} = \frac{\sigma_{all} (1 - \nu)}{E\alpha (T_g - T_o) f_n} \quad (3.23)$$

And at the inner boundary

$$\Delta\phi_{all} = \frac{\sigma_{all} (\beta^2 - 1) - (\beta^2 + 1) p_a + 2\beta^2 \frac{EJ}{K} \left[\frac{2p_a}{(\beta^2 - 1)E} + \alpha(T_g - T_o) \phi_a \frac{-u_g}{b} \right]}{E\alpha (T_g - T_o) (f_n - 1) \left[\frac{\beta^2 - 1}{1 - \nu} - 2\beta^2 \frac{J}{K} \right]} \quad (3.24)$$

In the two equations applicable to the inner boundaries, the allowable stress is compressive, so that σ_{all} used in these equations must be a negative quantity.

Inclusion of the effects of pressure and restraint in the equations admittedly makes them somewhat cumbersome. But the stresses which result can be significant to the overall structural analysis.

Not all of these equations are important for all of the insert materials considered in this program. Inserts of pyrolytic graphite washers can be considered only as short cylinders. Application of Equation (3.21) to pyrolytic graphite washer inserts shows that it is virtually impossible for outer radius tensile failure to be a critical failure mode. However, inner radius compressive failures are shown to be possible by Equation (3.22).

Tungsten inserts can be long or short cylinders. With this material, only outer radius tensile failures are considered; therefore, only equations (3.21) and (3.23) are important. Inner radius compressive failures have not been defined for this material.

All four equations are important for ATJ graphite inserts. These inserts may be long or short cylinders, and both tensile and compressive failures can occur.

A summary of the applicability of the equations and the materials are given in Table 3.1.

TABLE 3.1

APPLICATION OF LIMITING EQUATIONS TO NOZZLE INSERT MATERIALS

<u>Equation</u>	<u>Applied To</u>	<u>Important For</u>
3.21	Short cylinder, outer tensile	ATJ graphite, tungsten
3.22	Short cylinder, inner compressive	ATJ graphite, pyrolytic graphite
3.23	Long cylinder, outer tensile	ATJ graphite, tungsten
3.24	Long cylinder, inner compressive	ATJ graphite

The additional material properties necessary for the evaluation of the equations for the allowable temperature difference are presented in Table 3.2.

TABLE 3.2

MATERIAL PROPERTIES

<u>Material</u>	<u>ν</u>	<u>E(psi)</u>	<u>$\alpha/^{\circ}\text{F}$</u>	<u>α_{all} (Tensile) (psi)</u>	<u>α_{all} (Comp) (psi)</u>
Arc Cast and Extruded Tungsten	0.3	50×10^6	2.2×10^{-6}	94,000	(Not considered)
Gas Pressure Bonded Tungsten	0.3	31.4×10^6	2.2×10^{-6}	30,100	(Not considered)
ATJ Graphite	0.17	2×10^6	1.85×10^{-6}	3,000	-10,800
Pyrolytic Graphite	-0.2	3.55×10^6	1.2×10^{-6}	15,000	-10,500 and -13,000

The tensile strengths of the tungstens in Table 3.2 are the values measured in the laboratory. The values of E and α used for ATJ graphite are admittedly slightly high but are used to provide a margin in the analysis to compensate for the statistical variation in strength of this material. The mean coefficient of thermal expansion of ATJ is not constant but will vary between about 1.3×10^{-6} to about 2×10^{-6} per degree Fahrenheit over the temperature range of interest. The properties listed for pyrolytic graphite are values in the basal plane of the material. The analysis derived for

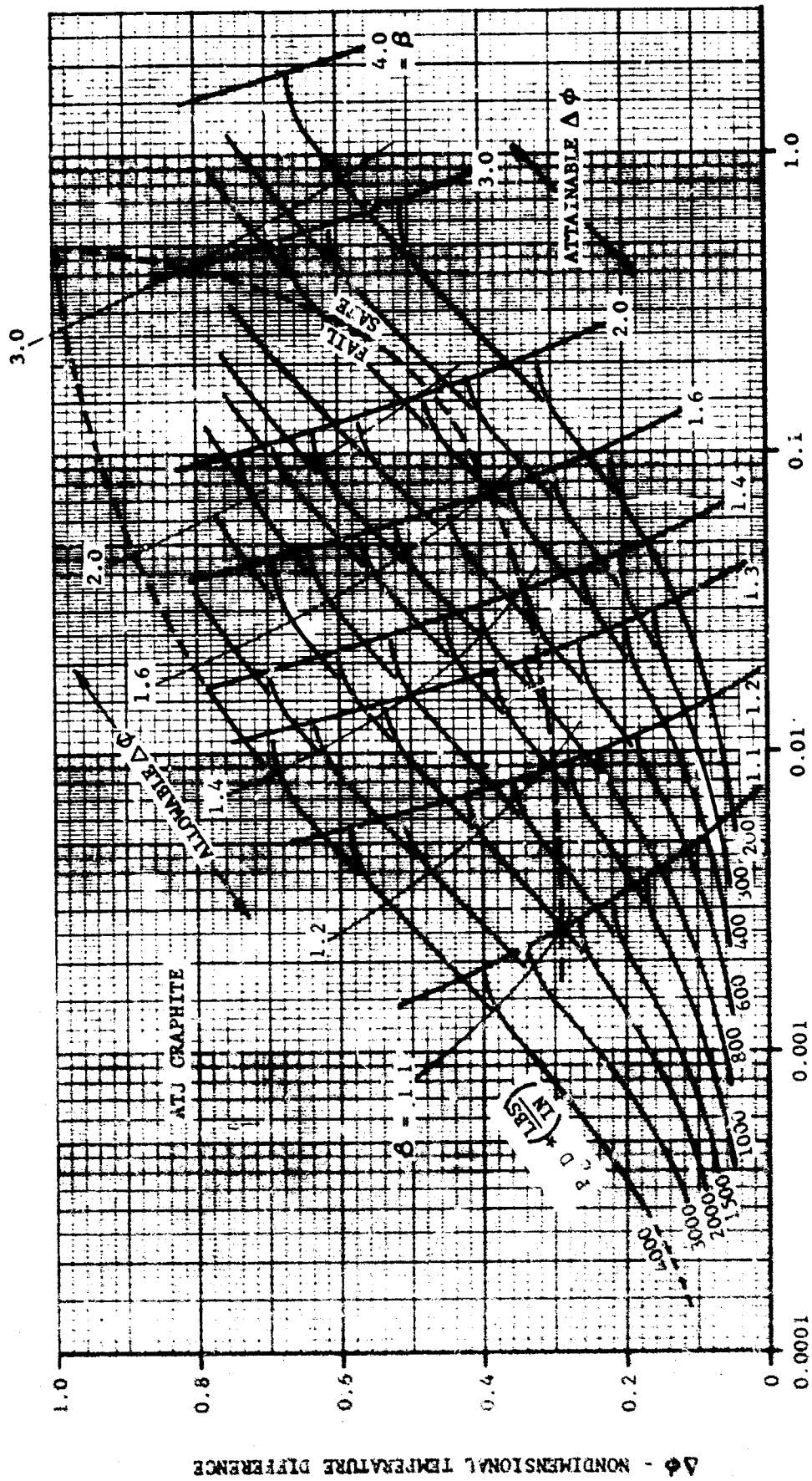
isotropic material applies to edge-grain-oriented (washer configuration) pyrolytic graphite when the axial Poisson effect is neglected. A special treatment was given to the structural analysis of pyrolytic graphite washers in order that a simplified method could be applied. This treatment is discussed later.

Figure 3-10 shows one type of design chart which results from this analysis. It involves Equation (3.23) applied to ATJ graphite. The data of Figure 3-5 was combined with the heat transfer parameter of Figure 3-6 and the conductivity data of Figure 3-7 to produce the attainable $\Delta\phi$ portion of the graph. The cross lines in Figure 3-10 identified by values of β and labeled attainable $\Delta\phi$ show the cutoff of the heating curves (labeled P_{CD}^*) when they have attained the maximum value of the temperature difference between faces of the insert. Equation (3.23) with the properties listed in Table 3.2 and values of f_n from Figure 3-9 was used to obtain the allowable $\Delta\phi$ values. The cross lines in Figure 3-10 identified by values of β and labeled allowable $\Delta\phi$ show the maximum temperature difference which can be tolerated by the insert. It will be noted that a "fail/safe" line has been drawn depicting the intersection of the β lines associated with the attainable $\Delta\phi$ with the β lines of the allowable $\Delta\phi$. This "fail/safe" line depicts the limiting value of β for an insert or, for a larger β , depicts the limit on the firing duration.

A similar chart for tungsten is shown in Figure 3-11. This chart is also based on Equation (3.23) and applies to a long cylinder outer radius tensile limitation.

It should be noted that these two charts are quite general and can be applied to any insert design so long as the relationship between the heating parameter and the inner wall temperature is as shown in Figure 3-6. Heating parameters which are not insensitive to the inner wall temperature introduce an additional complexity into the analysis, but can still be included to produce charts such as Figures 3-10 and 3-11.

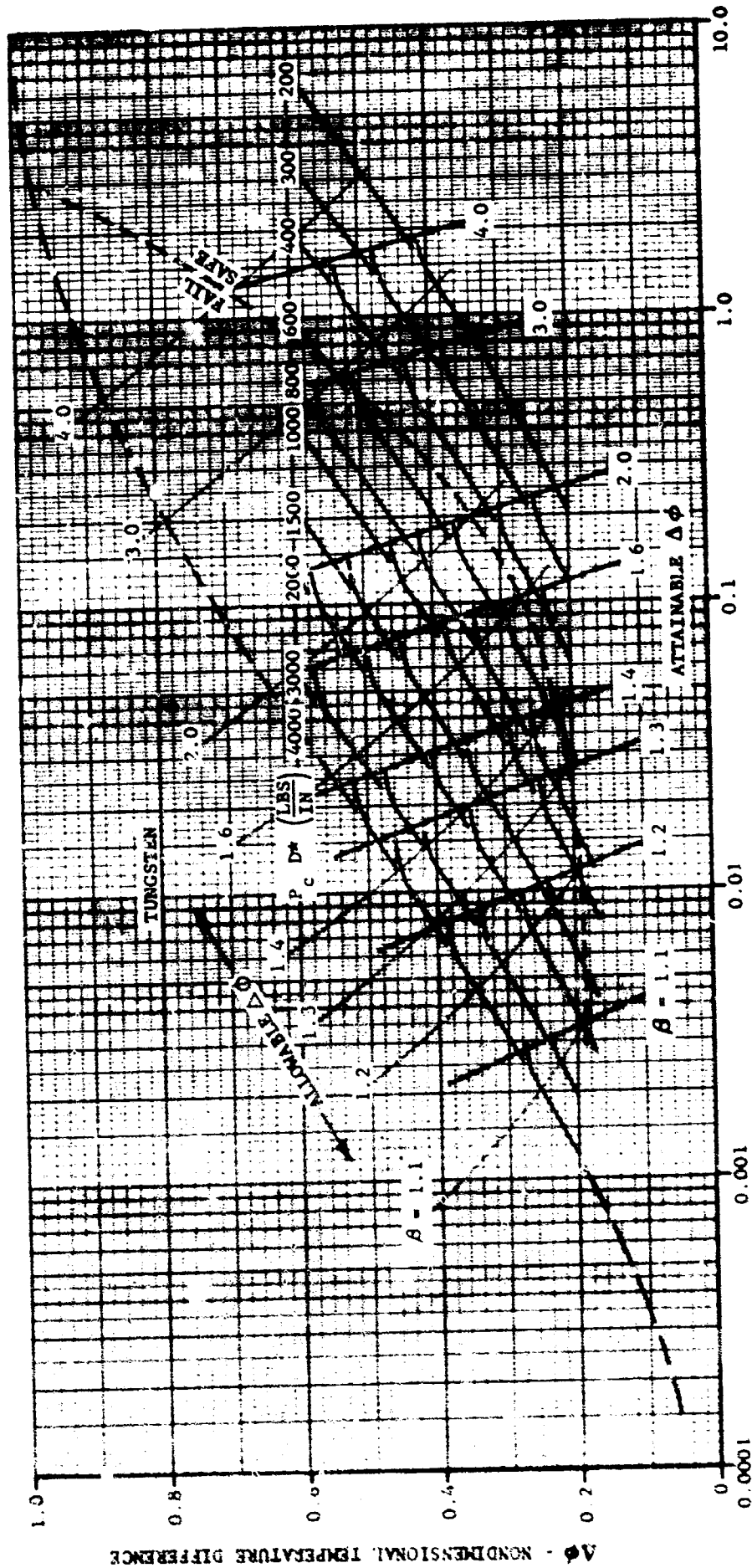
Only a portion of the P_{CD}^* curves are shown in Figures 3-10 and 3-11 due to the limitations in the thermal data; however, these curves, if extended, will show that, for large values of β , $\Delta\phi$ becomes asymptotic to unity as τ becomes large as suggested by the extension of the $P_{CD}^*=4000$ curve. If the "fail/safe" line is also extrapolated upwards, it can be seen that there will be some thickness ratio which can resist exceeding the allowable thermal stress at the outer surface of the insert for the entire range of heating conditions. For tungsten, the value of this invulnerable thickness ratio (β) is about 6. For ATJ the value is between 3 and 4.



R09870U

τ - NONDIMENSIONAL TIME

FIGURE 3-10. THERMAL STRESS DESIGN CHART FOR ATJ GRAPHITE LONG CYLINDER
BACK SIDE TENSILE FAILURE



RO9874 U

τ - NONDIMENSIONAL TIME

FIGURE 3-11. THERMAL STRESS DESIGN CHART FOR TUNGSTEN LONG CYLINDER
BACKSIDE TENSILE FAILURE

To illustrate the significance of the "fail/safe" line and its extrapolation, the following example is used. On Figure 3-11, consider the heating curve corresponding to $P_c D^* = 600$. Following the curve for increasing time and continued heating, all values of β are safe up to about 1.35. Moving further up the heating curve, failure will occur for β values between about 1.35 and 3. Values of β above about 3 are again safe. Therefore, with continued heating on the $P_c D^* = 600$ curve, it would be undesirable to design the throat insert with a thickness ratio between about 1.35 and 3. This region of undesirable thickness ratios has been coined the stress "window." If an insert were designed with a value of β between 1.35 and 3 for the $P_c D^* = 600$ heating condition, the firing duration should be limited to a value corresponding to $\tau = 0.035$ in order to preclude failure.

Other charts can be generated for all of the applicable combinations of equations and materials as shown in Table 3.1. These charts would be similar to those shown in Figures 3-10 and 3-11 and would include the parameters associated with pressure and restraint (p_a , J , and u_g). By the time design charts were being generated in the program, sufficient rocket motor testing had been conducted to shift emphasis away from ATJ and more heavily toward pyrolytic graphite and tungsten. For this reason, a complete development involving all four of Equations (3.21), (3.22), (3.23), and (3.24) for ATJ was not accomplished. Design charts were developed for the three conditions applicable for the other two materials.

The analysis of pyrolytic graphite washers was developed by the adoption of a somewhat special technique. The thermal and mechanical properties in only the a-b plane are involved in this analysis. In the simplified method which has been developed, it is necessary to use a constant thermal expansion coefficient. The available data show a great deal of scatter but generally indicate that the coefficient is not constant. However, if the initial temperature is taken as 1000°F instead of room temperature, a constant expansion coefficient does serve as a good approximation. A short computer study was conducted in order to evaluate the effects on temperature of starting from initial temperatures of 70 and 1000°F . It was found that the maximum temperature differences across the washer were quite comparable and at the times when these maximums existed, the temperatures were very close. Only the times at which these temperatures occurred were significantly different, and this difference was only about 2 seconds in 9. Thus whether starting from 70 or 1000°F , approximately the same maximum $\Delta\phi$ and shape of the temperature distribution could be obtained. This indicated that using the constant thermal expansion coefficient which approximates the thermal expansion above 1000°F in conjunction with the temperature response obtained with initial ambient conditions of 1000°F would result in a reasonably accurate structural analysis. The simplified method was applied using a constant thermal expansion coefficient.

Outer surface tensile failures of pyrolytic graphite washers were investigated for throat diameters between 5/8 inch and 5 inches using Equation (3.21) and considering that no back side restraint was provided. This is the most severe condition for the outer radius response. For wall thicknesses from thin to even beyond what would normally be considered reasonable, no failures could be predicted. The chart which was constructed for this analysis is not shown since it shows no more than is stated above.

The design chart generated for pyrolytic graphite inner surface compressive response using Equation (3.22) is shown in Figure 3-12. This is the same type of design chart shown previously with the exception that internal pressure, external restraint, and an initial clearance between the insert and backup structure have been included. In this chart the attainable $\Delta\phi$ and ϕ_a cross lines are independent of these additional factors, while the allowable $\Delta\phi$ cross lines are directly dependent on them.

If the value of P_c is fixed, the dependence on $P_c D^*$ is removed from the design charts. For a given material, geometrical limits of β can be defined as a function of the cylinder diameter, and another type of design chart emerges. This has been done for pyrolytic graphite and tungsten.

Fixing P_c at 700 psia results in a more directly usable design chart for pyrolytic graphite shown as Figure 3-13. Five curves are shown in this graph. Three of these curves can be considered as realistic design curves which consider partial restraint ($J = 1/5$) and an initial backside clearance ($u_g/b = 0.002$ and 0.001). These three curves are plotted for two strength values; the lower strength represents vendor data while the higher strength represents the data of Gobble and Salmen^{3.17}. The two other curves, 3 and 5, shown on the graph represent upper and lower bounds on the design for the lower strength material. The lower curve, 5, representing the lower design bound, considers total restraint to radial displacement without including internal pressure. This is not realistically attainable but represents the limit which would be approached as the backup structure becomes more rigid and the initial back side gap is removed. The upper curve, 3, is realistically more attainable and represents the upper design bound, which is approached as the back side gap is increased and the back side restraint is removed.

A similar design chart for tungsten with $P_c = 700$ psia is shown as Figure 3-14. This figure is for the long cylinder and therefore does not include any pressure or restraint effects. Both as-received arc cast and extruded tungsten and gas pressure bonded tungsten, as used in this program, are included in the figure. The corresponding tungsten design chart for short cylinders of arc cast material is shown as Figure 3-15. One of the curves shown in this figure considers $J = 1/50$ and no initial radial clearance behind the insert. The other curve considers no restraint. Only the

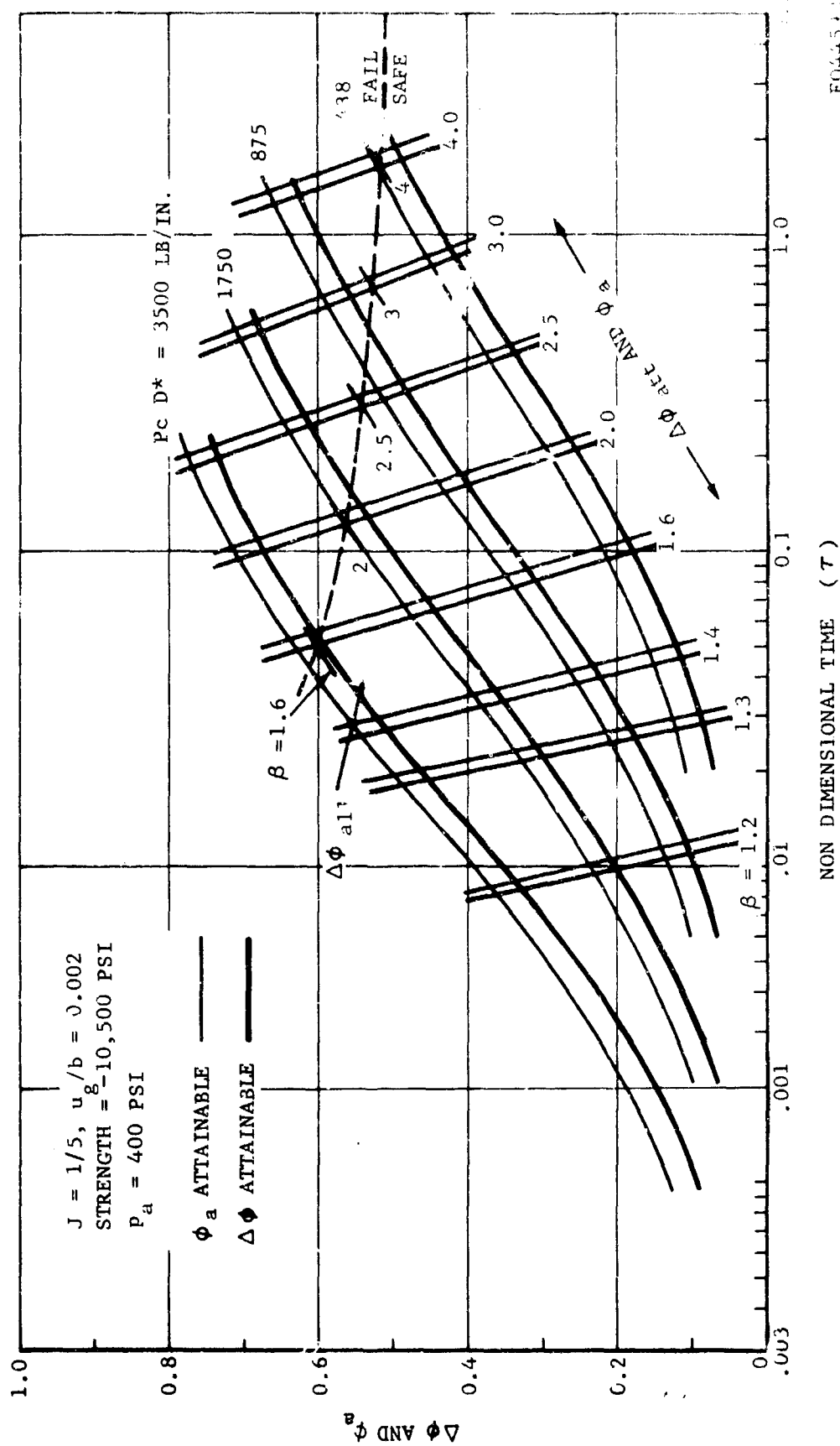
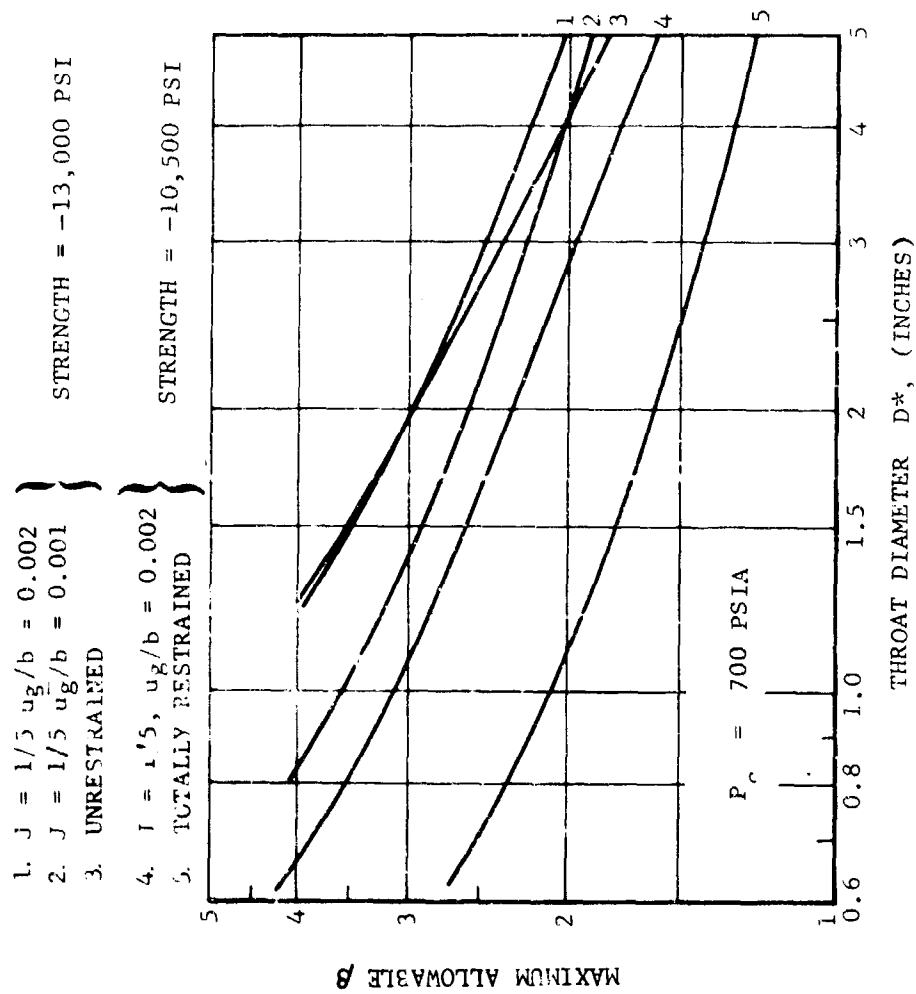
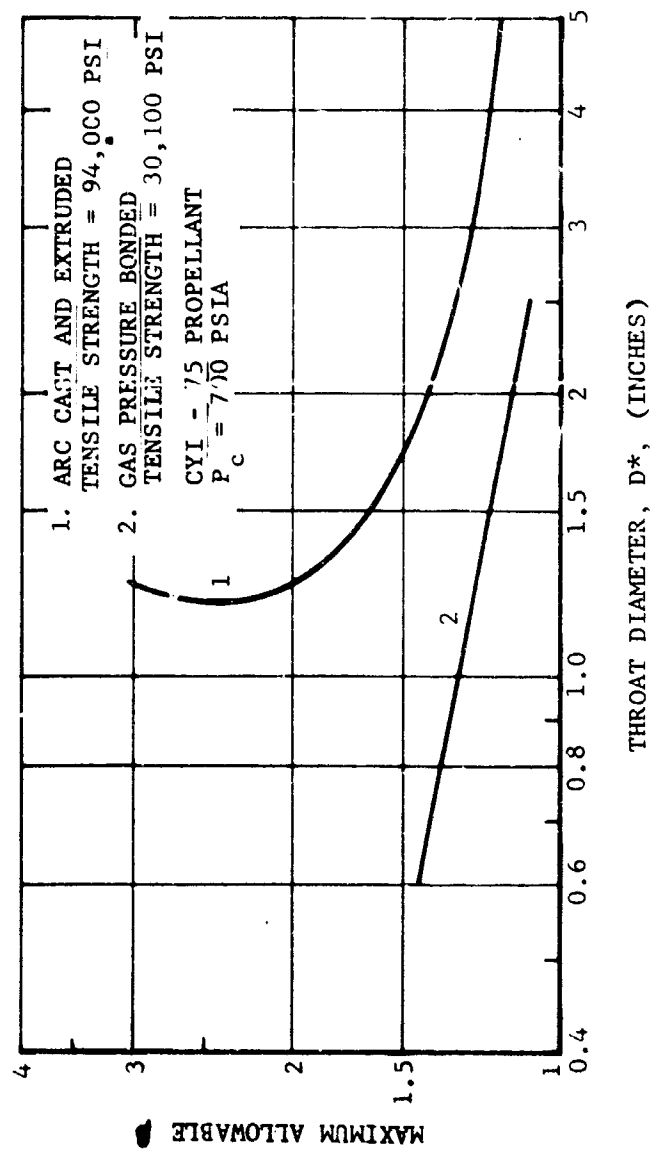


FIGURE 3-12. DESIGN CHART FOR FLYOLYTIC GRAPHITE INNER SURFACE COMPRESSION



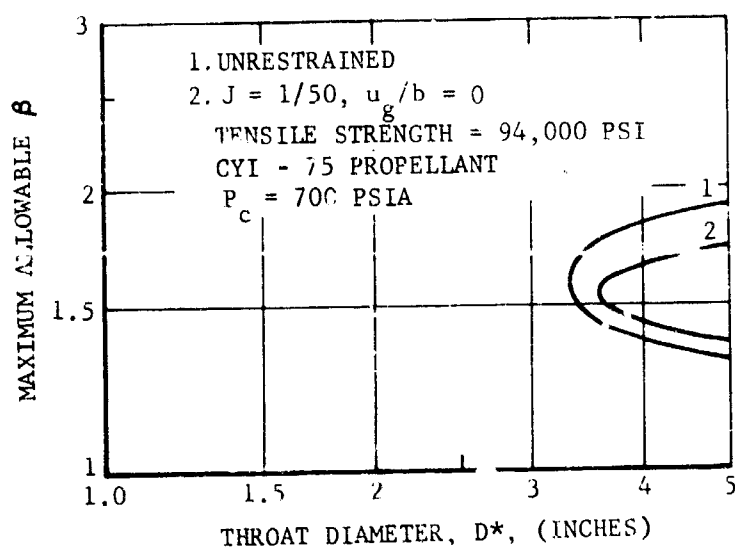
FO4460 U

FIGURE 3-13. PYROLYTIC GRAPHITE INNER SURFACE COMPRESSIVE RESPONSE STRUCTURAL CHART



FO4461 U

FIGURE 3-14. TUNGSTEN LONG CYLINDER OUTER SURFACE TENSILE RESPONSE STRUCTURAL CHART



FO4462 U

FIGURE 3-15. TUNGSTEN SHORT CYLINDER OUTER SURFACE
 TENSILE RESPONSE STRUCTURAL CHART

regions lying to the right of the curves are the unsafe design regions. The tremendous advantage that can be gained by utilizing short cylinders (and thus avoiding the axial effects) of high-strength tungsten is quite obvious from a comparison of Figures 3-14 and 3-15. In single-firing nozzles, this is an important consideration; however, in restartable nozzles which suffer from strength degradation because of grain growth, most of this advantage can be lost, as will be seen in Paragraph 3.6.

An upper design bound representing complete restraint is not really meaningful for tungsten; therefore, such a curve is not shown in Figure 3-15. An attempt was made to define an upper bound on the effects of restraint by considering the back side pressure to be equal to the bearing strength of an ATJ graphite backup structure. This bearing strength was taken as 8000 psi and the equation used is

$$\Delta\phi_{all} = \frac{\sigma_{all} - \frac{1}{\beta^2 - 1} \left[2p_r - (\beta^2 + 1) 8000 \right]}{E\alpha(T_g - T_o) f_n} \quad (3.25)$$

However, the insert became so safe that the design limits lay outside the range of the heating parameter used in the thermal portion of the analysis. A rough extrapolation of the data seems to indicate that all values of β are valid for initial firings for throat diameters up to about 10 inches.

The objective of this analysis has been to establish a simplified method or procedure by which the important design variables could be examined to discover problem areas or ranges in these variables over which brittle elastic fracture could be a problem. These areas or ranges could then be verified or examined by use of the more expensive computer analysis, thereby eliminating or minimizing a costly computerized random approach to finding problem areas. However, the extent to which the random approach is minimized depends on the accuracy of the simplified method. In order to obtain an indication of the accuracy of the method, comparisons were made with computer solutions. There are two general areas in which comparisons were necessary in order to provide a comprehensive evaluation: (1) the prediction of temperature as a function of time, and (2) the prediction of the stress response as a function of time. Since the method was based on an insulated back wall, a comparison was also made of the temperature and stress response when the insert has a conducting backup structure.

Comparisons of solutions from computer programs with those of the simplified method have been presented for ATJ and tungsten in Reference (3.3) and are not repeated here. These comparisons showed for tungsten that for the examples studied the hot wall temperature, the temperature difference across the walls, the time at which the maximum temperature occurs, and the shape parameter n of the simplified method gives a surprisingly good approximation to the computer solution. This is true for both an insulating and a conducting backup structure. The stress solutions from the computer and the simplified method also gave a good comparison.

The comparisons with ATJ were not quite so good. The maximum temperature differential and the time at which it occurs matched quite well, but the shape parameter, n , was as much as 25 percent in error at the time of peak surface temperature differential. A 25 percent error in n results in a much lower error in the loading function, f_n . No comparison was made with the stress solutions.

To investigate whether the simplified method for pyrolytic graphite gave a good approximation, spot checks, utilizing computer solutions for both the thermal and stress analyses, were made on the FAIL/SAFE curves of the design chart. It was found that the maximum allowable radius ratios, β , were between 5 and 10 percent conservative.

3.2.2 THERMOELASTIC ANALYSIS OF A THICK-WALLED CONICAL SECTION

The entrance and exit sections of a nozzle are considered to be cone frustums for purposes of this investigation. This consideration is a contractual requirement and removes the generally complicating involvement of double curvature in the analysis.

A detailed literature search of existing works directly related to the particular problem of thick-walled conical sections was made before a definite method of solution was adopted. References 3.4 through 3.9 are some of the more significant of these works. Several methods of solution were considered, including analytical solutions, analog computer simulation procedures, and approximate methods using digital computer techniques.

Because of the restrictive assumptions required in order to obtain an analytical solution, this approach was not considered to be fruitful in the present investigation. Analog simulation of the problem is a very powerful tool but, because of the complexity of the present problem, requires a prohibitive amount of equipment in order to obtain a reasonable degree of accuracy and, therefore, was not pursued further. A finite difference solution, making use of relaxation techniques and a digital computer, appeared to be the most promising. Sufficient information was available to indicate that reasonable accuracy could be expected to be achieved within an acceptable length of computer run time (References 3.4 and 3.5). Thus, this was the method of approach used, as outlined in the following discussion.

A biconical coordinate system was established as shown in Figure 3-16, and equilibrium equations were written in terms of this coordinate system. Making use of strain-displacement relations and the Duhamel-Neumann thermal stress-strain relations, the equilibrium equations were expressed in terms

The diagram illustrates a conical shell element. A vertex O is shown at the top left, with a horizontal distance r_c to the right and a vertical distance R down to the shell's axis. A cone angle ω is indicated. The shell is a curved surface with a central longitudinal axis labeled l . A coordinate system is defined with i as the longitudinal direction and j as the circumferential direction. The shell is divided into segments along both axes. Labels include $S_1(i, l)$, $P_1(i, l)$, $S_2(M, j)$, $P_2(M, j)$, $S_3(i, N)$, $P_3(i, N)$, $S_4(l, j)$, and $P_4(l, j)$, representing various stress and pressure components. The shell's boundary is labeled M and N .

FIGURE 3-16. COORDINATE SYSTEM USED FOR CONICAL SECTIONS

of R and ω displacements. Because of the assumed axial symmetry, the three equilibrium equations could be reduced to two equations in terms of the displacements U and V in the ω and R coordinate directions, respectively.

In addition to the assumption of axial symmetry, the material was assumed to be linearly elastic, homogeneous, and isotropic. Body forces were neglected, and the temperature and stress distribution problems were uncoupled. These are basic assumptions in the analysis and were made in order to simplify the initial solution. All are realistic and practical assumptions, the relaxation of which would have added considerable complexity to the solution, and this was not felt to be justified in the initial effort. The removal of some of these assumptions, however, (e.g., the consideration of nonlinear elastic, visco-elastic, or plastic material behavior) was considered to be likely for future efforts. Likewise, heterogeneous and/or anisotropic materials were of interest and could be treated in later efforts if the additional complexities introduced were felt to have been justified. Considering body forces and coupling the temperature and stress distribution problems introduce, in general, only higher order terms and therefore were of little consequence.

Both normal and shear loadings of arbitrary distribution (within the limitation of axial symmetry) were to be accommodated on all four boundaries; i.e., interior, exterior, and both ends.

The equilibrium and boundary condition equations, which are partial differential equations, were rewritten in difference form in order that they might be solved numerically. In the preliminary analysis, several assumptions were made in order to simplify the solution and make the checkout of the basic computer program simpler. These include the assumptions of (1) a single layer of material, (2) that material properties, with the exception of the coefficient of thermal expansion, do not vary with temperature, and (3) that the finite difference grid spacing in any one coordinate direction is uniform. All of these simplifying assumptions were to have been removed as required. Analytical work necessary for including the effects of temperature-dependent material properties in the basic formulation was accomplished, and these additions were to have been incorporated as required after the basic computer program was checked out. Thus, it would be possible to analyze conical sections made up of multiple layers of similar or dissimilar materials having temperature-dependent material properties and arbitrary loadings.

The method of successive over-relaxation was used for the solution of the difference equations with the cross section being defined by a finite difference grid and the number of grid nodes being arbitrary (within the upper limit of computer capacity, which is adequate). A relatively simple

point-by-point iteration procedure was used with periodic checks on rate of convergence and a detailed re-evaluation of residuals at specified intervals to minimize accumulative error.

The problem, as analyzed above, is general enough to be of real significance in solving practical problems and yet is specific enough to permit obtaining results within a reasonable amount of time and effort. A computer program was written in Fortran language for use on the Philco 2000 computer. However, difficulties were encountered in obtaining convergence of the numerical relaxation method for the general case of arbitrary surface loading conditions. Other problems involving certain mixed boundary conditions were solved with some success. In particular, these problems considered displacement conditions on the ends of the conical section. The program converged quickly (1-2 minutes of computer time) to a solution when only displacement boundary conditions were specified. However, when stress boundary conditions or mixed boundary conditions were specified, convergence was not obtained.

Attempts were made to make use of the fact that specifying boundary displacements does give convergence in order to solve the general mixed boundary value problem. By specifying boundary displacements based upon the magnitude of the applied boundary loadings, solving this displacement boundary value problem by the relaxational technique, and then calculating boundary stresses corresponding to these assumed displacements, the assumed displacements could be revised to give better agreement between the applied and calculated stresses. This process can then be repeated as necessary until sufficient accuracy is attained. Because of the nature of the existing finite difference equations, however, successive revision of the boundary displacements does not necessarily lead to the desired results. The coupling between adjacent boundary point displacements was too weak to transmit changes adequately.

Another attempt was made to obtain convergence by revising the original difference equations at the boundaries in order to eliminate forward and backward differencing techniques and to provide a more orderly system of difference equations with which to work. The details of such a method are similar to those outlined in Reference 3.10 for solutions of plane elasticity problems. However, again convergence was not obtained for the case of mixed boundary conditions, and the method was discarded.

Because of the difficulties encountered and the lack of contract time available for additional development, work was suspended at this point. The computer program which actually resulted then was one which would accept displacement boundary conditions but would not accept stress boundary conditions or mixed boundary conditions. This type of program was not considered sufficient to analyze conical sections in this investigation. As a consequence, no structural analysis was performed on these sections.

3.3 ANELASTIC BEHAVIOR

Elastic-perfectly plastic behavior was investigated in this analysis; no viscoelastic or time-dependent anelastic behavior was studied. The Tresca yield criterion was adopted for greater ease in investigating plastic behavior. An analysis was developed for determining the plastic behavior of hollow cylinders.

It was elected not to develop a computerized numerical methodology for the anelastic behavior of nozzle materials. Although such computer programs would greatly enhance capabilities for nozzle analysis, it was felt that they would find little practical application toward achieving the goals of the present restartable nozzle study. In addition, the property data required for efficient, accurate use of such programs do not exist in directly applicable form for most nozzle materials.

The assumption of ideal elastic-perfectly plastic (non-work-hardening) behavior would appear justified for tungsten, considering stress-strain curves at temperatures above the brittle-ductile transition temperature, such as those typically shown in Reference 3.11. However, examination of literature on various grades of graphites, i.e., Reference 3.12, and manufacturers' and supporting test data on pyrolytic graphite, such as in References 3.13 through 3.19, would seem to indicate that the graphites possess extremely work-hardening (or occasionally work-softening) characteristics, when not behaving as typical linearly elastic materials. Graphite is also a viscoelastic material, according to Reference 3.12, brittle to approximately 2800°F, plastic above 4500°F, and in a transition state between these two temperatures.

Below the brittle-ductile transition temperature, some types of tungsten also have no apparent yield region at all, exhibiting linear elastic brittle behavior. For such essentially completely brittle materials as tungsten at low temperatures, it is required to interpret any yield criterion as actually a failure criterion, since behavior is approximately linear elastic until failure. Scrutiny of the stress-strain curves presented for the graphites and pyrolytic graphite in References 3.12 to 3.17 indicate that for many of these, except at the higher temperatures, behavior is not linearly elastic and completely brittle. The work-hardening or softening portion of the almost bi-linear curves applies over most of the deformation range, until "brittle" failure. It appears quite adequate then to approximate materials so characterized as completely elastic, to brittle failure, on the first application of loading, using the "work-hardening modulus" as the elastic modulus. This appears to be the modulus usually tabulated for pyrolytic graphite, but not for other graphites, for which sonic moduli are found.^{3.12} It is only when loading is removed and then reapplied that the possibly true anelastic behavior comes into play for these materials, work-hardening or softening being reflected by a different

unloading (and subsequent reloading) modulus than used initially. (Such work-hardening is indicated in Figure 101 of Reference 3.19 for pyrolytic graphite.)

At the higher temperatures, the stress-strain curves also can usually be conservatively approximated by ideal elastic plus perfectly plastic behavior on first loading, again omitting the initial small elastic region but accounting for its effect on subsequent unloading and reloading. (It is observed that such work-hardening or softening behavior under cyclic loading requires care be taken in identification of the "initial" state of a material with respect to its use in a nozzle.) Thus, the assumption of elastic-perfectly plastic behavior appears quite valid for typical nozzle throat materials, if interpreted as above for application of first loading to the materials, with yield criteria replaced by brittle failure criteria where required.

Reference 3.20 has shown the comparative ease of use of the Tresca yield criterion and associated flow rule in place of the Mises criterion for isotropic materials. Analytic results are generally not expected to differ significantly between application of the two criteria for isotropic materials. The Tresca condition is a maximum resolved shear stress yield condition for isotropic materials. Since tungsten is elastically isotropic, fabrication and crystallographic orientation producing any plastic anisotropy exhibited, and since some polycrystalline graphites are not highly anisotropic, it would appear using a generalized Tresca condition would be as adequate as using the Mises criterion for yield. Reference 3.21 is a discussion of failure criteria. The analogy between yield by Mises or Tresca criteria and failure by, respectively, energy of distortion or maximum resolved shear stress becomes immediately apparent. For brittle materials, the latter failure criterion is typical. Thus, using a maximum resolved shear stress yield or failure criterion for tungsten and polycrystalline graphite would appear more easily justified than use of the Mises criterion.

For pyrolytic graphite, Reference 3.19 indicates brittle failures generally occur during compression of the basal plane by shear failure, the failure surface being a plane at 45 degrees to the load and across laminations (therefore, normal to the basal planes). This type of failure would agree with values of a-direction tensile and compressive strengths and trans-laminar shear strengths quoted in Reference 3.22.

For the purposes of structural analysis under this program, nozzle throat analyses are based on symmetrically loaded hollow infinite circular cylinder or thin annular plate models, or some analytic combination thereof. It is consistent with these models to assume, as in Reference 3.20, both that (1) the Tresca yield condition applies and that (2) yielding (or

failure) takes place under the action of the stresses in the plane of the cross-section only without influence of "axial" (plate surface normal) stress. Expressed mathematically, the criterion is

$$|\sigma_{\theta} - \sigma_r| = 2\mu \quad (3.26)$$

where μ is the shear strength and at the outer boundary of the material. The associated flow rule is

$$d\epsilon_{\theta}^P : d\epsilon_r^P : d\epsilon_z^P = 1:-1:0 \quad (3.27)$$

As in Reference 3.20, the conditions on axial load to satisfy this yield assumption may be determined a posteriori. In actuality, it is thus anticipated that at first yield or failure of cylinders (or plates in contact regions) the axial and circumferential stresses will have the same sense and similar magnitudes, while the radial stress will be small or of opposite sense. For surface traction free portions of plates, it is anticipated that if the radial stress is not of sense and magnitude similar to the (in this case) vanishingly small axial stress, it then opposes the circumferential stress in sense.

3.3.1 INITIAL YIELDING OR BRITTLE FAILURE OF A CYLINDRICAL INSERT

Consider an axisymmetric, long, cylindrical nozzle throat insert loaded also axisymmetrically with a net axial load P , internal and external pressures p_a and p_b , and temperature producing free thermal strains. Assume that this throat insert is made of an isotropic, homogeneous material with elastic-plastic properties invariant of location for a given thermal loading. For practical problems of isotropic throat inserts, initial yield on first firing will not occur between surfaces. For purposes of this analysis, yielding is considered to be initiated at the surface. The stresses are considered to result from thermal loading and from internal and external pressures. The stresses are given by adding the pressure stresses to the thermal stresses given by Equations (3.3) and (3.4) and including expressions for the radial stresses. At the inner boundary

$$\sigma_{\theta} = \frac{E\alpha}{1-\nu} (T_a - T_b) (f_n - 1) + \frac{\beta^2 + 1}{\beta^2 - 1} p_a - \frac{2\beta^2}{\beta^2 - 1} p_b \quad (3.28)$$

$$\sigma_z = \frac{E\alpha}{1-\nu} (T_a - T_b) (f_n - 1) + q \quad (3.29)$$

$$\sigma_r = -p_a \quad (3.30)$$

and at the outer boundary

$$q_\theta = \frac{E\alpha}{1-\nu} (T_a - T_b) f_n + \frac{2}{\beta^2 - 1} p_a - \frac{\beta^2 + 1}{\beta^2 - 1} p_b \quad (3.31)$$

$$\sigma_z = \frac{E\alpha}{1-\nu} (T_a - T_b) f_n + q \quad (3.32)$$

$$\sigma_r = -p_b \quad (3.33)$$

where q is a uniform axial stress resulting from an axial load, P , which is negative if compressive. These equations are for a long cylinder. If a short cylinder is considered, σ_z vanishes on both boundaries except for the quantity q , and ν is set equal to zero in the expressions for the hoop stress.

The above equations may be combined with Equation (3.26) to determine the point of first yield or failure for the combination of loads applied. At the same time, it is assumed in using Equation (3.26) for an isotropic material that, at any material point where yielding takes place, σ_z is algebraically intermediate to σ_θ and σ_r . This can be analytically expressed as

$$0 < \frac{q_\theta - \sigma_z}{\sigma_\theta - \sigma_r} < 1 \quad (3.34)$$

Consider the same polynomial temperature distribution, $(1-\xi)^n$, and the same thermal loading function, f_n , used in the thermoelastic analysis, Paragraph 3.2.1. For convenience, define the parameters

$$F = \frac{(1-\nu) (p_a - p_b)}{E\alpha (T_a - T_b)}$$

$$Q = \frac{(1-\nu) (1-p_a)}{2E\alpha (T_a - T_b)}$$

$$U = \left| \frac{(1-\nu) \mu}{E\alpha (T_a - T_b)} \right|$$

It is seen that $U \geq 0$ at all times.

There are three conditions which must be satisfied:

- (1) $|\sigma_\theta - \sigma_r| = 2\mu$
- (2) $|\sigma_\theta - \sigma_r|$ on the surface which is yielding is greater than $|\sigma_\theta - \sigma_r|$ on the opposite surface
- (3) σ_z is between σ_θ and σ_r

Utilizing Equation (3.26) and considering practical values of all parameters, yield or failure will take place first at the inner surface when F reaches the value F_a

$$F_a = \frac{\beta^2 - 1}{\beta^2} \left[U - 1/2 (f_n - 1) \right] \quad (3.35a)$$

This expression applies when $(\sigma_\theta - \sigma_r) > 0$. However, it is also required at this point that

$$F > 1/2 \quad (3.35b)$$

which assures that $|\sigma_\theta - \sigma_r|$ at $r = a$ is greater than $|\sigma_\theta - \sigma_r|$ at $r = b$. Also, for Equation (3.26) to be the correct portion of the yield surface, Equation (3.34) gives

$$- \frac{\beta^2}{\beta^2 - 1} F < Q < 1/2 (f_n - 1) \quad (3.35c)$$

which says that σ_z is intermediate to σ_θ and σ_r .

Yielding also occurs first at the inner surface under an alternate set of conditions if F achieves the value F_b

$$F_b = - \frac{\beta^2 - 1}{\beta^2} \left[U + 1/2 (f_n - 1) \right] \quad (3.36a)$$

This expression applies when $(\sigma_\theta - \sigma_r) < 0$.

It is required that at this point in stress history as well as space

$$F < G = - \frac{\beta^2 - 1}{\beta^2 + 1} (f_n - 1/2) \quad (3.36b)$$

and that

$$1/2 (f_n - 1) < Q < - \frac{\beta^2}{\beta^2 - 1} F \quad (3.36c)$$

Yielding otherwise occurs first at the outer surface according to Equation (3.26) for the problem under consideration when F reaches F_c

$$F_c = (\beta^2 - 1) (U - 1/2 f_n) \quad (3.37a)$$

However, in this case it is also required that

$$G < F < 1/2 \quad (3.37b)$$

and that

$$- \left(\frac{\beta^2 + 1}{\beta^2 - 1} \right) \frac{F}{2} < Q < 1/2 (f_n - F) \quad (3.37c)$$

Obviously, each pair of Equations, (3.35a) and (3.35b), (3.36a) and (3.36b), and (3.37a) and (3.37b), can be combined to determine conditions on the parameter U required in each case for yield or failure to occur in accord with F achieving one of its required values, provided the corresponding conditions on Q are met. Thus, yield occurs when $F = F_a$ at the inner

surface, if

$$U > 1/2 \left[f_n + \frac{1}{\beta^2 - 1} \right] \quad (3.35d)$$

provided that at yield

$$- \left[U - 1/2 (f_n - 1) \right] < Q < 1/2 (f_n - 1) \quad (3.35e)$$

Yield occurs when $F = F_b$ at the inner surface if

$$U > 1/2 \left(\frac{1}{\beta^2 + 1} \right) \left[(\beta^2 - 1) f_n + 1 \right] \quad (3.36d)$$

provided that

$$1/2 (f_n - 1) < Q < 1/2 (f_n - 1) + U \quad (3.36e)$$

Yield occurs when $F = F_c$ at the outer surface if

$$1/2 \frac{1}{\beta^2 + 1} \left[(\beta^2 - 1) f_n + 1 \right] < U < 1/2 \left[f_n + \frac{1}{\beta^2 - 1} \right] \quad (3.37d)$$

provided that

$$- \frac{\beta^2 + 1}{2} \left[U - 1/2 f_n \right] < Q < - \frac{\beta^2 + 1}{2} \left[\frac{\beta^2 - 1}{\beta^2 + 1} U - 1/2 f_n \right] \quad (3.37e)$$

Similar analyses could be performed considering that $|\sigma_z - \sigma_r| = 2\mu$ and placing the proper restrictions on the boundary on which yielding first occurs and requiring that σ_θ is intermediate to σ_z and σ_r .

For practical problems in this program, only yielding of tungsten is considered. Since corrosion considerations severely limit the maximum service temperature of ATJ graphite to about 4200°F, this material remains essentially brittle in nature throughout its service life and does not reach the plastic threshold temperature of 4500°F. Yielding of pyrolytic graphite in the a-b plane has never been observed in any nozzle firings. Large anelastic deformations do not occur in pyrolytic graphite at temperatures below about 4700°F. When the inner surface temperatures reach this value, the thermal loadings are usually rather small.

The initial yielding of tungsten is important on the inner surface when $F = F_b$. Yielding would not occur for $F = F_a$ since this condition requires $(\sigma_\theta - \sigma_r)$ to be positive and this in turn requires a tremendous value of p_a . Brittle tensile failure will occur on the outer surface of a tungsten insert before yielding will occur for $F = F_a$.

The magnitude of the compressive stress on the inner surface of the tungsten insert will always exceed the magnitude of the tensile stress on the outer surface. This is true since f_n is always less than 1/2, and

$$|f_n - 1| > f_n$$

and the thermal stresses contribute the major components of the stresses. It is found that, for most practical problems, the inner surface is fairly warm when the stresses build to a significant magnitude, so that the question of a brittle compressive failure mode for tungsten rarely arises.

Using the method of comparing an allowable $\Delta\phi$ with an attainable $\Delta\phi$ as was done in the thermoelastic analysis presented in Paragraph 3.2.1, and taking the tungsten properties as

$$E = 50 \times 10^6 \text{ psi}$$

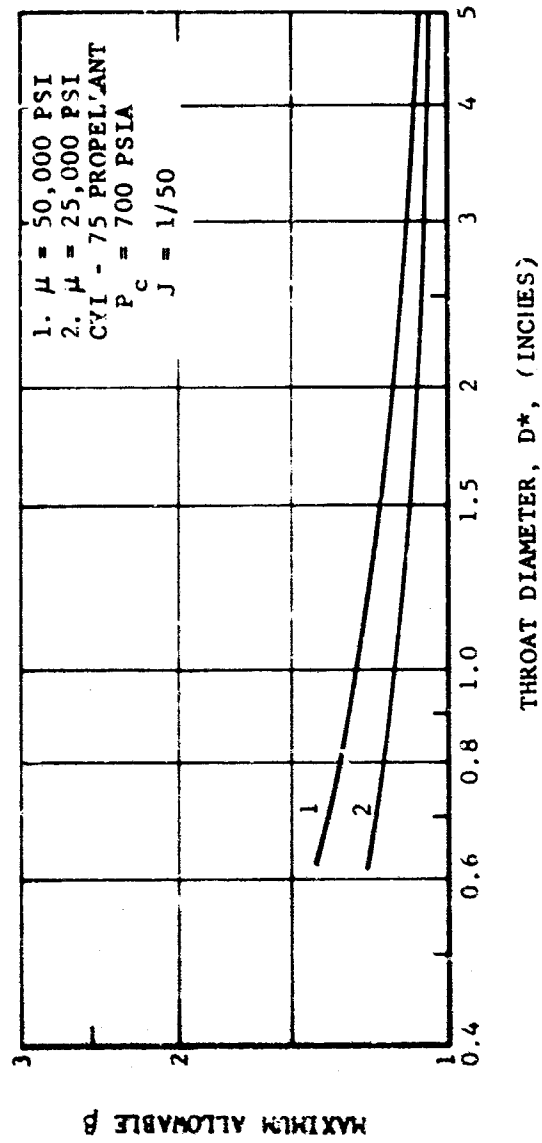
$$\alpha = 2.2 \times 10^{-6} / ^\circ\text{F}$$

$$\nu = 0.3$$

$$\mu = 25,000 \text{ psi and } 50,000 \text{ psi}$$

a graph which can be used as a design chart can be plotted. Such a graph is shown as Figure 3-17. It should be pointed out that the values of μ shown above are taken as reasonable values and are not intended to indicate precise values. These values can be used at least as representative for illustrative purposes.

It is seen by a comparison of Figure 3-14 with Figure 3-17 that compressive yield can occur on the inner surface before brittle tensile failure occurs on the outer surface. This does not indicate that the yielding will occur to the exclusion of brittle back side fracture. Indeed, a plastic inner zone can develop in a tungsten insert which still fractures on the back side. Figure 39 of Reference 3,23 shows an insert which has undergone such an occurrence. This figure shows a back side fracture whose propagation terminated in the inner plastic zone.



FO4463 U

FIGURE 3-17. TUNGSTEN LONG CYLINDER INNER SURFACE COMPRESSIVE YIELD CHART

3.3.2 PLASTIC FLOW OF AN ISOTROPIC ELASTIC-PERFECTLY PLASTIC CYLINDRICAL NOZZLE INSERT

Consider a cylindrical nozzle insert made of an isotropic, homogeneous, elastic-perfectly plastic material possessing uniform, temperature-independent, properties. Let the inner and outer radii of this cylinder be r_1 and r_2 , respectively, with associated internal and external pressures p_1 and p_2 , and net axial load P_z , where an average diameter, D , thickness, h , and boundary stresses are

$$D = r_2 + r_1 \quad h = r_2 - r_1$$

$$\sigma_r(r_1) = -p_1 \quad \sigma_r(r_2) = -p_2$$

Assume that under thermal and mechanical loading, elastic and plastic regions develop. Irrespective of their number and location, the assumptions of plane strain, which apply to all analyses of long cylindrical throat inserts, the yield condition (Equation 3.26), and the associated flow rule (Equation 3.27), require that the following holds,

$$E \epsilon_z = q + \frac{2E\alpha}{Dh} \int_{r_1}^{r_2} r T dr + \frac{2\nu}{Dh} (r_2^2 p_2 - r_1^2 p_1) \quad (3.38)$$

Let it be assumed that strains and displacements are small. Assume also that once a region becomes plastic, the load path is such that it remains plastic until loading is complete. Removing the absolute value signs from Equation 3.26, yielding is then defined by the positive or negative quantity τ_a with absolute value μ

$$1/2 (\sigma_\theta - \sigma_r) = \tau_a = \pm \mu \quad (3.39)$$

Equations (3.38) and (3.39) hold as long as within any plastic region $r_p \leq r \leq r_{p+1}$ the additional relation holds, for all r ,

$$x(r) - 2 < q/\tau_a < x(r) \quad (3.40)$$

where

$$x(r) = - \left[(1-2\nu) \sigma_r(r) + E\alpha T(r) \right] / \tau_a$$

$$+ \frac{2\nu \left[(\tau_a + p_2) r_2^2 - (\tau_a + p_1) r_1^2 \right]}{\tau_a Dh}$$

$$+ \frac{2E\alpha}{\tau_a Dh} \int_{r_1}^{r_2} r T dr \quad (3.41)$$

Consider any elastic region $a \leq r \leq b$. Equations (3.28), (3.29), (3.31), and (3.32) still apply. In addition

$$\sigma_z = E\epsilon_z - \frac{E\alpha T}{(1-\nu)} - 2\nu \frac{(b^2 p_b - a^2 p_a)}{(b^2 - a^2)} + \frac{2\nu E\alpha}{(1-\nu)(b^2 - a^2)} \int_a^b r T dr \quad (3.42)$$

The hoop strain, ϵ_θ , and radial displacement, u , in this elastic region are found from the relations

$$\begin{aligned} \epsilon_\theta = \frac{u}{r} = -\nu\epsilon_z - \frac{(1+\nu)a^2 b^2 (p_b - p_a)}{E(b^2 - a^2)r^2} - \frac{(1+\nu)(1-2\nu)(b^2 p_b - a^2 p_a)}{E(b^2 - a^2)} \\ + \frac{(1+\nu)\alpha}{(1-\nu)(b^2 - a^2)} \left\{ \frac{b^2}{r^2} \int_a^r r T dr + \frac{a^2}{r^2} \int_r^b r T dr \right. \\ \left. + (1-2\nu) \int_a^b r T dr \right\} \quad (3.43) \end{aligned}$$

Note however that, unlike the purely elastic analysis previously conducted, the locations a and b , and associated pressures p_a and p_b , are to be determined. At the boundaries of the to be determined plastic region $r_p \leq r \leq r_{p+1}$ consider that the actually still unknown stresses are imposed pressures,

$$\sigma_r(r_p) = -p_p \quad \sigma_r(r_{p+1}) = -p_{p+1}$$

Solution of the plastic flow problem for small radial displacements u , following Reference 3.20 if desired, gives

$$\sigma_r = -p_p + 2\tau_a \log_e \left(\frac{r}{r_p} \right) \equiv -p_{p+1} + 2\tau_a \log_e \left(\frac{r}{r_{p+1}} \right) \quad (3.44)$$

$$\sigma_\theta = \sigma_r + 2\tau_a \quad (3.45)$$

$$\sigma_z = E(\epsilon_z - \alpha T) + 2\nu(\tau_a + \sigma_r) \quad (3.46)$$

$$\begin{aligned} \epsilon_\theta = \frac{u}{r} = -\nu\epsilon_z + \frac{(1+\nu)(1-2\nu)}{E} \sigma_r + \frac{2(1-\nu^2)}{E} \left(\frac{r_\Delta}{r} \right)^2 \tau_a \\ + \frac{2(1-\nu)\alpha}{r^2} \int_{r_\Delta}^r r T dr \quad (3.47) \end{aligned}$$

Where r_Δ can be either r_p or r_{p+1} , and represents the radius at the transition from elastic to plastic behavior. In either case, continuity at the region interface requires

$$(p_a - p_b) = \frac{r_\Delta^2}{a^2 b^2} \left[(b^2 - a^2) \tau_a - \frac{E\alpha}{(1-\nu)} \int_a^b r T dr \right] \quad (3.48)$$

$$(p_{\Delta-1} - p_{\Delta+1}) = (p_a - p_b) + 2\tau_a \log_e \left(\frac{r_{p+1}}{r_p} \right) \quad (3.49)$$

However, the following sets of relations also apply, depending on the location of the interface r_Δ ,

$$\left. \begin{aligned} p_\Delta &\equiv p_{p+1} = p_a \\ p_{\Delta-1} &= p_p \\ p_{\Delta+1} &= p_b \end{aligned} \right\} \quad r_\Delta \equiv r_{p+1} = a \quad (3.50)$$

$$\left. \begin{aligned} p_\Delta &\equiv p_p = p_b \\ p_{\Delta+1} &= p_{p+1} \\ p_{\Delta-1} &= p_a \end{aligned} \right\} \quad r_\Delta \equiv r_p = b \quad (3.51)$$

It is seen that $(p_{\Delta-1} - p_{\Delta+1})$, chosen for notation compactness, actually represents the "pressure" drop across one elastic plus adjacent plastic zone of the nozzle.

Satisfaction of the surface pressure (boundary) conditions on the entire insert completes postulation of, and permits solution of, any such plastic flow problem. It is noted that an inverse approach is probably most practical for such problems.

3.4 DEVELOPMENT OF THEORY FOR STACKED PYROLYTIC GRAPHITE WASHER INSERTS

In Paragraph 3.2, the elastic response of pyrolytic graphite washer inserts was analyzed. This analysis did not treat the effects of axial loads or the high contact stresses which result when these loads are carried by a narrow annulus at the hot inner surface of the washers. These high contact stresses can result in permanent axial (c-direction) deformations of the washers as determined in the materials laboratory. (Refer to Section 4.)

A closed form elastic solution to the problem was also obtained. A solution is presented here. A computer program was also developed to treat the problem when variable material properties or multiple contact regions are involved.

The diagram shows a cross-section of a structure with two layers, labeled 1 and 2. Layer 1 is the bottom layer, and Layer 2 is the top layer. The structure is axisymmetric about a vertical Z-axis, indicated by the 'C SYMMETRY' label and the 'r' coordinate. The total height of the structure is 'c'. The bottom layer (1) has a height 'a' and is subjected to a uniform pressure 'P_a' acting upwards. The top layer (2) has a height 'b' and is subjected to a uniform pressure 'P_b' acting upwards. The top surface of Layer 2 is subjected to a uniform pressure 'P_c' acting downwards. The Z-axis is shown as a horizontal arrow pointing to the right, and the r-axis is shown as a vertical arrow pointing upwards.

Piece 1

- Load thermally and with p_a and p_b .
Temperature is monotonically decreasing radially outward.
- Assume plane sections remain plane;
 ϵ_z is a constant; plane strain prevails.
(In a washer stack, symmetry about the washer midplane is assumed.)
- Solve for σ_r , σ_θ , σ_z , and u with b , p_b , and ϵ_z unknown.

Piece 2

- Load thermally and with p_b and p_c .
Temperature is monotonically decreasing radially outward.
- Assume $\sigma_z = 0$ everywhere; plane stress prevails.
- Solve for σ_r , σ_θ , and u with p_b and b unknown.

Simultaneously

- Match u between Pieces 1 and 2 at $r = b$.
- In Piece 1, require $\sigma_z = 0$ at $r = b$.
- In Piece 1, require $2\pi \int_a^b \sigma_r dr = P$
There are now three equations in the three unknowns b , p_b , and ϵ_z .
- Solve the three equations simultaneously.

The solutions for the stresses and displacements in each piece were obtained in the usual way by utilizing the stress-strain equations of Hooke's Law, the strain-displacement relations,

$$\epsilon_r = \frac{du}{dr} \quad (3-52)$$

$$\epsilon_\theta = \frac{u}{r},$$

the equilibrium equation

$$\frac{d\sigma_r}{dr} + \frac{\sigma_r - \sigma_\theta}{r} = 0, \quad (3-53)$$

and the compatibility equation,

$$\epsilon_r - \frac{d(r\epsilon_\theta)}{dr} = 0. \quad (3-54)$$

Simultaneous solution for the three unknowns yielded three equations from which the unknowns could be determined. The first of these is

$$\frac{P}{\pi(b^2 - a^2)} = - \frac{E_r \nu_{rz} (\nu_{rz} \alpha_r + \alpha_z)}{\nu_{rz} (1 - \nu_{rz} \nu_{zr})} \left[\frac{2}{b^2 - a^2} \int_a^b Trdr - T_b \right] \quad (3.55)$$

For compressive axial loading, P is negative. The interface b may be determined from this equation and the process is an iterative one. The remaining two equations are:

$$p_b = - \frac{1}{b^2 [c^2 - a^2 - \nu_{rz} \nu_{zr} (c^2 - b^2)]} \left[E_r (\alpha_r + \nu_{zr} \alpha_z) (c^2 - b^2) \int_a^b Trdr \right. \\ \left. - E_r \alpha_r (b^2 - a^2) \int_b^c Trdr - p_a a^2 (c^2 - b^2) (1 - \nu_{rz} \nu_{zr}) - p_c c^2 (b^2 - a^2) \right] \quad (3.56)$$

and

$$\epsilon_z = - \frac{\nu_{rz}}{1 - \nu_{rz} \nu_{zr}} \left[\frac{2 (\alpha_r + \nu_{zr} \alpha_z)}{b^2 - a^2} \int_a^b Trdr - \frac{\nu_{rz} \alpha_r + \alpha_z}{\nu_{rz}} T_b \right] \\ - \frac{2 \nu_{rz}}{E_r} \frac{p_b b^2 - p_a a^2}{b^2 - a^2} \quad (3.57)$$

In these equations, the subscripts on α and E denote the direction in which they are measured. The Poisson's ratios are defined by

$$\nu_{ij} = - \frac{\epsilon_j}{\epsilon_i}$$

The stresses are given by the following equations for Piece 1:

$$\sigma_r = \frac{E_r (\alpha_r + \nu_{zr} \alpha_z)}{(1 - \nu_{rz} \nu_{zr}) r^2} \left[\frac{r^2 - a^2}{b^2 - a^2} \int_a^b Trdr - \int_a^r Trdr \right] \\ + \frac{p_b b^2 (r^2 - a^2) + p_a a^2 (b^2 - r^2)}{r^2 (b^2 - a^2)} \quad (3.58)$$

$$\sigma_r = \frac{E_r (\alpha_r + \nu_{rz} \alpha_z)}{(1 - \nu_{rz} \nu_{zr}) r^2} \left[\frac{r^2 + a^2}{b^2 - a^2} \int_a^b T r dr + \int_a^r T r dr - T r^2 \right] + \frac{p_b b^2 (r^2 + a^2) - p_a a^2 (b^2 + r^2)}{r^2 (b^2 - a^2)} \quad (3.59)$$

$$\sigma_z = \frac{E_r \nu_{zr}}{1 - \nu_{rz} \nu_{zr}} \left[\frac{2(\alpha_r + \nu_{zr} \alpha_z)}{b^2 - a^2} \int_a^b T r dr - \frac{\nu_{rz} \alpha_r + \alpha_z}{\nu_{rz}} T \right] + 2 \nu_{zr} \frac{p_b b^2 - p_a a^2}{b^2 - a^2} + \frac{\nu_{zr}}{\nu_{rz}} E_r \epsilon_z \quad (3.60)$$

and for Piece 2

$$\sigma_r = \frac{\alpha_r E_r}{r^2} \left[\frac{r^2 - b^2}{c^2 - b^2} \int_b^c T r dr - \int_b^r T r dr \right] + \frac{p_c c^2 (r^2 - b^2) + p_b b^2 (c^2 - r^2)}{r^2 (c^2 - b^2)} \quad (3.61)$$

$$\sigma_\theta = \frac{\alpha_r E_r}{r^2} \left[\frac{r^2 + b^2}{c^2 - b^2} \int_b^c T r dr + \int_b^r T r dr - T r^2 \right] + \frac{p_c c^2 (r^2 + b^2) - p_b b^2 (c^2 + r^2)}{r^2 (c^2 - b^2)} \quad (3.62)$$

The stress of interest is the axial stress at $r = a$ in Piece 1. This will be the greatest compressive axial stress in the constant-property body with the temperature distribution applied. The body will also be hottest at this point and therefore have the greatest tendency to deform. At $r = a$, this axial stress is given by the expression

$$\sigma_z = - \frac{E_r \nu_{rz} (\nu_{rz} \alpha_r + \alpha_z)}{(1 - \nu_{rz} \nu_{rz}) \nu_{rz}} (T_a - T_b) \quad (3.63)$$

T_b is found by solving Equation (3.56) for the interface, b . Assigning reasonable values to the material properties, it is found that at $r = a$

$$\sigma_z = - 30 (T_a - T_b) \quad (3.64)$$

so that the temperature difference across the plane strain region need be only a few hundred degrees Fahrenheit for this stress to be quite significant for producing permanent deformation.

The determination of the axial load, P , may be made with considerations of pressure loadings and restraint to axial expansion. Good design practices dictate that pyrolytic graphite washer inserts should not be constrained from axial expansion; restraint loading, then, will not be considered. The axial load resulting from pressure may be calculated by two different means, one of which is definitely conservative. The more conservative calculation assumes that the chamber pressure acts over the entire frontal area of washer. Alternately, the pressure differential across the washer thickness (pressure at upstream edge minus pressure at downstream edge) can be applied to the frontal area. In regions of high axial pressure gradients, this latter loading can be around half the first loading. Care should be taken in design that the pressure loads acting on the entrance section are not transmitted directly to the inner circle of the upstream pyrolytic graphite washer in the stack. If this is allowed to happen, even higher loads may result.

A computer program based on plane strain solution of a hollow cylinder was developed for this problem. By an iterative procedure, contact regions are defined. Where contact does not occur, the axial modulus, E_c , is made quite small (as much as a hundred orders of magnitude less than the actual E_c). This has the effect of imposing plane stress conditions upon the noncontacting regions and transforming the washer into a tension limited cylinder (axial tension cannot be supported).

This computer program is capable of analyzing anisotropic washers for axisymmetric loading. In addition to input of variable material properties, the loading consisting of internal and external pressures, the net axial load, and thermal load are required inputs to permit solution using this program. The principal axes of the material must coincide with the radial, circumferential, and axial directions of the washer. An arbitrary first guess of the value of r where contact between washers is lost is also input. By the iterative procedure, E_c is made as small as desired where any previous approximation has indicated a positive axial stress. The program ceases when iteration produces compressive stresses only in the regions of true E_c . Any arbitrary temperature distribution may be used since multiple contact regions can be determined.

3.5 THERMAL FATIGUE

At the beginning of the program, thermal fatigue was identified as a potential problem area. It was enveloped in an aura of mystery, since the subject itself, which is one of plastic straining, was not well developed and its application to brittle materials had hardly begun. The huge deficits of unknowns naturally raised certain fears of impending disaster for the flamefront materials when subjected to cyclic operation. This led to a rather extensive literature survey, some preliminary laboratory testing, a study of crack nucleation and propagation, and an extensive laboratory test plan. Many of these fears were allayed when, midway through the program, the first experimental thermal fatigue data on tungsten and pyrolytic graphite became available and indicated that thermal fatigue may not be a problem for up to 50 cycles. The nozzle testing program did not show thermal fatigue to be a problem for the duty cycles imposed.

This paragraph contains a rather detailed discussion of thermal fatigue as applicable to restartable solid rocket nozzles. Although at the end of the program, thermal fatigue was not considered to be the problem that was feared at the beginning of the program, this discussion has historical significance as well as value as a foundation for that time when further work becomes necessary. The literature survey, the important considerations of the dual brittle and ductile natures of the candidate materials, crack initiation and propagation, and an experimental program are included in the discussion. The investigation was designed to ferret out those most critical items and to determine the severity of the thermal fatigue problem for 40 restarts.

3.5.1 PRELIMINARY LABORATORY TESTS

In order to obtain a baseline indication of the thermal fatigue characteristics of the candidate flamefront materials, some rudimentary laboratory tests were conducted rather early in the program. These tests are discussed and results are presented in Paragraph 4.6. The results were inconclusive in that a definition of thermal fatigue as a problem area could not be made. Consideration was given to the meaningful extension of the laboratory work in order to obtain thermal fatigue data which could be applied to the restart nozzle analysis. The preliminary investigation which was conducted was designed to define some reasonable tests which might be run on the three candidate materials to see if thermal fatigue and/or associated brittle fracture is a problem. The approach used was to determine the critical variables for each material and to attempt to formulate several tests to delineate the scope of each variable. In implementing this approach, a literature survey was completed, the coupling of materials and temperature was examined, and several testing approaches were considered.

3.5.2 LITERATURE SURVEY

A very comprehensive review of thermal fatigue has been presented by Yen.^{3.25} Although this review centers around ductile metals, some of the factors are germane to refractory nozzle materials. There is a basic difference between mechanical fatigue at a constant temperature and thermal fatigue. The effect of a cyclic temperature on a specimen in a uniaxial test in which the specimen is constrained may be the same, stress-wise, as the effect of a cyclic load at a constant temperature in a fixed strain range. However, with the varying temperature conditions, there are associated changes in physical properties and microstructural variations which are dependent on both time and temperature. Correlation of thermal fatigue and mechanical fatigue at constant temperature, based on the cyclic plastic-strain range, can be made in some instances provided no major microstructural changes occur during the testing period. This has been done by Swindeman and Douglas^{3.26} for Inconel. However, Inconel is known to be metallurgically stable and to possess a rather uniform deformation mechanism within the range of the testing temperatures. The variation of mechanical properties and microstructure with temperature and time gives rise to difficulties in evaluating and interpreting the results of material testing at elevated temperature. For most materials, both the modulus of elasticity and coefficient of thermal expansion change with temperature. Thus, the history of the temperature distribution in reaching the extremes of the thermal cycle affects the degree and rate of the stress and strain to which the material is subjected. Annealing, hot-working, recrystallization, and grain growth may result from the temperature and time effects of the cycle. These factors may influence the stress-strain curve, the ductility, the strength, and even the deformation mechanism of the material. Corrosion of the nozzle material under operating conditions may lend thermal fatigue data obtained in the laboratory invalid for application because at elevated temperature the effect of temperature is superimposed on that of the strain, and any transformation is likely to be more pronounced.

The review of Yen summarized above is based on considerations applicable to ductile materials. Indeed the preponderance of fatigue and thermal fatigue data deals exclusively with ductile materials. Forrest,^{3.27} in discussing the literature on thermal fatigue, says on page 261, "No mention has been made of thermal fatigue in non-metals. The thermal fatigue resistance of ceramics is poor because of their brittleness and this is one of the reasons that has restricted their use." And Pope,^{3.28} on page 221 points out, "From the engineering point of view a less important variety of cast irons are the white and chilled cast irons which consist entirely or in part of a hard brittle white cast iron containing no graphite. Such irons are rarely used in components where fatigue is important, except perhaps as rolls in rolling mills. In any case, so little data are available on the fatigue properties that it has been necessary to ignore them in this account."

In searching the literature, it quickly becomes evident that fatigue behavior of brittle materials has not been the subject of extensive investigation. This is largely because brittle materials are not usually employed in structures subjected to large cyclic loads. In almost all of the thermal fatigue work reported to date, only ductile materials have been considered. In these materials, crack propagation is, in effect, slowed by the formation of a plastic region at the crack tip. It has recently been reported^{3.29} that for some very ductile materials crack nucleation is accomplished in less than 25 percent of the mechanical fatigue life, while propagation of the crack covers over 75 percent of the life. However, for brittle materials propagation of a crack to the critical length could occur relatively soon after nucleation and the major portion of the fatigue life could be involved with crack nucleation.

One item uncovered on brittle materials is that of Baron and Bloomfield.^{3.30} Cracking was produced in test pieces of chilled white iron, engineering gray iron, and two casts of nodular iron by repeated heating of one edge of the specimen while the mass of the specimen was water cooled. The large cool mass largely prevents expansion of the heated edge, and the resulting thermal stresses eventually initiate cracks normal to the edge. The temperature of the heated edge is the only index to loading or loading severity. The results of the tests are presented in Figure 3-18. It is interesting to note that the shapes of the curves can be roughly correlated to the ductility of the material. The white iron is quite brittle and exhibits a very flat fatigue curve. Taking the properties of the grey iron reported (tensile strength of 30,000 psi, modulus of 15.4×10^6 psi, and an elongation of 0.3 percent) a ductile strain of 0.04 percent is computed. The accuracy of prediction of ductility for this material is questionable; however, its brittleness should not be so pronounced as that of the chilled white iron. The nodular iron is ductile and characteristically exhibits elongations of about 8 percent or a little greater. The white iron has a fairly flat fatigue curve; the grey iron shows a curve with not only greater fatigue life but also with more slope; the nodular iron exhibits much greater life in the lower cycle range and a still greater slope.

For an extremely brittle material, such as the chilled white iron, one must critically question the implication of fatigue life. At a maximum temperature of 600°C, the fatigue life ranged from approximately 6 to 25 cycles as read from the curve. At a maximum temperature of 500°C, the range was approximately 80 to 700 cycles. Thus for an 18 percent decrease in the loading index, the fatigue life spans over two orders of magnitude. In a hardware application, one would have to be able to predict rather precisely the loading in order to have any confidence in such a fatigue life.

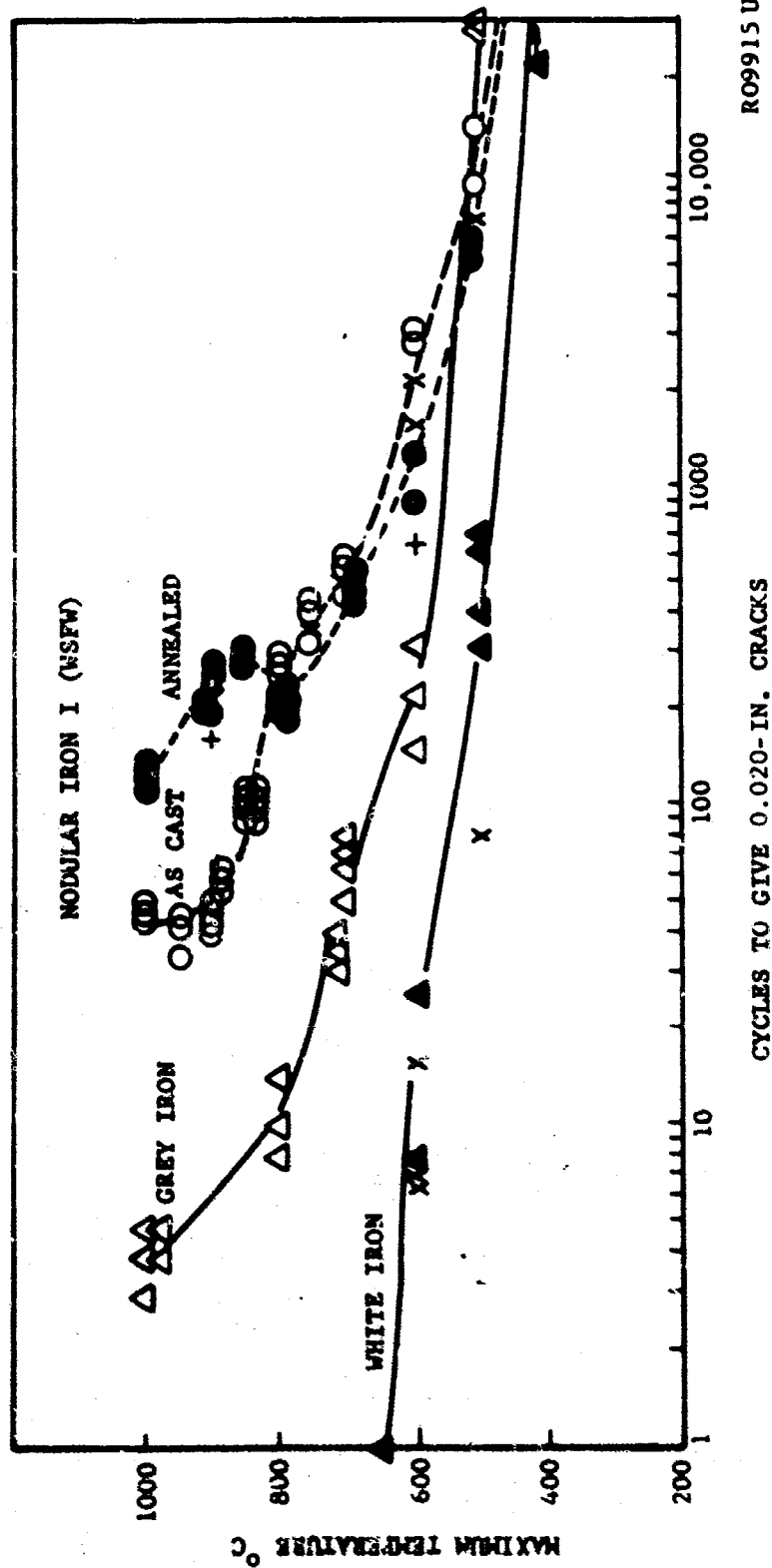


FIGURE 3-18. EFFECT OF THE MAXIMUM TEMPERATURE IN THE CYCLE ON THE FATIGUE LIFE (MINIMUM TEMPERATURE 40°C) (FROM REFERENCE 3-30)

In one rather extensive review^{3.31} of thermal fatigue, several literature items relating to brittle materials are covered. Since most of these items are of British publication, the originals were not sought. Those references dealing with thermal fatigue of brittle materials, mostly cast irons, are listed in this report as References 3.32 through 3.39.

The first experimental thermal fatigue data^{3.40} on tungsten and pyrolytic graphite became available about midway through the program. Tungsten and pyrolytic graphite rods 1/4 inch x 3 inches were cycled between 400 and 5000°F. Both notched and unnotched specimens were tested under full restraint. Some specimens were cycled 25 times and others 50 times in order to meet a 20-cycle objective. No thermal crack was observed in any of the test specimens. These data represent a giant stride toward establishing the existence of thermal fatigue problems with these two materials. However, since the testing reported did not include certain information which was felt to be pertinent nor did the investigation include certain considerations which were felt to have a great bearing on the applicability of the test data to restartable solid nozzles, the principal investigator was contacted by telephone.^{3.41} A brief discussion of the items covered follows:

- (1) The notch root radius of 0.005 inch was the lower limit of the machining technique used in the reported investigation. No attempt was made to introduce a sharper notch. As is pointed out below, a crack tip of 0.0001 inch radius is critical for tungsten. Such sharp cracks can be initiated by corrosive attack in solid nozzles.
- (2) The tungsten rods suffered column buckling at the higher temperatures. Such buckling substitutes an eccentrically caused stress distribution for full thermal restraint.
- (3) The samples were secured in the test fixture by set screws. Such devices raise the serious question of how well the specimens were restrained in tension at the low temperature portion of the cycle.
- (4) The groove was introduced into the pyrolytic graphite randomly. It was not known whether the groove was in the edge-grain of the material, or in the a-b faces, or in some oblique orientation. If the groove were introduced so as to propagate a crack across the basal planes of the material, the planes themselves would serve as crack stoppers. A groove across the edge grain of the material would be in the same direction as a critical crack in a pyrolytic graphite washer nozzle.

The data reported^{3,40} indicate that thermal fatigue may not be a serious problem for tungsten and pyrolytic graphite in restartable solid nozzle applications. It appears that this indication is of a preliminary nature only and further investigation, including the effects of corrosion initiated cracking, is certainly warranted before firm conclusions can be made.

3.5.3 DUCTILE AND BRITTLE CONSIDERATIONS

The refractory materials used in rocket nozzles are brittle over some portion of their operating temperature range. Indeed some graphites display essentially a brittle behavior over as much as 80 percent of their operating temperature range. Tungsten, depending upon recrystallization and how it was manufactured, has a brittle-ductile transition temperature of about 350°C. Pyrolytic graphite and ATJ graphite are definitely brittle at 1650°C and display no appreciable ductility below 2200°C. Thus, these materials may be subjected to thermal cycling in both the brittle and ductile ranges. As a consequence, the thermal fatigue behavior of the candidate materials is important not only in the ductile range but also in the brittle range.

Considering that brittle fracture is usually associated with the development of some critical crack length, such as is involved in the Griffith or Orowan theory, one might question the applicability of a fatigue life. Considering that fatigue is concerned with the nucleation and propagation of a crack in a brittle material, one would suspect that the development of a crack of critical length would be highly dependent upon any microstructural flaws which existed in the material initially. Since there can exist no plastic zone at the crack tip to attenuate crack growth, one would surmise that the crack might propagate very rapidly. The major portion of the fatigue life would then be the crack nucleation period, while the propagation would account for only a minor fraction of the life. Then fatigue life would depend upon the initial flaws in the material and would be more of a statistical phenomenon.

Any fatigue life data gathered for brittle materials might be expected to show a great deal of scatter. This can be seen in the data of Baron and Bloomfield shown in Figure 3-18. This scatter probably reflects the same sort of scatter that is exhibited by strength data of brittle materials. Also, one would expect the data to be dependent on the size of the test specimen. Since it has been reasoned that fatigue life is dependent on the existence of initial microstructural flaws, a small sample would have a lower probability of exhibiting such a flaw than a large sample, and should, therefore, show a greater fatigue life.

If a crack nucleates under plastic straining in the ductile range, the material may have quite an extended life if the thermal cycling is conducted without dropping below the brittle transition temperature. The propagation of the crack could proceed systematically in the ductile range, while one excursion into the brittle range may result in an immediate brittle fracture. Likewise, a crack nucleated in the brittle range may propagate slowly if subsequent thermal cycling is conducted only in the ductile range.

With the candidate refractory materials operating in a desirable temperature range, this program was faced not only with the difficult problem of classic thermal fatigue in the ductile range (which is complex enough), and not only with the difficult problem of thermal fatigue in the brittle range, but also with the problem of combining the two.

There were several alternatives:

- (1) Restrict the nozzle, after the first firing, to operation only in the ductile range of the particular material. The materials then could be investigated in the ductile region where some existing theory of thermal fatigue, based on repeated plastic straining, could be applied. This would severely restrict the cooldown of the graphites since they would probably be prohibited from falling below about 2000°C. It should be mentioned that ATJ may be restricted to operation below this temperature because of corrosion considerations and may thus actually become ductile. For tungsten this may not be so severe a restriction since this material could probably be permitted to drop to about 1500°C to assure its ductility after recrystallization.
- (2) Assume that it is too restrictive to prohibit temperatures to drop to the brittle range after the initial firing and that the materials will cycle in the brittle region. Since a shorter crack can be tolerated in the brittle regime, this is the critical regime. Assume that cracks will nucleate at least as easily in the brittle regime as in the ductile. Considering that within the brittle region materials properties (strength, modulus, and expansion coefficient)

do not vary over very wide ranges, there should not be much difference between thermal fatigue and mechanical fatigue. (The exception here may be tungsten, which could possibly undergo some microstructural changes during brittle straining.) Then all materials could be tested in the brittle range in mechanical fatigue with conservative application of the results to thermal fatigue over the entire thermal cycle range.

- (3) Define minimum and maximum temperature extremes which the materials will experience in the rocket nozzle and devise a conservative test (such as XX percent restraint) to investigate the materials while being cycled between these extremes.
- (4) Use a combination of the above approaches which can be selectively applied to the several materials. For instance, the brittle only assumption may be applied to ATJ since it will probably not be permitted to go ductile in a nozzle application. Tungsten and pyrolytic graphite could be cycled between temperature extremes.

3.5.4 SPECIFIC MATERIAL CONSIDERATIONS AND TEST PLANS

In order to maintain the greatest flexibility of duty cycle, all three candidate materials (tungsten, ATJ graphite, and pyrolytic graphite) are considered to operate in a high temperature range where some microstructural changes may take place. At the same time, all materials are considered to be thermally cycled into temperature regions where they are inherently brittle. This negates any standard thermal fatigue approach to the problem but necessitates the examination of material characteristics in the whole spectrum of its solid state. However, the task was to simplify, where possible, so as to work within the scope of the program. This immediately limited the definitiveness with which experiments could be planned and it should be emphasized that the program delineated below is subjected to this limitation. Since more is known about the ductile and brittle characteristics of tungsten as well as its recrystallization and oxidation behavior, this material is discussed first. This is followed by a discussion of ATJ graphite and pyrolytic graphite along with a proposed experimental plan for each material.

In view of the favorable negative indication of the thermal fatigue data^{3.40} discussed in Paragraph 3.5.2, a decision was reached that no experimental program would be conducted in this area. The discussion and program delineated below are included because of their significance to the problem and because they form a logical basis for the next step in this area when further work becomes necessary.

a. Tungsten. In determining the significant variables for this material, it should be realized that maximum flexibility in the restart capability is desirable. This dictates designing for the ambient temperature of deep space which is well below the ductile-brittle transition temperature for polycrystalline tungsten. Therefore, both high-temperature plastic thermal cycling and low-temperature brittle fracture must be considered with the thought that there may be a single limiting parameter.

(1) High Temperature Range. At the very high temperatures, classic thermal fatigue resulting from cyclic exhaustion of plastic strain is possible. In this type of failure mechanism, the important considerations are maximum temperature, time at temperature, heating and cooling rates, amount of plastic flow as determined by the degree of constraint and number of cycles to failure. The maximum temperature is probably most critical in that both plastic flow properties and microstructural changes occur more readily with increasing temperature. Both of these are detrimental to thermal fatigue life. For example, Kennedy^{3.42} has found that the thermal fatigue life of course-grained Inconel was one-half that of the fine-grained material in tests where the maximum temperature was well below those where grain growth occurs. One might expect that cycling into the temperature region where recrystallization and grain growth easily occur, as is the case for tungsten, would even be more detrimental. Similarly, the time at maximum temperature has been shown to slightly reduce the thermal fatigue life of stainless steel.

The final criterion for thermal fatigue failure embodies the amount of plastic flow per cycle as determined by the degree of constraint and the cooling rate and the number of cycles. For example, under fully constrained conditions, plastic flow of about one percent in compression may occur near 5000°F (2760°C) since the strength of tungsten is only about 2 to 6 ksi. With rapid cooling rates, very high residual tensile stresses will exist. With slow cooling rates, the material may creep to relieve the constrained condition. Considering the cooling rate in a typical 0.38-inch-thick shell, the tungsten could creep to a strain of at least 0.5 percent under a stress of 9 ksi in the time it takes to cool from 5500°F (3040°C) to 3500°F (1930°C). Even at temperatures as low as 2500°F (1370°C) where the cooling rate is very slow, some creep is possible at stresses on the order of 30 ksi. Thus, the restrained condition could be relieved by creep, and a similar cycle could be repeated on the subsequent firing. This would result in the classic type of thermal fatigue.

Superimposed upon these obvious variables is the fact that crack and void formation may take place during thermal cycling of nozzle materials. This could be quite serious since Coffin^{3.43} has shown that a mild stress concentration may reduce the fatigue life by a factor of five. Thus, cyclic propagation of sub-size Griffith cracks could prove deleterious to thermal fatigue life. That is, if the stress at the low temperature of the fatigue cycle were sufficiently small, cracks of a certain size would not propagate. These could, however, decrease the fatigue life in the high temperature range. Not only could sub-size Griffith cracks reduce the fatigue life, but void formation from high temperature creep and intergranular corrosion from the high temperature gaseous environment also could reduce the fatigue life.

(2) Surface Condition. In the inside surface of the nozzle, erosion and corrosion may produce an irregular surface with many sources of potential failure. For example, in Figure 3-19 cracks about 0.060 inch deep are found throughout the section of a tungsten washer that was fired only once. (This material was used on another program: Contract No. AF 04(611)-8387.) All of these cracks seem to emanate from the internal surface and form an intergranular crack as is seen at higher magnification in Figure 3-20. These cracks would be potential sources of intergranular corrosion during the next firing and would eventually cause failure. Perhaps even more important than the effect of the surface condition on classic thermal fatigue would be its enhancement of crack growth which could cause brittle fracture at ambient temperatures. That is, if intergranular corrosive attack or carbide precipitation at grain boundaries occurs, the energy required to propagate a crack intergranularly would be much less and long cracks would eventually form.

(3) Low Temperature Range. Propagation of Griffith-size cracks at low temperature may well be the limiting factor in the number of restarts a nozzle may achieve. The Griffith^{3.44} theory for brittle solids is an energy concept based upon the fact that the decrease in the strain energy of a system must be slightly greater than the increase in energy from the formation of new surfaces. The condition for the propagation of an existing crack of length $2C$ follows from the Inglis^{3.45} stress analysis,

$$\sigma = \sqrt{\frac{2ET}{\pi C}} \quad (3.65)$$

where σ is the applied stress on the system, E is the elastic modulus and T is the surface energy term.

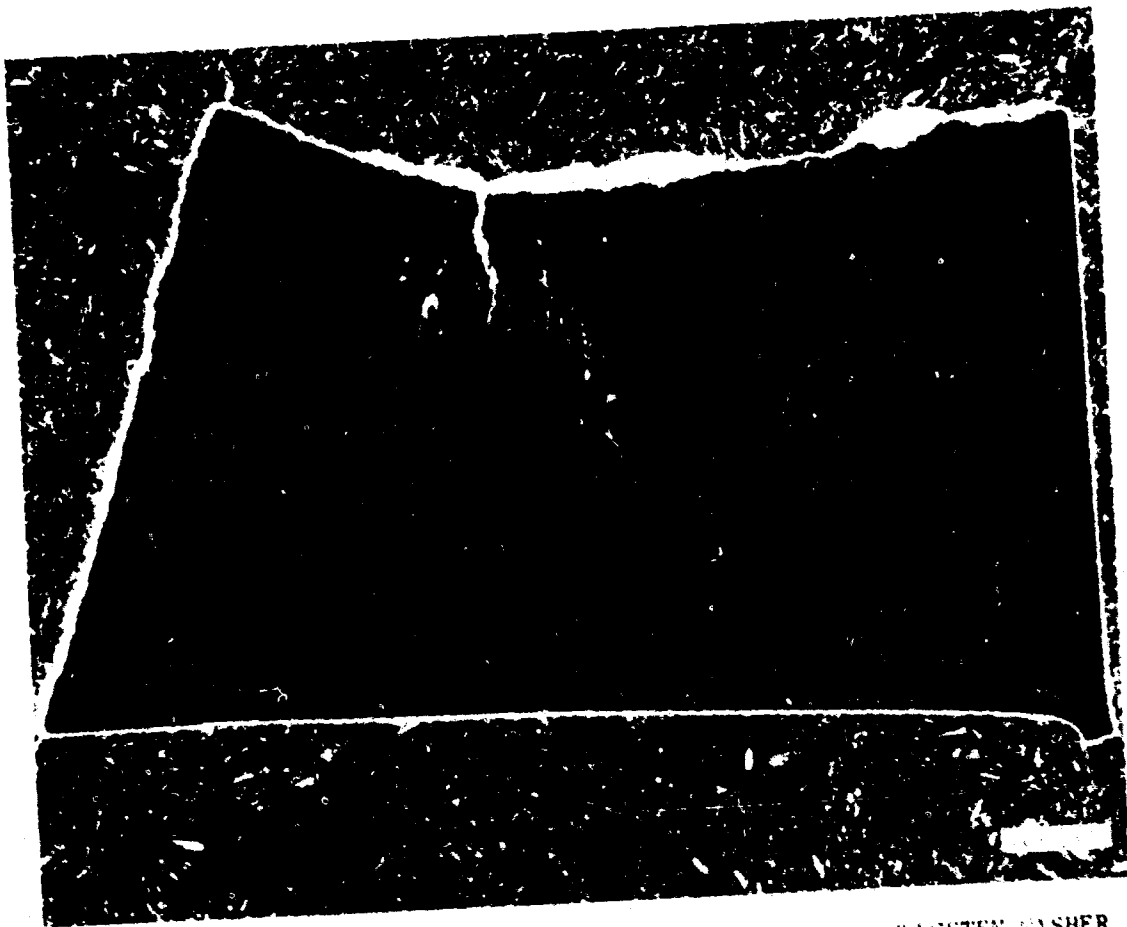
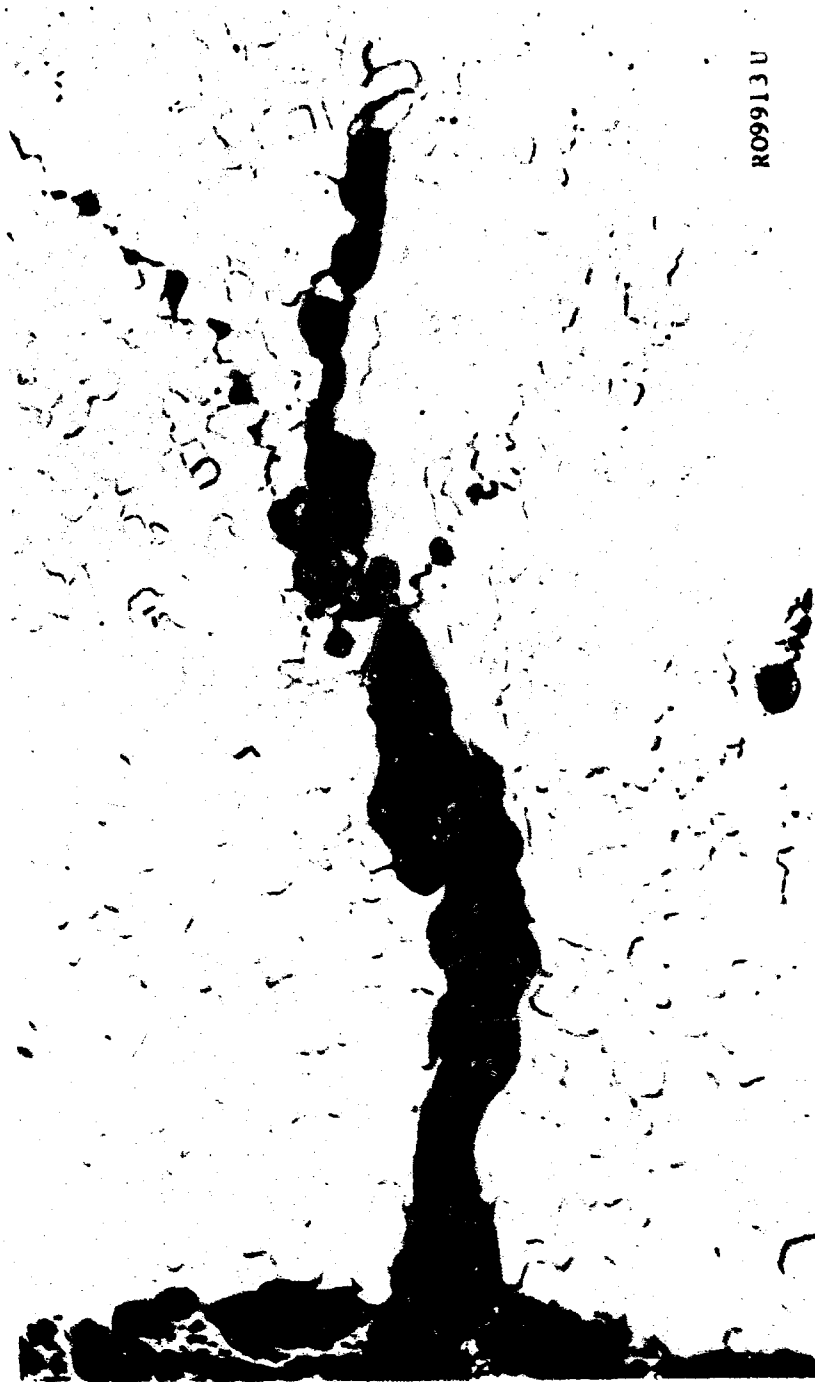


FIGURE 3-19. INTERGRANULAR CRACKS AT INNER SURFACE OF TUNGSTEN WASHER FIRED ONCE (14X)



RO9913 U

FIGURE 3-20. INTERGRANULAR CRACKS AT INNER SURFACE OF TUNGSTEN WASHER
FIRED ONCE (100X)

Orowan^{3.46} and Irwin^{3.47} applied the Griffith concept to more ductile materials independently modifying the classic Griffith theory to allow for plastic energy dissipation as well as the energy required to form new surfaces. Thus, they redefine Equation (3.65) to

$$\sigma = \sqrt{\frac{2G_c E}{\pi C}} \quad (3.66)$$

where G_c is the energy release rate taking into account both surface energy and plastic strain energy. Schroder, et al.,^{3.48} found that polycrystalline tungsten follows the Griffith type criterion in that the square-root characteristic of the crack length versus applied stress was observed. His measured values of the energy for crack propagation, however, were much larger than the true surface energy of tungsten. Some values for the true surface energy of several materials are given in Table 3.3 along with some theoretical or empirical estimates. Except as noted, the data in this table were taken from Reference 3.49.

TABLE 3.3

VALUES OF SURFACE TENSION

Metal	Surface Tension Experiments	Breger	Glauberger	Kunin	Zadumkin
Fe	1409 ergs/cm ²	2480	1427	1210	1180
Ag	927	2170	810	923	940
Na	191	777	208	206	223
Mo	2240 (Ref. 3.50)	----	----	681	1530
W	3000 (Estimated)	----	----	970	1900

Based upon the relatively good agreement between theory and experiment, the value for tungsten was estimated to be 3000 ergs/cm². Using the Irwin modification, Schroder^{3.48} calculated the fracture toughness, K_c ,

$$K_c^2 = G_c E \quad (3.67)$$

of recrystallized tungsten to be 6.2 ksi $\sqrt{\text{in.}}$. This yields a G_c value of 0.77 lb/in. or 135,000 ergs/cm² which is much more than one order of magnitude greater than the true surface energy value. This discrepancy is partially attributed to plastic deformation at the crack tip and the effect of grain boundaries. The grain boundary allows the very sharp characteristic of the crack to be removed when the crack tip intersects the grain boundary. Thus, the greater the grain boundary area, the more the crack is impeded while propagating transgranularly. This is one reason why Ault^{3.51} attributes large grain refractory metals to having a lower fracture energy than fine grained ones.

Another possibility for the high value measured for tungsten is that the specimens used had machined notches with root radii of about 0.003 inch. The resulting stress concentration is not sufficient to simulate a natural crack. Gerberich^{3.52} has confirmed that the root radius required to measure the true characteristics of crack propagation must be smaller than,

$$\rho_c = \frac{K_c^2}{20 \pi \sigma_{ys}^2} \quad (3.68)$$

where K_c is the fracture toughness and σ_{ys} is the yield strength of the material. Utilizing the measured value of K_c (which is an upper bound) and a yield strength of about 80 ksi gives a ρ_c of 0.0001 inch, which is much smaller than the 0.003-inch radius used. Tests with sharper notches, such as those introduced by fatigue cracking, would probably yield smaller values of K_c . Thus, the value of energy release rate for crack propagation of concern should be between the lower limit of 3000 ergs/cm² or 0.0171 lb/in. to an upper bound of 0.77 lb/in. Utilizing these two extremes allows the calculation of tensile stresses which may cause failure in tungsten inserts.

As a first case, assume a surface abrasion from machining or from the combined corrosive and stress environment of the first firing to give a small crack 0.006 inch deep. Utilizing the minimum and maximum values of fracture toughness gives a tensile failure stress ranging from 6740 to 45,000 psi. Since the upper value is probably more realistic, this may not be a limiting condition since the tensile stress would have to be developed at temperatures below the ductile-brittle transition temperature.

As a second case, assume that a fairly gross crack has developed either through a shock loading, repeated cycling, or from the corrosive environment. For example, take the average crack depth of 0.060 inch that is observed in Figure 3-19. With the range of fracture toughness possible, tensile stresses varying from 2130 psi to 14,300 psi may cause failure. Thus, any microscopic flaw of this dimension would probably cause failure. In summary, if high temperature creep is sufficient to relieve all stresses at temperatures below the ductile-brittle transition temperature, the classic type of thermal fatigue may predominate. On the other hand, if a tensile stress exists at low temperatures, there is a probability that brittle fracture will occur on the first or second cycle. The intermediate situation is that subsized Griffith cracks will form and grow at the high temperature reaching a size that will result in catastrophic failure at low stress level temperatures.

(4) Experimental Plan. A very few tests could be performed to determine which fracture phenomenon is likely to predominate. First, in order to represent the most extreme condition, consideration should be given to the effect of carbon diffusion into grain boundaries and how this might affect the energy for crack propagation. This is important, as carbon will

diffuse into the backside of an insert on the first firing; on the second cycle during heating, very high tensile stresses will be involved which may cause failure. Therefore, the following tests are recommended with a temperature cycle of 150°F (65°C) to 5000°F (2760°C) and a maximum cooling rate with the specimens at least 90-percent constrained from thermal expansion:

- (a) Two specimens with a polished surface
- (b) One specimen with a polished surface, carburized at the maximum backwall temperature for 5 minutes
- (c) One specimen with a shallow notch (0.005 inch to 0.010 inch deep)
- (d) One specimen with a shallow notch, carburized at the maximum backwall temperature for 5 minutes
- (e) One specimen with a deep notch (0.060 inch deep)
- (f) One specimen with a deep notch, carburized as above

Seven test specimens would be involved with a maximum number of 100 cycles being run on any one condition. In preparing these tests, it is recommended that fatigue cracking of machine notches be used to introduce natural cracks so that the seriousness of the problem may be assessed. With this spectrum of tests and the ability to monitor temperature and loading, information on the actual energy release rate, critical failure stress, and the effect of temperature and environment on crack growth would be forthcoming.

b. ATJ Graphite. Thermal fatigue behavior of ATJ graphite is discussed in the subsequent paragraphs.

(1) High Temperature Region. It is doubtful that the classic type of thermal fatigue would result in the temperature range being utilized for ATJ graphite. The maximum service temperature (about 2300°C) is in the range in which creep may occur^{3,53} but it is so slow that little microscopic flow could take place in order to obtain plastic thermal fatigue behavior. However, at this temperature some microscopic changes could take place which might be of significance at the lower temperatures.

(2) Low Temperature Region. Brittle fracture is possible in the whole spectrum of temperatures within which ATJ graphite is to be utilized. The classic type of Griffith concept is appropriate since the material is a very brittle solid capable of very little inelastic deformation. The limiting condition is that the pitch-coke graphites are extremely inhomogeneous and therefore have inherently large flaws which make them inherently weak to start with. Theoretical values for the true surface energy in

graphite crystals is given by Bruce.^{3.54} For the stress parallel to the basal planes it is 5470 to 6320 ergs/cm². From some data on pitch-coke graphite by Martens and Kotlensky^{3.55} the deduced value of surface energy from mechanical tensile tests ranges from 2000 to 4000 ergs/cm² which is within the range of the theoretical values. Based upon the range of true surface energy and the anisotropic effects of the crystallites, critical flaw sizes ranging from 0.01 to 0.05 inch may be calculated. Flaws of these sizes are already inherent in the molded graphite material so that sub-size Griffith crack propagation is probably the most likely failure mechanism at stresses short of the tensile strength.

(3) Experimental Plan. The experimental approach would be to determine if the high temperature does have an effect on the microstructure and/or fatigue life. It is also desirable to determine if a corrosive atmosphere can degrade the fatigue life of ATJ graphite. With these thoughts in mind, the following tests are suggested:

- (a) Since temperature may be of small consequence in determining fatigue behavior, run a standard S-N curve at room temperature in tension-tension fatigue with 1000 cycles being the upper limit of the run. A maximum of 20 specimens would be utilized with the initial stress level being 90 percent of the tensile strength. Adjustments may be made in the stress level to prolong or shorten the fatigue life.
- (b) Hold three specimens under the maximum tensile stress and temperature condition for 1 hour. With one specimen observe any microstructural changes. Run the other two at the stress level where failure previously occurred in about 100 cycles and compare.
- (c) Hold two specimens in a CO₂ atmosphere for 5 minutes at 4000°F (2200°C). Fatigue at room temperature using the same stress level as in test condition (b).

c. Pyrolytic Graphite. The extreme anisotropic behavior of pyrolytic graphite injects a large degree of uncertainty in projecting what the thermal fatigue behavior may be.

(1) High Temperature Region. Thermal cycling into the 5000°F (2760°C) range not only may cause creep and void formation, but it also may produce some interesting microstructural changes. Kotlensky^{3.55} has shown that hot-working pyrolytic graphite at temperatures near 5000°F (2760°C) will change the growth cone appearance and result in much higher tensile

properties. With deformations in the range of 12 to 22 percent, the growth cone appearance is completely removed and the tensile strength at room temperature is increased from 17,800 to 46,000 psi. With larger deformations up to 38 percent at 5000°F (2760°C), microcracks are introduced which result in a lower strength of 31,000 psi. Small deformations, up to 5 percent, did not change the microstructural appearance and resulted in minor strength increases. However, accumulative plastic strain from thermal cycling may have a similar result as a single large deformation so that this possibility should not be overlooked.

(2) Low Temperature Region. At room temperature, the tensile strength of pyrolytic graphite is about 15,000 psi in the direction of the layer planes and about 700 psi perpendicular to them. Fortunately, the directions of high strength and high thermal conductivity can be utilized in design. The apparent surface energy for crack propagation across layer planes in pyrolytic graphite may be calculated from mechanical property data^{3.55} to be about 26,000 ergs/cm² which is at least a factor of five greater than that of ATJ graphite. Of course, with the stress acting perpendicular to the layer planes, the resistance to crack propagation is extremely low and delamination will readily occur. The fact that the apparent surface energy in pyrolytic graphite is increased over ATJ means that for the same stress level greater flaws may be tolerated in pyrolytic graphite. However, the very fact that the strength of pyrolytic graphite is a factor of five greater than ATJ means that a material with a smaller initial flaw size has been manufactured. Actually, if the two materials are to be designed to their respective tensile strength levels at room temperature, the pyrolytic graphite can withstand smaller flaws than the ATJ. This means that prior structural changes may be more significant to pyrolytic graphite than to ATJ. From microcrack and mechanical properties observations, the apparent surface energy of hot-worked pyrolytic graphite is 85,000 ergs/cm² which is more than three times as great as as-deposited pyrolytic graphite. Thus, if the design stress for hot-worked pyrolytic graphite is similar to that of as-deposited pyrolytic graphite, a real advantage might be gained in that the resistance to microcrack propagation would be greater. It should be cautioned, however, that hot-work may degrade the basal shear strength by a factor of four^{3.56}. However, since this may not be a critical design problem, the hot-worked pyrolytic graphite should be considered as a potential material if necessary.

(3) Experimental Plan. Six specimens are required for the proposed plan. The tests listed below should be conducted with the specimens 90 percent constrained from thermal expansion.

- (a) Two specimens thermally cycled between 150°F (65°C) to 5000°F (2760°C) to a maximum run of 100 cycles.

- (b) One specimen initially treated with CO₂ gas at 5000°F (2760°C) for 5 minutes, cycled between 150°F (65°C) to 5000°F (2760°C) to a maximum run of 100 cycles.
- (c) One specimen with a surface flaw 0.010 inch deep cycled between 150°F (65°C) to 5000°F (2760°C) to a maximum run of 100 cycles.
- (d) One hot-worked pyrolytic graphite specimen cycled between 150°F (65°C) to 5000°F (2760°C) to a maximum run of 100 cycles.
- (e) One hot-worked pyrolytic graphite specimen with a surface flaw 0.010 inch deep cycled between 150°F (65°C) to 5000°F (2760°C) to a maximum run of 100 cycles.

3.6 CHANGES IN MATERIAL CHARACTERISTICS

Problems caused by changes in material characteristics are, of course, related to specific materials. Although many potential problems can be defined, the only one actually deemed important enough to investigate was that of tungsten.

The change of materials characteristics of ATJ graphite was not expected to be significant. Since ATJ graphite is severely limited as to maximum service temperature because of corrosion considerations, the material remains essentially brittle in nature throughout its service life. Changes in materials characteristics would be expected to be limited to such things as void formations or increase in void size, having a bearing, as a result, on the thermal fatigue characteristics of the material. It would not be expected that materials characteristics would change significantly within the allowable service temperature range.

The change of characteristics of pyrolytic graphite are expected to be generally reflected as a change in the degree of structural transformation which the material has undergone. These changes actually result in the formation of a different material. Within this program three different types of pyrolytic graphite were studied. These are as-deposited, heat-treated, and annealed pyrolytic graphite. Any changes in materials characteristics which are not reflected as these different types of materials can be regarded as a change in degree of transformation leading to these materials. Thus an as-deposited material, which has undergone some slight degree of heat-induced change, lies somewhere between as-deposited and heat-treated material. These two materials can serve as bounds on the slightly changed material. Thus, considering pyrolytic graphite to be in these three forms defines three discrete regions within a range in which this material may exist. All three forms of the material were utilized in the test phases of the program.

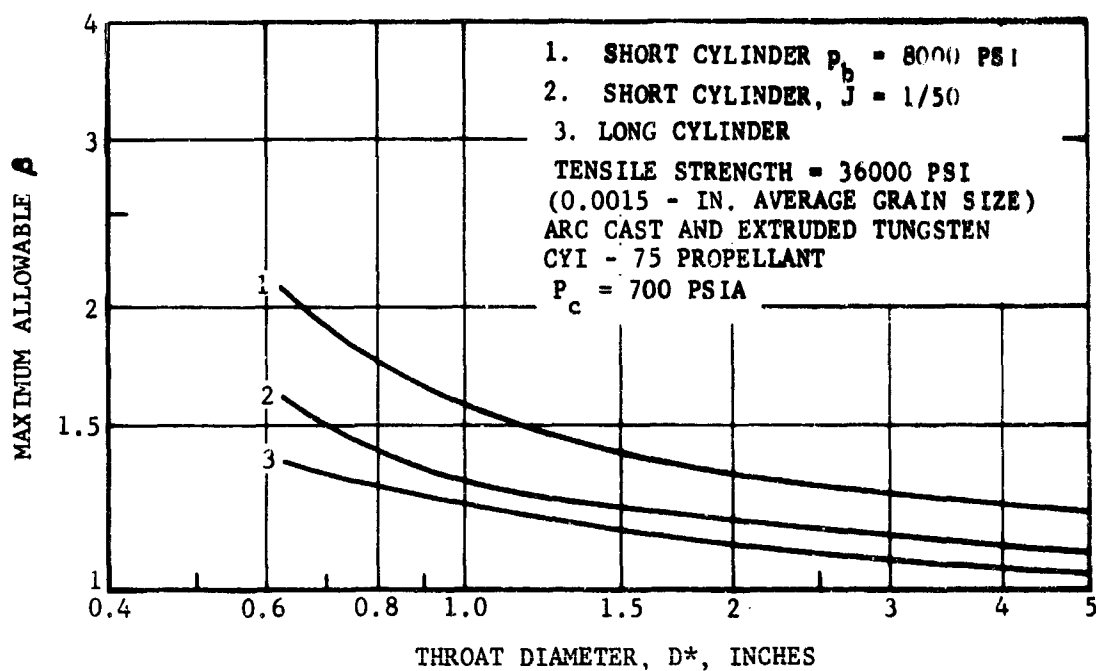
Work was conducted in the materials laboratory relating changes in properties of tungsten to grain size. Work was also conducted relating rate of grain growth to thermal cycling. These data are discussed in Section 4. It is shown that the strength of tungsten degrades very rapidly with only a slight increase in grain size, while the elastic modulus remains virtually constant over a great range of grain size. Since a slight growth in grain size results in a marked reduction in strength, rather severe limitations on the design strength of tungsten result. Although the data are limited insofar as indicating the rate of grain growth with respect to maximum temperature, one may conclude conservatively that any second or subsequent firing of a restartable nozzle should consider the strength to be markedly degraded as shown in Section 4. The change in coefficient of thermal expansion was determined to be unaffected by grain growth. The product of elastic modulus and coefficient

of thermal expansion is linearly related to the thermal stress response of the material. Thus, the thermal stress response of tungsten remains unaltered over a range in grain size, while the ability of the material to support this response is considerably degraded.

The effect of this reduced strength on the resistance to brittle tensile fracture may be investigated by inserting the new strength into Equations (3.21) and (3.23) of Paragraph 3.2.1. As an example of the effects of restarting a nozzle with a tungsten insert which has experienced some slight grain growth, Figure 3-21 has been constructed. It is similar to Figures 3-14 and 3-15 which are design charts constructed for tungsten with a tensile strength of 94,000 psi. Figure 3-21 illustrates the decline in the maximum β when the grains have grown to an average size of 0.0015 inch. It should be noted that even the insert restrained by ATJ ($p_b = 8000$ psi) will necessarily be quite thin if a tensile fracture is to be avoided. For larger grain sizes, the structural properties of the material are reduced to a level such that the failures theoretically take place only tenths of a second after initiation of the heating. In this analysis the heat transfer was applied as a step input (i.e., no startup transient was assumed). Since many solid rocket motors can achieve 90 percent of peak thrust in a few milliseconds, this step input assumption would be applicable to these motors.

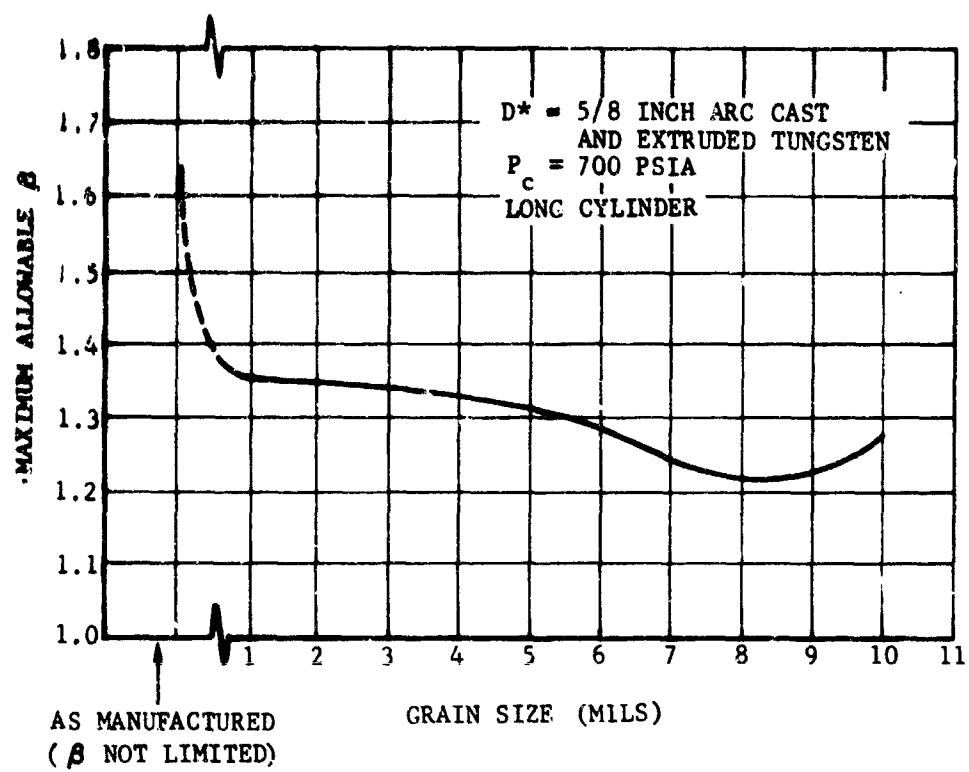
To illustrate the potentiality of tungsten inserts with large grains, a 5/8-inch diameter insert was examined for the full range of grain sizes measured in the materials studies. Figure 3-22 illustrates the maximum allowable β for the 5/8-inch D* nozzle as a function of the average tungsten grain size. This figure depicts a phenomenon which should receive further investigation. For grain sizes greater than 0.008 inch, the strength of the material is continuing to decrease, but the elastic modulus decreases more rapidly. This can be seen in Figure 4-15 which shows the variation in mechanical properties with grain size. Therefore, with increasing grain size, the allowable β begins to increase again for average grain sizes greater than 0.008 inch. Of course, this curve may be misleading since it was constructed from a relatively small number of data points; however, it may be a valid indication that large-grained tungsten can be a very good material for restartable rocket motor nozzle throat inserts.

Degradation of elastic modulus has not been studied in depth. No prediction can be made relative to the cause or ultimate degree of this degradation. But it will be recalled that the room temperature modulus of the as-received gas pressure bonded tungsten was only about 55 percent of what could normally be expected. Yet from all appearances, this was "sound" material. Here, then, are two examples of reduced modulus in material which was fired in this program. It opens up interesting speculation about the use of low-modulus tungsten.



FO4464 U

FIGURE 3-21. TUNGSTEN OUTER SURFACE TENSILE RESPONSE CHART FOR DEGRADED STRENGTH



FO4465 U

FIGURE 3-22. THE EFFECT OF GRAIN GROWTH ON THROAT INSERT DESIGN

Another indication of the effects of grain size in tungsten is given in Reference 3-23, where it is observed that there is a correlation between resistance to thermal stress cracking and large grain size. The materials of largest grain size, which were pure tungsten either cast or fully cold worked, showed the best crack resistance. The authors state it is likely that the large grain size favors resistance to crack propagation for three reasons:

- (1) The lower yield strength of coarse grain material would result in deformation at a lower applied stress. This deformation could favor reduction of stress concentrations and absorb sufficient energy from a propagating crack to terminate it.
- (2) Fewer grain boundaries exist for crack initiation. Since it is generally observed that crack initiation in tungsten is invariably intergranular, the presence of fewer grain boundaries would reduce the number of possible crack initiation sources.
- (3) Fewer grain boundaries exist (normal to) the direction of the principal fracture stress. Fracture propagation is generally intergranular, and cracks follow grain boundaries whenever a suitably oriented boundary exists. For coarse grain material, grain boundaries are not always present in the proper direction; in this event the propagating crack must enter a grain wherein the deformation which occurs may be sufficient to terminate the crack.

3.7 UNIQUE LOADING EFFECTS

Loadings on nozzle throat sections are attributable to temperature, pressure, and structural restraints. Unique loadings result from novel effects of these three causes and from residual effects resulting from prior structural behavior.

No unique effects are caused by pressure or structural restraints. However, thermal loading effects and residual states can be quite different from those considered for single-firing nozzles.

All structural analyses have considered that the initial condition of the nozzle insert includes uniform ambient temperature. If it is desired to restart the nozzle during some period of cooldown before uniform ambient conditions are reached, a new loading is imposed on the structure because of the resulting different temperature distribution. It has been shown in the thermal analysis that during all portions of the duty cycle, both firing and cooling, the temperature is either monotonically decreasing through the thickness or else is very nearly uniform at some level above the ambient temperature. The departure from uniformity in the temperature is not severe enough to cause a worse loading condition than that attained from an initial ambient uniform temperature. Nor is the monotonically decreasing temperature distribution worse than that which would have existed had the firing not been interrupted. Therefore, the assumption of an initial uniform temperature results in the most severe thermal loading obtainable. The lower the datum of this uniform initial temperature, the more severe will be the resulting loading. Since ambient temperature is the lowest datum for which corroborative test results could be obtained on this program, the assumption of an initial uniform ambient temperature results in a conservative structural analysis.

It has also been shown in the thermal analysis that alumina deposition retards the buildup of thermal gradients. Structurally, this means that the temperature difference across the insert is reduced while the shape of the temperature distribution is closer to being linear. The effect of the reduced temperature difference is more powerful than that of the shape of the distribution; this results in an decrease in the thermal stresses. Again, the assumption of an initial uniform ambient temperature results in a conservative structural analysis.

There are, then, no unique thermal loading effects to be considered.

Residual stresses resulting from permanent deformation have no significant importance for any of the throat materials except tungsten. Considering that the inner material of the insert undergoes a greater hoop permanent deformation than the material in the back side region (experimental results establish this as true) and that this is a compressive deformation, then the inner material will be in residual hoop tension while the back side

material is in residual hoop compression. These stresses are of the opposite sense of the thermal stresses developed during heating of the insert and represent a prestressed condition which must be overcome by the thermal stresses and are therefore subtractive to the thermal stresses. Thus, the thermal stresses developed in such a prestressed insert will always be less than those generated in an initially stress-free insert. Thus, the assumption that no residual stresses exist results in a conservative structural analysis.

No residual stress analysis was conducted during this program. Residual effects must be calculated from a complete history of the part--a statement of the residual boundary strains is not sufficient to allow a residual analysis to be performed. It is necessary to have a complete elastic and anelastic biography of the entire part. It is evident that purely plastic deformation does not account for all of the tungsten insert shrinkage observed in the test phases.

Complete radial restraint of thermal expansion of a tungsten insert up to temperatures near its melting point, even if the material were totally plastic and had no resistance to deformation, would cause at most a shrinkage of only 1-1/2 percent. This shrinkage is merely the $\Delta L/L$ or $\int \alpha dT$ of the material. Plastic deformation with some resistance to deformation would cause a somewhat smaller shrinkage. Actual shrinkages observed for single firings ranged upwards to 3 and 4 percent. The other effects which could contribute to the shrinkage are the tendency to extrude the insert with the conical back side through the die formed by the backup material and crystallographic changes which may occur in the material. The radial pressure exerted on the insert from the extrusion is of the order of 1000 psi. The inserts were noted to shrink a little each time they were heated. Any extrusion effect would then be a time-dependent phenomenon involving viscoelastic behavior of the material. Time-dependent phenomena were not included in the structural analysis.

It must be concluded that the phenomenon of tungsten shrinkage is not completely understood and until the causative mechanisms are defined and their effects on the residual state are known, no meaningful residual analysis can be conducted.

REFERENCES

- 3.1 Hatch, J. E., Schacht, R. L., Albers, L. U., and Saper, P. G., Graphical Presentation of Difference Solutions for Transient Radial Heat Conduction in Hollow Cylinders with Heat Transfer at the Inner Radius and Finite Slabs with Heat Transfer at One Boundary, NASA TR R-56, 1960.
- 3.2 Desmon, L. G., and Avis, G. B., "Transient Body Temperature Response Curves for Hollow Cylinders with Heated Interior and Insulated Exterior," "Cylheat" Handbook - Volume I, ABL-Hercules Report No. ABL/X-123, July 1964.
- 3.3 Second Quarterly Technical Report, An Investigation and Feasibility Demonstration of Nozzles for Restartable Solid Rocket Motors, Philco Secondary Publication No. C-2952, RPL-TDR-64-168, 20 December 1964 (Confidential).
- 3.4 Morgan, A. J. A. and Christensen, C. H., "Thermal Stresses in Missile Nose Cones," S.M.F. Fund Paper No. FF-24, Institute of the Aeronautical Sciences, New York, 1960.
- 3.5 Young, David, "Iterative Methods for Solving Partial Difference Equations of Elliptic Type," Transactions of the American Mathematical Society, Vol. 76, January-June, 1954, pp 92-111.
- 3.6 Bijlaard, P. P. and Dohrmann, R. J., "Thermal-Stress Analysis of Irregular Shapes," Transactions of the ASME, Series B (Journal of Engineering for Industry), November 1961, pp 467-477.
- 3.7 Bijlaard, P. P., and Dohrmann, R. J., "General Procedure for Analyzing Thick Shells of Irregular Shapes for Mechanical and Thermal Loading," Transactions of the ASME, Series B (Journal of Engineering for Industry), August 1963, pp 314-320.

- 3.8 Morgan, A. J. A., "A Proof of Duhamel's Analogy for Thermal Stresses," Journal of the Aero/Space Sciences, July 1958, pp 466-467.
- 3.9 Broglio, Luigi, Anisotropic Composite Thermal Structures for Hypersonic Flight, European Office Air Research and Development Command, Contract No. AF 61(052)-198, Tech. Note No. 1, University of Rome, February 1959.
- 3.10 Fox, L., "Mixed Boundary Conditions in the Relaxational Treatment of Biharmonic Problems," Proceedings of the Royal Society of London, Series A, Vol. 189, March-September 1947, pp 535-543.
- 3.11 Leggett, H. and Parechanian, H., Mechanical Properties of Wrought Tungsten, Air Force Materials Laboratory Research and Technology Division, Air Force Systems Command, Wright-Patterson Air Force Base, Ohio, ASD-TDR-63-585, Volume I, November 1963.
- 3.12 Dull, R. B., "Physical Properties of Some Newly Developed Graphite Grades," Volume XXVI of Research and Development on Advanced Graphite Materials, Air Force Materials Laboratory Research and Technology Division, Air Force Systems Command, Wright-Patterson Air Force Base, Ohio, WADD TR 61-72, May 1964.
- 3.13 "Pyrolytic Graphite/Facilities and Product Information," Pyrolytic Materials Engineering Handbook, Super-Temp Corporation, Santa Fe Springs, California, revised October 1964.
- 3.14 "Pyrolytic Graphite Engineering Handbook," Specialty Alloys Section, Metallurgical Products Department, General Electric Company, Detroit, Michigan, July 15, 1963.
- 3.15 D'Urso, S. F., "Pyrolytic Graphite Alloys," High Temperature Materials, Inc., Boston, Massachusetts, April 1964. Presented at ASTM Pyrolytic Graphite Symposium, March 30-31, 1964, Palm Springs, California.
- 3.16 "Pyroid, Bulk Pyrolytic Graphite," Engineering Data, Pyrogenics, Inc., Johns-Manville Aerospace Products Group, New York, N.Y., 1964.
- 3.17 Gobble, L. P., and Salmen, W. S., "Compressive Properties of Pyrolytic Graphite from Room Temperature to 5000°F," Symposium on Materials for Aircraft, Missiles, and Space Vehicles, ASTM STP No. 345, 1963.
- 3.18 Marcus, L., Modulus of Rupture Tests on Pyrolytic Graphite, Engineering Laboratories, Bell Aerosystems Company, Bell Laboratory Report BLR 62-1 (M), Revision A, 31 October 1962.
- 3.19 Kottlensky, W. V. and Fischbach, D. B., "Graphite," JPL Research Summary No. 36-8, Engineering Mechanics Division, Jet Propulsion Laboratories, May 1, 1961, pp 86-91.

- 3.20 Bland, D. R., "Elastoplastic Thick-Walled Tubes of Work-Hardening Material Subject to Internal and External Pressures and to Temperature Gradients," Journal of the Mechanics and Physics of Solids, 1956, Volume 4, pp 209-229.
- 3.21 Stepin, P., Strength of Materials, Chapter 8, Gordon and Breach, New York, 1963.
- 3.22 Donadio, R. N. and Pappis, J., The Mechanical Properties of Pyrolytic Graphite, Raytheon Company, Research Division, Waltham, Massachusetts. Presented at ASTM Pyrolytic Graphite Symposium, March 30-31, 1964, Palm Springs, California.
- 3.23 Olcott, E. L. and Batchelor, J. D., A Study of Tungsten Alloys for Rocket Nozzles, AFML-TR-65-101, April 1965.
- 3.24 First Quarterly Technical Report, An Investigation and Feasibility Demonstration of Nozzles for Restartable Solid Rocket Motors, Philco Secondary Publication No. U-2794, RPL-TDR-64-112, 21 September 1964.
- 3.25 Yen, T. C., "Thermal Fatigue - A Critical Review," Welding Research Council Bulletin 72, October 1961.
- 3.26 Swindeman, R. W. and Douglas, D. A., Jr., "The Failure of Structural Metals Subjected to Strain Cycling Conditions," Journal of Basic Engineering, Trans. ASME, Vol. 82, pp 203-212, June 1959.
- 3.27 Forrest, P. G., Fatigue of Metals, Pergamon Press, New York, 1962.
- 3.28 Pope, J. A., Metal Fatigue, Chapman and Hall, Ltd. London, 1959.
- 3.29 Boettner, R. C., Laird, C., and McEvily, A. J., Jr., Crack Nucleation and Growth in High Strain-Low Cycle Fatigue, Ford Motor Co., Scientific Laboratory Technical Report No. SL 64-50, July 15, 1964.
- 3.30 Baron, H. G. and Bloomfield, B. S., "Resistance to Thermal Fatigue Cracking of Several Types of Cast Iron," Armament Research and Development Establishment (Great Britain) ARDE Memo No. (Mx)53/61, October 1961, AD 265-818.
- 3.31 Glenny, E., "Thermal Fatigue," Metallurgical Reviews, Vol. 6, No. 24, 1961, pp 387-465.
- 3.32 Northcott, L. and Baron, H. G., J. Iron Steel Inst., Vol. 184, 1956, p 385.
- 3.33 Stumper, R., Iron Coal Trades Rev., Vol. 156, 1948, p 319.
- 3.34 Baron, H. G., New Scientist, Vol. 7, 1960, p 1287.

- 3.35 Baron, H. G. and Bloomfield, B. S., J. Iron Steel Inst., Vol. 197, 1961, p 223.
- 3.36 Riddihough, J., Metallurgia, Vol. 62, 1960, p 53.
- 3.37 Evans, E. R., Brit. Cast Iron Research Assoc., Research Rep. 407, 1955.
- 3.38 Bruckner, W. H. and Czyzewski, H., J. Amer. Ceram. Soc., Vol. 25, 1945, p 381.
- 3.39 Glenny, E. and Taylor, T. A., Powder Met., Vol. (1/2), 1958, p 189.
- 3.40 Design Report for Nozzle #1 - CSR Ancei Stop-Start Nozzle Program, TRW Report ER 6305-1, Contract No. AF 04(611)-9067, December 10, 1964.
- 3.41 Steigerwald, E., TRW Cleveland, Private Communication, January 22, 1965.
- 3.42 Kennedy, C. R., "Plastic Strain Absorption as a Criterion for High Temperature Design," Proc. Fourth Sagmore Conf., 1958, p 193.
- 3.43 Coffin, C. F., "Strass Fatigue in Austenitic Steels at Elevated Temperatures," ASTM Spec. Tech. Pub. No. 165, 1954, p 31.
- 3.44 Griffith, A., "The Phenomenon of Rupture and Flow in Solids," Philos. Trans. Royal Soc. London, Series A, 221, p 1921, 1963.
- 3.45 Inglis, C., "Stresses in a Plate Due to the Presence of Cracks and Sharp Corners," Trans. Inst. Naval Arch., London, 60, 219 (1913).
- 3.46 Orowan, E., "Fundamentals of Brittle Behavior in Metals," Fatigue and Fracture of Metals, John Wiley and Sons, Inc., New York, 1952, p 139.
- 3.47 Irwin, G. R., "Fracture Dynamics," Fracturing of Metals, American Society for Metals, Cleveland, 1948, p 147.
- 3.48 Schroder, K., Packman, P., Nash, G., Weiss, V., Crack Initiation in Metallic Materials, Syracuse University Research Institute Final Report, Contract N600(19)-59514, Navy Bur. Weap., 1964.
- 3.49 Surface Phenomena in Metals and Alloys, by V. K. Semchenko, Translated from Russian by N. G. Anderson, Pergamon Press, New York, 1961.
- 3.50 Taylor, J. W., Metallurgia, 50, No. 1, (1954), p 161.
- 3.51 Ault, R. T. and Stretnak, J. W., Initial Yielding and Fracture in Notched Sheet Molybdenum, Report ASD-TDR-62-223, 1962.

- 3.52 Gerberich, W. W., "Current Trends in Testing Methods, Design, and Materials for Fracture Toughness," Metals Engineering Quarterly, November 1964.
- 3.53 Seldin, E. J., "Creep and Recovery in Graphites at High Temperatures," Proc. Fifth Carbon Conference, Vol. 2, Pergamon Press, 1963, p 549.
- 3.54 Bruce, R. H., Journal Metal. Club, R.C.C. Glasgow, No. 10, p 41, 1958-1959.
- 3.55 Kotlensky, W. V. and Martens, H. E., "Mechanical Properties of Pyrolytic Graphite to 2800°C," Proc. Fifth Carbon Conf., Vol. 2, Pergamon Press, 1963, p 631.
- 3.56 Kotlensky, W. V., Private Communication, 1964.

SECTION 4

MATERIALS STUDIES

The materials studies effort was conducted in three areas. A literature survey was made, laboratory investigations were conducted, and post-firing examinations of test hardware were accomplished. The post-firing examinations are discussed in relation to the nozzle test program in Sections 5, 6, and 7, and in the comparison of analytical and experimental data in Section 8. The literature survey was conducted to provide material properties data and to support the laboratory studies. Materials laboratory studies were designed to examine the phenomenological characteristics of the materials of interest. Tungsten grain growth investigations studied both the rate of grain growth and the effects on mechanical properties. Tungsten carbon interaction studies examined eutectic formation and the use of diffusion barriers. Brief studies related to alumina deposition and reaction were conducted. An original investigation of the high temperature c-direction compressive deformation of pyrolytic graphite was made. Some preliminary thermal fatigue testing was also conducted. No materials laboratory work was done on reinforced plastics; comparative assessments of these materials were to be made in rocket firing tests.

4.1 LITERATURE SURVEY

The literature survey was divided into two portions. The first was a compilation of physical, thermal, and mechanical properties of materials. This was largely to provide support to the analytical phases of the program. The second portion was designed to search out meaningful data on the behavioral characteristics of materials in the rocket nozzle environment. This was to provide support to the laboratory investigations as well as to the nozzle test phases. The literature compiled in the second portion of the survey is discussed and referenced in those areas to which it is

related; e.g., the materials laboratory investigations, the nozzle test program, and the comparison of analytical and experimental data. The properties compilation produced no new discoveries. The following remarks seem appropriate in summary.

Data for gas pressure bonded microsphere tungsten are contained in the supplier's literature^{4.1}. What is essentially a second edition of this literature has recently been published^{4.2}. Limited data appear in the open literature^{4.3}. The gas pressure bonded tungsten used in the rocket motor tests was in the as-consolidated form. There is a dearth of property data on the material in this condition; most of the published data is for highly worked material. A summary report^{4.4} on tungsten issued by DMIC and the Polaris Materials Manual^{4.5} do an excellent job of compiling the physical, mechanical, and thermal properties of sintered, arc cast, and hot pressed tungsten. In addition, extensive property data for wrought tungsten are given in Reference 4.6. The compressive mechanical properties appear to be absent from the literature. The only data appear in two reports. Kirchner^{4.7} estimates the ultimate compressive strength at 4100°F to be 11,000 psi. Union Carbide^{4.8} sonically measured the modulus in compression up to 1800°C and obtained good agreement with other published data obtained from tensile tests at room temperature. However, the compressive sonic modulus diverges, with increasing temperature, from the tensile data.

The largest collection of data on the polycrystalline graphites has been found in reports from Union Carbide Corporation generated under Contract No. AF 33(616)-6915. Volume XXVI^{4.9} of this series contains a summary of property data. Values of Poisson's ratio are conspicuous by their absence. Caution should be exercised in using the published values of Young's modulus. The published values were determined by sonic methods which impose very small strains on the material. The stress-strain curves are bilinear and show that the initial slope is very high compared to the slope at large strains or stresses. Thus the initial slope (and the sonic modulus) may be over twice as high as the secant modulus at large strains.

In general, the data generated by Lockheed^{4.10} several years ago still stands as the most complete compilation of pyrolytic graphite properties. Additional data on the compressive properties are presented in Reference 4.11. More recent mechanical property data are published in Reference 4.12. A classified version of these data is contained in Reference 4.13. These later data were obtained with specimens which were carefully selected, machined, and tested. It, therefore, attempts to exclude the effects of material flaws which are inherently present in hardware-size pieces of the material. No material properties for heat treated pyrolytic graphite were found in the literature. The use of the material in this form is relatively new and the lack of property data should not be surprising. Thermal property data for annealed pyrolytic graphite were taken from Reference 4.14.

4.2 TUNGSTEN GRAIN GROWTH

The effect of grain size on the strength of tungsten is critical in determining the potential use of this material in nozzles for restartable rockets. With each successive firing, the tungsten grains can grow larger, the extent being dependent on the firing duration which in part determines both the temperature obtained and the residence time at temperature. Yet, with the initiation of the successive firings, the material must withstand the induced loadings while in the increasingly larger grain state. It is then imperative that the properties of the tungsten, as influenced by grain size, be known to compensate for variations from the initial material.

One material selected to evaluate the effect of grain size on the tensile strength and Young's modulus was Climax Molybdenum Company's Climet arc cast unalloyed tungsten. The composition of the material was

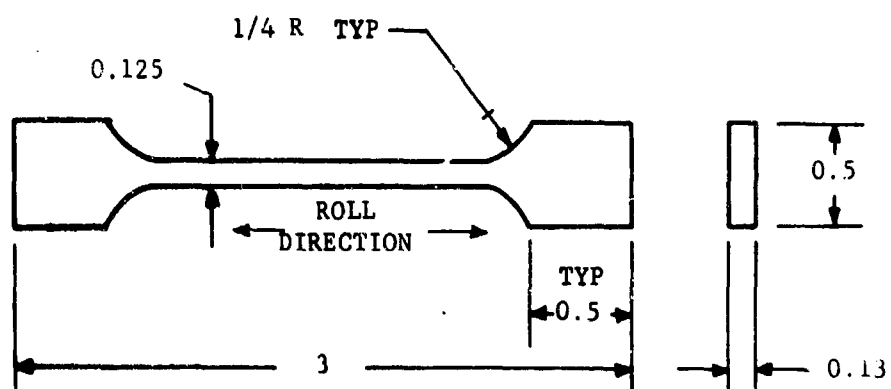
<u>Carbon</u>	<u>Iron</u>	<u>Nickel</u>	<u>Silicon</u>	
0.003	0.004	0.001	0.001	wt.%

with the balance tungsten by difference. The initial arc cast ingot was 7-1/4 inches in diameter. This ingot was processed as follows:

- (1) Extruded at 3100°F to a 1-1/4 inch by 4 inch billet of rectangular cross section.
- (2) Recrystallized at 3000°F.
- (3) Rolled in five increments to approximately 1/8 inch thickness using a rolling temperature of 3000° F each time.
- (4) Final recrystallization at 3000°F for one hour.
- (5) Cut to pieces 1/8 inch by 3 inches by 7 inches.
The 3 inch dimension was in the roll direction.

Test coupons corresponding to Figure 4-1 were cut from the slabs. These coupons were thermally cycled for various times to simulate successive firings, and were subsequently tested in tension at room temperature.

The thermal cycling consisted of heating the specimen by rf in a vacuum. The power was applied until the specimen reached a preselected temperature (about 25 seconds to 2400°C). When the specimen reached the temperature, power was discontinued. The specimen was then allowed to cool for five and one-half minutes prior to the next cycle. During this time, the specimen was below 800°C for approximately 3 minutes. After the final cycle, the specimen was allowed to cool at least 30 minutes prior to removal from the vacuum system.



R09614 U

FIGURE 4-1. TENSILE SPECIMEN USED FOR TUNGSTEN GRAIN GROWTH EVALUATION

This method of cycling resulted in a uniform grain size over the gauge section of the specimen. The gripping end, however, usually had smaller grains. These smaller grains were a consequence of the thermal gradient at the ends which resulted from conductive heat transfer to the supporting block of graphite and loss to the unheated upper section.

The thermal cycling history of the test specimens is listed in Table 4.1.

TABLE 4.1

TUNGSTEN GRAIN GROWTH HEATING CONDITIONS

Sample No.	Max. Temp (°C)	Time to Temp (sec)	Cycles to Temp	Avg Grain Size at Point of Fracture (in.)
1	1850	20	1	0.00075
2	2400	25	2	0.0015
3	2400	25	5	0.0070
4	2400	25	10	0.0045*
5	2400	25	10	0.0090
6	2400	25	10 min at 2400°C	0.0100
7	Room	0	As Received	

* Fractured in transition region of specimen near grips.

Following the temperature cycling, the specimens were electrolytically polished and etched in a solution containing 20 grams of NaOH per liter of water.

Figures 4-2 through 4-6 show the maximum grain size in the gauge section. This size is representative of the size that can be expected during the exposure to cyclic temperature. Marks resulting from the grinding required to shape the specimens are evident in these photomicrographs. These marks were not considered as detrimental, as the purpose was to observe the grain size.

Figures 4-7 through 4-12 show the grain size at the point of fracture resulting from tensile tests. It is this grain size that must be used to correlate mechanical property variation with grain size. Figure 4-7 shows both the maximum grain size and the grain at the point of fracture. Figures 4-13 and 4-14 show a comparison of grain sizes in material cycled the same as Sample 5 but which fractured during thermal cycling. These figures reveal additional cracking along the roll direction. This suggests that the fracture occurred prior to or during the early stage of the first heat cycle.



FIGURE 4-2. ARC CAST TUNGSTEN SAMPLE 2,
2 CYCLES TO 2400°C, LARGEST GRAIN (100X)



FIGURE 4-3. ARC CAST TUNGSTEN SAMPLE 3,
5 CYCLES TO 2400°C, LARGEST GRAIN (100X)



FIGURE 4-4. ARC CAST TUNGSTEN SAMPLE 5, 10 CYCLES TO 2400°C,
LARGEST GRAIN (100X)

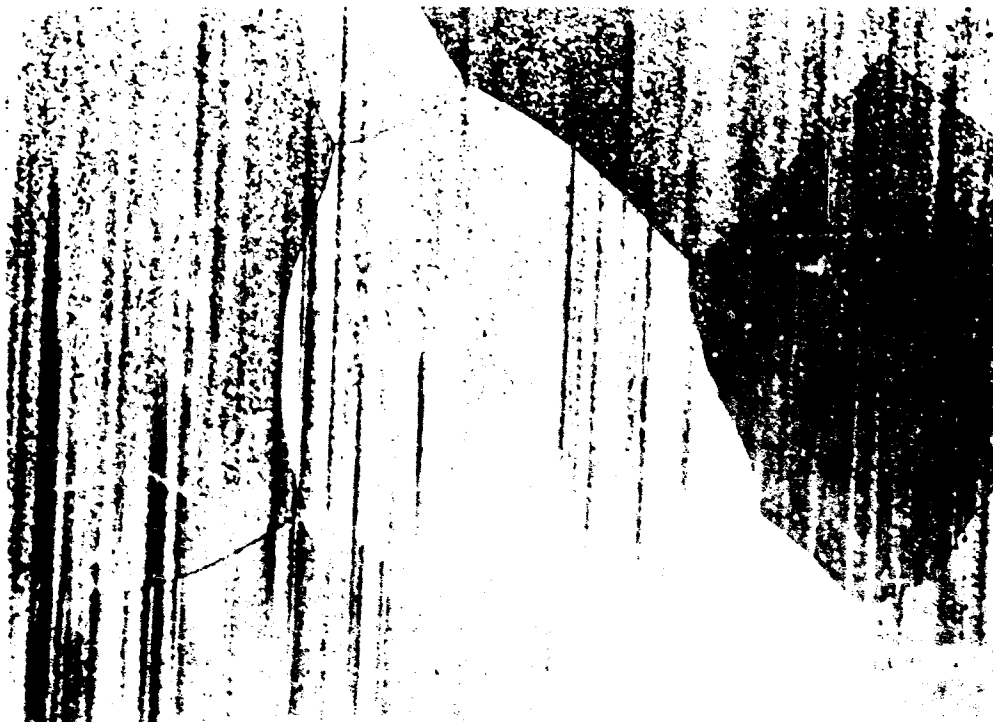


FIGURE 4-5. ARC CAST TUNGSTEN SAMPLE 6,
10 MINUTES AT 2400°C, LARGEST GRAIN (100X)

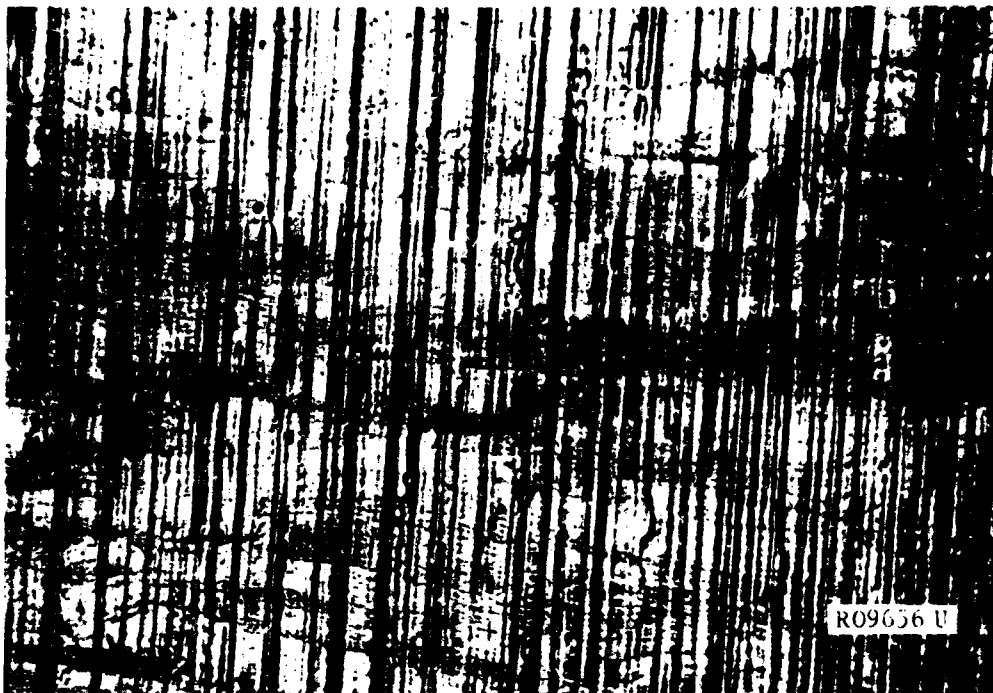


FIGURE 4-6. ARC CAST TUNGSTEN AS RECEIVED (200X)

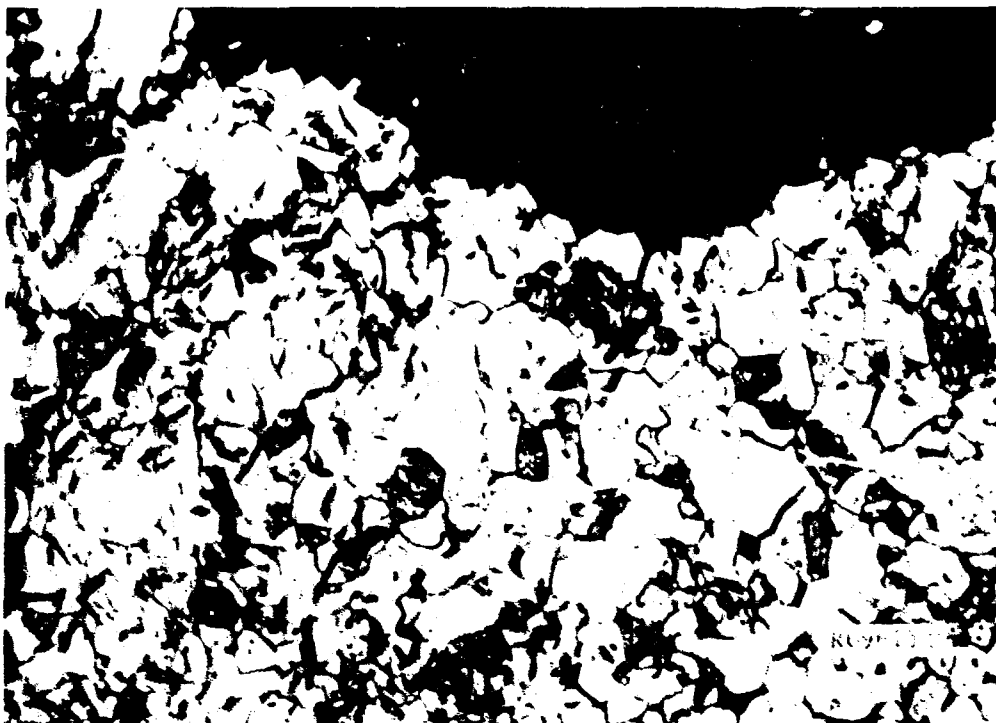


FIGURE 4-7. ARC CAST TUNGSTEN SAMPLE 1,
1 CYCLE 1-1850°C, LARGEST GRAIN
AND GRAIN AT FRACTURE (200X)

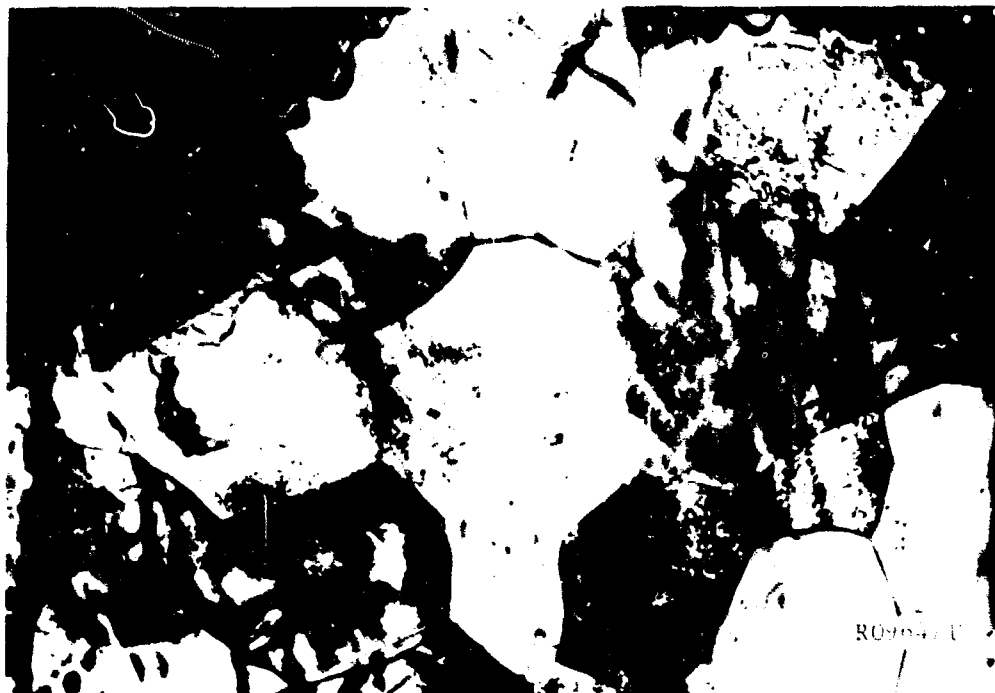


FIGURE 4-8. ARC CAST TUNGSTEN SAMPLE 2,
2 CYCLES TO 2400°C, GRAIN AT FRACTURE (200X)



FIGURE 4-9. ARC CAST TUNGSTEN SAMPLE 2,
5 CYCLES TO 2400°C, GRAIN AT FRACTURE (200X)

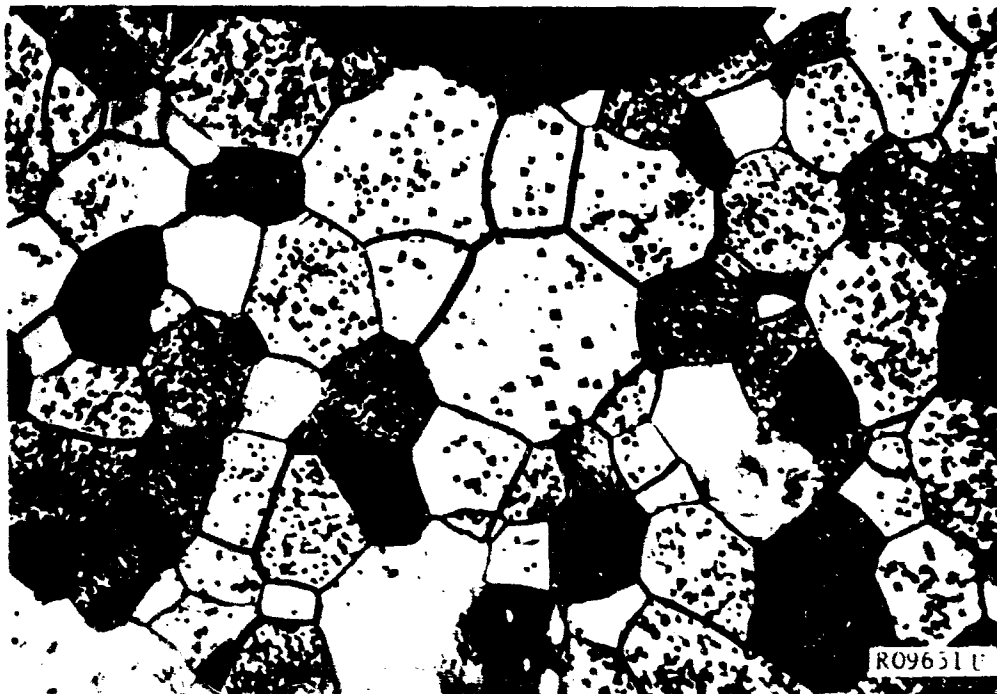


FIGURE 4-10. ARC CAST TUNGSTEN SAMPLE 5,
10 CYCLES TO 2400°C, GRAIN AT FRACTURE (200X)

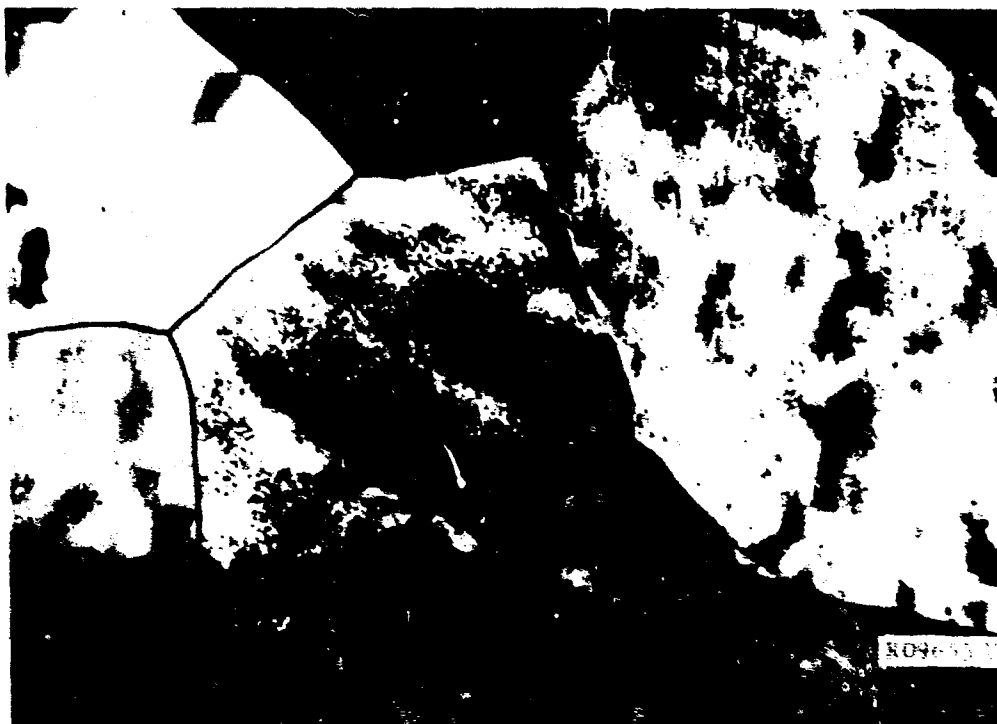


FIGURE 4-11. ARC CAST TUNGSTEN SAMPLE 6,
10 MP TO 2400°C, GRAIN AT FRACTURE (200X)



FIGURE 4-12. AS RECEIVED ARC CAST TUNGSTEN, SAMPLE 7,
AT FRACTURE (400X)



FIGURE 4-13. ARC CAST TUNGSTEN,
10 CYCLES TO 2400°C, CRACK DEVELOPED
DURING HEATING CYCLE (100X)



FIGURE 4-14. ARC CAST TUNGSTEN,
10 CYCLES TO 2400°C, CRACK DEVELOPED
DURING HEATING CYCLE (200X)

A plot of Young's modulus and tensile strength with grain size at the point of fracture is shown in Figure 4-15. The limited data to date indicate that the modulus is moderately insensitive to grain size up to a critical size. At this point, the modulus decreases with increasing size. The tensile strength appears to fall rapidly with the formation of grains and decreases slowly with increasing grain size. This suggests that the grain boundaries as formed are comparatively weak with little interlocking of grains.

The data of Klopp^{4.15} at 2500° to 4000°F show a similar dependence of strength on grain size as observed in the present work with similar material. Thus, the weakening of the structure exists over the region of transient thermal rise and is continued with further grain growth.

Each specimen failed by brittle fracture. The fracture was predominantly intergranular with the only evidence of transgranular fracture occurring on Sample 6. This transgranular fracture appeared to result from interlocked grains along the path of crack propagation. An intergranular fracture at this point would have required a two-grain width offset over a two grain distance.

The tensile strength variation suggests the material, with the formation of crystals, behaves as a polycrystalline as opposed to a single crystal material. The modulus behavior also suggests the polycrystalline behavior with low porosity (thin grain boundary). An examination of the samples after fracture revealed no grain-to-grain movement other than at the fracture line.

On the tungsten examined, there appears, as indicated in Figure 4-15, to be a deterioration of the mechanical properties with grain size increase as would be experienced in a restartable rocket motor. The limited data indicate a trend but without further verification should not be used in an absolutely quantitative sense.

Measurements of the coefficient of thermal expansion in the range of room temperature to 1000°C were made on all specimens listed in Table 4.1. All specimens displayed the same thermal expansion characteristics, indicating that grain growth does not affect this property in the range studied.

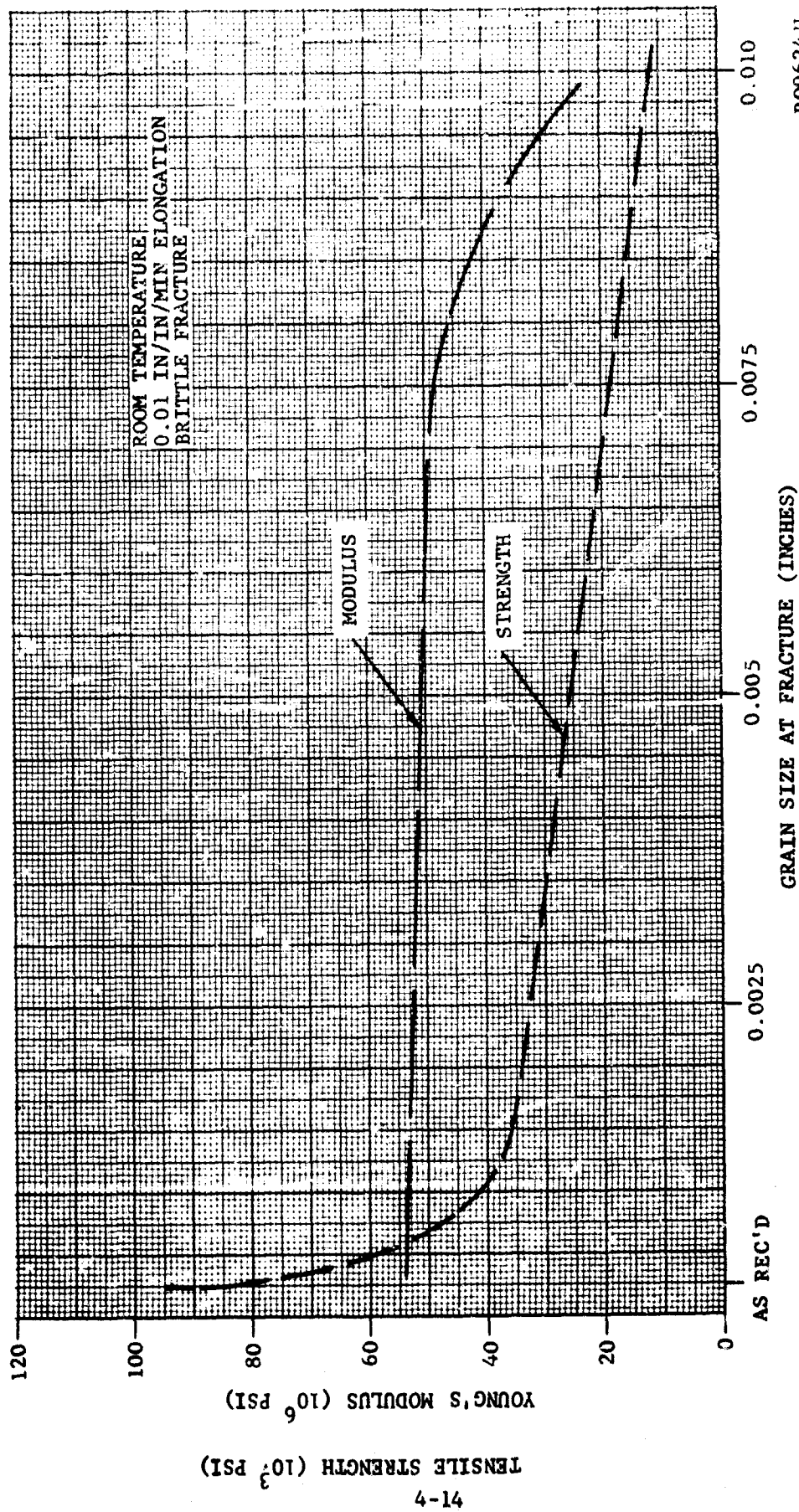


FIGURE 4-15. VARIATION OF YOUNG'S MODULUS AND TENSILE STRENGTH OF ARC CAST TUNGSTEN WITH GRAIN SIZE

The investigation of grain growth due to thermal cycling on the strength and modulus of tungsten was to be extended to the gas pressure bonded microsphere material of Allied Chemical Corporation. However, room temperature tests on the as-received material showed a tensile strength of 30,100 psi and a Young's modulus of 31.4×10^6 psi. These low values indicated that grain growth studies of this material would be rather pointless. One specimen held at 2500°C for 5 minutes displayed grain growth predominately within the particles as shown in Figure 4-16. This growth was not sufficient to make the hexagon-like structure typical of this material.

4.3 TUNGSTEN-CARBON REACTION STUDIES

The reaction between tungsten and carbon is of considerable interest because all materials which can be used as adjacent components of tungsten throat inserts are carbon based. If the interface temperature between the carbon and tungsten is higher than the melting point of the reaction product between carbon and tungsten, a liquid will be produced which may lead to alteration of contour, gas leakage, or even obtrusion of the insert. The reaction between tungsten and carbon results in the formation of W_2C and WC and takes place at relatively low temperatures. The literature shows a wide discrepancy in the minimum solidus temperature for the tungsten-carbon system. Temperatures range from a value of 2475°C reported by Hansen,^{4.16} a value of 2710°C reported by Rudy,^{4.17} to a temperature of 2732°C as reported by Nadler.^{4.18} This difference of some 250°C could be very important as the typical maximum backside tungsten-graphite interface temperature for many conditions is in this region.

There is very little agreement between the different investigators^{4.19, 4.20, 4.21} on diffusion of carbon into tungsten. Peterson^{4.22} has reviewed the data and concludes that the activation energy of carbon is probably of the order of 100,000 cal/mole. This would suggest a rather low rate of growth of a carbon bearing tungsten phase (assumed to be diffusion controlled) even at high as 2500°C. However, recent experimental observations, both at Philco^{4.23} and by Lally and Hiltz,^{4.24} suggest that a reaction between tungsten and carbon occurs rapidly as low as 1815°C. Lally and Hiltz state that there is a slow solid-state reaction at temperatures below 2500°C. Above this temperature, a liquid eutectic of W- W_2C is formed, and the rate of reaction becomes rapid. The liquid formed attacks in two directions, dissolving both the tungsten and the graphite.^{4.24} Observations at Philco, in general, confirm those of Lally and Hiltz.

The reaction between tungsten and carbon results in the formation of W_2C and WC and takes place at relatively low temperatures. In general, the commercial production of tungsten carbide is done at temperatures in the range of 1400-1700°C.^{4.25} The first eutectic between the tungsten-rich solid solution and the carbide W_2C is present at 1.5 percent carbon.

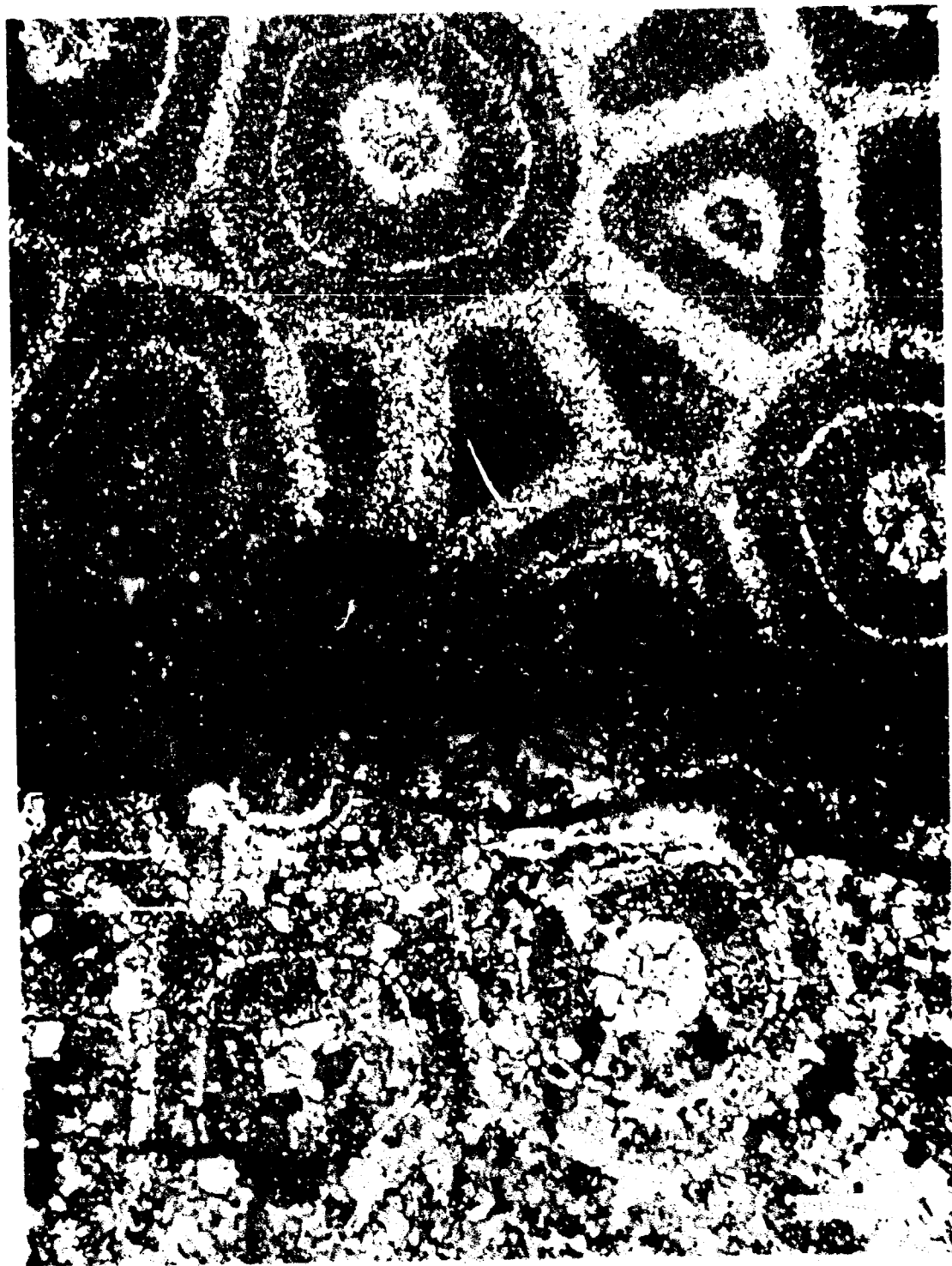


FIGURE 4-16. GRAIN GROWTH IN GAS PRESSURE BONDED TITANIUM.
ABOVE: AS RECEIVED. BELOW: AFTER HEATING AT 7500°C

The tungsten-carbon reaction studies were undertaken to determine the minimum temperature for these reactions between actual materials of interest for this restart program. The secondary objective was to investigate the effects of diffusion barriers.

The tungsten used for the experimental studies was obtained from Climax Molybdenum Company and contained by weight 0.003 percent carbon, 0.004 percent iron and less than 0.001 percent each of nickel and silicon. It was supplied in a sheet 1/8 inch thick. The source of carbon was ATJ graphite. These materials were considered typical of the types of materials which would be used in a nozzle. The samples were cut into specimens measuring 0.3 inch by 0.3 inch by 0.125 inch. They were arranged between blocks of ATJ graphite and placed in an induction coil where they were inductively heated using a 20 kw, 450 kc power supply.

The typical test was conducted as follows:

- (1) The faces of the tungsten sample were polished using 600 grit alumina paper.
- (2) The sample was placed between the ATJ blocks and set in the induction coil.
- (3) The chamber was evacuated to a pressure of 10^{-4} torr or lower.
- (4) The sample was heated to a temperature of approximately 1000°C and the pyrometer focused on the sample.
- (5) The sample was cooled to approximately room temperature.
- (6) The power was turned on to a predetermined level for the desired length of time.
- (7) The sample was allowed to cool to room temperature before removing from the chamber.

An attempt was made to duplicate the heating rates of the actual nozzle as much as possible. A typical time-temperature curve is shown in Figure 4-17. This heating rate is in the range of the rates experienced by actual inserts at the tungsten-graphite interface. The temperatures were measured with a continuously recording two-color optical pyrometer which had been calibrated against a N.B.S. tungsten filament and was adjusted to read the true temperature.

Some tests were conducted to determine the effectiveness of a material as a diffusion barrier. These materials, ThO_2 , ZrO_2 , and Ta, were in the

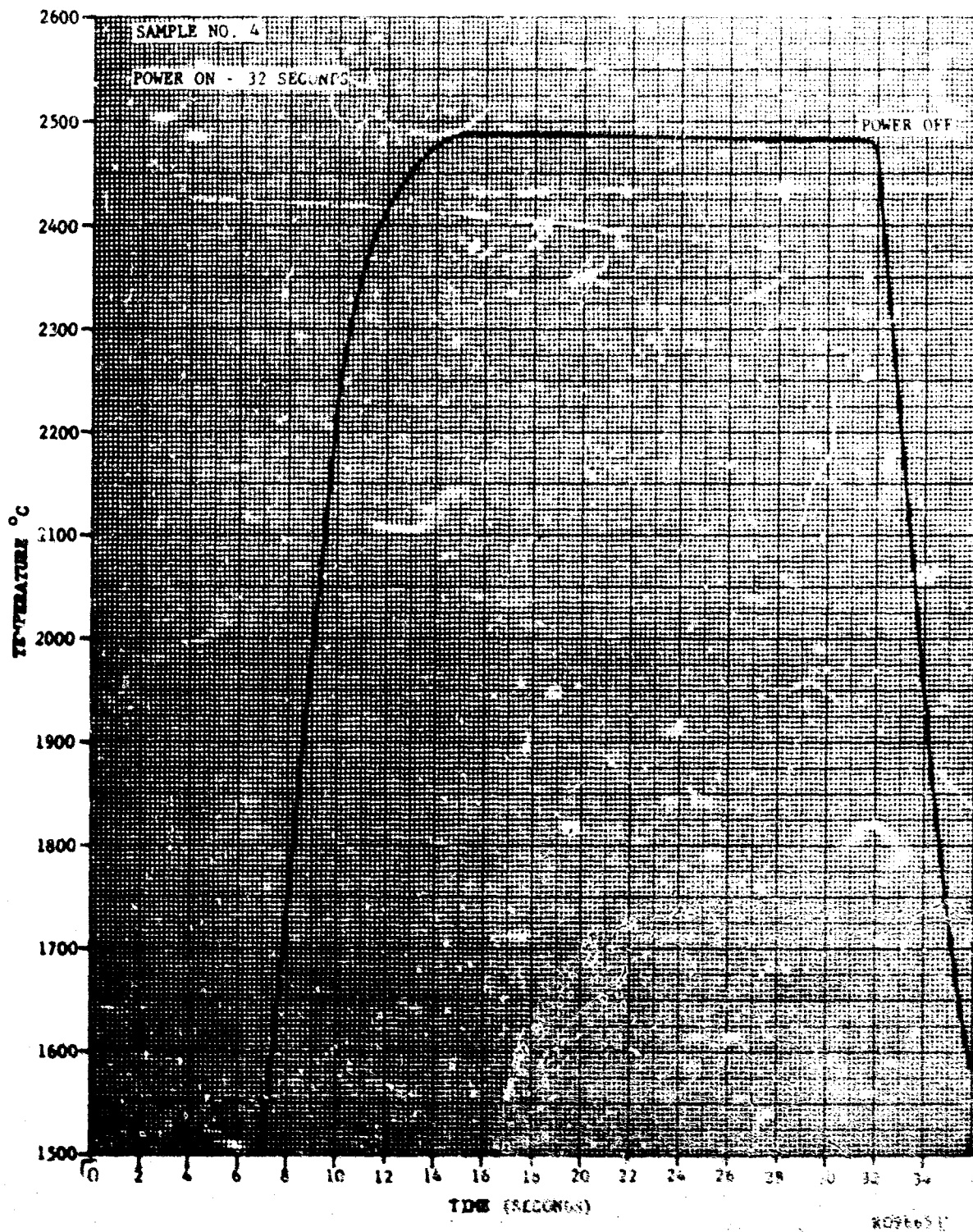


FIGURE 4-17. TYPICAL TIME-TEMPERATURE CURVE FOR TUNGSTEN-CARBON EXPERIMENTS

form of powders, -250 mesh size, and were reagent grade. The powders were sprinkled onto the surfaces of the ATJ and W and formed a diffusion barrier approximately 5 mils thick. One experiment was conducted using Ta foil as the diffusion barrier.

The results are listed in Table 4.2. Some specimens are shown after test in Figures 4-18 through 4-21. The results of these experiments indicate that above 2475°C (4500°F) incongruent melting occurs between tungsten and carbon. This melting results in the formation of WC and W₂C. Because of the presence of both of these compounds in the melted phase, the liquid phase must tend to form the stable compounds which have higher melting points. However, the solubility of carbon in the melt is high, and only a small amount of carbon is required to maintain a liquid. This condition would be very serious in a rocket nozzle where the interface temperature between the tungsten nozzle and the graphite backup is above the melting point of the eutectic composition. In this condition, the interface temperature is the lowest temperature in the tungsten. When the temperature of the interface becomes high enough for melting to occur, the reaction would be accelerated by the hotter unreacted tungsten. The composition of the melt would be continually changing, tending toward the formation of a higher melting composition. This condition could cause failure of the tungsten insert.

The use of a diffusion barrier appears to be promising. Generally, a higher melting material is more stable, and the diffusion of carbon through this material is much less. The initial tests were run at a temperature which was below the temperature where melting was observed between tungsten and carbon. The thickness of the carbide layer formed on the tungsten was decreased when diffusion barrier materials were used. The result of the Test No. 25 using thoria as the diffusion barrier where a liquid was formed at 2380°C may be misleading. This test was conducted in a vacuum and there is some indication^{4.26} that the thoria is not stable in a vacuum at these temperatures.

TABLE 4.2

SUMMARY OF TUNGSTEN CARBON EXPERIMENTS

Experiment No.	Time Power on (sec)	Atm	Temp (°C)	Carbide Layer Thickness (mil)	Remarks
4	32	Vac	2490	0.75-2	Sample was stuck to ATJ. Outer surface showed presence of liquid. See Figure 4-18.
5	35	Vac	2490	16	Sample stuck to graphite. Carbide layer showed liquid phase and appeared to be in 2 layers
6	300	Vac	2040	0.05	Sample not stuck to ATJ. Outer surface of W changed. See Figure 4-19.
11	300	1/2 Atm Ar	2410	17	Outer layer (W ₂ C) 10 mil. Inner layer (WC) 7 mil.
16	30	1/2 Atm Ar	2540	60	Sample deformed and slumped. Nearly all of original W was carbide. See Figure 4-20.
19	300	Vac	2410	17	Layer same as Experiment 11.
23	300	Vac	2410	0	W separated from ATJ by 1 mil Ta foil. Ta foil warped and made poor contact with W and ATJ.
24	300	Vac	2410	0	W separated from ATJ by 5 mil Ta powder. Ta powder sintered and reacted with carbon to form Ta ₂ C and small amount of TaC.
25	300	Vac	2380	1-5	W was separated from ATJ by ThO ₂ powder. Sample did not reach desired temperature of 2410°C because of arcing. X-ray diffraction showed liquid formed at interface to be W, W ₂ C, WC and an unknown cubic phase. See Figure 4-21.
26	300	Vac	2410	0	W separated from ATJ by ZrO ₂ powder. ZrO ₂ sintered and some reaction occurred at ZrO ₂ - C interface but none at ZrO ₂ - W interface.

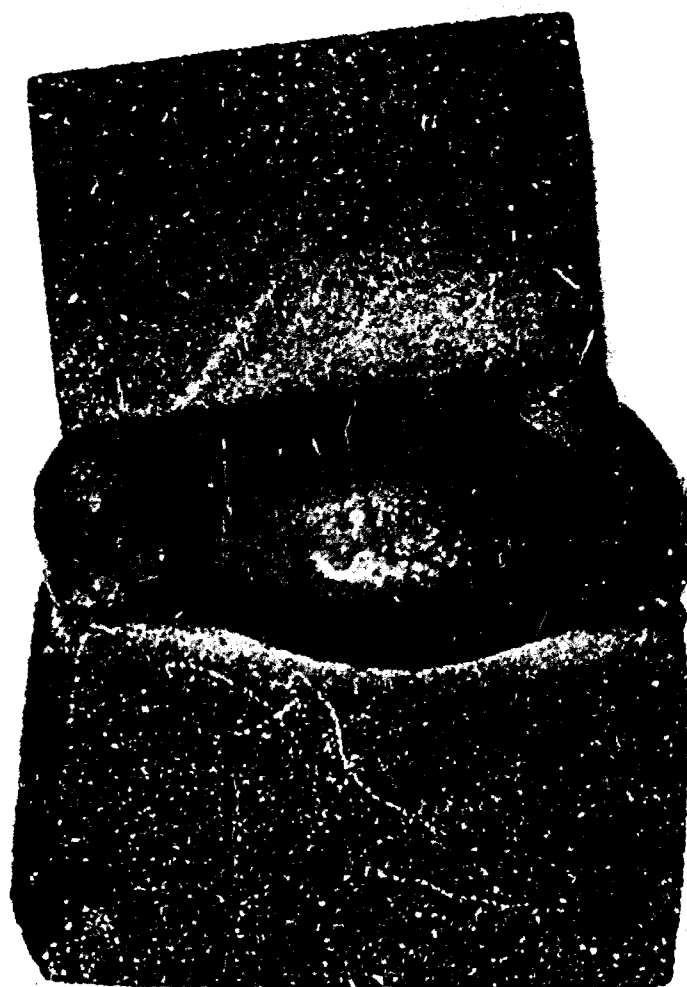


RO9658 U

FIGURE 4-18. TUNGSTEN-CARBON EXPERIMENT NO. 4 SHOWING MELTING AT THE INTERFACE.



FIGURE 9. TUNGSTEN-CARBON EXPERIMENT NO. 6 SHOWING SLIGHT SURFACE CHANGES.



RO9659 F

FIGURE 4-20. TUNGSTEN-CARBON EXPERIMENT NO. 16 SHOWING LIQUID PHASE FORMED AND DEFORMATION OF TUNGSTEN.

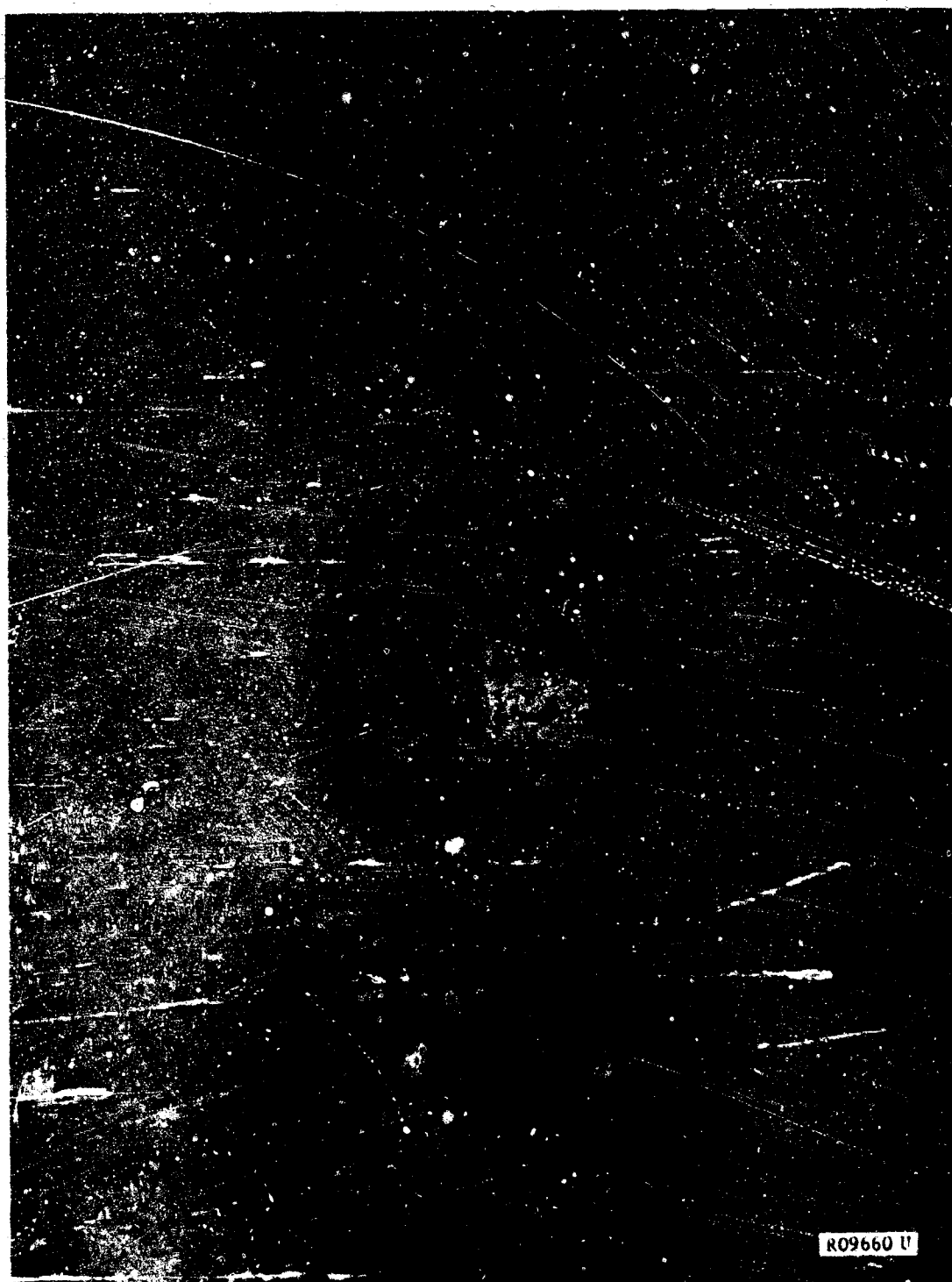


FIGURE 4-21. TUNGSTEN-CARBON EXPERIMENT NO. 25 SHOWING LIQUID PHASE WHICH OCCURRED WHEN USING ThO_2 AS A DIFFUSION BARRIER.

4.4 ALUMINA STUDIES

An excellent comprehensive discussion of the reactions between aluminum oxide and carbon has been presented by Foster, Lang, and Hunter.^{4.27} On graphites, the alumina deposit consists of an Al_4C_3 bonding layer at the graphite interface and an outer layer of a mixture of Al_2O_3 , Al_2OC , and $\text{Al}_4\text{O}_4\text{C}$. The Al_4C_3 layer is necessary in order for the deposit to stick. It is formed by the reaction between Al_2O_3 and C which gives off CO at high temperature. The mixture of alumina and the oxy-carbides may exist through the entire thickness of the deposit.

To verify this work, a brief experiment was conducted. Al_2O_3 , in the form of single crystal sapphire rod, was placed in a hole drilled in ATJ graphite. This sample was heated inductively in one-half atmosphere of N_2 to the melting point of the alumina. Initially, there was some gas evolution, probably CO. Thereafter, the melt came to equilibrium and formed a relatively low (20 to 30 degrees) contact angle indicating wetting of the graphite by the Al_2O_3 . After cooling, an interface of Al_4C_3 was observed between the graphite and the alumina. X-ray diffraction analysis of the melt showed it to contain Al_2O_3 , Al_2OC , and $\text{Al}_4\text{O}_4\text{C}$. This brief work confirmed the data reported by Foster, Lang, and Hunter and conclusively demonstrated the existence of a mechanism for alumina to wet and deposit on graphite.

The Al_4C_3 bonding layer is not stable in air since this compound hydrolyzes with the water vapor to give C_2H_2 and Al_2O_3 thereby destroying the interface which provides the bonding of the layer. In a vacuum, no water is available for hydrolysis. In addition, the oxy-carbides are stable in air but their stability in vacuum (space operation) injects a complicating factor which is not completely understood. Therefore, there are serious questions about the relative stability of the alumina layer in air and in vacuum. Alumina deposits which would become unbonded during cooldown in air and which would then be ejected on restart may remain bonded to graphite surfaces in space operation. Instead of being ejected on restart, these bonded layers may remain for several seconds until they can be melted and removed.

From thermochemical considerations, little or no chemical reactions between the condensed phase oxide Al_2O_3 and tungsten should be expected below 2760°C . This is substantiated by data from General Telephone and Electronics Laboratory^{4.28} which show no chemical interaction (no new compound phases) for tests performed at 3000°C for one minute. The Al_2O_3 did, however, wet and adhere to the tungsten. On the other hand, Lally and Hiltz^{4.24} noted that at temperatures below 2760°C , the liquid oxide rapidly attacks the tungsten setting up a eutectic system. Thus, disagreement exists regarding chemical reactions between Al_2O_3 and tungsten.

From the nozzle standpoint, the problem of condensed phase effects is not, however, a simple matter of measuring or following gross chemical reactions but is rather a matter of studying the effect of hardening due to movement or diffusion of extremely small quantities of the oxides or their decomposition products into the substrate metal. This is particularly important in the case of tungsten where the formation of fine oxide particles in the grain boundaries below the surface can cause a considerable decrease in tensile strength of the tungsten and thus alter its structural behavior. There are, of course, two possibilities: either the Al_2O_3 may penetrate into the interior and precipitate, or, what is more likely, oxygen resulting either from the sublimation-vaporization decomposition of the oxides or reactions of the oxides with the tungsten substrate may dissolve at the surface of the substrate and diffuse inward leading to variation in and degradation of physical properties.

As an experimental approach, high-purity Al_2O_3 was melted on a tungsten substrate at controlled temperatures and for controlled periods of time. By following microhardness and microstructure changes as a function of the two experimental variables, temperature and time, it was planned to gather quantitative data on the effect of oxygen penetration into the interior.

Briefly, the experimental procedure involved inductively heating a tungsten disk, 1 inch in diameter by 1/4 inch thick, containing high purity Al_2O_3 on the upper surface. This upper surface had previously been polished metallurgically and controlled hardness measurements had been taken. All tests were run at a total argon pressure of 200 psia for 300 seconds in a high pressure furnace assembly. The experimental temperature range studied was 2000 to 3000°C.

Initial experiments were conducted with fine grain, thoriated tungsten (Fansteel) because of its immediate availability. Although some minor surface hardness was detected at the higher temperatures, no clear-cut correlation developed between hardness and temperature or metallographic microstructure changes and temperature.

A similar series of experiments was made using tungsten fabricated at Philco Applied Research Laboratories by hot pressing Linde microspheres. Again, however, no clear-cut correlations between the experimental variables could be found.

On the basis of these experiments, the measurements of microhardness and microstructure changes were abandoned. The results of these experiments were negative in that they were inconclusive.

4.5 HIGH TEMPERATURE c-DIRECTION COMPRESSIVE DEFORMATION OF PYROLYTIC GRAPHITE

The purpose of this investigation was to determine the permanent c-direction deformation of pyrolytic graphite rapidly heated to very high temperatures and loaded in compression. No other data, such as mechanical or thermal properties, were sought or recorded. Only commercially available plate material was used in the experimental program.

It is well known that pyrolytic graphite undergoes a structural change at very high temperature which results in alterations of the dimensions of the material. In addition, the application of loads at high temperatures can result in very large deformations. Some of the most significant data on the change of dimensions of pyrolytic graphite at elevated temperature without load has been reported by Richardson and Zehms.^{4.29} Although their work showed that considerable deformation occurs with the application of temperature alone, the effects of loads were not considered. One item on the deformation under load has been reported from France.^{4.30} The primary concern in this instance was not the deformation but the ability to form a large single graphite crystal from pyrolytic graphite. Kotlensky^{4.31} has reported a 12 percent deformation in a specimen compressed in the c-direction with 5000 psi at 2800°C. However, the time involved was several tens of minutes. No data on these deformation characteristics associated with extremely high temperatures and very short times with load included as a parameter exist within the available literature.

The experimental apparatus consisted of a power source, vacuum jar, and a cluster of calibrated helical springs. The test setup is shown in Figure 4-22.

The test samples were nominal 1/2-inch cubes obtained from commercial 1/2-inch plates. It was felt that by using material from a single plate the influences of microstructural differences would be eliminated from the results. However, results from the planned series of tests indicated that additional data were highly desirable in order to broaden the spectrum of results. Additional testing was performed on samples obtained from a second plate of material.

The material used in the first series of tests was obtained from High Temperature Materials (Union Carbide). Although there was no information available relative to its processing parameters, it was considered to be typical fine grained, continuously nucleated pyrolytic graphite. The second plate was obtained from Super Temp Corporation. It was a disc from Polaris manufacture and conformed to the U.S. Navy specification. It was substrate nucleated and exhibited no oversized nodules. Samples from each manufacturer were tested in essentially different regimes so there were very little data to compare the two materials.

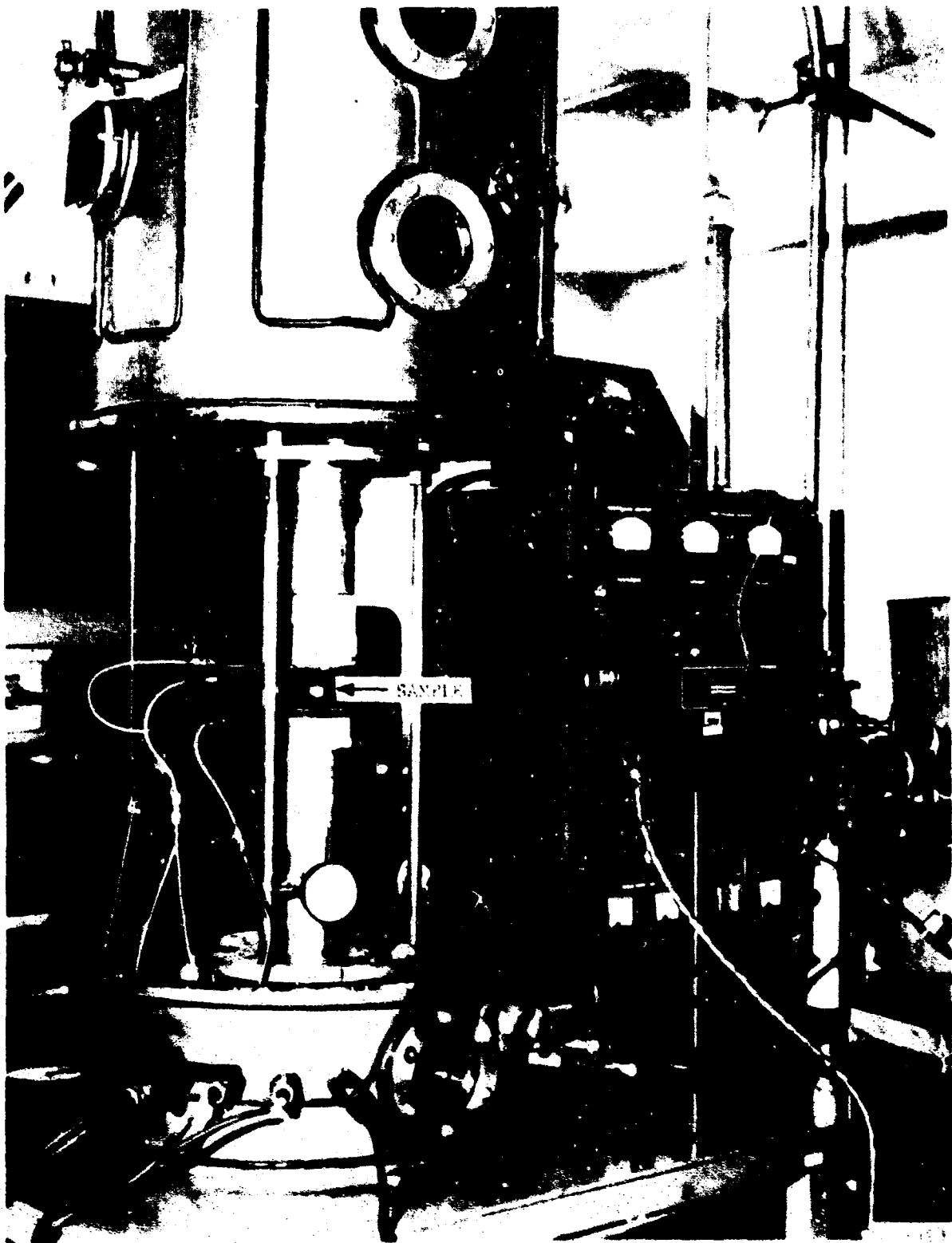


FIGURE 4-22. PYROLYTIC GRAPHITE COMPRESSIVE DEFORMATION APPARATUS

In both cases, the material was supplied with the a-b faces machined parallel. The plates were cut into nominal 1/2-inch cubes which were subsequently milled on the edge-grain faces to square up the sample. No further treatment, such as polishing, was given to any of the faces.

Samples were tested in a vacuum of 10^{-4} torr or lower and in approximately 1/2 atmosphere of argon. There was no discernible difference in the results when tested in vacuum or an inert atmosphere. Some of the high temperature ($>2700^{\circ}\text{C}$) tests run in a vacuum showed some slight loss of material but in no case was this loss greater than 0.005 weight percent.

The samples were resistively heated by a 40 volt 550 amp dc power supply through water-cooled electrodes. These electrodes were in direct contact with the a-b faces of the test samples.

Loading of the samples was effected with a cluster of calibrated helical springs. The spring constant of the cluster was 4700 lb/in. As the sample was heated, the springs were of course further compressed resulting in an increase of load. Deformation of the samples in turn relieved this increased load. The net result was that the true stresses are within 5 percent of the reported values.

The load was applied when the samples were at room temperature before the vacuum bell jar was closed and remained on the samples until the tests were completed. The samples were allowed to cool naturally to room temperature in the bell jar after the power was shut off. The samples cooled below red heat ($<500^{\circ}\text{C}$) in 30 seconds. The samples were probably at room temperature in less than 90 seconds as the copper electrodes were water cooled and at no time was there observed an appreciable increase in the water temperature.

Time was measured from the instant the sample reached test temperature. Figure 4-23 shows a typical temperature trace for a test. The samples reached temperature in approximately 12 seconds after the power was turned on. Average heating rates were approximately 210°C per second. Depending on the test temperature, there undoubtedly was some deformation which occurred during the latter portion of this initial heating.

Temperature was measured with a continuously recording two-color pyrometer which was calibrated against a NBS tungsten filament. The pyrometer was focused on one of the edge-grain faces through an optical flat which served as a window. The temperatures were compared to temperatures measured with a micro-optical pyrometer which was focused on the bottom of a hole drilled into the center of a specimen; the hole had a length to diameter ratio of 10. The temperatures compared to within $\pm 10^{\circ}\text{C}$ over the entire temperature range. This would be expected as the emissivity of pyrolytic graphite perpendicular to the c-axis is quite high.

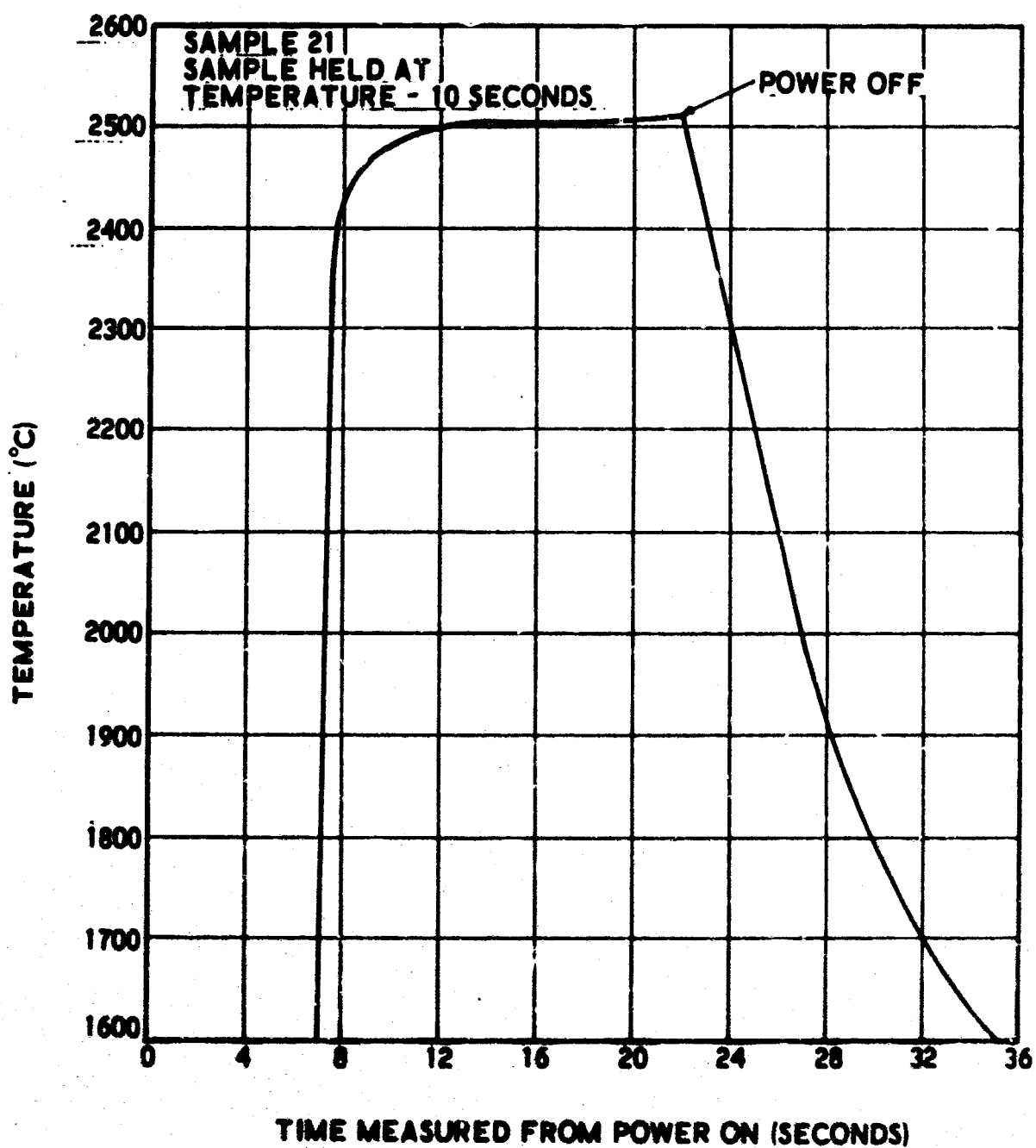


FIGURE 4-23. TYPICAL TEMPERATURE RESPONSE OF SPECIMENS

The dimensions were measured with a one-inch (0.0001) micrometer. In general the surfaces after a test were very nearly parallel. Each sample was measured at each corner, the center of each edge and the center after the test. The samples were measured in both the c-direction and the a-b directions.

The first determination made was the minimum temperature at which deformation would occur without load. This temperature was found to be 2600°C. In order to determine the threshold of permanent deformation with load, preliminary testing was conducted at a stress of 4200 psi, which is low relative to the range of stress of interest, while the specimen was held at temperature for 50 seconds. This testing was begun at a temperature of 2200°C. The threshold temperature on the plate obtained from HTM was found to be approximately 2300°C. The permanent deformation resulting from the above combination of stress and time was found to be 0.25 percent. This threshold temperature is 300°C lower than the minimum temperature for deformation to occur without load as found in this investigation and as reported by Richardson and Zehms.^{4.29} No effort was made to determine the minimum temperature at which deformation would occur when a sample was subjected to a load greater than 5000 psi or for times longer than 50 seconds.

The initial phase of the testing was concentrated within the range of 200°C above the threshold of permanent deformation. This was done in order to establish trends of the deformation with respect to time, load, and temperature and to determine the accumulative nature of deformation on specimens which were repeatedly tested. The results of this initial phase of testing are shown in Table 4.3. The percentage decreases for the accumulative tests are based on the original dimensions of the specimens before the first run. As would be expected, these results show that deformation increases with increasing time, temperature, and load.

The results of this phase of the testing are shown graphically in Figure 4-24 where time is used as the abscissa and in Figure 4-25 where temperature is the abscissa. Insufficient data were obtained to plot the data against stress. Each point plotted in Figure 4-25 represents one sample tested.

The second phase of testing involved higher temperatures and lower loads. These results are tabulated in Table 4.4. Extreme difficulty of applying the simple testing technique was encountered at the higher temperatures. Temperatures of 3000°C were attempted; however, no usable data were obtained above 2850°C and at this temperature only for low load. Rather large incremental increases in deformation were observed at the higher temperatures (above 2700°C). In 30 second's deformations of over 3-1/2 percent were obtained on specimens 36 and 40 with relatively low loads at the higher temperatures.

The results of this second phase are shown graphically in Figures 4-26 and 4-27 where deformation is plotted against time and temperature, respectively. Each point plotted represents one sample tested.

TABLE 4.3

PYROLYTIC GRAPHITE COMPRESSIVE DEFORMATION DATA PHASE 1 - HTM MATERIAL

Run No.	Stress (ksi)	Temp (°C)	Time at Temp (sec)	Initial c-Dimension (in)	Final c-Dimension (in)	Decrease (in)	Decrease (%)
14	13	2330	10	0.4648	0.4623	0.0027	0.58
19	13	2310	30	0.4647	0.4610	0.0037	0.80
15	13	2300	50	0.4649	0.4606	0.0043	0.92
11	13	2420	10	0.4649	0.4602	0.0047	1.01
20	13	2410	30	0.4649	0.4585	0.0064	1.38
16	13	2450	50	0.4649	0.4579	0.0070	1.51
21	13	2510	10	0.4648	0.4590	0.0058	1.25
23	13	2500	30	0.4650	0.4571	0.0079	1.69
22	13	2510	50	0.4648	0.4553	0.0095	2.04
21 2nd	13	2510	10		0.4565	0.0025	0.54
23 Run	13	2510	30		0.4540	0.0031	0.67
22	13	2520	50		0.4515	0.0038	0.82
21 3rd	13	2510	10		0.4520	0.0023	0.49
23 Run	13	2530	30		0.4515	0.0030	0.65
22	13	2530	50		0.4482	0.0035	0.75
17	20	2330	10	0.4650	0.4607	0.0043	0.92
25	20	2310	30	0.4650	0.4593	0.0057	1.22
18	20	2350	50	0.4649	0.4588	0.0061	1.31

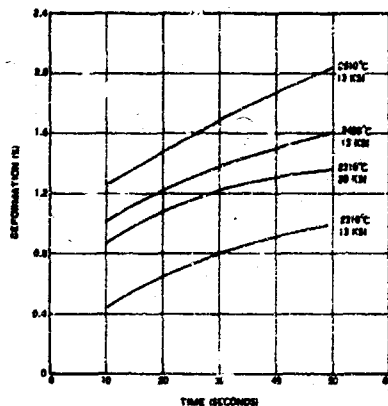
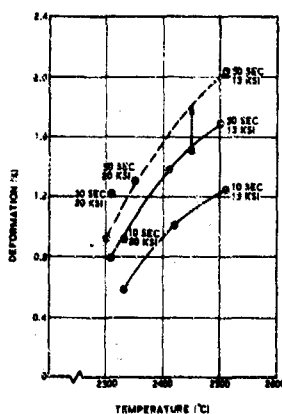


FIGURE 4-24. TIME DEPENDENCE OF DEFORMATION - PHASE 1
HTM MATERIAL



F03602 U

FIGURE 4-25. TEMPERATURE DEPENDENCE OF DEFORMATION - PHASE 1
HTM MATERIAL

TABLE 4.4

PYROLYTIC GRAPHITE COMPRESSIVE DEFORMATION DATA PHASE 2 - STC MATERIAL

Run No.	Stress (ksi)	Temp (°C)	Time at Temp (sec)	Initial c-Dimension (in)	Final c-Dimension (in)	Decrease (in)	Decrease (%)
31	13	2640	10	0.4520	0.4453	0.0067	1.48
30	13	2630	30	0.4519	0.4426	0.0093	2.06
32	13	2630	50	0.4519	0.4404	0.0115	2.54
39	11	2360	30	0.4520	0.4491	0.0029	0.64
38	11	2490	30	0.4525	0.4481	0.0044	0.97
37	11	2620	30	0.4520	0.4462	0.0058	1.28
35	11	2770	10	0.4517	0.4401	0.0116	2.57
36	11	2770	30	0.4517	0.4294	0.0223	4.94
42	7	2630	30	0.4524	0.4489	0.0035	0.77
41	7	2760	30	0.4523	0.4454	0.0069	1.53
40	7	2850	30	0.4520	0.4353	0.0167	3.69

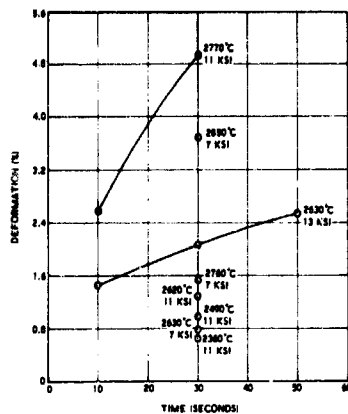
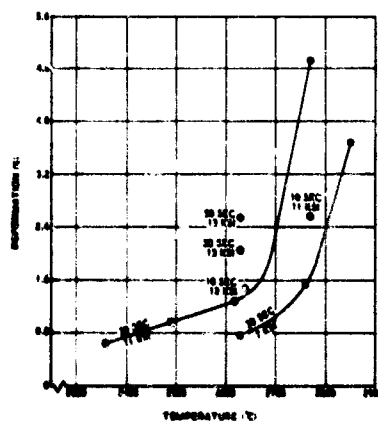


FIGURE 4-26. TIME DEPENDENCE OF DEFORMATION -
PHASE 2 STC MATERIAL



F03603 U

FIGURE 4-27. TEMPERATURE DEPENDENCE OF DEFORMATION -
PHASE 2 STC MATERIAL

Comparing data obtained from the two materials, to the extent that this can be done, leads to the observation that the STC material probably underwent a slightly lower deformation for a given set of test conditions than did that obtained from HTM. Caution should be exercised in attempting to combine data from the two phases of the testing since the two phases were conducted using materials obtained from different sources. The influences of microstructural differences of the two materials have not been assessed.

However, in order to obtain an indication of the relative influence of the three parameters time, temperature, and stress, the data from the two phases have been combined in order to develop surfaces in three space. These surfaces for constant temperature, time, and stress are shown in Figures 4-28, 4-29 and 4-30, respectively. The constant temperature surfaces shown in Figure 4-28 are the only ones that can be generated with the available data. Only traces in other surfaces could have been shown. The 2770°C surface has been generated with only three data points and cannot be considered to be precise. However, it is included for comparison with the 2310°C surface. The greater degree of steepness of the higher temperature surface is quite apparent.

Only one constant time surface is shown in Figure 4-29. This is the 30-second surface for which the most data exist. This surface shows very graphically the effect of temperature and stress upon the deformation, especially at the higher temperatures.

The majority of the test data was obtained at a stress of 13 ksi. This well defined surface is shown in Figure 4-30. Since the available data do not permit extension of this surface to the higher temperatures, traces of the 11 ksi and 7 ksi surfaces are shown. The marked increase in the effect of temperature at these stress levels is quite apparent. It appears that the 13 ksi surface extends only to the onset of greatly increased deformations.

Figure 4-31 shows percent deformation versus time for a series of samples which were retested. These samples were all tested at the same temperature (2520°C) and load (13,000 psi). The curve labeled first run is the deformation versus time for samples 21, 22, and 23. For the second run the samples were rerun under identical conditions as the first run (i.e., sample 21 was heated to 2520°C with a 13,000 psi load for 10 seconds, making a total of 20 seconds at temperature). The percent deformation for the second run is the percent change in c-axis length from the first to the second run. Likewise, the percent change for the third run is the percent change in c-axis length from the second to the third run. Figure 4-32 shows the same data replotted so that the deformation is accumulative (i.e. each data point is the change in length from the original) versus accumulative time (time sample was at temperature). The slope of the curve for the 10-second runs is much steeper than the slope for the longer runs. This would indicate that for a given length of time at temperature, if this

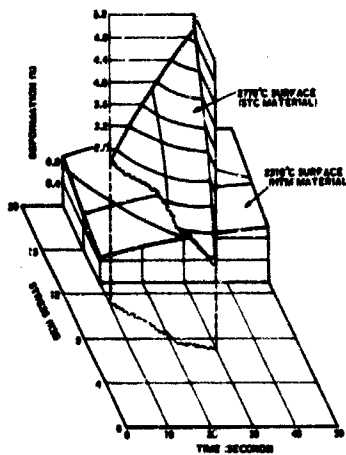


FIGURE 4-28. DEFORMATION SURFACE FOR CONSTANT TEMPERATURE

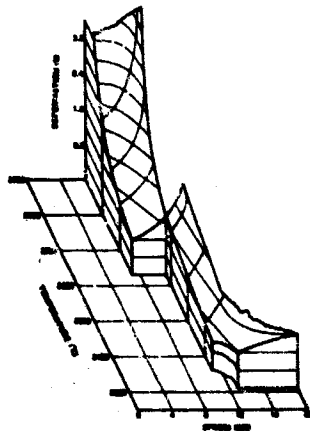
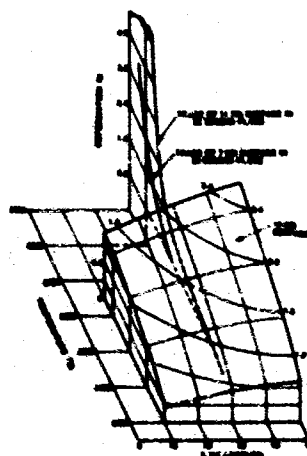


FIGURE 4-29. DEFORMATION SURFACE FOR CONSTANT TIME OF 30 SECONDS



P03604 U

FIGURE 4-30. CONSTANT STRESS SURFACE

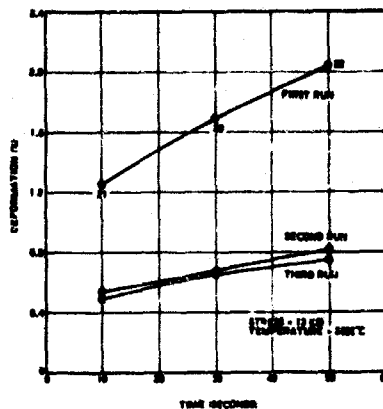
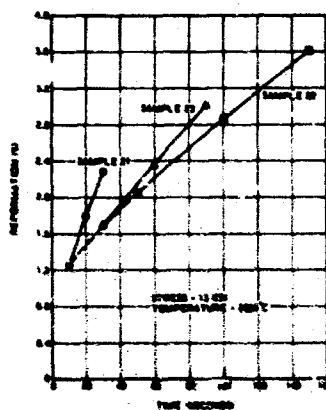


FIGURE 4-31. DEFORMATION VERSUS TIME FOR REPEATED LOADING



F03605 U

FIGURE 4-32. ACCUMULATIVE DEFORMATION VERSUS TIME FOR REPEATED LOADING

time were accumulated by a series of very short runs, the deformation would be much higher than if the time were achieved in a small number of long runs. This is an unexpected and, at present, an unexplained phenomenon which may be due to the experimental techniques.

Other samples besides those used for establishing the threshold temperature and those listed in Tables 4.3 and 4.4 were tested. One sample tested at 2770°C and 20 ksi fractured at a time of 23 seconds. Subsequent testing at this temperature was conducted at 11 ksi. A sample tested at 2850°C and 13 ksi fractured in 17 seconds. Only one data point, at 7 ksi, was obtained at this temperature. Another sample, tested at 3000°C and loaded to 13 ksi shattered in 5 seconds. As a consequence, no further testing was attempted at this extreme temperature.

Measurements of the deformed samples were made in the a and b directions as well as in the c-direction. These measurements indicated that the volume change of the samples in all cases were negligible. Both the a and b dimensions showed an increase for all samples.

All data obtained from samples which successfully completed their testing cycles have been reported.

The onset of large, rapid permanent deformation in pyrolytic graphite compressed in the c-direction appears to occur in the range of 2600-2700°C. The c-direction deformation increased rapidly above this temperature even when tested at stresses as low as 7 ksi. This is the same temperature range in which large plastic deformations occur when the material is tested in tension in the direction of the basal planes.^{4.10}

In order to determine whether the deformations recorded were partly due to structural transformation of the material, several samples were subjected to X-ray diffraction. Since this transformation is more likely to occur at the higher temperatures, only the phase 2 material was examined. The surfaces of three samples were studied. A sample of untested material (STC), sample 36 which experienced a 4.94 percent deformation at 2770°C, and sample 38 which underwent a 0.97 percent deformation at 2490°C were examined. All three samples displayed a unit cell c_0 dimension of 6.837 Å. This dimension is typical of as-deposited pyrolytic graphite and indicated that no measurable structural transformation occurred at the faces of the samples during testing.

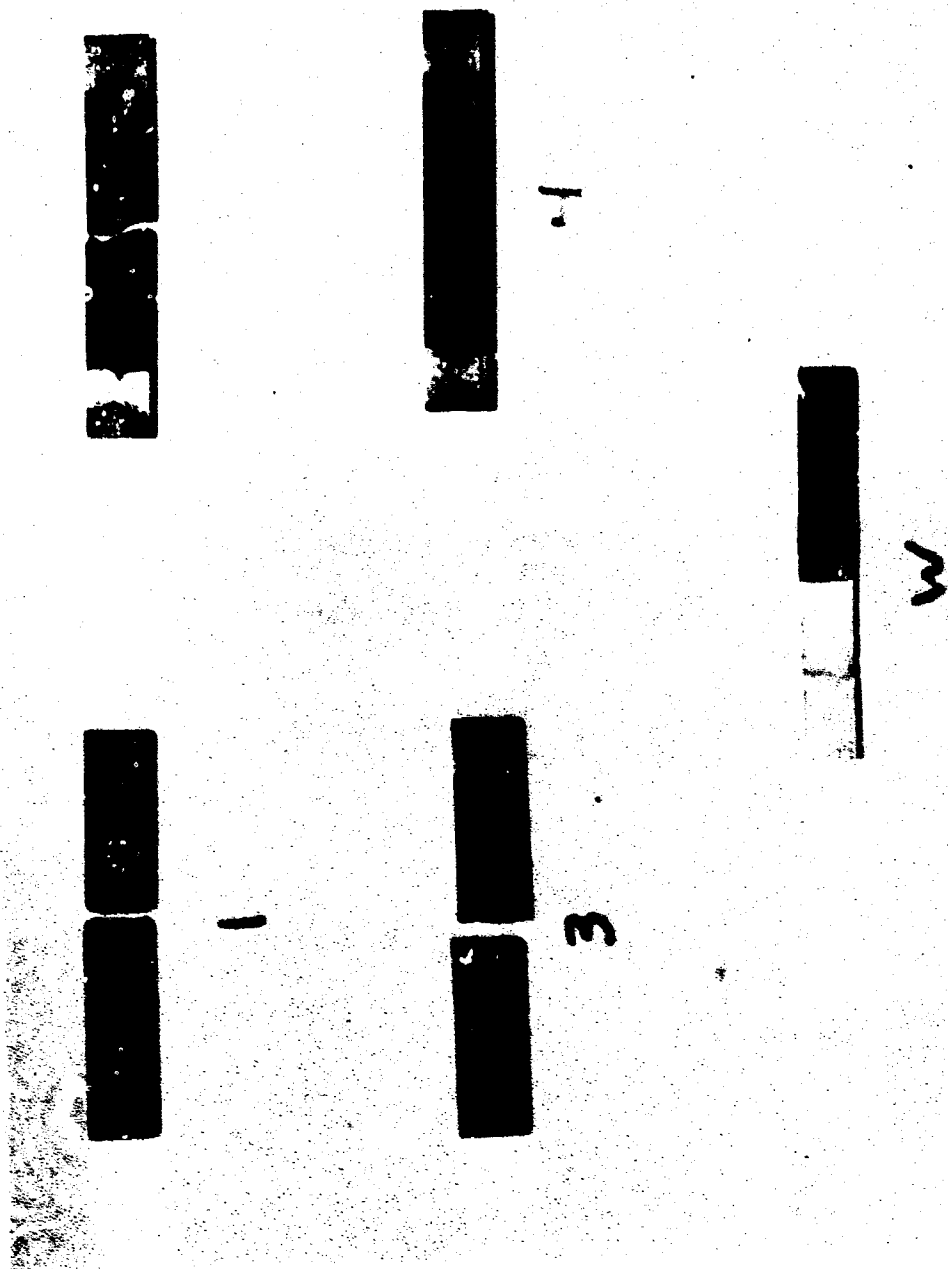
Samples 36 and 38 were split in halves and the interior material, which experienced the test temperature, was examined. Sample 38 showed a c_0 dimension of 6.832 Å which is only slightly different from the value for the as-deposited material. Sample 36, which experienced the greatest deformation at high temperature, showed an (004) doublet indicating varying values of the c_0 dimension and thus varying degrees of structural transformation. The two measured values of c_0 are 6.768 and 6.716 Å. The latter value is representative of a highly transformed material.

Since the heated samples were in contact with the water-cooled electrodes, the contact surfaces were cooler than the interior of the material. This probably accounts for the absence of transformation at the faces of the samples. During the observation of the samples with the disappearing filament pyrometer, it was found that the sample had a constant temperature zone over 90 percent of the thickness. Approximately 5 percent of the sample at each end was at a much lower temperature. No attempt has been made to determine the true nature of any distribution of temperature in the test samples. The temperatures reported are those measured at the center of the visible face of the samples.

4.6 THERMAL FATIGUE TESTS

To obtain a first look at thermal fatigue of the candidate materials, some preliminary testing was undertaken. The tungsten used was in the form of a 3 inch by 0.4 inch by 0.125 inch bar obtained from Climax Molybdenum Company. The material was supplied in the form of a 1/8 inch sheet and was the same material used in other material experiments. The graphite used was ATJ in the form of 1/4 inch by 1/2 inch by 3 inch bars. The samples were heated in a vacuum bell jar which could be back-filled with argon. The power supply was a 4000 amp, 10 volt ac source. The samples were clamped onto water cooled copper electrodes. The clamp consisted of a copper plate, 1/8 inch thick, which was held in place by four screws. This copper plate was not directly cooled, but a copper spacer, the same thickness as the sample, was put behind the sample to provide a better conduction path to the cooled electrode. The power was applied to the sample by adjusting a variable transformer to a preset power level and the full preset power left on for 30 seconds. The variable transformer was then adjusted to zero. The samples reached temperature in approximately 12 seconds. After power shut off, a temperature below 400°C was achieved in 30 seconds by the graphite and in 15 seconds by the tungsten. The tungsten was allowed to cool for a total of 45 seconds and the temperature reached approximately 150-200°C. The graphite samples were allowed to cool for 90 seconds. The temperature was measured with a continuously recording 2-color pyrometer which had been calibrated to read true temperature. The samples are shown after testing in Figure 4-33. The results are tabulated in Table 4.5.

After testing, while still clamped onto the water cooled electrodes, Sample 1 displayed a gap of about 0.015 inch. However, upon removal from the electrodes, the specimen showed no net change in length. This would indicate that the specimen had not been tightly clamped and some slippage had occurred, at least on the first heating. Samples 2 and 3 suffered gross loss of material from sublimation in the regions of their fractures. Thus they broke in regions of very porous, weak material.



R09916 U

FIGURE 4-33. THERMAL FATIGUE SAMPLES AFTER TEST

TABLE 4.5

PRELIMINARY THERMAL FATIGUE TEST DATA

<u>Sample No.</u>	<u>Material</u>	<u>ATM</u>	<u>Maximum Temperature</u>	<u>Result</u>
1	ATJ Graphite	Vacuum 10^{-5} Torr	2500°C	Sample broke after 90th heat.
2	ATJ Graphite	Vacuum 10^{-5} Torr	3100°C	Sample broke during 2nd heating.
3	ATJ Graphite	10"Ar	3150°C	Sample broke during 14th heating.
4	ATJ Graphite	20"Ar	2900°C	Sample cycled 100 times without failure.
W	W	Vacuum 10^{-5} Torr	2600°C	Sample cycled 100 times without failure. No indication of cracking.

It would be difficult to estimate the exact degree of constraint afforded by the electrodes; however, Sample W did suffer plastic deformation during test as evidenced by a slight out-of-plane joggle caused by a slight misalignment of the holding fixture.

This preliminary testing was to be used to indicate whether thermal fatigue was definitely a problem. However, no such clear results came from these tests. Had the specimens cracked after a few cycles, it could be concluded that thermal fatigue was potentially a serious problem. With the results obtained, no such conclusion can be reached without further study.

REFERENCES

- 4.1 "Properties of High Purity Tungsten," Technical Information Bulletin, General Chemical Division, Allied Chemical Corporation, Morristown, N. J.
- 4.2 "Allied Chemical Tungsten," General Chemical Division, Allied Chemical Corporation, Morristown, N. J., June 1965.
- 4.3 Maykuth, D. J., Ratliff, J. L. and Ogden, H. R., "A Metallurgical Evaluation of a New Tungsten Product," AIAA Fifth Annual Structures and Materials Conference, Palm Springs, California, April 1-3, 1964.
- 4.4 The Engineering Properties of Tungsten and Tungsten Alloys, DMIC Report 191, September 27, 1963.
- 4.5 Nozzle and Insulation Materials for A-3, Polaris Materials Manual, Volume I, Lockheed Missiles and Space Company, December 1962.
- 4.6 Mechanical Properties of Wrought Tungsten, Report No. ASD-TDR-63-585, Volumes I and II, November 1963.
- 4.7 Kirchner, W. R., "Development of Advanced Polaris First Stage Propulsion System," Bulletin of the 18th Meeting JANAF-ARPA-NASA Solid Propellant Group, Volume I, June 1962, pp. 1-27.(C)
- 4.8 Research on Physical and Chemical Principles Affecting High Temperature Materials for Rocket Nozzles, Quarterly Progress Report, Union Carbide Research Institute, ARPA Order No. 34-63, Task 4, Contract No. DA-30-069-ORD-2787, September 30, 1964.
- 4.9 Dull, R. B., Physical Properties of Some Newly Developed Graphite Grades, Volume XXVI of WADD TR 61-72, Research and Development on Advanced Graphite Materials, May 1964.
- 4.10 Pyrolytic Graphite Final Report, Volume I, Chapter 4, LMSC-801376, 1 June 1962.(C)

- 4.11 Gobble, L. P. and Salmen, W. J., "Compressive Properties of Pyrolytic Graphite from Room Temperature to 5000°F," Symposium on Materials for Aircraft, Missiles, and Space Vehicles, ASTM STP No. 345, 1963, pp. 119-128.
- 4.12 Gebhardt, J. J. and Berry, J. M., "Mechanical Properties of Pyrolytic Graphite," AIAA Journal, Volume 3, No. 2, February 1965, pp. 302-308.
- 4.13 Mechanical Properties of Pyrolytic Graphite, Final Report No. DIN: 024-Final, Contract NOW 61-0481-C-(FEM), December 1964.(C)
- 4.14 Pappis, J. and Blum, S. L., "Properties of Pyrolytic Graphite," J. Amer. Cer. Soc., Volume 44, No. 12, December 1961, pp. 592-597.
- 4.15 Klopp, W. O., Witzke, W. R., and Raffo, P. L., Presentation at the AIME Symposium on High Temperature Refractory Metals, New York, February 17-20, 1964. See also Klopp, W. D. and Raffo, P. L., Effects of Purity and Structure on Recrystallization, Grain Growth, Ductility, Tensile, and Creep Properties of Arc-Melted Tungsten, NASA TN D-2503, November 1964.
- 4.15 Hansen, M., Constitution of Binary Alloys, McGraw-Hill Book Co., New York, New York, 1958.
- 4.17 Rudy, E., Investigation of Phase Equilibrium Relations in Ternary and Higher Order Systems of Transition Metals, Second Progress Report, Aerojet-General Corporation, Sacramento, California, 1964.
- 4.18 Nadler, M. R. and Kempter, C. F., "Some Solidus Temperatures in Several Metal-Carbon Systems," J. Phy. Chem., 64, 1471, 1960.
- 4.19 Pirani, M. and Sandor, J., J. Inst. Metals, 73, 385 (1947).
- 4.20 Klein, R., J. Chem. Phys., 22, 1406 (1954).
- 4.21 Zioikker, C., Physcia, 7, 189 (1927).
- 4.22 Peterson, N. L., Diffusion in Refractory Metals, WADD Technical Report 60-793, March 1961.
- 4.23 Unpublished work, Hall, J., Philco Research Laboratories, June 1964.

- 4.24 Lally, F. J. and Hiltz, R. H., J. of Metals, June 1962, p. 424-428.
- 4.25 Schwarzkopf, P. and Kieffer, R., Refractory Hard Metals, The MacMillan Company, New York, N. Y., 1953.
- 4.26 Tinklepaugh, J. R. and Crandall, W. B., Cermets, Reinhold Publishing Company, New York, N. Y., 1953, p. 161.
- 4.27 Foster, L. M., Lang, G. and Hunter, M. S., "Reactions Between Aluminum Oxide and Carbon," J. Amer. Ceram. Soc., Volume 39, No. 1, January 1, 1956, pp. 1-11.
- 4.28 Experimental Study of Factors Controlling the Effectiveness of High-Temperature Protective Coatings for Tungsten, Fifth Progress Report Contract AF 33(657)-8787, November 1, 1963 - March 1, 1963, General Telephone and Electronics Laboratories, Inc., Bayside Laboratories, Bayside, N. Y.
- 4.29 Richardson, J. H. and Zehms, E. H., Structural Changes in Pyrolytic Graphite at Elevated Temperatures, Report No. SSD-TDR-63-340, December 1, 1963.
- 4.30 Gremion, R. and Maire, J., "Modification of the Structure of Pyrolytic Graphite by Compression at High Temperature Evolution of a Single Crystal," presented at the Sixth Biennial Conference of Carbon, University of Pittsburgh, June 17-21, 1963.
- 4.31 Kotlensky, W. V., "Materials Research-Graphite," JPL Space Program Summary 37-25, Volume IV, February 29, 1964.

CONFIDENTIAL

SECTION 5

ROCKET MOTOR TESTS

Fourteen nozzles with 5/8-inch diameter throats were tested at nominal conditions of 700 psia chamber pressure and 325 pounds thrust. The purposes of these tests were (1) to evaluate design concepts, (2) to provide a comparison of material performances in the various nozzle sections, (3) to establish a range of restart capabilities for the primary nozzle materials, and (4) to corroborate analysis where applicable. The rocket motor tests were conducted on the Aeronutronic Solid Propellant Simulator at the Newport Beach facility. All tests utilized a simulation of CYI-75, an aluminized solid propellant with a combustion temperature of 6175°F. Duty cycles were varied for each test to provide the maximum amount of useful information over the spectra of materials and design concepts that were investigated. A summary of these rocket motor tests, including the materials investigated, duty cycles employed, test conditions, throat performances, and conclusions, is presented in Table 5.1. For nozzle sketches and post test photographs see References 5.1 and 5.2.

As a result of this phase of the test effort, certain conclusions applicable to restartable nozzles can be reached concerning material applicability, duty cycle limitations, and problem areas that require additional investigation. To facilitate the presentation of these conclusions and observations, each of the four basic sections of the nozzle (i.e., the throat, the entrance or aft closure, the exit cone, and the backup structure or insulation) is treated as an entity. It must be remembered that interdependency among these sections exists in practice and is the final determinant of overall nozzle performance.

CONFIDENTIAL

CONFIDENTIAL

TABLE 5.1
RESTART ROCKET MOTOR TESTS - SUMMARY

Test No.	Materials			Insulation	Pulse Cycle	P _c (lb)	Thrust Performance				Remarks
	Thrust	Entrance	Exit				AD _c (in.)	ΔP _c (%)	ΔP _c (psi)	$\frac{dP}{dt}$ (psi/sec)	
1	ATJ Graphite	ATJ Graphite	ATJ Graphite	Asbestos Phen. (FN 5062) High Silica Phen. (FN 5067) Cool to Amb	On - 16 sec 676 Cool to Amb	316 302	0.0351 0.0470	5.6 7.1	11.3 14.8	1.1 1.5	High erosion rate of ATJ throat of this size prohibits use except for a small number of short pulses.
2	Graphitite 'GK'	ATJ Graphite	ATJ Graphite	Asbestos Furfuryl Same as 1 above	On - 17 sec 702	303	0.0108	1.7	3.7	0.32	Spallation of 'GK' noted. Asbestos furfuryl and carbon cloth laminate eliminated as insulator candidate on basis of poor performance.
3	Pyrolytic Graphite (As deposited) Plate C ₀ = 6.84 Å	ATJ Graphite	ATJ Graphite	Asbestos Phen. (RFD 150) High Silica Phen. (FN 5067) Cool to Amb	On - 16 sec 740 Cool to Amb On - 16 sec 732 Cool to Amb On - 16 sec 776 Cool to Amb On - 31 sec 723	302 287 273 306	0 0 0 0.0030	0 0 0 0.48	0 0 0 0.95	0 0 0 0.05	Performance of conical ATJ entrance is poor under these conditions. Asbestos phenolic evaluated as best insulator of those tested. Little difference between FN 5062 and RFD 150.
4	Pyrolytic Graphite (Heat Treated) Plate C ₀ = 6.74 Å	ATJ Graphite	ATJ Graphite	Asbestos Phen. (FN 5062) Cool to Amb	On - 31 sec 749 Cool to Amb On - 60 sec 732 Cool to Amb On - 31 sec 634	301 316 304	0 0.041 0	0 6.6 0	0 13.6 0	0 0.34 0	Pulse length limited to less than 60 seconds for PG of this configuration. Conical ATJ entrance performance is at best marginal at this total time.
5	Pyrolytic Graphite (As deposited) Shell C ₀ = 6.84 Å	ATJ Graphite	ATJ Graphite	Asbestos Phen. (FN 5062) Cool to Amb	On - 16 sec 683	324	0.024	3.9	7.9	0.75	PG shell type throat performance is unsatisfactory
6	Pyrolytic Graphite (Annealed) Plate C ₀ = 6.71 Å	ATJ Graphite	ATJ Graphite	Asbestos Phen. (FN 5062) Cool to Amb	On - 31 sec 714 Cool to Amb On - 60 sec 758	305 316	-0.0005 0.078	-0.08 12.4	-0.2 26.2	~ 0.65	Conical ATJ entrance marginal. Confirmation of insulator performance predictions. Confirmation of PG plate pul- ^{se} limit of less than 60 seconds.

CONFIDENTIAL

CONFIDENTIAL

TABLE 5.1 (Continued)

Test No.	Throat	Entrance	Wall	Insulation	P _c (psia)	Throat Performance				Remarks	
						ΔP _t (in.)	ΔA _t (%)	ΔA _c (%)	$\frac{dA_c}{dt}$ (in./sec)		
7	Throat: 110 mil Arc-Cut (110 mil Arc-Cut)	ATJ Graphite Plus 2 PG Nubbers	ATJ Graphite	Cork filled Asbestos Phen. (13 MP)	On - 26 sec Cool to Amb	716 308	-0.02	-3.1	-6.2	-0.38	Observed throat on third cycle gross gas leakage behind throat. Pressure unit erosion. Addition of PG Nubbers improves entrance performance.
					On - 36 sec Cool to Amb	714 302	-0.01	-7.1	-3.5	-0.15	
					On - 24-1/2 sec	696 293	-	-	-	-	
8	Throat: 100 mil Arc-Cut (100 mil Arc-Cut)	ATJ Graphite Plus 2 PG Nubbers	ATJ Graphite	Asbestos Phen. (FM 5062)	On - 61 sec Cool to Amb	704 306	-0.001 to -0.010	-0.16 to -1.6	-0.32 to -3.2	0.00 to 0.08	Entrance unsatisfactory at this total firing time even with PG Nubbers. Initial erosion and gas leakage behind throat. Erosion cracked during second cycle.
					On - 61 sec Cool to Amb	693 290	0 to 0	0 to 0	0 to 0	0 to 0	
					On - 56 sec	654 293	-0.006 to -0.04	-0.94 to -6.5	-2.0 to -12.5	-0.05 to -0.36	Improved entrance is reflected in improved throat performance on initial cycle as compared to test No. 6. Entrance performance still unsatisfactory at this duty cycle level.
					On - 34 sec Equilibrate	712 278					ATJ blown through throat from entrance section on last cycle. Insulator characteristic and critical predictions completed.
					On - 20 sec Equilibrate	591 284	0.190	11.5	72.5	1.57	Graphite 'G' with upstream 'G' shows some improvement over ATJ/J-P-C. Entrance and is reflected in J-P-C. and throat performance. Entrance still marginal at this increased total firing time. Insulation is marginal at this total firing duration.
					On - 9 sec	463 282					
10	Pyrolytic Graphite (As deposited) Plate C ₀ = 0.845 Å	Graphite 'G' Plus 2 PG Nubbers	ATJ Graphite	High Silica Phen. (FM 5067)	On - 58 sec Cool to Amb	722 302	-0.014	-2.8	-5.6	-0.15	
					On - 28 sec Equilibrate	681 279					
					On - 36 sec Equilibrate	620 267	0.223	36.0	25.0	0.98	
					On - 21 sec Equilibrate	517 282					
					On - 28 sec	424 273					
11	Pyrolytic Graphite (As deposited) Plate C ₀ = 0.839 Å	ATJ Graphite Plus 2 PG Nubbers	ATJ Graphite	Asb. Phen. (FM 5062)	On - 58 sec Cool to Amb	735 304	0.03	4.84	9.8	0.26	Entrance performance satisfactory. Gas generator blew through nozzle at end of first cycle and chamber liner failure at end of last cycle obscure erosion results to some extent.
					On - 39 sec Equilibrate	638 303					
					On - 24 sec Equilibrate	546 296	0.156	24.0	53.7	0.91	
					On - 23 sec	470 288					

CONFIDENTIAL

CONFIDENTIAL

TABLE 5.1 (Continued)

Test No.	Materials				P _e	P	Thrust Performance				Remarks
	Thrust (lb)	Carbon Cloth Phenolic Plus 2 PC Washers	Ball Graphitic "G"	Insulation Low Resin Silica Phenolic (PM 5019-25)			ΔP (in.)	ΔA (in.)	ΔA (in.)	ΔA (in.)	
12	Friction (100 mil Gas Press. Standard)				712	315	-0.020 to -0.025	-3.2 to -4.0	-6.2 to -7.9	-0.2 to -0.25	Overall entrance performance improved with carbon cloth phenolic over polycrystalline graphite entrance (slightly higher erosion, but vast structural improvement). No gas leakage behind press fit throat insert. Little or no exit erosion. Gross alumina deposition on throat after 5-1/2 second cycle.
					642	268	0 to -0.016	0 to -2.55	0 to -3.25	0 to -1.45	
13	Toughness	Graphite Cloth Phenolic Plus 2 PC Washers	Graphitic "G"	Asbestos Phen (PM 5062)	696	294	-0.003 to -0.008	-0.4 to -1.2	-0.88 to -2.5	-0.00 to -1.5	Entrance performance is definitely superior to graphite entrance, and slightly improved over carbon cloth due to a slightly lower erosion rate of graphite cloth. Slight gas leakage behind pressed fit insert. Little exit erosion. Insert cracked on first application of thermal load but did not affect performance.
					699	308	0	0	0	0	
					694	312	0	0	0	0	
14	Pyrolytic Graphite (As deposited) Plate C _g = 6.844 g	Graphite Cloth Phenolic Plus 2 PC Washers	ATJ Graphite	Asbestos Phen (PM 5062)	639	263	-0.009	-1.4	-2.8	-0.14	Performance of graphite cloth phenolic substantiated. Erosion results substantiate analysis in that several short pulses with short coast times are equivalent to one long pulse where the sum of the short pulse firing times equals the firing duration of the long single pulse. Confirmation of 60 sec limit for 90 without cooling.
					591	251	0.034	3.85	7.85	0.18	

CONFIDENTIAL

CONFIDENTIAL

5.1 NOZZLE THROAT SECTIONS

The basic throat materials and material subgroupings that were considered for restart nozzle application are depicted in Figure 5-1. It should be mentioned that ablative plastics, carbides, nitrides, borides, oxides, etc., were not considered as candidates for restartable rocket nozzle throat materials based on experience and prior results.

The rocket motor tests showed that polycrystalline graphites should be eliminated from further consideration in this program. Assuming a 5 percent area enlargement limit, ATJ graphite as a throat material is limited to short pulses of six seconds or less, with adequate cooldown between pulses, and a maximum of eight to ten restarts based on the erosion results gathered with these tests. The use of a higher density polycrystalline graphite such as Graphitite GK extends these limits slightly but not significantly. For most missions and envisioned future mission requirements, this limitation is prohibitively restrictive. That is not to say that the use of polycrystalline graphites as throat materials, along with the ablative plastics, must be rejected for use in the very large rocket nozzles, but an experimental treatment of this problem is beyond the scope of this investigation.

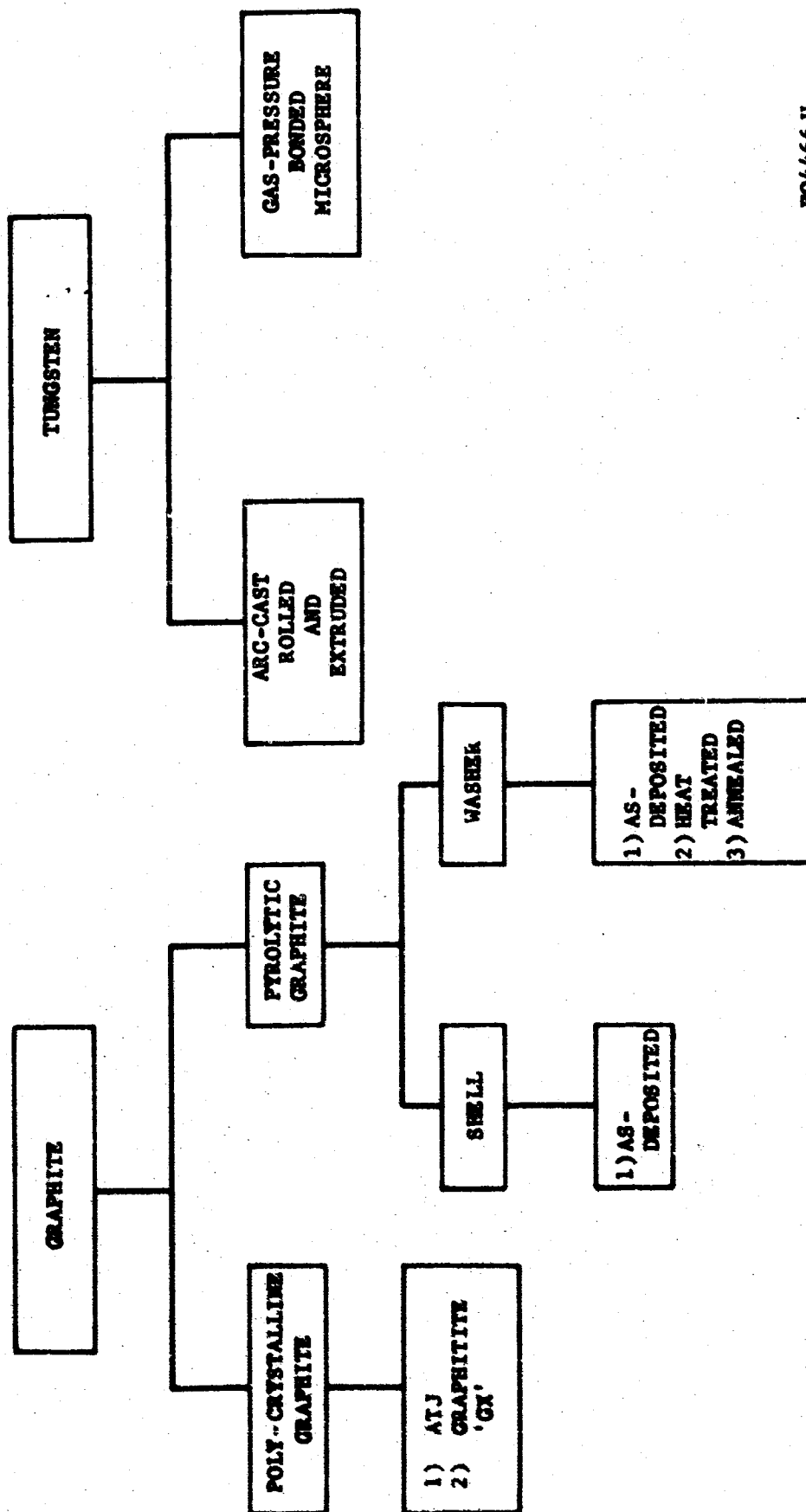
By the same token, present state-of-the-art fabrication inadequacies of the shell configuration, or a-b plane deposited form of pyrolytic graphite, preclude its use in a restart application. Although this method of utilizing pyrolytic graphite shows some merit in theory, its actual performance is unreliable.

Thus, in effect, pyrolytic graphite throats of the stacked edge grained washer configuration, and tungsten become the primary candidates for restartable nozzle throat materials.

The use of edge grained pyrolytic graphite throats is primarily a function of chemical corrosion.

Firing times without an adequate cooldown period are limited to 50 to 60 seconds (for the throat diameter and radial thicknesses used in these tests) and are independent of pulse length or number of pulses (i.e., 10-5 second pulses with short down times may be treated as a single 50 second firing). Duty cycle limits for pyrolytic graphite nozzles of the configuration used in these rocket motor tests have been established in terms of number of cycles versus firing time/cycle for the minimum and maximum delay times. These limits are shown in Figure 5-2. The curves are grouped with the analogous curves for the development and demonstration test phases to facilitate scaling comparisons. Indications are that annealing or partial annealing of pyrolytic graphite can extend the total allowable firing duration to a degree. The use of a maximum pulse length before adequate

CONFIDENTIAL



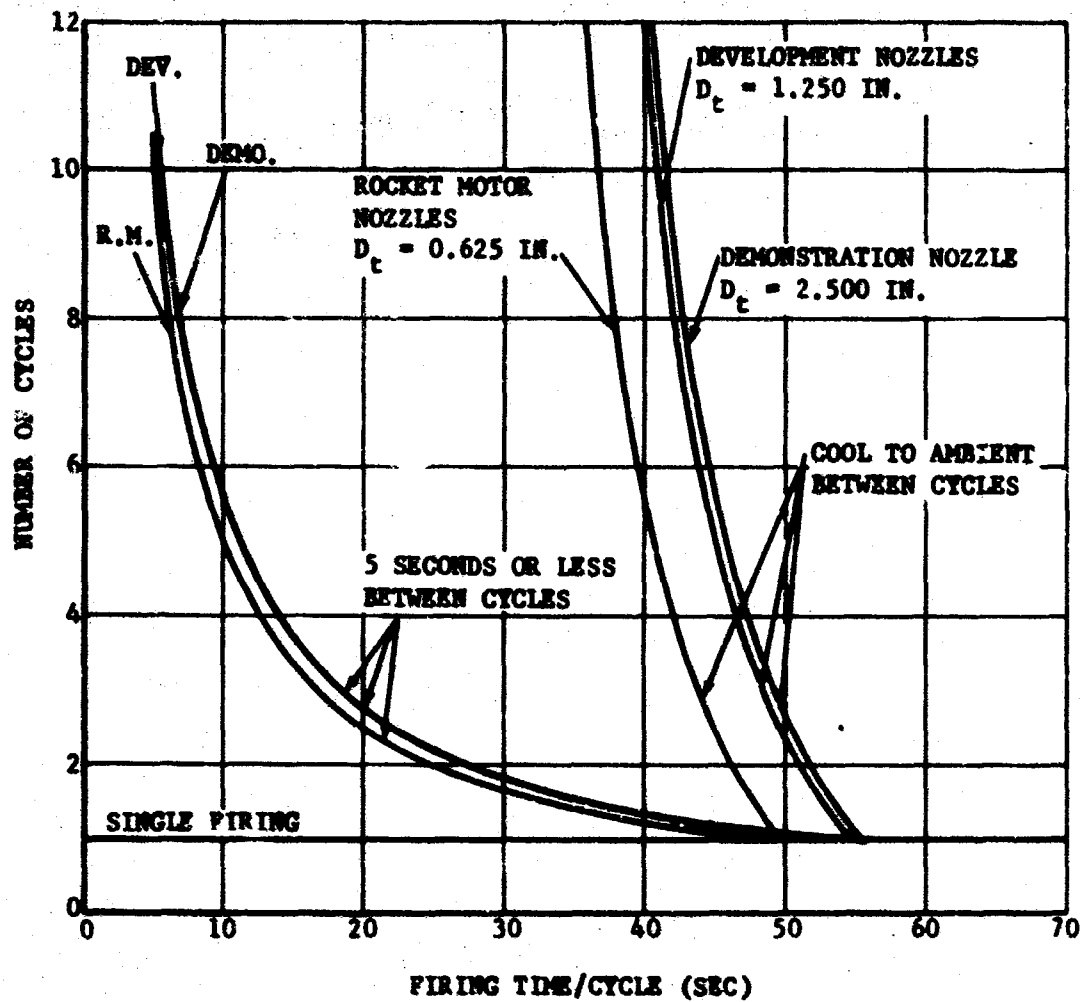
FO4466 U

FIGURE 5-1. NOZZLE THROAT MATERIAL CANDIDATES FOR RESTARTABLE SOLID PROPELLANT ROCKET MOTORS.

CONFIDENTIAL

THIS PAGE IS UNCLASSIFIED

CONFIDENTIAL



FO4467 C

FIGURE 5-2. DUTY CYCLE LIMITS PYROLYTIC GRAPHITE THROATS

CONFIDENTIAL

CONFIDENTIAL

cooling effectively reduces the maximum allowable pulse length of subsequent cycles slightly due to washer gapping and creation of resultant sites for selective erosion. Design mechanics such as allowance for thermal expansion does not appear to be a limiting problem.

Although tungsten has exhibited excellent erosion resistance, it has some serious restart limitations when compared to polycrystalline graphite for short pulses, or to edge-grained pyrolytic graphite for firing times up to 60 seconds. There is the possibility of fracture after a small number of pulses due to property changes which occur during thermal cycling. Dimensional changes during long firings and carbon diffusion while hot can seriously limit its capabilities. Leakage behind the insert, especially after several firings, can also be a limitation. However, due to its excellent erosion resistance, tungsten should be given further consideration, although many of its properties are not known. Since the success of tungsten as a throat material is primarily dependent upon its interaction or compatibility with surrounding nozzle materials, and its physical retention, no meaningful duty cycle curves such as those for pyrolytic graphite can be established.

5.2 NOZZLE ENTRANCE SECTIONS

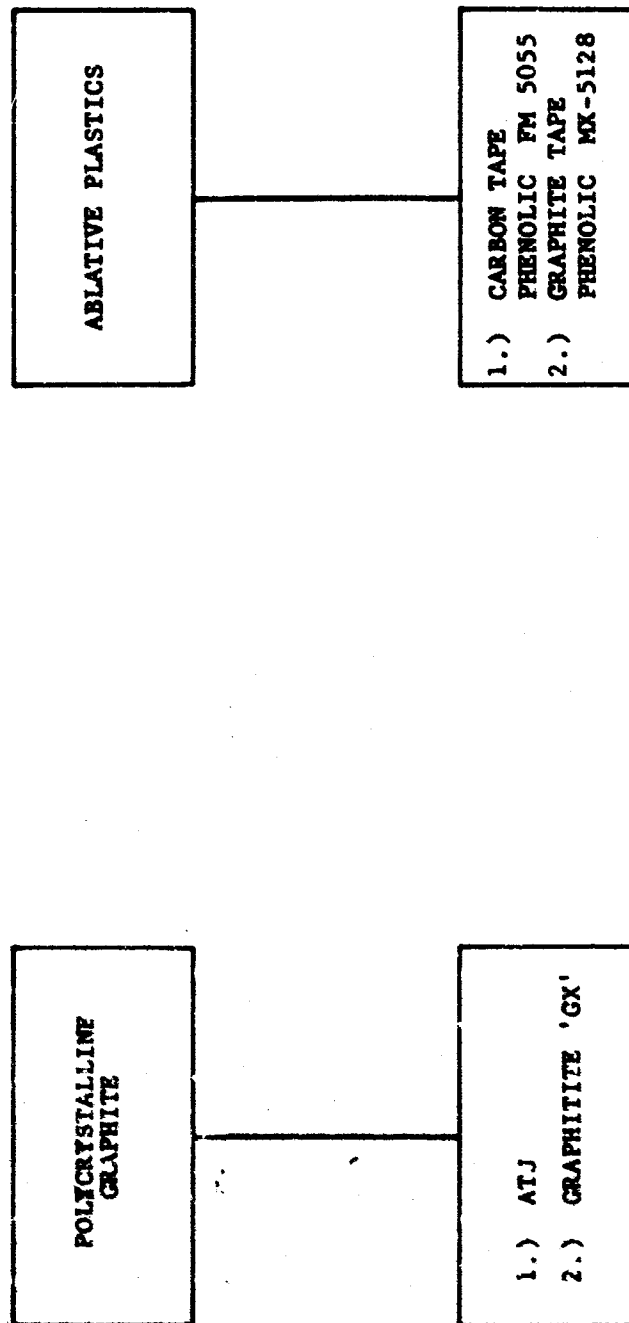
The primary entrance materials and their subgroupings that were considered in this program are depicted in Figure 5-3.

Neither of the two grades of polycrystalline graphite examined in the entrance sections can be considered as adequate for restart applications, particularly where many multiple starts are to be affected. In all tests, the ATJ graphite or Graphitite GX entrance sections cracked on either the first or second cycles. These cracks worsened on subsequent restarts, and, where the duty cycles were severe enough, the entrance sections failed completely. This failure invariably occurred while the remainder of the nozzle was still in a condition acceptable for restart. Duty cycle limits for the ATJ graphite entrance configuration and thickness used in these rocket motor tests in terms of number of cycles versus firing time/cycle for the minimum and maximum delay times are shown in Figure 5-4. These curves are plotted with the comparable curves for the development and demonstration test phases to show the scaling effect as in Figure 5-2. It must be emphasized that these curves, of necessity, do not take catastrophic failures into account, and for this reason the ATJ graphite appears more serviceable than an ablative plastic in this entrance section application. It is, however, this very mode of failure that has occurred with ATJ with monotonous regularity during the rocket motor tests that accents its inadequacies and lack of reliability as an entrance flamefront material.

To provide a broader aspect to the duty cycle limitations of ATJ graphite entrances (Figure 5-4 is restricted to the 400-mil entrance cone size used

CONFIDENTIAL

CONFIDENTIAL



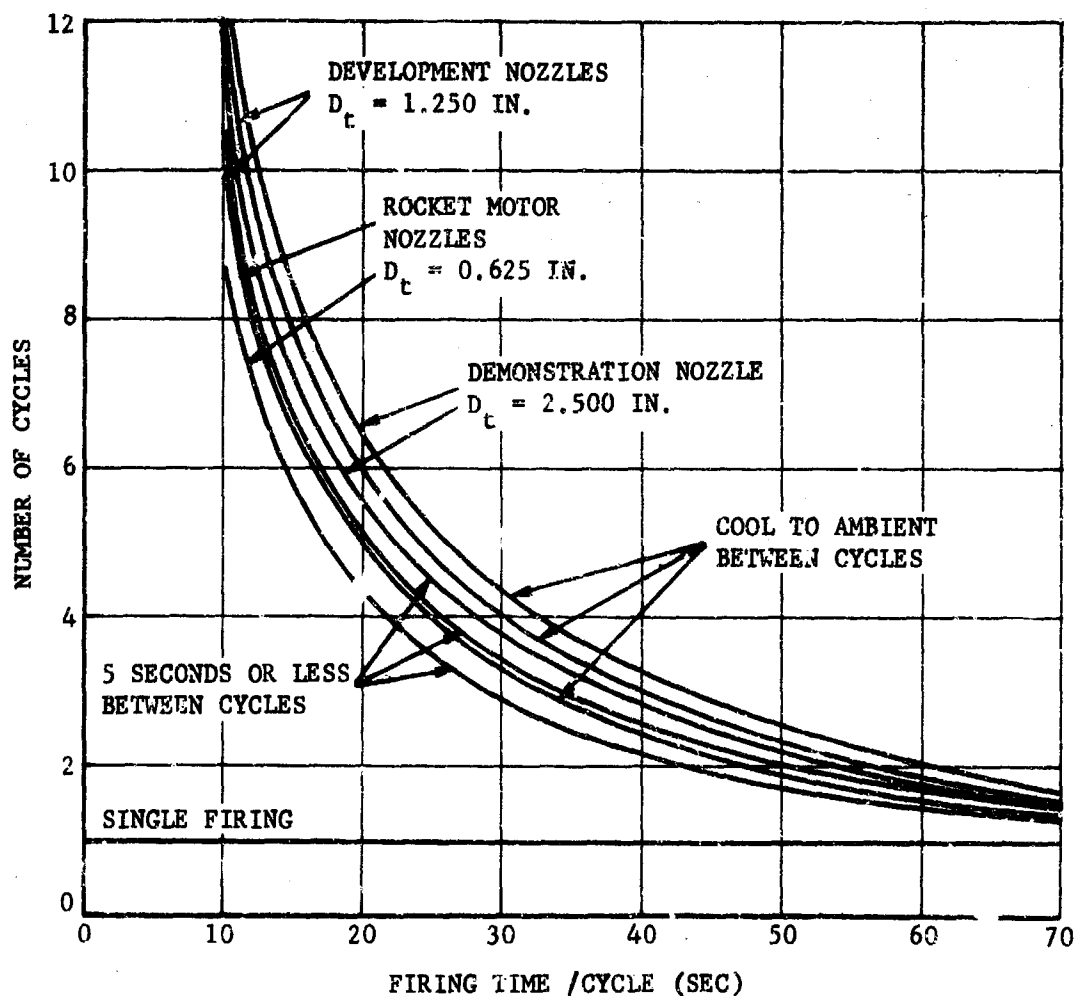
FO4468 U

FIGURE 5-3. NOZZLE ENTRANCE MATERIAL CANDIDATES FOR RESTARTABLE SOLID PROPELLANT ROCKET MOTORS

CONFIDENTIAL

THIS PAGE IS UNCLASSIFIED

CONFIDENTIAL



F04469 C

FIGURE 5-4. DUTY CYCLE LIMITS - ATJ GRAPHITE ENTRANCES

CONFIDENTIAL

CONFIDENTIAL

in the rocket motor tests since it is based solely on experimental data) and to allow some latitude in nozzle design, a plot of total allowable firing time versus section thickness has been constructed in Figure 5-5. This curve is derived from a simple empirical approach in which only cone thickness is varied. Although this method introduces some errors inherent in its over simplification, it can provide a rough estimate of total firing time as a function of entrance cone thickness. Thus, it can be utilized in mission requirement-weight limitation tradeoff studies. For convenience, and to provide comparative data, the ablative plastic (carbon cloth phenolic) family of curves is shown on the same plot. As in Figure 5-3, these curves do not consider catastrophic failure of the ATJ graphite.

The performances of carbon cloth phenolic and graphite cloth phenolic in the rocket motor entrance section were comparable. Both showed superior performance to the polycrystalline graphites in terms of physical integrity. Although their erosion rates were slightly higher than the polycrystalline graphites, this erosion was a uniform regression free of catastrophic failures. As a result, a more adequate protection of the throat was achieved. Duty cycle limits for carbon cloth phenolic entrances of the configuration and thickness used in these tests are shown in Figure 5-6 for minimum and maximum coast times. As mentioned above, Figure 5-5 shows allowable firing time for a range of carbon cloth phenolic entrance section thicknesses.

5.3 NOZZLE EXIT SECTIONS

No particular limitations appear to be critical for exit materials of either the graphite class or for the ablative plastics. The gross regression noted on the rocket motor tests involving several of the tungsten insert nozzles can be attributed entirely to gas leakage behind the tungsten. In cases where leakage was overcome, little exit erosion occurred. Minimal amounts of erosion of the exit section occurred in all tests involving graphite as the throat material. The exit materials considered in this program were the same as the entrance materials (see Figure 5-3).

5.4 NOZZLE INSULATION

Figure 5-7 shows the various insulation materials that were considered for restart application. Table 5.2 presents a detailed summary of the fabrication procedures for all the plastics used in this program. Although the scope of this program did not permit an extensive investigation of the many types and classes of insulations in use, it is felt that those considered were representative of the overall reinforced plastics group.

CONFIDENTIAL

CONFIDENTIAL

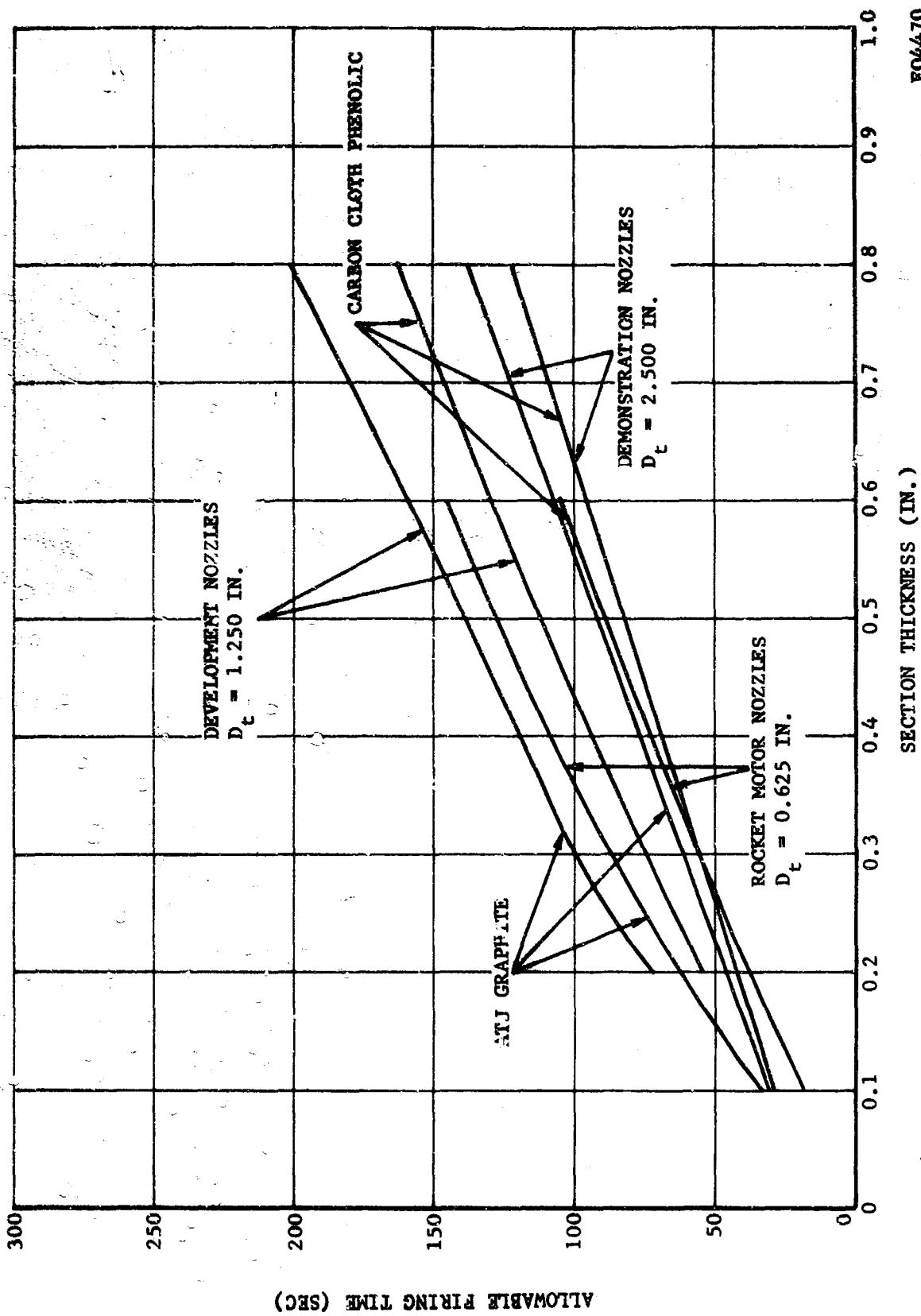


FIGURE 5-5. MAXIMUM ALLOWABLE FIRING TIME VERSUS THICKNESS FOR ENTRANCE SECTIONS

CONFIDENTIAL

CONFIDENTIAL

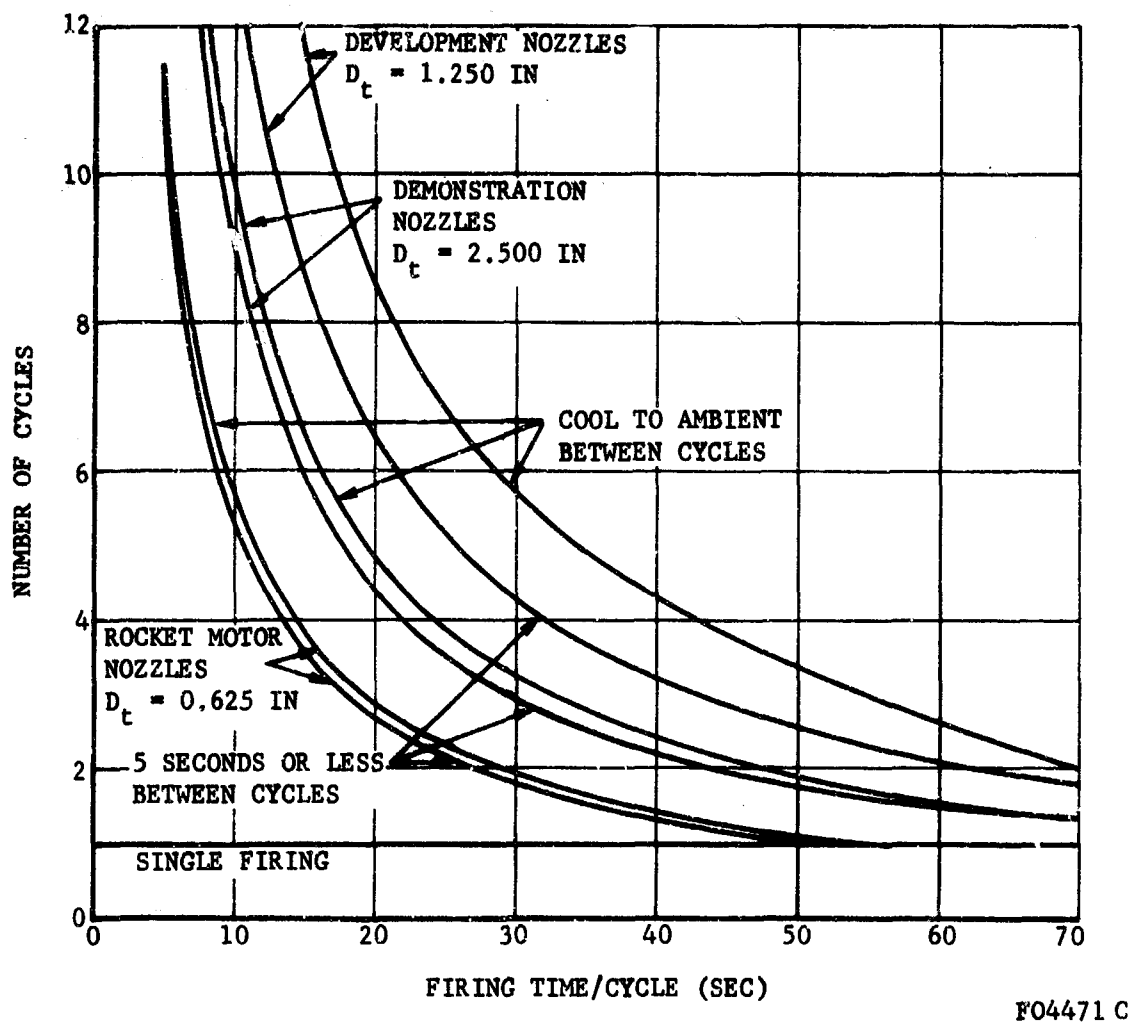
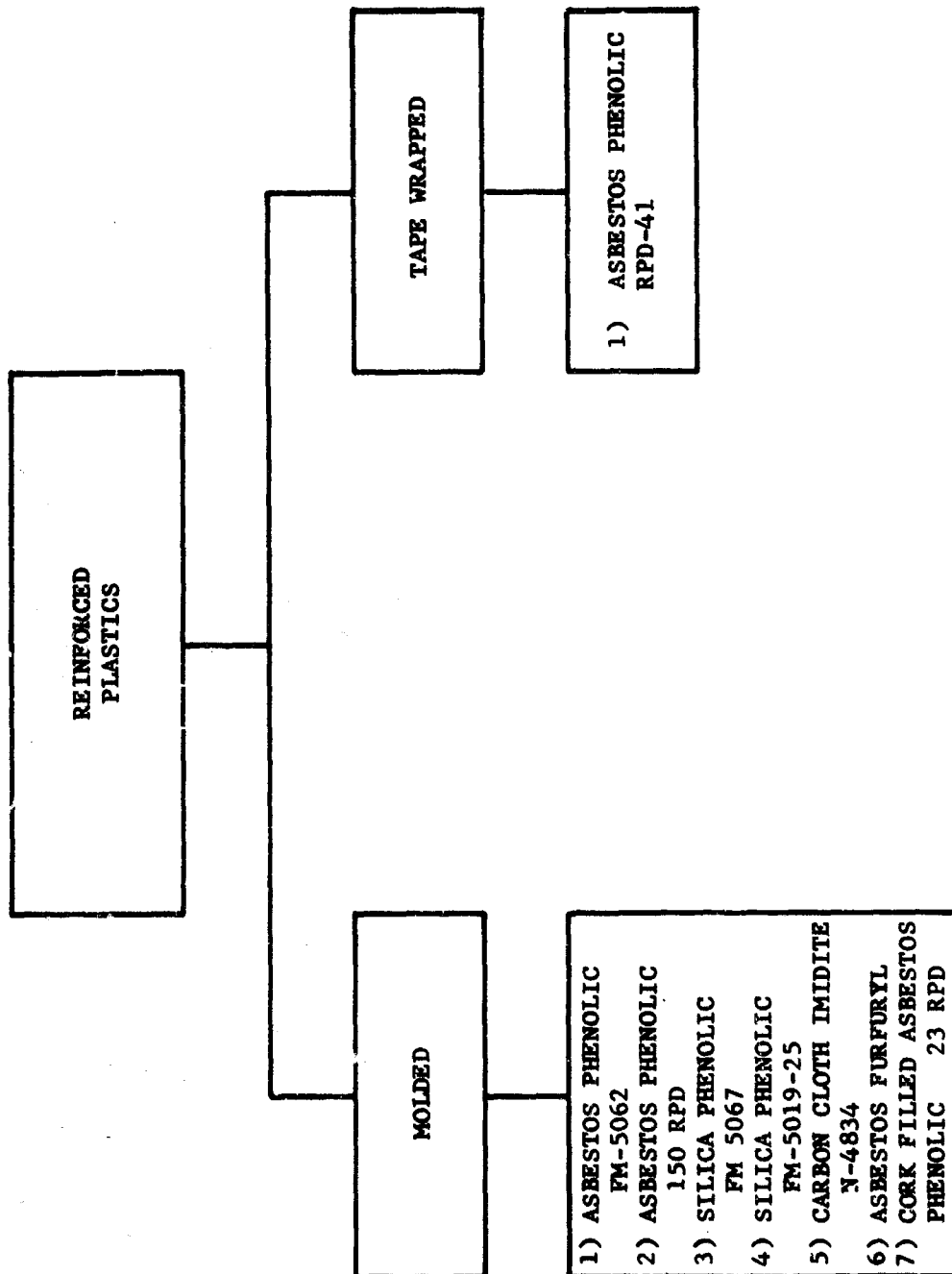


FIGURE 5-6. DUTY CYCLE LIMITS - CARBON CLOTH PHENOLIC ENTRANCES

CONFIDENTIAL

CONFIDENTIAL



FO4472 U

FIGURE 5-7. NOZZLE INSULATION MATERIAL CANDIDATES FOR RESTARTABLE SOLID PROPELLANT ROCKET MOTORS

CONFIDENTIAL

THIS PAGE IS UNCLASSIFIED

CONFIDENTIAL

TABLE 5.2
NOZZLE MATERIALS AND FABRICATION PROCEDURES

Material No.	Description	Vendor	Cure Cycle	Pressure	Density
1. PN 5062	Asbestos-phenolic	U.S. Polymeric	Preheat at 180°F. Cure at 300°F for 4 hours	2000 psi	1.80
2. PN 5067	High silica-phenolic	U.S. Polymeric	Preheat at 145°F. Cure at 300°F for 4 hours	2000 psi	1.75
3. M-4834	Carbon cloth-Imidite (1/2 in. x 1/2 in. squares)	Marwco	1. 250°F for 30 minutes 2. 500°F for 4 hours 3. 700°F for 4 hours	1. Contact pressure 2. 200 psi 3. 200 psi	Not determined
4. None	Asbestos-furfuryl (bulk asbestos fiber and 6-4/L ester resin)	Karbo, Inc.	1. 300°F for 16 hours 2. 350°F in air circulating oven for 8 hours	1. 600 psi 2. None	1.70
5. 150 RPD	Asbestos-phenolic	Raybestos Manhattan	Preheat at 180°F. Cure at 325°F for 3 hours	2000 psi	1.74
6. 23 RPD	Cork filled asbestos-phenolic (1/2 in. x 1 in. pieces cut from the mat)	Raybestos Manhattan	Cure at 325°F for 3 hours	150 psi	1.40
7. MS-5128	Graphite tape-phenolic (1-1/2 in. width)	Fiberite Corp.	Preheat at 160°F. Cure 8 hours at 325°F	1000 psi	Not determined
8. PN 5055	Carbon tape-phenolic 1-1/2 in. width	U.S. Polymeric	Preheat at 190°F for 2 hours. Cure 8 hours at 320°F	1000 psi	Not determined
9. PN 5019-25	High-silica-phenolic	U.S. Polymeric	Preheat at 180°F for 30 minutes. Cure 250°F for 1 hour and 325°F for 3 hours.	3000 psi	Not determined
10. RPD 61	Asbestos phenolic tape, 1-1/2 in. width	Raybestos Manhattan	Preheat at 200°F for 1 hour. Five hours at 320°F	1000 psi	Not determined

CONFIDENTIAL

THIS PAGE IS UNCLASSIFIED

CONFIDENTIAL

Asbestos furfuryl and carbon cloth imidite were eliminated as suitable insulation materials for a restart application because of their high char rate and/or their lack of structural integrity. Both the molded asbestos and silica phenolics showed merit, the former because of its relatively low char rate (even under protracted heat soak conditions), and the latter due to its inherent structural integrity after long firing durations. The effects of variation in resin content, raw material source, method of fabrication, and the use of fillers were then investigated for the two primary insulator candidates. The use of a low resin content silica phenolic (FM 5019-25) resulted in improved performance over the initial silica phenolic tested (FM 5067). A measure of this performance was a decrease in char rate to a level comparable to the asbestos phenolic while maintaining the superior structural integrity of the silica phenolic family. This feature provides support to the theory that a minimization of resin content may be advantageous in restart application where adequate performance is required after numerous heat soak or coast periods. Variation in material source (asbestos phenolic FM 5062 versus 150 RPD) had no effect on performance for the two types tested. For this application, the molding method of fabrication proved superior to the tape wrap method (asbestos phenolics FM 5062 and 150 RPD versus asbestos phenolic RPD-41). The use of a cork filler in the case of asbestos phenolic (23 RPD) showed no advantage over the unfilled material, and resulted in a higher char rate coupled with a deterioration of structural integrity. Tables 5.3 and 5.4 present summaries of insulation evaluation for the entrance and throat sections, respectively.

Duty cycle limits have been established for asbestos phenolic (FM 5062) of the thickness used in these tests. They are shown graphically for entrance and throat insulation applications in Figures 5-8 and 5-9, respectively, and are plotted with the comparable curves for the development and demonstration test phases as was done for entrance sections to show scaling effects. Figures 5-10 and 5-11 provide a broader basis for the use of asbestos phenolic insulators in a restart application. These figures show the effects of thickness variations on total allowable run time and are derived from the experimental data for the specific insulation thicknesses used coupled with the use of the empirical equation for calculating char thickness detailed in References 5.1 and 5.2 with run times calculated for limiting values of char thickness.

CONFIDENTIAL

TABLE 5.3

ENTRANCE INSULATOR EVALUATION-ROCKET MOTOR TESTS

MATERIAL	DESCRIPTION	K													CHAR GRADE
		TEST NO.													
		1	2	3	4	5	6	7	8	9	10	11	12	13	
ASBESTOS PHENOLIC	1. FM-5062		Q033		Q036	Q034	Q035		Q034	Q033		Q032		Q034	2
	2. 150 RPD			Q034											2
	3. 23 RPD (CORK FILLED)							Q056							4
HIGH SILICA PHENOLIC	1. FM-5067		Q053	Q056	Q055					Q052					1
	2. FM-5019-25 (LOW RESIN)											Q037			1
C.C. IMIDITE	1. N-4834		Q076												3
ASBESTOS FURFURYL	—		Q064												5

 $K = \rho_c / \sqrt{E}$ where ρ_c = char thickness

 t = firing time

 K = characteristic constant
of char growth

Char Grade: An empirical order of
structural integrity
where 1 = best
1+n = worst.

NOTE: K has exhibited independence of soak times for these subscale tests

TABLE 5.4
THROAT INSULATOR EVALUATION - ROCKET MOTOR TESTS

MATERIAL	DESCRIPTION	K											CHAR GRADE
		TEST NO.											
		7	8	9	10	11	12	13					
ASBESTOS PHENOLIC	1. FM-5062		0.045	0.040		0.046			0.046				2
	2. 150 RPD												—
HIGH SILICA PHENOLIC	1. FM-5067				0.073								1
	2. FM-5019-25 (LOW RESIN)								0.046				1

$K = \delta_c / \sqrt{t}$ Where: δ_c = char thickness

t = firing time

K = characteristic constant
of char growth

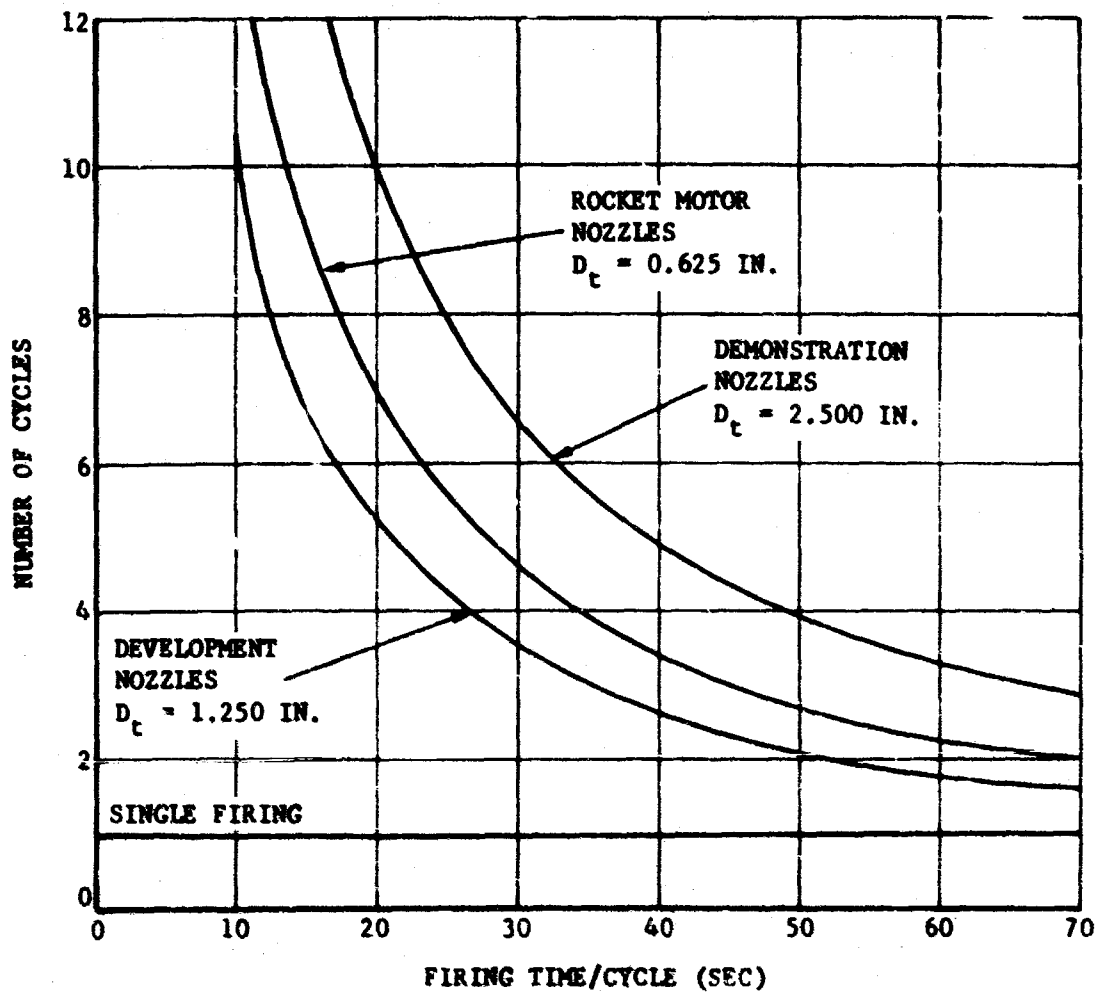
Char Grade: An empirical order
of structural
integrity where

1 = best

1+n = worst

NOTE: K has exhibited independence of soak times for these subscale tests

CONFIDENTIAL

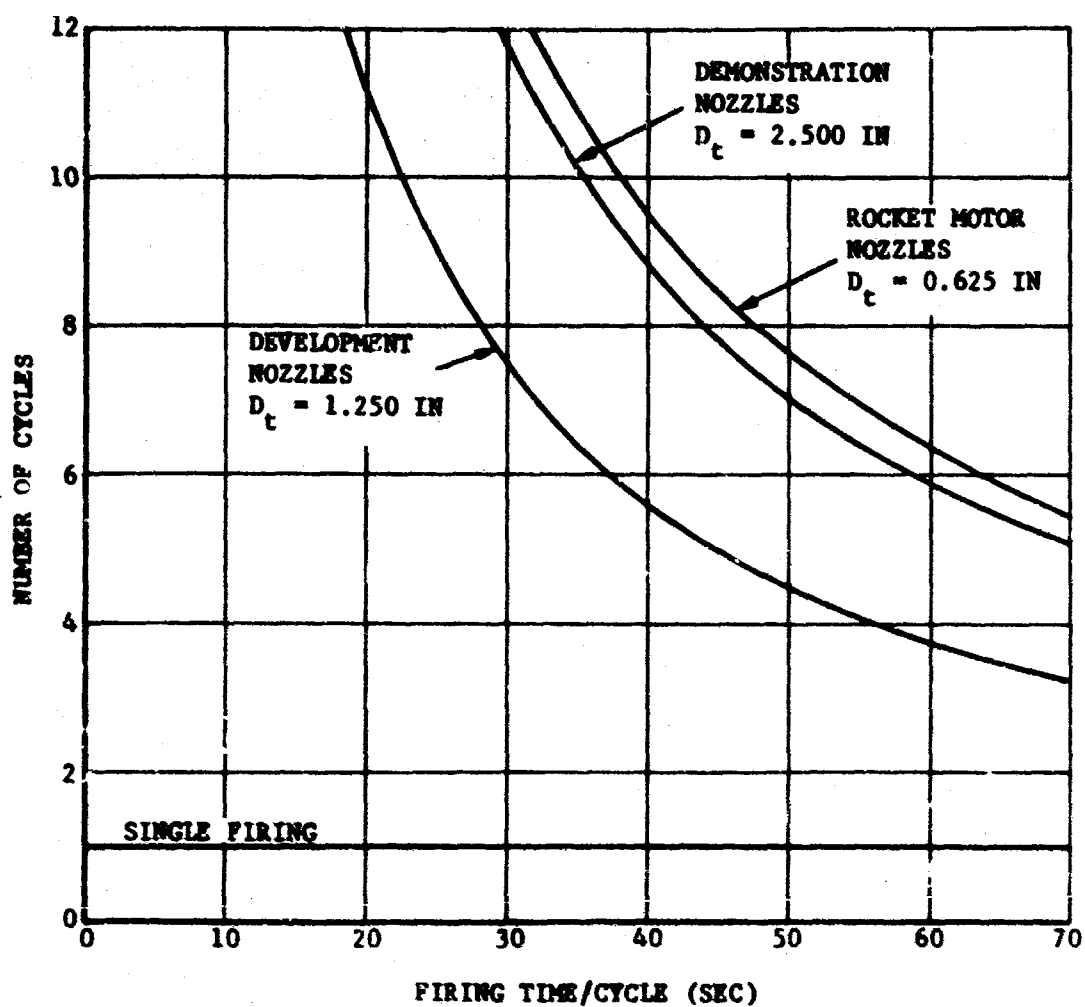


FO4473 C

FIGURE 5-8. DUTY CYCLE LIMITS ASBESTOS PHENOLIC INSULATION BEHIND ENTRANCE SECTION

CONFIDENTIAL

CONFIDENTIAL

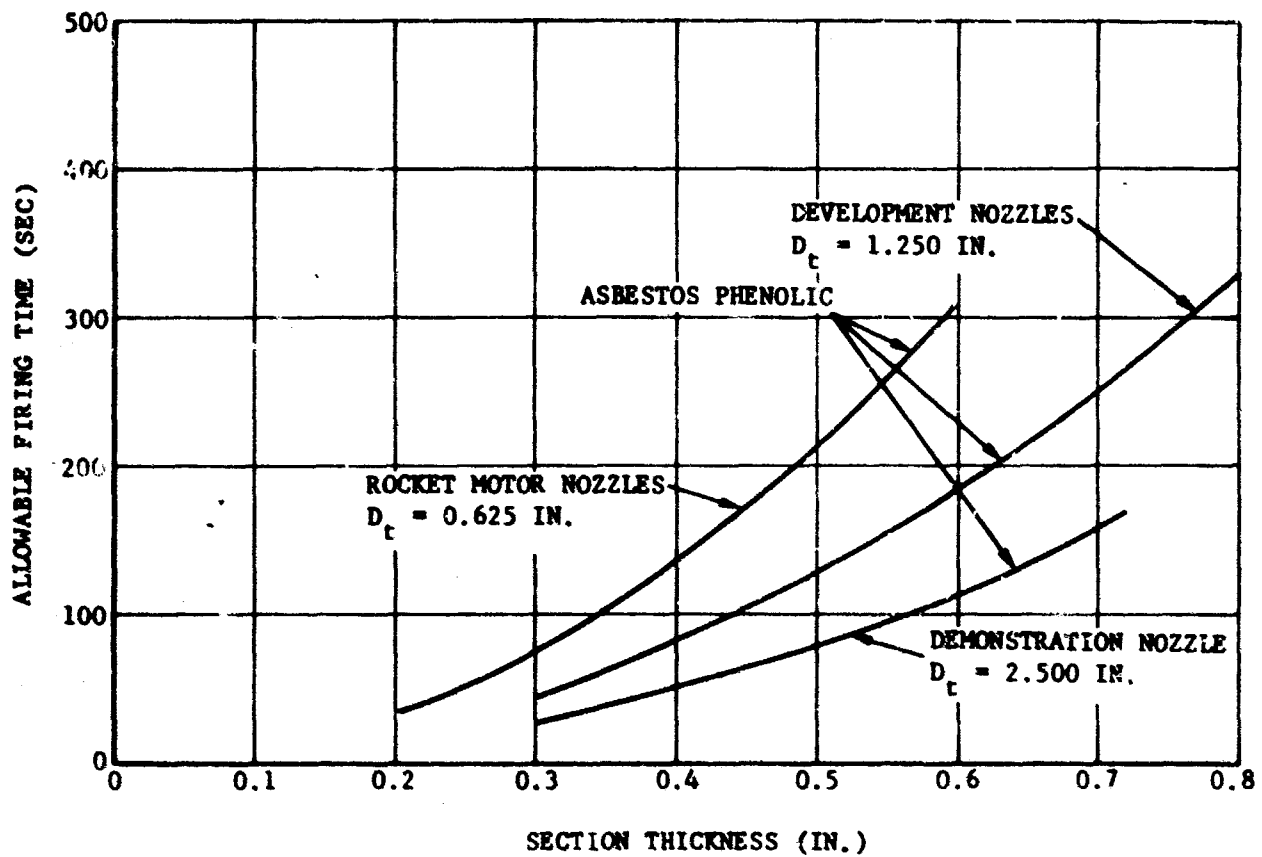


FO4474 C

**FIGURE 5-9. DUTY CYCLE LIMITS - ASBESTOS PHENOLIC INSULATION
BEHIND THEROAT SECTION**

CONFIDENTIAL

CONFIDENTIAL



FO4475 C

FIGURE 5-10. MAXIMUM ALLOWABLE FIRING TIME VERSUS THICKNESS FOR ENTRANCE INSULATION

CONFIDENTIAL

CONFIDENTIAL

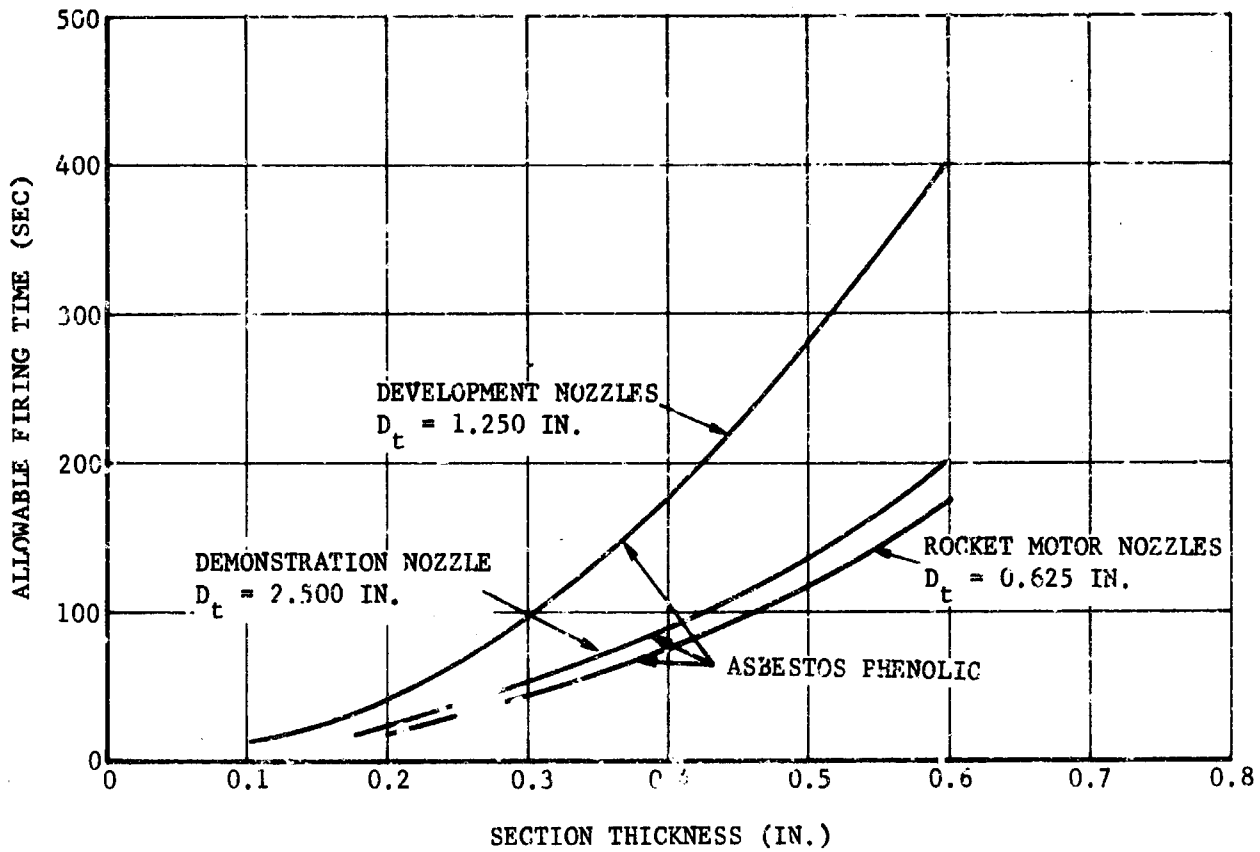


FIGURE 5-11. MAXIMUM ALLOWABLE FIRING TIME VERSUS THICKNESS FOR THROAT INSULATION

F04476 C

CONFIDENTIAL

REFERENCES

- 5.1 Armour, W. H., et al., "An Investigation and Feasibility Demonstration of Nozzles for Restartable Solid Rocket Motors," Contract AF 04 (611)-9904, Second Quarterly Report RPL TDR-64-158, Aeronutronic Publication No. C-2952, 20 December 1964.
- 5.2 Armour, W. H., et al., "An Investigation and Feasibility Demcnstration of Nozzles for Restartable Solid Rocket Motors," Contract AF 04 (611)-9904, Third Quarterly Report RPL TDR-65-53, Aeronutronic Publication No. C-3023, 22 March 1965.

CONFIDENTIAL

SECTION 6

DEVELOPMENT MOTOR TESTS

Five nozzles with 1.25-inch diameter throats were tested in the development phase of the program. The propellant simulated (CYI-75), combustion temperature (6175°F), and nominal chamber pressure (700 psia) were identical to those of the rocket motor tests. A larger motor was used for these tests and the thrust developed was approximately 1100 pounds. This test series was designed to (1) utilize the knowledge gained in the program to design nozzles for particular duty cycles, (2) to provide additional data for the demonstration tests, and (3) to bring all previous laboratory efforts and analysis, combined with the results of the rocket motor tests, together. The development tests are, therefore, the bridge between the rocket motor tests and demonstration test. Two basic duty cycles were used for these tests, the second of which was modified for the last two tests as a result of simulator limitations. A summary of these five development motor tests, including the particular duty cycle employed, materials utilized, test conditions, throat performance, and conclusions is presented in Table 6-1.

Presentation of observations and conclusions drawn from the development motor tests follows the same format as that utilized in the rocket motor tests (Section 5) in that each nozzle section is treated separately. However, a more detailed discussion of individual test results can be made for these development tests due to the limited scope and the reduction of nozzle variables in this phase. Figures 6-1 through 6-5 show the nozzle configurations used in these tests as well as summarizing nozzle material performance in terms of erosion data.

6.1 DEVELOPMENT NOZZLE THROAT SECTIONS

As a result of the rocket motor tests, edge grained pyrolytic graphite and tungsten were the only logical throat candidates for consideration in the development motor test phase (see Paragraph 5.1).

CONFIDENTIAL

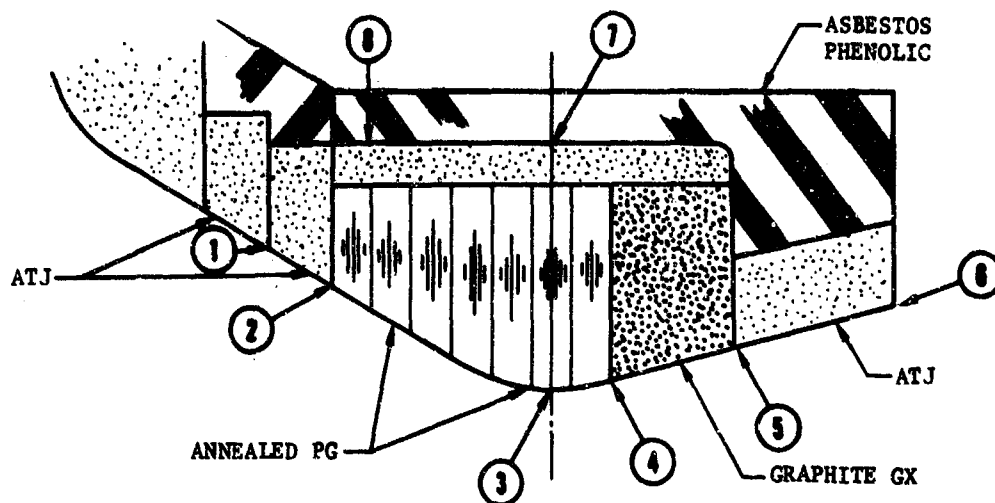
CONFIDENTIAL

TABLE 6.1
RESTART DEVELOPMENT TESTS - SUMMARY

Test No.	Materials					Thrust Performance					Remarks
	Thrust	Entrance	Exit	Insulation	Duty Cycle	P _c (psia)	F (lb)	ΔP (in.)	ΔA (%)	ΔT (°C)	
1	Pyrolytic Graphite (annealed) Plate C ₀ = 6.716 Å	ATJ Graphite Plus 3 Annealed PG Plates	Graphite 'CX' Plus ATJ Graphite	Asbestos Phen (PM 5062)	On - 20 sec	642	1112	-0.018	-1.44	-0.27	Loss of slurry in last 5 sec pulse of phase 2 and last 5 sec pulse of phase 3 caused oxygen flow rate to jump from about 4.7% to 78% of the total flow. The entrance ATJ washers all cracked during the first 2 phases.
					Off - 100 sec			to	to	to	
					On - 15 sec			-0.030	-2.4	-0.43	
					Cool to Amb						
					On - 15 sec	642	1129	0	0	0	
2	Tungsten (Split Arc-Cast)	ATJ Graphite Plus 2 PG Washers	Graphite 'CX' Plus Carbon Cloth Phenolic	Asbestos Phen (PM 5062)	On - 6x5 sec	602	1117	0.052	4.2	8.6	Thrust insert obstructed about 1/16 in./phase. No gas leakage behind insert. Radial dimensions of insert decreased with each phase. All ATJ entrance washers cracked during phase 1.
					Off - 100 sec			to	to	to	
					On - 15 sec	652	1160	-0.04	-3.2	-6.36	
					Cool to Amb						
					On - 15 sec	669	1077	-0.012	-1.57	-2.97	
3	Pyrolytic Graphite (As deposited) Plate C ₀ = 6.844 Å	ATJ Graphite Plus 3 PG Washers	Graphite 'CX' Plus ATJ Graphite	Asbestos Phen (RFD 41)	On - 100 sec			to	to	to	Loss of slurry on 6th phase of phase 2 resulting in an C flow of about 77% of total and aborting phase 2 results. No cracking of improved ATJ entrance during phase 1. Chamber liner failure due to O ₂ rich phase 2.
					Off - 100 sec			-0.003	-0.25	-0.27	
					On - 10 sec			to	to	to	
					Cool to Amb			-0.014	-1.2	-2.4	
					On - 10x5 sec	625	1042	-	-	-	
4	Tungsten (Arc-Cast)	Carbon Cloth Phenolic Plus 3 PG Washers	Graphite 'CX' Plus ATJ Graphite	Asbestos Phen (PM 5062)	On - 40 sec	655	1108	-0.042	-3.4	-6.6	Thrust insert obstructed about 1/16 in./phase. Slight gas leakage behind insert and localized exit grooving. Carbon cloth entrance performance was structurally superior to ATJ although the erosion rate (2.75 mils/sec avg for both phases) was high. Upstream P.G. washer cracked.
					Off - 100 sec			to	to	to	
					On - 10 sec						
					Cool to Amb						
					On - 30 sec	685	1068	-0.027	-2.24	-4.28	
5	Pyrolytic Graphite (Heat-treated) Plate C ₀ = 6.761 Å	Carbon Cloth Phenolic Plus 3 Heat Treated PG Plates	Graphite 'CX' Plus Carbon Cloth Phenolic	Asbestos Phen (PM 5062)	On - 40 sec	656	1093	0	0	0	Loss of slurry on last pulse of phase 2 caused oxygen flow rate jump to 78% from 4.7% partially negating phase 2 results. Entrance performance was good (dr/dt of about 2 mils/sec for phase 1).
					Off - 100 sec						
					On - 10 sec						
					Cool to Amb						
					On - 30 sec	651	1029	0.046	3.7	7.6	
					Off - 60 sec						
					On - 4x5 sec						

CONFIDENTIAL

CONFIDENTIAL



STATION NO.	BEFORE		AFTER						TOTAL	
	DIA. INCHES		PHASE I		PHASE 2		PHASE 3		Δr_{or}^c INCHES	dr/dt or $d\delta c/dt$
			DIA. INCHES	dr/dt MIL/SEC	DIA. INCHES	dr/dt MIL/SEC	DIA. INCHES	dr/dt MIL/SEC		
①	4.06	10.6	4.06	0	4.24	2.6	—	—	—	—
②	3.28	6.9	3.28	0	3.46	2.6	3.60 to 3.66	1.17 to 1.67	0.32 to 0.38	1.6 to 1.9
③	1.25	1.0	1.22 to 1.232	-.258 to -.425	1.247 to 1.284	-.043 to 0.49	1.302 to 1.315	0.52 to 0.87	0.052 to 0.065	0.26 to 0.33
④	1.64	1.75	1.64	0	1.64	0	1.64	0	0	0
⑤	2.50	4.0	2.50	0	2.50	0	2.54	0.67	0.04	0.2
⑥	3.81	9.3	3.81	0	3.81	0	3.89	1.34	0.08	0.4
⑦	—	—	—	—	—	—	—	—	0.20	2.0
⑧	—	—	—	—	—	—	—	—	0.32	3.2

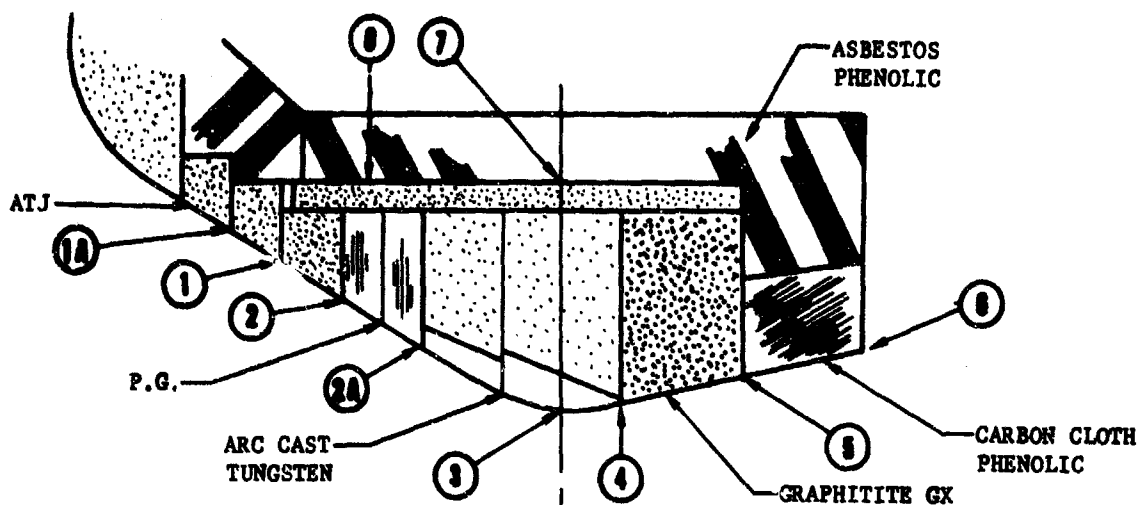
FIGURE 6-1. RESTART DEVELOPMENT TEST NO. 1
MATERIALS PERFORMANCE

FO4477 C

6-3

CONFIDENTIAL

CONFIDENTIAL



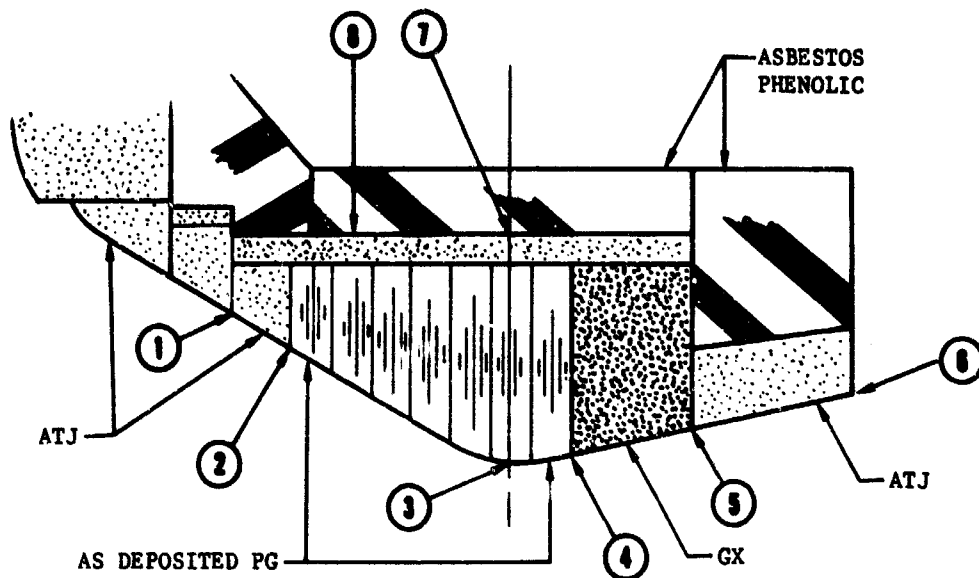
STATION NO.	BEFORE		AFTER						TOTAL	
	DIA. INCHES		PHASE I		PHASE 2		PHASE 3		ΔD or Δc INCHES	$\frac{dr}{dt}$ or $\frac{d \Delta c}{dt}$ MIL/SEC
		ϵ	DIA. INCHES	$\frac{dr}{dt}$ MIL/SEC	DIA. INCHES	$\frac{dr}{dt}$ MIL/SEC	DIA. INCHES	$\frac{dr}{dt}$ MIL/SEC		
10	4.20	11.3	4.23	0.43	4.25 to 4.33	0.29 to 1.43	4.31 to 4.38	0.83 to 2.16	0.11 to 0.18	0.55 to 0.9
1	3.52	7.95	3.52	0	3.54 to 3.61	0.29 to 1.29	3.59 to 3.66	0.80 to 2.00	0.07 to 0.14	0.35 to 0.7
2	2.82	5.11	2.95	1.85	2.98 to 3.03	0.43 to 1.15	3.11 to 3.16	1.33 to 3.00	0.29 to 0.34	1.45 to 1.70
2A	1.74	1.9	1.74	0	1.74 to 1.76	0 to 0.29	1.81	0.83 to 1.17	0.07	0.35
3	1.249	1.0	1.209	-.57	1.181 to 1.190	-.271 to -.400	1.176 to 1.178	-.05 to -.234	0.071 to -.073	-.355 to -.365
4	1.73	2.0	—	—	THROAT OBTRUSION MASKED REGRESSION				—	—
5	2.50	4.0	.253	0.43	2.53	0	2.53	0	0.03	0.15
6	4.23	11.4	4.23	0	—	—	4.25 to 4.34	—	0.02 to 0.11	0.1 to 0.55
7	—	—	—	—	—	—	—	—	0.20	2.0
8	—	—	—	—	—	—	—	—	0.29	2.9

FIGURE 6-2. RESTART DEVELOPMENT TEST NO. 2
MATERIALS PERFORMANCE

F04478 C

CONFIDENTIAL

CONFIDENTIAL



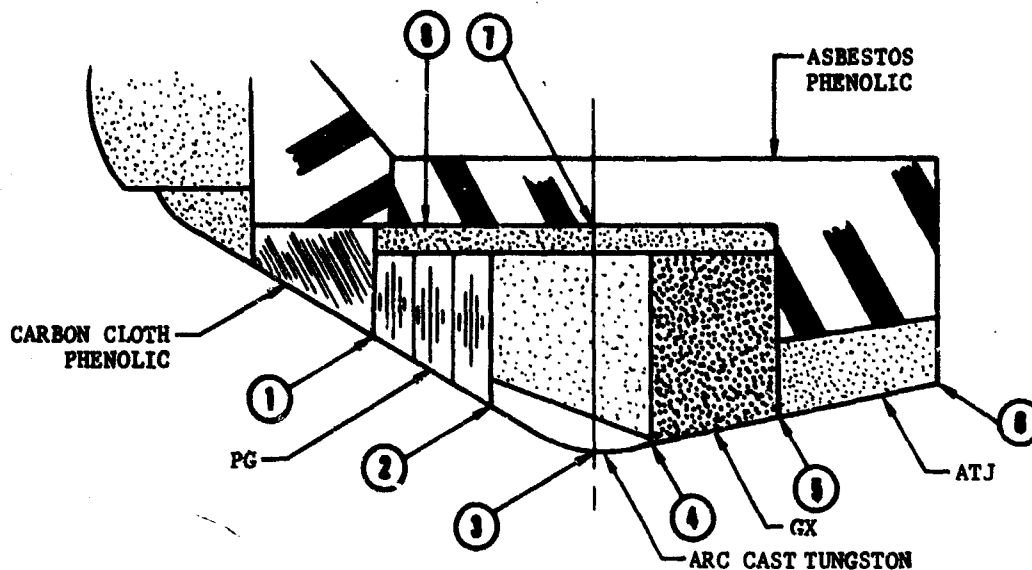
STATION NO.	BEFORE		AFTER				TOTAL	
	DIA. INCHES	ϵ	PHASE I		PHASE 2		Δ Dia INCHES	dr/dt or d ϵ /dt MIL/SEC
			DIA. INCHES	dr/dt MIL/SEC	DIA. INCHES	dr/dt MIL/SEC		
①	4.18	11.2	4.28 to 4.31	1.0 to 1.3	INVALID DUE TO THRUST CHAMBER MALFUNCTION			
②	3.50	7.85	3.72 to 3.74	2.2 to 2.4				
③	1.249	1	1.249	0				
④	1.65	1.76	1.65	0				
⑤	2.45	3.9	2.45	0				
⑥	3.80	9.75	3.80	0				
⑦	—	—	—	—	—	—	0.43	4.3
⑧	—	—	—	—	—	—	0.55	5.5

FIGURE 6-3. RESTART DEVELOPMENT TEST NO. 3
MATERIALS PERFORMANCE ,

FO4479 C

CONFIDENTIAL

CONFIDENTIAL



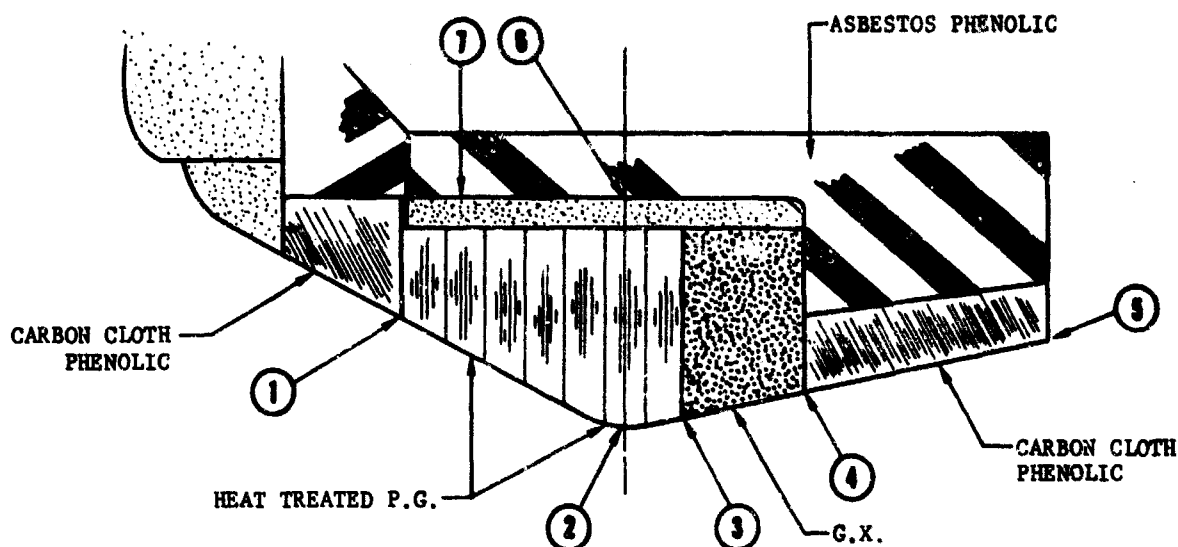
STATION NO.	BEFORE		AFTER				TOTAL	
	DIA. INCHES	<	PHASE 1		PHASE 2		ΔD or Δc INCHES	dr/dt or ddc/dt MIL/SEC
			DIA. INCHES	dr/dt MIL/SEC	DIA. INCHES	dr/dt MIL/SEC		
①	3.342	7.2	3.52 to 3.59	1.8 to 2.5	3.89 to 4.09	3.0 to 5.7	0.55 to 0.75	2.75 to 3.75
②	1.704	1.9	1.75	0.5	1.89	1.4	0.19	0.95
③	1.249	1.	1.207	-0.42	1.180	-0.27	-0.069	-0.345
④	1.73	2.	MASKED BY OBTRUSION PROCESS					
⑤	2.48	3.9	2.48	0	2.49 to 2.50	0.1 to 0.2	0.01 to 0.02	0.05 to 0.10
⑥	3.92	9.75	3.92	0	3.92	0	0	0
⑦	—	—	—	—	—	—	0.25	2.5
⑧	—	—	—	—	—	—	0.40	4.0

FIGURE 6-4. RESTART DEVELOPMENT TEST NO. 4
MATERIALS PERFORMANCE

FO4480 C

CONFIDENTIAL

CONFIDENTIAL



STATION NO.	BEFORE		AFTER				TOTAL	
	DIA. INCHES	€	PHASE I		PHASE 2 *		ΔD or Δc INCHES	dr/dt or $Disc/dt$ - MIL/SEC.
			DIA. INCHES	dr/dt MIL/SEC	DIA. INCHES	dr/dt MIL/SEC.		
①	3.38	7.33	3.58-3.70	2.0-3.2	—	—	—	—
②	1.248	1.0	1.248	0	1.294	0.46*	0.046	0.23*
③	1.44	1.33	1.60	1.6	1.63	0.3*	0.19	0.95*
④	2.50	4.0	2.55	0.5	2.59	0.4*	0.09	0.45*
⑤	4.23	11.5	4.25	0.2	4.35	1.0*	0.12	0.60*
⑥	—	—	—	—	—	—	0.30	3.0
⑦	—	—	—	—	—	—	0.45	4.5

* LOST SLURRY FLOW

FO4481C

FIGURE 6-5. RESTART DEVELOPMENT TEST NO. 5
MATERIALS PERFORMANCE

CONFIDENTIAL

CONFIDENTIAL

The rocket motor tests did not, however, present any clear cut choice among the annealed, as-deposited or heat treated (partially annealed) states of pyrolytic graphite. In an attempt to obtain more comparative data in this area Development Tests 1, 3 and 5 utilized nozzle throat stacks composed of the aforementioned materials. An examination of Table 6.1 shows that the development tests did nothing to establish a performance superiority of any one of these materials over the other two. When the simulator functioned properly, none of the nozzles exhibited any erosion under the duty cycles imposed. Duty cycle limits for pyrolytic graphite nozzles of the configuration used in these Development Motor tests have been established in terms of number of cycles versus firing time per cycle for the minimum and maximum delay times. These limits are shown in Figure 5-2 with the analogous curves for the rocket motor tests and the demonstration test.

Tests 2 and 4 utilized tungsten as the throat material. The arc cast rolled and extruded tungsten was chosen as opposed to the gas pressure bonded micro-sphere type primarily because of availability and compatibility with scheduling requirements. They differed from each other in that Test 2 utilized a two segmented insert split radially at the sonic line while Test 4 consisted of a single piece insert. Performances were identical in that neither showed any throat regression for the duty cycle employed. There was, in fact, a decrease in radial dimension of the throat in each case. This is discussed more fully in Paragraph 8.2. Both inserts obtruded approximately 0.062 inch per test phase. This supports the conclusion that the success of tungsten as a throat material is primarily dependent upon design criteria rather than a predictable thermal erosion/corrosion response, as is true for pyrolytic graphite. The logical inference is, therefore, that although tungsten presents a superior corrosion resistance than pyrolytic graphite it is inherently less reliable in restart application due to a failure mode which must be considered catastrophic.

6.2 DEVELOPMENT NOZZLE ENTRANCE SECTIONS

ATJ graphite and carbon cloth phenolic were chosen as entrance materials for the development test phase. These materials were considered representative of the material families investigated in the rocket motor tests (see Figure 5-3). As stated in Paragraph 5.2, neither material proved better than marginal for restart application. The primary purposes of this test phase, in terms of entrance sections, were (1) an attempt to design a polycrystalline graphite entrance that would not fail catastrophically under restart conditions and (2) to determine more precisely the erosion rate of an ablative plastic entrance section. The initial three tests of this series utilized ATJ graphite as an entrance material, and the latter two tests employed carbon cloth phenolic entrances. Development nozzle No. 1, Figure 6-1, used stepped ATJ washers forward of the throat. These washers cracked badly during the first phase of the duty cycle. These cracks worsened during the second phase of the duty cycle, and it is highly questionable whether the entrance section would have survived another firing phase. The entrance of development nozzle No. 2 was similar to that of the

CONFIDENTIAL

CONFIDENTIAL

first nozzle, and its performance was equally poor. The condition of the ATJ graphite after completion of firing was marginal at best. Development nozzle No. 3 employed an entrance section in which the ATJ graphite washers were allowed virtually unrestrained axial motion. No cracking of the ATJ was noted after the test, indicating the soundness of design approach. However, a comparison of Station (2) of Figure 6-3 with Stations (1) of Figures 6-4 and 6-5 at approximately the same values shows little or no advantage in regression rate as compared to carbon cloth phenolic entrance sections. As Figures 6-4 and 6-5 show, the carbon cloth phenolic entrance sections of development nozzles 4 and 5 are comparable. Both performed satisfactorily from a structural standpoint, but their relatively high erosion rates, compared to both tungsten and pyrolytic graphite throat sections, leave much to be desired.

Duty cycle limits for the ATJ graphite entrance configuration and thickness used in these development tests in terms of number of cycles versus firing time/cycle for the minimum and maximum delay times are shown in Figure 5-4. These curves are plotted with the comparable curves for the rocket motor and demonstration test phases to show the scaling effect as in Figure 5-2. To provide a broader aspect to the duty cycle limitations of ATJ graphite entrances and to allow some latitude in nozzle design, a plot of total allowable firing time versus section thickness has been constructed in Figure 5-5. The derivation of this curve is explained in Paragraph 5-2. For convenience, and to provide comparative data, the ablative plastic (carbon cloth phenolic) family of curves is shown on the same plot. Duty cycle limits for carbon cloth phenolic entrances of the configuration and thickness used in these tests are shown in Figure 5-6 for minimum and maximum coast times.

An obvious and vital conclusion which cannot be overemphasized can be drawn from the rocket motor and development test series:

The restart test series has shown that a problem exists with nozzle entrances that is equal to, if not greater than, that of the throat. This problem centers about creation of an entrance that will perform adequately from both a thermal and structural standpoint. Invariably, the overall nozzle performance has suffered from an entrance section performance which is, at best, marginal. Many of the duty cycle limitations of throat materials, particularly tungsten, are critically limited by poor entrance performance. Although an ablative entrance has shown an overall improvement over graphite entrances, its erosion rate is high enough to be unacceptable where pulses of long duration are a part of the duty cycle. A concentrated effort in terms of material and design evaluation geared toward solving this problem or at least alleviating it to the extent that entrance performance is comparable to throat performance will be required.

CONFIDENTIAL

CONFIDENTIAL

6.3 DEVELOPMENT NOZZLE EXIT

The development nozzle exit sections in all cases corroborated the conclusions drawn from the rocket motor tests, i.e., no problems areas have been uncovered for nozzle exit sections in terms of restart capabilities. Future efforts should be directed toward weight and design optimization.

6.4 DEVELOPMENT NOZZLE INSULATION

Of those materials considered in the rocket motor tests (Figure 5-7), FM-5062 molded asbestos phenolic and RPD-41 tape grade asbestos phenolic were chosen for use in the development test phase. The choice of asbestos phenolic FM-5062 was based on its relatively superior properties, as discussed in Paragraph 5.4. The tape grade asbestos phenolic (RPD-41) was chosen for two reasons. The primary reason for utilizing the asbestos tape insulator was so that special thermocouples could be wrapped in precise locations within the insulation in an effort to obtain thermal response data for the corroboration of the ablation analysis. The second reason for using RPD-41 was to verify the superior performance of the molded asbestos phenolic noted in the rocket motor tests. Regrettably, the low resin silica phenolic (FM 5019-25) could not be included in this phase since it would require a number of controlled experimental firings to establish the credibility of its superior properties. A study such as this was considered to be beyond the scope of this program. Tables 6.2 and 6.3 present summaries of insulator evaluation for the entrance and throat sections, respectively. As these tables show, the molded FM-5062 asbestos phenolic exhibits a superior performance over the tape grade in terms of lower char growth versus time. This verifies the data obtained in the rocket motor tests.

Duty cycle limits have been established for asbestos phenolic (FM 5062) of the thickness used in these tests. They are shown graphically for entrance and throat insulation applications in Figures 5-8 and 5-9, respectively, and are plotted with the comparable curves for the rocket motor and demonstration test phases. Figures 5-10 and 5-11 provide a broader basis for the use of asbestos phenolic insulators in a restart application. These figures show the effects of thickness variations on total allowable run time and are derived in the manner described in Paragraph 5.4.

CONFIDENTIAL

TABLE 6.2

ENTRANCE INSULATOR EVALUATION - DEVELOPMENT MOTOR TESTS

<u>Material</u>	<u>Description</u>	<u>K</u> <u>Test No.</u>				
		1	2	3	4	5
Asbestos	1. FM 5062	0.032	0.029		0.040	0.045
Phenolic	2. RPD 41			0.055		

$$K = \delta_c / \sqrt{t}$$

where

δ_c = char thickness, inches

t = firing time, seconds

K = characteristic constant
of char growth

TABLE 6.3

THROAT INSULATOR EVALUATION - DEVELOPMENT MOTOR TESTS

<u>Material</u>	<u>Description</u>	<u>K</u> <u>Test No.</u>				
		1	2	3	4	5
Asbestos	1. FM 5062	0.020	0.020		0.025	0.030
Phenolic	2. RPD 41			0.043		

$$K = \delta_c / \sqrt{t}$$

where

δ_c = char thickness, inches

t = firing time, seconds

K = characteristic constant
of char growth

CONFIDENTIAL

SECTION 7

DEMONSTRATION TESTS

The design, fabrication, and test of the demonstration nozzle represents the culmination of all efforts expended in the rocket motor and development test phases of this program. The purpose of this demonstration test was to show the feasibility of scaling up a nozzle design utilizing the experience from the prior two test phases and to demonstrate the ability of such a nozzle to satisfactorily undergo a duty cycle which is of maximum severity and contains a rigorous number of varied firing cycles.

7.1 TEST CONDITIONS

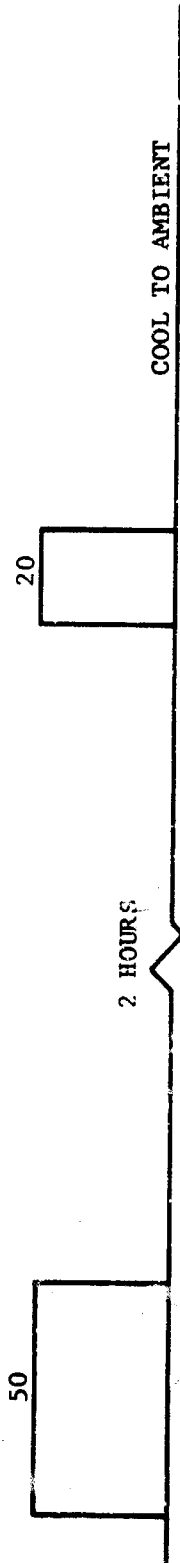
The demonstration nozzle contained a 2.50-inch diameter throat and was tested at nominal conditions of 700 psia chamber pressure and 5190 pounds of thrust. Firings were conducted on an Aeronutronic Solid Propellant Simulator at the El Toro remote test site. The propellant simulation (CYI-75 with a 6175°F theoretical combustion temperature) was identical to that used in the previous test phases of this program.

7.2 DUTY CYCLE

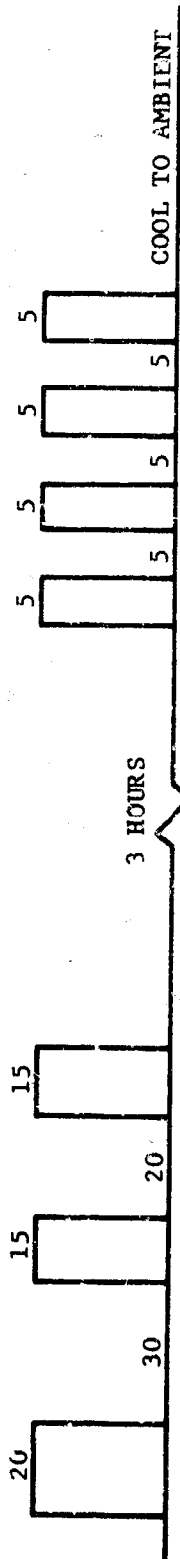
The specific duty cycle established for this test was based on two primary factors. It was considered the most severe combination of firing conditions that could be imposed on the nozzle while maintaining a satisfactory performance. The duty cycle was also chosen as being representative of a fictitious but realistic mission requirement. Figure 7-1 illustrates the demonstration nozzle duty cycle.

CONFIDENTIAL

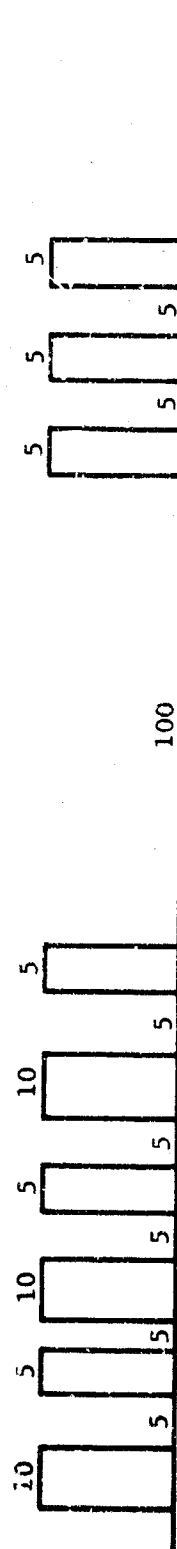
PHASE 1 - LAUNCH AND INITIAL ADJUSTMENT



PHASE 2 - MIDCOURSE CORRECTIONS



PHASE 3 - FINAL CORRECTIONS AND/OR INTERCEPT



NUMBERS REPRESENT TIME IN SECONDS EXCEPT WHERE OTHERWISE INDICATED

FIGURE 7-1. PROPOSED DEMONSTRATION NOZZLE DUTY CYCLE

FO4482 U

CONFIDENTIAL

THIS PAGE IS UNCLASSIFIED

CONFIDENTIAL

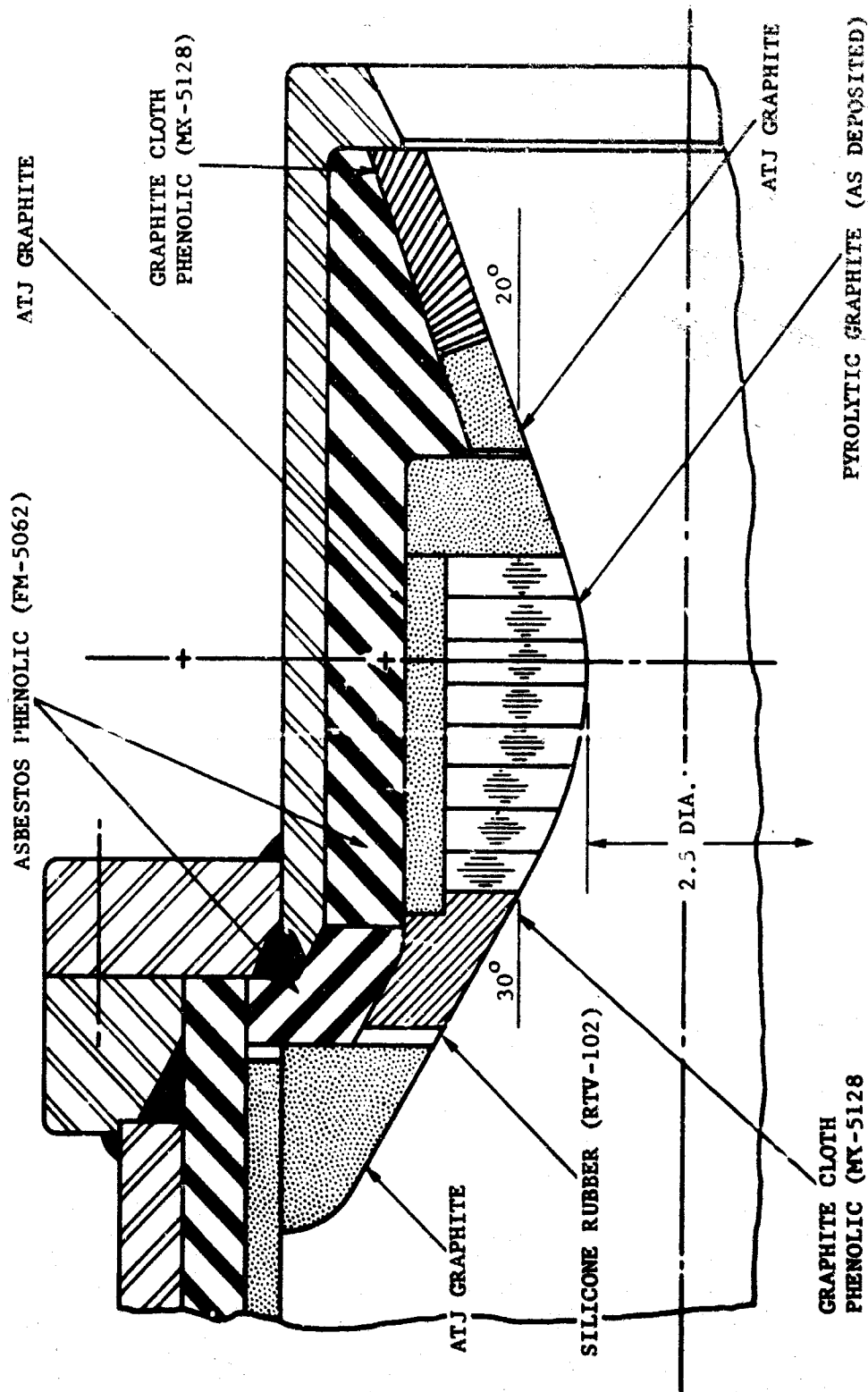
7.3 NOZZLE DESIGN

The nozzle designed for the demonstration test is illustrated in Figure 7-2. The contour and internal configuration is basically the same as that used throughout the earlier test phases. The basis for materials usage and specific design criteria are described in the following paragraphs.

The choice of as-deposited pyrolytic graphite for the throat material was based on several considerations. As explained in Sections 5 and 6, edge grained pyrolytic graphite and tungsten were the only logical throat candidates for restartable solid propellant rocket nozzles of this size and subjected to this test environment. Pyrolytic graphite was chosen rather than tungsten because of the more predictable behavior of the former. Prior test efforts have shown that its use is primarily a function of chemical corrosion and its thermal response. Provisions for thermal expansion can be easily and reliably made in nozzle design. Although tungsten offers superior corrosion resistance with the attending possibility of an extended duty cycle, its reliability is questionable. Because of problematical design considerations such as throat obstruction at extended firing durations due to insert backside melting resulting from a tungsten-carbon reaction, and from shrinkage, the use of tungsten carries with it a possibility of failure. It was believed advantageous to accept the possible lower duty cycle limits of pyrolytic graphite than to chance the catastrophic failure mode of tungsten. The ultimate choice of the as-deposited state of pyrolytic graphite over the annealed or partially annealed states was dictated by a lack of sufficient data concerning the advantages of the latter two forms over the former.

The pyrolytic graphite throat stack is contained in an 0.5-inch thick ATJ graphite ring which overhangs the upstream pyrolytic graphite washer 0.25 inch and has a 5 mil clearance between its ID and the OD of the throat. The overhang is calculated to result in the forward surfaces of the ATJ and pyrolytic graphites being in the same radial plane when both are fully expanded during firing. The clearance between the ATJ and pyrolytic graphite allows unrestricted radial thermal expansion of the pyrolytic graphite while providing sound structural support for the hot pyrolytic graphite washers. Axial thermal expansion of the pyrolytic graphite is provided for by a gap forward of the entrance section. The width of this gap is designed to 110 percent of the maximum pyrolytic graphite and ATJ graphite expansion. The gap is filled with an RTV type silicone which forms a char which is easily crushed to 10 percent of its original thickness. Thus, the pyrolytic graphite is virtually unrestrained in thermal expansion. This procedure has been found by Aeronutronic to eliminate delamination and "elephant footing" of the pyrolytic graphite which would otherwise occur. Based on the previous tests, described in Sections 5 and 6, there was no requirement for springs or other devices to account for axial thermal expansion.

CONFIDENTIAL



FO4483 U

FIGURE 7-2. NOZZLE DESIGN FOR DEMONSTRATION TEST

CONFIDENTIAL

THIS PAGE IS UNCLASSIFIED

CONFIDENTIAL

The heat sink limitation of the throat was based on two complementary considerations. The first of these considerations was a limiting b/a, or washer to throat diameter ratio, which was imposed to prevent spallation of the throat surface. A detailed discussion of this effect is contained in Paragraph 3.2 of this report. The complementary restriction to heat sink size was a requirement for a specific insulation thickness designed for the 200 seconds of firing in the proposed duty cycle. This thickness requirement was determined from the empirical predictions illustrated in Figures 5-10 and 5-11. The aforementioned factors, coupled with nozzle holder size, effectively dictated the internal dimensions of the nozzle.

The decision to utilize an ablative plastic entrance was a direct outgrowth of the earlier test phases and, in a sense, parallels the reasoning behind the decision to use pyrolytic graphite rather than tungsten as a throat material. The high probability of catastrophic failure of a polycrystalline graphite entrance which was adequately demonstrated during the earlier test phases dictated the use of an ablative plastic entrance and the acceptance of an inherently higher erosion rate. It must be re-emphasized that this decision was made with an awareness that both types of entrances considered leave much to be desired in terms of satisfactory performance (see Paragraph 6.2).

The combination of materials utilized in the nozzle exit section was chosen primarily as being representative of materials and material configurations that could easily be converted to a flight weight nozzle. No specific problem areas were anticipated for this section of the nozzle.

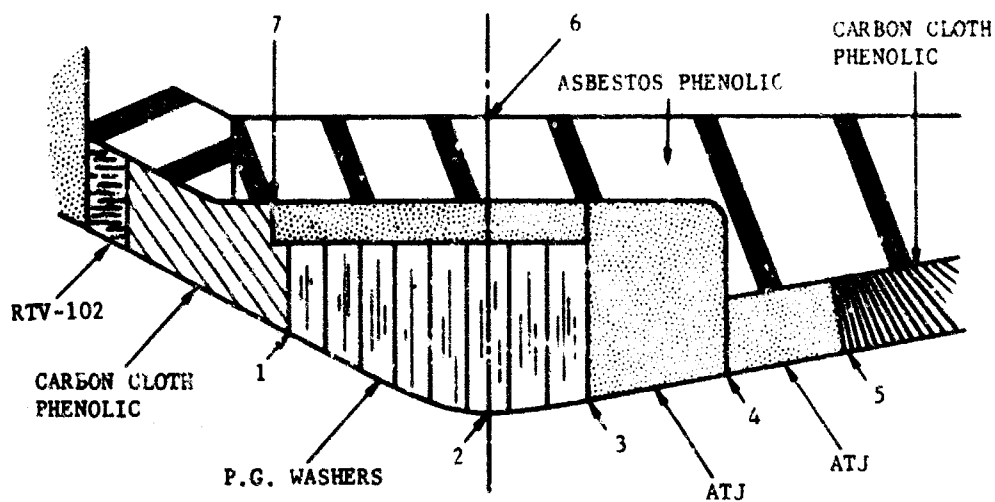
7.4 TEST RESULTS

7.4.1 NOZZLE NO. 1

A demonstration nozzle was fabricated from the design described above, and tested under the conditions outlined in Paragraph 7.1. Approximately two seconds prior to completion of the initial 50-second firing (see Figure 7-1), a chamber burn through occurred due to malfunction of the simulator slurry injection system. The nozzle was apparently unharmed, but accomplishment of the 20-second firing of Phase 1 was delayed. The duty cycle was continued after repairs were effected on the chamber and simulator. A second catastrophic failure of the simulator caused an explosion of the motor chamber which destroyed the nozzle. Data was recorded, and nozzle performance for the 48-second firing was compiled. This performance coupled with post test insulator analysis is shown in Figure 7-3. It is of interest to compare the nearly identical throat erosion performance and insulation performance (K values) for the aborted 50-second test with the full 200-second duty cycle run on the nozzle described in the following paragraph.

CONFIDENTIAL

CONFIDENTIAL



STATION NO.	BEFORE		AFTER 50 SECONDS			
	DIAM IN	ϵ	DIAM IN	dr/dt MIL/SEC	δc IN	K
1	4.28	2.9	4.88-4.98	6.2-7.2	—	—
2	2.62	1	2.664	0.45	—	—
3	3.23	1.6	3.45	2.3	—	—
4	4.22	2.7	4.22	2.05	—	—
5	5.21	4.3	5.30	0.93	—	—
6	—	—	—	—	0.29	0.416
7	—	—	—	—	0.18	0.546

FOI484 C

FIGURE 7-3. RESTART DEMONSTRATION TEST NO. 1 NOZZLE PERFORMANCE

CONFIDENTIAL

CONFIDENTIAL

7.4.2 NOZZLE NO. 2

A second demonstration nozzle was fabricated from the same design as the original and fired in accordance with the duty cycle shown in Figure 7-4. This actual duty cycle differed from the planned one (Figure 7-1) in minor detail only. Table 7.1 shows the nozzle throat performance throughout the various phases of the duty cycle. The gross erosion which occurred in one quadrant of the nozzle took place during the first 50-second pulse and has been attributed to simulator malfunction which allowed an oxygen rich flow over the affected quadrant. A comparison of chamber pressure throughout the various phases of the duty cycle (Figure 7-5) with the erosion data of Table 7.1 indicates the overall adequate performance of the nozzle except during the simulator malfunction. Figure 7-6 is a pictorial representation of cumulative erosion rate versus time data taken from Table 7.1. The average erosion rate of 0.427 mil/sec (Table 7.1) for the total firing time of 200 seconds compares favorably with the 0.450 mil/sec erosion rate experienced on the original demonstration nozzle (Figure 7-3).

The performance of the FM-5062 asbestos phenolic in both the entrance and throat sections was almost precisely as predicted. Table 7.2 gives the K values based on char thickness and total run time. The close comparison with the K values obtained in the original demonstration test (Figure 7-3) is significant since the insulation of the original nozzle was subjected to but one 50-second firing whereas the insulation of this nozzle underwent 19 separate firings with the various associated heat soak durations. This substantiates the empirical method for the prediction of insulator char growth derived in Reference 5.1, and utilized throughout the program to calculate insulator requirements. As the use of this equation implies, char formation for an insulation material is a function of total actual firing time and is independent of the number of restarts as well as the duration of heat soak. This can be explained by the apparent fact that heat soak back time during coast periods is totally offset by the lag time on restart.

The exit section of the nozzle performed as was expected. Erosion was uniform and varied inversely as to exit area ratio as shown in Figure 7-7. No particular problems were anticipated or encountered with the exit portion of the demonstration nozzle.

Figures 7-8 and 7-9 are photographs of the nozzle throat from the entrance and exit sections, respectively, and illustrate the throat condition after Phase 1 of the duty cycle (75 seconds of firing). Figure 7-10 is a photograph of the sectioned nozzle after completion of the 200-second duty cycle. Figure 7-11, a picture of the same segment, illustrates the nozzle contour after completion of testing.

CONFIDENTIAL

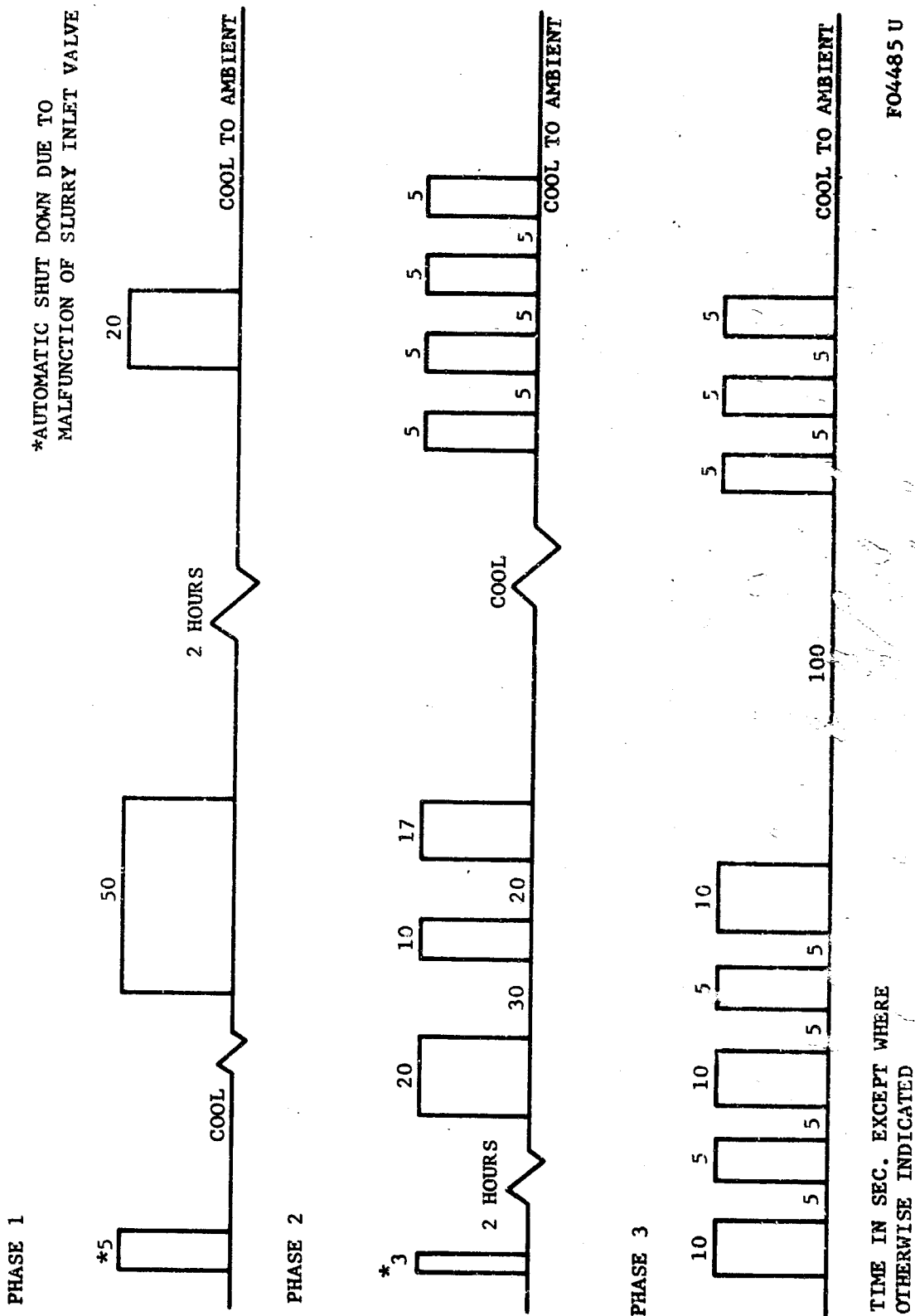


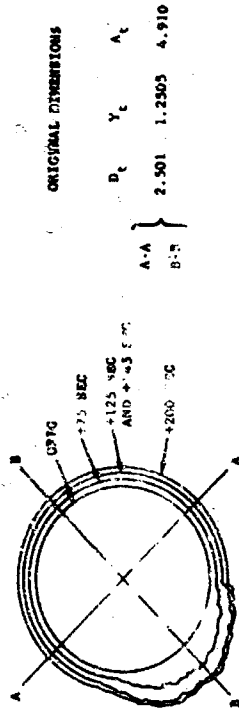
FIGURE 7-4. DEMONSTRATION DUTY CYCLE AS ACTUALLY FIRED

CONFIDENTIAL

THIS PAGE IS UNCLASSIFIED

CONFIDENTIAL

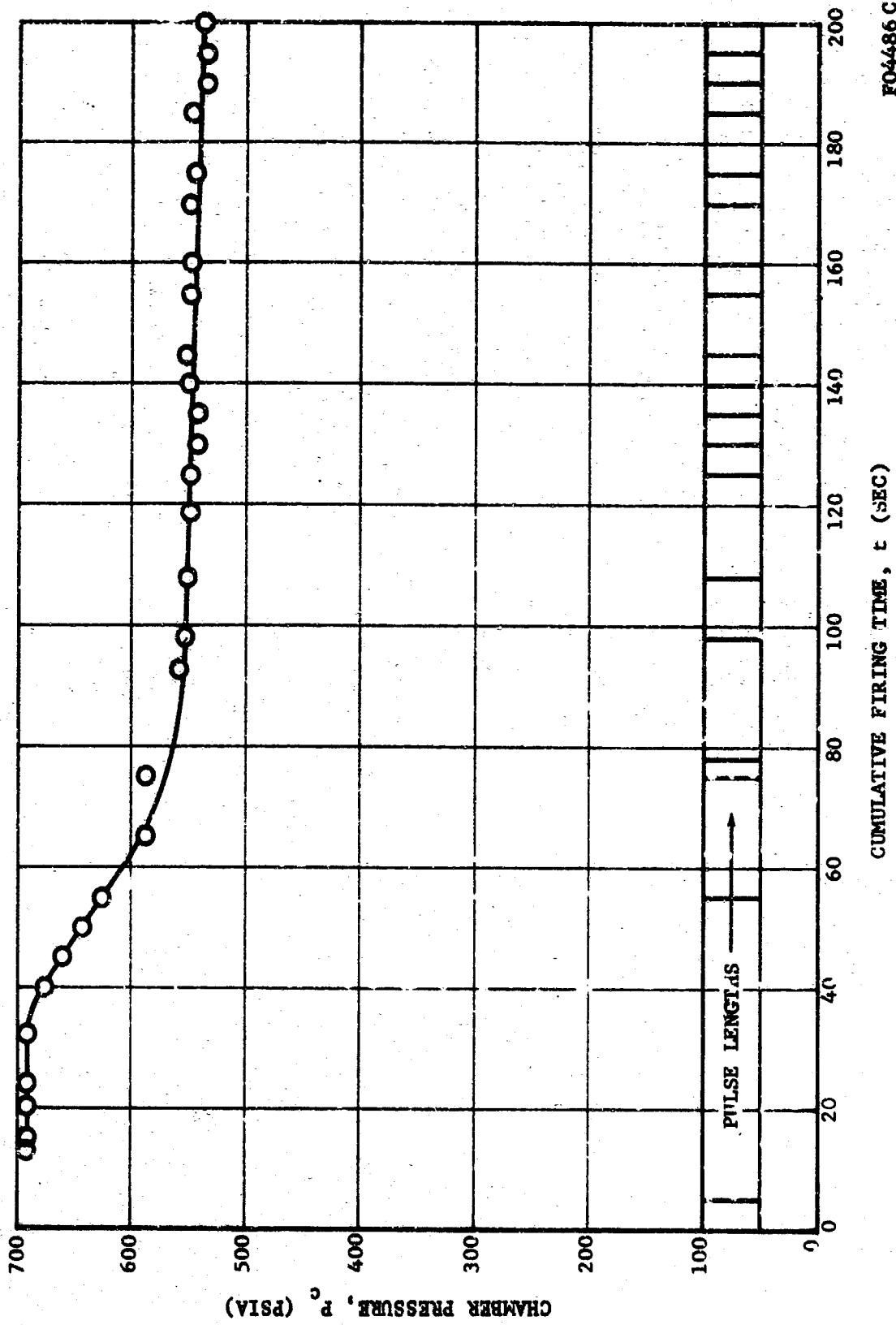
TABLE 7.1
RESTART DEMONSTRATION NOZZLE THROAT PERFORMANCE



Firing Conditions	Time between shots (sec)		Total Δt (sec)		D _c (in.)		A _c (in.)		Y _c (in.)		Total Δt _c (in.)		Δt _c (in.)		dr/dt (mm)		tot dr/dt (mm)		ΔA _c (in.)		cum ΔA _c (in.)	
	55	55A	55B	55C	55D	55E	55F	55G	55H	55I	55J	55K	55L	55M	55N	55O	55P	55Q	55R	55S	55T	55U
Fire 5 sec																						
Cool to ambient																						
Fire 50 sec																						
Cool 2 hours																						
Fire 20 sec																						
Cool to ambient																						
Fire 3 sec																						
Cool 2 hours																						
Fire 20 sec																						
Cool 30 sec																						
Fire 10 sec																						
Cool 10 sec																						
Fire 17 sec																						
Cool to ambient																						
Fire 5 sec-off 5 sec/fire																						
5 sec-off 5 sec/fire 5 sec																						
off 5 sec/fire 5 sec-cool																						
Fire 10 sec-off 5 sec																						
Fire 5 sec-off 5 sec																						
Fire 10 sec																						
Cool 100 sec																						
Fire 5 sec-off 5 sec																						
Fire 5 sec-off 5 sec																						
Fire 5 sec																						
Cool to ambient																						

CONFIDENTIAL

CONFIDENTIAL

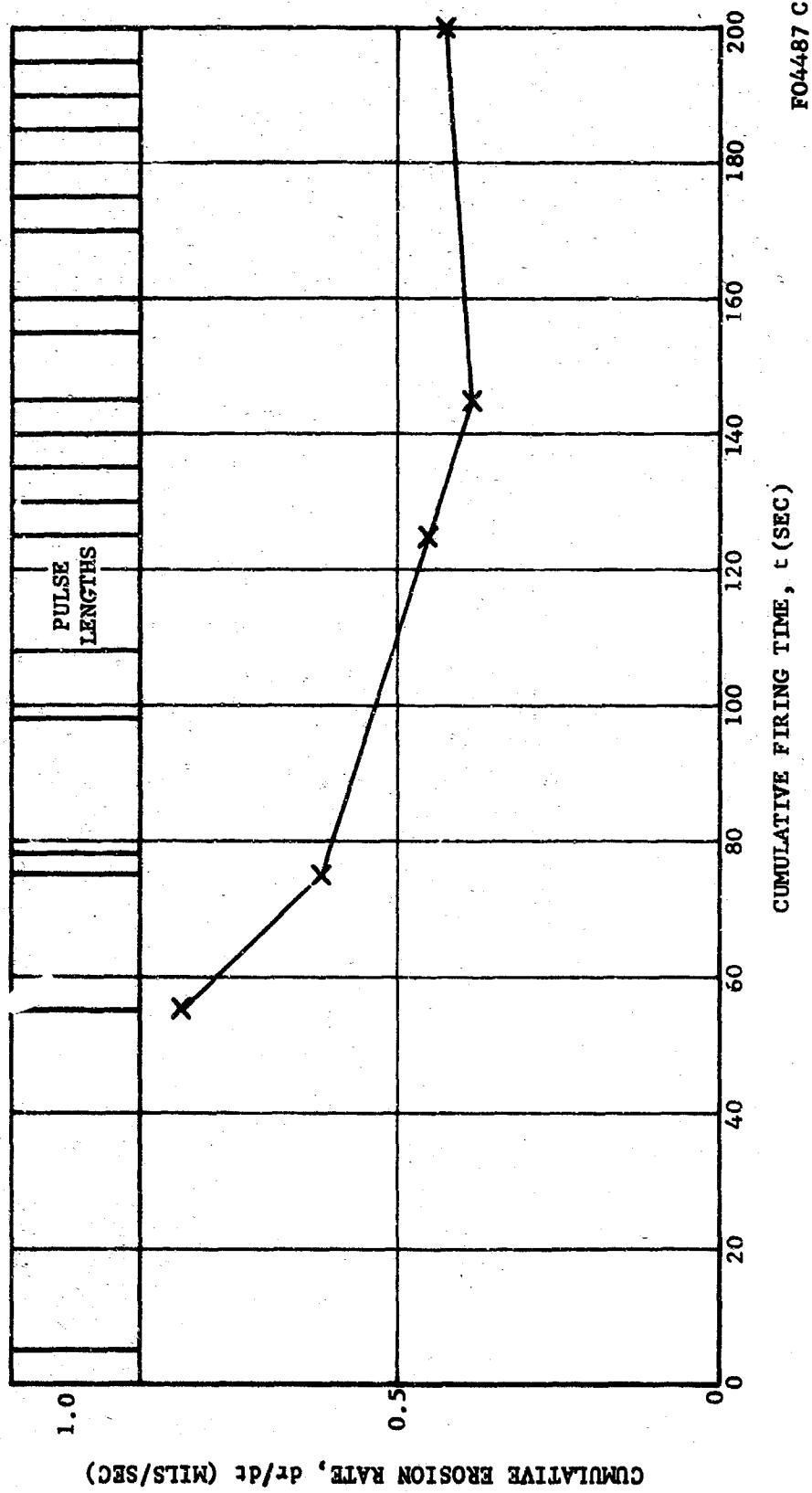


FO4486 C

FIGURE 7-5. DEMONSTRATION NOZZLE CHAMBER PRESSURE VERSUS CUMULATIVE FIRING TIME

CONFIDENTIAL

CONFIDENTIAL



FO4487 C

FIGURE 7-6. DEMONSTRATION NOZZLE CUMULATIVE THROAT EROSION RATE VERSUS CUMULATIVE FIRING TIME

CONFIDENTIAL

CONFIDENTIAL

TABLE 7.2
INSULATOR EVALUATION-DEMONSTRATION MOTOR TEST

<u>Material</u>	<u>Description</u>	<u>K</u>	
		<u>Entrance</u>	<u>Throat</u>
Asbestos Phenolic	FM-5062	0.056	0.042

$k = \delta_c / \sqrt{t}$

where

δ_c = char thickness, inches

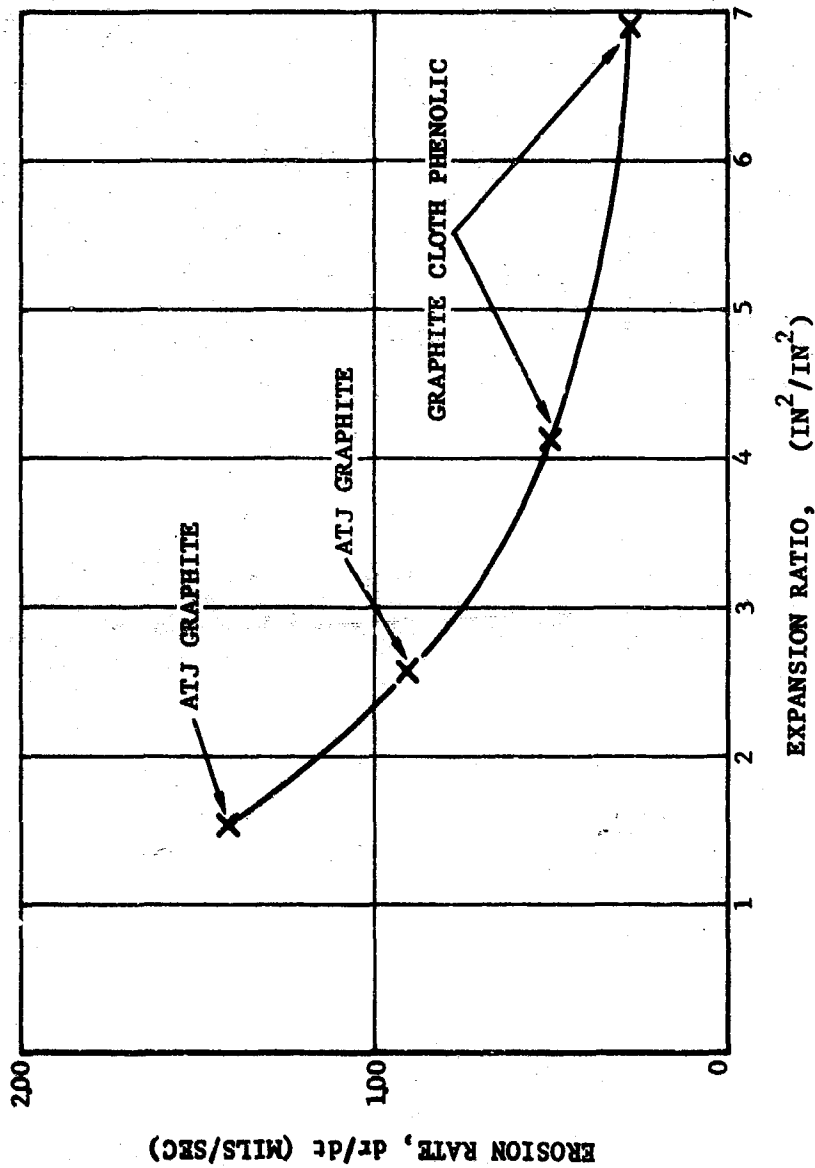
t = firing time, seconds

K = characteristic constant of char growth

CONFIDENTIAL

THIS PAGE IS UNCLASSIFIED

CONFIDENTIAL



FO4488 C

FIGURE 7-7. EROSION RATES OF EXIT CONE SEGMENTS VERSUS EXPANSION RATIO FOR DEMONSTRATION NOZZLE

CONFIDENTIAL

CONFIDENTIAL



FIGURE 7-2 DEMONSTRATION NOZZLE THROAT AFTER 75 SECONDS FIRING TIME

7-14

CONFIDENTIAL

THIS PAGE IS UNCLASSIFIED

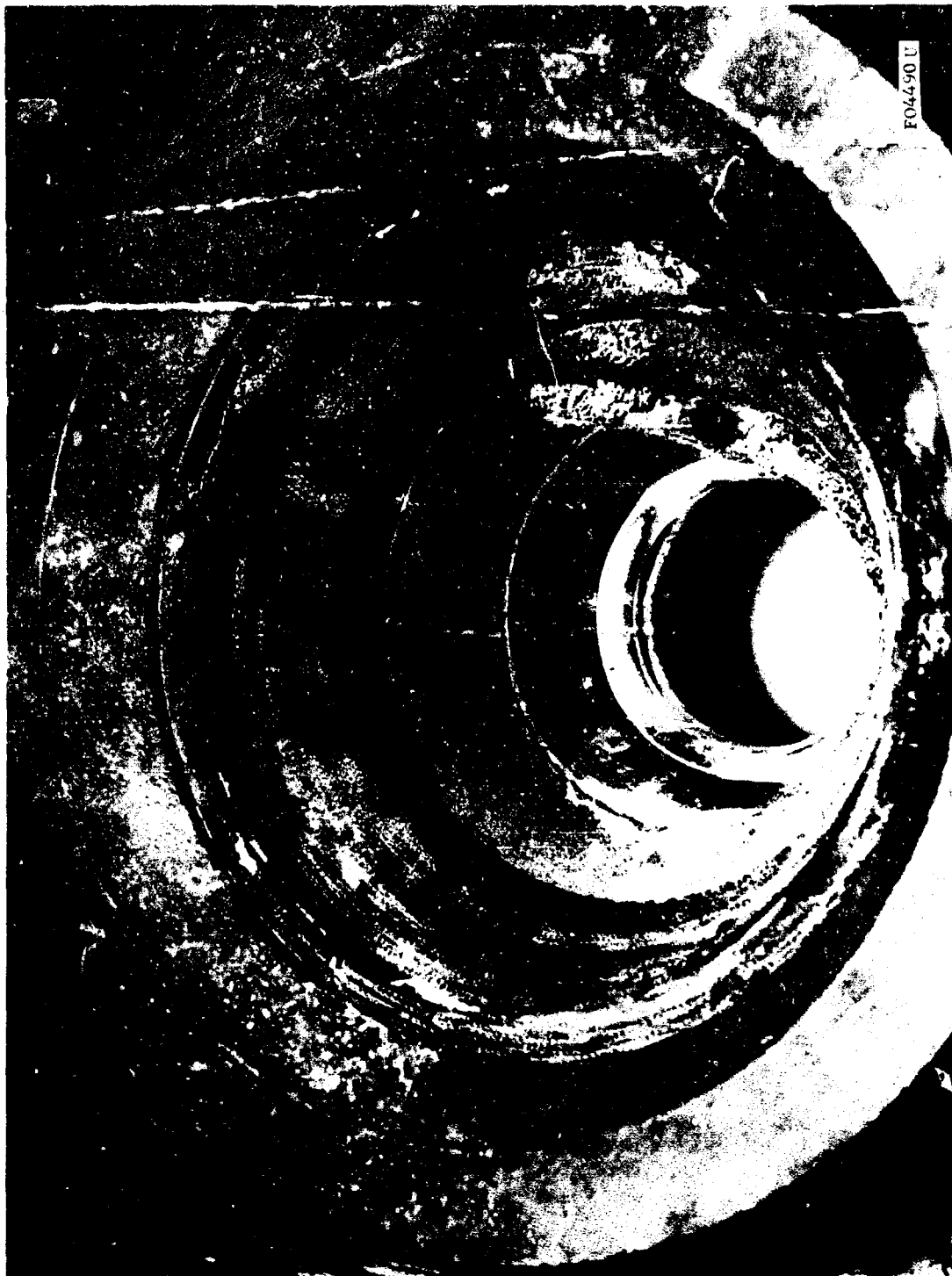


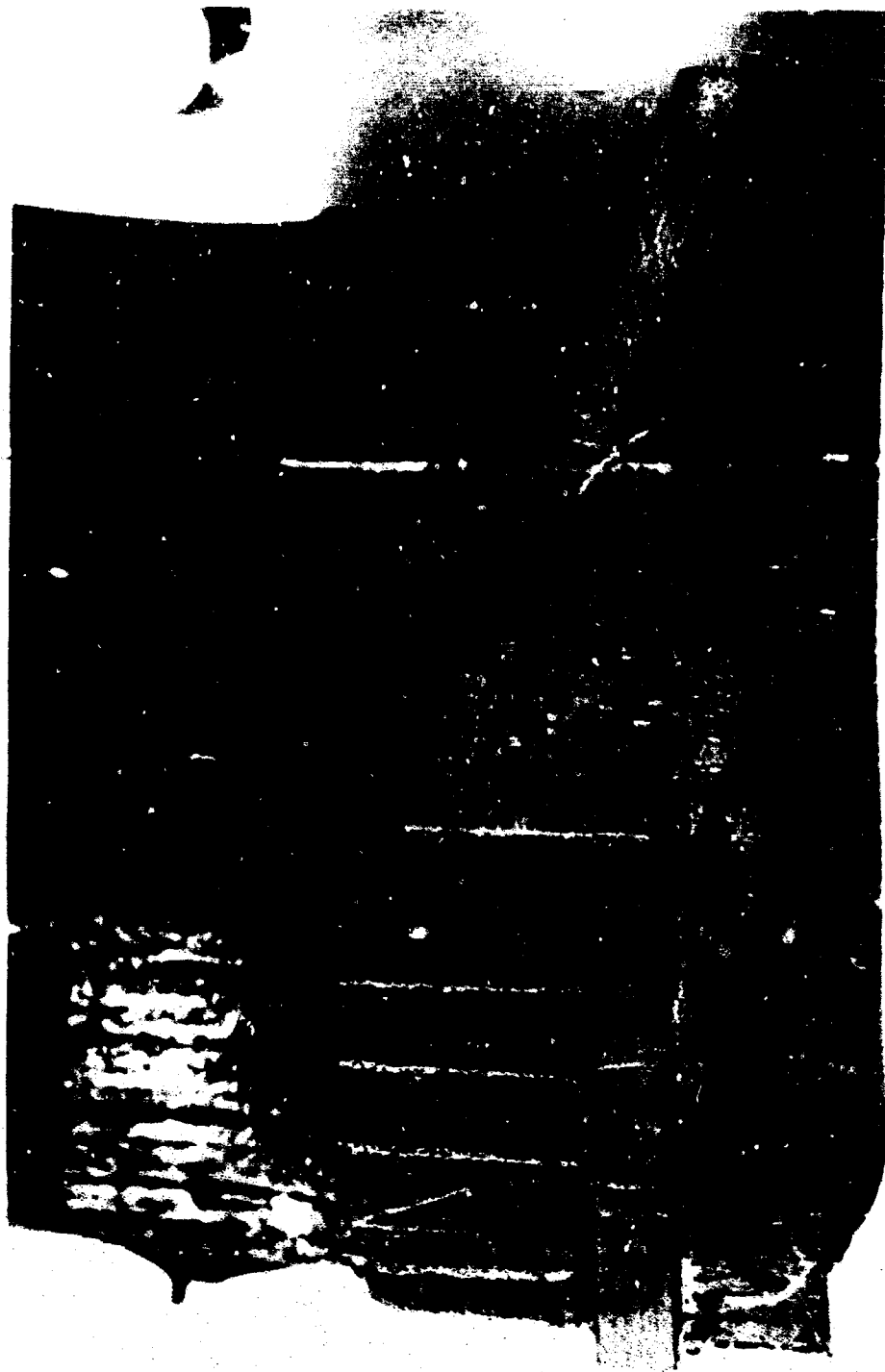
FIGURE 7-9 DEMONSTRATION NOZZLE THROAT AND EXIT CONE AFTER 75 SECONDS FIRING TIME



FO4491 U

FIGURE 7-10 DEMONSTRATION NOZZLE THROAT CROSS SECTION
AFTER TEST (200 SECONDS)

CONFIDENTIAL



FO4492 U

FIGURE 7-11 DEMONSTRATION NOZZLE CONTOUR AFTER TEST (200 SECONDS)

7-17

CONFIDENTIAL

THIS PAGE IS UNCLASSIFIED

CONFIDENTIAL

The performance of the entrance section can only be described as inadequate . It was found necessary to replace entrance sections after Phase 1 (75 seconds) and Phase 2 (145 seconds) since they were deemed unserviceable after each phase. If the duty cycle were extended beyond the 200 secondr, a third entrance section would have been required. The graphite cloth phenolic was replaced with equivalent ATJ graphite sections for Phases 2 and 3 of the duty cycle. Performances of all entrance sections were comparably poor. The demonstration test reaffirmed the data obtained from the rocket motor and development test's in terms of nozzle entrance sections for restartable solid rocket motors (see Paragraph 6.2). It is obvious from the test phases of this program that a satisfactory solution to this problem is the pacing item for the advancement of restartable solid propellant rocket nozzle technology.

CONFIDENTIAL

CONFIDENTIAL

SECTION 8

COMPARISON OF ANALYTICAL AND EXPERIMENTAL DATA

Within this section, data are presented from the series of rocket motor and development nozzle tests to illustrate the relationships and the correlations between various analyses used in this program and the actual test results. Much of the material presented here has been previously discussed elsewhere in this report; however, it is believed that a better understanding of capability and comparability of the various analyses can be obtained if they are presented in comparison with the corresponding test results.

Each component of the nozzle - entrance section, throat, exit section, and insulation - is discussed separately. The materials used in each component form the basis for discussion. A direct comparison of test results with analysis can be made only for the throat sections and for the insulation materials. Difficulties have been encountered in both the thermal and structural analyses of the entrance sections. These difficulties have precluded any analytical prediction of the behavior of these sections. No problems were anticipated in the exit sections of the subscale nozzles; therefore, no analyses were performed.

The primary objective of the rocket motor tests was not to provide a basis for correlation of analytical work but rather to investigate problem areas individually by providing materials evaluations and problem definitions. Only as a secondary objective was there to be a correlation of analytically predicted phenomenological occurrences with those observed in the tests. These events include the occurrence of certain structural responses such as the development of fractures and spallation, and occurrence of erosion and the deposition and removal of condensed phases such as alumina.

CONFIDENTIAL

The development nozzle tests were designed to apply the data and knowledge gained from previous tests and analyses so that a translation of technology could be made to the demonstration nozzle tests. Also, additional problem areas were sought especially in terms of sealing and in application of duty cycles to designs. Additional correlation of analysis with test data was sought in this test phase.

8.1 ENTRANCE SECTIONS

The major effort devoted to entrance sections was in the structural area, since so many failures and problems were encountered in this area. Thermal analysis was limited due to severe erosion-corrosion problems.

8.1.1 ENTRANCE SECTION CORROSION

Regression or corrosion rates of the graphite entrance section can be calculated using the simplified equilibrium corrosion theory presented in Paragraph 2.5.3. Figure 8-1 shows the surface temperature versus time for three locations in development nozzle number 3 (as deposited pyrolytic graphite throat). Also given are the calculated heat transfer coefficients at two designated locations in the entrance section and at the throat. With these coefficients and the temperature history, the "theoretical" surface regression was calculated for the entrance section; that is, locations (1) and (2) in Figure 8-1. After the first pulse or phase of the duty cycle imposed on this nozzle, diameter measurements were made at locations (1) and (2). Pretest measurements were also recorded.

The calculated and measured values are given below:

<u>Location</u>	<u>Calculated Δr</u>	<u>Measured Δr</u>
(1)	0.035 inch (0.029)	0.050 to 0.065 inch
(2)	0.067 inch (0.052)	0.110 to 0.120 inch

As can be seen, the agreement is not too good, especially since the total corrosion is reduced (numbers in parentheses above) when consideration is made for the Al_2O_3 deposit on the entrance section at least up to surface temperatures of $3700^\circ F$. As mentioned previously in Paragraph 2.5.3, the theory of corrosion in rocket nozzles is poorly understood at present and much additional effort is required in this area. The influence of particle erosion may have contributed to the large surface regressions measured as well as the result of pyrolysis gas flow. It is not clear at this time which mechanisms are predominant in causing these "higher than calculated" rates. Observation of the onset of surface loss and its characteristics are not readily measurable for the entrance section as they are in the throat region.

CONFIDENTIAL

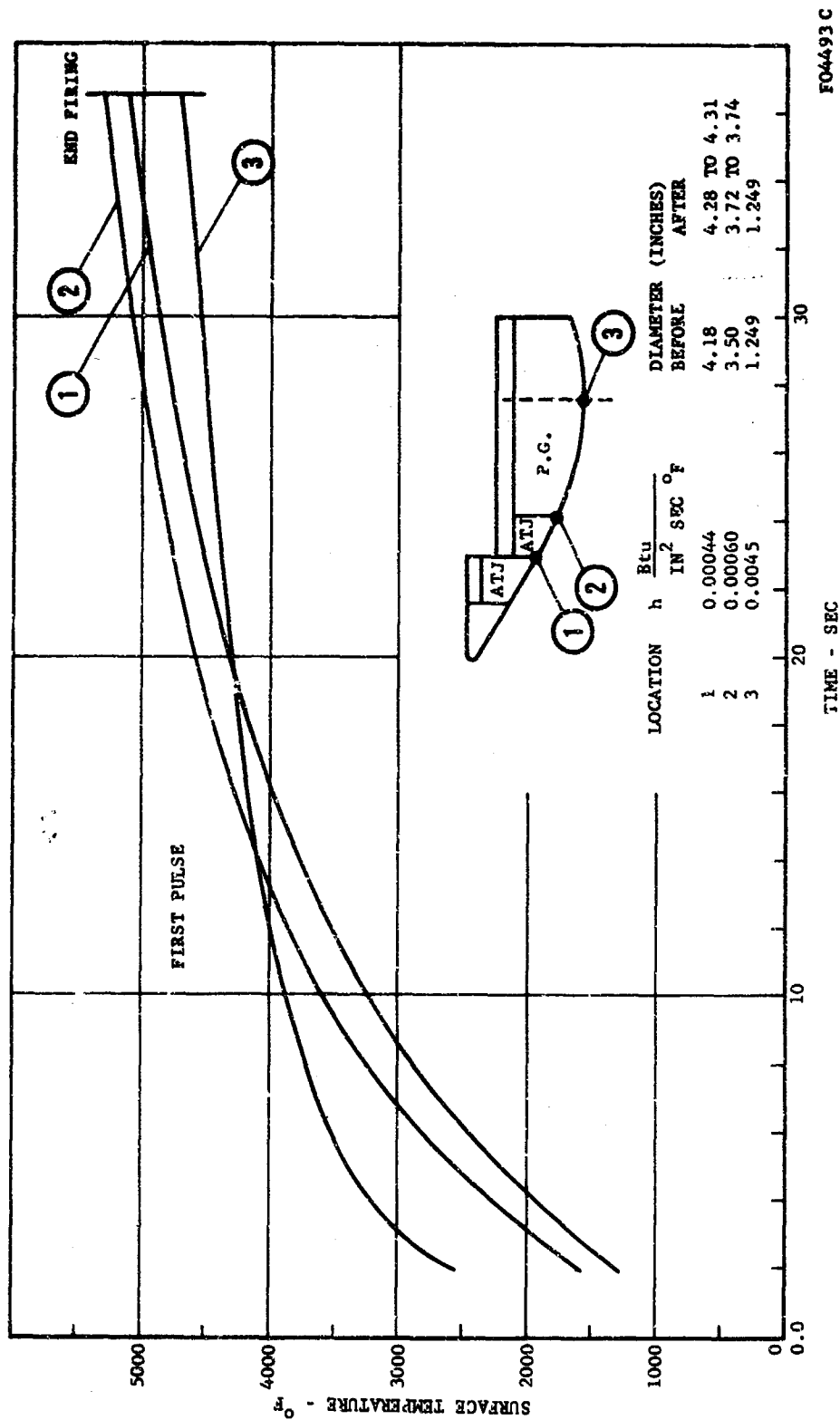


FIGURE 8-1. SURFACE TEMPERATURE VERSUS FIRING TIME FOR 1.25 INCH AS-DEPOSITED P.G. DEVELOPMENT NOZZLE (TEST NO. 3)

FO4493 C

CONFIDENTIAL

CONFIDENTIAL

8.1.2 ENTRANCE SECTION - STRUCTURAL ANALYSIS

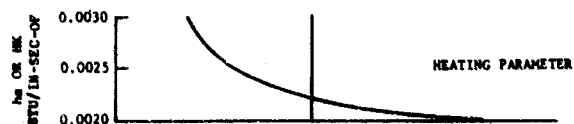
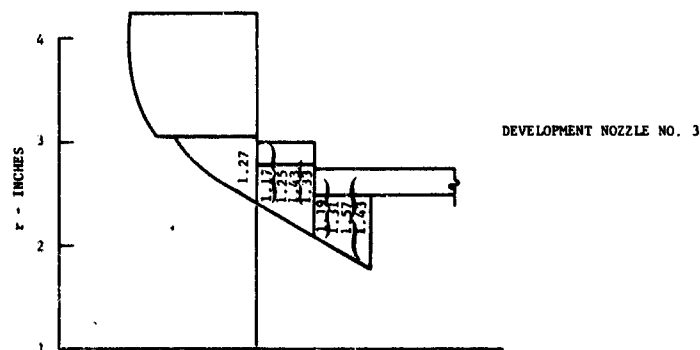
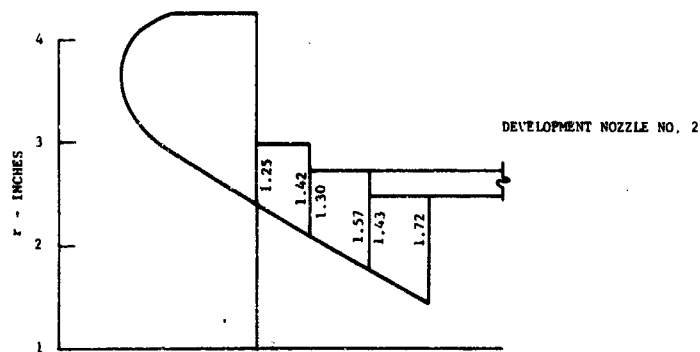
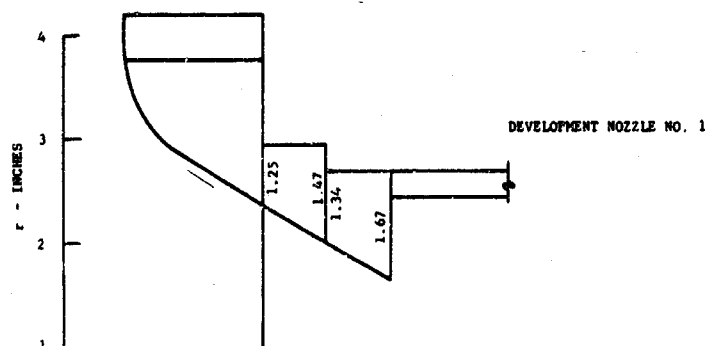
Generally, because of the failure to generate a working computer program for the structural analysis of conical sections, no structural analysis could be performed on the entrance sections. Entrance sections performed rather poorly from a structural viewpoint and/or from a surface regression viewpoint in all of the nozzles tested in this program. Although the reinforced plastics developed no structural problems when used as entrance flamefront materials, their regression rates were quite high. Though the basic regression rates of the polycrystalline graphites were not so high, they developed severe crack patterns which accelerated the material loss. In many cases, this resulted in loss of a sizable portion of the entrance flamefront material either by abundant surface regression or by pieces being blown out through the throat.

Since no structural analysis tools existed for the examination of these components, physical rationale based on behavior characteristics of cylindrical sections, was employed to redesign these entrance sections for the development test nozzles. It is known that short cylinders experience a lowered stresses response (by a factor of 1- ν) compared to long cylinders. Thus, the first step in the redesign was to section the entrance into washers with conical flamefront contours and cylindrical backside contours. These washers were then split circumferentially into two rings to create a washer within a washer with an intimate fit at the interface. This interface then served as a crack-stopper for any tensile cracks which would be initiated on the outer surface of the outer washer. By having the two washers fit intimately, the stress response would be virtually identical to that of an unsplit washer since axial effects essentially vanish. The outer washer could then be expected to develop fracture surfaces initiating at the outer radius, but these cracks would not propagate past the circumferential interface of the two parts. The outer cracked part would still be in place to provide backup restraint as long as the ablating insulator provided backup to it.

There were three nozzles on which these design changes were incorporated and for which any analytical predictions could be made. These were the first three development nozzles. The entrance section designs are shown in Figure 8-2 along with the heating parameter. The β ratios at the upstream and downstream faces of the washers are shown in the figure. The first two entrance sections merely incorporated a washer design without the crack stopper feature. Due to scheduling, the second nozzle had to be designed before the first nozzle was fired. However, the third entrance section was designed with the benefit of the results of the firing of the first nozzle.

Relating the heating parameter to the allowable β ratios for those washers lying downstream of the entrance nose piece shows that the allowable β ratios lie in a very narrow range of about 1.43. The upstream faces of

CONFIDENTIAL



FO4548 C

FIGURE 8-2. DEVELOPMENT NOZZLE ATJ ENTRANCE SECTIONS

CONFIDENTIAL

CONFIDENTIAL

the washers in development nozzles 1 and 2 have ratios of β at or below this value, while the β ratios at the downstream faces exceed this value. High values of α and E were used for ATJ so this analysis should be conservative, assuming that a washer is a good approximation to the short conical components.

In the first two nozzles, all of the washers cracked during the first firing. This was not anticipated since a conservative approach was used in their design. The nature of the fractures (in the radial-axial plane) indicated that they resulted from hoop tensile stress. This indicated that the analysis, based on the minimum β ratio for the short conical components, was not adequate and that a more conservative design could be obtained by basing the analysis on the maximum β ratios at the downstream faces of the washers.

The entrance section of the third development nozzle was designed to incorporate circumferential crack stoppers if the backside tensile fractures should develop again. This technique was also carried to the massive nose piece of the entrance. In this design, only one value of β exceeds the 1.43 limit and that was for the downstream face of the aftmost washer when the outer ring is included. None of these washers cracked during the first firing. This indicated that, by basing the analysis on the greatest (or downstream) value of β , satisfactory analysis could be performed. Testing difficulties prevented obtaining meaningful results on subsequent firings of this nozzle.

This design technique has limitations for small diameter components. To stay below small ratios of β at the downstream face, thin (radially) washers become necessary. When the washer radial thickness is less than that needed to provide for normal surface regression, this limitation has been exceeded.

8.2 THROAT SECTIONS

Correlations of convective heat transfer, chemical corrosion, and structure behavior are presented in this section. Also presented are materials phenomena as experienced during the test phases of this program.

8.2.1 CONVECTIVE HEAT TRANSFER

A comparison is made between the analytically predicted convective heat transfer coefficient at the nozzle throat with that obtained during the development motor tests. The analytical prediction, presented in Paragraph 2.1.3, is modified herein to account for the effects of deposition of Al_2O_3 on the nozzle throat.

CONFIDENTIAL

In this discussion of the correlation procedure, only the first starting cycle is treated; the effects of ablation on the heat transfer coefficient may be neglected for the nozzle in question. The effect of deposition may be approximately accounted for by the following procedure:

The one-dimensional characteristic mass flow velocity is defined as

$$C^* = \frac{P_c A^* g_c}{\dot{W}} \quad (1)$$

where

P_c = chamber pressure

A^* = throat area

g_c = conversion factor 32.2 lbm ft/lb_f sec²,

\dot{W} = propellant weight flow

By requiring isentropic perfect gas flow in the inviscid stream and employing Bernoulli's equation, C^* may be also given by

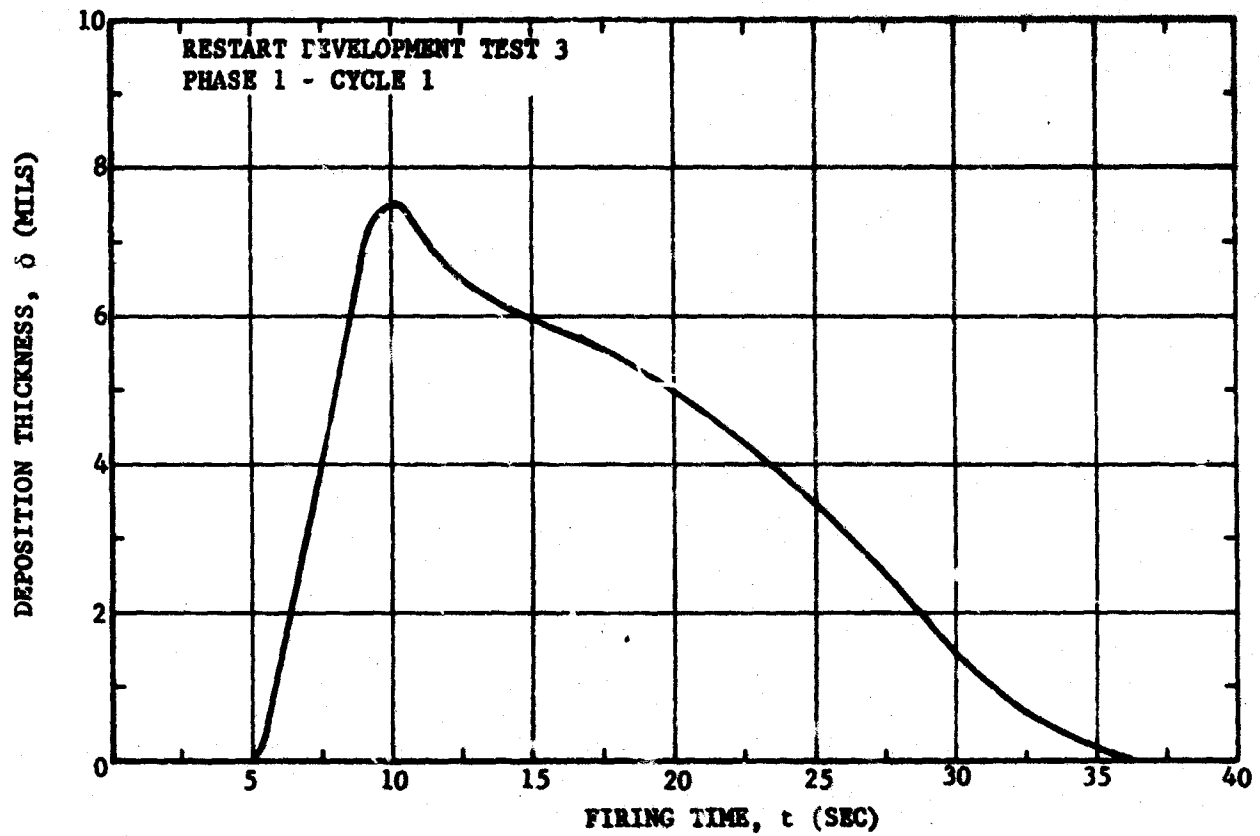
$$C^* = \frac{1}{\sqrt{\gamma}} \left(\frac{\gamma+1}{2} \right)^{\frac{\gamma+1}{2(\gamma-1)}} \left(\frac{P_c}{RT_c} \right)^{1/2} \quad (2)$$

In their early solid rocket internal ballistic calculations, von Karman and Malina (Reference 8.1) proved that an appreciable chamber pressure change did not correspond to a significant change in chamber temperature; therefore, C^* is assumed constant throughout the firing period of uniform propellant mass flux. The deposition thickness at the nozzle throat is only a function of the instantaneous chamber pressure and may be written as

$$\delta = r_o^* \left[1 - \left(\frac{P_{co}}{P_c} \right)^{1/2} \right] \quad (3)$$

where the zero subscript refers to the initial condition at the start of the run. Figure 8-3 shows the throat deposition thickness as a function of time for the nozzle in question; the plot is calculated from a measured chamber pressure versus time distribution.

CONFIDENTIAL



FO4494 C

FIGURE 8-3. Al_2O_3 DEPOSITION ON NOZZLE THROAT VERSUS TIME

CONFIDENTIAL

CONFIDENTIAL

A reasonably accurate expression for the total heat absorbed by a throat washer is

$$\frac{Q_T}{A} = \frac{T_{\text{equil}}}{A} \left[(\rho v c)_{\text{PG}} + (\rho v c)_{\text{ATJ}} \right] + \int_{t=0}^{t_{\text{equil}}} \left(\dot{q}_{\text{abl}} \right) dt \quad (4)$$

ρ is the material density, V is the volume, C is the specific heat (Btu/lbm^{°R}), pyrolytic graphite refers to the pyrolytic graphite washer, ATJ is the back-up piece, T_{equil} is the radial isothermal temperature, A is the hot side surface area of the washer (assumed independent of time), and \dot{q}_{abl} is the heat ablation (Btu/sec). For pyrolytic graphite backed with an ATJ heat sink, it has been found that the radial isothermal condition (T_{equil}) is reached approximately 30 seconds after shutdown. As indicated above, the ablation is negligible during the firing portion of the first run cycle. From $t = t_f$ to $t = t_{\text{equil}}$ there is some ablation; however, as was determined from study of the thermocouple traces, its effect on Q_T/A is considered small. Correctly speaking, there should be an axial heat conduction term in Equation 4, but its magnitude is usually small compared to the terms included.

In order to initiate the solution it is necessary to create a locus of Q_T/A versus h_{eff} values by repeated runs of the conduction-ablation program, using proper solid material thermal properties and the CYI-75 adiabatic wall temperature at the throat (6600^{°R}). The conduction-ablation program solves for the wall surface temperature, T_w , as a function of time for an assumed h_{eff} , the Q_T/A then being calculated by employment of (t_f is the 36.5 second firing time)

$$\frac{Q_T}{A} = \int_0^{t_f} h_{\text{eff}} (T_{\text{aw}} - T_w) dt \quad (5)$$

The resulting curve is shown on Figure 8-4. Equation 4 is then employed to give Q_T/A from the experimental thermocouple T_{equil} value. Using accepted thermal property data and a throat washer area of 2.27 in.², Equation 4 gives a measured Q_T/A value of 342 Btu/in.², which corresponds to an h_{eff} of 0.0056 Btu/in.²sec^{°R} (Figure 8-4).

CONFIDENTIAL

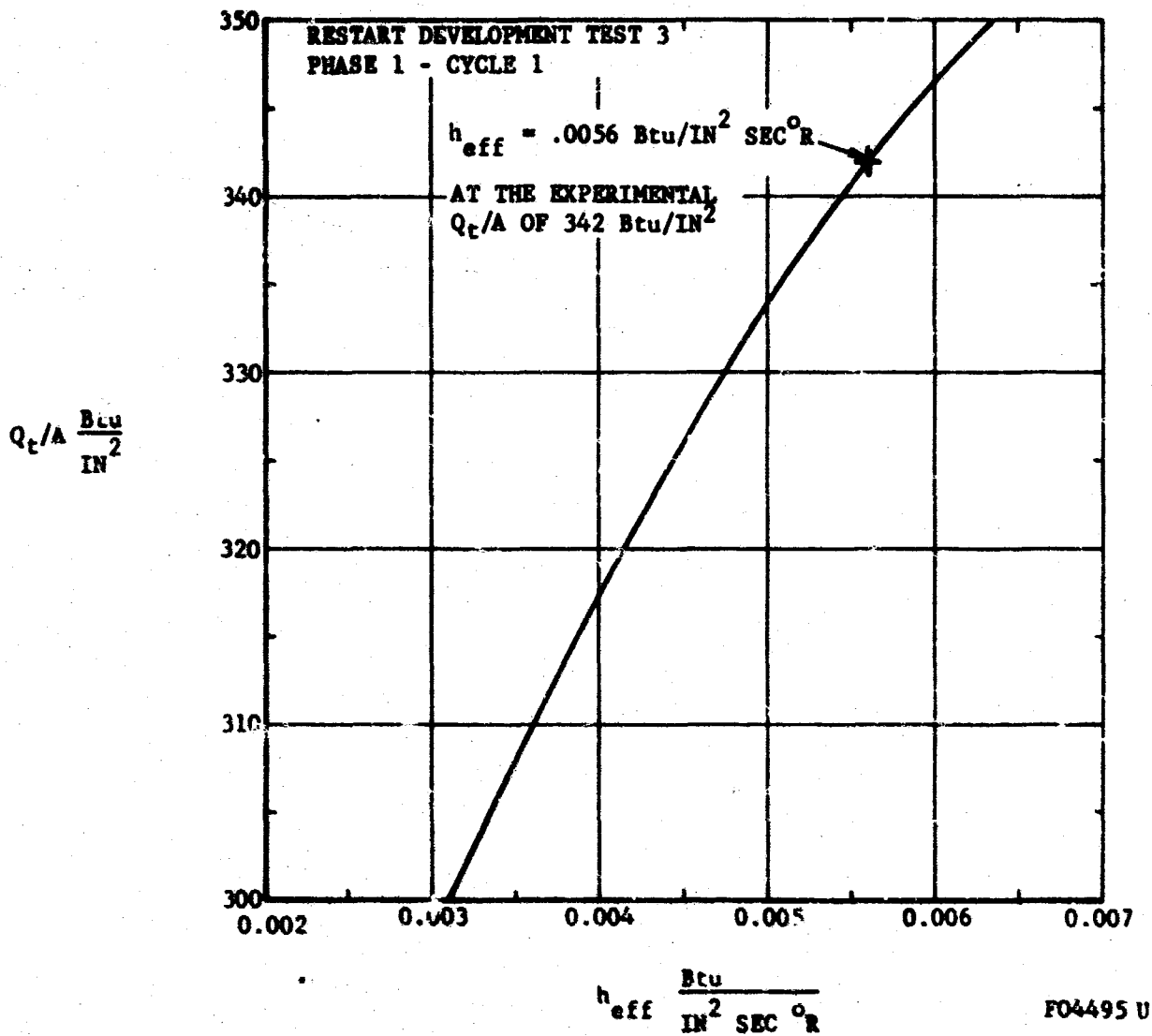


FIGURE 8-4 CONDUCTION - ABLATION PROGRAM CALCULATIONS OF TOTAL HEAT FLUX OVER A RANGE OF ASSUMED h_{eff} VALUES

CONFIDENTIAL

THIS PAGE IS UNCLASSIFIED

CONFIDENTIAL

This "measured" value of h_{eff} is now compared to the theoretical value obtained from a summation of the washer and deposit layer thermal resistivities written in the form

$$h_{eff} = \left[\frac{1}{t_f} \left\{ \int_0^{t_f} \left(\frac{1}{h_g} \right) dt + \int_0^{t_f} \left(\frac{\delta}{K} \right) dt \right\} \right]^{-1} \quad (6)$$

As is seen, the quantity h_{eff} differs from the gas side coefficient h_g (determined from the boundary layer solution) due to the presence of the deposited Al_2O_3 layer. Of course, there is a degree of measurement involved in Equation 6 since the deposition thickness δ was obtained from an experimental pressure versus time distribution. Employment of the boundary layer theory throat h_g value ($8.18(10^{-3})$ Btu/in.²sec^{OR}), which is assumed constant for the run period (an approximation), together with a t_f of 36.5 seconds and a K of $6.02(10^{-5})$ Btu/sec in.^{OR} gives a theoretical h_{eff} of 0.00572 Btu/in.²sec^{OR}, a value that is exceedingly close to the "measured" h_{eff} . The several assumptions made in this calculation, i.e., the supposedly correct value of K taken from solid rather than liquid Al_2O_3 measurements, and the constancy of h_g as a function of time, must be valid, or at least the errors induced by them should cancel each other out. It is thus seen that a throat h_g calculated from the real gas boundary layer program does accurately correlate, when adjusted for deposition, with the experimental data, and, as will now be shown, is decidedly superior to the Reference 2.1 perfect gas value or one obtained from the Bartz (Reference 8.2) pipe flow type correlation. The Bartz formula for the heat transfer coefficient is simply

$$h_g = \frac{0.026 C_p}{(D^*)^{0.2}} \left(\frac{\mu^{0.2}}{P_r^{0.6}} \right)_c \left(\frac{P_c R_c}{C^*} \right)^{0.8} \left(\frac{D^*}{r_c} \right)^{0.1} \left(\frac{A^*}{A} \right)^{0.9} \sigma \quad (7)$$

where

$$\sigma = \left[\frac{1}{2} \left(\frac{T_w}{T_c} \right) \left(1 + \frac{\gamma-1}{2} M^2 \right) \right]^{\frac{W}{5} - 0.8} \left[1 + \frac{\gamma-1}{2} M^2 \right]^{-\frac{W}{5}} \quad (7a)$$

The quantities are standard or have been defined elsewhere in this report. Although the original Bartz correlation employed the chamber C_p value, it has been determined that better results are obtained when a local "average"

CONFIDENTIAL

specific heat based on the local stagnation enthalpy and temperature differences across the boundary layer is employed, i.e.,

$$C_p = \frac{H_o - H_{w,z}}{T_{o,z} - T_{w,z}} \quad (6)$$

Figures 8-5 and 8-6 illustrate the uncorrected-for-deposition gas side coefficients for the three heat transfer theories, together with their respective throat h_{eff} values as corrected for deposition by employment of Equation 6. Also shown in the throat "experimental" value of h_{eff} (Equation 4 and Figure 8-4). The superiority of the real gas calculation, at least in the throat region, is clearly evident.

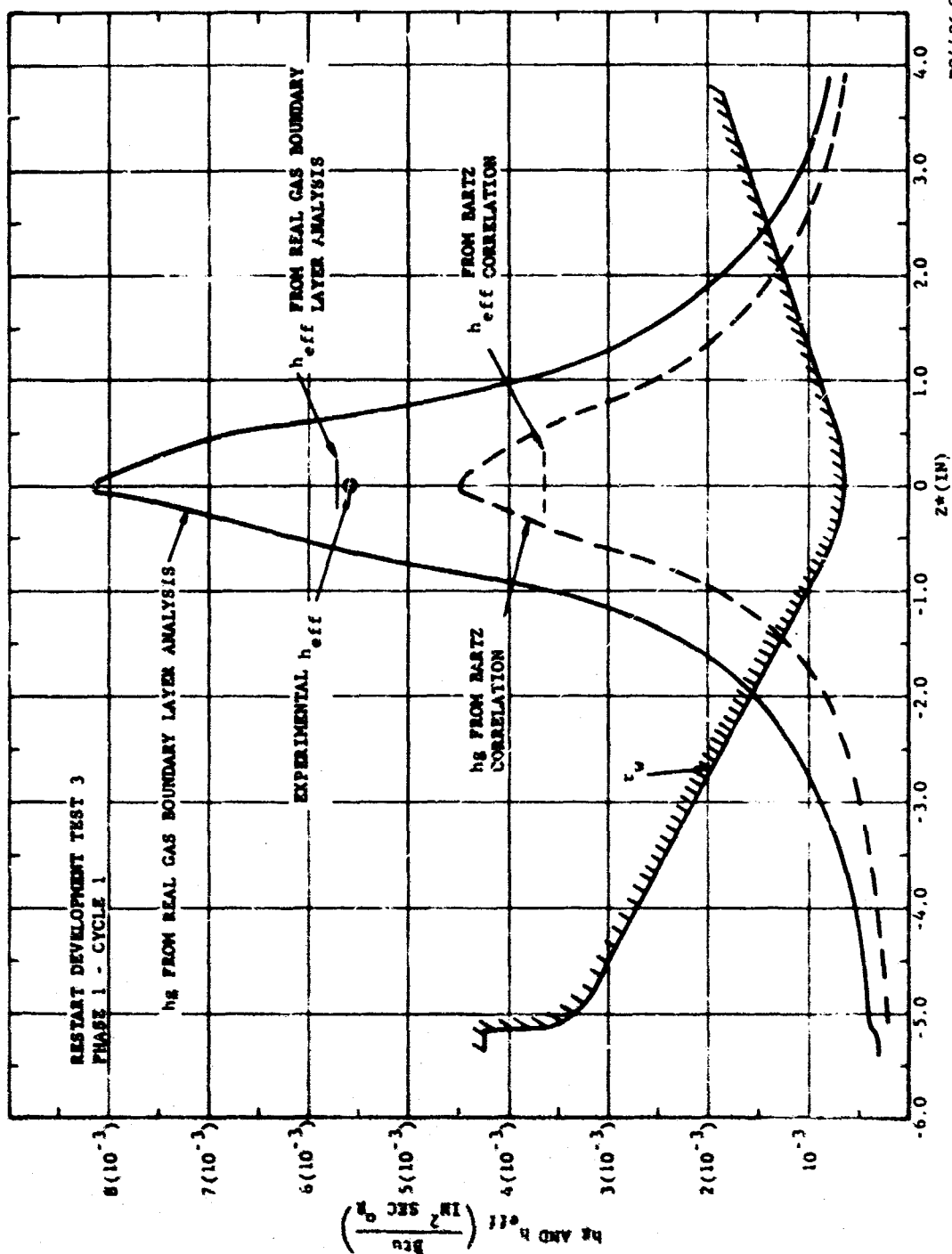
8.2.2 THROAT SECTION CORROSION

Duty cycle and firing time restrictions were imposed on pyrolytic graphite and tungsten throat inserts based on allowable maximum surface temperatures. These maximum surface temperatures were chosen as a result of the theoretical equilibrium corrosion rate calculations modified by data acquired through various programs utilizing propellants with similar exhaust properties. Thus, the theoretical maximum temperature has been somewhat altered by experience since, as mentioned in Paragraph 2.5.3, corrosion theory is not yet adequate and reliable.

Several observations can be made from the firings conducted under this program. The limit imposed on pyrolytic graphite was 5000°F. It has been found in the thermal analysis that this surface temperature will be achieved at the same time whether the nozzle is subjected to a continuous firing or to a duty cycle of several pulses. Thus, ten 5-second pulses have the same effect in producing this surface temperature as a single 50-second firing.

In examining the rocket motor test results, the occurrence of a given degree of erosion can be determined more accurately than the initiation of erosion. The time at which a five percent area change has occurred was chosen as the experimental data which would be correlated. This comparison between experimental and analytical data is shown in Figure 8-7. The analytical predictions are based on the time to reach a 5000°F throat temperature, at which temperature surface regression is assumed to occur; whereas, the experimental results are for time sufficient to achieve a 5 percent throat area change. The discrepancy in the firing times for 5 seconds or less between cycles is attributed to the start transient alumina deposition and the time from the initiation of surface regression to a 5 percent area change. The consideration of alumina deposition increases the firing time for a single pulse to achieve throat regression from 46.3 seconds to 49.5 seconds. The experimental time for a 5 percent

CONFIDENTIAL



FO4496 C

FIGURE 8-5. COMPARISON OF THE HEAT TRANSFER COEFFICIENTS OBTAINED FROM THE REAL GAS BOUNDARY LAYER ANALYSIS AND THE BARTZ CORRELATION

CONFIDENTIAL

CONFIDENTIAL

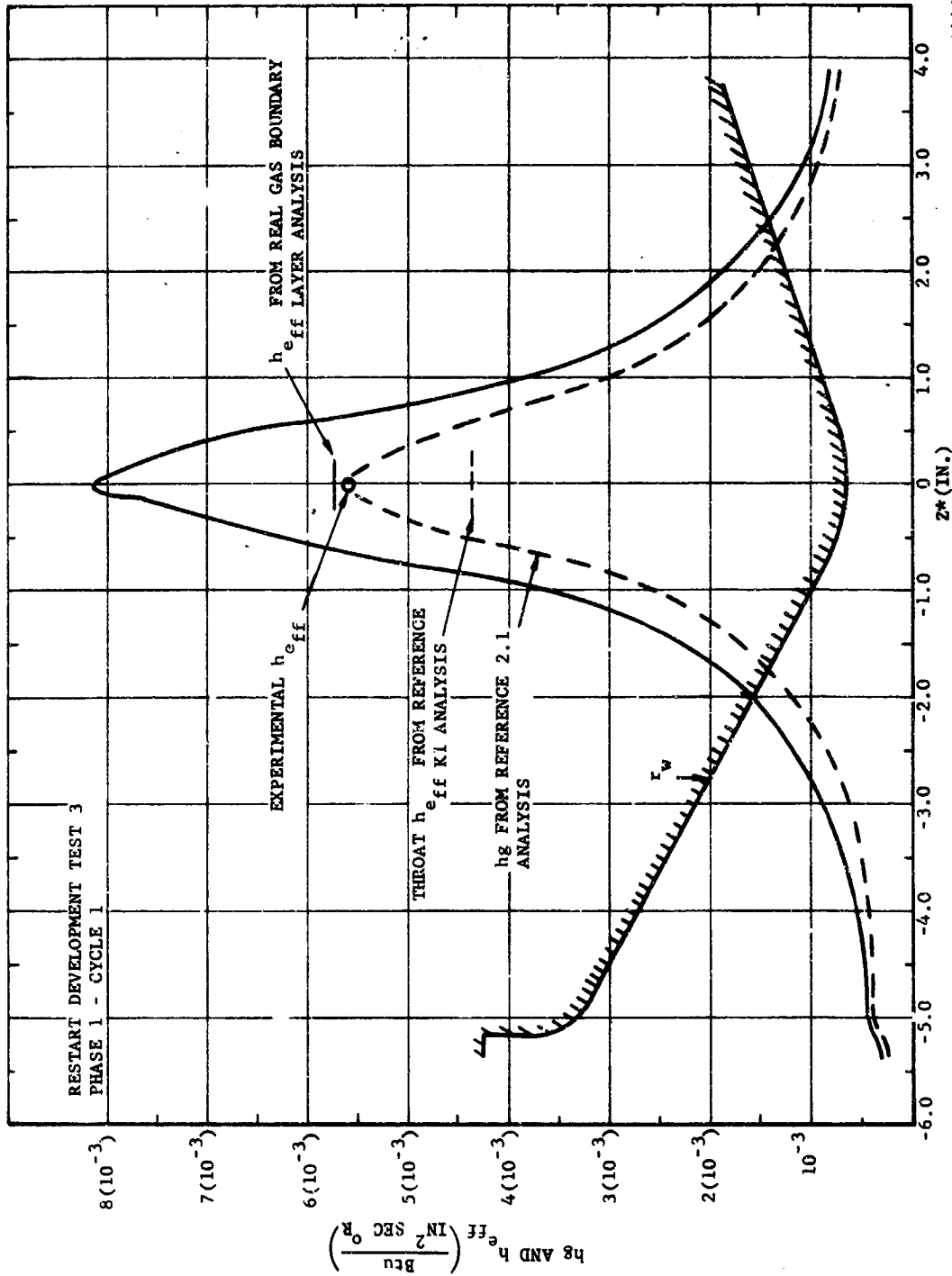


FIGURE 8-6 COMPARISON OF THE HEAT TRANSFER COEFFICIENTS OBTAINED FROM THE REAL GAS BOUNDARY LAYER ANALYSIS AND THE PERFECT GAS ANALYSIS OF REFERENCE K1.

FO4497 C

CONFIDENTIAL

CONFIDENTIAL

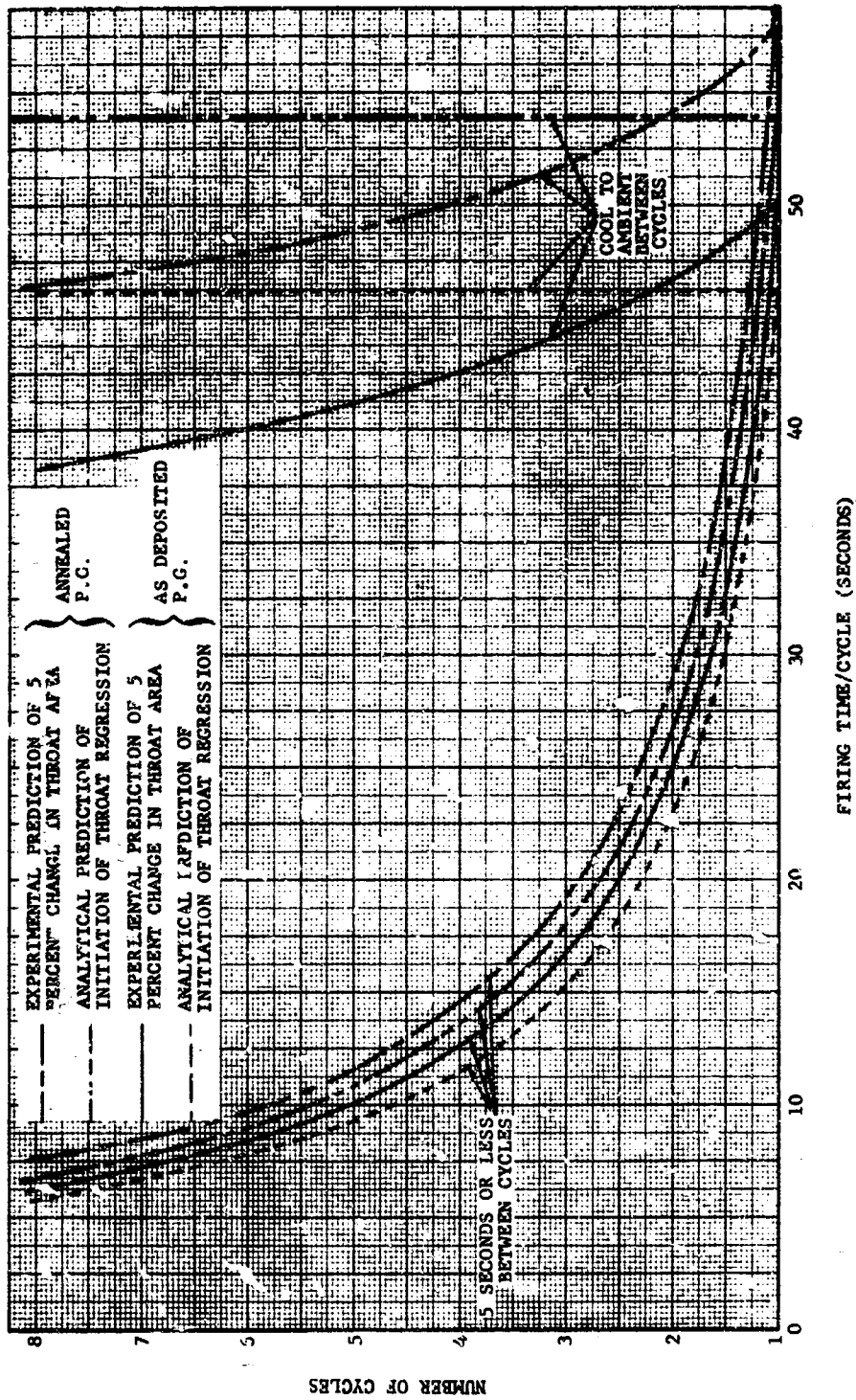


FIGURE 8-7. ANALYTICAL AND EXPERIMENTAL COMPARISONS OF DUTY CYCLE LIMITATIONS ON ROCKET MOTOR TESTS

CONFIDENTIAL

CONFIDENTIAL

area change is 50 seconds; this indicates that the assumption of the initiation of surface regression at 5000°F may be slightly off. However, by eliminating alumina deposition the thermal analyses used in this program may be used to very accurately predict the duty cycle limitations of pyrolytic graphite throat inserts similar to the rocket motor tests. The only restriction that should be imposed on the thermal analysis is the fact that after the first firing the throat insert will experience a change from its original geometry. The influence of geometry change on duty cycle is indicated in Figure 8-7 and imposes a definite limitation to the analysis.

An examination of the development motor tests shows approximately the same results. As shown in Figure 8-1 for test No. 3 the surface temperature at the throat was calculated to reach 4750°F at the end of the 36.5 second firing. The post-test measurement showed no throat surface regression. The 5000°F limit imposed does not appear to be excessively optimistic.

The interpretation of the data obtained for the tungsten inserts is more difficult, since the effects of plastic deformation have clouded somewhat the post-test measurements. The maximum surface temperature imposed on tungsten for this environment was 5500°F. The same reasons were used as with pyrolytic graphite, however, less data were available upon which confidence could readily be placed. Data acquired from the rocket motor tests may be clouded somewhat by the fact that backside gas leakage had occurred. However, neglecting this, the following can be shown:

<u>Nozzle</u>	<u>Firing Time</u>	<u>Measured Erosion</u>	<u>Predicted Surface Temperature (°F)</u>
0.625 inch dia 800 mils thick	61	0	5530
0.625 inch dia 180 mils thick	50	0	5520
1.25 inch dia 0.400 mil thick	35	0	~5200
1.25 inch dia 0.400 mil thick	45	0	~5400

On all of these inserts, final diameters were less than the original diameter (see Sections 5 and 6). However, it was noted on several of these inserts that fine axial grooves occurred in the surface. Also, tungsten carbide was found on the surface indicating a carbon reaction from either the pyrolysis products (Paragraph 2.5.4) or from carbon carried by the degradation of the entrance section. However, it does appear that the 5500°F surface temperature limit is conservative, but it is not known by how much, since some localized grooving (corrosion) did occur.

CONFIDENTIAL

CONFIDENTIAL

8.2.3 THROAT SECTIONS - STRUCTURAL ANALYSIS

The structural responses observed in the tests consisted of the occurrence or nonoccurrence of specific phenomena: either the insert spalled or it did not; it fractured or it did not; anelastic deformation occurred or it did not. The comparison of analytical predictions of these occurrences with the observed test results forms the basis of the correlation between the two.

a. Pyrolytic Graphite. Pyrolytic graphite was used in the test phases as shown in Table 8.1.

TABLE 8.1

PYROLYTIC GRAPHITE TEST UTILIZATION					
<u>Test</u>	<u>D^a (in.)</u>	<u>b (in.)</u>	<u>β</u>	<u>u_g (mils)</u>	<u>u_g/b (approx)</u>
RM 3, 10, 11, 14	0.625	1.5	4.8	1-2	0.0007-0.0013
Dev 3	1.25	2.5	4.0	3-5	0.0012-0.002
Demo 1, 2	2.5	3.0	2.4	5	0.0017

As discussed in Paragraph 3.2.1, the structural analysis would predict that these designs were ultrasafe from fractures resulting from backside tensile stresses. No such fractures were observed. Thus it can be concluded that these analytical predictions were verified by test. However, it cannot be concluded that the analysis is precise since it was impractical to attempt to design the washers near their failure points. Nonetheless, it still appears that backside tensile fracture is an almost impossible failure mode to induce in pyrolytic graphite.

The occurrence of spallation on the inner surface of pyrolytic graphite washers could be predicted depending upon the backside restraint provided and the a-b compressive strength of the material. In the rocket motor tests, the geometric ratio, β , was quite high at 4.8. This is actually outside the range of values used in the analytically derived design charts. However, assuming that some extrapolation is valid, the following remarks can be made. The washers would have been safe, theoretically, if the inserts had been free to expand radially during the run. At the peak stress condition, the washers require about 5 mils on the radius for this expansion, whereas only 1 or 2 mils was provided. Some slight extrapolation of curve 2 of Figure 3-13, the applicable design chart, shows the rocket motor test nozzles to be marginal for spallation. Some gross surface roughening, much too coarse to be classed as purely chemical corrosion, was observed in the pyrolytic graphite in tests 3, 10, and 11, but not

CONFIDENTIAL

in test 14. This roughening has been called spallation. In these tests the picture is somewhat clouded because of the unsatisfactory behavior of the entrance sections. On some of the test nozzles, the excessive surface regression, as well as the loss of pieces, of the entrance sections resulted in unfavorable effects on the throat material.

The development nozzle design falls within the range of the design charts. Referring to Figure 3-13, the two curves with $u_g/b = 0.002$, and the curve for $u_g/b = 0.001$, can be used for this comparison. The curve for the lower strength of -10,500 psi and $u_g/b = 0.002$ shows the design to be definitely unsafe, as does the curve for u_g/b of 0.001 and a strength of -13,000 psi. The curve for -13,000 psi strength and $u_g/b = 0.002$ shows the design to be marginal. No spallation was observed in this nozzle after test.

The two demonstration nozzles were designed on the basis of the favorable results of the development nozzle. Referring again to Figure 3-13 the design point for these nozzles falls about midway between the two curves for $u_g/b = 0.002$. Thus, the analysis would predict spallation for a strength of -10,500 psi and no spallation for a strength of -13,000 psi. No spallation was observed in this nozzle after test.

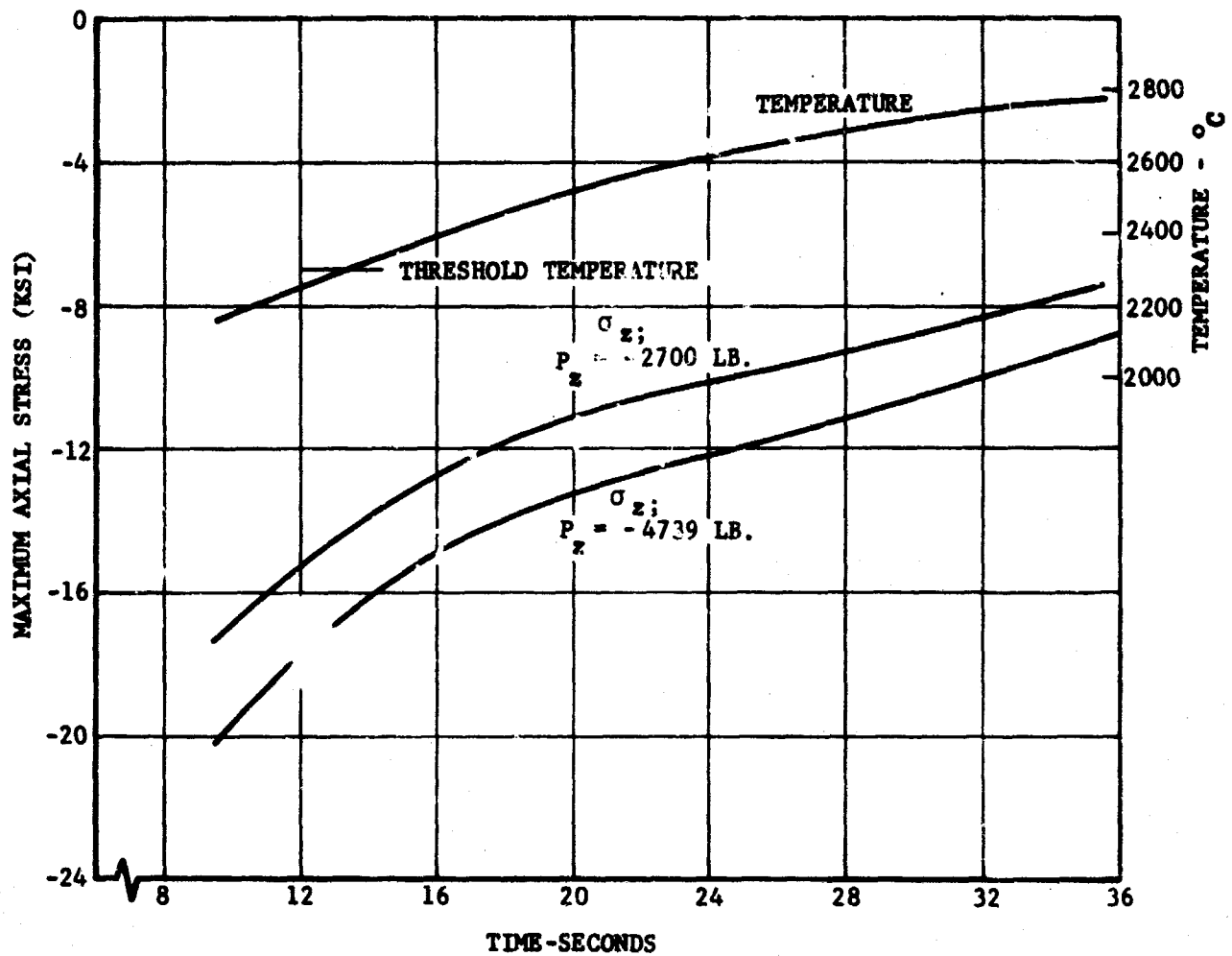
Spallation in pyrolytic graphic is sensitive to the a-b compressive strength of the material and to the degree of restraint to radial expansion provided. It would appear from the test results that the greater strength of -13,000 psi is probably more applicable than the lesser value of -10,500 psi. Although a phenomenon, which has been referred to here as spallation, was observed in the rocket motor tests, the actual occurrence of such a structurally related event should be demonstrated in the laboratory so that chemical effects are absent. Although Gobble and Salmen^{3.17} have shown that basal-plane compression causes fracture at 45 degrees to the applied stress in a compression specimen, it should be demonstrated that such fractures are translatable to spallation in an elastic body of revolution with some c-direction restraint.

The backside restraint imposed on the washers, even with a carefully controlled backside clearance, is questionable. Deposits from the combustion products and from the pyrolysis products which find their way behind the washers reduce this clearance and increase the restraint to some degree.

The phenomenon defined as elephant footing in Paragraph 3.1 has been examined analytically. Although the analysis was not completed until after the rocket motor tests were completed and the development nozzles were designed, analysis was conducted to see if this occurrence could be predicted for the rocket motor nozzles. The event was not observed in any of the rocket motor nozzles. Figure 8-8 shows the predicted axial stress at the inner surface of the washers along with the predicted temperature as a function of time. Two curves are shown in the figure representing two values of axial load. The greater load is computed by assuming that the

CONFIDENTIAL

CONFIDENTIAL



FO4498 U

FIGURE 8-8. PREDICTED PYROLYTIC GRAPHITE INNER SURFACE
TEMPERATURE AND AXIAL STRESS - ROCKET MOTOR TEST NOZZLES

8-19

CONFIDENTIAL

THIS PAGE IS UNCLASSIFIED

CONFIDENTIAL

chamber pressure of 700 psi acts over the frontal area of the washer. The lesser load assumes that a pressure differential of 400 psi acts across the opposing faces of the washer. This represents the greatest axial pressure difference across a distance equal to the thickness of a single washer. As can be seen from this figure, at the time the inner surface reaches the threshold temperature for c-direction permanent deformation, the stresses are above 14,000 psi compression. Referring to Figure 4-24 and the curve labeled 2310°C, 13 ksi, a permanent deformation of about 1/2 percent could be expected if this load were held for 10 seconds. Referring again to Figure 8-8, when the inner surface temperature has reached 2400 to 2500°C, the stresses are still in the range of -13,000 psi. In this case, the laboratory data, shown in Figure 4-24, indicate that if these conditions prevailed for 10 seconds, a permanent deformation of 1 to 1-1/4 percent could be anticipated. When the inner surface has reached 2760°C, the axial stresses exceed -8000 psi, and the laboratory data, Figure 4-26, indicate over 1.6 percent deformation could be expected in another 30 seconds.

A plot of the radial distribution of axial stress is shown in Figure 8-9. The peak stress at the inner surface is not greatly sensitive to total load carried. The annulus over which the load is carried is reduced as the load is decreased. With the annulus decreasing, the triangular area under the curve (which approximates the load, $P_z = 2\pi \int \sigma_z r dr$) drops rather abruptly with only a slight decrease in stress. The significant point about the stress distribution is that the high stresses exist only over a very small radial distance. Stresses in excess of -10,000 psi only exist to a depth of 0.045 inch for the lower load curve. It would require only a small deformation in this area to redistribute the load and relieve these high stresses. The relationship between degree of deformation and the stress relief afforded has not been developed.

The predicted radial distribution of axial stress for the demonstration nozzles when the predicted inner surface temperature has reached 2430°C is shown in Figure 8-10. The high load curve assumes the axial load to be the product of chamber pressure and washer frontal area, and the low load curve assumes a pressure differential of 210 psi acting across the washer. The same comparisons can be made with the laboratory data as was done above by referring to the 2420°C curve of Figure 4-24. For the low load curve of Figure 8-10, only about a 30-mil annulus is at a stress above -10,000 psi. Localized redistribution could relieve these high stresses to a value where no discernible permanent deformation would occur. This should be investigated but has not been on this program. From the computed structural data and the laboratory data, a prediction of some degree (approximately 1 percent) of permanent c-direction deformation to a depth of not over 1/16-inch would be made. This deformation could not be detected on the demonstration nozzles after test.

b. Annealed Pyrolytic Graphite. This material was used in the nozzle throats in rocket motor tests 6 and 9, and in development test 1.

CONFIDENTIAL

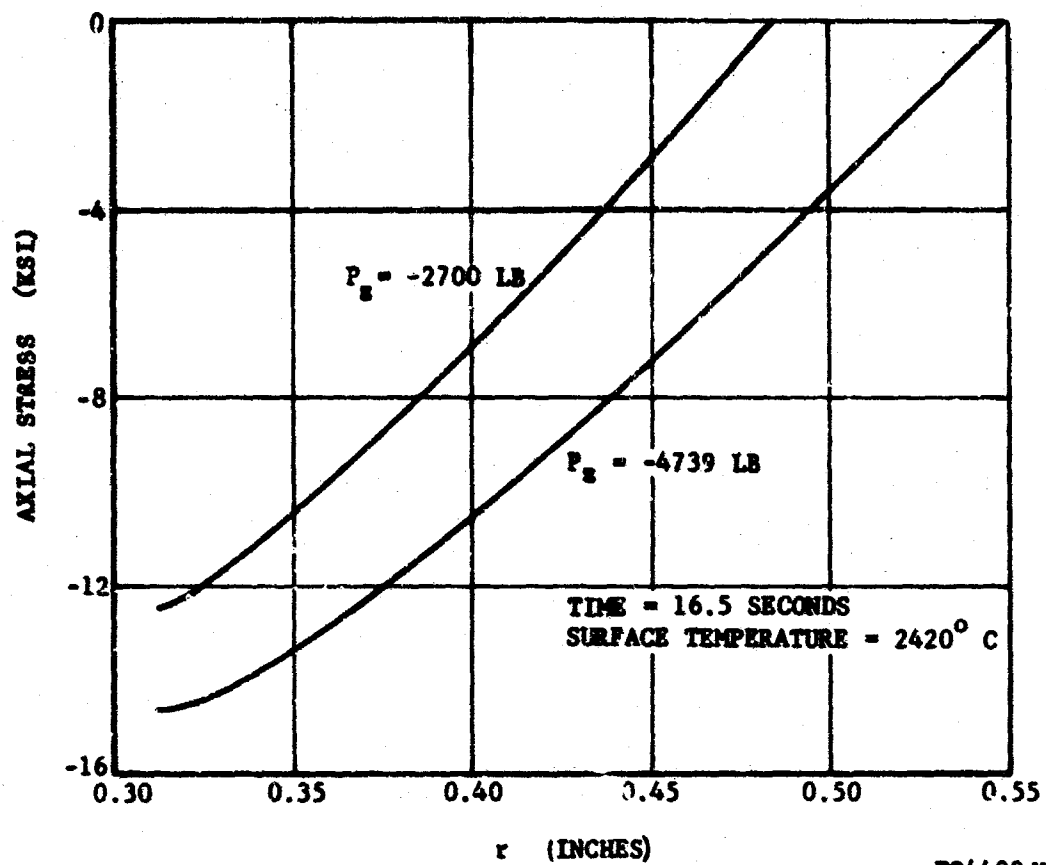


FIGURE 8-9. PREDICTED AXIAL STRESS DISTRIBUTION OF PYROLYTIC GRAPHITE ROCKET MOTOR TEST NOZZLES

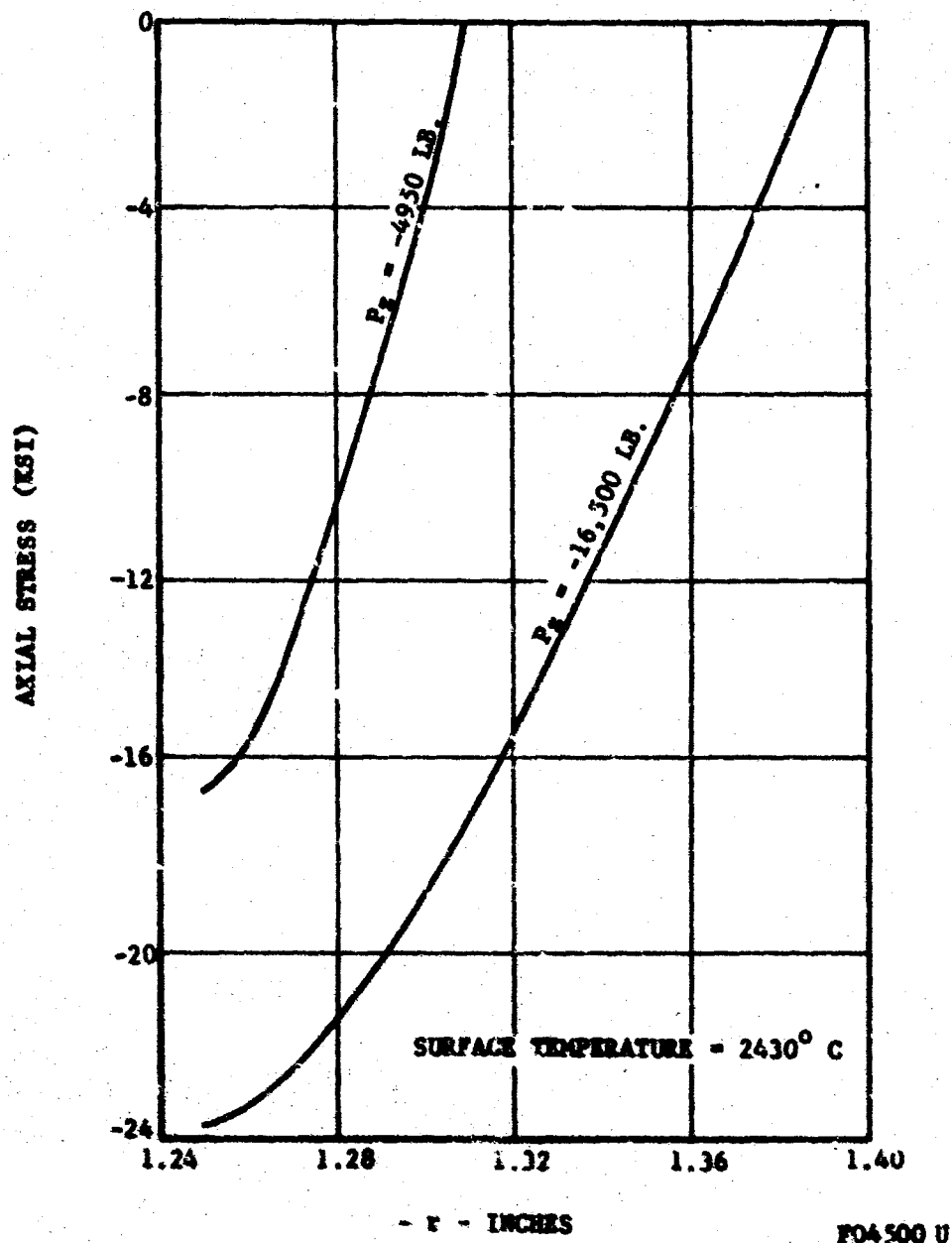


FIGURE 8-10. PREDICTED AXIAL STRESS DISTRIBUTION
IN PYROLYTIC GRAPHITE - DEMONSTRATION TEST NOZZLES

CONFIDENTIAL

The tensile stress behavior on the outer surface of this material should be much better than that of as-deposited pyrolytic graphite. The reasons for this lie in the material properties: compared to as-deposited pyrolytic graphite, the annealed material has a higher a-b conductivity, a lower a-b thermal expansion, and a high a-b tensile strength. Thus not only will the thermal loading be lower but the structural response will also be lower while the strength is higher. Since analysis has shown that it is virtually impossible to fail as-deposited washer inserts in tension, the same would be even truer for the annealed material. Thus no tensile failures would be predicted for the inserts of these test nozzles; and none occurred.

Before the rocket motor tests were conducted with this material, the compressive behavior at the inner surface could not be predicted. It is known that at room temperature the annealed material has about half the a-b compressive strength of the as-deposited material. But the higher temperature strength and the mode of compressive failure were not known. It could reasonably be expected that both the strength and the mode could be dependent upon the c-direction bonding of the material. This bonding is Van der Waal (electrostatic) and is greatly reduced by annealing. Thus it might reasonably be expected that the annealed material might be more sensitive to compressive loading than the as-deposited material, even though no precise predictions based on calculated magnitudes could be made.

In both rocket motor tests 6 and 9, the annealed material wrinkled, producing kinks in the a-b plane as a result of the inner surface hoop compressive stress. The washers in these nozzles had a backside radial clearance of 1 to 2 mils ($u_g/b \approx 0.001$) comparable to the clearance provided for the as-deposited pyrolytic graphite washers used in this test phase. The wrinkles appeared on both tests and extended in a continuous fashion throughout the length of the washer stack as if a wrinkle occurring in one washer had been embossed on the adjacent washers. Where these wrinkles appeared on the inner edge of the annealed material, a site for selective corrosive attack was created. As a consequence, corrosion grooves were produced along the length of the insert. The results of this phenomenon are graphically shown in Figures 8-11 and 8-12. It appears that wrinkling of the soft annealed material rather than spallation occurs from the inner surface compressive hoop stress. This is a new problem definition resulting from the rocket motor tests.

In development nozzle 1, the clearance behind the annealed pyrolytic graphite washers was increased to about 4 mils ($u_g/b \approx 0.0016$). The wrinkles developed again as a result of the motor firing but to a lesser degree than observed in the rocket motor tests. Not all wrinkles extended to the outer radius of the washer stack.

c. Heat Treated Pyrolytic Graphite. This material was used in the nozzle throats in rocket motor test 4 and in development test 5. The structural behavior of heat treated pyrolytic graphite should be superior to that of the as-deposited material for the same reasons cited above for

CONFIDENTIAL

CONFIDENTIAL



FIGURE 8-11. WRINKLES AND EROSION GROWTH IN ANNEALED PYROLYTIC GRAPHITE ROCKET MOTOR TEST 8

8-24

CONFIDENTIAL

THIS PAGE IS UNCLASSIFIED

CONFIDENTIAL



FIGURE 8-12. EDGE VIEW OF KINKS IN ANNEALED PYROLYTIC GRAPHITE ROCKET MOTOR TEST 6

8-25

CONFIDENTIAL

THIS PAGE IS UNCLASSIFIED

CONFIDENTIAL

the annealed material, although the properties of the heat treated material are not changed to the same degree as the annealed material. Analysis indicated that no tensile failures could be expected for as-deposited washer inserts; therefore, no tensile failures would be predicted for the heat treated material. None were observed.

Whereas spallation was shown to be marginal for the pyrolytic graphite rocket motor nozzles, heat treated material should show a small margin, assuming a higher compressive strength for this material. No spallation was observed in the rocket motor nozzle 4.

Certain testing difficulties obfuscated the observance of any structural phenomena on the inner surface of development nozzle 5. Neither spallation or permanent c-direction deformation could be detected because of these difficulties.

d. Tungsten. Two structural phenomena could be analytically predicted: backside tensile fractures and inner surface yielding. It may be recalled that the effects of grain growth on the strength and modulus of arc cast material were studied in the laboratory. However, it was found that the grain size of the tungsten inserts exceeded the range studied in the laboratory rather early in the duty cycle. Thus the occurrence of backside tensile fracture could be predicted for the initial firing, but the question of the effects of large grain size reappears for predictions made for subsequent firings. It is impossible to estimate accurately the grain size for second and subsequent firings. It appears quite safe though to assume that the grain size exceeds some nominal minimum. A minimum of 0.0015 inch is convenient since analyses have been performed with the corresponding strength of 36,000 psi.

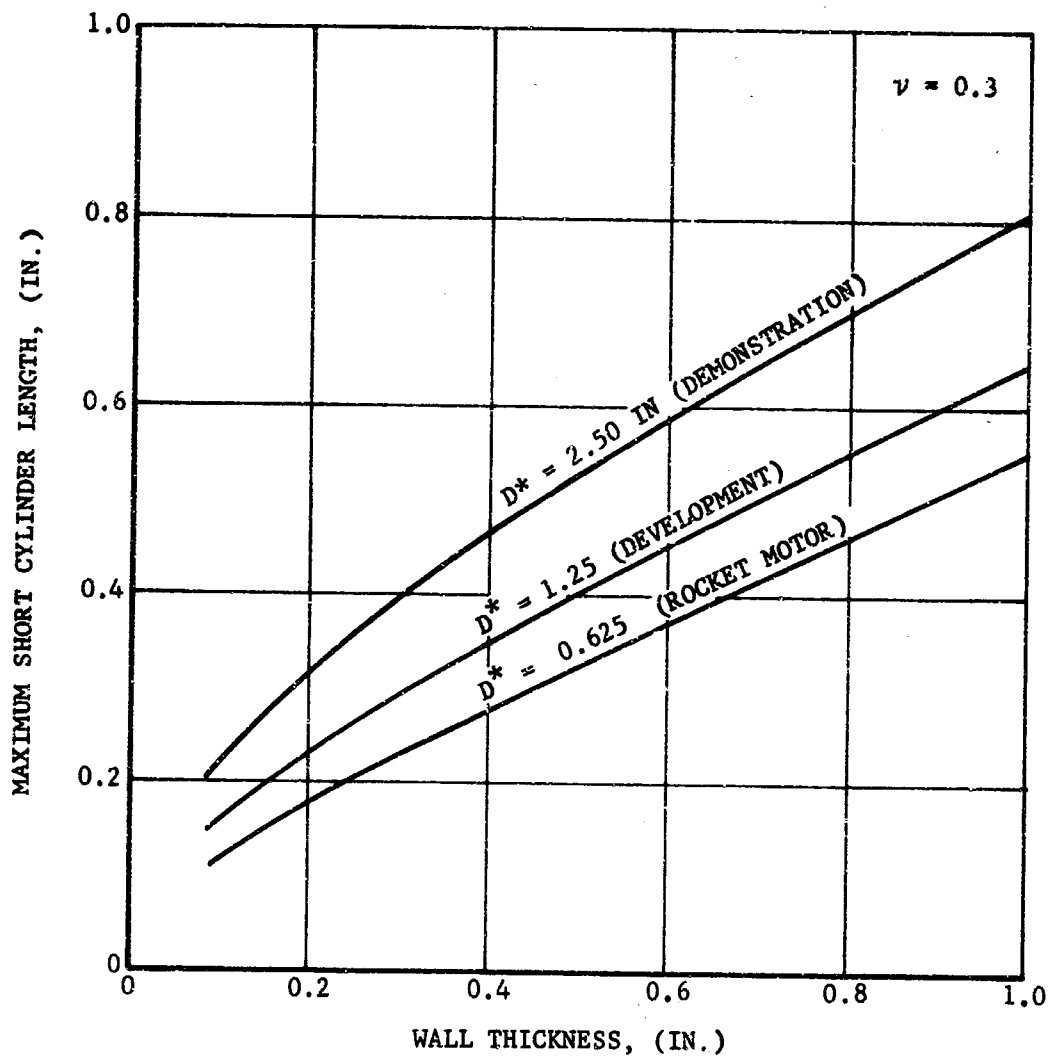
All of the tungsten inserts fired in the test phases were, according to the definition of Paragraph 3.2.1, long cylinders. The short cylinder lengths for the test inserts are shown in Figure 8-13. The test insert design data are shown in Table 8.2.

Comparing the design data in Table 8.2 with the limiting lengths in Figure 8-13 shows that the inserts were all long cylinders. Since the inserts of the rocket motor tests were not well restrained, the axial and hoop stresses should be approximately equal and fracture from either should be equally likely.

Using the long cylinder data of Figure 3-14, for unrestrained inserts, none of the inserts should have suffered a tensile fracture on the first firing with the exception of the insert of rocket motor test 13. Thus for the first firing predictions, there is perfect correlation between analytical predictions and observed test results. However, the predictions for subsequent firings, assuming an average grain size of 0.0015 inch and the accompanying strength of 36,000 psi, indicated that all of the arc cast inserts would

CONFIDENTIAL

CONFIDENTIAL



FO4501 U

FIGURE 8-13. SHORT CYLINDER LENGTH LIMITS (TUNGSTEN)

CONFIDENTIAL

THIS PAGE IS UNCLASSIFIED

TABLE 8.2

TUNGSTEN TEST INSERT DATA

<u>Test</u>	<u>Material</u>	<u>Length, inch (approx)</u>	<u>Wall Thickness, inch (approx)</u>	<u>β</u>	<u>Tensile Fracture</u>	
					<u>Predicted</u>	<u>Subsequent</u>
RM 7	Arc Cast and Extruded	1	0.180	1.58	No	Yes
RM 8	Arc Cast and Extruded	1	0.800	3.56	No	Yes
RM 12	Gas-Pressure Bonded	1	0.180	1.58	No	Unknown
RM 13	Gas-Pressure Bonded	1	0.800	3.56	Yes	-
Dev 2 (2-piece)	Arc Cast and Extruded	0.7 and 1.25	0.400	1.64	No	Yes
Dev 4	Arc Cast and Extruded	1.9	0.400	1.64	No	Yes

CONFIDENTIAL

CONFIDENTIAL

CONFIDENTIAL

have fractured. (No predictions could be made for the gas pressure bonded material.) Referring to the appropriate curve of Figure 3-21, the rocket motor inserts would not survive for β 's greater than 1.36 and the development inserts would not survive for β 's greater than 1.2. The inserts which had β 's in excess of these values by not more than 37 percent did survive all subsequent firings without fracture. The insert of rocket motor test 8 was the only one which fractured on subsequent firing. It fractured on the second firing. Its β ratio, as shown in Table 8.2, was 3.56. This is considerably above the predicted safe design value and considerably above the values for the inserts which did survive all firings.

There seem to be two possible causes for this discrepancy. One is that the analysis is faulty and the other is that the strength and grain size assumption for subsequent firings is inaccurate. For the insert of rocket motor test nozzle 7, $\beta = 1.58$, a minimum strength of 54,500 psi is required for the insert to survive all firings. For the insert of development nozzles 2 and 4, $\beta = 1.64$, a minimum strength of 89,500 psi is required for survival. Looking at the grain growth data obtained from the sectioned inserts after firing, Paragraph 8.2.4, it would appear that some grain growth would have occurred during the first firing of the three inserts under discussion. And some degradation of strength below the as-received value would have accompanied this growth so that the necessary strengths quoted above probably would not have been maintained.

If the inserts had been short cylinders, the rocket motor 7 insert would have been marginal to survive a strength loss to 36,000 psi according to curve 2 of Figure 3-21, but the development inserts 2 and 4 could not have survived a similar strength loss.

It appears then that there is insufficient correlation between analytical predictions and test results for tensile fracture on second or subsequent firings for these tungsten inserts.

According to Figure 3-17, all of the tungsten inserts would have undergone inner surface yielding by a wide margin on all firings. This yielding was observed.

The reduction in throat diameter experienced for each cycle for all of the tungsten inserts is shown in Table 8.3. It is interesting to note that the throat shrinkage is relatively significant as long as the circumferential integrity of the insert is maintained. All four of the thinnest inserts continued to shrink during all cycles and the thicker inserts experienced significant shrinkage until they fractured. These fractures were in the r-z (radial-axial) planes and extended throughout the thickness and length of the insert. These fractures, then, could be expected to relieve the rotational restraint on the insert and, as a consequence, reduce the magnitude of the compressive hoop stress in the inner region of the insert, thus reducing the degree of anelastic deformation observed. The test results

CONFIDENTIAL

CONFIDENTIAL

TABLE 8.3
TUNGSTEN INSERT DATA

Type of Tungsten	Wall Thickness (mils)	Test No.	Firing Duration (seconds)	Average Throat Diameter Reduction (mils)	Remarks
Arc Cast and Extruded	180	RM 7	26	19	
			36	11	No cracks. Insert obtruded on next cycle.
	800	RM 8	60	10	
			60	2	Cracked early in this cycle.
	400	Dev 2	56	38	Reduction in throat diameter attributable to carbide formation.
			35	40	
			35	24	
	400	Dev 4	30	8	No cracks. Throat change due to material deformation.
			50	42	
			50	27	No cracks. Throat change due to material deformation.

CONFIDENTIAL

CONFIDENTIAL

TABLE 8.3 (Continued)

Type of Tungsten	Wall Thickness (mils)	Test No.	Firing Duration (seconds)	Average Throat Diameter Reduction (mils)	Remarks
Gas Pressure Bonded	180	RM 12	50	25	
			5-1/2	11	No cracks. Majority of change on second cycle due to alumina deposition.
	800	RM 13	25 (5-sec pulses)	8	Cracked on first or second pulse.
			45 (5-5 sec pulses) (1-20 sec pulse)	0	

CONFIDENTIAL

CONFIDENTIAL

show that the anelastic deformation was virtually stopped when fractures appeared in the thicker inserts, thus tending to support the above rationale.

It may also be noted in Table 8.3 that the thinner inserts deformed more and in a shorter time than did the thicker inserts. For the thinner inserts there is less cross section in tension and thus less mass of the insert to resist compressive deformation. And for the thicker inserts there is more material which must be forced to move for the inner boundary to shrink. The test results consistently support this as being the case.

8.2.4 MATERIALS PHENOMENA - TUNGSTEN INSERTS

There were a total of six tungsten inserts fired during the program. These inserts and their duty cycles are summarized in Table 8.4.

The arc cast and extruded tungsten inserts were made from a single bar of material obtained from Climax Molybdenum Company. The chemistry provided by the supplier was:

<u>C</u>	<u>Fe</u>	<u>Ni</u>	<u>Si</u>	
0.001	<0.002	<0.001	<0.002	Weight Percent

with the balance W by difference. With a starting ingot 7-1/4 inches in diameter, the processing was:

- (a) Extruded at 3100°F to 2-3/4 inches diameter.
- (b) Recrystallized at 3000°F for 1 hour.
- (c) Machined to 2-3/8 inches diameter.

The gas pressure bonded tungsten used in the rocket motor tests was consolidated by Allied Chemical Corporation as a pilot plant production item. No chemical or processing data are available for this material. Its use was not carried into the development tests.

There are several materials and related items associated with these inserts. Grain growth, carbide formation and flow, and composition of deposits are the particular items which will be included in this discussion.

Although a precise thermal history of the material is quite desirable when examining these phenomena, no such history is available. For this reason, analytical predictions will often be used as an indication of the approximate temperature levels reached.

a. Rocket Motor Test 7 Insert. This insert was obtruded after three starts and a total firing time of about 87 seconds. A photograph of the sectioned insert is shown in Figure 8-14. The blotchy material on the

CONFIDENTIAL

CONFIDENTIAL

TABLE 8.4

TUNGSTEN INSERT SUMMARY

<u>Test</u>	<u>Insert Description</u>	<u>Duty Cycle</u>
Rocket Motor 7	180-mil wall arc cast and extruded	26 seconds Cool to ambient 36 seconds Cool to ambient 24-1/2 seconds Insert obtruded
Rocket Motor 8	800-mil wall arc cast and extruded	61 seconds Cool to ambient 61 seconds Cool to ambient 56 seconds
Rocket Motor 12	180-mil wall gas pressure consolidated (cylindrical backside)	50 seconds Cool to ambient 5-1/2 seconds
Rocket Motor 13	800-mil wall gas pressure consolidated	Five 5-second pulses with 5 seconds between pulses. Cool 25 minutes. Five 5-second pulses with 5 seconds between pulses. Cool to equilibrium (33 seconds). Fire for 20 seconds
Development 2	2-piece arc cast and extruded	20 seconds Cool 100 seconds 15 seconds Cool to ambient 15 seconds Cool 100 seconds Four 5-second pulses spaced 5 seconds apart Cool to ambient Six 5-second pulses spaced 5 seconds apart
Development 4	1-piece arc cast and extruded	37 seconds Cool 103 seconds 10 seconds Cool to ambient 27 seconds Cool 63 seconds Four 5-second firings spaced 5 seconds apart

8-33

CONFIDENTIAL

CONFIDENTIAL

P03477 U



FIGURE 8-14. SECTIONED INSERT OF ROCKET MOTOR TEST NO. 7

8-34

CONFIDENTIAL

THIS PAGE IS UNCLASSIFIED

CONFIDENTIAL

surface is fused silica caused when the insert impacted an earthen embankment after being ejected. Note that the contour of the section is well preserved even though the insert was pretty well battered by the impact.

Two samples were taken from the nozzle after firing was completed. The results of X-ray diffraction analysis are shown in Table 8.5. It is interesting to note that tungsten carbides were found in the exit cone. These carbides had evidently flowed downstream from the insert during firing. The sample taken from the backup material adjacent to the insert backside showed no carbides. Visual inspection of the insert confirmed that there was no gross melting on the backside although there was some carbide present. It may be concluded then that the insert obtruded because it became very soft at the elevated temperature and there was sufficient force to cause it to be ejected. It may not be concluded that carbide melting on the backside was a major factor in the loss of the insert.

TABLE 8.5

X-RAY DIFFRACTION DATA OF ROCKET MOTOR TEST NO. 7 SAMPLES

Sample	$\alpha\text{Al}_2\text{O}_3$	Percent of Compound in Sample				Al_4C_3	Remarks
		Al_2O_3	WO_3	WC	Al_2O_3		
1	70-80	low	low	trace	trace		Sample taken from exit section approximately 1 inch downstream of insert.
2	10-15		trace			4-6	Sample taken from ATJ behind insert section. Sample mostly normal graphite. One peak ~ Al 100 percent intensity line 5 percent plus or minus.

The duty cycle to which the nozzle was subjected unquestionably brought the entire insert above the temperatures necessary for grain growth and tungsten-carbide reactions to occur. Analytical predictions indicated that the flame-front material at the throat would reach 2400°C (4350°F) in about 10 seconds and the backside would reach this temperature in about 23 seconds. For each of the three firing cycles, the entire insert would have been expected to

CONFIDENTIAL

have been above this temperature. The average grain size in the throat region is approximately 0.016 inch. This is about five times as large as would be expected from the materials laboratory studies for three excursions to 2400°C.

Even so, there remains a patch of small grains evident in Figure 8-14. This patch lies along a well defined striation line, and it is quite probable that the initial microstructure in this region influences the rate of grain growth.

b. Rocket Motor Test 8 Insert. Figure 8-15 is a view of the backside of the tungsten insert used in rocket motor test 8. This photograph shows the deposits which resulted partly from the backside flow. At the inner surface and extending aft are the carbide deposits which have flowed over the inner surface.

Figure 8-16 is a view from upstream. Deposits are evident. General roughness of the contour, material loss from the upstream face near the inner surface, and the radial fracture can all be seen in this figure.

Figure 8-17 shows the untouched fracture surface. The insert had been sectioned prior to photographing. After sectioning, the insert did not fall apart at the fracture but was securely held together at or near the inner surface. It had to be mechanically broken to part it. From the appearance of the fracture surface, it can be deduced that the most probable mechanism of bonding was by carbides.

Figure 8-18 is a photograph of the sectioned insert which has been polished and etched. Loss of upstream material by carbide formation is quite evident. This section includes the fracture which is seen as the channeling at about the middle of the upstream surface.

Figure 8-19 is an enlargement at the lower portion of the section shown in Figure 8-18. The surface carbide layer is quite evident. Carbide migration into the grain boundaries can be traced to a considerable depth. Carbides were detected to a depth at about 3/16 inch. Toward the aft region of the insert near the inner surface, a small grain within a grain can be clearly seen. This small grain was being dissolved at a very rapid rate when the insert cooled off. Grain growth in this region, being extremely rapid, has resulted in random directional grain enlargement probably between grains of minimum crystal misorientation as is suggested by this included grain which has almost been annihilated by the larger surrounding grain.

The tremendous variation in grain size can be seen from the flamefront surface to the aft backside corner. In the region near the hottest surface, exaggerated grain growth is evident along the insert length. The average grain cross section is approximately 3.5×10^{-3} in.². The resulting grains in this portion of the specimen tend to be somewhat longer in the radial direction than in the axial direction.

CONFIDENTIAL

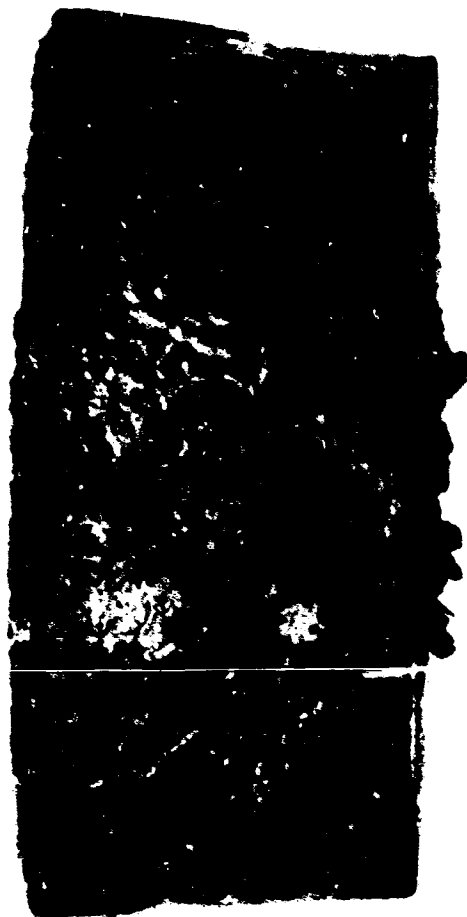
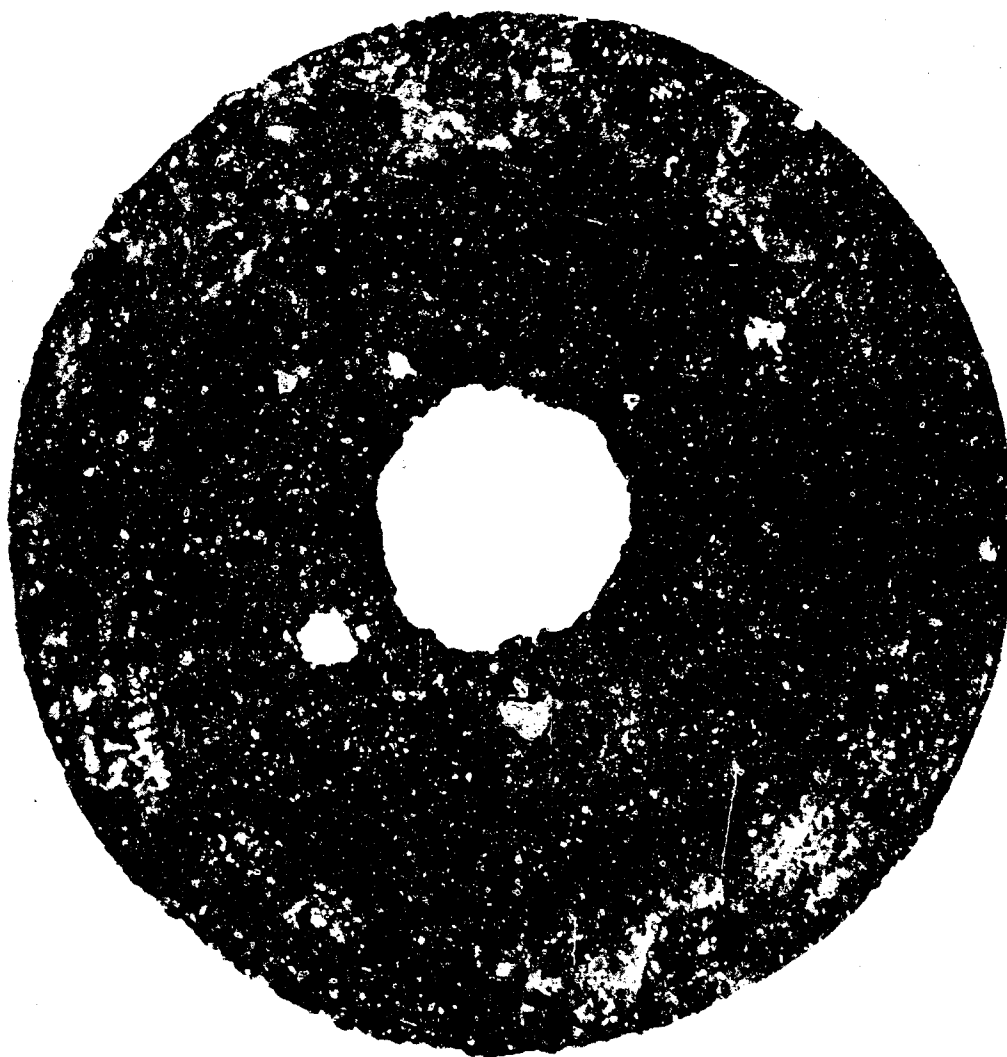


FIG 478 U

FIGURE 8-15. BACKSIDE VIEW OF INSERT OF ROCKET MOTOR TEST NO. 8



F03479 U

FIGURE 8-16. VIEW FROM UPSTREAM OF INSERT OF ROCKET MOTOR TEST NO. 8



F03480 V

FIGURE 8-17. FRACTURE SURFACE OF INSERT OF ROCKET MOTOR TEST NO. 8



F034811

FIGURE 8-18. SECTIONED INSERT OF ROCKET MOTOR TEST NO. 8

CONFIDENTIAL



FIGURE 8-19. SECTIONED INSERT OF ROCKET MOTOR TEST NO. 8

8-41

CONFIDENTIAL

THIS PAGE IS UNCLASSIFIED

CONFIDENTIAL

Analytical predictions indicate that the flamefront material would reach 2400°C (4350°F) in about 21 seconds and that the backwall temperature would achieve this value in about 60 seconds. Thus, according to these predictions, the entire insert would have exceeded this temperature in each of the three firing cycles.

The grain size in the area farther removed from the flame surface and lying along a striation line of enlarged grains is approximately 1.1×10^{-3} in.² and exhibits a more equiaxed structure indicative of more uniform grain boundary movement. Within this region a band of relatively small crystals is apparent.

The region adjacent to the outside surface is in contact with a graphite support and therefore expected to be cooler. The grain size in this portion of the nozzle is approximately 3.4×10^{-4} in.².

The nozzle material at the lowest temperature is that at the outside surface at the aft end of the insert. As expected, the grain growth in this region is less than elsewhere although some growth is evident. This material, surrounded by finer grained material, is not understood. It is to be expected that grain growth would be less than that in material closer to the interior structure. The larger grained material lying radially outward from the finer grained material could be the consequence of a local variation in raw material stock (compositional or structural variations) which could be more amenable to grain growth.

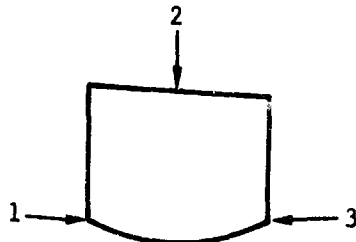
X-ray diffraction analysis data for samples taken from the insert are given in Table 8.6. The sample taken from the recessed upstream face showed a preponderance of alumina. The sample taken from the backside showed high concentrations of tungsten carbides. There was considerable backside leakage behind this insert which was evidenced by exit section erosion. The sample taken from the material which appeared to flow at the downstream edge of the insert (see Figure 8-15) was composed almost entirely of tungsten and tungsten carbides. This material came from the flamefront material. The hydrocarbons reacted with the insert material and the elemental tungsten melted and the mixture flowed from the contoured surface to form the ragged tail on the insert.

CONFIDENTIAL

CONFIDENTIAL

TABLE 8.6

X-RAY DIFFRACTION ANALYSIS OF ROCKET MOTOR TEST NO. 8 SAMPLES



Sample	$\gamma\text{Al}_2\text{O}_3$	Percent of Compound in Sample				C	Remarks
		$\alpha\text{Al}_2\text{O}_3$	W	WC	$\alpha\text{W}_2\text{C}$		
1	50	25	15	10	Trace		Unknown compound, low percent, also present
2	5		25	15	50	5	
3		Trace	65	5	30		Sample taken from material which appeared to flow at downstream edge.

c. Rocket Motor Test 12 Insert. The second firing of this insert (see Table 8.4) was conducted to examine alumina deposition and to check for thermal shock in the material after grain growth had been induced on the first firing. Alumina deposition is quite evident in Figure 8-20. There was a complete cone of deposits at the termination of firing, but most of this cone was lost when the nozzle was disassembled. Backside deposition which resulted from backside gas flow can also be seen in Figure 8-20. This insert had a cylindrical backside in contrast to the other tungsten inserts which all had conical backsides.

Figure 8-21 shows a section of the fired nozzle with an enlargement of a portion of the section. Material loss caused by carbide formation from the upstream portion of the insert can be noted. The typical hexagonal structure of the gas pressure bonded material has been preserved even though considerable grain growth has occurred. It was noted that the grain growth did not progress across these hexagonal boundaries on either of the two gas pressure bonded inserts fired.

No grain growth correlation was made nor could it reasonably be attempted. No laboratory data were generated as noted in Paragraph 4.2. The hexagon-like structure typical of the gas pressure bonded material was still evident since grain growth was predominately within the particles. This is the same type of behavior observed in the laboratory sample which was heated.

CONFIDENTIAL



F03483 U

FIGURE 8-20. INSERT OF ROCKET MOTOR TEST NO. 12

8-44

CONFIDENTIAL

THIS PAGE IS UNCLASSIFIED

CONFIDENTIAL



FIGURE 8-21. SECTIONED INSERT OF ROCKET MOTOR TEST NO. 12

8-45

CONFIDENTIAL

THIS PAGE IS UNCLASSIFIED

CONFIDENTIAL

d. Rocket Motor Test 13 Insert. Figure 8-22 is a view from upstream showing fractures and loss of material at the inlet region of the insert. It is postulated that the loss of inlet material and widening of the fractures at the inlet are both due to carbide formation and runoff. The insert did not fall apart when the nozzle was disassembled; rather, the two halves of the fractured insert were well bonded together with carbides.

Figure 8-23 shows the fracture surfaces of the insert. Note the sharpness of the backside contour, the aft end contour, and the outer region of the forward contour. There was a very thin carbon-carbide layer on all of these surfaces. No evidence of backside leakage was found although some minor leakage did occur.

Figure 8-24 shows a polished and etched section which lies just below the fracture surface. An enlargement of a region of this section is also shown. The region of grain growth is detectable in this photo as that region with the salt and pepper appearance. The enlargement shows that the grain growth has not obliterated the hexagonal pattern characteristic of the gas pressure bond material.

e. Development Test 2 Insert. This insert was a two-piece item with the split between the two pieces at about the sonic line. Figure 8-25 is a view from upstream showing deposition, carbide, preservation of roundness of the throat, and the interface between the two pieces of the insert.

Figure 8-26 is a polished and etched section of the insert. Apparent general surface roughness is a combination of deposits and streaking of the flame-front material. The toothed effect which is evident in the photo at the aft feather edge of the insert was caused by taking samples for X-ray diffraction analysis and not by this streaking.

Figure 8-27 shows an enlargement of the polished section in the region of the interface of the two pieces of the insert. It can be noted that there is some very slight loss of material at the inner corner of the downstream element. A few huge grains are noticeable at the inner surface of the upstream element. The adjacent grains are quite small by comparison. This irregular grain growth pattern is not evident in the downstream piece where there does not appear to be much variation in grain size through the thickness of the component.

Striations are much more evident in this insert than in the arc cast and extruded inserts fired in rocket motor tests 7 and 8. The grain growth has been much less in this insert and the initial character of the material has been better preserved.



703485 U

FIGURE 8-22. VIEW FROM UPSTREAM OF INSERT OF ROCKET MOTOR TEST NO. 13



F01486 U

FIGURE 8-23. FRACTURE SURFACE OF INSERT OF ROCKET MOTOR TEST NO. 13

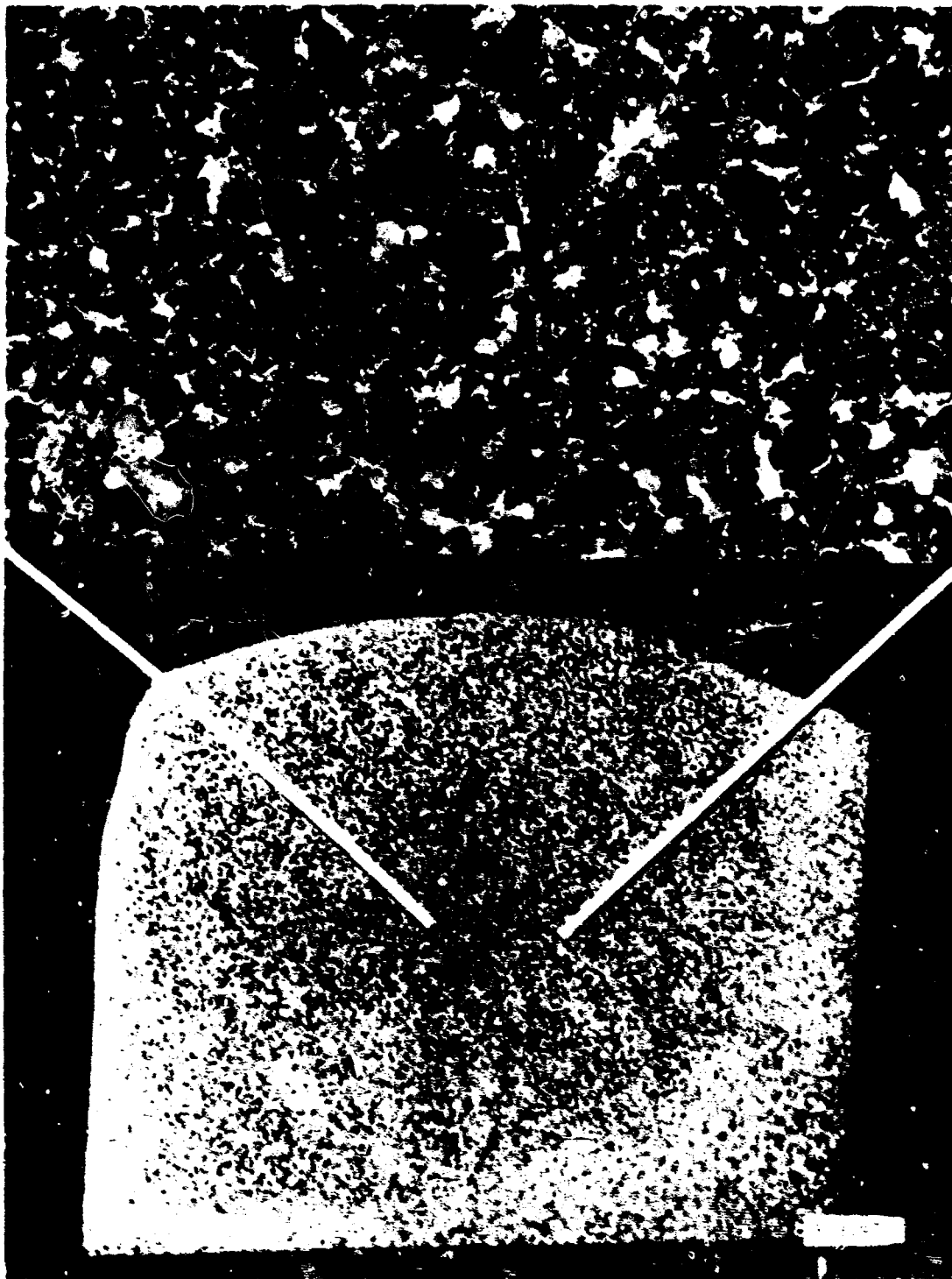


FIGURE 8-24. SECTIONED INSERT OF ROCKET MOTOR TEST NO. 13



F03488 U

FIGURE 8-25. UPSTREAM VIEW OF INSERT OF DEVELOPMENT TEST NO. 2



FIGURE 8-26. SECTIONED INSERT OF DEVELOPMENT TEST NO. 2



FCI-001

FIGURE 8-27. SECTIONED INSERT OF DEVELOPMENT TEST NO. 2

CONFIDENTIAL

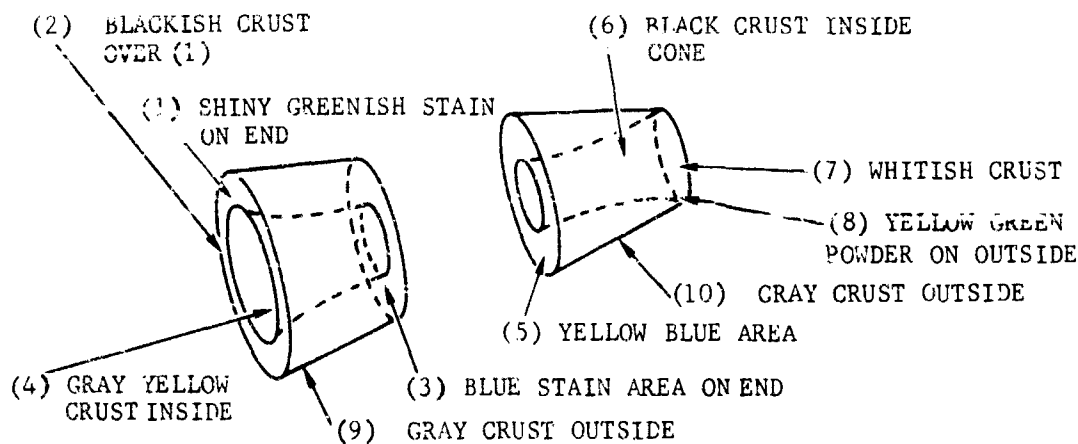
Calculations indicated that one percent material would reach 2400°C (4350°F) in 9 seconds and that the backwall would get this hot in 25 seconds. From the duty cycle imposed, the entire insert would have attained or exceeded this temperature five times. Three of these excursions would have been from ambient temperature.

Some very large grains were evident near the interface of the two pieces of the insert. These grains were of the order of 0.07-inch in size. The material back of the larger grains at the flamefront material varied in grain size from about 0.0025 to 0.004 inch with the grains nearer the flamefront generally exhibiting a slightly larger average size. This is the size range which might be anticipated for 3 or 4 excursions to 2400°C according to the laboratory data presented in Paragraph 4.2.

X-ray diffraction data are given in Table 8.7.

TABLE 8.7

X-RAY DIFFRACTION ANALYSIS DATA DEVELOPMENT TEST NO. 2 SAMPLES



Sample*	Percent of Compound in Sample					Unidentified**
	$\alpha\text{W}_2\text{C}$	$\alpha\text{Al}_2\text{O}_3$	WO_3	Al_4C_3	WC	
1	85-90	2-5	5-10	-	-	-
2	5-10	80-90	-	2-5	-	2-5
3	-	45-55	45-55	-	-	-
4	-	90-95	-	-	-	5-10
5	-	45-55	45-55	-	-	-
6	20-25	60-70	-	5-10	-	5
7	5-10	70-80	5-10	-	-	5-10
8	-	-	100	-	-	-
9	40-50	trace	5-10	-	40-50	-
10	55-65	trace	5-10	-	30-35	-

* No $\text{Al}_4\text{O}_4\text{C}$ or Al_2OC present.

** Unidentified portions were the same (identical peak positions) for each sampling.

CONFIDENTIAL

1. Development Test 4 Insert, Figure 8-28 shows a polished and etched section of this one-piece arc-melt and extruded tungsten insert. Surface streaking is apparent on the flameside material as it was for the insert of the second development test nozzle.

Figures 8-29 and 8-30 are enlargements of the polished sections shown in Figure 8-28. The great difference in grain size between the two figures is quite marked. In Figure 8-29, which shows the larger grains, there is an abrupt decrease in grain size in the radial direction -- the grains are huge near the inner surface and abruptly become much smaller outward from this region. The grain size in this region is approximately 0.03 inch for the large grains and back of these grains varies radially from about 0.004 inch to about 0.0027 inch. On the other side of the insert, Figure 8-30, behind the larger grains at the flamefront surface, the grain size varies between 0.003 inch and 0.0035 inch.

That portion of the insert with the largest grains, shown in Figure 8-29, reached a higher temperature than the remainder of the insert. Close inspection of Figure 8-28 reveals corroborative evidence to this effect. There is discernable streaking on the flamefront surface near this region and the upstream edge of the insert has been slightly rounded.

According to analytical prediction, the flamefront material realized a temperature of 4700°F or greater four times and the backside material achieved a temperature of 4700°F or greater twice during the duty cycle. These temperatures would be more than sufficient to cause both grain growth and backside carbide reactions.

In Figure 8-30 the striations are not all parallel. In this case, this insert was fabricated from the end of the tungsten billet. The arc melting of the tungsten into the ingot form could be expected to produce this effect at the end of the bar which was first melted.

There was no backside leakage behind this insert since a good fit was obtained with the backup graphite. Still carbide formation was evident on the backside of the tungsten insert. X-ray diffraction data for samples removed from this insert are given in Table 8.8. It is noted in this table that the sample taken from the backside of the insert (sample 1) was almost all carbide. This carbide was observed to exist uniformly over the backside surface to an estimated depth of 0.002 inch.

CONFIDENTIAL

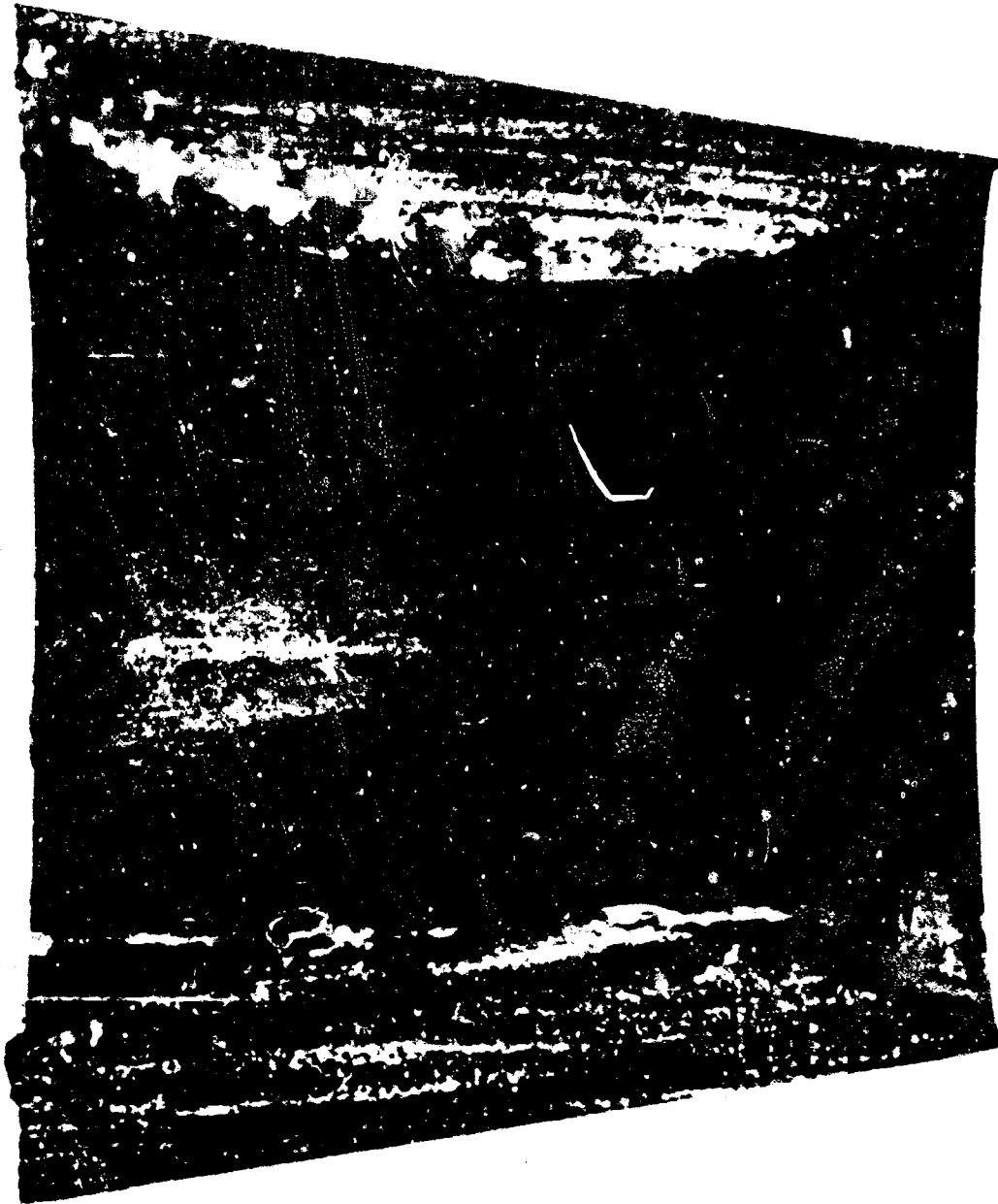


FIGURE 8-28. SECTIONED INSERT OF DEVELOPMENT TEST NO. 4.



FIGURE 8-29. SECTIONED INSERT OF DEVELOPMENT TEST NO. 1

CONFIDENTIAL

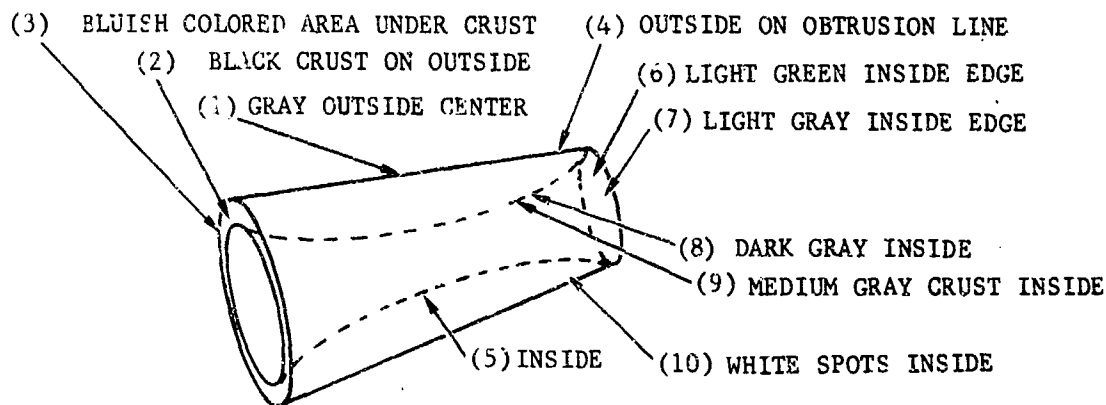


CONFIDENTIAL

CONFIDENTIAL

TABLE 8.8

X-RAY DIFFRACTION ANALYSIS DATA DEVELOPMENT TEST NO. 4 SAMPLES



Sample	$\alpha\text{Al}_2\text{O}_3$	Percent Compound in Sample					W
		WC	$\alpha\text{W}_2\text{C}$	Al_4O_3	WO_3	R- Al_2O_4	
1	-	75-85	10-15	-	5	-	-
2	90-95	trace	2-4	2-4	-	-	-
3	-	5-10	85-90	-	1-3	-	-
4	-	-	5-10	-	90-95	-	-
5	2-5	2-5	2-5	trace	5-10	-	80-90
6	2-4	-	-	2-4	90-95	-	-
7	80-90	-	-	-	10-20	-	-
8	70-80	-	2-5	trace	2-5	10-20	-
9	20-30	2-5	2-5	2-5	2-5	50-60	-
10	60-70	2-5	-	-	trace	20-30	-

g. Discussion. One factor which obscures the tungsten grain growth phenomenon is that large grains grow faster than small grains. Once grain growth is initiated, larger grains can be formed by the violation of a single grain boundary. If grain growth be viewed as merely a succession of doubling grain size, i.e., two grains combine to form a single larger grain, then the grain size goes up by powers of two. A region which has experienced the causative mechanism to a degree sufficient to produce only half the effect that another region has experienced would have only one-fourth the grain size of the other region. In effect, this is what happens. The causative mechanism is a combination of temperature and time, and extremely high temperatures appear to produce a given grain size in less than a proportionate time than do lower temperatures.

CONFIDENTIAL

Initial microstructure or substructure is probably an influencing factor in grain growth. As can be noted in Figures 8-14, 8-19, 8-27, and 8-29 some non-monotonic grain size gradients as well as some abrupt changes in grain size were produced in the inserts. Some of these effects appear to be associated with the striations evident in the material. These striations are associated with the processing of the material. The abrupt changes in grain size in Figures 8-27 and 8-29 appear to be associated with isotherms.

A rough correlation can be made between the laboratory data and the experimental data for the two development tests. The smaller grains which exist behind the large grains in the flamefront material are in the size range which might be expected for the number of temperature excursions to 2400°C which were experienced. An attempt was made to correlate the observed grain growth with the number of excursions to and total time above certain temperature levels. These data are presented in Table 8.9. In this table, there is a wide discrepancy between the rocket motor test data and the development test data. Degradation of the entrance sections of the rocket motor test nozzles had the effect of increasing the heat transfer coefficient at the insert and thereby increasing the temperature level which the insert actually attained. It would appear, then that grain growth is quite sensitive to these higher temperatures. This is confirmed by the insert of development test number 4. Where this insert becomes locally hotter, grain growth was quite exaggerated and abruptly fell off behind the hotter region.

The observation of carbide formation on the backside of the inserts of the rocket motor tests was somewhat obscured by backside leakage. The combustion products were available in these cases to induce carbide formation. It can, in general, be concluded that the backside carbide formation was almost in proportion to the degree of backside leakage.

The correlation of carbide formation is much better for the development test inserts. The backsides of these two inserts were at or above the critical temperature of 2475°C (4480°F) only briefly. Uniform carbide coatings were observed on the backsides of the two inserts to an estimated depth of about 2 mils. No incongruent melting was observed as might be expected had the inserts been held at this or higher temperatures for longer times.

No attempts were made to determine any effects of alumina on any of the tungsten material. The equipment available to probe for the presence of grain boundary materials was not sensitive enough to detect compounds having low atomic number constituents.

CONFIDENTIAL

TABLE 8.9
TUNGSTEN GRAIN SIZE AND TEMPERATURE HISTORY SUMMARY*

Test	Flamefront Material					Backside Material					
	Average Grain Size	Estimated Number of Excursions to and Total Time Above				Average Grain Size	Estimated Number of Excursions to and Total Time Above				
RM 7	0.016	3 71 sec	3 41 sec	2 11 sec	None	5500°F	4350°F	4700°F	5000°F	5300°F	5500°F
RM 8	0.047	3 132 sec	3 94 sec	3 58 sec	2 6 sec	None	0.008	3 28 sec	1 1 sec	None	None
Dev. 2	0.004**	5 87 sec	5 73 sec	4 18 sec	1 1 sec	None	0.011	2 4 sec	None	None	None
Dev. 4	0.004**	4 82 sec	4 67 sec	3 38 sec	1 10 sec	None	0.0025	3 20 sec	None	None	None
							0.003	3 39 sec	2 7 sec	None	None

*Temperature data in table are based on analytical predictions and assume that integrity of entrance section is maintained and ignores deposition effects.

**Average grain size behind large flamefront grains.

CONFIDENTIAL

CONFIDENTIAL

8.3 EXIT SECTIONS

All exit sections performed well in the rocket motor and development tests. The flamefront materials of these sections were polycrystalline graphites, or a combination of polycrystalline graphite followed by carbon cloth phenolic for all nozzles. As discussed in Sections 5 and 6, erosion of exit sections occurred on some tests because of backside gas leakage of tungsten inserts. This is not considered to be an exit section problem since its solution lies in the throat region. No other erosion and no cracking of these exit sections was observed.

The problem of gas leakage was attacked by providing a better fit between the tungsten insert and the ATJ backup. This reduced the exit section erosion as evidenced by the results of tests 12 and 13 of the rocket motor series and the results of the development tests.

Because experience had shown that exit sections of subscale rocket nozzles present no inherent problems, no analysis was performed for the rocket motor test nozzles. It was felt that analyses developed for these sections would be useful only in lending a degree of sophistication to design technology which already existed. This confidence has been justified by the successful performance of the exit sections.

A note of caution is in order at this point. Flightweight nozzles, composed of minimum sections would have additional considerations attendant to their designs. These considerations include methods of retention of the flamefront materials, large expansion ratios resulting in large diameter components, small wall thicknesses, and thin outer shells.

The methods of retention may result in high localized contact stresses or the creation of stress concentrations.

Large diameter, thin wall components can behave as shells, wherein the temperature distribution is approximately linear. Recalling from Paragraph 3.2.1 that the thermal stresses are proportional to the product of the temperature difference across the wall and a loading function, f_n , the loading function takes on its maximum value for a linear temperature distribution and can thus be two or three times greater than for a thicker section. The temperature difference then needs to be only one-half or one-third its value for thicker sections in order to develop the same stress response. Although the temperature in exit sections is not so extreme as for other components, it does not need to be in order to produce the same degree of structural response.

Thin outer shells may not produce the same degree of radial restraint as is produced by thicker sections of lower modulus materials such as is obtained in throat sections. Thus, the reduction of tensile response by backside restraint is lessened and this can be important for flamefront materials which have tensile strengths much lower than their compressive strengths.

CONFIDENTIAL

8.4 INSULATION

To determine the ability of the ablation analysis in predicting ablation characteristics and the limitations imposed on the ablation analysis by the lack of accurate ablation property data, the ablation analysis was applied to the demonstration and development motor firings. The predicted and measured ablation characteristics were compared using the following correlations:

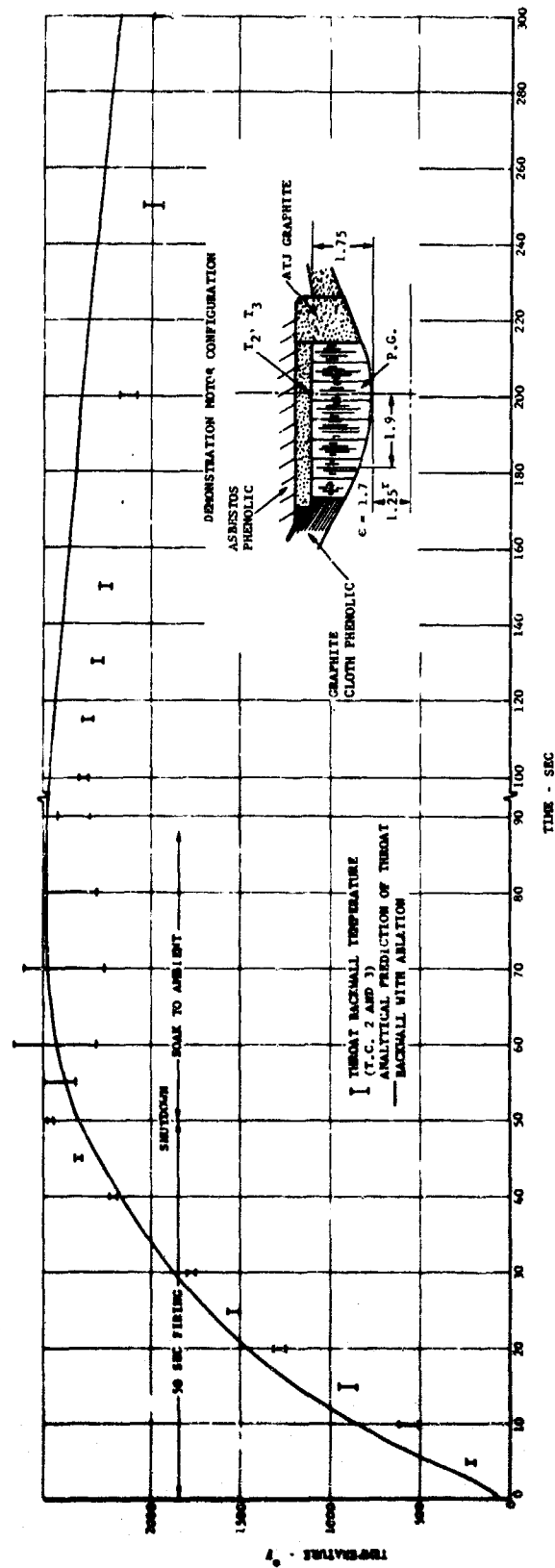
- (1) Pyrolytic graphite (PG) backwall temperature response
- (2) Heat dissipated during soak back
- (3) Final char thickness

These correlations represent important parameters in defining duty cycle limitations and rocket motor design criteria and are also easily acquired from the motor firings.

The pyrolytic graphite backwall temperature response, although directly related to heat dissipated after insert equilibration, gives a good indication of the behavior of ablation during equilibration and the total heat absorbed by the heat sink during firing (verification of analytical convective and radiative boundary conductions). The measured and predicted pyrolytic graphite backwall temperatures are shown in Figures 8-31 and 8-32 for the development and demonstration motor firings, respectively. In Figure 8-31 the correlation between the analytical prediction and measured values is very good during the firing and soak periods. However, during the period immediately following shutdown, the thermocouple measurements experience a large decrease in temperature. This phenomena has been discussed in Paragraph 2.4 and is considered to be caused by an instantaneous increase in pyrolysis gas mass flow (the increase in pyrolysis gas mass flow is caused by the large chamber pressure decay during shutdown). The deviation in the predicted ablation analysis and measured temperatures before shutdown is attributed to the delay in pyrolysis mass flow through the developed char. This is evident by comparing the analytical prediction, assuming no ablation, with the actual results. The difference between the measured and predicted results during the soak period is largely caused by the deposition phenomena and the convective boundary condition employed in the analysis. The convective boundary condition employed in the development nozzle thermal analysis causes approximately 6 percent and 3 percent more heat to be absorbed by the pyrolytic graphite washers than actually occurred during the first and second firings, respectively.

The throat backwall thermal response for the demonstration test is shown in Figure 8-32. The effect of the start transient and alumina deposition on the backwall temperature is evident during the first 30 seconds of firing. (The rate of pressure rise and the time to reach a nearly steady chamber

CONFIDENTIAL



FO4504 C

FIGURE 8-32. PREDICTED AND MEASURED THERMAL RESPONSE OF TROAT INSERT FOR DEMONSTRATION TEST

CONFIDENTIAL

CONFIDENTIAL

pressure was considerably less for the demonstration than for the development firing as shown in Figure 8-33. The deviation between the predicted and measured temperatures in the 40- to 50-second period is attributed to the pyrolysis gas mass flow rate that results when the effects of gas momentum change and gas storage are not considered. The thermal analysis, using the radiation and convective boundary conditions employed in the demonstration nozzle, predicted approximately 9 percent more heat to be absorbed by the throat washer than actually occurred.

The ability of the thermal analysis in predicting the thermal response during the soak period can, in part, be determined by comparing the measured and predicted cooldown rates. Figures 8-34 and 8-35 present the measured and predicted cooldown rates for the pyrolytic graphite development and demonstration firings, respectively. Only the soak back heat transfer mechanisms that were found to be important in Paragraph 2.4 were included in the thermal analysis of Figures 8-34 and 8-35 (i.e., two-dimensional conduction, ablation, intersurface radiation, and radiation to space).

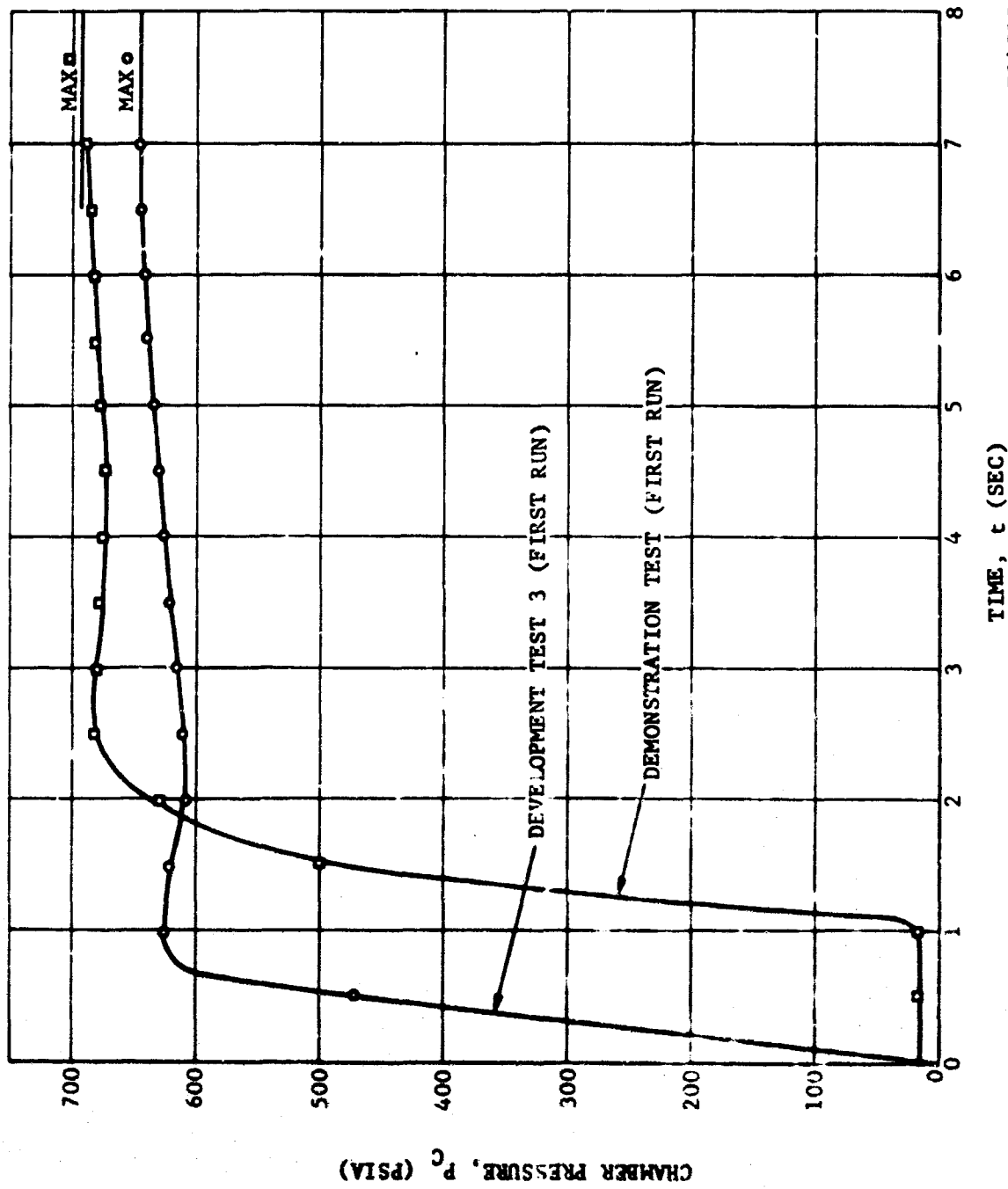
The enthalpy change of the throat washer during soakback for the development and demonstration nozzles was found from the thermocouple trace after insert equilibration. After the equilibration period (insert approaches a radial isothermal condition) the change in pyrolytic graphite backwall temperature (dT/dt) is related directly to the enthalpy change of the washer ($dH/dt = c dT/dt$). In Paragraph 2.4.3 it was found that the heat dissipated by ablation is considerably larger than the heat removed from the pyrolytic graphite washers by the other cooldown mechanisms. Therefore, the measured and predicted enthalpy change of the pyrolytic graphite washers is almost entirely a result of ablation.

In Figure 8-34 the effect of heat content level at the initiation of heat soak on ablation performance is shown when complete cooldown to ambient condition was not reached. The predicted enthalpy change at the end of the first soak period is slightly less than the initial enthalpy change at the initiation of the second soak period. Also, the enthalpy change during the second soak period reaches a peak at approximately 50 seconds; whereas the first soak period enthalpy change is always decreasing. That is, at the end of the first soak period, the ablation rate was approaching steady state. By firing the motor a second time (see Figure 8-34), the enthalpy level of the washer was increased, thereby increasing the heat transferred to the pyrolysis zone; consequently the ablation rate and radial temperature gradient in the char increased.

In Figure 8-35, the effect of initial char thickness and heat content level on the ablation phenomena is shown. During the first cooldown, the motor reached ambient conditions; therefore, on restart, the enthalpy change versus time will be of the shape as that obtained during the first soak period, but will be of a lower level.

CONFIDENTIAL

CONFIDENTIAL



FO4505 C

FIGURE 8-33. INITIAL CHAMBER PRESSURE VS TIME COMPARISON

CONFIDENTIAL

CONFIDENTIAL

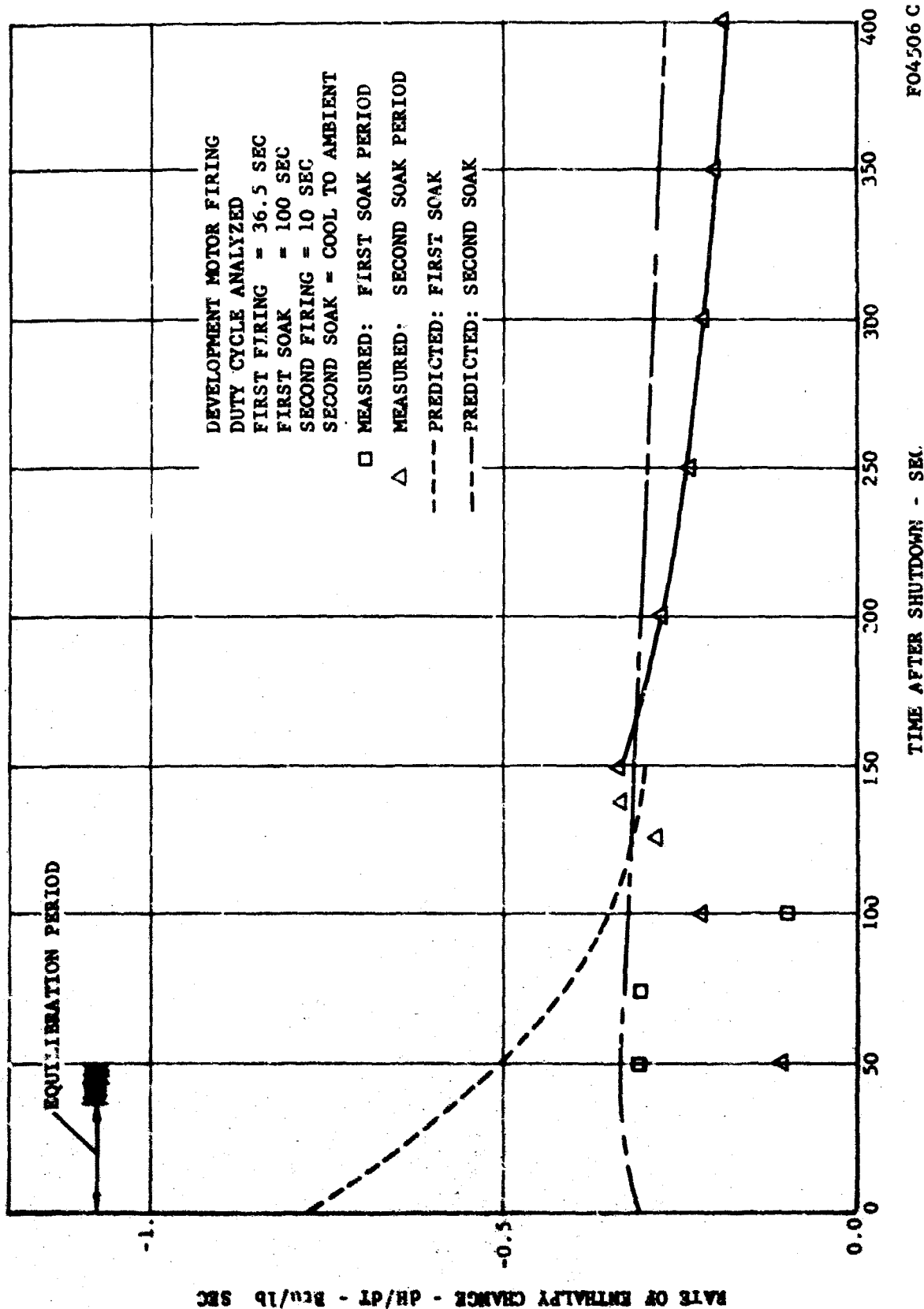
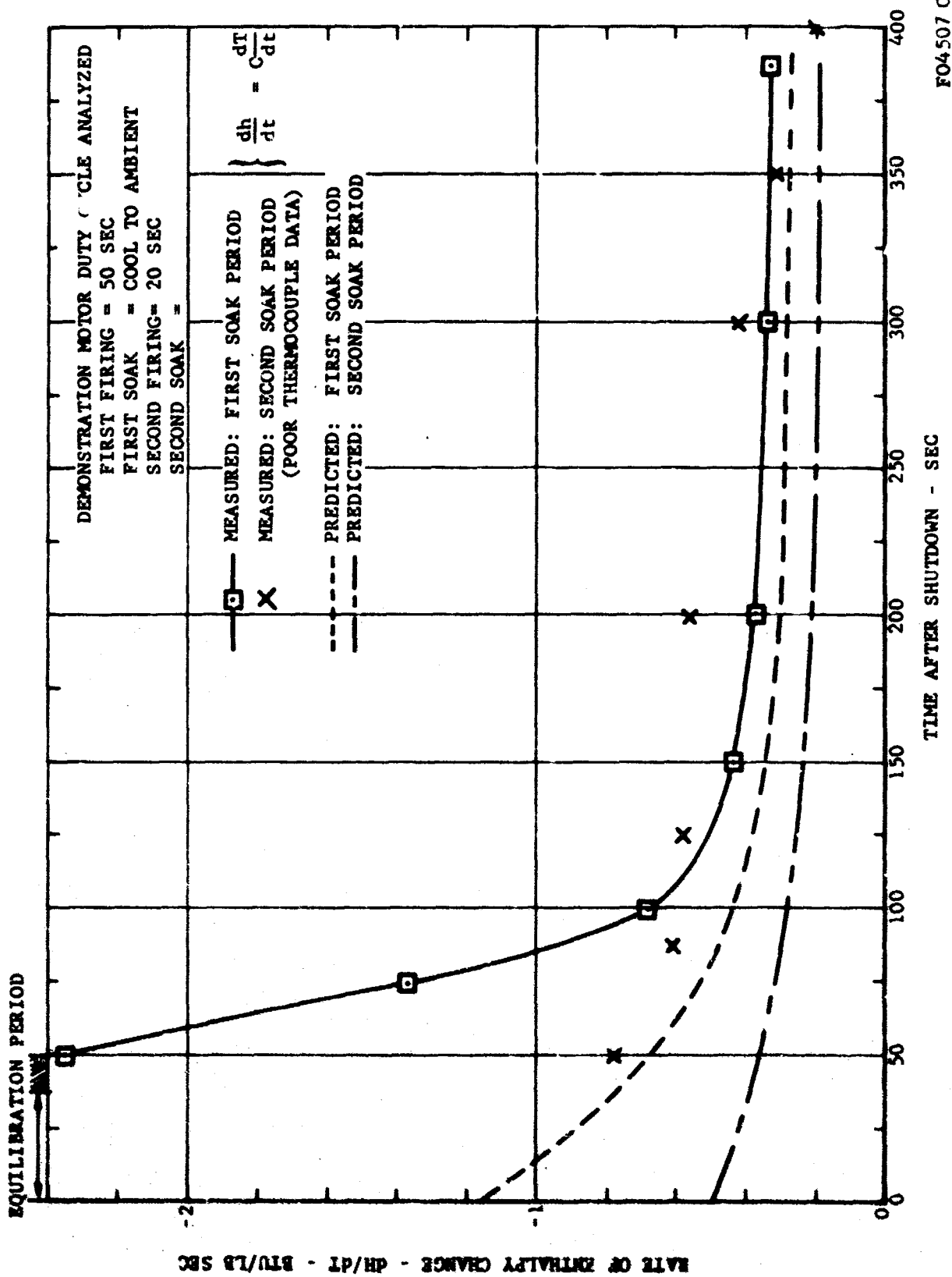


FIGURE 8-34. RATE OF ENTHALPY CHANGE OF THROAT WASHER VERSUS SOAK TIME FOR AS-DEPOSITED P.G. DEVELOPMENT MOTOR FIRING

FO4506 C

CONFIDENTIAL

CONFIDENTIAL



FO4507 C

FIGURE 8-35. RATE OF ENTHALPY CHANGE OF THROAT WASHER VERSUS SOAK TIME FOR DEMONSTRATION MOTOR FIRING

CONFIDENTIAL

CONFIDENTIAL

By comparing Figures 8-31 and 8-32 during the first soak period, it can be seen that the backwall temperature for the demonstration nozzle (see Figure 8-35) after equilibration is higher than that of the development nozzle (Figure 8-34). Therefore, as expected, the enthalpy change during the first soak period is larger for the demonstration nozzle (Figure 8-35) than that of the development (Figure 8-34).

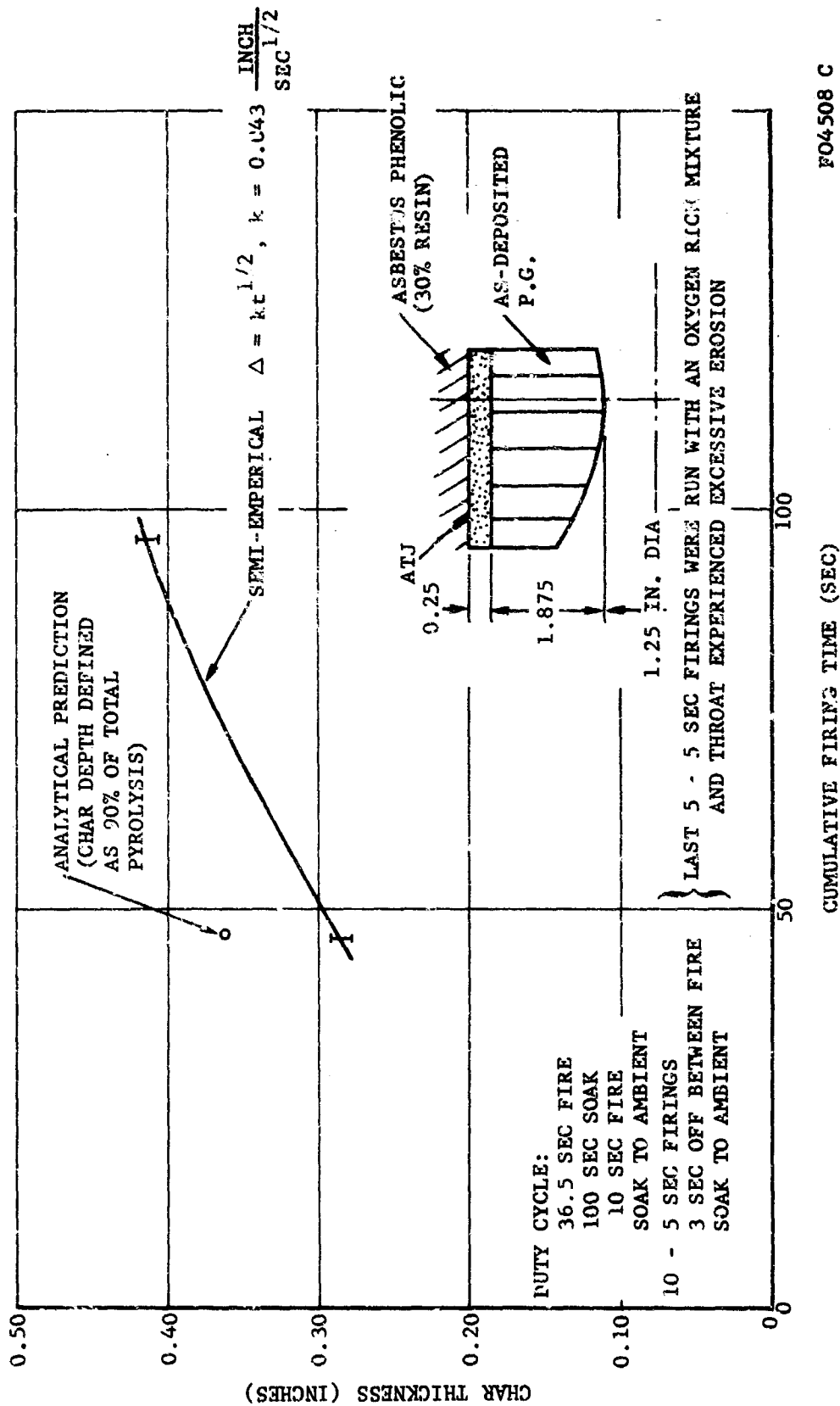
The correlation between the predicted and measured enthalpy change that is indicated in Figures 8-34 and 8-35 is largely dependent on the accuracy of the thermocouple data and the ablation property values employed in the thermal analysis. As indicated in Figures 8-36 and 8-37, the predicted char depths are larger than those measured, yet the predicted enthalpy change is of the same level as that indicated by the thermocouple data. This indicates that both the predicted ablation rates and the corresponding amount of energy absorbed by the ablation phenomena are in error. These errors are of course reflected by inaccuracies in the ablation properties. Of the ablation properties employed in the analysis, the Arrhenius rate constants, char thermal conductivity, and carbonaceous char-reinforcement chemical reactions are considered of primary importance. The accuracy of the thermocouple data used in determining the enthalpy change is highly questionable as evidenced by the scatter in Figures 8-34 and 8-35. This thermocouple discrepancy may be attributed to the pyrolysis products and the time at which the thermocouple is at high temperatures. The latter has been found to affect both the thermocouple calibration and contact resistance.

The predicted final char depth, after the first cooldown to ambient is shown in Figures 8-36 and 8-37 for the demonstration and development nozzle firings, respectively. The semi-empirical determined char depths in both figures were based on the final measured char depth and the equation $r = k t^{1/2}$, where t is the cumulative firing time. Use of this equation in determining the char depth is valid only when the nozzle cooled to an ambient condition.

The predicted char depth is overly conservative as noted in Figures 8-36 and 8-37. The correlation presented in Figure 8-36, however, is approximate, since, during the last 25 seconds of firing, the slurry orifices plugged and the propellant combination was oxygen rich causing the throat to undergo excessive corrosion-erosion. Therefore, the heat that is to be dissipated by ablation is less (loss of heat sink material and reduced heating during firing). The conservatism of the analytical predicted char depths is felt to be influenced primarily by inaccuracies in the ablation property data and the conservative prediction of the heat absorbed during firing. As Figures 8-31 and 8-32 indicate, the predicted heat absorbed during firing is higher than the measured, therefore causing the predicted char depth to be larger than measured. Also, the ablation analysis did not include the highly endothermic carbon-silica reaction. The heat absorbed by this reaction was required to be dissipated by

Best Available Copy

CONFIDENTIAL

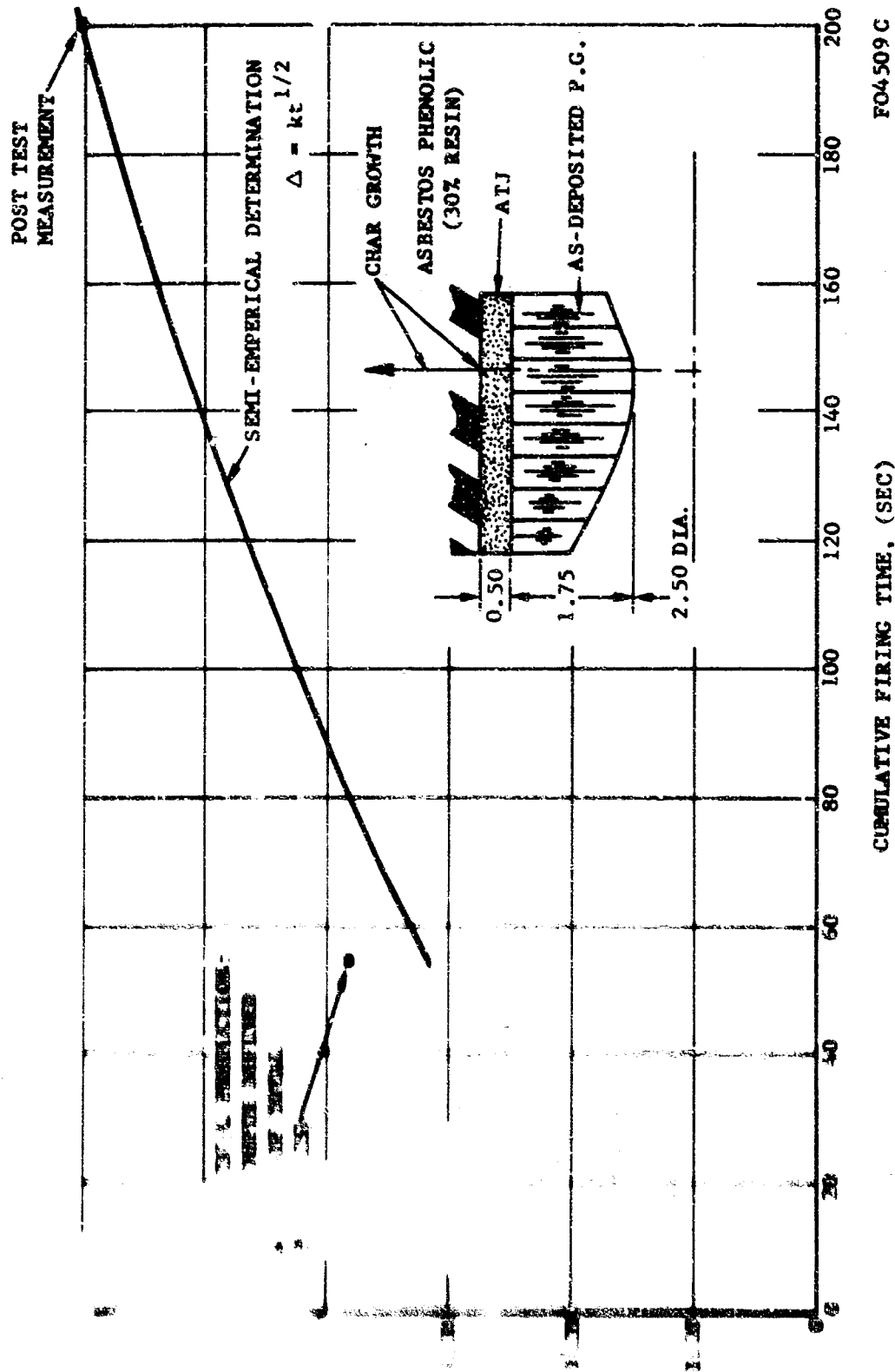


FO4508 C

FIGURE 8-36. CHAR GROWTH VERSUS CUMULATIVE FIRING TIME FOR DEVELOPMENT NOZZLE

CONFIDENTIAL

CONFIDENTIAL



FO4509 C

CUMULATIVE FIRING TIME, (SEC)

FIGURE 8-37. CHAR GROWTH VERSUS CUMULATIVE FIRING TIME RESTART DEMONSTRATION NOZZLE

CONFIDENTIAL

CONFIDENTIAL

virgin pyrolysis in the analytical model, resulting in a conservative prediction of char depth. From post-test analysis, the char was found to have a considerable amount of SiC indicating that this reaction should be included in the analysis.

8.5 ALUMINA DEPOSITION

Rocket motor nozzle materials performance can be significant and advantageously affected by alumina deposition since the nozzle thermal response of an aluminized solid propellant rocket motor is a strong function of this deposition. This relationship between alumina deposit and thermal response is discussed in Paragraph 2.4 of this report. A physical model was developed to describe deposition behavior by utilizing the various test data of this program coupled with laboratory results from this and prior programs. A complete description of the model is presented in Paragraph 2.4.

The primary purpose of this paragraph is to correlate results of the physical model with the semi-empirical calculations of alumina deposition as determined from the rocket motor and development tests. The latter calculations are derived from Equation (3) of Paragraph 8.2.1, and are plotted as a function of firing time for the edge grained pyrolytic graphite rocket motor nozzles in Figures 8-38, 8-39, 8-40, and 8-41. Deposition for those rocket motor nozzles having tungsten throats (i.e. tests 7, 8, 12 and 13) could not be calculated in the aforementioned manner since plastic deformation of the tungsten throats during firing, coupled with the throat obtusion process, masked any deposition with a significant positive ΔP_c response. Alumina deposition calculations were also impractical on nozzles such as rocket motor test-14 where many short cycles with cooldown periods insufficient to obtain throat measurements were employed.

There are three basic factors related to deposition behavior that can be acquired from the rocket motor tests. These are:

- (1) Measurement of deposition thickness versus time at the throat utilizing the aforementioned technique
- (2) Visual observation of flow separation in exit cone
- (3) Visual observation of sparks in periphery of the plume.

CONFIDENTIAL

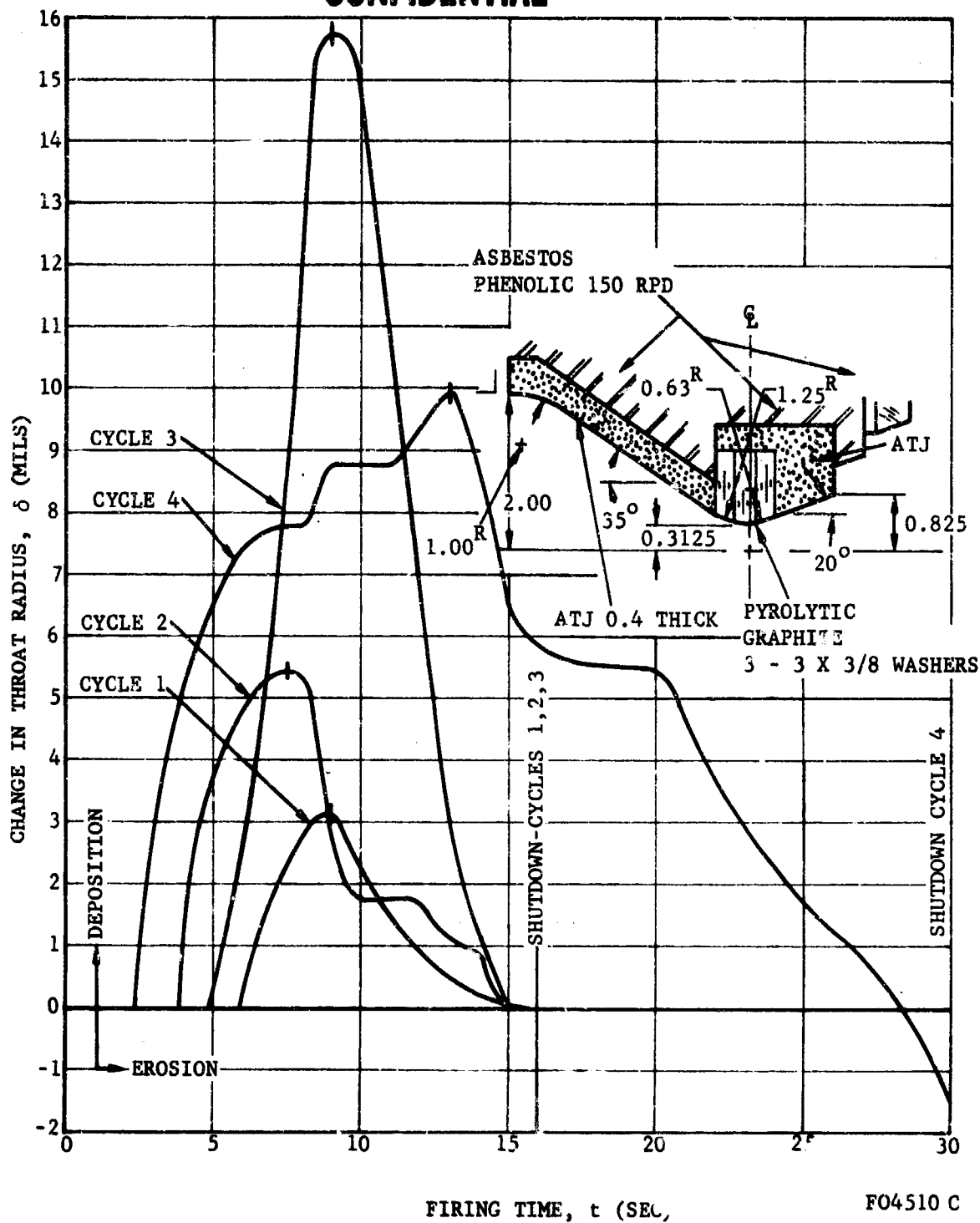


FIGURE 8-38. NOZZLE THROAT RADIUS CHANGE VERSUS FIRING TIME
RESTART ROCKET MOTOR TEST NO. 3
(AS-DEPOSITED PYROLYTIC GRAPHITE)

CONFIDENTIAL

CONFIDENTIAL

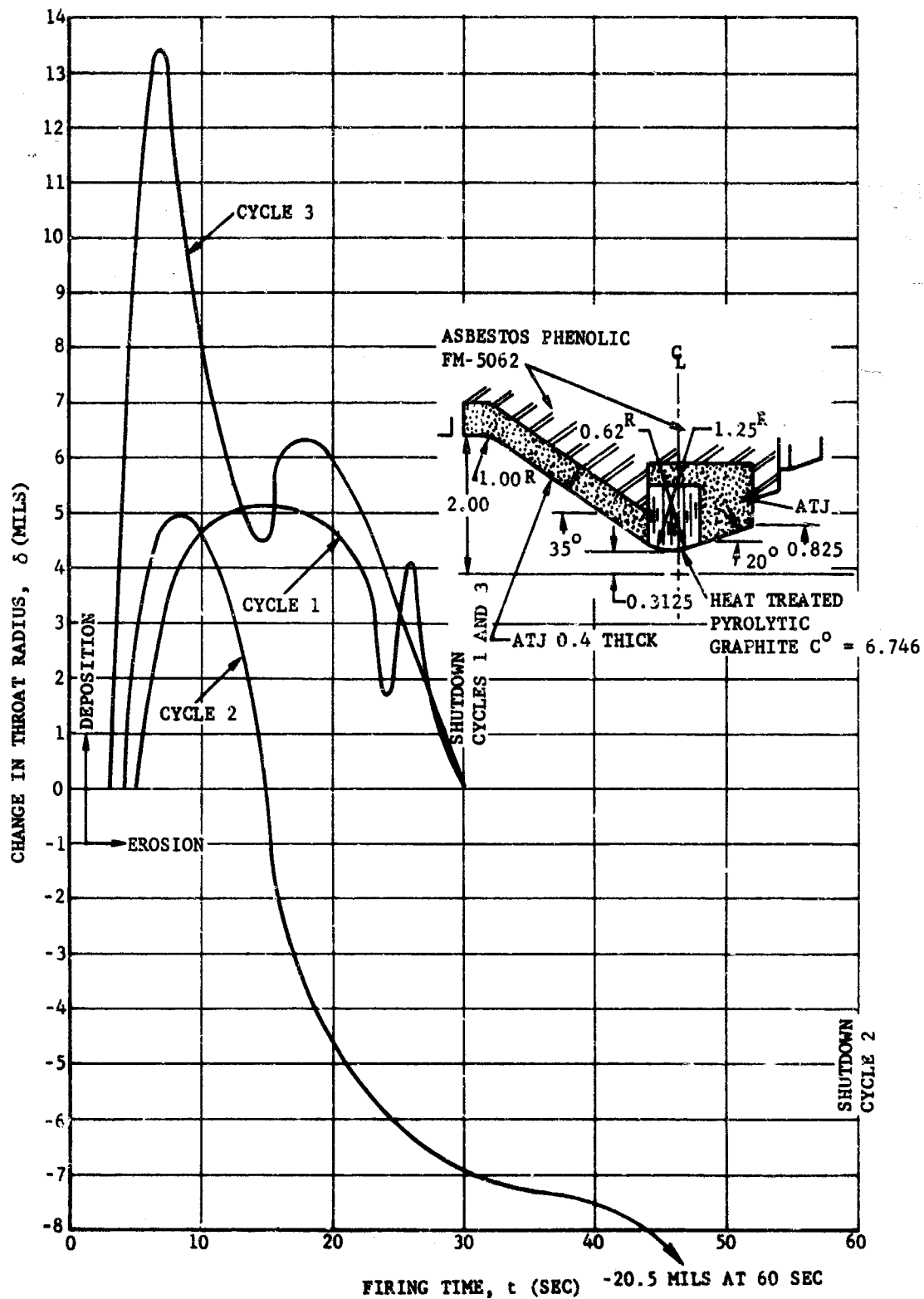


FIGURE 8-39. NOZZLE THROAT RADIUS CHANGE VERSUS FIRING TIME
RESTART ROCKET MOTOR TEST NO. 4
(HEAT TREATED PYROLYTIC GRAPHITE)

FO4511 C

8-74

CONFIDENTIAL

CONFIDENTIAL

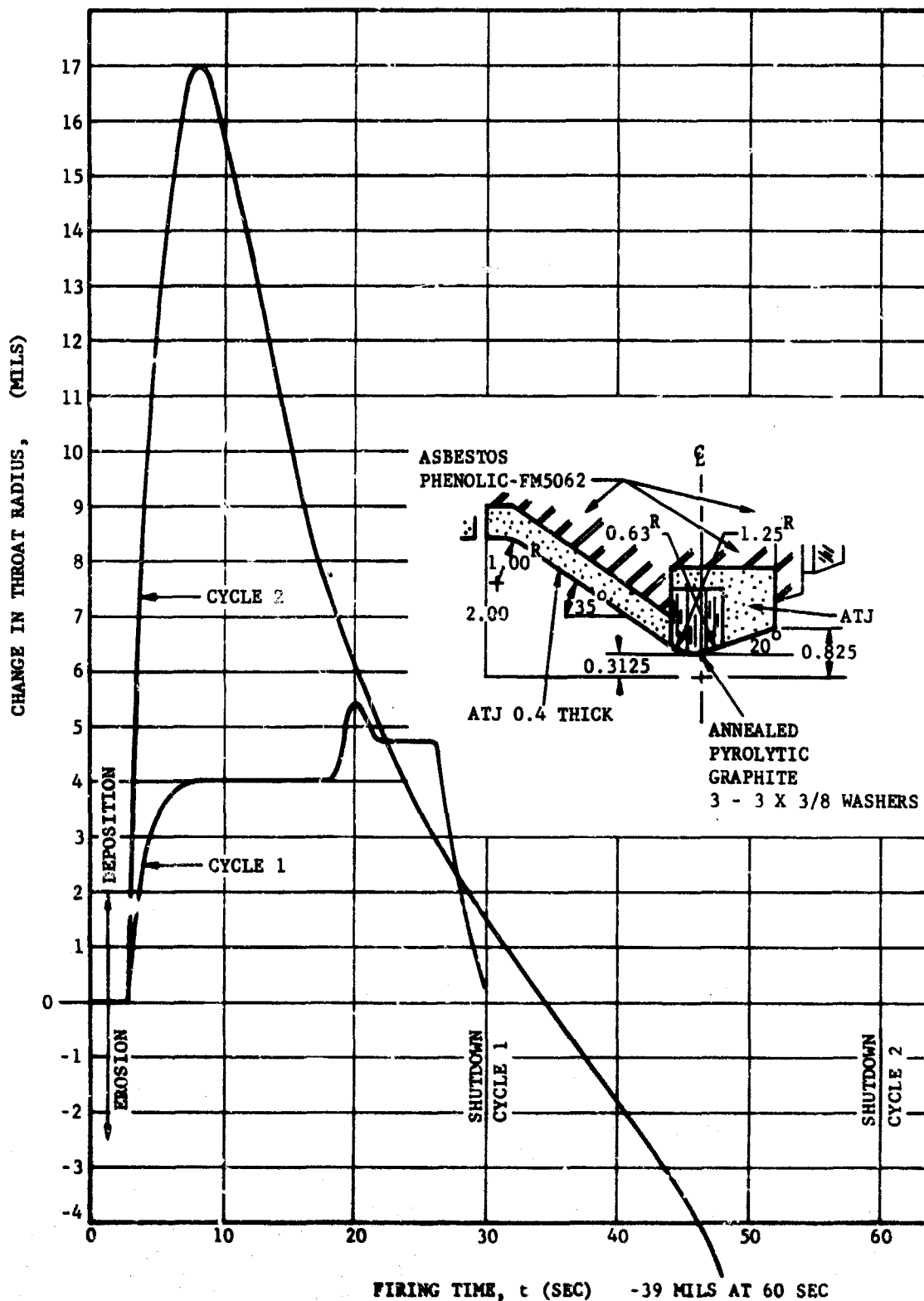


FIGURE 8-40. NOZZLE THROAT RADIUS CHANGE VERSUS FIRING TIME
RESTART ROCKET MOTOR TEST NO. 6
(ANNEALED PYROLYTIC GRAPHITE)

FO4512 C

8-75

CONFIDENTIAL

CONFIDENTIAL

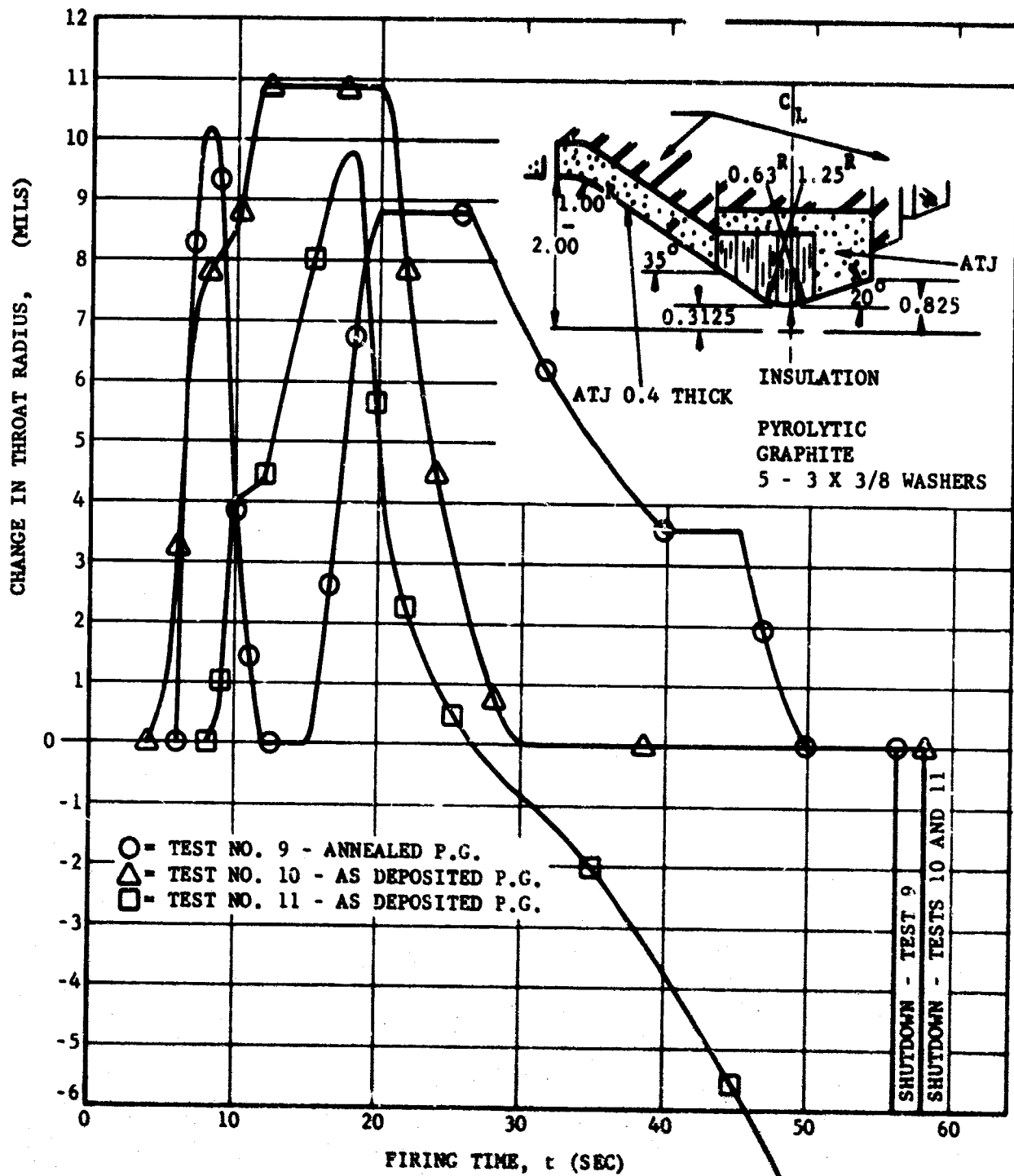


FIGURE 8-41. NOZZLE THROAT RADIUS CHANGE VERSUS FIRING TIME
 RESTART ROCKET MOTOR TESTS 9, 10 AND 11

FO4513C

8-76

CONFIDENTIAL

CONFIDENTIAL

As can be seen in Figures 8-38 through 8-41, there is a period in the firing in which alumina is being stored at the throat (increase in deposit thickness). This period (defined as Period 1) is shown in Step (3) of Figure 2-5. Liquid alumina flows from the entrance section to the pyrolytic graphite insert and solidifies, causing a mass storage of alumina. The mass storage period is followed by a period at which the alumina mass entering the throat is equal to the mass leaving (defined as Period 2); the length of this period being dependent on the upstream alumina behavior and the rate at which solid alumina at the throat is liquifying. As noted in the deposition figures, Period 2 may be followed by a mass loss or a mass stored period (defined as Period 3). Period 3 represents Step (4) and/or (5) in Figure 2-5 and alternatives 1 and 2 of Paragraph 2.4.2a may apply; that is, if during Period 3 mass is stored, the mass leaving the entrance is transient in the positive sense. This may be caused by (1) an increased impingement rate, (2) by an increased liquification rate, and/or (3) increasing local wall shear in the entrance or upstream throat insert sections. The depletion of mass in Period 3 is caused by an increase in local solid liquification rate and/or a decrease in upstream mass flow. If Period 3 is a mass loss situation, Step (5) of Figure 2-5 follows; whereas, if Period 3 is a mass storage situation, Period 2 follows.

When the nozzle undergoes pulsing, the deposit behavior is described by alternatives 3 and 4 of the physical model (Paragraph 2.4.2) since entrance surface regression may be experienced during the previous pulse and/or an initial deposit may be present during start up. By comparing total deposit present on the throat ($\int_0^t \delta dt$), Figure 8-42, it can be seen that as the number pulses increases, $\int_0^t \delta dt$ increases. This effect can be attributed to surface regression and/or initial deposit "seeding" at start up. That peculiar decrease in $\int_0^t \delta dt$ for Cycle 2 of the heat treated pyrolytic graphite nozzle is a result of an early throat regression during this cycle. The reason for the regression is unexplainable, and therefore $\int_0^t \delta dt$ for Cycle 2 of rocket motor test 4, as shown in Figure 8-42, must be considered a questionable data point.

The effect of throat insert material on the deposit behavior is clearly evident in Figure 8-42, where it is shown that as the gas side surface material thermal conductivity increases, total deposition also increases. That is, the heat conducted away from the deposit is dependent on the thermal conductivity of the surface material and interface contact resistance. Therefore, as the thermal conductivity of the surface material increases, the heat and thus time required to melt the deposit also increase.

CONFIDENTIAL

CONFIDENTIAL

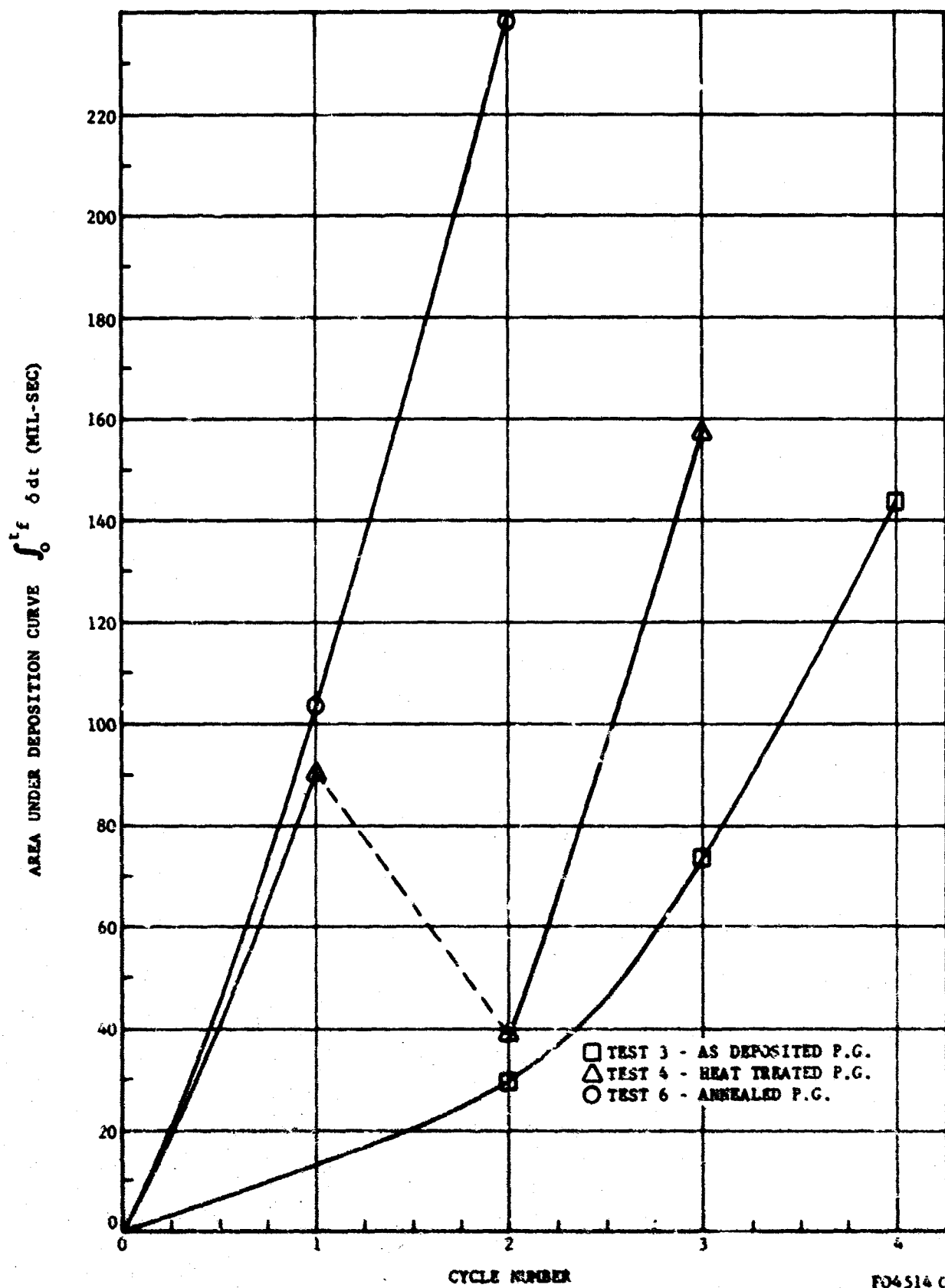


FIGURE 8-42. $\int_0^{t_f} \delta dt$ VERSUS CYCLE NUMBER

8-78

CONFIDENTIAL

CONFIDENTIAL

The effect of pyrolytic graphite stack thickness upstream of the throat, i.e., entrance section location of pyrolytic graphite-ATJ interface, can be found by comparison of Figure 8-41 with the initial pulses of Figures 8-38, 8-39, and 8-40. The transient deposition thickness, the $\int_0^t \delta dt$, and the time of deposit removed are all greater for nozzles shown in Figure 8-41, than the comparable nozzles having smaller pyrolytic graphite throats axially (Figures 8-38 through 8-40). This may be explained with reference to Step (3) of Figure 2.5. From Step (3), it can be seen that the deposit thickness is very dependent on the pyrolytic graphite location (thermal conductivity of pyrolytic graphite-ATJ). The presence of pyrolytic graphite at high inlet area ratios provides both a larger distance over which the impingement may be experienced and also a greater heat sink effect. That is, with pyrolytic graphite at large area ratios where the heat flux is small, a significantly longer time is required to melt the deposit than if the pyrolytic graphite were replaced with ATJ. The deposition resulting in second and third pulses (when applicable) of Figures 8-38, 8-39, and 8-40 are influenced by the previous pulses (i.e., surface regression and initial deposition) and therefore are not included in the above correlation.

Deposition calculations were also made for development test 3, Cycle 1, for comparison with Figures 8-38 through 8-41. This deposition is plotted as a function of time and is shown in Figure 8-3 of Paragraph 8.2.1. No deposition calculations were possible for the demonstration nozzle due to a masking of the deposition by nozzle throat erosion.

CONFIDENTIAL

CONFIDENTIAL

REFERENCES

- 8.1 Van Karman, T., and Malina, F. J., "Characteristics of the Ideal Solid Propellant Rocket Motor," Collected Works of Theodore van Karman, Vol. IV, 1956, pp. 94-106.
- 8.2 Bartz, D. R., "A Simple Equation for Rapid Estimation of Rocket Nozzle Convective Heat Transfer Coefficients," Jet Propulsion, pp 49-51, January 1957.

CONFIDENTIAL

CONFIDENTIAL

SECTION 9

CONCLUSIONS

- (U) The objectives of this program were to define and investigate the problems associated with restartable solid propellant rocket nozzles. The problems were to be investigated analytically and experimentally, with verification to be attained from nozzle firings. The scope of the program was limited to a first effort in the investigation of restartable nozzles.

9.1 (C) SUMMARY OF RESULTS

The major achievements deal with an increase in the understanding of material behavior and the development of analytical techniques for predicting nozzle responses. Initially in the program, some potential problem areas were outlined for investigation. These problems were those associated with restart operation without the benefit of any prior detail investigation. As such, several of these problem areas were found to be nonexistent:

- (U) (1) Adverse radial temperature gradients during cooldown and restart to impose more severe thermal stresses.
- (C) (2) The requirement for springs or other devices for edge grain pyrolytic graphite throat sections. After examination of nozzles after several restarts, the use of these devices was unnecessary.
- (C) (3) The cooldown mechanism of the nozzle after firing was found to be chiefly by conduction and convection caused by pyrolysis (ablation)

CONFIDENTIAL

CONFIDENTIAL

of the insulation materials. In the throat and entrance section, this is the principle cooldown mechanism with radiation being an order of magnitude less.

- (U) (4) The behavior of alumina deposits was an initial problem area. This was effectively studied in both the laboratory and in the rocket motor tests. The detailed phenomena of deposition is still not understood. However, the behavior of deposits on the nozzle and their influence of duty cycles was studied. Also, in atmospheric firings, it was found that hydrolysis of the deposit aids in its removal. The consequence of space environment testing (vacuum) is not known.
- (U) (5) The result of repeated thermal loading on materials properties was studied. No adverse changes in polycrystalline and pyrolytic graphite were encountered. Heat treatment and annealing of pyrolytic graphite appears to aid nozzle performance; however, the data are meager and not conclusive at this time.
- (U) Other studies were made as the program progressed and new problem areas uncovered. Materials investigations produced data on tungsten-carbon reactions. Above 2475°C, incongruent melting occurs between tungsten and carbon. The solubility of carbon in the melt is high, and only a small amount of carbon is required to maintain a liquid. The use of a diffusion barrier appears to be promising. The first data on the high temperature c-direction compressive deformation of pyrolytic graphite were generated in this program. Large permanent deformations occur above 2600°C under stresses as low as 7000 psi in very short times. Studies were made on the effect of tungsten grain growth on elastic properties. For the materials used, there appeared to be a degradation in tensile strength with increasing grain size (caused by thermal cycling), while the elastic modulus and coefficient of thermal expansion are not significantly altered over a wide range of grain size. However, it should be pointed out that this reduction may have been caused by segregation of impurities from the grains to the grain boundaries. All specimens exhibited intergranular fracture, implying brittle behavior. The effects of working and grain boundary impurities were not studied, and the only correlation made was with grain size as a variable. The reader should not assume from these studies and results that grain size alone can determine the elastic properties of tungsten.

CONFIDENTIAL

CONFIDENTIAL

- (2) The radiation, conduction (soak back), ablation and convective (pyrolysis gas flow) modes of nozzle cooldown were analyzed in order to predict thermal transients and ablative char growths in restartable nozzles. It was found that the principal mode of cooldown for the throat insert was that of ablation while radiation, depending on the exit area ratio, is an order of magnitude lower. The radial temperature gradients in the throat insert during cooldown are very small. As a result, the thermal loading is also quite small. The exit zone cooldown is due mainly to radiation to space, whereas the entrance section benefits largely from ablation, with radiation comparable to ablation during the first 2 to 4 minutes after shutdown. The effects of alumina deposition on the nozzle throat during firing have been investigated, and it was found that an analysis neglecting alumina is applicable at firing times greater than 30 seconds for a 5/8-inch ID pyrolytic graphite insert. At times less than 30 seconds the difference in surface temperature by neglecting and including alumina deposits is of the order of 1000°F. These same analyses may be employed to determine similar effects for larger size nozzles. However, the difference is expected to decrease with increasing nozzle scale. These thermal analyses result in duty cycle limitations of various nozzle configurations and in curves directly applicable to nozzle design.
- (U) In the structural analysis, simple methods have been developed for predicting the elastic behavior of nozzle inserts. Failure is based on brittle tensile fracture originating at the outer surface of the insert or on spallation at the inner surface. The effects of outer surface restraint to thermal growth and of internal pressure have been included. The effects of restraint can be quite significant while the effects of internal pressure are so small that they easily become lost in the scatter of data. An analysis for predicting the existence and locations of plastic zones within the nozzle inserts has been developed. It is possible to get plastic zones to exist for some depth at the inner and outer surfaces of the insert. It appears that it is impossible to achieve an interior plastic zone or to make the two surface zones join. Large contact stresses are possible between washers which make up the nozzle insert. These stresses are highest at the inner surface of the insert during firing. This is also the hottest portion of the nozzle, and, as a result, plastic deformation can occur in this region. The important factors which must be considered in thermal fatigue of the refractory nozzle materials have been delineated. Corrosion initiated cracking appears to be a potential problem for restartable nozzles.
- (C) The inclusion of the changes of tungsten properties with grain growth due to thermal cycling leads to the prediction that, without considering the constraint provided by the backup structure, a tungsten insert will fail after only slight grain growth. There is a small probability of the tungsten surviving the second application of the maximum thermal loading.

CONFIDENTIAL

CONFIDENTIAL

- (C) It has been determined that starting (firing) from the initial condition of uniform ambient temperature provides the most severe thermal loading. A restart from any cooldown temperature distribution is less severe as far as thermal loading is concerned.

9.1.1 (U) ASSESSMENT OF CURRENT RESTART ANALYTICAL CAPABILITY

- (U) It may be generally concluded that the state of the art of restartable nozzles has been greatly advanced even though there remain many unanswered questions. Any assessment of restart analytical capability must be tempered with an understanding that there is an uncertainty in the precision of material properties, both thermal and mechanical. The ability of an analysis to predict the behavior of hardware is, of course, directly related to the accuracy of these properties.
- (U) The capability for analyzing corrosion is poor. This is true not only for restartable but also for single firing nozzles. From the test results obtained, some empirical data on corrosion rates have been compiled. But these data must be restricted to the chemistry, temperature, and times for which they were gathered and contain no fundamental information such as reaction rates with particular species.
- (U) Thermal analytical capability is very good. Techniques for handling the various modes of heating and cooling are available. The ability to treat the effects of ablation of the insulators and the pyrolysis gases as they influence the thermal behavior exists. From these analyses, not only can the temperature history of a nozzle be determined, but they can also be used for predicting heat sink capacity requirements, insulation requirements, and time restrictions on duty cycles.
- (U) Structural analytical capability is considered to be good although many areas remain to be investigated. Brittle tensile fracture on the outer insert surface or spallation on the inner surface can be simply predicted. Stacked PG washers can be analyzed. This is a significant contribution to the state of the art. The existence and location of plastic zones can be predicted. However, the residual state of stress after removal of load cannot be assessed.

9.1.2 (C) ASSESSMENT OF CURRENT RESTART CAPABILITY WITH MATERIALS INVESTIGATED

At this time, the restart capability of several materials of interest to nozzle systems can be inferred. For insulation material, no current limitations exist. The basic requirement is a low char rate, which asbestos phenolic and low resin silica phenolic possess. However, some new resin systems which are thermally stable to higher temperatures may provide improved performance. A very strong virgin material and strong char are the structural requirements, and the above materials are adequate in this regard. Thus, it may be assumed that the restart capability of these materials is very good.

CONFIDENTIAL

CONFIDENTIAL

- (C) Polycrystalline graphite used in the entrance section cannot be considered as adequate, structurally, for restart applications. To date, it has shown poor performance. However, carbon and graphite cloth phenolic have shown good structural performance at the expense of increased erosion. The erosion resistance of these materials is not so good as the graphites. Another consideration, however, is the cooldown of the entrance. In this respect, the reinforced phenolics appear to be more efficient than the graphite system. This efficiency decreases after several restarts, since the char layer of these moderately conducting materials becomes quick thick. Although the same material systems as applied to the inlet were used in the exit cone of the nozzle, the performance was much better. Polycrystalline graphite can be used downstream of the throat section very adequately for its good erosion resistance. Carbon cloth phenolic appears to be an excellent material for large area ratios. There do not appear to be restart limitations on these materials when applied to the exit cone.
- (C) Polycrystalline graphite as a throat material is limited to short pulses, of the order of four to six seconds with adequate cooldown between pulses in this environment. Except for its poor resistance to corrosion, it appears to have no particular restart limitation. However, grain boundary corrosion could lead to cracks which may induce thermal fatigue failure since all of the thermal cycling is done in the brittle range for this material. Pyrolytic graphite, when used in the edge grain configuration, is an excellent material and has no particular limitation except chemical corrosion. This limits it to firing times in a duty cycle of less than 60 seconds. For these long firing times, surface regression can become a problem and gapping due to surface plastic deformation can induce subsequent surface loss on restart. Changes in the materials properties during firing and soak down are currently not known. However, the use of partially transformed (heat treated) and fully transformed (annealed) material have shown excellent results in nozzle firings.
- (C) For tungsten, there is the possibility of fracture after a small number of pulses due to the property changes which occur during thermal cycling. It has excellent erosion resistance; however, dimensional changes during long firings and carbon diffusion, while hot, can seriously limit its applicability. Leakage behind the insert, especially after several firings, is also a limitation. Little is currently known about its thermal fatigue behavior. Thus, compared to the polycrystalline graphite for short times and pyrolytic graphite for firing times up to 60 seconds, tungsten has some serious restart limitations.

9.2 (C) RESIDUAL PROBLEM AREAS

In discussing further work, problems exist which would increase both the breadth and depth of the investigation.

CONFIDENTIAL

CONFIDENTIAL

- (C) There definitely exists a strong need for further work in the materials area. This includes both the generation of materials property data as well as the behavior characteristics of candidate materials. What happens when very large tungsten grains are grown? The data presented show that the modulus of elasticity starts dropping at a certain grain size. Is it possible that the modulus will drop so low at very large grain size that the structural response will be even less than the lowered strength of the material? Even more basic, what is the influence of grain boundary contamination on elastic properties as a function of grain size?
- (C) Restart tests have indicated that tungsten is a primary candidate for a throat material. Design optimization geared toward elimination of insert backside gas leakage, inhibition of the tungsten-carbon backside reaction, and a retardation of the obtrusion process is paramount. The obtrusion process will in all probability be eliminated if the first two problems are satisfactorily solved.
- (U) Experimental data is needed to determine the erosion threshold of the tungsten. This has been done by analytical techniques which predict the time at which the tungsten flamefront temperature surpasses its melting point, but no experimental data to corroborate this exist since no tungsten throat regression was achieved in the restart tests.
- (U) Carbide formation and melting and the effectiveness of diffusion barriers for tungsten in a restart situation needs further investigation.
- (U) A wide field of investigation exists for pyrolytic graphite. Heat treatment and annealing bring about alterations of the material. These changes related to degree and method of treatment are not understood and need further investigation. A further investigation is indicated to determine the relative performances of annealed, stress relieved, and as-deposited pyrolytic graphite. At present, only an analytically predicted performance comparison can be made based on relative thermal and structural properties. Actual test results to date under controlled and comparable conditions are of a quantity insufficient to substantiate any analytical hypotheses.
- (C) Techniques for machining annealed pyrolytic graphite must be developed if it is to be considered further as a nozzle throat material. Present methods are entirely inadequate. A detailed laboratory evaluation of the physical and thermal characteristics of the pyrolytic graphite in the annealed state is desirable, both for a corroboration of what little work has been done in the past on this material and as a basis for evaluation with the other forms of pyrolytic graphite.
- (U) The c-direction compressive deformation of pyrolytic graphite needs additional investigation to extend the present data. Higher temperatures achieved at higher heating rates coupled with higher stresses applied at the instant of attainment of test temperature should be included in such an extension.

CONFIDENTIAL

CONFIDENTIAL

- (C) Other materials should be examined. Boron pyrolytic graphite, doped tungsten, and tungsten alloys should be investigated for their potential application to restartable solid rocket nozzles.
- (U) Alumina deposition and removal is an urgent area for further work. The problem is complicated because not only alumina is involved. Aluminum carbide exists at the surface of at least the carbonaceous materials and probably to some degree at the surface of tungsten. This is covered by a thin layer of aluminum oxy-carbides, and the alumina deposit lies on this layer. The stability of the oxy-carbides is an important factor in this total deposit. Also, the influence of the environment should be studied.
- (U) Refinement is needed in the analysis of the convective cooldown due to the ablation pyrolysis gases. An improvement is needed in determining the gas temperature in the chamber as a function of time, both during firing and cooldown. Since the convection is a major mechanism in the cooldown of the nozzle, errors in the convection calculation can cause considerable errors in the cooldown time.
- (C) Erosion-corrosion and ablation of the surface materials need to be understood. Knowledge in this area is presently limited. This knowledge is needed not only to predict surface regression but also to predict the heat which is carried away by the material lost. This, of course, affects the accuracy of the thermal analysis.
- (C) Thermal contact resistance between nozzle components influence the temperature history of the nozzle. These contact resistances are not well known. They must change during firing as thermal expansion and pressure loads change the contact pressures between components. They must also change during cooldown, and what is the effect on subsequent restart? For thin sections exposed to the flame, these contact resistances have a great influence on the temperatures of these sections.
- (U) Need exists for the improvement in material property data. It must be realized that reproducibility of material is a major factor. The lack of industry-wide standards as well as the difficulty of production of consistent material by a single manufacturer are factors which must be considered when assessing the applicability of published material data. The ability of an analysis to predict behavior of a piece of hardware is no better than the properties used.
- (U) Time dependent structural behavior should be investigated. The deformations which occur and the resulting residual stress distribution which exists at time of restart should be analyzed and experimentally verified.
- (U) Thermal fatigue, including the effects of corrosion induced cracks, should be investigated.

CONFIDENTIAL

CONFIDENTIAL

- (C) The failure of graphite entrance sections to perform adequately after several restarts remains a large problem area. Also, the structural analytical capability in this region of the nozzle is poor. Further efforts are required in both areas.

CONFIDENTIAL

APPENDIX A

CONVECTION HEAT TRANSFER

A.1 BOUNDARY LAYER SOLUTION

The presently operating numerical routine is an adaption of the analysis of Reference A.1 which employs the integral equations of momentum and thermal energy written in the form

Momentum

$$\frac{d\phi}{dz} + \phi \left(\frac{1 + \delta^*/\phi}{u_e} \frac{du_e}{dz} + \frac{1}{\rho_e u_e} \frac{d(\rho_e u_e)}{dz} + \frac{1}{r_w} \frac{dr_w}{dz} \right) = \frac{C_f}{2} \left(1 + \left(\frac{dr_w}{dz} \right)^2 \right)^{1/2} \quad (A.1)$$

Thermal Energy

$$\frac{d\phi}{dz} + \phi \left(\frac{1}{\rho_e u_e} \frac{d(\rho_e u_e)}{dz} - \frac{1}{H_e - H_w} \frac{dH_w}{dz} + \frac{1}{r_w} \frac{dr_w}{dz} \right) = C_h \left(\frac{H_{aw} - H_w}{H_e - H_w} \right) \left(1 + \left(\frac{dr_w}{dz} \right)^2 \right)^{1/2} \quad (A.2)$$

where

$$\phi = \int_0^{\Delta} \frac{\rho u}{\rho_e u_e} \left(1 - \frac{u}{u_e} \right) dy, \quad \delta^* = \int_0^{\Delta} \left(1 - \frac{\rho u}{\rho_e u_e} \right) dy$$

and

$$\phi = \int_0^{\Delta} \frac{\rho u}{\rho_e u_e} \left(1 - \frac{H - H_w}{H_e - H_w} \right) dy$$

C_f is the turbulent skin friction coefficient $2 \tau_w / \rho_e u_e^2$; C_h is the Stanton number $q_w / \rho_e u_e (H_{aw} - H_w)$; q_w is the heat flux per unit area; H is the total enthalpy $(u^2 + v^2)/2 + \int C_p dh$; $H_{aw} = H_e - (1 - r_h)(u_e^2 + v_e^2)/2$; r_h is the recovery factor; r_v is the local nozzle wall radius; y is the distance perpendicular to the nozzle surface; u is the velocity component parallel to the nozzle surface; z is the distance along the nozzle centerline; and ρ is the fluid density. Δ , the location of the outer edge of the thermal boundary layer, is allowed to differ from δ , the location of the edge of the velocity boundary layer. It is implicitly assumed that $\Delta > \delta$, which is the normal case when $P_r < 1.0$. The "e" subscript denotes an inviscid stream condition. To include thermochemistry effects, it is noted that the use of enthalpy rather than temperature as a fundamental dependent variable is made throughout, contrary to Reference A.1.

To determine the θ , ϕ , and δ^* thicknesses, it is necessary to assume values of u/u_e and $(H - H_w)/(H_e - H_w)$ as a function of y and a suitable density-enthalpy relation. The profile assumptions made in Reference A.1, and retained in the present calculations, are that

$$\frac{u}{u_e} = \left(\frac{y}{\delta} \right)^n, \quad \frac{H - H_w}{H_e - H_w} = \left(\frac{y}{\Delta} \right)^n \quad (A.3)$$

where $n = 1/7$ for both profiles. The program is designed to employ different values of n , if desired. These assumptions are strictly accurate only in the case of a smooth, nonporous wall with a zero pressure gradient, unity Prandtl number, and $u_e X/\nu_e \geq 10^5$.

As was discussed in Paragraph 2.1.2, a linear density-enthalpy relation of the form

$$\frac{\rho}{\rho_e} = \frac{\rho_w}{\rho_e} + \left(1 - \frac{\rho_w}{\rho_e} \right) \left(\frac{h - h_w}{h_e - h_w} \right) \quad (A.4)$$

is assumed. The viscosity is represented by

$$\mu = \mu_e \left(\frac{h - H_r}{h_e - H_r} \right)^\omega \quad (A.5)$$

where $\omega \approx 0.60$. H_r is an enthalpy factor which facilitates an accurate viscosity fit.

The turbulent, skin friction coefficient expressions employed in Reference A.1 are related to the experimental expressions derived by Coles (see Reference A.2 for a summary of his work) from adiabatic supersonic flat plate data. The adiabatic (no wall heat transfer) skin friction relation is written as a function of a "sublayer temperature" defined by

$$\frac{T_e}{T_{aw}} = 1 + 17.2 \left(\frac{T_e}{T_{aw}} - 1 \right) \left(\frac{\bar{C}_f}{2} \right)^{1/2} - 305 \left(\frac{T_e}{T_{aw}} - \frac{T_e}{T_{aw}} \right) \left(\frac{\bar{C}_f}{2} \right) \quad (A.6)$$

the \bar{C}_f (equivalent to the incompressible coefficient), being related to the C_f adiabatic by a relation involving the density-viscosity product. The \bar{C}_f is a complicated function of the momentum (or energy) thickness Reynolds' number, the functional form depending on the Reynolds' number range under consideration. Once the adiabatic skin friction value is obtained, it is necessary to determine the actual skin friction - with heat transfer by a further assumption. The analysis of Reference A.1 chooses to present two options: (1) the skin friction value for a nonadiabatic wall equals the adiabatic wall value, and (2) the nonadiabatic wall is determined from the incompressible value by the arithmetic mean temperature relation

$$C_f = \frac{\bar{C}_f}{\left[\frac{1}{2} \left(\frac{T_w}{T_e} + 1 \right) \right]^{\frac{3-\omega}{4}}} \quad (A.7)$$

where ω is the viscosity power (Equation (A.5)). The first option, although relatively accurate for heated air nozzle flows, is quite bad for the correlation of liquid propellant ($N_2O_4 - N_2H_4$) nozzle heat transfer. It may be inferred that the situation for even higher temperature solid propellants would not improve. The second option (Equation A.7)) seems to be somewhat more accurate than the first when correlating liquid propellant motor tests; however, the experimental heat flux in the region near the throat (see Reference A.1, page 27) is still significantly higher than the theoretical value.

The applicability to high temperature nozzle flows of the skin friction laws employed in Reference A.1 may be questioned on two counts. The first uncertainty is whether high temperature thermochemistry flows may be represented by the above skin friction model which was empirically defined by testing of a thermally and calorically perfect gas air stream. Equation (A.6) may be "generalized" by writing h (enthalpy) instead of T , keeping the form of the equation unchanged; however, the correctness of this substitution is definitely open to question. The suitability of Equation (A.7) is questionable because it ignores the effect of stream kinetic energy on the skin friction value (which is relatively small up to the throat but does increase in importance in the supersonic expansion region).

Another complaint which may be raised concerns the excessive complexity of the incompressible skin friction versus Reynolds' number expressions used in Reference A.1; such complexity is not warranted because of the empirical nature of the theory with attendant data scatter.

It was decided, therefore, to employ a simpler incompressible skin friction versus Reynolds' number relation and couple this to an incompressible-to-compressible skin friction transformation based on the reference enthalpy idea.

The incompressible skin friction law derived in this contract's work is written as (see Figure A-1)

$$\frac{C_{f1}}{2} = \alpha (Re_1)^{-\beta} \quad (A.8)$$

where

$$\left. \begin{array}{l} \alpha = 0.0253 \\ \beta = 0.401 \end{array} \right\} \quad 10 \leq Re_1 < 200$$

$$\left. \begin{array}{l} \alpha = 0.00935 \\ \beta = 0.214 \end{array} \right\} \quad 200 \leq Re_1 < 10^4$$

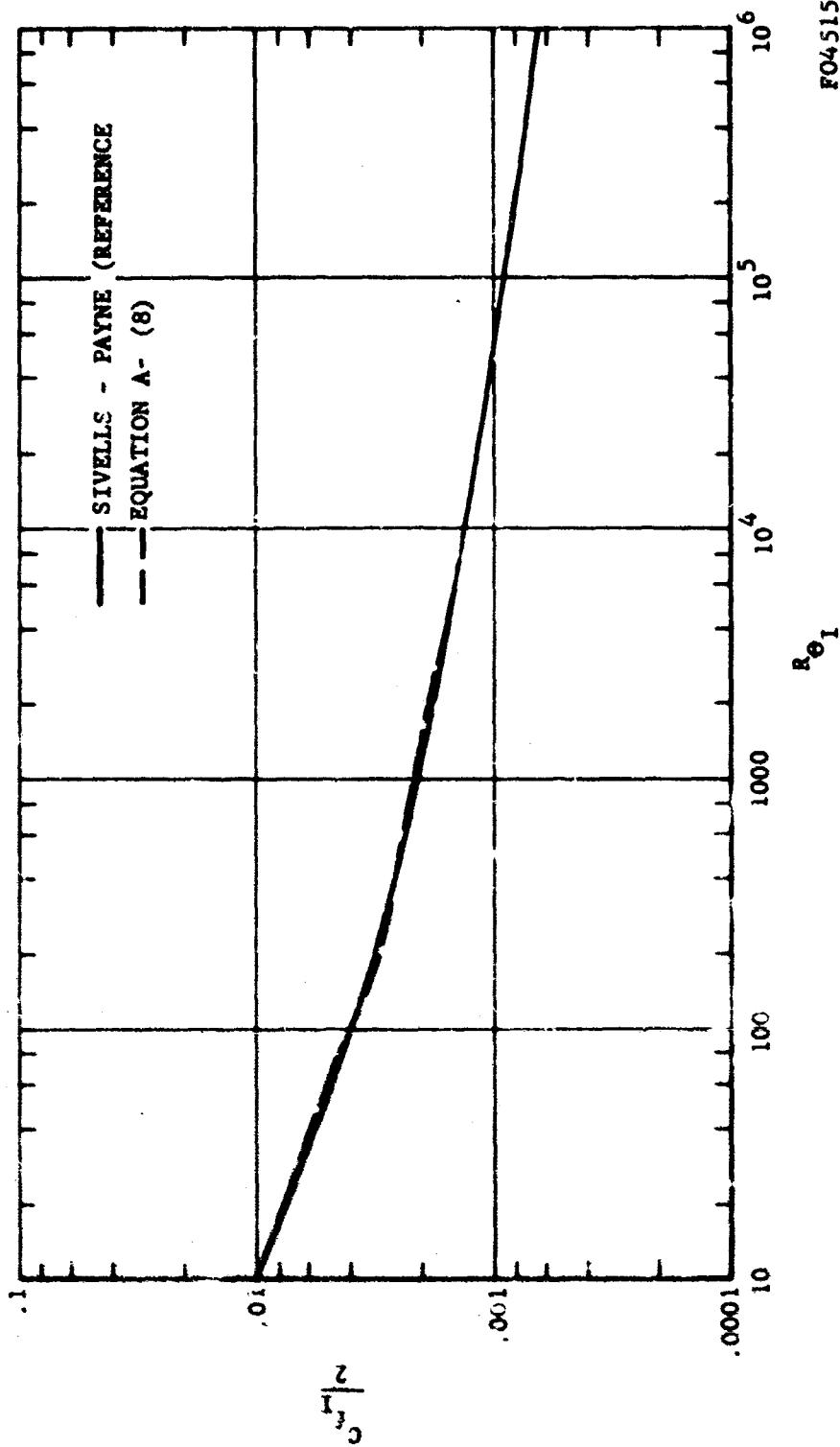
$$\left. \begin{array}{l} \alpha = 0.00508 \\ \beta = 0.140 \end{array} \right\} \quad 10^4 \leq Re_1 < 10^6$$

Re is the momentum thickness Reynolds' number $\rho_e u_e \theta / \mu_e$. The α and β coefficients accurately fit the implicit skin friction correlation given for zero blowing by Sivells and Payne (Reference A.3). It is of some interest to note that Spence (Reference A.4) has also shown that a power law of this form with coefficients of similar magnitude will follow from certain velocity power law and boundary layer substructure assumptions.

The reference enthalpy concept states that skin friction in a compressible flow may be represented by a suitable incompressible expression with the enthalpy-related quantities evaluated by using

$$h^* = .5 (h_e + H_w) + .22 (H_{aw} - h_e) \quad (A.9)$$

h^* is only a function of the distance along the nozzle surface; i.e., h is constant throughout the boundary layer thickness at a particular downstream



FO4515 U

FIGURE A-1. INCOMPRESSIBLE SKIN FRICTION COEFFICIENT AS A FUNCTION OF THE MOMENTUM THICKNESS REYNOLDS' NUMBER

location. Although this relation was originally derived to correlate theoretical laminar flat plate calculations (Reference A.5), it seems to have a wide range of validity, as is evident by its successful application over a large temperature range to both laminar and turbulent boundary layers, with and without wall heat transfer. The reason for its applicability to turbulent boundary layer flow is suggested by the analysis of Burggraf (Reference A.6), who derived a relation for temperature similar to Equation (A.9) by assuming that the characteristic temperature for turbulent flow is the value at the edge of the laminar sublayer. Assuming that the idealization of dividing the boundary layer into a laminar sublayer and turbulent outer layer is valid, this finding gives some support to the reference temperature or enthalpy expression. It should also be mentioned that Spence (Reference A.4) showed that employment of the reference enthalpy expression in the determination of the reference density ρ^* involved in the coordinate transformation

$$\bar{y} = \int_0^y \left(\frac{\rho}{\rho^*} \right) dy, \quad \bar{\delta} = \int_0^\delta \left(\frac{\rho}{\rho^*} \right) dy \quad (\text{A.10})$$

reduced a wide range of experimental compressible flow velocity profiles $u/u_e = f(y/\delta)$ to, very closely, a single profile $u/u_e = g(\bar{y}/\bar{\delta})$. Because the specification of a proper reference condition amounts to the shrinking of a large field of compressible skin friction versus Reynolds' number, Mach number, and wall temperature values to a single incompressible Reynolds' number dependence, it is seen that Equation (A.9) has a definite pragmatic value. Any theoretical extension to flows with wall blowing and roughness would necessitate a complete re-evaluation of this procedure, however. As shown by Tetervin (Reference A.7) evaluation of the compressible skin friction employing the incompressible expression can be achieved by transforming Equation (A.8) from

$$\frac{\tau_w}{\rho_e u_e^2} = \alpha \left(\frac{\rho_e u_e \theta}{\mu_e} \right)^{-\beta} = \frac{C_{f1}}{2}$$

to

$$\frac{\tau_w}{\rho^* u_e^2} = \alpha \left(\frac{\rho^* u_e \theta^*}{\mu^*} \right)^{-\beta} = \frac{C_f}{2} \left(\frac{\rho}{\rho^*} \right) \quad (\text{A.11})$$

where $\theta^* = (\rho_e/\rho^*) \theta$. This direct transformation holds for a general flow with free stream gradients, a range of applicability which is not obvious from the usual means of derivation (transformation back and forth between flat plate $C_f/2$ dependencies on R_x and R_θ).

Employment of Equation (A.4) enables Equation (A.11) to be written as

$$\frac{C_f}{2} = \frac{\alpha \left[R_\theta \left(\frac{h_e - H_r}{h^* - H_r} \right)^\omega \right]^{-\beta}}{\rho_e / \rho_w + (1 - \rho_e / \rho_w) \left(\frac{h^* - H_w}{h_e - H_w} \right)} \quad (\text{A.12})$$

This is the relationship employed in the numerical program. The α, β values, which are applicable over discrete ranges of $R_{\theta T}$, are assumed to be applicable over the same ranges of R_θ .

The Stanton number employed in the energy integral, C_h , is determined from Von Karman's relation (Reference A.8)

$$C_h = \frac{C_f / 2}{1 + 5 (C_f / 2)^{1/2} (Pr - 1 + \ln [1 + 5/6 (Pr - 1)])} \quad (\text{A.13})$$

Pr is the Prandtl number $\mu C_p / K$. This relationship was employed in Reference A.1 and is considered as good as any in representing Reynolds' analogy between skin friction and heat transfer.

The actual routine in which Equations (A.1) and (A.2) are integrated was left unchanged from the method employed in Reference A.1. This method is an adaption of the Adams-Moulton method for the simultaneous solution of several ordinary differential equations. The various integrals employed in the analysis (displacement thickness, etc.), are the same as in Reference A.1 except for differences caused by using an arbitrary n (velocity distribution power) rather than $1/7$, and the density-enthalpy relation of Equation (A.4) rather than the thermally perfect density-temperature equation $\rho / \rho_e = T_e / T$. The process of integration of the conservation equations at a particular axial location is considered complete when the ratio of the thermal to velocity boundary layer thicknesses converges to a particular value. The integration technique was carried out in a machine language subroutine (FAP) rather than in FORTRAN, thus preventing changes in the solution system and requiring some care in making modifications to the rest of the program.

Solution of Equations (A.1) and (A.2) is carried out coupled with a determination of the inviscid, nonturbulent stream flow given by a combined inviscid flow field-chemical equilibrium scheme. Paragraph A.2 discusses this method.

A.2 FREE-STREAM NOZZLE FLOW

The program contains the option of using the one-dimensional mass conservation relation

$$\rho A U = \dot{m} \quad (\text{A.14})$$

or a two-dimensional theory based on the integral relations method of Holt (Reference A.9). \dot{m} is the mass flow in lbm/sec, ρ is the fluid density, A the nozzle cross sectional area ($\delta^{**} < r_w$), and U is the flow velocity parallel to the nozzle centerline.

The analysis of Reference A.10 basically follows the Dorodnitsin strip method of integral relations (Reference A.10) which is actually a generalization of the Karman integral theory of boundary layer analysis. Solution of the various conservation relations describing the flow field is achieved by integrating from the nozzle axis of symmetry out to $(N - (n-1))/N$ times the width of the flow field of interest, where N is the total number of strips used and n is the strip number under consideration. For example, for a one-strip division of the nozzle, integration is carried out over the total half width of the nozzle. For a two-strip division, the integration is successively carried out to $1/2$ and 1 times the total half width. Thus, for every conservation equation used, N integral relations can be written.

The conservation relations assumed are the conservation of mass and the irrotationality condition

Mass

$$\frac{\partial(\rho v r)}{\partial z} + \frac{\partial(\rho v r)}{\partial r} = 0 \quad (A.15)$$

Irrotationality

$$\frac{\partial v}{\partial z} - \frac{\partial u}{\partial r} = 0 \quad (A.16)$$

v and r are, respectively, the velocity and coordinate perpendicular to the nozzle centerline. Integration of Equations (A.15) and (A.16) across r from 0 to r (a general point in the flow field) gives

$$\frac{d}{dz} \left[r_w^2 \int_0^1 (\rho v) \eta d\eta \right] - (\rho v)_1 r_w \left[r_w \frac{d\eta}{dz} + \eta \frac{dr_w}{dz} \right] + \eta r_w (\rho v)_1 = 0 \quad (A.17)$$

$$\frac{d}{dz} \left[r_w^2 \int_0^1 v d\eta \right] - v_1 \left[r_w \frac{d\eta}{dz} + \eta \frac{dr_w}{dz} \right] - U_1 + U_0 = 0 \quad (A.18)$$

η is the radial coordinate normalized to the wall radius, i.e., $\eta = r/r_w$. The η subscript denotes evaluation at a general radial location while the 0 subscript denotes the nozzle centerline value.

For a single integration strip the integration is carried out from the nozzle centerline to the wall, and a linear variation of ρU and V as a function of η is assumed. Some analysis has been performed with a two strip division (see Reference A.1) but due to its excessive complexity, it was not employed. On completing the integration and substitution of the linear profiles,

$$\frac{d(\rho v)_0}{dz} + 2 \frac{d(\rho v)_1}{dz} + \frac{2}{r_w} \frac{dr_w}{dz} \left[(\rho v)_0 + 2(\rho v)_1 \right] = 0 \quad (A.19)$$

$$\frac{dV_1}{dz} + U_1 \left[\left(\frac{d^2 r_w}{dz^2} \right) \left(\frac{dr_w}{dz} \right)^{-1} - \frac{1}{r_w} \frac{dr_w}{dz} \right] - \frac{2}{r_w} \left(\frac{dr_w}{dz} \right)^{-1} (U_1 - U_0) = 0 \quad (A.20)$$

and, in addition

$$V_1 = U_1 \frac{dr_w}{dz} \quad (A.21)$$

the 1 subscript denotes the value at the wall (actually at the edge of the displacement thickness, but since $\delta^* < r_w$ there is little error in assuming that the integration is carried to the wall). $V_0 = 0$ by symmetry.

The chemical equilibrium, minimum free energy routine is the same as the one described in Paragraph 2.1. A range of pressure points between the chamber value and a suitable exit cone value is selected, and the program computes the corresponding state points including $\rho q = \rho \sqrt{U^2 + V^2}$. These streamline state points are connected to the nozzle flow through the employment of Equations (A.19) and (A.20).

Although Holt defined proper criteria, assuming a perfect gas, by which Equations (A.14) and (A.20) may be applied through the sonic point, it is better, in view of the equilibrium chemistry model, to utilize a separate sonic region analysis.

The method of Hall (Reference A.11) is a solution of the mass conservation and irrotationality relations in the region near the sonic line, where the velocity perturbations in the axial and radial directions are small compared to the critical sound speed at the throat. These velocity perturbations are expanded in inverse powers of R , the radius of curvature of the nozzle profile

at the throat measured in throat half-heights. Successively improved solutions result from the use of higher order terms in the expansions; terms of order $1/R^3$ are included. The involved relationships are given in Equations (83) through (90) of Reference A.11. Although they were derived in terms of a calorically and thermally perfect gas, it is assumed that the γ may be evaluated from

$$\gamma = \left(\frac{\partial \ln p}{\partial \ln \rho} \right)_{s, (q)_{max}} \quad (A.22)$$

Integration of Equations (A.1) and (A.2) along Z gives the momentum and thermal energy defect thicknesses, plus the local skin friction and heat transfer values.

A complete listing of the boundary layer convective heat transfer program is not given here for several reasons. The first reason is that documentation of the program is not yet finished so that a complete listing of the variables and their corresponding Fortran statements is not yet available. Budget and time limitations and higher priorities attached to other aspects of the program have prevented a complete documentation during the course of the work. Another reason is that important segments of the numerical analysis, notably the integration routine of the conservation equations, were originally programmed by JPL (Reference A.1) in IBM machine language, not in Fortran, so that understanding the inner workings of the program in detail is a difficult procedure for most readers. It is hoped to eventually re-program these segments in Fortran; however, in the interim a documentation of the combined Fortran-machine language program is now underway at Aeronutronic and will be sent to RPL, Edwards AFB, upon its completion.

REFERENCES

- A.1 Elliot, D. G., Bartz, D. R., and Silver, S., Calculation of Turbulent Boundary-Layer Growth and Heat Transfer in Axisymmetric Nozzles, Jet Propulsion Laboratory, Technical Report No. 32-387, California Institute of Technology, Pasadena, California, 15 February 1963.
- A.2 Coles, D., "The Turbulent Boundary Layer in a Compressible Fluid," The Physics of Fluids, Vol. 7, No. 9, September 1964, pp 1403-1423.
- A.3 Sivells, J. C. and Payne, R. G., A Method of Calculating Turbulent-Boundary-Layer Growth at Hypersonic Mach Numbers, AEDC TR-59-3, Arnold Engineering Development Center, March 1959.
- A.4 Spence, D. A., "Velocity and Enthalpy Distributions in the Compressible Turbulent Boundary Layer on a Flat Plate," Journal of Fluid Mechanics, 8, July 1960, pp 368-387.
- A.5 Eckert, E. R. G., Survey on Heat Transfer at High Speeds, WADC TR 54-70, April 1954.
- A.6 Burggraf, O. R., "The Compressibility Transformation and the Turbulent Boundary Layer Equations," Journal of the Aerospace Science, 29, April 1962, pp 434-439.
- A.7 Tetervin, N., "The Application of the Reference-Enthalpy Method to Friction Formulas," Journal of the Aerospace Sciences, 29, May 1962, p 493.
- A.8 Van Karman, T., "The Analogy Between Fluid Friction and Heat Transfer," Trans. ASME, 61, 1939.
- A.9 Holt, M., The Design of Plane and Axisymmetric Nozzles by the Method of Integral Relations, University of California, Report No. AFOSR 3140, Berkeley, September 1962.

REFERENCES (Continued)

- A.10 Dorodnitsyn, A. A., Method of the Integral Relations for the Numerical Solution of Partial Differential Equations, Report of the Institute of Exact Mechanics and Computing Technique, Akad. Nauk SSSR, 1958.
- A.11 Hall, I. M., Transonic Flow in Two-Dimensional and Axially Symmetric Nozzles, ARC No. 23, 347, December 1961.

APPENDIX B

RADIATIVE HEAT TRANSFER

The restartable solid rocket nozzle has been divided into two characteristic periods of operation for analyzing the radiative boundary condition. During firing, the chamber and nozzle surfaces intercept energy emitted by the combustion products. The amount of energy absorbed by the surfaces is dependent on the surface temperature, surface emissivity, and emission properties of the free stream. During the cooldown period, radiative energy exchange will occur between the surfaces of the motor components, between the surfaces and the pyrolysis gas products, and between the surfaces and the ambient environment. A description of the radiation analyses developed to predict the radiative boundary conditions of a restartable solid rocket motor is presented below. The results of applying these analyses to specific rocket motors were presented in Paragraph 2.4.

B.1 COOLDOWN PERIOD

It was necessary to formulate analytical solutions for three specific types of cooldown radiative transfer:

- (1) Transparent media (gray walls)
- (2) Absorbing media (gray walls)
- (3) Absorbing media (black walls)

The third case is a special case of the second. A fourth possibility, transparent media (black walls), can be deduced directly from the first case. Analyzing the cooldown behavior of a nozzle requires a breakdown of the nozzle into nodal points (finite volumes), each of which will be

used in the conduction computer program. Nodal points on the interior surface of the nozzle are such that an energy balance requires the specification of the radiant heat flux to each nodal point on the nozzle surface. Therefore, it is required that the three types of radiative transport be analyzed in such a manner to facilitate the application of the results to a numerical conduction solution.

B.1.1 TRANSPARENT MEDIA (GRAY WALLS)

When the free stream of a nozzle is transparent to thermal radiation, the radiant interchange between a point on the surface and its surroundings can be expressed by the method devised by Oppenheim (B.1). For a gray surface, the net radiant heat flux to an elemental area (dA_1) may be written as the difference in the incident and emitted plus reflected radiant energy.

$$\dot{q}_1 = H_1 - J_1 \quad (B.1)$$

The energy leaving dA_1 is

$$J_1 = \epsilon_1 E_1 + r_1 H_1 \quad (B.2)$$

where $E_1 = \sigma T_1^4$ and ϵ_1 and r_1 are the emissivity and reflectivity of dA_1 respectively. The energy incident on dA_1 is the energy leaving adjacent surfaces in the direction of dA_1 , or

$$H_1 = J_1 F_{1-1} + J_2 F_{1-2} + \dots + J_n F_{1-n} \quad (B.3)$$

If the temperatures, emissivities, and shape factors (F_{1-n}) are specified, the radiant heat flux may be found by solving simultaneously a combination of Equations (B.2) and (B.3) written for each surface. It may be noted that combining Equations (B.1) and (B.2) reduces the heat flux to a form.

$$\dot{q}_1 = \frac{\epsilon_1}{r_1} (J_1 - E_1) \quad (B.4)$$

Determination of the shape factors, F_{1-n} , is required for the solution of Equation (B.3). An analysis similar to that described in Reference B.2 has been programmed for computer solution.

A shape factor, F_{dA_1-2} , is defined as that fraction of the total radiant energy which leaves a diffuse area dA_1 and is incident on an area A_2 . Then from Reference B.3 the shape factor is

$$F_{dA_1-2} = \frac{1}{\pi} \int_{A_2} \frac{\cos \theta_1 \cos \theta_2}{R^2} dA_2 \quad (B.5)$$

where R is the distance between areas dA_1 and dA_2 , and θ_1 and θ_2 are the angles between R and the normals to area dA_1 and dA_2 , respectively. For a geometry similar to that of a nozzle, Equation (B.5) is simplified if cylindrical coordinates are employed and a new angle, β , is defined according to Figure B-1, i.e., the angle between the axis of the nozzle and a line, tangent to the area in question, that intersects the axis of the nozzle.

Expressing $\cos \theta_2$, $\cos \theta_1$, R and dA_2 in terms of the coordinate system described previously, an integral of the form,

$$F_{dA_1-2} = \frac{1}{\pi} \int_l f(\beta) dl \int_{\psi} g(\psi, \beta, r) d\psi \quad (B.6)$$

is obtained from Equation (B.5). The quantities $f(\beta)dl$ and $g(\psi, \beta, r)$ will vary depending on the location in the nozzle. That is, the expression $f(\beta)dl$ when dA_2 is on the injector face is different than when dA_2 is on the surface of the nozzle. Also, there are many different expressions for $g(\psi, \beta, r)$ which are dependent on the conditions listed below:

$$(1) \quad l_{dA_1} < l_{dA_2}, \quad l_{dA_1} = l_{dA_2}, \text{ and } l_{dA_1} > l_{dA_2}$$

$$(2) \quad \beta_{dA_1} > 90^\circ, \quad \beta_{dA_2} > 90^\circ$$

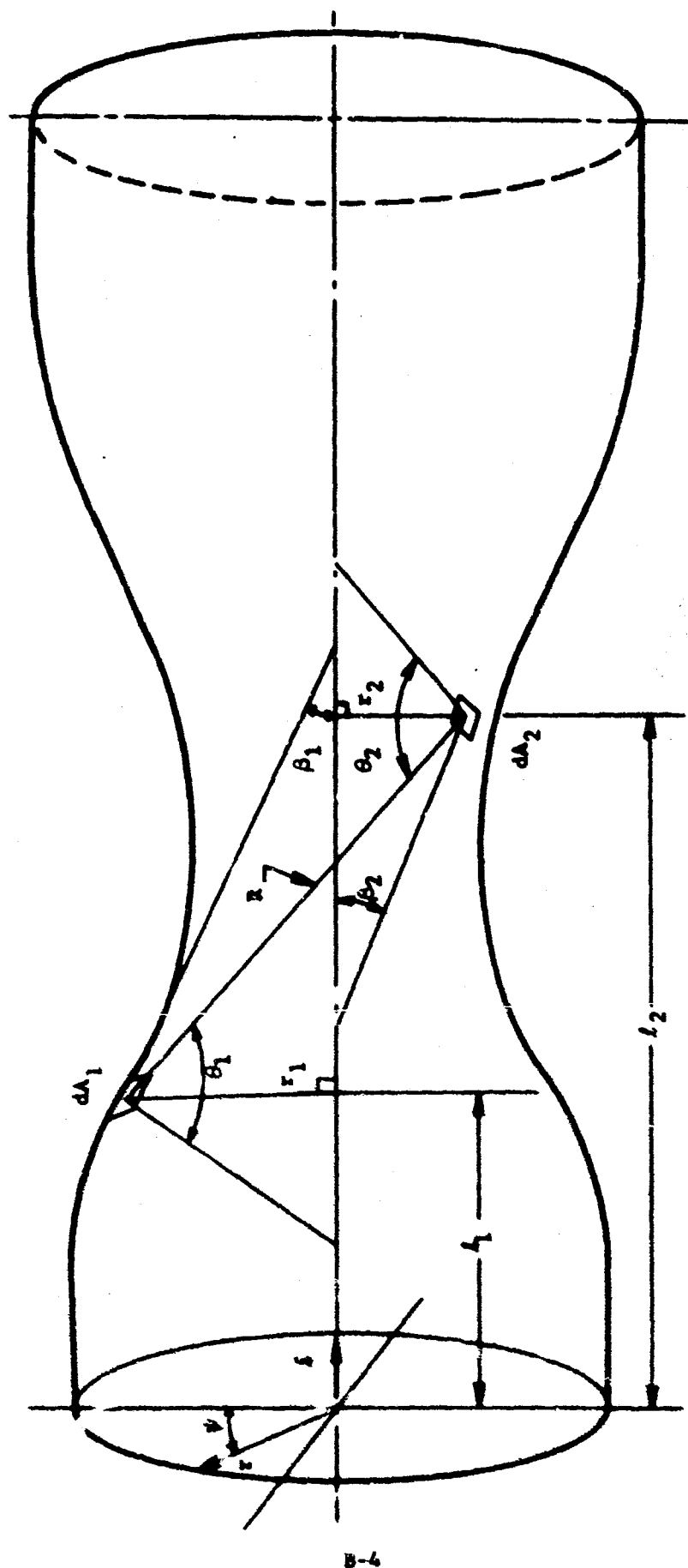
$$(3) \quad dA_1 \text{ on injector face and } dA_2 \text{ on injector face.}$$

With the expression, $g(\psi, \beta, r)$, known as a function of nozzle position, the integral

$$\int_{\psi} g(\psi, \beta, r) d\psi \quad (B.7)$$

is easily evaluated from standard integral tables.

The limits of integration in Equation (B.7) are defined as the percent of the total area of dA_2 (see Figure B-1) that is seen by dA_1 . An algebraic expression is easily obtained for the limits of integration by consideration of the intensity vectors originating at a point dA_1 on the entrance section of the nozzle. Since the cross section of the throat is circular in a plane perpendicular to the nozzle axis and the intensity vectors from dA_1 passing through the throat describe a cone, the cross section of the intensity vectors at any point in the exit cone will also be circular in a plane normal to the axis of the nozzle. The intersection of the intensity vector cone with the nozzle surface at the axial position of dA_2 , defines the limits of integration at point 2.



R08200U

FIGURE B-1. COORDINATE SYSTEM FOR THE SHAPE FACTOR ANALYSIS OF A ROCKET NOZZLE

With the integral, Equation (B.7), evaluated at the proper limits, the shape factor may be evaluated numerically as follows

$$F_{dA,-2} = B f(\theta) \Delta l \quad (B.8)$$

Equations (B.2), (B.3), (B.4), (B.7), and (B.8) were programmed for the Philco 2000 high speed digital computer to obtain the shape factors and radiant heat fluxes for the internal surface elements of any combustion chamber and nozzle configuration.

The internal surface of the nozzle is divided up into finite areas by the conduction-ablation program (Appendix C), permitting a numerical energy balance on each node. To avoid solving Equations (B.2), (B.3) and (B.4) at each time increment in the finite difference conduction solution, the surface nodes have been interconnected by resistors, R_{1-2} . The resistors enable the radiant heat flux between any two nodes to be expressed as

$$q_{1-2} = \frac{T_1 - T_2}{R_{1-2}} \quad (B.9)$$

and for gray walls

$$q_{1-2} = A_1 F_{1-2} \sigma (T_1^4 - T_2^4) \quad (B.10)$$

then

$$\frac{1}{R_{1-2}} = A_1 F_{1-2} \sigma (T_1^2 + T_2^2) (T_1 + T_2) \quad (B.11)$$

The net radiant heat flux to any node is then the sum of the heat flux to each separate node

$$q_{rad} = \frac{T_1 - T_2}{R_{1-2}} + \frac{T_1 - T_3}{R_{1-3}} + \dots + \frac{T_1 - T_n}{R_{1-n}} \quad (B.12)$$

If in the transient state the radiant heat flux at time $t = m\Delta t$ is evaluated at the temperatures found at time $t = (m-1)\Delta t$, use of Equations (B.11) and (B.12) will, therefore, eliminate the complicated solution of Equations (B.2), (B.3), and (B.4) and permit a finite difference solution to the conduction equations.

The quantity, $A_1 F_{1-n}$, which is a function of both the shape factor, F_{1-n} , and the emissivity, ϵ , is determined by use of the radiation program

just described and in a manner prescribed by Reference B.4. The method given in Reference B.4 is straightforward and only the end result is given in this report.

Setting $T_1 = 1$ and T_2, T_3, \dots, T_n equal to zero, the heat fluxes are calculated by the radiation program with the specified emissivities as input. Since area 1 is the only surface that emits, the heat flux at point 2 represents the heat flux between 1 and 2. Therefore, from Equation (B.10),

$$A_1 \bar{F}_{1-n} = \frac{q_n}{\sigma}$$

and

(B.13)

$$A_1 \bar{F}_{1-3} = \frac{q_3}{\sigma} \quad , \quad \dots$$

The same procedure is followed for T_2, T_3, \dots, T_n .

B.1.2 ABSORBING MEDIA (GRAY WALLS)

The presence of an absorbing media in a rocket nozzle may seriously alter the radiative transfer during cooldown, depending, of course, on the opacity of the mixture. The chemical species that affect the optical properties of typical pyrolysis products below 3000°F are primarily condensed carbon, water vapor, carbon dioxide, and carbon monoxide. Of these, condensed carbon is likely to be of major importance.

During cooldown, a nonzero chamber pressure will result from the degassing of the ablative materials in the nozzle. For testing at either atmospheric or space pressures, the assumption of an optically thin media will suffice for a large range in path length and particle concentration. From References B.5 and B.6 the emissivity (or absorptivity, if $\alpha = \epsilon$ is assumed) of an optically thin particle cloud may be written as

$$\epsilon_\lambda = 1 - \exp[-NR\sigma_t(\lambda)] \quad (B.14)$$

where N is the particle density, R is the path length, and $\sigma_t(\lambda)$ is the total cross section ($\sigma_t(\lambda)$ represents the energy absorbed and scattered by a particle of a certain size and shape). For the optically thin case, Equation (B.14) reduces to

$$\epsilon_\lambda = NR\sigma_t(\lambda) \quad (B.15)$$

For the case of gray walls and an absorbing media, the network method of Oppenheim is employed with slight alterations to include the effects of the absorbing media. That is, the radiant interchange between two elements is reduced by the amount of energy absorbed or scattered by the media. The energy incident on an area element has the added contribution of that energy emitted and multiple scattered by the cloud in the direction of the area. With this, Equation (B.3) becomes

$$H_1 = J_1 F_{1-1} \tau_{1-1} + J_2 F_{1-2} \tau_{1-2} + \dots + J_n F_{1-n} \tau_{1-n} + \bar{\epsilon}_{g-1} \bar{E}_g \quad (B.16)$$

From Reference B.7 the last term in Equation (B.16) may be written as

$$\sum_n \int_{A_n} \frac{\bar{E}_g}{\pi} \epsilon \frac{\cos \theta_1 \cos \theta_n}{R^2} dA_n \quad (B.17)$$

This is equivalent to saying that the gas volume involved between two areas, A_1 and A_n , is determined by the solid angle originating at dA_1 and intersecting A_n . The total volume is then the sum of the individual volumes.

The term, ϵ , in Equation (B.17) is related to Equation (B.15) by the following expression

$$\epsilon = \frac{NR \int_0^\infty \bar{\sigma}_t(\lambda) E(\lambda) d\lambda}{\sigma T^4} = NR \bar{\sigma}_t \quad (B.18)$$

where E is the emissive power at the wavelength, λ , and σT^4 is the total blackbody energy over all wavelengths.

Substituting Equations (B.15), (B.17) and (B.18) into (B.16) and then combining (B.16) with (B.2) yields

$$J_1 = \epsilon_1 E_1 + \tau_1 \sum_n \left[\int_{A_n} \frac{\bar{E}_g}{\pi} N \bar{\sigma}_t \frac{\cos \theta_1 \cos \theta_n}{R} dA_n + \int_{A_n} \frac{J_n}{\pi} \frac{\cos \theta_1 \cos \theta_n}{R^2} dA_n - \int_{A_n} \frac{J_n}{\pi} N \bar{\sigma}_t \frac{\cos \theta_1 \cos \theta_n}{R} dA_n \right] \quad (B.19)$$

Let

$$dF_{1-n} = \frac{\cos \theta_1 \cos \theta_n}{\pi R^2} dA_n \quad (B.20)$$

and

$$dG_{1-n} = \frac{\cos \theta_1 \cos \theta_n}{\pi R} dA_n \quad (B.22)$$

Returning to the radiation computer program discussed in the previous paragraph, it may be noted that dF_{1-n} has already been calculated for the nozzle configuration. Evaluation of the integrals in Equation (B.19) requires a knowledge of the variation in temperature and the absorption coefficient ($N \sigma_t$) in the nozzle. Since dG_{1-n} can be reduced to finite difference form in much the same manner as dF_{1-n} (i.e., $dA_n = f(\beta) \Delta l$), the cloud volume is then divided into incremental hollow conical volume elements. (The intensity vectors leaving a point on the surface of a nozzle encloses a definite volume of gas with suspended particles before reaching an area dA_2 on the nozzle surface. When dA_2 is revolved around the nozzle axis on the circumference of the nozzle, the resulting gas volume is a hollow conical volume.) To solve Equation (B.19), a temperature and absorption coefficient representing the average for the conical volume is used and assumed constant for the integral of that particular surface element, dA_n .

It may be noted that the nozzle surface may not necessarily represent the absorbing media's boundary, as Equation (B.17) states. That is, the condensation of carbon particles may occur on a local basis in the nozzle. If this is the case, Equation (B.19) is invalid and an added approximation is required in the evaluation of the radiant heat flux. If the shape factor from the area dA_1 to A_n (A_n representing an area on the nozzle where the absorption coefficient reduces to zero somewhere in the path length between dA_1 and A_n) is small, then, evidently, the last term in Equation (B.19) is even smaller than the third. If $F dA_{1-n}$ is large, dA_n in the first integral of Equation (B.19) must be replaced by an imaginary surface area at the plane of initial condensation. In many cases when the shape factor is large, the ratio of the distance between elements and cloud path length is near unity and use of Equation (B.19) is permitted.

The assumption of average temperature and absorption coefficients between dA_1 and dA_n reduces Equation (B.19) to

$$J_1 = \epsilon_1 E_1 + r_1 \sum_n \left[(E_g N \bar{\sigma}_t)_{1-n} G_{1-n} + F_{1-n} J_n - (N \bar{\sigma}_t)_{1-n} J_n G_{1-n} \right] \quad (B-23)$$

where the subscript (1-n) signifies that the quantity is evaluated between areas 1 and n, and G is defined by Equation (B.22).

B.1.3 ABSORBING MEDIA (BLACK WALLS)

An absorbing media surrounded by black walls is treated as a special case of the preceding gray wall analysis. There are two reasons for subdividing the gray and black wall analyses: (1) the fact that no radiation energy

is reflected by a black wall eliminates the use of Equation (B.23) and (2) the black wall analysis is very simply applied as a boundary condition to the conduction program used in this program.

Applying a radiative energy balance to a black surface element in much the same manner that was done in the previous paragraph yields,

$$q_{\text{rad}-i} = \sum_n \left\{ F_{i-n} (E_i - E_n) - (N\bar{\sigma}_t)_{i-n} G_{i-n} (E_i - E_n) + (N\bar{\sigma}_t)_{i-n} G_{i-n} [E_i - (E_g)_{i-n}] \right\} \quad (\text{B.24})$$

Equation (B.24) can be further subdivided into the heat exchange between surface elements

$$q_{i-n} = [F_{i-n} - (N\bar{\sigma}_t)_{i-n} G_{i-n}] \sigma [T_i^4 - T_n^4] \quad (\text{B.25})$$

and between a surface element and the absorbing gas

$$q_{i-g} = \sum_n (N\bar{\sigma}_t)_{i-n} G_{i-n} \sigma [T_i^4 - (T_g)_{i-n}^4] \quad (\text{B.26})$$

Equation (B.25) is of the same form as Equation (B.11) where

$$F_{i-n} = F_{i-n} - (N\bar{\sigma}_t)_{i-n} G_{i-n} \quad (\text{B.27})$$

Therefore, Equation (B.25) is applied in exactly the same manner as was Equation (B.11) for the transparent gas-gray wall case.

Assuming an isothermal gas, Equation (B.26) reduces to

$$q_{i-g} = (h_r)_{i-g} (T_i - T_g) \quad (\text{B.28})$$

and

$$(h_r)_{i-g} = \frac{\sum_n (N\bar{\sigma}_t)_{i-n} G_{i-n} [E_i - (E_g)_{i-n}]}{T_i - T_g} \quad (\text{B.29})$$

B.2 APPLICATION OF COOLDOWN RADIATIVE ANALYSES

The total absorption cross section, $\bar{\sigma}_t$, of a carbon particle cloud has been presented by Stull and Plass in Reference B.8 for various sized particles. In the rocket nozzle, it is likely that the products of ablation are saturated with carbon and as the gas expands in the nozzle (for vacuum exhaust), carbon will condense out. It is expected, therefore, that the particle size will change in expanding through the nozzle, presenting difficulties in the evaluation of $\bar{\sigma}_t$.

The product, $N\bar{\sigma}_t$, has been calculated for the ablation products of various ablative materials. In performing these calculations, thermochemical considerations were required to determine the amount of solid carbon encountered in the chamber and nozzle volume. The data of Reference B.8 were applied to the predicted solid carbon amount, resulting in $N\bar{\sigma}_t$. $N\bar{\sigma}_t$ for the pyrolysis products of carbon both phenolic. This is shown in Figures B-2 and B-3 at various soak back temperatures and pressures.

The dependence of $N\bar{\sigma}_t$ on particle size is negligible as shown by Figure B-2. This phenomena was also reported by Thring^{B.9} for hydrocarbon flames. Therefore, it is concluded that knowledge of particle size is not important, and the major difficulty lies with the determination of the pressure and temperature decay during cooldown.

The importance of carbon cloud radiation during cooldown was determined using the temperature and pressure decay measurements presented in Section 2.4. Using the pyrolysis temperature presented in Figure 2-9 (or 2000°F at 140 seconds after shut down) and a soakback pressure of 20 psia the term $N\bar{\sigma}_t R$ (cloud emissivity - $N\bar{\sigma}_t$) reaches a maximum of 0.029 at $\epsilon = 1.5$. At 140 seconds, the measured surface temperature in the annealed P.G. throat insert is approximately 1620°F (see Figure 2-9). Therefore, the radiative and convective interchange between the throat insert and the free stream is negligible compared to the heat dissipated by ablation. However, for rocket motors employing a good heat sink material in the entrance and a heat barrier material in the throat, the pyrolysis temperature may be low enough that the thermal analysis must include carbon cloud radiation. For the materials studied in this program, the effect of carbon cloud radiation and convection during cooldown may be omitted from thermal considerations, leaving only the radiative interchange between flame front surfaces and radiation to the ambient environment as the soak-back boundary conditions.

B.3 FIRING PERIOD

Little is known of the emission properties of high temperature alumina clouds and what data do exist can only be applied after making very questionable assumptions. Experimental data on alumina emission properties have been obtained for optically thin clouds with temperatures reaching 5200°R.

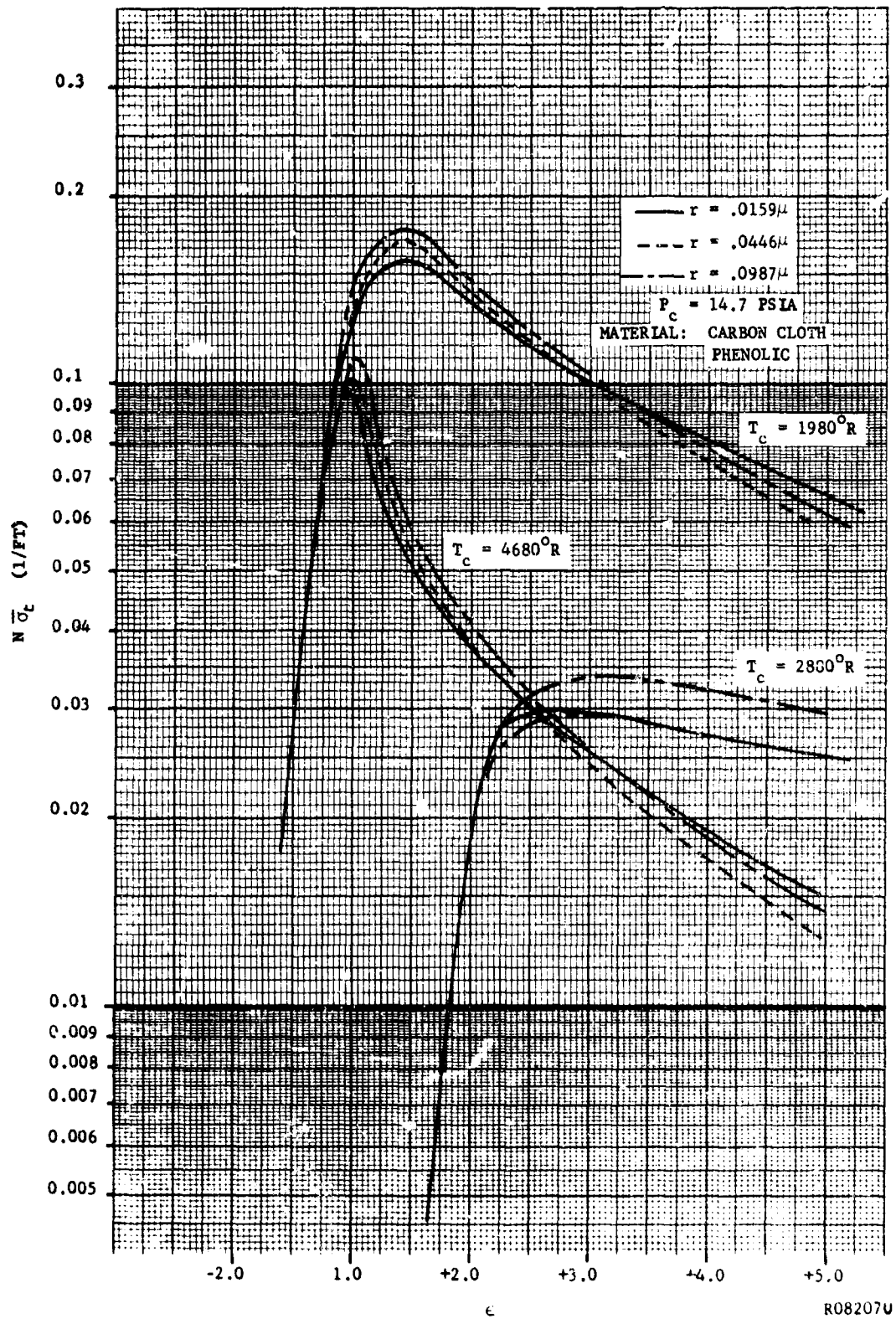


FIGURE B-2. ABSORPTION COEFFICIENT OF A CARBON PARTICLE CLOUD
VERSUS AREA RATIO FOR OPTICAL THIN CONDITION

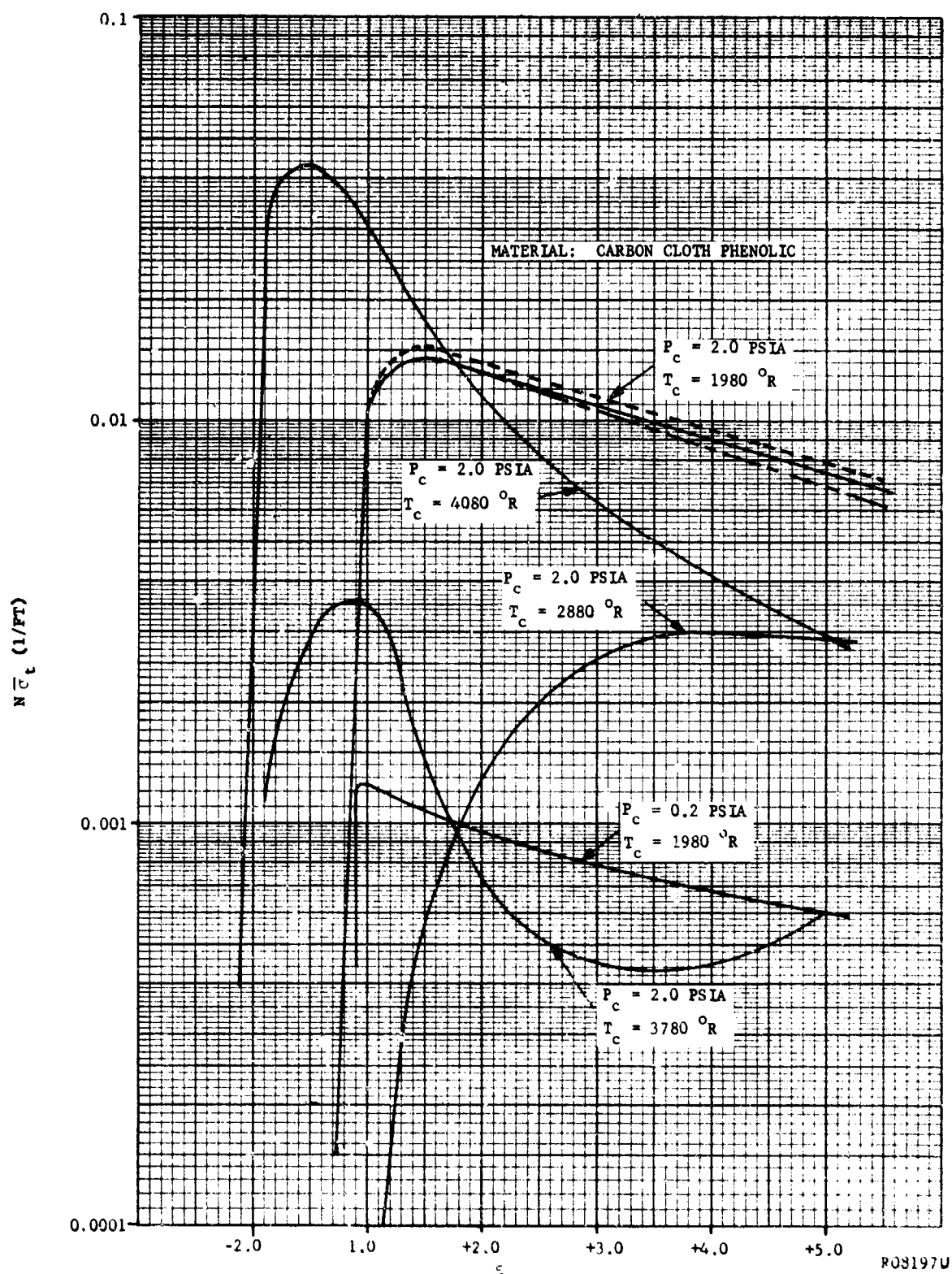


FIGURE B-3. ABSORPTION COEFFICIENT OF A CARBON PARTICLE CLOUD
VERSUS AREA RATIO FOR OPTICAL THIN CONDITION

Optically thin cloud measurements do not provide emission data sufficient to analyze the important effects of scattering associated with a high temperature alumina cloud. Reference B.6 postulates an approach to account for the scattering and multiple scattering effect of finely dispersed alumina particles. However, this approach requires the experimental determination of scattering coefficients (see Reference B.6 for details). An analysis based upon optically thin cloud emission data to predict the radiative heat transfer to rocket motor flame front surfaces, which eliminates the effect of scattering, is given in Reference B.6. In this analysis, the maximum cloud total hemispherical emissivity can approach unity. From recent alumina cloud emission data, (References B.10 and B.11) it was found that the maximum total hemispherical emissivity is between 0.25 and 0.35. Comparing the results of References B.10 and B.11 with the semi-empirical predictions of Reference B.6 indicates the importance of scattering in radiative transfer.

Early in this program, the alumina cloud hemispherical emissivity was calculated using the analysis of Reference B.6. As the data of References B.10 and B.11 became available, however, the technique employed in the calculation of emissivity was revised to include scattering. The revised technique incorporated the expression derived in Reference B.6 to include the chamber pressure, particle concentration, path length, and temperature effect on emissivity, with the maximum measured emissivity ϵ_m ; i.e.,

$$\epsilon = \epsilon_m (1 - e^{-N\bar{\epsilon}l})$$

and $N = 1.59 \times 10^{-4} \frac{\phi P M}{T r^3}$

where

ϕ = weight ratio of particles to gas

P = static pressure

T = static temperature

M = gas molecular weight

l = path length

r = particle radius

$\bar{\epsilon}$ = absorption coefficient (data obtained from Reference B.5).

The maximum cloud emissivity is related to the absorption and scattering cross sections of the dispersed alumina particles by (Reference B.11)

$$\epsilon_m = g \left(\frac{Q^a}{Q^t} \right)^{1/2}$$

where g is the cloud geometric factor

Q^a = absorption cross section

Q^t = sum of the absorption and scattering cross section

These cross sections are dependent on particle size, particle concentration, and temperature. However, due to the lack of cross section data, the maximum emissivity used in this program was assumed to be 0.3 as reported in Reference B.10.

B.4 SURFACE EMISSIVITY

For simplification, the emissivities of the flame front surfaces were regarded as a function of material only. The emissivities employed in this program were 0.9, 0.7, and 0.4 for PG, ATJ, and tungsten, respectively. The emissivities of solid and/or liquid alumina wall coatings are considerably different from those of the nozzle surface materials (~ 0.3) and should be included in the radiative boundary condition. However, to include the effect of deposition on wall emissivity, the surface coverage of Al_2O_3 must be determined as a function of position and time. At the present time, it is impossible to predict the deposit behavior; therefore, to be conservative, the effect of deposits on wall emissivity was omitted.

REFERENCES

- B.1 Oppenheim, A. K., "Radiation Analysis by Network Method," Trans. ASME, Vol. 78, 1956, pp 725-735.
- B.2 Robbins, W. H., An Analysis of Thermal Radiation heat Transfer in a Nuclear-Rocket Nozzle, NASA TN D-586, January 1961.
- B.3 Eckert, E. R. G. and Drake, R. M., Heat and Mass Transfer, McGraw-Hill Book Co., New York, 1959.
- B.4 McAdams, N. H., Heat Transmission, McGraw-Hill, 1954, p 72.
- B.5 Carlson, D. J., et al., Alumina Absorption and Emittance, Final Report, Philco Research Laboratories Report No. U-2627, May 1964.
- B.6 Price, F. C., et al., Internal Environment of Solid Rocket Motors, Philco Research Laboratories Report No. U-2709, August 1964.
- B.7 Bevans, J. T. and Dunkle, R. V., "Radiant Interchange Within an Enclosure," Trans. ASME, February 1960.
- B.8 Stull, V. R. and Plass, G. N., "Emissivity of Dispersed Carbon Particles," J. Opt. Soc. Am., Vol. 50, February 1960.
- B.9 Thring, M. W.; Foster, P. J.; McGrath, I. A.; and Ashton, J. S., "Prediction of the Emissivity of Hydrocarbon Flames," International Developments in Heat Transfer (ASME), 1961, p 796.
- B.10 Bauer, E. and Carlson, D. J., "Mie Scattering Calculations for Micron Size Alumina and Magnesia Spheres," J.Q.S.R.T., 4, pp 363, 1964.
- *B.11 Fontenot, J. E., "Thermal Radiation from Solid Rocket Plumes at High Altitude," AIAA Journal Technical Note, May 1965, pp 970.

APPENDIX C

CONDUCTION-ABLATION HEAT TRANSFER

This appendix presents a detailed discussion of the analysis used in predicting the thermal response of a solid propellant rocket motor nozzle subjected to any stop-start duty cycle. This discussion describes the manner in which the phenomena associated with transient conduction and ablation were handled in the development of the analytical model.

The formulation of an analytical model to predict the performance of a nozzle under stop-start conditions requires definition of the mechanisms involved in thermal and chemical degradation of materials, radiative and convective heat transfer, and alumina deposition. By defining the various mechanisms associated with stop-start, an analytical model can be constructed which will predict such characteristics as temperature distributions, char thickness, heat absorbed during firing, and change in heat content during soak for the structural and insulation components of the rocket motor nozzle.

The approach taken in developing an analytical model consisted of using an existing three dimensional transient conduction computer program as a foundation in the analysis. The mechanisms associated with restart were included in the computer program as subroutines.

C.1 INTERNAL ENERGY BALANCE

The ablation phenomenon is a very complicated form of heat transfer. To devise a conduction-ablation analysis (and, correspondingly, an analytical tool to predict char growth and temperature profiles) requires a firm understanding of pyrolysis and the ablative modes of heat transfer. The internal ablation-conduction portion of the ablation model used in this

analysis is the well known "charring ablation" concept of Munson and Spindler^{C.1}.

The three dimensional transient conduction computer program utilizes a finite difference scheme in solution of the Fourier conduction equation. The program applies an energy balance to each finite volume (node) in the system. In two dimensional form this energy balance is:

$$\frac{1}{r} \frac{\partial}{\partial r} \left(r k_r \frac{\partial T}{\partial r} \right) + \frac{\partial}{\partial z} \left(k_z \frac{\partial T}{\partial z} \right) + \frac{1}{r} \frac{\partial}{\partial r} (r \dot{w} H_g) + \sum \dot{q} \Delta H = \rho c \frac{\partial T}{\partial t} \quad (C.1)$$

In this equation, the first two terms account for the radial and axial conduction, respectively; the third term accounts for the energy associated with the transpiration of the pyrolysis gas through the char; the fourth term accounts for decomposition, cracking, and any other chemical reactions experienced in the ablator; and the last term accounts for heat storage in the solid.

C.2 PYROLYSIS

To solve Equation (C.1), the pyrolysis rate of the ablator must be specified. Specification of this phenomenon is very important in the evaluation of ablator performance under stop-start conditions. For example, under stop-start conditions, the pyrolysis zone heating rate is variable dT/dt , and will effect the type and degree of reactions experienced in this zone. Therefore, the pyrolysis law used in the ablation analysis must be dependent on heating rate, temperature level, and post-thermal history. The most widely accepted pyrolysis law to date which includes the above dependencies is that of Friedman:

$$\frac{d(\rho/\rho_v)}{dt} = -A \left(\frac{\rho - \rho_c}{\rho_v} \right)^n \exp \left[-E/RT \right] \quad (C.2)$$

The constants A, n, and E, commonly defined as the rate constant, degree of reaction, and activation energy, respectively, are determined empirically.

It has been generally concluded that pyrolysis in an internal ablating material is reaction rate controlled. This phenomenon is then dependent upon (1) the rate at which the chemical reaction products leave the pyrolysis zone, (2) temperature level, (3) total pressure, and (4) heating rate, dT/dt . In performing TGA experiments to determine the rate

constants of Equation (C.2), it is desirable to simulate the magnitudes of these four parameters existing at the locations where Equation (C.2) is to be applied. It is impossible, however, to exactly simulate the removal rate of the pyrolysis gas in TGA experiments. Therefore, it is necessary to assume that the removal rates of the chemical reaction products in the TGA and rocket motor are equal.

Figure C-1 is a plot of various Thermal Gravimetric Analyses (TGA) performed on phenolic resin composites. The original weight of the ablative material (W_0) is based on 100 percent phenolic (reinforcement free). All TGA samples used in Figure C-1 were post-cured except for that of Coffman which explains the initiation of pyrolysis at low temperatures. The TGA data presented in Figure C-1 were performed at low heating rates ($dT/dt \leq 360^\circ\text{C/hr}$) and under a variety of free stream conditions. Since the decomposition dependence on temperature is function of heating rate, free stream pressure (see Figure C-2), and chemical composition (oxygen content), and unpredictable error will result when the TGA data of Figure C-1 are multiplied by the appropriate heating rate and applied to rocket nozzle conditions in the form of an Arrhenius expression (Equation C.2). Therefore, four Arrhenius rate laws were chosen for this program all of which were obtained under a variety of free stream conditions. Table C.1 is a summary of these Arrhenius constants required in Equation C.2.

TABLE C.1

ARRHENIUS PYROLYSIS RATE LAWS FOR PHENOLIC RESINS

<u>Investigator</u>	<u>n</u> <u>Degree of</u> <u>Reaction</u>	<u>B</u> <u>(1/sec)</u>	<u>E</u> <u>Activation</u> <u>Energy</u> <u>(cal)</u>
Farmer (Ref. C.2)	1	4.67	15,200
Friedman (Ref. C.3)	1	6.75	15,200
Friedman (Ref. C.3)	5	2.78×10^{14}	55,000
Munson and Spindler (Ref. C.1)	1	1×10^6	22,100

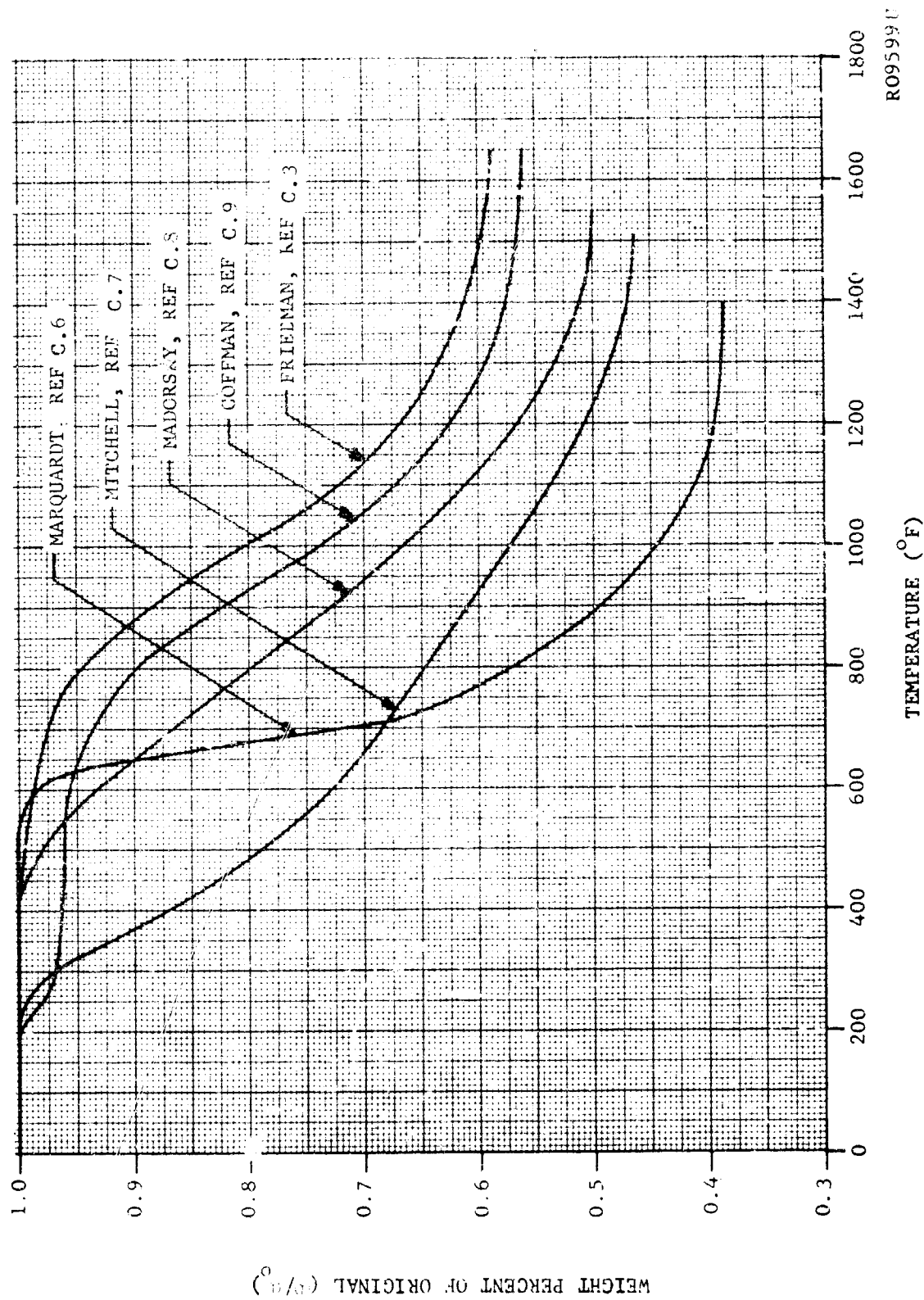


FIGURE C-1. PYROLYSIS OF PHENOLIC RESIN ON REINFORCEMENT FREE BASIS

C.3 GAS-CHAR REACTIONS

The heat absorbed by pyrolysis (heat of decomposition) and transpiration of the pyrolysis gases through the char (gas enthalpy change) requires the determination of the chemical composition of the pyrolysis gas at various pyrolysis zone temperature levels. Knowing the chemical composition of the pyrolysis gas as a function of temperature, and knowing the original chemical composition of the ablator, thermochemical calculations can be performed on the ablator, assuming thermochemical equilibrium between gas and char. This assumption is valid if the interconnected pores in the char have a sufficiently large surface area and the flow velocities are relatively small.

The average specific heat of the pyrolysis products for asbestos, silica, graphite cloth, and carbon cloth phenolics are shown in Figure C-2. The chemical stoichiometry of phenolic used in the thermochemical calculations was approximated as $(C_6H_6O)_n$. Asbestos and silica were assumed inert with respect to the char. This assumption is only valid at temperatures up to 1800°F . In the temperature region of 1800°F to 2700°F , condensed SiO_2 will react with the carbonaceous char to produce condensed SiC and gaseous CO . The reaction is endothermic and, depending upon any kinetic limitations arising from the solid-solid reaction, can be far more important from a heat absorption standpoint than the resin degradation process. Above 2700°F , SiC is unstable with respect to gaseous SiO and the latter becomes the important product species. Thus, if the char temperature exceeds 1800°F , silica-carbon reactions will occur and cause the average specific heat to increase. Since the data shown in Figure C-2 do not reflect this increase, char thicknesses predicted using these data and the ablation program will be larger than the measured char thickness.

The heat of decomposition of phenolic was assumed to be 500 btu/lb as reported in Reference C.1. The heat of ablation, of which the heat of decomposition is a part, is the property usually reported by various investigators. The complexity in determining the heat of decomposition from the heat of ablation results in a very approximate value. Another possible method in determining the heat of decomposition of phenolic is to utilize the polymeric structure of phenolic and to find the energy required to break the material down to the resultant pyrolysis products. This method is approximate in that the chemical structure of phenolic is questionable.

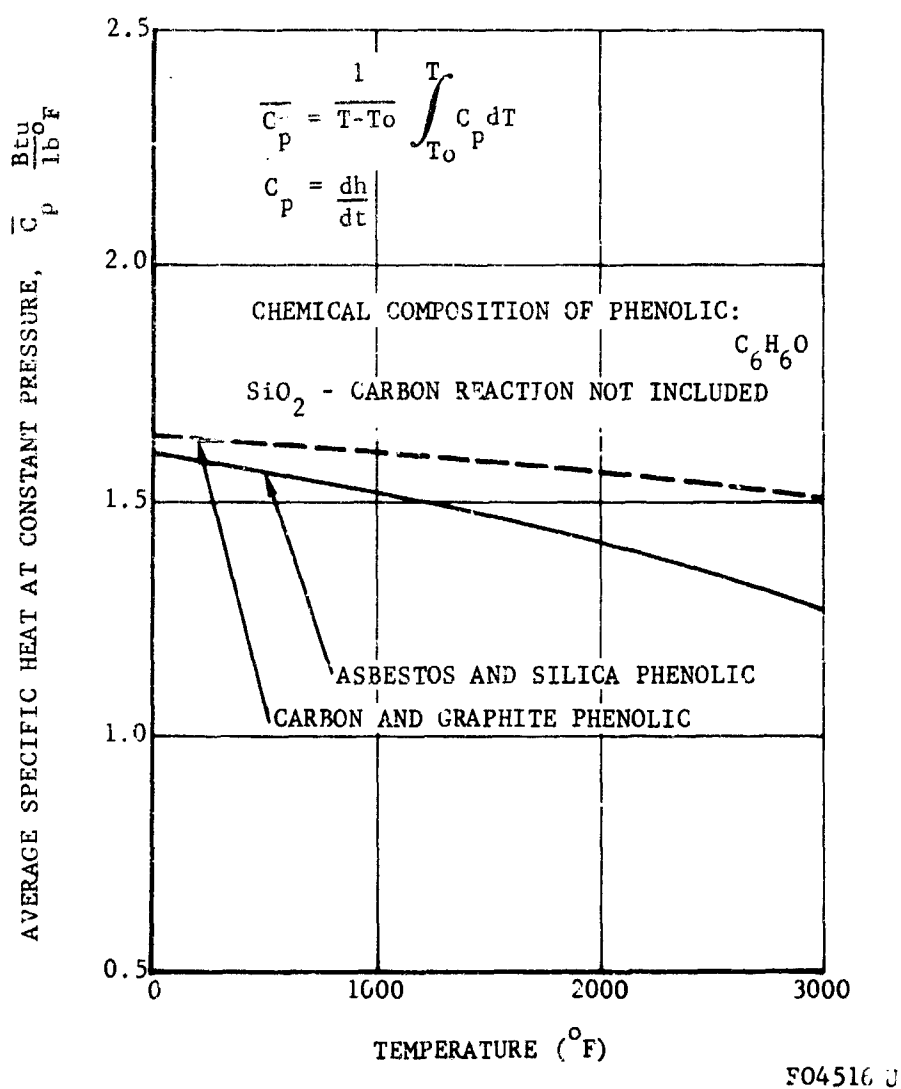


FIGURE C-2. AVERAGE SPECIFIC HEAT AT CONSTANT PRESSURE OF PYROLYSIS PRODUCTS OF PHENOLIC RESIN

C.4 THERMOPHYSICAL PROPERTIES

The thermophysical properties required in the solution of Equation C.1 include the specific heat, density, and thermal conductivity of the rocket motor materials. However, the definition of thermal conductivity and solid specific heat for an internal ablating material is not definite until the mathematical model separates and defines the other modes of heat transfer. The thermal conductivity represented in Equation C.1 does not include the effects of convection, decomposition, or any other chemical reactions but does include internal radiation between voids in the char and transpiring gas for ablating materials.

With thermal conductivity defined in this manner, experimental determination is difficult for a partially degraded material because of the effect of pyrolysis of the material and the influence of the transpiring pyrolysis gas. This problem has also been found by many other investigators (Ref. C.1, C.4, and C.5), and has led them to the following assumption: The thermal conductivity and specific heat of a partially degraded material can be found by a linear interpolation between the appropriate values of the char and virgin materials. Mathematically this is stated as

$$K = \left(\frac{\kappa_v - \kappa_c}{\rho_v - \rho_c} \right) (\rho - \rho_v) + \kappa_v \quad (C.3)$$

$$C = \left(\frac{C_v - C_c}{\rho_v - \rho_c} \right) (\rho - \rho_v) + C_v \quad (C.4)$$

Thermal conductivities of the virgin material and the char of various ablative materials are presented in Table C.2.

The laboratory conditions and specimens to be used in the determination of char and virgin material thermal properties should reproduce as closely as possible the temperature level, char porosity, and char density that occur in actual motor firings. Since the char thermal conductivity is very dependent on char porosity and density, the effect of coking in the char by the pyrolysis gas must also be included. However, this program was not a basic investigation of materials properties; therefore, properties available from the literature were employed.

TABLE C 2

VIRGIN AND CHAR THERMAL CONDUCTIVITIES OF
ASBESTOS AND SILICA PHENOLIC

<u>Material</u>	<u>Investigator</u>	<u>Remarks</u>	<u>Temperature °F</u>	<u>Thermal Conductivity (Btu/in sec^{°F} x 10⁶)</u>	
				<u>Char</u>	<u>Virgin</u>
Asbestos Phenolic	Schmidt	40% Resin	200		1.9
	Ref C.10	See Table C.3	700		3.5
	Acrojet	40% Resin			
	Ref C.11	Sp Gr Virgin= 1.84 Char = 0.91	Independent of temperature*	15.0	4.2
	Atlantic Research	Sp Gr Virgin= 1.58 Char = 1.26	70 1200	4.6 5.4	8.3
	Ref C.12				
Silica Phenolic	Schwartz	42% Resin	70		6.2
	Ref C.13	See Table C.3			
	Mixer	45% Resin	100		5.4
	Ref C.14		400		4.2
	Vidya	30% Resin	Independent	9.6	4.1
	Ref C.5	See Table C.3	of temperature*		
	Tapco	Virgin: 1 to plies	200	2.9	5.5
	Ref C.18	See Table C.3	400	3.4	6.4
			700	3.4	
	Hitco	Virgin: 1 to plies	200		5.1
	Ref C.15		500		5.2
	Atlantic Research	50% Resin	70	5.9	5.4
	Ref C.12	Sp Gr Virgin= 1.51 Char = 1.25	1200	6.6	
	Schwartz	25% Resin	70		7.2
	Ref C.13	See Table C.3			
	Super Temp	30% Resin	70		5.2
		Sp Gr Virgin= 1.70			

* Value to be used that is independent of temperature.

The densities and specific heats of the virgin material and char of various ablating materials are presented in Table C.3. These properties were also obtained from the literature.

The lack of thermal-physical property data for ablating materials was a serious problem area in this program. Therefore, the results obtained from the ablation portion of the thermal analysis should be considered as only approximate.

C.5 GAS MOMENTUM AND MASS BALANCE

To complete the internal portion of the ablation model, relationships must be formulated, based on mass and momentum considerations, to account for the amount, location, and motion of the pyrolysis gas. To solve Equation C.1, a finite difference technique is required which divides that part of the ablator undergoing chemical reactions (char and pyrolysis zone) into incremental volumes. The local rate of pyrolysis is determined from Equation C.2. The local rate of pyrolysis gas formation per unit cross-sectional area is then given by

$$\dot{m}_i = \dot{\rho}_i V_i$$

where $\dot{\rho}_i$ is found from Equation C.2 and V_i is the node volume.

The pyrolysis gas mass flow leaving the incremental volume is the sum of all the gas produced in the upstream nodes plus that generated at the node in question, plus or minus the mass storage rate resulting from permeability, porosity, and free stream pressure change:

$$\dot{m}_{L-1} = \sum_{i=2}^{\infty} \dot{m}_i + \dot{m}_1 \pm \dot{m}_s \quad (C.5)$$

If the chemical reactions that occur between the pyrolysis gas and char or the char and reinforcements involve a gas, the above mass balance has an added term to account for the gaseous mass addition or depletion.

TABLE C.3

VIRGIN AND CHAR DENSITIES AND SPECIFIC HEATS
FOR VARIOUS ABLATING MATERIALS

Material	Resin Content (%)	Virgin Density $\left(\frac{\text{lb}}{\text{ft}^3}\right)$	Char Density $\left(\frac{\text{lb}}{\text{ft}^3}\right)$	Virgin Specific Heat $\left(\frac{\text{Btu}}{\text{lb}^\circ\text{F}}\right)$	Char Specific Heat $\left(\frac{\text{Btu}}{\text{lb}^\circ\text{F}}\right)$	Code Name	Reference
Asbestos Phenolic	30-40	115	79.4	--	--	150 RPD	Blaes, Ref C.16
	30-40	109	80	--	--	150 RPD	Blaes, Ref C.16
	40	112	--	0.315	--	--	Schmidt, Ref C.10
	37-40	124	60	--	--	CTL 301	Mitchell, Ref C.7
	38	114.8	--	0.27	--	--	Schwartz, Ref C.13
	42	103.6	--	0.29	--	--	Schwartz, Ref C.13
Silica Phenolic	31	106	93.7	--	--	Cl100-48	Blaes, Ref C.16
	40	113	96	0.24	0.20	--	Tapco, Ref C.18
	25	103.6	--	0.22	--	--	Schwartz, Ref C.13
	21	116.1	--	0.27	--	--	Schwartz, Ref C.13
	30	110	91	0.30	0.273	Astrolite	Mensak, Ref C.17
	30	--	--	0.30	0.60	--	Vidya, Ref C.5
Carbon Cloth Phenolic	30	88	67.1	--	--	CCA-1	Blaes, Ref C.16
	50	90	--	--	--	--	Schmidt, Ref C.10
	34	91.7	76.7	0.29	0.25	--	Tapco, Ref C.18
Graphite Phenolic	40	89.3	73.7	0.26	0.22	--	Tapco, Ref C.18
	40	--	--	0.34(ave)	--	--	Schmidt, Ref C.10
	30	--	--	0.33(ave)	--	--	Schmidt, Ref C.10

The momentum equation that could be employed in the ablation analysis is based upon a simplified theory of slow flow through porous media

$$\dot{m} = - \left[\frac{L_m \rho_g}{\mu_g P_0} \right] \frac{dP}{dy} \quad (C.6)$$

and the permeability coefficient empirically defined in terms of porosity is

$$L_m = a + b \exp [c P_0]$$

P_0 = porosity

P = pressure

Incorporation of the momentum equation in the ablation model requires that porosity be specified as a function of the density change of the ablator and that an equation of state be used. However, in this program, it was found that the inaccuracies produced in the ablation analysis by the use of the approximate thermophysical properties presented above did not justify the inclusion of momentum considerations and the mass storage term of Equation C.5 in the ablation model. That is, the effect of momentum and mass storage of the pyrolysis products is important when the combustion products static pressure changes rapidly (i.e., at startup and shutdown); whereas, the heat transferred to the pyrolysis zone via the char is very dependent on the char thermal conductivity.

C.6 FLAME FRONT BOUNDARY CONDITIONS

In general, chemical potentials will exist between the flame front surface of a rocket motor and its fluid environment. Such potentials are normally dissipated by chemical reactions which transfer solid surface material into a more mobile fluid phase. The resultant surface regression is controlled by the rates of mass transport of the reactants and products to and from the surface and/or by chemical kinetic reaction limitations. It is usual practice to regard surface sublimation as a special case of corrosion. However, it is more difficult to assess the heat and mass transfer when chemical reactions and sublimation occur together. That is, both solid-gas and gas-gas versions of the same reaction can occur, and the reactions are not confined to the solid surface. Unfortunately, the precise analytical solution of the general case cannot be achieved with currently available techniques. However, a good qualitative understanding of the important mechanism of corrosion does exist.

In the development of a surface regression model, a reasonable approach is to assume initially that chemical corrosion can be uncoupled from the other mechanisms of surface regression. Considering the present limitations in detailed knowledge of surface regression mechanisms, no other alternative is deemed possible. Using the corrosion theories presented by Vidya^{C.5} and Rocketdyne^{C.19}, the surface regression due to chemical corrosion can be determined. The contribution of sublimation to the surface regression of chars may be assumed negligible in comparison with the other surface regression mechanisms.

The most practical and widely accepted solution to the corrosion problem is the theory developed by Denison and Bartlett^{C.20} and ^{C.21}. To obtain a practical solution to the multicomponent boundary layer heat and mass transfer equations with chemical reactions, Denison and Bartlett made the following assumptions: (1) The diffusion coefficients for the various molecular species in the boundary layer are equal, and (2) the Prandtl and component Lewis numbers are unity. This enabled them to derive expressions for the rate of heat transfer to the wall and the rate of chemical corrosion of the wall surface. Then the heat flow to the surface, including transpiration and radiation, is

$$\begin{aligned}
 -k \left. \frac{dT}{dy} \right|_w &= \rho_e U_e (St)_a (H_e - H_w) + \dot{m}_g (H_c - H_w) \\
 &+ \dot{m}_c (H_g - H_w) + \dot{m}_e (H_c - H_w) \pm \dot{q}_{rad}
 \end{aligned}
 \tag{C.7}$$

The first term represents the heat conducted from the surface. The second represents both the heat transferred by convection and the chemical energy of recombination of free stream gases at the wall. The third, fourth, and fifth terms represent, respectively, the energy resulting from the mixing of the pyrolysis gas with the boundary layer gas and the energies involved in the chemical and mechanical removal of the surface. The sixth term is the radiation boundary condition.

The mass loss due to chemical corrosion can be specified only if (1) chemical corrosion can be uncoupled from mechanical erosion, spallation, and chunking, and (2) either thermochemical equilibrium is assumed or the chemical reaction rates are specified (kinetically controlled). That is, the mass loss of surface material resulting from mechanisms other than chemical corrosion will result in a chemical alteration of the boundary layer by reaction with those chemical species originating in the free stream that would otherwise react with the wall material at the surface. Inclusion of the mechanical erosion, spallation, and chunking

mass loss in evaluating chemical corrosion is invalid since chemical attack of this mass by the combustion products is not necessarily a surface or boundary layer phenomenon.

The technique employed in applying the conduction-ablation analysis to this program, however, eliminated the flame front surface regression boundary condition. Instead of including surface regression, a design surface temperature was selected for the heat sink materials. This surface temperature represented a thermal level above which excessive surface regression (see Paragraph 2.6 for discussion) would result. This approach then reduces Equation C.7 to

$$-K \frac{dT}{dy} \Big|_w = \rho_e U_e St (H_e - H_w) \pm \dot{q}_{\text{rad}}$$

REFERENCES

- C.1 Munson, T. R. and Spindler, R. J., "Transient Thermal Behavior of Decomposing Materials, Part I, General Theory and Application to Convective Heating," IAS 30th Annual Meeting, New York, January 22-24, 1962.
- C.2 Farmer, R. W., Thermogravimetry of Plastics, Part I: Empirical Homogeneous Kinetics, ASD TDR 62-1043, February 1963.
- C.3 Friedman, H. L., The Kinetics of Thermal Degradation of Charring Plastics, General Electric TIS R61SD45, August 1961.
- C.4 Tick, S. J., Huson, G. R., and Griese, R., "Design of Ablative Thrust Chambers and Their Materials," AIAA Paper No. 64-261, 1st Annual Meeting, Washington, D.C., July 1964.
- C.5 McCuen, P. A., Schaefer, J. W., Lundberg, R. E., and Kindall, R. M., A Study of Solid-Propellant Rocket Motor Exposed Materials Behavior, Final Report, Vidya Report No. 149, February 1965.
- C.6 Batha, D. R., et al., Thrust Chamber Cooling Techniques for Spacecraft Engines, Marquardt Corp., Report No. 5981, July 1963.
- C.7 Mitchell, R. L., "Ablation of a Reinforced Phenolic Plastic Subjected to a Low Heat Rate," Thesis, University of California at Berkeley.
- C.8 Madorsky, S. and Straus, S., Thermal Degradation of Polymers at Temperatures up to 1200°C, WADC TR 59-64, April 1960.
- C.9 Coffman, J., Kibler, G., Riethof, T. and Watts, A., Carbonization of Plastics and Refractory Materials Research, WADD TR 60-646, July 1960.

REFERENCES (Continued)

- C.10 Schmidt, D. L., Pyrolyzed Rayon Fiber-Reinforced Plastics, ML TDR 64-47, April 1964.
- C.11 McFarland, B., Joerg, P., and Taft, M., Criteria of Plastic Ablation Materials as Functions of Environmental Parameters, Part I, Aerojet-General ASD TR 61-439, August 1961.
- C.12 Atlantic Research, WADD TR 60-109.
- C.13 Schwartz, H. S., Comparative Erosion Resistance of Plastic Materials in a Supersonic Rocket Exhaust and Subsonic Air Arc Plasma, WADD TR 60-649, September 1960.
- C.14 Mixer, R., Margnowski, A., and Chamberlain, A Study of the Mechanism of Ablation of Reinforced Plastics, WADC TR 59-668, 1960.
- C.15 Hitco PB 7-24A, 1959.
- C.16 Blaes, H. M., et al., Application of Materials to Advanced Rocket Nozzle and Hot Gas Control Systems, Fourth Quarterly Report, Publication No. U-2750, Philco Research Laboratories, July 1964.
- C.17 Mensak, J., Boericke, R., "Effect of Pulsed Mode on Operational Life of Rocket Engines," 6th Liquid Propulsion Symposium, Volume I, September 1964.
- C.18 TAPCO, Development of Advanced Nozzle Designs for Large Solid Propellant Rocket Motors, Final Report, AD 336-366, June 1963.
- C.19 Rivers, W. J., Van Wyk, R., Seader, J. D., Friedman, H. A., and Chu, H. N., Effect of Rocket Engine Combustion on Chamber Materials, Part I, Rocketdyne, AFRPL-TR-65-13, January 1965.
- C.20 Denison, M. R., "The Turbulent Boundary Layer on Chemically Active Ablating Surfaces," Journal of Aerospace Sciences, Vol. 28, 1961.
- C.21 Bartlett, E. P. and Denison, M. R., "Experimental Ablation Rates in a Turbulent Boundary Layer," Journal of Heat Transfer, Vol. 83, 1961.

Unclassified

Security Classification

DOCUMENT CONT. DATA - R&D		
(Security classification of title, body of abstract and indexing annotation must be entered when the overall report is classified)		
1. ORIGINATING ACTIVITY (Corporate author) Aeronutronic Division, Philco Corporation Ford Road, Newport Beach, California		2a. REPORT SECURITY CLASSIFICATION Confidential
		2b. GROUP 4
3. REPORT TITLE An Investigation and Feasibility Demonstration of Nozzles for Restartable Solid Rocket Motors (U)		
4. DESCRIPTIVE NOTES (Type of report and inclusive dates) Final Report		
5. AUTHOR(S) (Last name, first name, initial) W. H. Armour, R. M. Edmiston, H. M. Moody, et al		
6. REPORT DATE 31 March 1966	7a. TOTAL NO. OF PAGES 397	7b. NO. OF REFS 139
8a. CONTRACT OR GRANT NO. AF 04(611)-9904		8b. ORIGINATOR'S REPORT NUMBER(S)
b. PROJECT NO.		
c.	9b. OTHER REPORT NO(S) (Any other numbers that may be assigned this report)	
d.	AFRPL-TR-66-53	
10. AVAILABILITY/LIMITATION NOTICES In addition to security requirements which must be met, this document is subject to special export controls and each transmittal to foreign governments or foreign nationals may be made only with prior approval of AFRPL (RPPR-STINFO), Edwards, Calif.		
11. SUPPLEMENTARY NOTES		12. SPONSORING MILITARY ACTIVITY Rocket Propulsion Laboratory Research and Technology Division Air Force Systems Command, Edwards, Calif.
13. ABSTRACT Analytical and empirical studies were conducted to define and investigate problems associated with restartable solid propellant rocket nozzles. Thermal analysis covered the complete temperature history from startup through cooldown of the duty cycle. In addition to conventional convection, conduction, and radiation, the effects of the pyrolysis gases of charring ablators were included. The structural analysis included the investigation of the thermo-elastic behavior of cylindrical and washer inserts, the existence of plastic zones, the effects of contact pressures in stacked washer inserts, and the effects of property degradation of tungsten due to grain growth. The materials investigation included tungsten-carbon reactions, tungsten grain growth and the resulting effects of properties, and the high temperature c-direction compressive deformation of pyrolytic graphite. Rocket nozzle firings were used for verification of analyses and further problem definition. It was found that the strength of tungsten is degraded by 50 percent or more with very slight grain growth. Large permanent c-direction compressive deformations are attainable in pyrolytic graphite above 2600°C with stresses of 7000 psi in 30 seconds. Ablation of char-forming insulators provides the principal mode of cooldown by the pyrolysis process and by heat transfer to the resulting gases as they leave the nozzle. Radiation was found to be an order of magnitude lower in significance. Higher thermal loads result from initial uniform ambient temperature conditions than from restarting from any point during cooldown. Thermal stress design charts have been constructed for the candidate throat materials. A very simple design chart based on brittle fracture and yielding		

DD FORM 1 JAN 64 1473

Unclassified

Security Classification

14. KEY WORDS	LINK A		LINK B		LINK C	
	ROLE	WT	ROLE	WT	ROLE	WT

INSTRUCTIONS

1. **ORIGINATING ACTIVITY:** Enter the name and address of the contractor, subcontractor, grantee, Department of Defense activity or other organization (*corporate author*) issuing the report.

2a. **REPORT SECURITY CLASSIFICATION:** Enter the overall security classification of the report. Indicate whether "Restricted Data" is included. Marking is to be in accordance with appropriate security regulations.

2b. **GROUP:** Automatic downgrading is specified in DoD Directive 5200.10 and Armed Forces Industrial Manual. Enter the group number. Also, when applicable, show that optional markings have been used for Group 3 and Group 4 as authorized.

3. **REPORT TITLE:** Enter the complete report title in all capital letters. Titles in all cases should be unclassified. If a meaningful title cannot be selected without classification, show title classification in all capitals in parenthesis immediately following the title.

4. **DESCRIPTIVE NOTES:** If appropriate, enter the type of report, e.g., interim, progress, summary, annual, or final. Give the inclusive dates when a specific reporting period is covered.

5. **AUTHOR(S):** Enter the name(s) of author(s) as shown on or in the report. Enter last name, first name, middle initial. If military, show rank and branch of service. The name of the principal author is an absolute minimum requirement.

6. **REPORT DATE:** Enter the date of the report as day, month, year, or month, year. If more than one date appears on the report, use date of publication.

7a. **TOTAL NUMBER OF PAGES:** The total page count should follow normal pagination procedures, i.e., enter the number of pages containing information.

7b. **NUMBER OF REFERENCES:** Enter the total number of references cited in the report.

8a. **CONTRACT OR GRANT NUMBER:** If appropriate, enter the applicable number of the contract or grant under which the report was written.

8b, 8c, & 8d. **PROJECT NUMBER:** Enter the appropriate military department identification, such as project number, subproject number, system numbers, task number, etc.

9a. **ORIGINATOR'S REPORT NUMBER(S):** Enter the official report number by which the document will be identified and controlled by the originating activity. This number must be unique to this report.

9b. **OTHER REPORT NUMBER(S):** If the report has been assigned any other report numbers (either by the originator or by the sponsor), also enter this number(s).

10. **AVAILABILITY/LIMITATION NOTICES:** Enter any limitations on further dissemination of the report, other than those

imposed by security classification, using standard statements such as:

- (1) "Qualified requesters may obtain copies of this report from DDC."
- (2) "Foreign announcement and dissemination of this report by DDC is not authorized."
- (3) "U. S. Government agencies may obtain copies of this report directly from DDC. Other qualified DDC users shall request through _____."
- (4) "U. S. military agencies may obtain copies of this report directly from DDC. Other qualified users shall request through _____."
- (5) "All distribution of this report is controlled. Qualified DDC users shall request through _____."

If the report has been furnished to the Office of Technical Services, Department of Commerce, for sale to the public, indicate this fact and enter the price, if known.

11. **SUPPLEMENTARY NOTES:** Use for additional explanatory notes.

12. **SPONSORING MILITARY ACTIVITY:** Enter the name of the departmental project office or laboratory sponsoring (paying for) the research and development. Include address.

13. **ABSTRACT:** Enter an abstract giving a brief and factual summary of the document indicative of the report, even though it may also appear elsewhere in the body of the technical report. If additional space is required, a continuation sheet shall be attached.

It is highly desirable that the abstract of classified reports be unclassified. Each paragraph of the abstract shall end with an indication of the military security classification of the information in the paragraph, represented as (TS), (S), (C), or (U).

There is no limitation on the length of the abstract. However, the suggested length is from 150 to 225 words.

14. **KEY WORDS:** Key words are technically meaningful terms or short phrases that characterize a report and may be used as index entries for cataloging the report. Key words must be selected so that no security classification is required. Identifiers, such as equipment model designation, trade name, military project code name, geographic location, may be used as key word, but will be followed by an indication of technical context. The assignment of links, roles, and weights is optional.

ABSTRACT (Continued)

which requires knowledge of only the chamber pressure and throat diameter has been devised. Tests showed the analysis techniques developed to be satisfactory. With these analytical techniques, limitations on duty cycles can be determined. These limitations are couplings of firing times and cooldown times. The results of rocket firing tests are presented. The current capability of analyzing restartable nozzles is assessed and major problems which require further investigation are defined.